DOE-BES Principal Investigators' Meeting

Physical Behavior of Materials

May 2 – 4, 2017

Gaithersburg Marriott Washingtonian Center

Gaithersburg, MD

Program and Abstracts

Chairs: Irena Knezevic (Univ. Wisc.) and Xiang Zhang (UC, Berkeley)

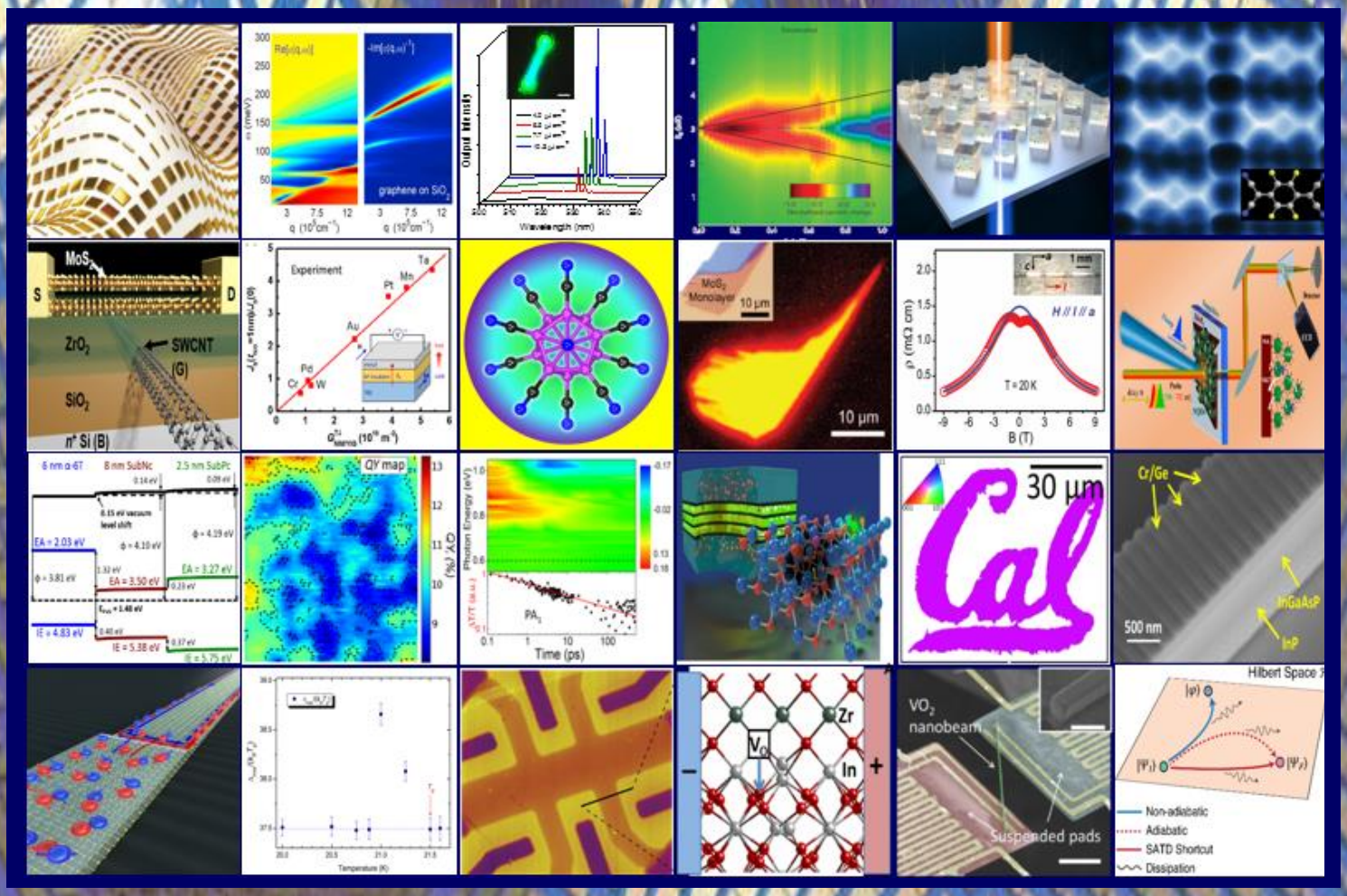

U.S. Department of Energy

Office of Science – Basic Energy Sciences

Division of Materials Sciences and Engineering

Cover Images:

1	2	3	4	5	6
7	8	9	10	11	12
13	14	15	16	17	18
19	20	21	22	23	24

1- An ultrathin invisibility skin cloak for visible light, Xiang Zhang
2- Dielectric function and plasmons in supported graphene, Irena Knezevic
3- Lasing in robust cesium lead halide perovskite nanowires, Peidong Yang
4- Collective spin effects on polymer magnetoresistance, Christoph Boehme
5- Broken symmetry dielectric resonators for high quality factor Fano metasurfaces, Igal Brener
6- Molecular self-assembly in a poorly screened environment: F_4TCNQ on graphene/BN, Michael Crommie
7- MoS_2 transistors with 1-nanometer gate lengths, Ali Javey
8- Amplification of spin current via antiferromagnetic insulator, Chia Ling Chien
9- Stability of $B_{12}(CN)_{12}^{2-}$: Implications for Li and Mg ion batteries, Puru Jena
10- Near-unity photoluminescence quantum yield in MoS_2, Ali Javey
11- Discovery of chiral magnetic effect in condensed matters, Qiang Li
12- Order of magnitude enhancement of monolayer MoS_2 emission by near-field energy transfer from nanocrystals, Anton Malko
13- Understanding the interfacial energetics for high efficiency energy cascade solar cells, Barry Rand
14- Spatially non-uniform trap state densities and emission quantum yields in hybrid perovskite films, Masaru Kuno
15- Ultrafast spectroscopy of photoexcitations in organometal trihalide perovskites, Z. V. Vardeny
16- Impact of point defects on efficiency of nitride LEDs, Chris Van de Walle
17- Direct growth of single crystalline III-V semiconductors on amorphous substrates, Ali Javey
18- Lasing and anti-lasing in a single cavity, Xiang Zhang
19- Coexistence of superconducting and topological states in one single material, Feng Liu
20- Onset of temperature chaos at mesoscopic length scales, Raymond L. Orbach
21- Tailoring oxide interface by oxygen surface adsorbates, Cheng Cen
22- Interfacial control of oxygen vacancies in heterostructures, Jeffrey Eastman
23- Anomalously low electronic thermal conductivity in metallic VO_2, Junqiao Wu
24- Accelerating quantum control with superadiabatic driving, David D. Awschalom

This document was produced under contract number DE-SC0014664 between the U.S. Department of Energy and Oak Ridge Associated Universities.

The research grants and contracts described in this document are supported by the U.S. DOE Office of Science, Office of Basic Energy Sciences, Materials Sciences and Engineering Division.

FOREWORD

The 2017 "Physical Behavior of Materials" Principal Investigators' meeting is sponsored by the Division of Materials Sciences and Engineering (DMS&E) of the Department of Energy, Office of Basic Energy Sciences (BES), and it is held on May 2–4, 2017, at the Gaithersburg Marriott Washingtonian Center, Gaithersburg, Maryland. This booklet is a collection of extended abstracts of the projects presented at this meeting.

This Principal Investigators' meeting is intended to facilitate exchange of ideas and dissemination of the latest scientific discoveries among participants. It also fosters synergistic activities among researchers in the Physical Behavior Program. For BES and the participating investigators, it serves the purpose of providing an overview of the whole program that helps identify promising new research areas and future directions. This meeting brings together leading experts in diverse fields of interest to our program and is designed to stimulate crosscutting and inspiring of new ideas.

The Physical Behavior of Materials program supports ground-breaking research activities in a broad range of topics in materials science and condensed matter physics. The primary mission of the program is to support transformative fundamental science and use-inspired basic research that promise to advance our knowledge of material's physical behavior under external stimuli. The primary scientific interests of the program include electronic, electromagnetic, magnetic and thermal properties of materials that are relevant to the Basic Energy Sciences mission. The program has a rich portfolio in many exciting, high-risk high-reward projects using both experimental and theoretical approaches.

The 2017 Principal Investigators' meeting is chaired by Prof. Irena Knezevic of University of Wisconsin and Prof. Xiang Zhang of UC, Berkeley and LBNL, and is attended by over 80 scientists. There are 30 oral presentations in 14 oral sessions and 47 presentations in two poster sessions. The oral presentations are organized to group similar topical research areas. We gratefully acknowledge the contributions of all the attendees for participating at this meeting and sharing their ideas with other meeting participants. We also gratefully acknowledge the outstanding support of Linda Severs from the Oak Ridge Institute for Science and Education, and Teresa Crockett of the DMS&E, and the staff of the Gaithersburg Marriott Washingtonian Center.

Refik Kortan, Ph.D.
Program Manager
Division of Materials Sciences and Engineering
Office of Basic Energy Sciences
Department of Energy
May 2017

Table of Contents

Session XI

Session XIII

Session XIV

Poster Sessions

Poster Abstracts

Physical Behavior Principal Investigators' Meeting
May 2-4, 2017
Gaithersburg Marriott Washingtonian Center

Meeting Chairs:
Irena Knezevic (Univ. Wisconsin) and Xiang Zhang (LBNL / UC Berkeley)

Monday, May 1, 2017	
	*** Dinner (On your own) ***
Tuesday, May 2, 2017	
7:30 – 8:30 am	Registration & *** Breakfast***
8:30 – 8:40 am	**Welcome, *Meeting Chairs***
8:40 – 9:10 am	**"Division and Program Updates"** Linda Horton *Director, Division of Materials Sciences and Engineering* Refik Kortan *Program Manager, Physical Behavior of Materials*
Session I	***Chair: Xiang Zhang (LBNL)***
9:10 – 9:40 am	Hongjie Dai (Stanford Univ.) *"Novel materials for renewable energy"*
9:40 – 10:10 am	Junqiao Wu (LBNL) *"Electrons that conduct electricity but (almost) not heat in a metal"*
10:10 – 10:40 am	Feng Liu (Univ. Utah) *"Formation of Dirac and topological states on semiconductor surface and strain engineering"*
10:40 – 11:00 am	*** Break ***
Session II	***Chair: Irena Knezevic (Univ. Wisconsin)***
11:00 – 11:30 am	Xiang Zhang *(LBNL)* *"Sub-wavelength metamaterial design, physics and applications"*
11:30 – 12:00 am	Thomas Koschny *(AMES Lab.)* *"Metamaterials"*

12:00 – 12:30 pm	Igal Brener *(Sandia Lab.)* *"Light-matter interaction phenomena using subwavelength engineering of material properties"*
12:30 – 1:30 pm	**Working Lunch (*poster introductions: session I*)**
Session III	***Chair: Katherine Willets (Temple Univ.)***
1:30 – 2:00 pm	Barry Rand *(Princeton Univ.)* *"Charge transfer states at organic heterojunctions I: Structure-property relationships"*
2:00 – 2:30 pm	Noel Giebink *(Penn. State Univ.)* *"Charge transfer states at organic heterojunctions II: Role in energy conversion and nonlinear optics"*
Session IV	***Chairs: Knezevic, Zhang***
2:30 – 5:30 pm	Poster Session I
5:30 – 6:30 pm	*** Dinner *(Scientific Highlights of the Day: Discussion and Input from Attendees)****
Session V	***Chair: Puru Jena (Virginia Commonwealth Univ.)***
6:30 – 7:00 pm	Yet-Ming Chiang *(MIT)* *"Electrochemically driven phase transitions in battery storage compounds"*
7:00 – 7:30 pm	Anil Virkar *(Univ. Utah)* *"Thermodynamic, kinetic and electrochemical studies on mixed proton, oxygen ion and electron (hole) conductors"*
7:30 – 8:00 pm	Scott Barnett *(Northwestern Univ.)* *"Properties, electrochemical activity, and stability of solid oxide cell materials under extreme conditions"*
8:00 – 8:30 pm	Vitalij Pecharsky *(Ames Lab.)* *"Complex hydrides – A new frontier for future energy applications"*
Session VI	***Chairs: Knezevic, Zhang***
8:30 – 10:00 pm	Continuation of Poster Session I

Wednesday, May 3, 2017

7:30 – 8:30 am	***Breakfast***

Session VII	***Chair: Mark Stockman (Georgia State Univ.)***
8:30 – 9:00 am	David Schuster (Univ. Chicago) *"Quantum metamaterials"*
9:00 – 9:30 am	Nathaniel Stern (Northwestern Univ.) *"Probing coherent states of light and matter in two-dimensional semiconductors"*
9:30 - 10:00 am	Hanan Dery (Univ. Rochester) *"Spin transport in group IV materials and 2D membranes"*
10:00 – 10:30 am	Peidong Yang (LBNL) *"Physical chemistry of inorganic halide perovskite nanostructures"*
10:30 – 11:00 am	*** *Break* ***

Session VIII	***Chair: Jing Shi (UC Riverside)***
11:00 – 11:30 am	Valy Vardeny *(Univ. Utah)* *"Optical, electrical and magnetic studies of hybrid organic-inorganic perovskite semiconductors"*
11:30 – 12:00 am	Christoph Boehme *(Univ. Utah)* *"Coherent control of spin states in organic electronics – spin-spin interaction and collective spin effects on magneto-optoelectronic materials properties"*
12:00 – 12:30 pm	Raymond Orbach (Univ. Texas) *"The mesoscale: A laboratory for dynamical measurements"*
12:30 – 1:30 pm	**Working Lunch (*poster introductions: session II*)**

Session IX	***Chair: Gerbrand Ceder (UC Berkeley)***
1:30 – 2:00 pm	Alain Karma *(Northeastern Univ.)* *"Phase-field modeling of materials interfaces and nanostructures"*
2:00 – 2:30 pm	Yuri Mishin *(George Mason Univ.)* *"Interfaces in electronic and structural materials"*

Session X	***Chairs: Knezevic, Zhang***
2:30 – 5:30 pm	**Poster Session II**
5:30 – 6:30 pm	*** Dinner *(Scientific Highlights of the Day: Discussion and Input from Attendees)****

Session XI	***Chair: Harry Atwater (Caltech)***
6:30 – 7:00 pm	Shanhui Fan *(Stanford Univ.)* *"Nanophotonics-enhanced solar cells"*
7:00 – 7:30 pm	David Waldeck *(Univ. Pittsburgh)* *"Directing charge transport in quantum dot assemblies"*
7:30 – 8:00 pm	Masaru Kuno *(Notre Dame Univ.)* *"Probing local, hybrid perovskite photophysics through spatially- and temporally-resolved absorption/emission microscopy"*
8:00 - 8:30 pm	Cheng Cen *(W. Virginia Univ.)* *"Develop on-demand nanoplasmonic device concepts in a semiconductor compatible hybrid system"*

Session XII	***Chairs: Knezevic, Zhang***
8:30 – 10:00 pm	Continuation of Poster Session II

Thursday, May 4, 2017

7:30 – 8:30 am	***Breakfast***
Session XIII	***Chair: John Neumeier (Montana State Univ.)***
8:30 – 9:00 am	Dillon Fong *(Argonne Nat. Lab.)* *"Proximity effects in charged oxide heterostructures"*
9:00 – 9:30 am	Qiang Li *(Brookhaven Nat. Lab.)* *"Chiral materials and unconventional superconductivity"*
9:30 – 10:00 am	Hariharan Srikanth *(Univ. South Florida)* *"Complex magnetism and emergent phenomena in correlated electron oxide materials"*
10:00 – 10:30 am	*** *Break* ***
Session XIV	***Chair: Svetlana Boriskina (MIT)***
10:30 – 11:00 am	Steven Cronin *(Univ. Southern Calif.)* *"Energy carrier transport in functionalized two-dimensional layered chalcogenides"*
11:00 - 11:30 am	Zhuomin Zhang *(Georgia Tech)* *"Measurements of near-field thermal radiation between flat plates for energy conversion applications"*
11:30 – 12:00 am	Closing Remarks by Meeting Chairs and PM

Session I

Project title:

Novel materials for renewable energy

PI's and affiliations:

Hongjie Dai, Department of Chemistry, Stanford University, Stanford, CA 94305

Program Scope:

Fundamental research on rechargeable aluminum ion battery

Aim 1. Basic investigation and understanding of graphitic cathodes for rechargeable aluminum ion battery

Aim 2. Investigation of new cathode materials and electrolytes for rechargeable aluminum ion battery

Aim 3. Fundamental understanding of the intercalation mechanism and side reactions in rechargeable aluminum ion battery

The proposed research will be integrated into our ongoing program of novel materials for renewable energy and will facilitate other projects in the general areas of advanced batteries and electrocatalysis.

Recent Progress

(1) Rechargeable High Capacity Al Ion Battery with Natural Graphite Cathode

We recently developed a rechargeable Al-ion battery with Al anode exhibiting reversible electrochemical deposition and dissolution in a room temperature ionic liquid (IL) electrolyte formed by mixing 1-ethyl-3-methylimidazolium chloride ([EMIm]Cl) and aluminum chloride ($AlCl_3$) to afford redox active chloroaluminate anions ($AlCl_4^-$ and $Al_2Cl_7^-$). The Al anode was paired with a graphitic cathode material that allowed for reversible chloroaluminate anions intercalation/de-intercalation during charge-discharge cycles. The rate capability could be significantly improved by constructing a highly porous 3D graphitic foam that allows fast ion diffusion/intercalation. A drawback of our previous rechargeable Al battery was the low specific cathode capacity of < 70 mAh/g down to low C rate, which required much improvement in order to match the high capacity of the Al anode side and thus increase the energy density of AIB.

In this BES project, we developed a rechargeable AIB using a film of SP-1 natural graphite flakes (NG) with polyvinylidene fluoride (PVDF) binder as the cathode of rechargeable Al-ion battery (Al/NG cell). Our AIB cell exhibited clear discharge voltage plateaus in the ranges 2.25 to 2.0 V and 1.9 to 1.5 V and the graphite cathode exhibited a much improved specific capacity over pyrolytic graphite up to ~110 mAh/g and ~ 98% Coulombic efficiency at a current density of ~ 100 mA/g. Charge-discharge cycling at a current density of 660 mA/g showed highly stable AIB cells, with little capacity decay over > 6000 cycles at a ~99% Coulombic efficiency. Further, the reversible structural evolutions of the natural graphite particles during charging and discharging were characterized by *in-situ* Raman spectroscopy, powder X-ray diffraction, X-ray photoelectron spectroscopy and X-ray absorption spectroscopy.

We investigated various graphite materials for AIB cathode and found that in general, natural graphite was found superior to synthetic graphite to afford higher capacity and well-defined voltage plateaus in charge-discharge characteristics of the battery. Two synthetic graphite materials, KS6 and MCMB widely used as Li ion battery anode materials, were found to give much lower capacity than that of NG without clear discharge voltage plateaus. This was attributed to that KS6 and MCMB materials exhibited lower crystallinity and higher defect density than natural graphite based on Raman and XRD measurements. The results indicated that graphite materials with high crystallinity and low defect density were strongly desired for high performance Al ion battery. In general, we found that graphite materials commonly used for lithium ion batteries performed poorly for AIB. This is an important result to the AIB field.

To investigate $AlCl_4^-$ anions deep inside graphite layers, we performed DFT calculations. Simulation of $AlCl_4^-$ anions between two graphene layers revealed a transition pathway from two $AlCl_4^-$ anions to one $Al_2Cl_7^-$ anion and a Cl^- anion. We found that when two $AlCl_4^-$ anions entered graphite layers and were close enough, a Cl^- would be firstly separated from an $AlCl_4^-$ anion, bringing about a metastable $AlCl_4^-$ and $AlCl_3$-Cl^- pair. $AlCl_3$ would further be bonded with $AlCl_4^-$ anion and then form $Al_2Cl_7^-$ anion with a stand-alone Cl^- ion. The optimized geometries of both $AlCl_4^-$ anion and $Al_2Cl_7^-$ anion were slightly flattened due to the graphene layers. Also, from both calculation models, a stoichiometry of carbon versus $AlCl_4^-$ is ranged around $C_{20}(AlCl_4)$, corresponding to a theoretical capacity of 120 mAh/g.

(2) High Coulombic efficiency aluminum-ion battery using an AlCl3-urea ionic liquid analog electrolyte

High-rate (fast charge/discharge) rechargeable batteries with long cycle lives are urgently needed for grid-scale storage of renewable energy, as it is becoming increasingly important to replace fossil fuels. Batteries based on aluminum offer a viable alternative due to aluminum's three-

electron redox properties (offers potential for high capacity batteries), stability in the metallic state, and very high natural abundance. Furthermore, the development of these batteries based on non-flammable electrolytes of low toxicity is critical for minimizing safety hazard and environmental impact. For this reason, ionic liquids (ILs) have been investigated for energy storage due to their low vapor pressure and wide electrochemical windows, unfortunately with the caveat of high cost in most cases. A new class of ionic liquids, referred to as ionic liquid analogues (ILAs) or so-called deep eutectic solvents, generally formed through a mixture of a strongly Lewis acidic metal halide and Lewis basic ligand, have gained significant attention due to their comparable electrochemical and physical properties with reduced cost and minimal environmental footprint.

Recently, our group developed a secondary Al battery system based on the reversible deposition/stripping of aluminum at the Al negative electrode and reversible intercalation/deintercalation of chloroaluminate anions at the graphite positive electrode in a non-flammable 1-ethyl-3-methylimidazolium chloroaluminate (EMIC-$AlCl_3$) ionic liquid electrolyte. However, room for improvement exists as the parameter space for the Al battery remains largely unexplored. A consideration is our existing Al battery electrolyte uses 1-ethyl-3-methylimidazolium chloride (EMIC), which is relatively expensive.

In this work, we investigated the performance of a rechargeable Al battery using an ILA electrolyte based on urea, a superior compound in terms of cost (~ 50 times cheaper than EMIC) and eco-friendliness. A high efficiency battery that is stable over ~180 cycles and a variety of charge-discharge rates using an Al anode, graphite powder cathode, and cheap urea-$AlCl_3$ ionic liquid analogue electrolyte was successfully established. Intercalation/deintercalation of graphite during charging/discharging was confirmed by in-situ Raman experiments, and a stage 2 GIC was observed. Reversibility of the process was confirmed by recovery of the G-band at 1584 cm^{-1} with no increase of the D-band intensity observed. Raman spectroscopy and Al NMR of the electrolyte suggested the presence of $AlCl_4^-$, $[AlCl_2 \cdot (urea)_n]^+$ and $Al_2Cl_7^-$ ionic species in the electrolyte.

Future Plans

We plan to continue our fundamental research on rechargeable aluminum ion battery along the lines below

1. Basic investigation and understanding of graphitic cathodes for rechargeable aluminum ion battery. We hope to elucidate the physics of anion intercalation of graphite in details.

2. Investigation of new cathode materials and electrolytes for rechargeable aluminum ion battery. We will continue to explore new cathode materials including sulfides and new electrolytes for AIB.

3. Fundamental understanding of side reactions in rechargeable aluminum ion battery

Publications

Di-Yan Wang, Chuan-Yu Wei, Meng-Chang Lin, Chun-Jern Pan, Hung-Lung Chou, Hsin-An Chen, Ming Gong, Yingpeng Wu, Chunze Yuan, Michael Angell, Yu-Ju Hsieh, Yu-Hsun Chen, Cheng-Yen Wen, Chun-Wei Chen, Bing-Joe Hwang, Chia-Chun Chen and Dai. "Advanced rechargeable aluminium ion battery with a high-quality natural graphite cathode" ***Nature Communications,*** Article number: 14283 (2017) Published February 13, 2017.

Michael Angell, Chun-Jern Pan, Youmin Rong, Chunze Yuan, Meng-Chang Lin, Bing-Joe Hwang, and Dai. "High Coulombic efficiency aluminum-ion battery using an AlCl3-urea ionic liquid analog electrolyte" ***PNAS***, 114(5):834-839, 2017.

Yingpeng Wu, Ming Gong, Meng-Chang Lin, Chunze Yuan, Michael Angell, Lu Huang, Di-Yan Wang, Xiaodong Zhang, Jiang Yang, Bing-Joe Hwang, and Dai. "3D Graphitic Foams Derived from Chloroaluminate Anion Intercalation for Ultrafast Aluminum-Ion Battery" ***Advanced Materials***, 2016, 28, 9218–9222

Electrons that conduct electricity but (almost) not heat in a metal

Junqiao Wu, University of California, Berkeley, and Lawrence Berkeley National Laboratory

Program Scope

The goal of the program is to advance and expand the fundamental understanding of the materials science of semiconductors. The research focuses on the relationships between synthesis and processing conditions and the structure, properties, and stability of semiconductor materials systems. Progress in these areas is essential for the performance and reliability of a number of technologies that lie at the heart of the DOE mission, including solar power conversion devices, solid state sources of visible light, visual displays, and a large variety of sensors and power control systems for energy generation, conservation, distribution, and use.

Recent Progress

In conventional metals, itinerant electrons carry both charge and heat. As a consequence, electrical conductivity and the electronic contribution to thermal conductivity are typically proportional to each other, known as the Wiedemann-Franz law that is robust in all conventional metals. We found a large violation of this law near the insulator-metal phase transition in metallic vanadium dioxide (VO_2). In the metallic phase of VO_2, the electronic contribution to thermal conductivity amounts to only 10% of what would be expected from the Wiedemann-Franz law. The results are explained in terms of independent propagation of charge and heat in a strongly correlated electron system, where the electrons move in unison in a new, non-quasiparticle mode, in stark contrast to the conventional Drude mode.

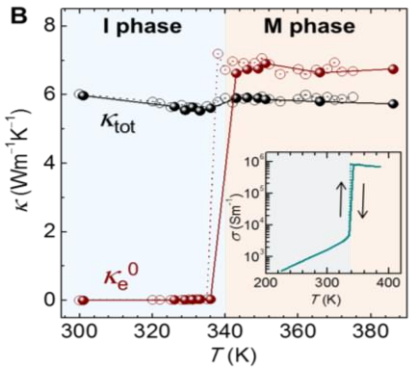

Measured thermal conductivity (κ_{tot}) of VO_2 across its metal-insulator transition. Also shown is the electronic thermal conductivity (κ_e^0) expected from the Wiedemann-Franz law. Inset is the measured electrical conductivity.

Future Plans

On the basis of this discovery, we will study the electronic thermal physics of strongly correlated materials in general. The generality of non-quasiparticle transport in these materials will be explored, and the validity of the Wiedemann-Franz law will be tested in comparison to conventional conductors and semiconductors. Applications of these materials for smart thermal management technologies and thermoelectrics will be developed.

References

Sangwook Lee, Kedar Hippalgaonkar, Fan Yang, Jiawang Hong, Changhyun Ko, Joonki Suh, Kai Liu, Kevin Wang, Jeffrey J. Urban, Xiang Zhang, Chris Dames, Sean A. Hartnoll, Olivier Delaire, Junqiao Wu, Anomalously low electronic thermal conductivity in metallic vanadium dioxide, Science, 355, 371 (2017).

Publications

Including publications from PI's DOE Early Career award (2015-2016, UC Berkeley) and support of PI by the Electronic Materials Program (2016-present, LBNL)

- Sangwook Lee, Kedar Hippalgaonkar, Fan Yang, Jiawang Hong, Changhyun Ko, Joonki Suh, Kai Liu, Kevin Wang, Jeffrey J. Urban, Xiang Zhang, Chris Dames, Sean A. Hartnoll, Olivier Delaire, Junqiao Wu, Anomalously low electronic thermal conductivity in metallic vanadium dioxide, Science, 355, 371 (2017).

- Jiwei Hou, Xi Wang, Deyi Fu, Changhyun Ko, Yabin Chen, Sangwook Lee, Kevin X. Wang, Seffattin Tongay, Jie Yao, Kai Liu, Junqiao Wu, Modulating Photoluminescence of Monolayer Molybdenum Disulfide by Phase Transition in Active Substrates, Small, 12, 3976 (2016).

- Yabin Chen, Shuai Zhang, Weiwei Gao, Feng Ke, Jinyuan Yan, Bivas Saha, Changhyun Ko, Joonki Suh, Bin Chen, Joel W. Ager III, Wladyslaw Walukiewicz, Raymond Jeanloz, Junqiao Wu, Pressure-induced structural transition and phase diagram of CdxZn1-xO alloys, Appl. Phys. Lett., 108, 152105 (2016).

- Jaehyeon Kim, Jonghoon Kim, Muhammad Ejaz Khan, Jae-Hyeon Ko, Joonki Suh, Junqiao Wu, Yong-Hyun Kim, Jeong Young Park, and Ho-Ki Lyeo, Control of heat transport at graphene-metal interfaces with modified flexural phonons, Sci. Rep., 6, 34428 (2016).

- Jose J. Fonseca, Sefaattin Tongay, Mehmet Topsakal, Alexander V. Luce, Changyun Ko, Junqiao Wu, Oscar D. Dubon, Bandgap Restructuring of the Layered Semiconductor Gallium Telluride in Air, Adv. Mater., 28, 6465 (2016).

- Sangwook Lee, Fan Yang, Joonki Suh, Sijie Yang, Yeonbae Lee, Guo Li, Hwan Sung Choe, Aslihan Suslu, Yabin Chen, Changhyun Ko, Joonsuk Park, Kai Liu, Jingbo Li, Kedar Hippalgaonkar, Jeffrey J. Urban, Sefaattin Tongay, Junqiao Wu, Anisotropic in-plane thermal conductivity of black phosphorus nanoribbons at temperatures higher than 100K, Nature Commun., 6, 8573 (2015).

- Kai Liu, Cheng-Lun Hsin, Deyi Fu, Joonki Suh, Sefaattin Tongay, Michelle Chen, Yinghui Sun, Aiming Yan, Joonsuk Park, Kin M. Yu, Wenli Guo, Haimei Zheng, Daryl Chrzan, Junqiao Wu, Self-passivation of point defects: effects of high-energy particle irradiation on elastic modulus of multilayer graphene, Adv. Mater., 27, 6841 (2015).

Formation of Dirac and Topological States on Semiconductor Surface and Strain Engineering

Feng Liu
University of Utah

Program Scope

This project encompasses a comprehensive study of physical mechanisms that lead to formation of exotic quantum electronic states on semiconductor surfaces and explores a novel approach of strain engineering of such states. It covers four correlated research topics: (1) Mechanistic study of epitaxial growth of an overlayer of Dirac and topological states on semiconductor surfaces, which is atomically bonded but electronic isolated from the underlying substrates. (2) Self-assembled growth of topological states arising from non-conventional lattice symmetry in semiconductor surfaces. (3) Strain engineering of topological surface/edge states and topological nanomechanical architecture. (4) Nanostructured topological materials. The common theme of the proposed research is to understand a new class of "surface-based" 2D Dirac and topological materials chemically supported (i.e., non Van der Waals type) on a substrate. The theoretical studies will be done in collaboration with experiments including Prof. Lagally funded by the DOE-BES "Materials Synthesis and Processing" program.

We will employ a multiscale approach, combining several state-of-the-art theoretical and computational techniques, ranging from first-principles density-functional-theory (DFT) electronic structure calculations to semi-empirical tight-binding (TB) model Hamiltonian analyses and calculations and to classical molecular dynamics (MD) simulations. Specifically, surface equilibrium structure and associated energetics will be calculated by DFT and MD methods. Electronic band structure will be studied using both DFT and TB methods with the TB parameters fit to the DFT band structures in supercells of slab geometry to represent a surface. Band topology will be revealed by analyzing the bulk (thin film) Bloch wavefunctions and the topological surface (edge) states using DFT and TB bands and iterative Green's function and Wannier function method. In addition, DFT as well as classical MD simulations will be carried out to directly simulate topological nanomechanical architectures resulted from the strain induced bending of thin films to study strain engineered topological states and spin manipulation.

Our studies will significantly improve our fundamental understanding of physical origins of surface-based Dirac and topological states in solid material systems, in terms of lattice geometry, spin-orbit coupling (SOC), orbital composition and surface/interface interactions. It will open up a new route towards realizing topological quantum phases in a new class of surface-based 2D materials. It will foster a new field of research by taking the effect of stress/strain to new territories on topological order of materials, beyond strain engineering of self-assembled nanostructures and of electronic properties that we have studied in the past decade within the

DOE-BES program. We believe many of our theoretical findings will provide useful guidance for future experimental efforts in growing surface-based 2D materials as we propose, realizing novel topological phases, strain engineering of topological states and spin texture, and nanostructured topological materials. These studies have also technological impact on advancing electronic and optoelectronic materials for energy applications, to fulfill the mission of Department of Energy.

Recent Progress

During the last two years, we have published twenty-six journal papers fully or partially supported by this DOE grant, including one Nature Materials, two PRL, one Nature Communications, one Advanced Materials, three Nano Lett and one ACS Nano papers. Three postdoctoral research associates and two graduate students have been fully or partially supported by this DOE project. The PI gave fourteen invited talks at national/international conferences, and twenty-three departmental colloquium/seminar presentations. Below is a brief summary of four topics of research achievements pertaining to this project:

(a) Topological edge states in a high-temperature superconductor FeSe/SrTiO3(001) film[1].

Superconducting and topological states are two most intriguing quantum phenomena in solid materials. The entanglement of these two states, the topological superconducting state, will give rise to even more exotic quantum phenomena. While many materials are found to be either a superconductor or a topological insulator, it is very rare that both states exist in one material. Recently, we demonstrated by first-principles theory as well as scanning tunneling spectroscopy and angle-resolved photoemission spectroscopy experiments that the recently discovered 'two-dimensional (2D) superconductor' of single-layer FeSe also exhibits 1D topological edge states within an energy gap of ~40meV at the M point below the Fermi level. It is the first 2D material that supports both superconducting and topological states.[1,2] Our finding will provoke an exciting opportunity to study 2D topological superconductors through the proximity effect, which may help advance our fundamental understanding of physical properties associated with the topological superconducting state, such as Majorana fermions. It will pave the way to building novel quantum and spintronics devices by interfacing a

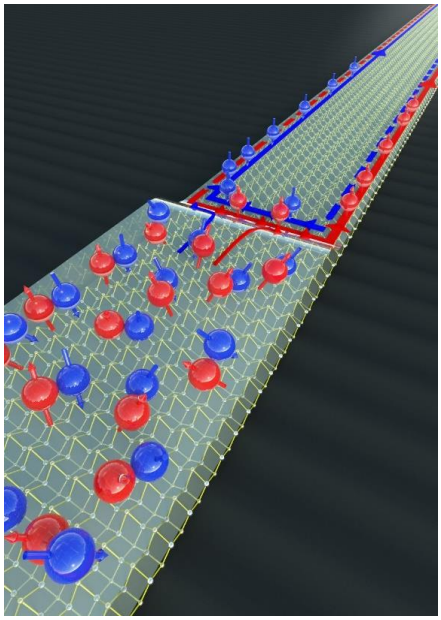

Fig. 1. Schematic illustration of a superconductor-topological insulator P-N junction in doped FeSe/SrTiO3, showing the electron doped superconducting bulk states on one side (low left) and the hole doped topological edge states on the other side (top right).

superconductor with a topological insulator through a p-n junction (see Fig. 1) since n- and p-type FeSe is respectively a superconductor and topological insulator. This work was published last year as one of the "cover" articles in Nature Materials[1], commented by Nature Materials News & Views column[2] and covered by news media.

(b) Quantum Spin Hall Phase in 2D Trigonal Lattice[3]

The quantum spin Hall (QSH) phase is an exotic phenomena in the condensed-matter physics. Recently, we show that a minimal basis of three orbitals (s, px, py) is required to produce a QSH phase via nearest-neighbor hopping in a two-dimensional trigonal lattice.[3] Tight-binding model analyses and calculations show that the QSH phase arises from an spin-orbit coupling (SOC) induced s-p band inversion or p-p band gap opening at Brillouin zone center (Γ point), whose topological phase diagram is mapped out in the parameter space of orbital energy and SOC. Remarkably, based on first-principles calculations, this exact model of QSH phase is shown to be realizable in an experimental system of Au/GaAs(111) surface (see Fig. 2) with an SOC gap of ~73 meV, facilitating the possible room-temperature measurement. Our results significantly extend the search for substrate supported QSH materials to new lattice and orbital types.

(c) Formation of Dirac State in Chemical Functionalized Si Surface and THz Plasmonics[4].

Graphene, the first discovered 2D Dirac material, has had a profound impact on science and technology. In the last decade, we have witnessed huge advances in graphene related fundamental

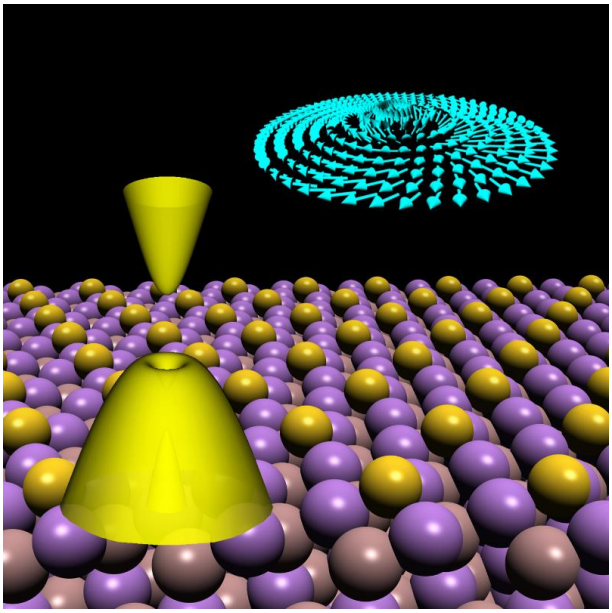

Fig. 2. Schematic illustration of a topological insulating state [3D band structure (middle left) and spin texture of topological edge state(top right)] form with a trigonal lattice of Au overlayer on GaAs(111) surface (bottom).

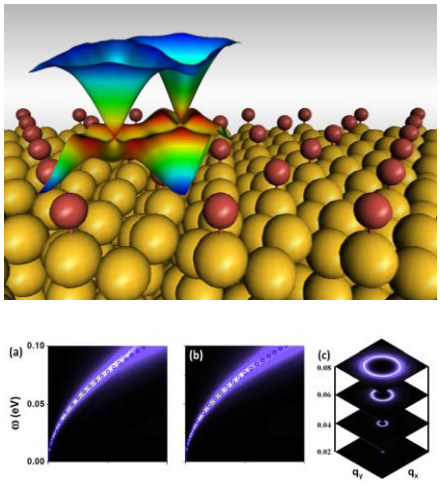

Fig. 3. Up: Si(111) surface with 1/3 Br coverage. Inset: 3D plot of anisotropic surface Dirac band. Down: Anisotropic THz Plasmonics: EELS of the hole doped Dirac band. (a,b) excitation along (q_x,q_y) direction, respectively. (c) 2D momentum space plotting of the EELS at different excitation energies.

and applied research. Recently, based on first-principles calculations, we propose a new surface-based 2D Dirac material on the Si(111) surface with 1/3 monolayer halogen coverage, such as Br (Fig. 3, up).[4] The sp^3 dangling bonds form a honeycomb superstructure on the Si(111) surface that results in an anisotropic Dirac band with a group velocity ($\sim 10^6$ m/s) comparable to that in graphene. Most remarkably, the Si-based surface Dirac band can be used to excite a tunable THz plasmon through electron or hole doping (Fig. 3, down). These unique surface electronic properties can be retained by covering with an insulating protection layer like 2D BN. Our results demonstrate a new way to design Dirac states on a traditional semiconductor surface, so as to make them directly compatible with Si technology. We envision this new type of Dirac material to be generalized to other semiconductor surfaces with broad applications.

Future Plans

We plan to expand our current studies in the following areas:

(a) Search for new inorganic and organic topological materials
(b) Explore different epitaxial growth routes towards formation of topological quantum phases on semiconductor surfaces
(c) Continue exploring a new research direction in "topological nanomechanical architecture"
(d) Exploring topological phases in nanostructured materials, such as nanotube arrays
(e) Continue the efforts of experimental collaborations.

References

1. "Topological Edge States in High-Temperature Superconductor FeSe/SrTiO3(001) Film", Z. F. Wang, H. Zhang, D. Liu, C. liu, C. Tang, C. Song, Y. Zhong, J. Peng, F. Li, C. Nie, L, Wang, X. J. Zhou, X, Ma, Q. K. Xue and Feng Liu, *Nature Mat.*, **15**, 968 (2016).
2. "Topological Insulators and Superconductivity: The integrity of Two Sides", W.-F. Tsai and H. Lin, *Nature Mat.*, **15**, 927 (2016).
3. "Quantum spin Hall phase in 2D trigonal lattice", Z. F. Wang, Kyung-Hwan Jin & Feng Liu, *Nature Commun*. **7**, 12746 (2016).
4. "Self-Assembled Si(111) Surface States: 2D Dirac Material for THz Plasmonics", Z. F. Wang and Feng Liu, *Phys. Rev. Lett*. **115**, 026803 (2015).

Publications

1. “Topological Edge States in High-Temperature Superconductor FeSe/SrTiO3(001) Film”, Z. F. Wang, H. Zhang, D. Liu, C. liu, C. Tang, C. Song, Y. Zhong, J. Peng, F. Li, C. Nie, L, Wang, X. J. Zhou, X, Ma, Q. K. Xue and Feng Liu, Nature Mat., 15, 968 (2016).
2. “Quantum spin Hall phase in 2D trigonal lattice”, Z. F. Wang, Kyung-Hwan Jin & Feng Liu, Nature Commun. 7, 12746 (2016).
3. “Direction-Controlled Light-Driven Movement of Microribbons”, Y. Zhang, C. Peng, B. Cui, Z. Wang, X. Pang, R. Ma, Feng Liu, Y. Che, J. Zhao, Adv. Mat., 28, 8538 (2016).
4. "Large-Gap Quantum Spin Hall State in MXenes: d-Band Topological Order in a Triangular Lattice", C. Si, K.-H. Jin, J. Zhou, Z. Sun, and Feng Liu. Nano Lett. 16, 6584 (2016).
5. “Strain engineering of graphene: a review”, C. Si, Z. Sun and Feng Liu, Nanoscale, 8, 3207 (2016).
6. "Effect of Chlorine Substitution on Lattice Distortion and Ferroelectricity of CH3NH3PbI3", W. L. Yan, G. H. Lu and Feng Liu, J. Phys. Chem. C 120, 17972 (2016).
7. “Graphene processing using electron beam assisted metal deposition and masked chemical vapor deposition growth”, A. Merrell and Feng Liu, J. Vac. Sci. Technol. B 34, 4 (2016).
8. “Interface Orbital Engineering of Large-gap Topological States: Decorating Gold on a Si(111) Surface, B. Huang, K. Jin, H. L. Zhuang, L. Zhang, and Feng Liu, Phys. Rev. B 93, 115117 (2016).
9. “Thickness dependence of surface energy and contact angle of water droplets on ultrathin MoS2 films”, Y. Guo, Z. Wang, L. Zhang, Xiao. Shen and Feng Liu, Phys. Chem. Chem. Phys., 18, 14449 (2016).
10. “Electronic structure evolution of single bilayer Bi(111) film on 3D topological insulator Bi2SexTe3-x surfaces”, T. Lei, K. Jin, N. Zhang, J. Zhao, C. Liu, W. Li, J. Wang, R. Wu, H. Qian, Feng Liu and K. Ibrahim, J. Phys.: Condens. Matter. 28, 255501 (2016).
11. “Electrophobic Interaction Induced Impurity Clustering in Metals”, H.-B. Zhou, J.-L. Wang, W. Jiang, J. A. Aguiar, G.-H. Lu1, and Feng Liu, Acta Materialia, 119, 1 (2016).
12. “Formation of Ideal Rashba States on Layered Semiconductor Surfaces Steered by Strain Engineering”, W. Ming, Z.F. Wang, M. Zhou, M. Yoon, and Feng Liu, Nano Lett., 16, 404 (2016).
13. "Formaiton of a quantum spin Hall state on a Ge(111) surface", P. Li, M. Zhou, L. Zhang, Y. Guo and Feng Liu, Nanotechnology, 27, 095703 (2016).
14. “Tunable Topological States in Electron-Doped HTT-Pt”, X. Zhang, Z. Wang, M. Zhao, Feng Liu, Phys. Rev. B, 93, 165401 (2016).
15. “Structural, electronic, and magnetic properties of tris(8-hydroxyquinoline)iron(III) molecules and their magnetic coupling with ferromagnetic surface: first-principles study”, J. Phys.: Condens. Matter 28, 176004 (2016).

16. “Intrinsic Two-Dimensional Organic Topological Insulators in Metal-Dicyanoanthracene Lattices”, L. Z. Zhang, Z. F. Wang, B. Huang, B. Cui, Zhiming Wang, S. X. Du, H.-J. Gao, and Feng Liu, Nano Lett., 16, 2072 (2016).
17. “Engineering electronic structure of a 2D topological insulator Bi(111) bilayer on Sb nanofilms by quantum confinement effect", G. Bian, Z.F. Wang, X. Wang, C. Xu, S. Xu, T. Miller, M. Hasan, Feng Liu, T.-C. Chiang, ACS Nano, 10, 3859 (20016).
18. “Selectively doping Barlowite for quantum spin liquid: a first-principles study”, Z. Liu, X. Zou, J.-W. Mei, and Feng Liu, Phys. Rev. B 92, 220102(R) (2015).
19. “Alloy Engineering of Defect Properties in Semiconductors: Suppression of Deep Levels in Transition-Metal Dichalcogenides”, B. Huang, M. Yoon, B. G. Sumpter, S.-H. Wei, and Feng Liu, Phys. Rev. Lett. 115, 126806 (2015).
20. “Self-Assembled Si(111) Surface States: 2D Dirac Material for THz Plasmonics”, Z. F. Wang and Feng Liu, Phys. Rev. Lett. 115, 026803 (2015).
21. “Tailoring graphene-based electrodes from semiconducting to metallic to increase the energy density in supercapacitors”, J. Vatamanu, X. Ni, F. Liu and D. Bedrov, Nanotechnology 26, 464001 (2015).
22. “First-principles study of the organometallic S=1/2 kagome compound Cu(1,3-bdc)”, Z. Liu, J.-W. Mei, and Feng Liu, Phys. Rev. B 92, 165101 (2015).
23. “Surface confined quantum well state in MoS2(0001) thin film”, J.-T. Sun, S. R. Song, S. Meng, S. X. Du, F. Liu and H. J. Gao, Appl. Phys. Lett. 107, 161602 (2015).
24. “Highly Anisotropic Dirac Fermions in Square Graphynes”, L. Z. Zhang, Z. F. Wang, Z. M. Wang, S. X. Du, H.-J. Gao, and Feng Liu, J. Phys. Chem. Lett., 6, 2959 (2015).
25. “Mechanical modeling of graphene using the three-layer-mesh bridging domain method”, A. Sadeghirad, N. Su, Feng Liu, *Comput. Methods Appl. Mech. Engrg*. **294** 278–298, (2015).
26. “Quantum Hooke’s Law to Classify Pulse Laser Induced Ultrafast Melting”, H. Hu, H. Ding and Feng Liu, *Sci. Rep.* **5**, 8212 (2015).

Session II

Sub-wavelength Metamaterial Design, Physics and Applications

PI: Xiang Zhang
Co-investigators: Stefano Cabrini, Yuen-Ron Shen, Feng Wang, Eli Yablonovitch
Materials Sciences Division, Lawrence Berkeley National Laboratory, Berkeley, CA 94720
e-mail: xzhang4@lbl.gov

Program Scope / Definition: The overarching goal of this program is to investigate unique metamaterials and explore unprecedented optical properties and promising applications in subwavelength metamaterials. The first mission is to design new metamaterials with extreme light manipulation, which will enable the nanoscale revolution to create an entirely new paradigm for harnessing coherence in light and matter. The second mission is to discover new properties of metamaterials with novel structures, functions, and properties beyond ideal materials and systems. The third mission is to explore dynamic control of metamaterials, which will help to understand the processes underlying physical transformations and master beyond-equilibrium matter. The unique properties arising from the specific designs of the metamaterials open up exciting new venues for the device development for DOE missions. For example, the concentrating and manipulating of light at the nanoscale enables efficient photochemical processes such as energy harvesting and catalysis. Moreover, the intrinsic resonant and broadband electromagnetic responses of metamaterials make them the outstanding candidate to control and manipulate the ultrafast optical pulses at an unprecedented small time and length scales, advancing the researches on systems away from equilibrium at LBNL --- one of the key DOE grand challenges.

This program has five co-investigators with strong expertise in theoretical design, numerical modeling, structure fabrication and optical characterization. **Shen, Yablonovitch and Zhang** are in charge of the design and modeling of metamaterials. **Shen, Cabrini and Zhang** are responsible for metamaterials synthesis and fabrication. Various optical characterizations have been performed by **Zhang and Wang**.

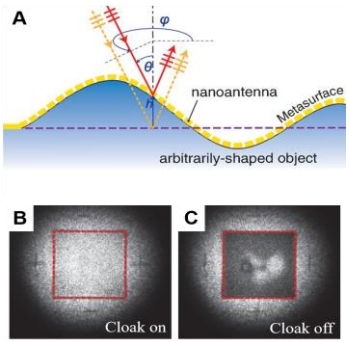

Fig. 1: (A) A illustration of a metasurface skin cloak with an ultrathin layer of metallic nanoantenna to locally modify the reflected light to provide a phase shift to compensate the phase difference between the solid and dashed lines. This skin cloak can restore both the wavefront and the phase of the scattered light and thus the object is hidden. (B and C) Optical images when the cloak is on (B) and off (C)

Recent Progress: Here I will highlight our achievements within the three missions of our program: *(A) Extreme light manipulation using metasurface, (B) New properties of metamaterials with extraordinary nonlinearity*, and *(C) Dynamic control of metamaterials by ultrafast acousto-plasmon interactions.*

(A) Extreme Light Manipulation Using Metasurface: We peviously designed carpet cloak that hides an object by restoring the optical wavefront as if it were reflected from a flat surface [1]. However, there are several substantial limitations. It requires refractive index modulation over a large volume, leading to a bulky cloak device. The sophisticated three-dimensional fabrication with very high spatial resolution makes it challenging to scale up to hide

large objects in practical applications. In addition, the varying index has to be less than that of the environment in certain regions, so that the cloak usually is embedded in a dielectric prism of higher index, which, however, introduces an additional phase in the reflected light and makes the optical cloak visible by phase-sensitive detection.

To overcome these limitations, we developed an ultrathin invisibility skin cloak (Fig. 1 (A)) by using the unique properties of metasurfaces [2]. We created a metasurface tightly wrapped over an object. The ultrathin layer of this skin cloak barely 80 nanometers in thickness reroutes the light and completely restores the wavefront scattered from the object by compensating the phase difference using phase-shifting resonant elements. Our experiment shows that an arbitrarily shaped 3D object of 36 mm by 36 mm gets hided in the visible light (see Fig. 1 (B) and (C)). The ultra-thin cloak is valuable for hiding the detailed layout of microelectronic components or for security encryption purposes. It is also scalable for hiding macroscopic objects and can be applied for altering the apparent shape of an object, making it appear to be something else.

(B) New properties of metamaterials about the extraordinary nonlinearity: Nonlinear optics phenomena play important roles in materials sciences, physics and chemistry. A major challenge in nonlinear optics is the inherent phase mismatch between the interacting waves propagating inside the nonlinear materials. The mismatch prevents microscopic nonlinear sources from combining constructively, resulting in destructive interference and thus very low efficiency. To increase the amounts of nonlinear light, a compensation technique must be used. The most widely used methods include birefringent phase matching, angle phase matching, and quasi–phase matching. Implementing each technique poses a number of challenges. One intrinsic limitation is that all conventional compensating schemes work only in a specific direction: either in the forward direction or the backward direction, but not both (Fig. 2 (A)).

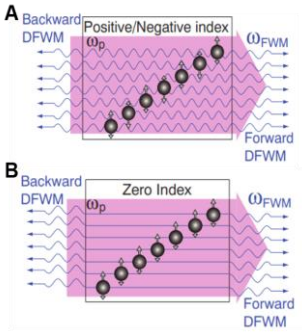

Fig. 2 (A) The conventional methods for phase matching only allow compensation in one directions. (B) A zero-index metamaterial creates a phase mismatch–free environment for nonlinear propagation, eliminating the requirement for phase matching.

We have experimentally demonstrated that the optical momentum conservation is always preserved regardless of the direction in which the light waves are generated, using a zero refractive index optical metamaterial [3]. The zero index medium eliminates the need for phase matching, because in a zero-index material the photons carry zero momentum and satisfy momentum conservation for any combination of photon directions (Fig. 2 (B)). Each source coherently emits equally in both directions and all the sources add up coherently to generate the net nonlinear emission, which guarantees a constructive interference and an increase of the signal in both directions with propagation length. This phase mismatch-free quality holds promise for quantum computing and networking, and future light sources based on nonlinear optics.

To predict nonlinear properties, Miller [4] found empirically that the nonlinear susceptibility could be predicted from the linear susceptibilities, which allows a rapid determination of nonlinear

susceptibilities from linear properties. However, for nonlinear metamaterials, we found [5] that the Miller's nonlinear oscillator model does not apply in general to nonlinear metamaterials because the Miller's theory only considers the far-field linear response and misses the importance of the mode overlap between the nonlinear polarization and its harmonic modes. We developed a microscopic description to effectively predict the nonlinear susceptibility [5]. The nonlinear emission can be given by an integral of the nonlinear polarization $\chi^{(2)}_{nnn}(\omega)E_n(\omega)E_n(\omega)$ and the mode at second harmonic frequency, $E_n(2\omega)$ (Fig. 3). The value of the overlap integral depends on the local field and the relative sign of the contributions. Good mode overlap, meaning constructive interference between the nonlinear polarization mode and its harmonics, leads to very high far-field nonlinear emission. The predictive capability of this nonlinear scattering theory enables rapid design of optimal nonlinear nanostructures for other applications.

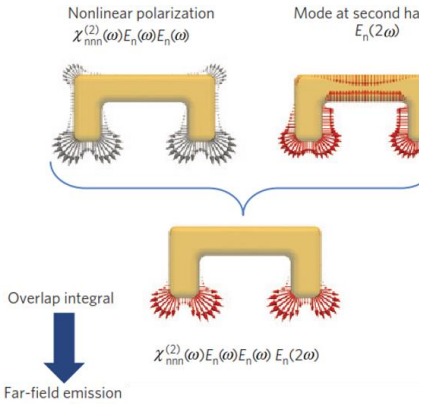

Fig. 3. The overlap integral of the microscopic nonlinear polarization, calculated from the linear fields at the fundamental frequency ω, and the mode at the second harmonic yields the far-field nonlinear emission.

(C) Dynamic Control of Metamaterials by Ultrafast Acousto-Plasmon Interactions: Dynamic control of the metamaterial response is of great importance in optoelectronics, optical communication, chemistry, and biology. Nanoplasmonic resonators have a large absorption cross-section and, therefore, can efficiently absorb energy from a laser pulse, and then the rapid impulsive thermal expansion generates coherent acoustic phonons. The local strain deforms the nanostructure, causing geometry and refractive index changes, which in turn modulate the plasmonic resonance.

By designing plasmonic nanostructures exhibiting multimodal phonon interference, we have successfully detected the spatial properties of complex phonon modes below the optical wavelength at the nanoscale through the interplay between plasmons and phonons [6] -- previously only possible using an X-ray free-electron laser. In our experiment (Fig. 4 (A)), the gold Swiss-cross nanostructures support two mechanical eigenmodes, the antisymmetric (B) and the symmetric eigenmode (C). The superposition between the modes dictates the mechanical dynamics, whose phase and amplitude can be detected with localized surface plasmon polaritons. Each probe plasmon polarization yields a projection of the dynamics, allowing us to sense the mechanical displacement along each axis, corresponding to the two mechanical eigenmodes. Applications of this technique can leverage the advances in coherent control of electromagnetic fields to selectively detect phonons on narrow tips and complex nanostructures, revolutionizing the scientific approaches to study electron transport and their interaction with coherent phonons at the nanoscale.

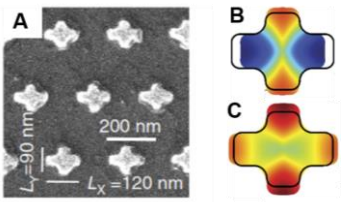

Fig. 4. (A) The 35-nm-thick gold Swiss-cross nanostructures support two mechanical eigenmodes, the antisymmetric (B) and the symmetric eigenmode (C).

Future Plans:

The future goals are to explore exciting optical properties and to develop promising applications of subwavelength metamaterials. We intend to explore quantum effects in metamaterials and quantum phenomena of photon assisted by metamaterials like photon entanglement, as well as to understand the interaction between quantum emitters with metamaterials such as quantum interference phenomena by engineering anisotropic quantum vacuum. We will additionally explore the extraordinary nonlinear properties in metasurfaces. Nonlinear metasurfaces are ultrathin electromagnetic nanostructures, which enables to tailor the nonlinear optical response on the subwavelength scale and paves the way for the generation of harmonic waves in ultrathin flat nanophotonic devices. Another mission is to explore new metamaterial transformation and control photons with new transformation symmetry such as parity-time (PT) symmetry. The notion of PT symmetry started from quantum mechanics used to describe electron motions. In metamaterials, it means that the system combines balanced loss and gain. It has opened up many novel opportunities like unidirectional invisibility [7], single mode micro-ring laser [8], lasing and anti-lasing [9]. This new physics may enable us to explore one-way lasing for non-equilibrium photon flux control and memory effects with linear responses at exceptional points.

References:

[1] J. Valentine, J. Li, T. Zentgraf, G. Bartal & X. Zhang, *Nature Materials* **8**, 568 - 571 (2009).
[2] X. Ni, Z. J. Wong, M Mrejen, Y. Wang, & X. Zhang, *Science* **349** (6254), 1310-1314 (2015).
[3] H. Suchowski, K. O'Brien, Z.J. Wong, A. Salandrino, X. Yin & X. Zhang, *Science* **342**, 1223 (2013).
[4] R. C. Miller, *Appl. Phys. Lett.* **5**, 17-19 (1964).
[5] K. O'Brien, H. Suchowski, J. Rho, A. Salandrino, B. Kante, X. Yin, & X. Zhang, *Nature Materials* **14**, 379-383 (2015).
[6] K. O'Brien, N. D. Lanzillotti-Kimura, J.Rho, H. Suchowski, X. Yin, & X. Zhang, *Nature Communications* **5**, 4042 (2014).
[7] X. Yin & X. Zhang, *Nature Materials* **12**, 175–177 (2013).
[8] L. Feng, Z. J. Wong, R.M. Ma, Y. Wang & X. Zhang, *Science* **346**(6212), 972-975 (2014)
[9] Z. J. Wong, Y.-L. Xu, J. Kim, K. O'Brien, Y. Wang, L. Feng & X. Zhang, *Nature Photonics* **10**, 796–801 (2016).

DOE Publications Relevant To This Subtask:

[1] H. Suchowski, K. O'Brien, Z.J. Wong, A. Salandrino, X. Yin & X. Zhang, *Science* **342**, 1223 (2013).
[2] Z. Ye, T. Cao, K. O'Brien, H. Zhu, X. Yin, Y. Wang, S. G. Louie & X. Zhang, *Nature* **513**, 214-218 (2014). DOI: 10.1038/nature13734.
[3] K. O'Brien, N. D. Lanzillotti-Kimura, J.Rho, H. Suchowski, X. Yin, & X. Zhang, *Nature Communications* **5**, 4042 (2014). DOI: 10.1038/ncomms5042.
[4] H. Ramezani, H.K. Li, Y. Wang, & X. Zhang, *Phys. Rev. Lett.* **113** (26), 263905 (2014).
[5] D.J. Cho, W. Wu, F. Wang, & Y.R. Shen, *Phys. Rev. B* **89**, 035434 (2014).
[6] K. O'Brien, H. Suchowski, J. Rho, A. Salandrino, B. Kante, X. Yin, & X. Zhang, *Nature Materials* **14**, 379-383 (2015).
[7] X. Ni, Z. J. Wong, M Mrejen, Y. Wang, & X. Zhang, *Science* **349** (6254), 1310-1314 (2015).
[8] H. Ramezani, Y. Wang, E. Yablonovitch & X. Zhang, IEEE *Journal of Selected Topics in Quantum Electronics* **22**, 5000706 (2016).
[9] K.L. Tsakmakidis, R.W. Boyd, E. Yablonovitch & X. Zhang, *Optics Express* **24**, 17916 (2016).
[10] H. Ramezani, M. Dubois, Y. Wang, & X. Zhang, *New Journal of Physics* **18**, 095001 (2016).

Metamaterials

Costas M. Soukoulis, Thomas Koschny, Jigang Wang
Ames Laboratory, Iowa State University, Ames, Iowa.

Program Scope

Many of the technologies, that underpin our economy and enable our standard of living, depend on advanced materials. Therefore, the engine for progress in many disciplines is the discovery and understanding of new materials, and their properties. Metamaterials are novel artificial materials that enable the realization of innovative properties unattainable in naturally existing materials. This program explores theoretical understanding, analysis, development, fabrication, and experimental characterization of electromagnetic metamaterials, and investigates their feasibility for various applications. In view of the complexity of electromagnetic interactions in metamaterials, the combination of theory, state-of-the-art models and computational techniques are essential to understand these structures, and we collaborate with experimentalists to fabricate and characterize some of these materials.

Recent Progress

Graphene for THz plasmonic metasurfaces: Graphene — a one-atom-thick continuous sheet of carbon atoms — has special properties that make it a desirable material for manipulating terahertz waves, i.e., electromagnetic radiation with frequencies between microwaves and far infrared. Some metamaterials could benefit from replacing conventional metal films with graphene, which provides a unique, qualitative advantage over metals with the unprecedented ability to tune its electromagnetic response, i.e., complex sheet conductivity, for a given application as well as its capacity to support deeply subwavelength surface plasmons at THz frequencies. Graphene also offers the advantage of a potential enhancement of terahertz wave confinement. Experimental data has shown significantly worse performance of graphene than has been estimated by theoretical work. The major obstacle in developing plasmonic

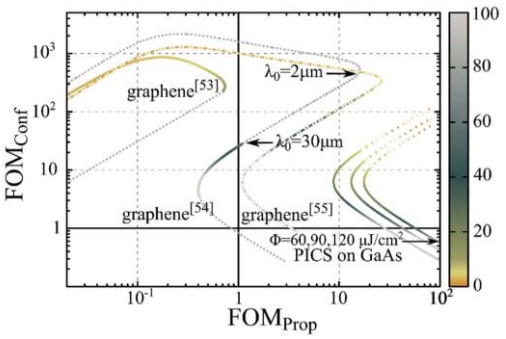

Fig. 1. Sheet conductivities of graphene and competing photo-conducting surfaces (PICS) from experimental data, classified according to the relevant figures-of-merit (FOM) for use in metamaterials: dissipative loss and confinement. Taken from our recent analysis [1].

applications is dissipative loss, which limits the propagation length of surface plasmons and broadens the bandwidth of surface-plasmon based resonances. We performed a new analysis [1] of plasmonic materials and geometries, which fully considers the tradeoff between propagation length and degree of confinement. It is based on a two-dimensional analysis of two independent figures of merit and the analysis is applied to graphene and competing relevant plasmonic materials, e.g., noble metals, aluminum, silicon carbide, doped semiconductors, photo-induced conducting surfaces, etc. The analysis provides guidance on how to improve the performance of any particular plasmonic application and substantially eases the selection of the plasmonic material. We also explore different approaches tunable metasurfaces based on tunable Goos–Hänchen effect and mechanical state transitions due to plasmon mediated optical force in Graphene.

Dielectric resonant dark-state optical metamaterials: Metamaterials made with metallic constituents have proven very successful at microwave and THz frequencies, but suffer from significant dissipative losses and broken geometric scaling in the optical domain. One important approach to reduce dissipative losses is to make use of dielectrics rather than metals for building the electromagnetic resonators. We develop a novel concept that uses generic, dark resonant states in dielectrics together with purposefully designed, non-resonant coupling to radiation in order to implement the desired electromagnetic response. In dielectrics, dark resonances can be constructed with a high quality factor. However, being dark, these modes do not posses large electric or magnetic dipole moments that can radiate, i.e. couple to propagating modes. This is an advantage because: (i) we can construct small non-resonant scatterers that couple to the dark resonant state and provide an arbitrary, specifically designed electric, magnetic, or chiral dipole moment, which will in turn radiate and couple to the propagating waves resulting in an effective resonant response in either permittivity, permeability, or chiral parameter – determined purely by the geometry of the non-resonant scatterers, not by the dark resonator; (ii) the radiating moment, hence the radiation damping and Q-factor of the resonant response, can be controlled readily and

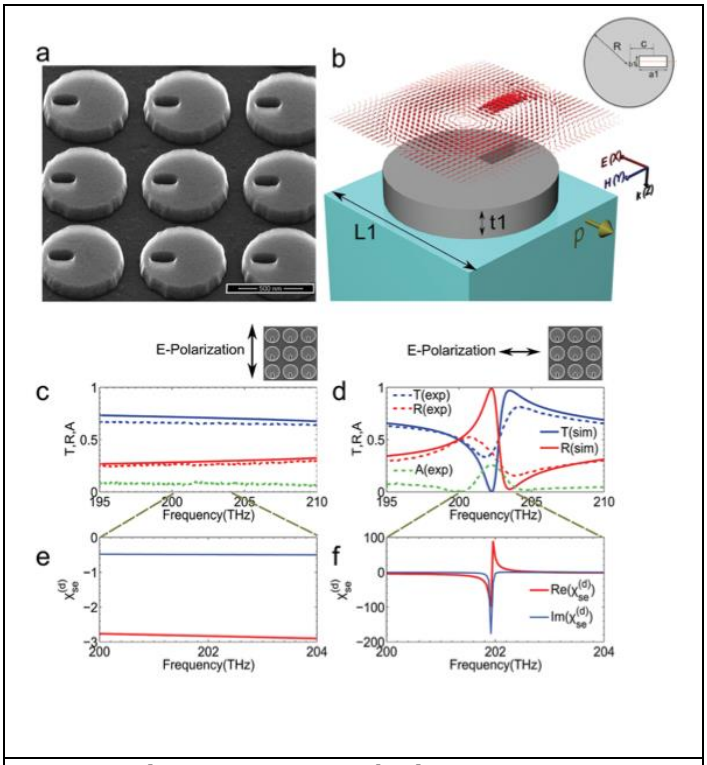

Fig. 2. Dielectric resonator with electric response using a resonant dark state in a disc. (a) SEM pictures of a fabricated sample. (b) Schematic of dark mode and structure. (c-d) Simulated and measured Transmission and reflection spectra; Retrieved electric surface susceptibility χ_{se}. [2]

independent of the actual resonant dark state. This separation of resonant energy storage (dark mode) and configurable electromagnetic response (non-resonant scatterers) allows for great versatility in the design of low-loss metamaterials and metasurfaces. We have designed, numerically simulated and, in collaboration with J. Valentine (Vanderbilt Univ.) and I. Brener (CINT, Sandia), fabricated as well as experimental characterized two implementations. The first one, shown in Fig. 2, is based on dark magnetic Mie modes in arrays of silicon discs and provides a resonant electric permittivity at optical frequency of ~ 200THz (1.5μm, telecom band) in the NIR. The mode is dark because the magnetic moments perpendicular to the surface are in-phase and cannot radiate for large samples. Coupling to propagating waves is provided by the tiny slot. The second implementation uses the dark bound states in a dielectric film, which modes are quantized by a grating structure on its surface below the diffraction edge. Asymmetric protrusions of the dielectric film as shown in Fig. 3c, provide a small magnetic moment to couple the dark resonant bound state to radiation and, hence, turning the structure into a resonant metasurface with magnetic response at ~ 200THz (1.5μm). The same geometry is also shown to provide electric resonant response as well as simultaneous electric and magnetic response, just be altering the coupling to the same dark resonant state. This approach of separating the nature of the actual resonance from the coupling to the radiation field in metamaterials and implementing the resonance by dark resonant states is very general and enables a lot of freedom in designing suitable metamaterial resonators.

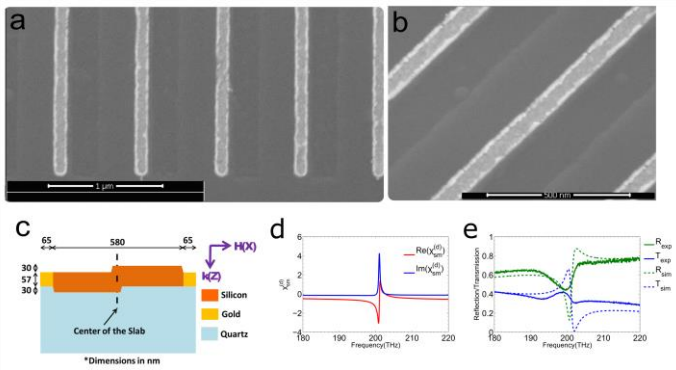

Fig. 3. Dielectric resonator with magnetic response using a resonant dark state in a thin dielectric layer. SEM pictures of a fabricated sample: (a) top view, (b) perspective view. (c) A schematic of the structure. (d) Retrieved magnetic surface susceptibility $\chi_{sm}(d)$. (e) Simulated and measured Transmission and reflection spectra. [3]

Active metasurfaces and lasers based on dark resonant states: The high Q-factor afforded by dielectric dark resonant states together with subwavelength mode volume provides a route to miniaturization of laser systems. Especially if surface emitting lasers with non-trivial beam characteristics are desired, we can design metasurfaces that combine tight near-field coupling between quantum emitters (the gain medium) with resonant dark states, leading to "lasing" directly into the bound photonic modes of the dark states rather than propagating waves of light. Then, coupling to the free-space radiation field can be managed by a metasurface that allows precise control over the amount of radiation damping as well as the precise nature of the generated beam (beam profile, direction, polarization, etc.). These structures are conceptionally analog to Spasers but allow for more control, higher Q-factors, and lower lasing thresholds. For

example, a macroscopically populated dark state may evanescently couple to both electric and magnetic currents of the metasurface, providing directional emission only to the air side, not back into the structure, without a lossy mirror and without a "vertical cavity", enabling the thickness of the lasing structure to be substantially smaller than the wavelength of the emitted radiation. We explore an example of such a lasing system in [4]. Here, we propose a metamaterial laser system that offers radiation damping tunability, along with many other features, such as directionality, subwavelength integration, and simple layer-by-layer fabrication.

Future Plans

Exploration of intercalated graphene for THz: We will experimentally explore the THz properties of intercalated multilayer graphene, which shows promise of behaving like decoupled stacks of individual graphene layers. If so, it could reach and exceed the effective bulk conductance of 30nm noble metal films and provide a lower loss alternative conductor in THz metamaterials at nm thickness. Finally, we will explore tunable, mutually biased, dielectric insulated multilayer graphene stacks for THz modulators with large modulation ratio.

Tunable, photo-induced conducting surfaces: We will explore photo-induced conducting surfaces (PICS) as alternatives to graphene at THz frequencies. Experimentally, photo-induced sheet conductivities on GaAs surfaces have proven to exceed the best available samples of graphene while still providing graphene's key properties of tunability and well confined surface plasmons, potentially allowing for photo-imprinted resonant metasurfaces and plasmonics.

Enhanced nonlinearity by radiation control: Metal-based metasurfaces been shown to have huge nonlinearities, which are tunable in frequency. Using resonant dark states, we will design metasurfaces that separately control linear and nonlinear radiation damping, leading to tailored optical nonlinearities for advanced THz generation.

Development of computational tools: We will develop further our self-consistent FDTD calculations for non-linear and gain materials, enabling realistic simulations that include spontaneous emission and noise to model luminescence and the transition from luminescence to lasing and allow comparison with experimental data. The simulation tools will provide guidance to the experiment on how full loss compensation and lasing/spasing can be achieved.

References

[1] B. Dastmalchi, P. Tassin, Th. Koschny, C. M. Soukoulis, "A New Perspective on Plasmonics: Confinement and Propagation Length of Surface Plasmons for Different Materials and Geometries," *Adv. Opt. Mater.* **4**, 177 (2016).

[2] A. Jain, P. Moitra, Th. Koschny, J. Valentine, C.M. Soukoulis, "Electric and Magnetic Response in Dielectric Dark States for Low Loss Subwavelength Optical Meta Atoms," *Adv.Opt.Mater.* **3**, 1431 (2015).

[3] A. Jain, T. James, J. Nogan, T. S. Luk, G. Subramania, S. Liu, I. Brener, Th. Koschny, C. M. Soukoulis, (*unpublished*, 2017).
[4] S. Droulias, A. Jain, Th. Koschny, C. M. Soukoulis, "Novel Lasers Based on Resonant Dark States," *Phys. Rev. Lett.* **180**, 073901 (2017).

Publications

1. C. M. Soukoulis, Th. Koschny, P. Tassin, N. Shen and B. Dastmalchi, "What is a good conductor for metamaterials or plasmonics," Nanophotonics 4, 69 (2015).
2. Y. Fan, N. Shen, Th. Koschny and C. M. Soukoulis, "Tunable terahertz meta-surface with graphene cut-wires," ACS Photonics 2, 151 (2015).
3. G. Kenanakis, A. Xomalis, A. Selimis, M. Vamvakaki, M. Farsari, M. Kafesaki, C. M. Soukoulis, and E.N. Economou, "A three-dimensional terahertz metamaterial with asymmetric transmission," ACS Photonics 2, 287 (2015).
4. V. Ginis, P. Tassin, Th. Koschny and C. M. Soukoulis, "Tunable THz frequency comb generation using time-dependent graphene sheets," Phys. Rev. B. 91, 161403(R) (2015).
5. P. Zhang, C. Fietz, P. Tassin, Th. Koschny and C.M. Soukoulis, "Numerical investigation of the flat band Bloch modes in a 2D photonic crystal with Dirac cones," Opt. Express 23, 10444 (2015).
6. A. C. Tasolamprou, L. Zhang, M. Kafesaki, Th. Koschny and C. M. Soukoulis, "Frequency splitter based on the directional emission from surface modes in dielectric photonic crystal structures," Opt. Express 23, 13972 (2015).
7. P. Liu, S. Yang, A. Jain, Q. Wang, H. Jiang, J. Song, Th. Koschny, C. M. Soukoulis, and Liang Dong, "Tunable meta-atom using liquid metal embedded in stretchable polymers," J. of Appl. Phys. 118, 014504 (2015).
8. Q. Zhao, Z. Xiao, F. Zhang, J. Ma, M. Qiao, Y. Meng, C. Lan, Bo LI, Ji Zhou, Peng Zhang, N. Shen, Th. Koschny, and C. M. Soukoulis, "Tailorable zero phase delay and localized subwavelength resonances," Advanced Mater. 27, 6187 (2015).
9. Aditya Jain, P. Moitra, Th. Koschny, J. Valentine and C. M. Soukoulis "Electric and Magnetic response in Dielectric Dark states for Low Loss Subwavelength Optical Meta Atoms," Advanced Opt. Mater. 3, 1431 (2015).
10. G. Kenanakis, C. M. Soukoulis, and E.N. Economou, "Casimir forces of metallic microstructures into cavities," Phys. Rev. B 92, 075430 (2015).
11. A. Akbarzadeh, J. A. Crosse, Mohammad Danesh, Cheng-Wei Qiu, Aaron J. Danner, and C. M. Soukoulis, "Interplay of optical force and ray-optic behavior between Luneburg lenses," ACS Photonics 2, 1384 (2015).
12. B. Dastmalchi, P. Tassin, Th. Koschny and C. M. Soukoulis, "A new perspective on plasmonics: Confinement and propagation length of surface plasmons for different materials and geometries," Advanced Opt. Mater. 4, 177 (2016).
13. V. Ginis, P. Tassin, Th. Koschny and C. M. Soukoulis, "Broadband metasurfaces enabling arbitrarily large delay-bandwidth product," Appl. Phys. Lett. 108, 031601 (2016).
14. G. Kenanakis, E. N. Economou, C. M. Soukoulis, and M. Kafesaki, "Controlling THz and far-IR waves with chiral and bianisotropic metamaterials," EPJ Appl. Metamater. 2, 15 (2016).

15. M. Fang, Z. Huang, Th. Koschny, and C. M. Soukoulis, “Electrodynamic modeling of quantum dot luminescence in plasmonic metamaterial,” ACS Photonics 3, 558 (2016).
16. A. Akbarzadeh, Th. Koschny M. Kafesaki, E. N. Economou and C. M. Soukoulis, “Graded-index optical dimer formed by optical force,” Opt. Express 24, 11376 (2016).
17. N. Shen, P. Zhang, Th. Koschny and C. M. Soukoulis, “Metamaterial-based lossy anisotropic epsilon-near-zero medium for energy collimation,” Phys. Rev. B 93, 245118 (2016).
18. Y. Yang, L. Jing, B. Zheng, R. Hao, W. Yin, E. Li, C. M. Soukoulis, and H. Chen, “Full-polarization 3D meta-surface cloak with preserved amplitude and phase,” Advanced Mater. 28, 6866 (2016).
19. Y. Fan, N. Shen, F. Zhang, Z. Wei, H. Li, Q. Zhao, Q. Fu, P. Zhang, Th. Koschny, and C. M. Soukoulis, “Electrically Tunable Goos–Hänchen Effect with Graphene in the Terahertz Regime,” Advanced Opt. Mater. 4, 1824 (2016).
20. A. Tasolamprou, O. Tsilipakos, M. Kafesaki, C. M. Soukoulis, and E. N. Economou “Toroidal eigenmodes in all-dielectric metamolecules,” Phys. Rev. B 94, 205433 (2016).
21. S. Droulias, A. Jain, Th. Koschny and C.M. Soukoulis, “Novel lasers based on resonant dark states,” Phys. Rev. Lett. 118, 073901 (2017).
22. P. Zhang, N. Shen Th. Koschny and C. M. Soukoulis, “Mechanical state transition induced by surface-plasmon-polariton-assisted gradient force enhancement in graphene sheet pair,” ACS Photonics 4, 181 (2017).
23. R. Peng, Z. Xiao, Q. Zhao, F. Zhang, Y. Meng, Bo Li, Ji Zhou, Y. Fan, P. Zhang, N. Shen, Th. Koschny, and C. M. Soukoulis, “Temperature-Controlled Chameleonlike Cloak,” Phys. Rev. X 7, 011033 (2017).

Light-matter interaction phenomena using subwavelength engineering of material properties

PI: Igal Brener

Team members: Michael B. Sinclair, Willie Luk, Sheng Liu, Salvatore Campione, John Klem, Ines Montano,

Sandia National Laboratories, Albuquerque, NM 87185, USA

Program Scope

The overarching goal of this project is to achieve fundamental understanding and control of light–matter interaction through engineering material properties at the subwavelength scale. Our approach involves the use of localized and propagating metamaterial photon modes coupled to semiconductor heterostructures. The metamaterials will allow tailoring of the photonic mode properties, while the semiconductor heterostructures will enable the production of electronic and vibrational transitions with desired characteristics. Two distinct classes of metamaterials will be utilized which will allow complementary aspects of the light–matter interactions to be investigated. One thrust will investigate strong coupling of the localized modes of planar metamaterial nanocavities to semiconductor transitions; while a second thrust will explore the coupling of the propagating modes of hyperbolic metamaterials to semiconductor transitions. The ultimate goal is to control the flow of energy between photons, phonons, and electrons in ways that are not possible with natural materials.

Recent Progress

1. Enhanced Optical Nonlinearities in Metasurfaces-Semiconductor Coupled Systems.

Metasurfaces can be designed to exhibit strong magnetic and electric resonances that can couple efficiently to a variety of excitations in semiconductors and their heterostructures. For metallic metasurfaces, past studies of this coupling have included phonons [1], intersubband transitions [2-4] and plasmons [5]. This coupling can be exploited for fundamental studies of light matter interaction or for optoelectronic functionality such as light modulation, tunable spectral filtering or optical nonlinearities. We have obtained record second order nonlinearities using metallic metasurfaces that are coupled with resonant electronic transitions in semiconductors such as intersubband transitions. [6,7] Additionally, since the nonlinear unit in this case is a single resonator coupled to the semiconductor heterostructure, additional functionality can be obtained at the second harmonic wavelength. [7] For example, we can tailor the radiated phase of each resonator to form a phased-array source. Using this principle, we have created beam and polarization splitters operating at the second harmonic wavelength. [7] This is new functionality that has no counterpart in conventional nonlinear optical materials. Representative results are shown in Fig. 1

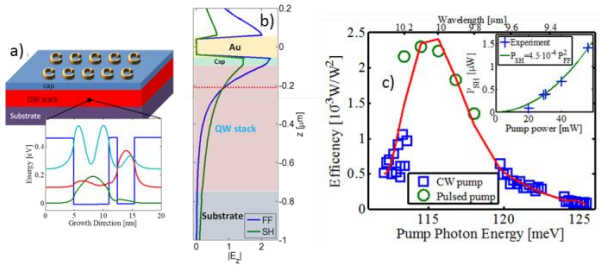

Figure 1: a) Schematic of the coupled system used for SHG, and band diagram of the nonlinear heterostructure. b) Profile of the z-directed electric field below the resonator showing strong overlap with the nonlinear medium. c) Measured SHG as a function of the pump energy/wavelength.

2. Linear and Nonlinear Optical Properties of All-Dielectric Metamaterials made form III-V Semiconductors

All-dielectric metamaterials consisting of arrays of high-index, subwavelength-size Mie resonators have attracted much attention recently due to their much lower loss at optical frequencies compared with their metallic counterparts. Moreover, these Mie resonators interact strongly with both electric and magnetic fields and therefore enable manipulation of the electromagnetic permittivity and permeability. Great success has been achieved in using these metamaterials for nonlinear optical processes, ultrathin optical components and advanced wavefront engineering. However, most of this work has been done using silicon, which lacks second-order optical nonlinearities and is not an efficient light emitter.

Recently, our group demonstrated a new class of dielectric metamaterials based upon III–V semiconductors that exhibit strong intrinsic optical nonlinearities and allow for full integration with optoelectronic functionality.

We have developed a top-down fabrication process to create such III-V metamaterials that can go beyond a single layer of resonators. [8] The fabrication procedure includes an oxidation step that creates a low index layer below each III-V nanoresonators. (Fig. 2(c)). The ability to create multilayer III-V metamaterials enables new degrees of freedom in device engineering. Figure 2 (a) & (b) show that the multilayer metamaterials can act as broadband mirrors with nearly 100 percent reflectivity, outperforming even gold mirrors. [8] Furthermore, since the thickness of the different layers is determined by epitaxy, exquisite control of the spectral location of magnetic and electric dipole resonances can be achieved using "split-resonator" designs (Fig. 2 (c) & (d)).

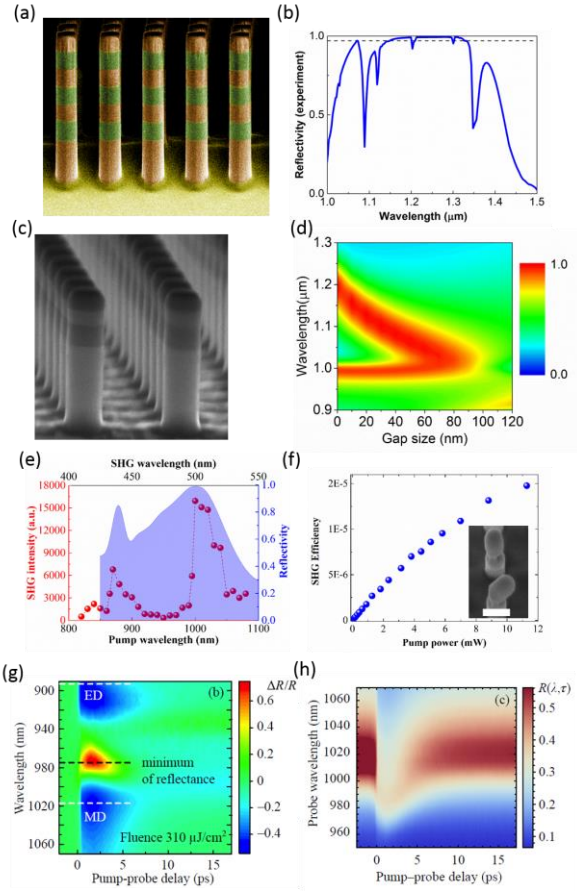

Figure 2: Examples of novel linear and nonlinear optical properties enabled by GaAs dielectric metasurfaces. (d) spectral location of magnetic and electric dipole resonances as a function of the gap size. (f) Power dependence of SHG. (g)-(h) Time-resolved reflectance data from a GaAs metasurface pumped at the magnetic dipole resonance.

These III-V metamaterials exhibit strong resonantly enhanced second-harmonic generation with conversion efficiencies exceeding 10^{-5}, several orders of magnitude higher than with metallic metasurfaces. [9] Due to the direct bandgap of the constituent semiconductor, photoexcited carriers can also induce other types of strong nonlinearities such as transient saturation and/or resonance shift on an ultrafast timescale. Using transient reflectance spectroscopy, we demonstrated a picosecond-scale absolute reflectance modulation of up to 0.35 at the magnetic dipole resonance of the metasurfaces and a spectral shift of the resonance by 30 nm (Fig. 2(g) and (h)). [10]

3. Ultrafast Metasurfaces

Noble metals such as gold and silver are the most commonly adopted plasmonic materials, but their plasmonic properties are hardly tunable. As an alternative, doped semiconductors, such as Si, III-V semiconductors, and transparent conducting oxides offer tunability, with their plasma frequency ω_p tunable by either inter- or intra-band optical excitation. In the simplest form, the plasma frequency is given by $\omega_p^2 = ne^2/m^*$. In the case of interband excitation, the modulation of ω_p is achieved by increasing the electron density n; alternatively, using intraband optical pumping, one can modify the effective mass m^* of the plasmonic material due to its conduction band non-parabolicity and the momentum-dependent effective mass $m = m(k)$. In this section, we present our recent efforts of ultrafast control of various plasmonic/metasurface systems by either inter- or intra-band optical excitation.

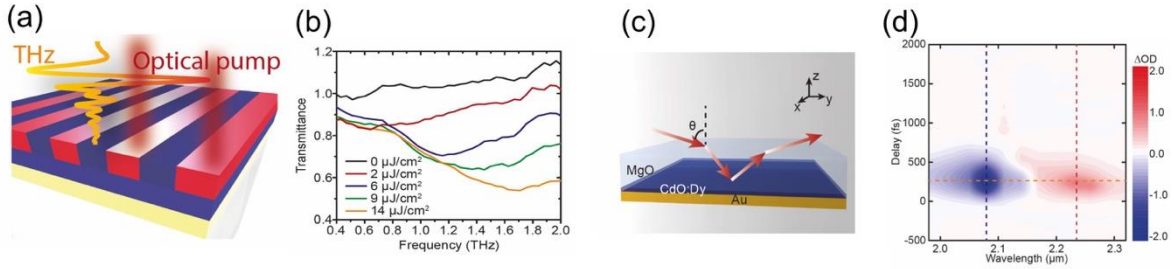

Figure 3: (a) Schematic of a transient GaAs metasurface induced by a structured femtosecond optical pump beam. (b) Measured transmittance spectra of the photo-imprinted GaAs metasurface as a function of pump fluence. (c) Schematic of the CdO-based perfect absorber. (d) The relative absorption change as a function of wavelength and delay time.

First, we demonstrated the ultrafast formation of macroscopic terahertz (THz) metasurfaces through all-optical creation of spatially modulated carrier density profiles in a deep-subwavelength GaAs film. [11] The switch-on of the transient plasmon mode, governed by the GaAs effective electron mass and electron-phonon interactions, is revealed by structured-optical pump THz probe spectroscopy, on a time scale of 500 femtoseconds. By modulating the carrier density using different pump fluences, we observe a wide tuning of the electric dipole resonance of the transient GaAs metasurface from 0.5 THz to 1.7 THz (Fig. 3(a) & (b)).

Second, we show a novel plasmonic amplitude and polarization switch using a cadmium-oxide (CdO)-based perfect absorber (Fig. 3(c)). With the aid of high-mobility epitaxially-grown dysprosium-doped CdO as the gateway plasmonic material, [12] we realize a high-quality factor, polarization-selective, Berreman-type perfect absorber at a wavelength of 2.08 μm. Upon sub-bandgap resonant optical pumping, the perfect absorption resonance strongly redshifts due to the transient increase of the ensemble-averaged effective electron mass of CdO, leading to a very large *absolute p*-polarized reflectance change from 1.0% to 86.3% (Fig. 3(d)). The switching time is sub-picosecond and is governed by electron-phonon coupling. By combining the exceedingly high modulation depth with the polarization selectivity of the perfect absorber, we experimentally demonstrate a reflective polarizer with a polarization extinction ratio of 91 that can be switched on and off within 800 fs.

Future Plans

Our activities will proceed along four main directions:

i) Metasurface-Mediated Photon Emission: taking advantage of our recently developed III-V all-dielectric metamaterials, we are now able to embed different emitters grown epitaxially (i.e.,

quantum dots, quantum wells, etc) and study the coupling to a variety of modes intrinsic to the Mie resonators and alter the far field emission using metasurfaces.

ii) Strong coupling to Metamaterials: Impact on Condensed Matter Excitations: We will explore coupling of metamaterials to phonons and intersubband plasmons with the aim to alter or modify some macroscopic behavior such as electronic transport, phase transitions, etc.

iii) Optical Nonlinearities from Coupled Metamaterials-Semiconductors: here we plan on using broken gap semiconductor heterostructures to harness even higher resonant optical nonlinearities while coupling them to metallic metasurfaces. We also plan on investigating other optical nonlinearities using III-V all-dielectric metamaterials.

iv) Ultrafast and Spatiotemporal Phenomena in Metamaterials: using spatially and temporally structured pump beams, we plan to photoexcite dielectric metamaterials built from direct bandgap semiconductors and study their transient optical behavior.

References

[1] D. J. Shelton, I. Brener, J. C. Ginn, M. B. Sinclair, D. W. Peters, K. R. Coffey, and G. D. Boreman, Nano Lett. **11**, 2104 (2011).

[2] A. Benz, S. Campione, J. F. Klem, M. B. Sinclair, and I. Brener, Nano Lett. **15**, 1959 (2015).

[3] A. Benz, S. Campione, M. W. Moseley, J. J. Wierer Jr., A. A. Allerman, J. R. Wendt, and I. Brener, ACS Photonics **1**, 906 (2014).

[4] A. Benz, S. Campione, S. Liu, I. Montano, J. F. Klem, A. Allerman, J. R. Wendt, M. B. Sinclair, F. Capolino, and I. Brener, Nature Communications **4**, 2882 (2013).

[5] Y. C. Jun, J. Reno, T. Ribaudo, E. Shaner, J.-J. Greffet, S. Vassant, F. Marquier, M. Sinclair, and I. Brener, Nano Lett. **13**, 5391 (2013).

[6] O. Wolf, A. A. Allerman, X. Ma, J. R. Wendt, A. Y. Song, E. A. Shaner, and I. Brener, Appl. Phys. Lett. **107**, 151108 (2015).

[7] O. Wolf, S. Campione, A. Benz, and A. P. Ravikumar, Nature Communications **6**, 7667 (2015).

[8] S. Liu, G. A. Keeler, J. L. Reno, M. B. Sinclair, and I. Brener, Advanced Optical Materials **4**, 1457 (2016).

[9] S. Liu, M. B. Sinclair, S. Saravi, G. A. Keeler, Y. Yang, J. Reno, G. M. Peake, F. Setzpfandt, I. Staude, T. Pertsch, and I. Brener, Nano Lett. **16**, 5426 (2016).

[10] M. R. Shcherbakov, S. Liu, V. Zubyuk, A. Vaskin, P. P. Vabishchevich, G. A. Keeler, T. Pertsch, T. Dolgova, I. Staude, I. Brener, and A. A. Fedyanin, Nature Communications **accepted 2017**.

[11] Y. Yang, N. Kamaraju, S. Campione, S. Liu, J. L. Reno, M. B. Sinclair, R. P. Prasankumar, and I. Brener, ACS Photonics **4**, 15 (2017).

[12] Y. Yang, K. kelley, E. Sachet, S. Campione, T. S. Luk, J.-P. Maria, M. B. Sinclair, and I. Brener, Nat Photon **accepted 2017**.

Two-year list of publications supported by BES

1. "Phased-array sources based on nonlinear metamaterial nano cavities", Omri Wolf, Salvatore Campione, Alexander Benz, Arvind P. Ravikumar, Sheng Liu, Ting S. Luk, Emil A. Kadlec, Eric A. Shaner, John F. Klem, Michael B. Sinclair & Igal Brener, Nature Communications **6**, 7667 (2015)
2. "Realizing high-quality, ultra-large momentum states and ultrafast topological transitions using semiconductor hyperbolic metamaterials", S. Campione, T.S. Luk, M.B. Sinclair, JOSA B **32**, 1809 (2015).
3. "Tailoring dielectric resonator geometries for directional scattering and Huygens' metasurfaces", Salvatore Campione, Lorena I. Basilio, Larry K. Warne, and Michael B. Sinclair, Opt. Express **23**, 2293 (2015)
4. "Optical properties of transiently-excited semiconductor hyperbolic metamaterials", S. Campione, T.S. Luk, S. Liu, and M.B. Sinclair, Opt. Mater. Express **5**, 2385 (2015).
5. "A Small-Footprint IR Source with Beam Control", Omri Wolf, Salvatore Campione, Igal Brener, John Klem, Michael Sinclair, Optics and Photonics News, December 2015, p54.
6. "Enhanced optical nonlinearities in the near-infrared using III-nitride heterostructures coupled to metamaterials", Omri Wolf, Andrew A. Allerman, Xuedan Ma, Joel R. Wendt, Alex Y. Song, Eric A. Shaner and Igal Brener, Appl. Phys. Lett. **107**, 151108 (2015)
7. "Epsilon-Near-Zero Modes for Tailored Light-Matter Interaction", Salvatore Campione, Sheng Liu, Alexander Benz, John F. Klem, Michael B. Sinclair, and Igal Brener, Phys. Rev. Applied **4**, 044011 (2015)
8. "Near-Infrared Strong Coupling between Metamaterials and Epsilon-near-Zero Modes in Degenerately Doped Semiconductor Nanolayers,", S. Campione, J.R. Wendt, G.A. Keeler, and T.S. Luk, ACS Photonics **3**, 293 (2016).
9. "Highly Directional Room-Temperature Single Photon Device", Nitzan Livneh, Moshe G. Harats, Daniel Istrati, Hagai S. Eisenberg, and Ronen Rapaport, Nano Letters **16**, 2527 (2016)
10. "III–V Semiconductor Nanoresonators—A New Strategy for Passive, Active, and Nonlinear All-Dielectric Metamaterials", Sheng Liu, Gordon A. Keeler, John L. Reno, Michael B. Sinclair, Igal Brener, Adv. Opt. Mat. 2016, DOI: 10.1002/adom.201600240
11. "Resonantly Enhanced Second-Harmonic Generation Using III−V Semiconductor All-Dielectric Metasurfaces", Sheng Liu, Michael B. Sinclair, Sina Saravi, Gordon A. Keeler, Yuanmu Yang, John Reno, Gregory M. Peake, Frank Setzpfandt, Isabelle Staude, Thomas Pertsch, and Igal Brener, Nanoletters **16,** 5426 2016.
12. "Electrically controlled mutual interactions of flying waveguide dipolaritons", Itamar Rosenberg, Yotam Mazuz-Harpaz, Ronen Rapaport, Kenneth West, and Loren Pfeiffer, Phys. Rev. B **93,**195151 (2016)
13. "Experimental verification of epsilon-near-zero plasmon polariton modes in degenerately doped semiconductor nanolayers", S. Campione, I. Kim, D. de Ceglia, G.A. Keeler, and T.S. Luk, *Opt. Express* **24**, 18782 (2016).
14. "Transient GaAs plasmonic metasurfaces at Terahertz frequencies," Y. Yang, K. Natarajan, S. Campione, S. Liu, J.L. Reno, M.B. Sinclair, R.P. Prasankumar, and I. Brener, ACS Photonics, Article ASAP, DOI: 10.1021/acsphotonics.6b00735
15. "Broken symmetry dielectric resonators for high quality-factor Fano metasurfaces,", S.

Campione, S. Liu, L.I. Basilio, L.K. Warne, W.L. Langston, T.S. Luk, J.R. Wendt, J.L. Reno, G.A. Keeler, I. Brener, and M.B. Sinclair, ACS Photonics, Article ASAP, DOI: 10.1021/acsphotonics.6b00735 (2016).
16. "All-Dielectric Metamaterials Using III–V Semiconductors", S. Liu et al., Optics and Photonics News, December 2016.
17. "Femtosecond Optical Polarization Switching Using a Cadmium-Oxide-Based Perfect Absorber", Yuanmu Yang, Kyle Kelley, Edward Sachet, Salvatore Campione, Ting S. Luk, Jon-Paul Maria, Michael B. Sinclair and Igal Brener. *Accepted for publication* in Nature Photonics 2017.
18. "Spectral filtering using active metasurfaces compatible with narrow bandgap III-V infrared detectors", Omri Wolf, Salvatore Campione, Jin Kim, and Igal Brener, Optics Express **24**, 21512 (2016).
19. "Efficient Collection of Light from Colloidal Quantum Dots with a Hybrid Metal–Dielectric Nanoantenna ", Livneh, N., Harats, M. G., Yochelis, S., Paltiel, Y., & Rapaport, R., ACS Photonics **2**, 1669 (2015). http://doi.org/10.1021/acsphotonics.5b00433
20. "Ultrafast all-optical tuning of direct-gap semiconductor metasurfaces", Maxim R. Shcherbakov, Sheng Liu, Varvara V. Zubyuk, Aleksandr Vaskin, Polina P. Vabishchevich, Gordon Keeler, Thomas Pertsch, Tatyana V. Dolgova, Isabelle Staude, Igal Brener and Andrey A. Fedyanin, Nature Communications, *accepted for publication* 2017.
21. "Design, fabrication and characterization of a hybrid metal-dielectric nanoantenna with a single nanocrystal for directional single photon emission", Moshe G. Harats, Nitzan Livneh, and Ronen Rapaport, Optical Materials Express **7**, 834 (2017).

Session III

Charge transfer states at organic heterojunctions I: Structure-property relationships

Barry P. Rand,[1,2] Antoine Kahn,[1] and Noel C. Giebink[3]

[1] Department of Electrical Engineering, Princeton University, Princeton, NJ 08544
[2] Andlinger Center for Energy and the Environment, Princeton University, Princeton, NJ 08544
[3] Department of Electrical Engineering, The Pennsylvania State University, University Park, PA 16802

Program Scope

Charge transfer from a donor-type to an acceptor-type molecule forms the basis for the photovoltaic effect observed within conjugated molecular systems. The charge transfer (CT) state is a bound geminate charge pair that defines an intermediate state in both charge generation and recombination processes. As such, the CT state possesses a binding energy ($\sim 10 k_b T$) that still needs to be overcome in order to produce a free charge pair. While some important realizations have been made concerning CT states recently regarding their role in limiting open-circuit voltage, there still remains a lack of fundamental knowledge regarding what controls CT state energy and the efficiency by which they may be dissociated, and whether or not Frenkel excitons become free charge via the formation of CT states. This research program sets out to comprehensively investigate the various nanoscale environmental factors that determine CT state behavior (dielectric, structural, dynamic, and energetic), as well as to quantify their spatial extent and density of states (DOS) energetic distribution.

We will utilize sensitive spectral response measurements, impedance spectroscopy, X-ray scattering, and spectroscopic ellipsometry to probe the structure and optical response of thin films, as well as to extract dielectric properties. Surface-sensitive techniques such as ultraviolet photoelectron spectroscopy (UPS), inverse photoelectron spectroscopy (IPES), and X-ray photoelectron spectroscopy (XPS) will be utilized to probe energy levels. Finally, time-resolved and steady-state photoluminescence (PL), electroluminescence (EL), electroabsorption, and pump-probe spectroscopy measurements will be used to probe CT state energetics and dynamics. In this way, the PIs assembled in this collaborative proposal represent a complementary team uniquely suited with the ability to transform our understanding of CT states.

Recent Progress

In order to probe the fundamental nature of CT states, as well as how they relate to limiting photovoltaic function in organic solar cells, we have been exploring microns-scale grains of rubrene[1] like that shown in Fig. 1(a), and compare its properties to that of an amorphous rubrene/C_{60} interface. The amorphous interface is very reminiscent of highly disordered systems like bulk heterojunctions that form the basis for all of the most efficient solar cells to-date. And it is known that even the most efficient of solar cells today feature energy losses of at least 0.5 eV, at least twice that of inorganic systems.

As one can see, the CT states at each of these heterojunctions are markedly distinct, as shown via external quantum efficiency (EQE) spectral measurements in Fig. 1(c). The result, plotted in Fig. 1(d) reveals a step function-like CT state absorption spectrum in the range 1-1.6 eV that is clearly different from the Gaussian lineshape observed for the disordered case shown in Fig. 1(c) in red. Further, EL measurements of the crystal planar heterojunction and amorphous bulk heterojunction

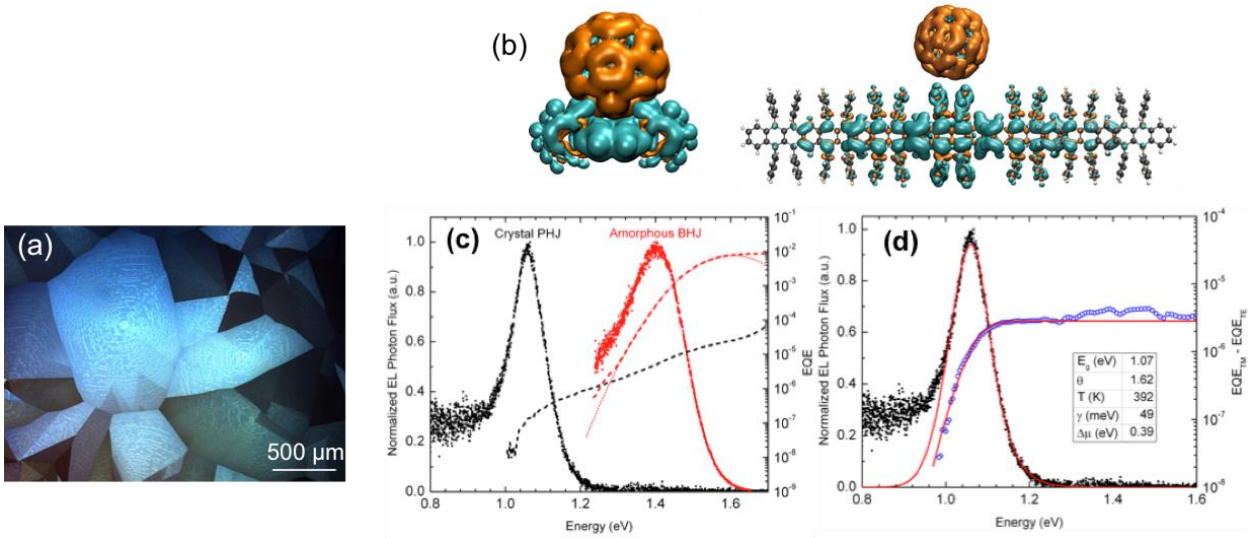

Figure 1. (a) Polarized optical microscope image of the crystalline rubrene template layer showing single-colored crystal domains occasionally exceeding 1 mm in size. (b) Left, the calculated (by T. Van Voorhis, MIT) lowest energy CT state of a single rubrene and C_{60}. Right, diagram showing delocalized positive charge across seven rubrene molecules in the lowest-energy crystalline CT state. (c) EL shows a single, narrow peak for the crystal PHJ device and a broader, blue shifted peak for the amorphous BHJ device. The dashed curves are EQE data for the respective devices. The amorphous BHJ device includes a Marcus fit to the EQE data (dotted curve). (d) A band model with shared fit parameters based on a 2D DOS (shown in red solid lines) fits both the polarized EQE (blue) and EL data (black).

devices (Fig. 1(c)) show a single, narrow CT state emission peak for the crystal device and a broader, blue shifted peak for the amorphous device.

In fact, the absorption and emission spectrum for the crystal device are reminiscent to that observed for inorganic quantum wells and other 2D electronic materials[2] having a step function-like DOS. In this context, we applied a 2D DOS direct bandgap model[3] to the EL and EQE data of the crystal planar heterojunction device. Using this reciprocity approach, we simultaneously fit these two data sets to yield a shared set of parameters (see inset of Fig. 1(d)) and found that such a model provides a consistent description of the data. Compared to a CuZnSnSSe solar cell,[3] the crystal planar heterojunction device has a ~20% smaller energy broadening parameter, γ, underscoring the narrowness of its emission peak as a result of the highly ordered system. Finally, we collaborated with the group of Troy Van Voorhis at MIT, whose calculations (Fig. 1(b)) support the idea of not only delocalized CT states in the crystalline device, but also that the delocalization is in-plane, and supports the notion of a 2D DOS.

Through temperature dependent open-circuit voltage (V_{OC}) measurements (Fig. 2), we address whether or not a crystalline layer and associated band-like CT DOS has the capability of lowering energy losses at the donor/acceptor interface. Energy losses for a donor/acceptor interface can be quantified by the difference between the room temperature qV_{OC} and E_{CT} at 0 K, a metric that we found to be 0.57 ± 0.038 eV for an ensemble of DA heterojunctions reported in the literature.[4-5] The amorphous rubrene device has an energy loss of 0.54 eV. Remarkably, the crystal device presents a difference of 0.35 eV, thereby exhibiting a reduced energy loss of 220 meV, nearly six standard deviations below the mean.

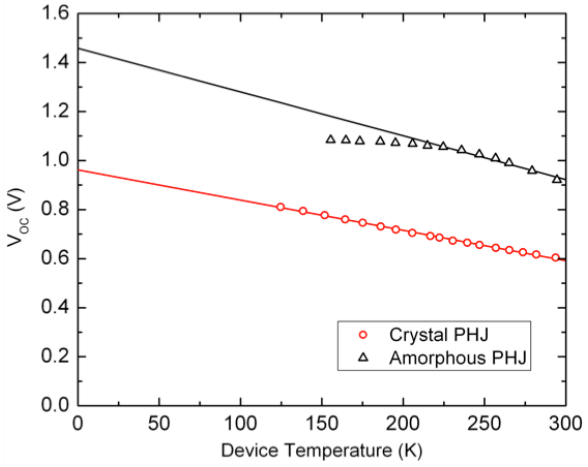

Figure 2. Temperature-dependent open-circuit voltage for the crystal and amorphous devices. Open-circuit voltage linearly increases as temperature decreases, but the amorphous device saturates below 225 K whereas the crystal one does not, even down to 125 K, indicating that charge separation occurs more easily in this device due to increased delocalization and reduced binding energy.

According to the above, the CT state DOS should be inherently dependent on the molecular structure of the DA interface, as well as by the degree of order found in the donor or the acceptor phase. By studying rubrene (Fig. 3), a combination of UPS and IPES measurements on crystalline vs. amorphous rubrene reveals a significant increase in the band gap of the amorphous film with respect to the crystalline one. This increase is carried mostly by a shift in the HOMO position with respect to the vacuum level, although some shift also appears on the LUMO position. With a higher degree of molecular packing in the crystalline phase, electronic polarization, which is typically of the order of 0.5-1 eV in molecular solids and plays a major role in defining electron and hole single particle levels,[6] is stronger than in the amorphous phase. This typically results in a reduction of the materials ionization energy and an increase in its electron affinity, thus reducing the single particle energy gap. It is unclear why the impact is stronger on the HOMO than on the LUMO for rubrene at this time. Yet, the CT state energy, which depends on the energy difference between the LUMO of the acceptor and the HOMO of the donor (rubrene in this case), should be affected by the crystallinity of the layer. Investigating the CT state manifold in crystalline vs. amorphous

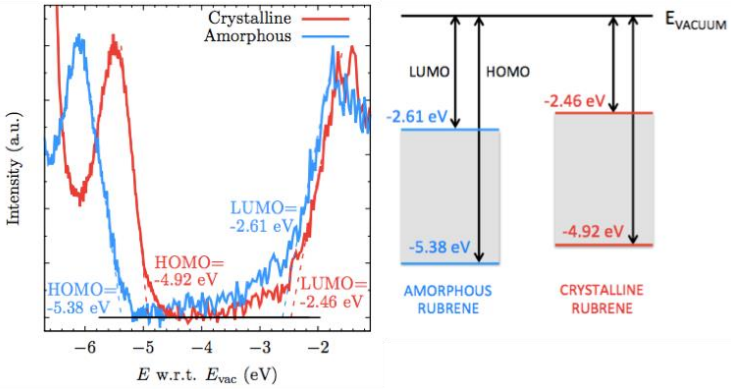

Figure 3. (left) Combined UPS and IPES spectra of the HOMO and LUMO, respectively, of crystalline vs. amorphous rubrene. The significant shift in the HOMO position reflects the decrease in ionization energy upon crystallization of the layer; (right) corresponding energy diagrams showing the ionization energy and electron affinity of the two layers.

rubrene/acceptor systems, as in Fig. 1(c), already reveals a considerable energy shift.

Future Plans

Continued research in correlating observations with differences in structural order should contribute to further unraveling correlations between CT state energy and delocalization, DA interface energetics, and materials structure. In particular, over the next year we intend to study additional donor/acceptor interfaces beyond the rubrene/C_{60} system, such as acceptors other than C_{60}, in particular a perylene compound (PTCBI) and the higher order fullerene C_{70}. As donors, we intend to study pentacene compounds (rubrene being tetracene based) as well as subphthalocyanine. To further unravel how delocalized CT states allow for lower energy losses, we will conduct electroabsorption measurements, as well as temperature dependent current-voltage, EQE, and emission measurements.

References

[1] B. Verreet, P. Heremans, A. Stesmans, B.P. Rand, "Microcrystalline organic thin film solar cells," *Adv. Mater.*, **25**, 5504-5507 (2013).

[2] (a) W. Stolz, J.C. Maan, M. Altarelli, L. Tapfer, K. Ploog, "Absorption spectroscopy on Ga 0.47 In 0.53 As/Al 0.48 In 0.52 As multi-quantum-well heterostructures. II. Subband structure," *Phys. Rev. B*, **36**, 4310-4315 (1987); (b) K.F. Mak, C. Lee, J. Hone, J. Shan, T.F. Heinz, "Atomically thin MoS_2: a new direct-gap semiconductor," *Phys. Rev. Lett.*, **105**, 136805 (2010); (c) G. Livescu, D.A.B. Miller, D.S. Chemla, M. Ramaswamy, T.Y. Chang, N. Sauer, A.C. Gossard, J.H. English, "Free carrier and many-body effects in absorption spectra of modulation-doped quantum wells," *IEEE J. of Quantum Electron.*, **24**, 1677–1689 (1988).

[3] J.K. Katahara, H.W. Hillhouse, "Quasi-Fermi level splitting and sub-bandgap absorptivity from semiconductor photoluminescence," *J. Appl. Phys.*, **116**, 173504 (2014).

[4] U. Hörmann, J. Kraus, M. Gruber, C. Schuhmair, T. Linderl, S. Grob, S. Kapfinger, K. Klein, M. Stutzman, H.J. Krenner, W. Brütting, "Quantification of energy losses in organic solar cells from temperature-dependent device characteristics," *Phys. Rev. B* **88,** 235307 (2013).

[5] T.M. Burke, S. Sweetnam, K. Vandewal, M.D. McGehee, "Beyond Langevin Recombination: How Equilibrium Between Free Carriers and Charge Transfer States Determines the Open-Circuit Voltage of Organic Solar Cells," *Adv. Energy Mater.* **5,** 1500123 (2015).

[6] I.G. Hill, A. Kahn, Z.G. Soos, R.A. Pascal Jr, "Charge-separation energy in films of π-conjugated organic molecules." *Chem. Phys. Lett.*, **327**, 181-188 (2000).

Publications from DOE-sponsored research (last 2 years)

A.N. Brigeman, M.A. Fusella, Y. Yan, G.E. Purdum, Y.-L. Loo, B.P. Rand, N.C. Giebink, "Revealing the full charge transfer state absorption spectrum of organic solar cells," *Advanced Energy Materials*, **6,** 1601001 (2016).

J. Endres, I. Pelczer, B.P. Rand, A. Kahn, "Determination of energy level alignment within an energy cascade organic solar cell," *Chemistry of Materials*, **28**, 794 (2016).

Y.L. Lin, M.A. Fusella, O.V. Kozlov, X. Lin, A. Kahn, M.S. Pshenichnikov, B.P. Rand, "Morphological tuning of the energetics in singlet fission organic solar cells," *Advanced Functional Materials*, **26**, 6489 (2016).

Y. Yan, Y. Yuan, B. Wang, V. Gopalan, N.C. Giebink, "Sub-wavelength modulation of $\chi^{(2)}$ optical nonlinearity in organic thin films," *Nature Communications*, **8**, 14269 (2017). (*partial support*)

O.V. Kozlov, F. de Haan, R.A. Kerner, B.P. Rand, D. Cheyns, M.S. Pshenichnikov, "Real-time tracking of singlet exciton diffusion in organic semiconductors," *Physical Review Letters*, **116**, 057402 (2016). (*partial support*)

N.C. Davy, G. Man, R.A. Kerner, M.A. Fusella, G. Purdum, M. Sezen, B.P. Rand, A. Kahn, Y.-L. Loo, "Contorted hexabenzocoronenes with extended heterocyclic moieties improve visible light absorption and performance in organic solar cells," *Chemistry of Materials*, **28**, 673 (2016). (*partial support*)

Charge transfer states at organic heterojunctions II: Role in energy conversion and nonlinear optics

Noel C. Giebink,[1] Barry P. Rand,[2,3] and Antoine Kahn[2]

[1] Department of Electrical Engineering, The Pennsylvania State University, University Park, PA 16802

[2] Department of Electrical Engineering, Princeton University, Princeton, NJ 08544

[3] Andlinger Center for Energy and the Environment, Princeton University, Princeton, NJ 08544

i) Program Scope

Charge transfer from a donor-type to an acceptor-type molecule forms the basis for the photovoltaic effect observed within conjugated molecular systems. The charge transfer (CT) state is a bound geminate charge pair that defines an intermediate state in both charge generation and recombination processes. As such, the CT state possesses a binding energy ($\sim 10 k_b T$) that still needs to be overcome in order to produce a free charge pair. While some important realizations have been made concerning CT states recently regarding their role in limiting open-circuit voltage, there still remains a lack of fundamental knowledge regarding what controls CT state energy and the efficiency by which they may be dissociated, and whether or not Frenkel excitons become free charge via the formation of CT states. This research program sets out to comprehensively investigate the various nanoscale environmental factors that determine CT state behavior (dielectric, structural, dynamic, and energetic), as well as to quantify their spatial extent and density of states (DOS) energetic distribution.

We will utilize sensitive spectral response measurements, impedance spectroscopy, X-ray scattering, and spectroscopic ellipsometry to probe the structure and optical response of thin films, as well as to extract dielectric properties. Surface-sensitive techniques such as ultraviolet photoelectron spectroscopy (UPS), inverse photoelectron spectroscopy (IPES), and X-ray photoelectron spectroscopy (XPS) will be utilized to probe energy levels. Finally, time-resolved and steady-state photoluminescence (PL), electroluminescence (EL), electroabsorption, and pump-probe spectroscopy measurements will be used to probe CT state energetics and dynamics. In this way, the PIs assembled in this collaborative proposal represent a complementary team uniquely suited with the ability to transform our understanding of CT states.

ii) Recent Progress

Much of the knowledge on CT state properties in current literature is based on partial fits to a weak, low-energy shoulder in the solar cell absorption spectrum that is buried beneath much stronger excitonic absorption from the pure donor and acceptor materials. This unfortunate situation increases uncertainty in the extracted parameters of the lowest energy CT state and has so far prevented observation of additional, higher energy CT states thought to play an important role in efficient photocurrent generation.

We recently addressed this challenge by introducing a simple approach to extract CT state absorption from the overlapping excitonic background by exploiting the natural alignment of CT states at a planar heterojunction (PHJ).[1] Because the CT transition dipole is predominantly oriented orthogonal to the heterojunction interface (see Fig. 1(a)), transverse magnetic (TM)-polarized light couples to the CT transition whereas transverse electric (TE)-polarized light does not. The difference between TM and TE-polarized external quantum efficiency (EQE) measurements therefore eliminates the common-mode isotropic donor and acceptor excitonic absorption to uncover the full underlying CT absorption spectrum.

Applying this method to bilayer OPV cells with C_{60} as an acceptor and a series of different donors, we found strong CT absorption anisotropy for nanocrystalline pentacene/C_{60} and microcrystalline rubrene/C_{60} that uncovered the existence of at least two different CT states in the former and a continuum CT absorption spectrum in the latter. The distinct CT absorption peaks observed for pentacene/C_{60} (see Fig. 1(a)) are tentatively assigned to different crystalline phases of pentacene at the heterojunction whereas the featureless 'step-like' spectrum identified for the highly ordered rubrene/C_{60} interface (see Fig. 1(b)) suggests the intriguing possibility of a 'band-like' continuum CT DOS.

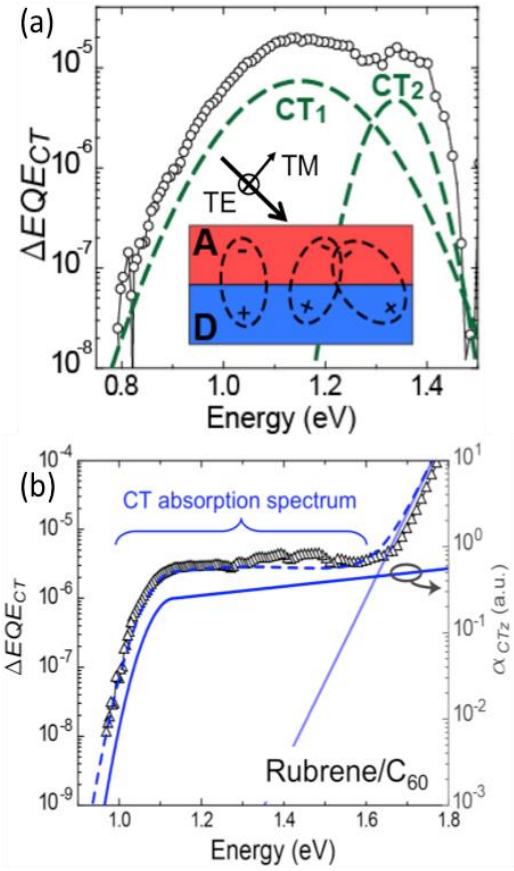

Figure 1. Difference between TM- and TE-polarized low energy EQE spectra, which in (a) reveals the existence of two distinct CT states at a nanocrystalline pentacene/C_{60} heterojunction. The inset schematically indicates the natural orientation of CT state transition dipoles orthogonal to the heterojunction interface that preferentially absorb TM-polarized light. (b) 'Step-like' CT state absorption spectrum observed in a crystalline rubrene/C_{60} bilayer OPV.

An unexpected application that emerged from our investigation of oriented CT states is the opportunity to create new organic nonlinear optical materials. A long-standing challenge in the field for organic and inorganic nonlinear optical materials alike lies in modulating the second order nonlinear optical susceptibility, $\chi^{(2)}$, at sub-micron length scales. We addressed this challenge by exploring the large hyperpolarizability (β) of intermolecular charge transfer states, naturally aligned at an organic semiconductor DA interface as described above to control the magnitude and sign of $\chi^{(2)}$ at arbitrarily short length scales.[2] The second order susceptibility in organic nonlinear optical materials depends on high dipole moment CT transitions that maximize β. These CT transitions are traditionally intramolecular in nature, driven between electron donor D and acceptor A moieties on individual molecules that are electrically poled into alignment within a glassy polymer matrix to break inversion symmetry.

However, intermolecular CT states existing at the interface between separate D and A molecules also provide a basis for achieving large β and they are naturally suited for non-centrosymmetric CT alignment by stacking donor-acceptor-spacer multilayers as shown in Fig. 2a. The ability to modulate $\chi^{(2)}$ at short periods follows from the ability to structure and reverse the DA interface orientation using standard nanofabrication techniques such as, for example, grating-shadowed oblique-angle deposition. Our recent work using the donor pentacene and acceptor C_{60} has validated this approach, demonstrating $\chi^{(2)} \approx 28$ pm/V for second harmonic generation (SHG) at a fundamental wavelength of 800 nm in composites such as that shown in Fig. 2a. Figure 2b shows the second harmonic power measured as a function of sample tilt angle for DA bilayers with 20 nm of C_{60} deposited on top of pentacene with varying thickness. As compared to either the bare C_{60} or pentacene reference films, the DA bilayers yield an approximate 6-fold increase in second harmonic power that is independent of pentacene thickness. Figure 2c displays the dependence of p-polarized second harmonic power on the polarization angle of the fundamental beam obtained for a typical bilayer tilted 45°. This polarization pattern together with the fact that the p-polarized SHG is much stronger than s-polarized SHG together suggest that the susceptibility tensor is dominated by $\chi^{(2)}_{zzz}$ as expected for pentacene/C_{60} CT transitions oriented orthogonal to the DA interface.

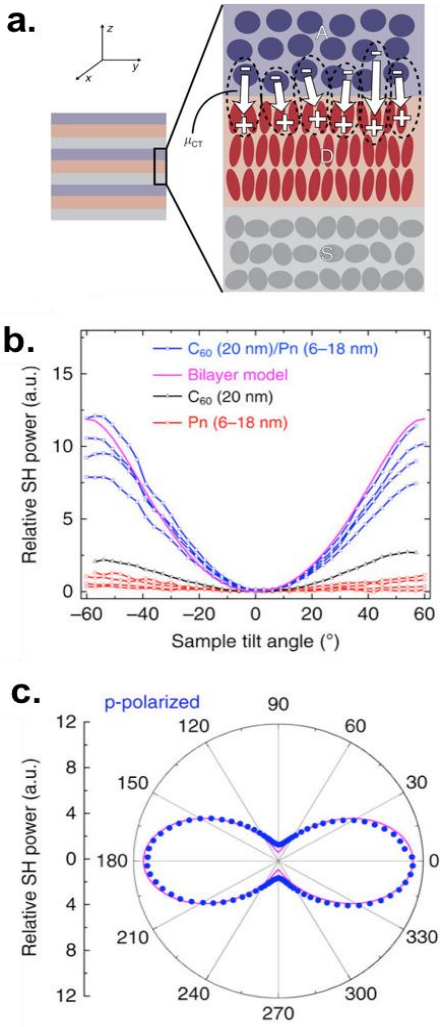

Figure 2. (a) Stacking pairs of organic semiconductor donor (D) and acceptor (A) thin films separated by insulating spacer (S) layers leads to a high density of naturally-aligned charge transfer states (white arrows), resulting in the creation of a non-centro-symmetric, $\boldsymbol{\chi^{(2)}}$ -active composite material. **(b)** Tilt scan results of p-polarized SHG from pentacene/C_{60} bilayers with fixed C_{60} and varying pentacene thickness. **(c)** Polar plot show the dependence of p-polarized SHG on pump polarization angle, consistent with $\boldsymbol{\chi^{(2)}}$ exhibiting $\boldsymbol{C_{\infty v}}$ symmetry.

To explore the possibility of modulating $\chi^{(2)}$ by reversing the CT state orientation, we constructed a series of asymmetric donor-acceptor multilayers via oblique-angle deposition on the surface of a shallow photoresist grating. By depositing the acceptor layers only on the 'windward' grating facets, it is possible to periodically vary the lateral distribution of DA interface and thus also the magnitude of $\chi^{(2)}$. Backward-wave second harmonic diffraction measurements were subsequently used to confirm $\chi^{(2)}$ modulation for grating-shadowed composites at periods of Λ=280 nm, which is the shortest period to date and could open up a new backward quasi-phase matching regime for integrated frequency conversion and nonlinear nanophotonic applications.

iii) Future Plans

Our future work is focused on moving beyond the single CT state picture of organic heterojunctions and on understanding the *distribution* of CT states, that is, the CT density of states (DOS). In particular, we are exploring the form and breadth of the CT state DOS, how it is populated in the initial charge transfer event, how CT states relax as they evolve toward dissociation or recombination, and how free carriers relax as they move toward extraction or non-geminate recombination via CT states. Relaxation will be investigated via transient CT photoluminescence spectroscopy, where initial data collected for a small molecule bulk heterojunction displays a sub-nanosecond dynamic ~80 meV red-shift marking both the time and energetic scale of CT state relaxation. Coupled with temperature-dependent steady-state CT photoluminescence, these data will be used to test our current hypothesis of CT states relaxing within the DOS toward charge separation during their lifetime, with relatively little impact from applied electric field, followed by further relaxation of the free charge carriers that do not reach a thermal equilibrium occupation of the available site energies before they are extracted at contacts or recombine non-geminately.

iv) References

[1] Brigeman, A. N., Fusella, M. A., Yan, Y., Purdum, G. E., Loo, Y.-L., Rand, B. P. & Giebink, N. C. Revealing the Full Charge Transfer State Absorption Spectrum of Organic Solar Cells. *Adv. Energy Mater.* **6**, 1601001, (2016).

[2] Yan, Y., Yuan, Y., Wang, B., Gopalan, V. & Giebink, N. C. Subwavelength modulation of chi2 optical nonlinearity in organic thin films. *Nat. Comm.* **8**, 14269, (2017).

v) Publications from DOE-sponsored research (last 2 years)

A.N. Brigeman, M.A. Fusella, Y. Yan, G.E. Purdum, Y.-L. Loo, B.P. Rand, N.C. Giebink, "Revealing the full charge transfer state absorption spectrum of organic solar cells," *Advanced Energy Materials*, **6,** 1601001 (2016).

J. Endres, I. Pelczer, B.P. Rand, A. Kahn, "Determination of energy level alignment within an energy cascade organic solar cell," *Chemistry of Materials*, **28**, 794 (2016).

Y.L. Lin, M.A. Fusella, O.V. Kozlov, X. Lin, A. Kahn, M.S. Pshenichnikov, B.P. Rand, "Morphological tuning of the energetics in singlet fission organic solar cells," *Advanced Functional Materials*, **26**, 6489 (2016).

Y. Yan, Y. Yuan, B. Wang, V. Gopalan, N.C. Giebink, "Sub-wavelength modulation of $\chi^{(2)}$ optical nonlinearity in organic thin films," *Nature Communications*, **8**, 14269 (2017). (*partial support*)

O.V. Kozlov, F. de Haan, R.A. Kerner, B.P. Rand, D. Cheyns, M.S. Pshenichnikov, "Real-time tracking of singlet exciton diffusion in organic semiconductors," *Physical Review Letters*, **116**, 057402 (2016). (*partial support*)

N.C. Davy, G. Man, R.A. Kerner, M.A. Fusella, G. Purdum, M. Sezen, B.P. Rand, A. Kahn, Y.-L. Loo, "Contorted hexabenzocoronenes with extended heterocyclic moieties improve visible light absorption and performance in organic solar cells," *Chemistry of Materials*, **28**, 673 (2016). (*partial support*)

Session V

DOE award # DE-SC0002626, Massachusetts Institute of Technology
DOE award # DE-SC0014435, Rice University

Electrochemically-Driven Phase Transitions in Battery Storage Compounds

PIs: Yet-Ming Chiang[1], Ming Tang[2], co-PI: W. Craig Carter[1]
[1]Massachusetts Institute of Technology, Dept. of Materials Science and Engineering, Cambridge, MA 02139, ychiang@mit.edu
[2]Rice University, Dept. of Materials Science and Nanoengineering, 6100 Main Street, Houston, TX 77005, mt20@rice.edu

Program Scope

Compounds of interest for ion storage in advanced batteries frequently exhibit phase transformations as the working ion concentration varies. Under large electrochemical driving forces inherent to practical use, systems are often driven far from equilibrium. This program combines experiments and theory to develop a predictive understanding of the interaction between composition, transformation strain, crystallite size and shape, and the electrochemical conditions driving the phase transition. Behavior at nanoscopic to mesoscopic scale under electrical overpotentials that vary in magnitude and with time are studied. The systems to be studied have fundamental and practical interest, and include lithium and sodium transition metal olivines, AMPO4 (A = Li, Na; M = Fe, Mn, + additives) exhibiting a wide range of transformation strains. Phase-field modeling of phase stability and transformation pathways is combined with *operando* experiments in which electrochemical titration is conducted simultaneously with structure characterization at DOE facilities. Understanding of phase transformation pathways is expected to lead to new materials design concepts, and electrochemical duty cycles, that improve capacity utilization at high charge/discharge rates, control voltage and capacity hysteresis, and improve life by reducing cycling-induced mechanical fatigue. The main questions to be addressed are:

(i) How does the magnitude of the phase transformation strain, and the magnitude of the electrochemical driving force, dictate the phase transformation pathway? Our approach takes advantage of a unique series of carefully curated olivines samples developed over more than a decade. *Operando* synchrotron X-ray diffraction, pair distribution function (PDF) analysis and high resolution TEM are used to characterize phase behavior under controlled electrochemical driving force. Phase-field and phase transformation models are used to identify transformation mechanisms and to interpret deviations from equilibrium transformation paths. Large deviations from equilibrium are found to be the rule rather than the exception.

(ii) What is the relationship between transformation strain and electrochemical performance? While it can be assumed that the rate-limiting kinetic steps and atomic species change with the transformation mechanism, it is not currently possible to predict electrochemical capacity and rate performance from basic structural knowledge. Systematic study of the olivine family makes such correlations possible for the first time.

(iii) What is the role of plasticity? While elastic response dominates at small strain while plasticity dominates at high strain, many materials of interest for energy storage fall in the middle – where strains are large enough that the elastic limit is surely exceeded, yet the parent/daughter phases remain structurally similar. The bridge between elastic and plastic response is being studied in this program experimentally and theoretically.

Recent Progress

1) Disorder as a Mechanism of Phase Transformation Strain Accommodation

Olivine $NaFePO_4$ (NFP), heretofore relatively unstudied, is of interest to this project as it is the intercalation compound (unlike silicon) with the largest volume change (17 %) across a first-order transition of any intercalation compound known to us. Over the past year, we have elucidated how strain is accommodated in NFP using a combination of experimental techniques including *operando* SR-PXD, pair distribution function (PDF) analysis as well as transmission electron microscopy (TEM). Figure 1(A) compares NFP to materials previously studied under this program. Figure 1 (B) displays *operando* SR-PXD data for a $FePO_4$/Na half-cell undergoing charge and discharge; the horizontal axis is the Na content (from 212 PXD scans).

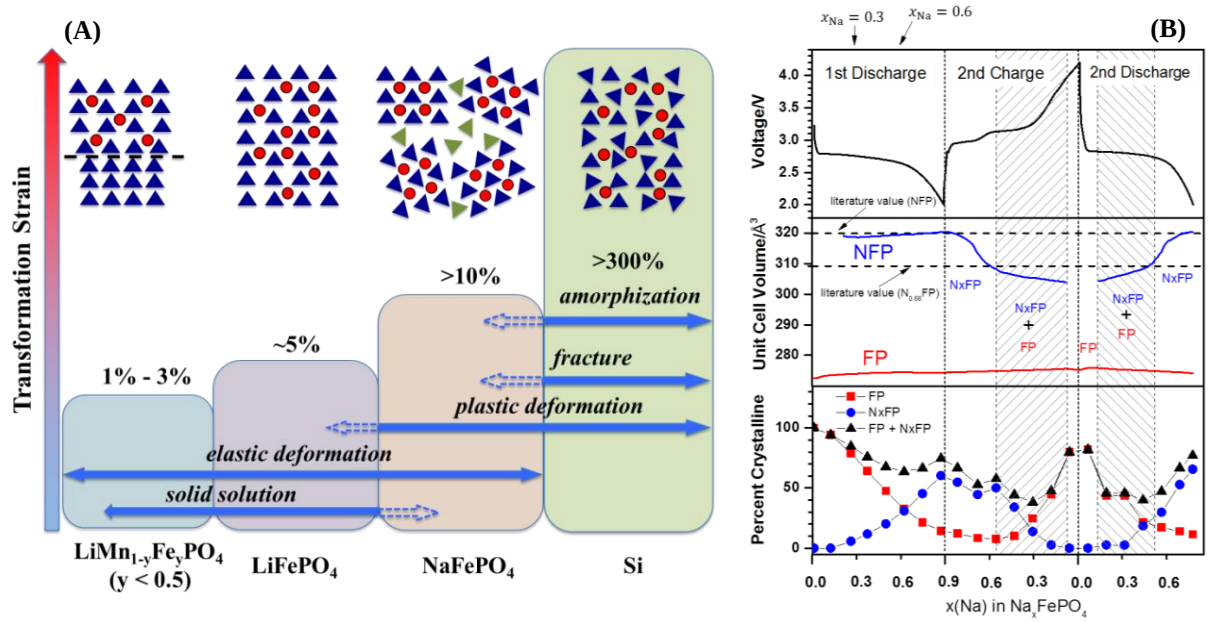

Figure 1 (A) Systems studied, corresponding transformation strains, and phase transformation behaviors observed. Voltage profile of sodium iron phosphate cell (B – upper), refined unit cell volume of observed crystalline phases (B – middle) and calculated mole percentage of crystalline phases against initial amount of crystalline FP phase (B – lower) obtained from *operando* PXD data.

During the first discharge (first Na insertion, there is 20% decrease in the total crystalline phase percentage compared to the starting FP (Figure 1 (B), lower-left). During the second charge (desodiation), further loss of crystallinity occurs, especially across the two-crystalline-phase field (the shaded region). Formation of a disordered phase is implied, but the nature of this phase is not clear from the SR-PXD results alone. Thus we used pair distribution function (PDF) analysis (with colleagues at APS) to characterize the short-range order of the newly formed disordered phase. Two-phase and three-phase structure models were tested for PDF data of samples discharged to compositions x_{Na}=0.3 and x_{Na}=0.6, respectively. A satisfactory fit could not be obtained without addition of a third, amorphous phase, which interestingly has short-range order that can be fit with two domain parameters close to those of NFP, and a third parameter close to that of FP. These results suggest a unique strain-accommodation mechanism, not previously reported, wherein an amorphous phase is formed that is able to orient topotaxially against FP or NFP, forming coherent or semicoherent interfaces.

2) Mesoscale Nucleation and Growth in Multi-Particle Assemblies

A second important question addressed in this project is how nucleation and growth proceeds in large multiparticle ensembles appropriate to battery electrodes. A large set of electrochemical data from potentiostatic (PITT) measurements for nanoscale $LiMn_yFe_{1-y}PO_4$ was obtained and analyzed by the Johnson-Mehl-Avrami-Kolmogolov (JMAK) model.[1] While the JMAK analysis has been repeatedly applied to olivine cathodes in literature[2,3], its major assumptions (infinite system, homogeneous nucleation) are not satisfied by nanoscale particles, raising question for such an exercise. Here, we showed for the first time why such analysis can be valid for nanoparticulate systems, if it occurs within a mesoscopic system of secondary particles composed of nanoscale primary particles. We show that the Avrami exponent *n* can be generally expressed as $n = a + b*c$, where parameter *a* is related to nucleation kinetics (a=0, instantaneous nucleation; a = 1, constant nucleation rate), *b* represents the growth dimensionality and *c* is controlled by phase boundary migration mechanism (diffusion- vs interface-limited). In $LiMn_yFe_{1-y}PO_4$ samples of varying Mn:Fe ratio and particle size, under different overpotentials and temperatures, we find that the Avrami exponent *n* systematically varies between 0.5 and 1.5 (Figure 2). These results lead to the following new insights:

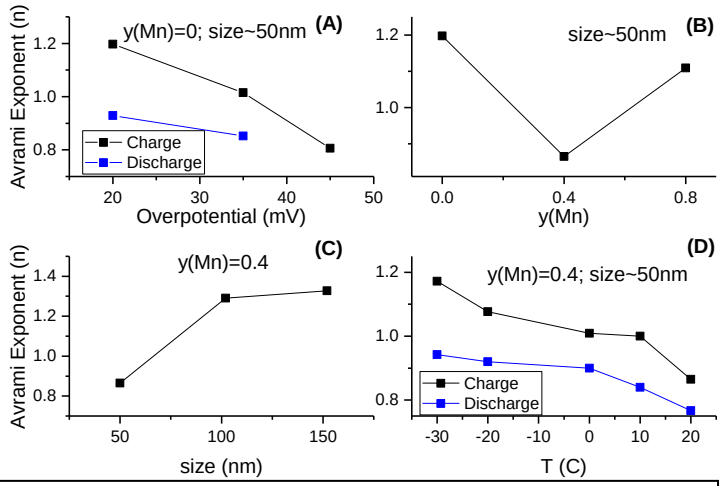

Figure 2. Effect of (A) applied overpotential, (B) Mn-content y(Mn), (C) particle size and (D) temperature on the Avrami exponent from fitting the JMAK equation to PITT measurement of nanoscale olivine $LiMn_yFe_{1-y}PO_4$.

1) Nucleation occurs through heterogeneous nucleation on two-dimensional particle surface followed by one-dimensional phase growth (i.e. b =1) into individual primary particles.
2) Phase boundary movement is controlled by Li diffusion, i.e. c = 1/2.
3) Variation of Avrami exponent indicates the variation in nucleation rate since $n = a + 1/2$ based on 1) and 2). Nucleation rate decays with time; the decay rate is directly correlated with a nucleation barrier modulated by particle size, composition, overpotential and temperature.

Complementary to the JMAK analysis is our recent discovery of a *hybrid-mode growth mechanism* during intercalation-induced phase transformations in secondary particles[4]. Delithiation of $LiFePO_4$ microrods during *operando* hard x-ray transmission microscopy (TXM) shows that growth of $FePO_4$ domains along (100)/(001) particle surface is much faster than the phase boundary movement into the particle, Fig. 3(A,B). Detailed analysis and phase-field simulation reveal that $FePO_4$ growth is governed by two distinct mechanisms along different directions: it is *surface-reaction-limited* (SRL) along [100] but bulk-diffusion-limited in the [100]/[001] direction. This observation provides the first direct confirmation of the SRL phase boundary migration mechanism, and also sheds light on how nucleation and growth may proceed in secondary particles. We propose that the SRL growth provides a deterministic mechanism for accelerating

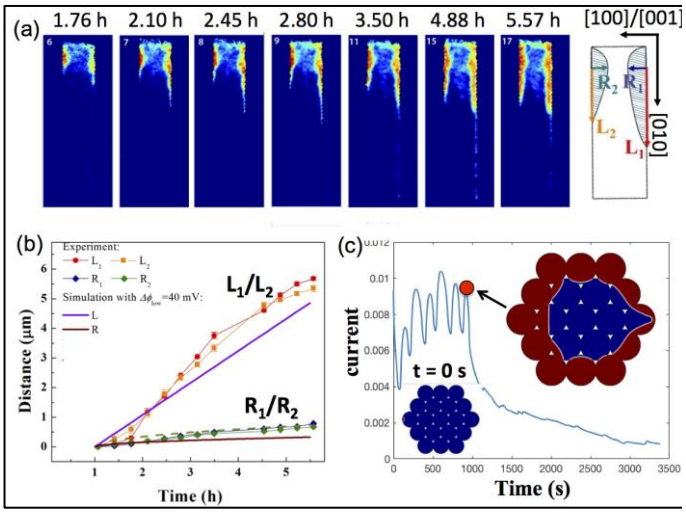

Figure 3 (a) Operando TXM chemical maps of the delithiation of a $LiFePO_4$ microrod. Red – $FePO_4$; Blue – $LiFePO_4$. (b) The [010] (square) vs [100]/[001] (diamond) dimensions of $FePO_4$ domains compared against simulation (solid lines). (c) Current vs time upon delithiation of a 200nm secondary particle from phase-field simulation.

nucleation in inter-connected primary particles as the new phase can propagate rapidly between them through SRL growth once a nucleation event occurs in one particle. Our simulation predicts that the peak current observed in potentiostatic experiments corresponds to when nearly all the primary particles in a secondary particle are "activated" by fast SRL growth and start transforming as shown in Fig. 3(C). An important implication of this prediction is that the peak current time should scale with secondary particle size, which is currently being verified.

Future Plans

We have identified several additional intercalation compounds with unusually large volume or shear strain, in which we will investigate the generality of the disordering response. It is hypothesized that such *in-situ* disordered electrodes may have attractive electrochemical properties, which will be studied in the project. *Operando* TXM experiments will be performed to directly image the nucleation and growth process in secondary particles to examine the JMAK interpretation of the PITT measurement and our model predictions. We will further extend the theoretical study of the mesoscopic nucleation and growth kinetics in electrodes to consider the effect of misfit stress. Specifically, we hypothesize that stress-induced phase boundary morphology instability will occur in single crystalline and secondary particles. Such possibility will be analyzed by theory and simulation to predict the conditions for its manifestation.

References

1. Fanfoni, M., and M. Tomellini. "The Johnson-Mehl-Avrami-Kohnogorov model: a brief review." *Il Nuovo Cimento D* **1998**, *20*, 1171.
2. Allen, Jan L., T. Richard Jow, and Jeffrey Wolfenstine. "Kinetic study of the electrochemical $FePO_4$ to $LiFePO_4$ phase transition." *Chemistry of materials* **2007**, *19*, 2108.
3. Oyama, Gosuke, Yuki Yamada, Ryuichi Natsui, Shinichi Nishimura, and Atsuo Yamada. "Kinetics of Nucleation and Growth in Two-Phase Electrochemical Reaction of Li_xFePO_4." *The Journal of Physical Chemistry C* **2012**, *116*, 7306.
4. L. Hong, L. Li, Y.-K. Chen-Wiegart, J. Wang, F. Wang, K. Xiang, L. Gan, W. Li, F. Meng, J. Wang, Y.-M. Chiang, S. Jin, M. Tang, "Two-Dimensional Li Diffusion Behavior and Hybrid Phase Transformation Kinetics in Olivine Lithium Iron Phosphate ($LiFePO_4$)", under review.

Published and Accepted Journal Publications of DOE Sponsored Research in 2015-2017

1. K. Xiang, W. Xing, D. B. Ravnsbæk, L. Hong, M. Tang, Z. Li, K. M. Wiaderek, O. J. Borkiewicz, K. W. Chapman, P. J. Chupas, Y.-M. Chiang, "Accommodating High Transformation Strains in Battery Electrodes via Formation of Nanoscale Intermediate Phases: Operando Investigation of Olivine $NaFePO_4$", *Nano Letters* **2017**, *17*, 1696. DOI: 10.1021/acs.nanolett.6b04971
2. D. B. Ravnsbaek, K. Xiang, W. Xing, O. J. Borkiewicz, K. M. Wiaderek, P. Gionet, K. W. Chapman, P. J. Chupas, M. Tang, Y.-M. Chiang, "Engineering the Transformation Strain in $LiMn_yFe_{1-y}PO_4$ Olivines for Ultrahigh Rate Battery Cathodes", *Nano Letters* **2016**, *16*, 2375. DOI: 10.1021/acs.nanolett.5b05146
3. T. Heo, M. Tang, L.-Q. Chen, B. C. Wood, "Defects, Entropy, and the Stabilization of Alternative Phase Boundary Orientations in Battery Electrode Particles", *Advanced Energy Materials* **2016**, *6*, 1501759. DOI: 10.1002/aenm.201501759
4. J. Ye, Y. An, E. Montalvo, P. G. Campbell, M. A. Worsley, I. C. Tran, Y. Liu, B. C. Wood, J. Biener, H. Jiang, M. Tang, Y. M. Wang, "Solvent-directed sol-gel assembly of 3-dimensional graphene-tented metal oxides and strong synergistic disparities in lithium storage", *Journal of Materials Chemistry* **2016**, *4*, 4032. DOI: 10.1039/C5TA10730J
5. Y. An, B. C. Wood, J. Ye, Y.-M. Chiang, Y. M. Wang, M. Tang and H. Jiang, "Mitigating mechanical failure of crystalline silicon electrodes for lithium batteries by morphological design", *Physical Chemistry Chemical Physics* **2015**, *17*, 17718. DOI: 10.1039/C5CP01385B
6. Li, B., Gong, Y. J., Hu, Z. L., Brunetto, G., Yang, Y. C., Ye, G. L., Zhang, Z. H., Lei, S. D., Jin, Z. H., Bianco, E., Zhang, X., Wang, W. P., Lou, J., Galvao, D. S., Tang, M., Yakobson, B. I., Vajtai, R., Ajayan, P. M., "Solid-Vapor Reaction Growth of Transition-Metal Dichalcogenide Monolayers", *Angewandte Chemie-International Edition* **2016**, *55*, 10656. DOI: 10.1002/ange.201604445
7. Wu, J. J., Hu, Z. L., Jin, Z. H., Lei, S. D., Guo, H., Chatterjee, K., Zhang, J., Yang, Y. C., Li, B., Liu, Y., Lai, J. W., Vajtai, R., Yakobson, B., Tang, M., Lou, J., Ajayan, P. M., "Spiral Growth of SnSe2 Crystals by Chemical Vapor Deposition." *Advanced Materials Interfaces* **2016**, *3*, 16. DOI: 10.1002/admi.201600383
8. P. Dong, A. C. Chipara, P. Loya, Y. Yang, L. Ge, S. Lei, B. Li, G. Brunetto, L. D. Machado, L. Hong, Q. Wang, B. Yang, H. Guo, E. Ringe, D. S. Galvao, R. Vajtai, M. Chipara, M. Tang, J. Lou, P. M. Ajayan, "Solid−Liquid Self-Adaptive Polymeric Composite", *ACS Applied Materials & Interfaces* **2016**, *8*, 2142. DOI: 10.1021/acsami.5b10667

Title: Thermodynamic, Kinetic and Electrochemical Studies on Mixed Proton, Oxygen Ion and Electron (Hole) Conductors

PI: Anil V. Virkar, University of Utah

Program Scope

The principal objective of the project is to investigate multi-species transport in predominantly ionic conductors which have applications in fuel cells, electrolyzers, oxygen separators, hydrogen separators, and in sodium and lithium batteries. Much of the literature is focused on transport properties (e.g. conductivities) of such materials or charge transfer at electrode/electrolyte interfaces. In predominantly ionic conductors, focus has been on ionic conductivity, effects of which are easily measureable – e.g. current flowing through a device or electrocatalytic activity of electrodes. Local thermodynamic equilibrium (even when a system is away from thermodynamic equilibrium), however, determines stability [1-3]. Stability is governed by chemical potentials of electrically neutral species. Thus, local thermodynamic equilibrium in an oxygen ion conductor is primarily dictated by the chemical potential of neutral oxygen, μ_{O_2}; that in a proton conductor by μ_{H_2}; that in a lithium ion conductor by μ_{Li}, etc. Concepts from non-equilibrium thermodynamics lead to an important result which shows that even in a predominantly ionic conductor, the electronic conductivity, no matter how small, cannot be ignored since it has a profound effect on local equilibrium [4-6]. Thus, to investigate multi-species transport, electronic transport must be included in the general equations of transport [5-8]. In the relevant mathematical formulas, the electronic conductivity can be allowed to approach zero only in an asymptotic limit. Solution to multi-species coupled transport equations leads to one very general and a very important result: (a) If ionic (e.g. O^{2-}) and *electronic* (no matter how small) currents through an *electrolyte* (e.g. zirconia) are *anti-parallel* (current defined in the usual sense as coulomb.s^{-1} – so if electrons are moving along positive 'x', the corresponding positive current is flowing along '-x'; etc.), chemical potential of the corresponding neutral species (e.g. μ_{O_2}) is mathematically bounded by the electrode values. (2) If ionic and electronic currents through an electrolyte are *parallel,* chemical potential of the corresponding neutral species need not be mathematically bounded by electrode values. If the chemical potential becomes too high or too low, the electrolyte can degrade/fail [6-9]. The former is the galvanic mode. The latter is the electrolytic mode. For these reasons, electrochemical devices exhibit greater tendency to degradation in the electrolytic mode. Experimental evidence [10,11] of this behavior has been reported in the literature, which confirms our theoretical predictions [5-8]. The origin of this result lies in non-equilibrium thermodynamics and Onsager coupling. The focus of our work is on predominantly oxygen ion conductors, proton conductors, and monovalent cation conductors and their properties when removed from thermodynamic equilibrium.

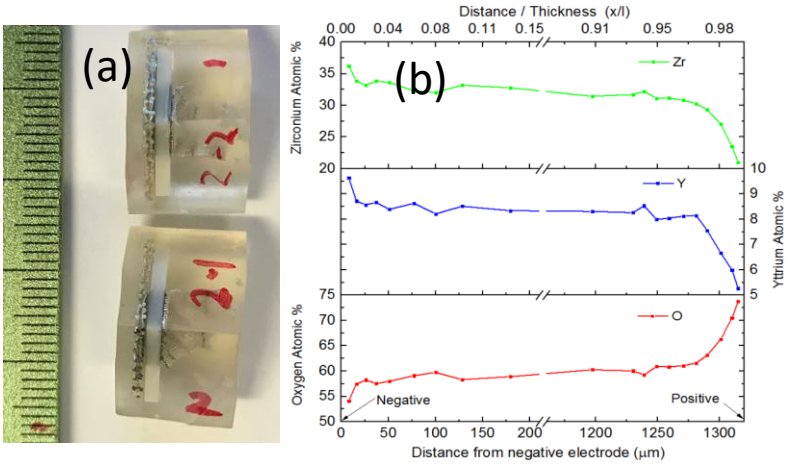

Figure 1: (a) Two cut halves of the sample after electrochemical tests. (b) Concentrations of O, Y and Zr from the negative electrode (left) to the positive electrode (right) through the YSZ disc. The initial concentration of O was uniform ~60%. After transport, O concentration has increased to ~72% (right) and decreased to ~54% (left). Y and Zr concentrations have changed accordingly. This shows that the defect chemistry is vastly changed.

Recent Progress

Recent work has been on the following topics: **(1)** Synthesis of oxygen ion conductors removed from thermodynamic equilibrium to create new defect chemistries. Figure 1(a) shows cross-sections (two halves mounted in plastic molds) of a yttria-stabilized zirconia (YSZ) disc with Sr-doped $LaMnO_3$ (LSM) + Gd_2O_3-doped CeO_2 (GDC) electrodes tested at 700°C in air at a fixed DC current of 0.2 A for 24 h. Figure 1(b) shows EDS plots of oxygen, yttrium and zirconium concentrations across the YSZ disc after electrochemical tests. This testing is in electrolytic mode where O^{2-} ion and electron/hole currents through YSZ are *parallel*. The EDS map shows that under the positive electrode, oxygen concentration increased from the initial ~60% to ~72% (these are approximate numbers, especially the value of ~72%, and only indicate trends – absolute numbers will need to be verified with additional tests). Just under the negative electrode, oxygen concentration decreased to ~54% from the initial ~60%. The Y and Zr concentrations have proportionately changed consistent with the local stoichiometry, which is now position dependent. These are remarkable results and in agreement with our theoretical predictions [5-8]. Since oxygen partial pressure in the atmosphere is ~0.21 atm, this means the chemical potential of oxygen in YSZ, just under the electrodes, has exceeded electrode bounds. By this electrolytic process, we have created a YSZ with negligible oxygen vacancy concentration under the positive electrode, and a very high oxygen vacancy concentration under the negative electrode. This also means p-type conductivity under positive electrode and n-type under negative electrode. **(2)** A novel method for measuring the electronic conductivity of predominantly ionic conductors. Most of the measurements reported to date use the Hebb-Wagner polarization method using blocking electrodes [12]. However, this creates stoichiometric changes and it is difficult to estimate the electronic conductivity as a function of p_{O_2} or μ_{O_2} (it is deduced by fitting to a model, but is not an absolute measurement). We have developed a novel technique based on an embedded probe. We have measured electronic conductivity of YSZ using this approach. **(3)** Measurement of local thermodynamics in an oxygen ion conductor. We have fabricated YSZ discs with two embedded screen electrodes and two surface electrodes. By electrochemically pumping oxygen out, a nonstoichiometric YSZ was made. With embedded probes, local electrochemical potential of electrons, $\tilde{\mu}_e$ was measured. This allowed the measurement of oxygen chemical potential as a function of position, $\mu_{O_2}(x)$. **(4)** Determination

of electrode polarization resistance by electrochemical impedance spectroscopy is usually not possible on a full cell due to overlapping spectra. We are investigating embedded screen probes (sputter-deposited gold) to separately measure cathode and anode polarizations of proton exchange membrane fuel cells (PEMFC). **(5)** We have developed a DC method to investigate the ionic conductivity and the electrode polarization resistance. Using this approach, we have measured the polarization resistance of Pt on YSZ in air at a temperature as low as 270^{o}C. The DC measurement avoids the uncertainties associated with the interpretation of electrochemical impedance spectra (EIS) using frequency dependent circuit elements which include empirical fitting parameters. **(6)** Spray pyrolysis method for depositing nanosize cathodes on electrolytes. These cathodes have a particle size from ~5 to ~20 nm. The deposited cathode is well-bonded to the electrolyte surface. This allows one to minimize the electrode thickness (lowering concentration polarization) while maintaining high electrocatalytic activity. **(7)** We have made potentiometric measurements at room temperature using YSZ-based sensors. This is made possible using a very high impedance meter (an input impedance > 200 TΩ). The results showed that partial pressure of oxygen could be measured in H_2-H_2O mixtures at room temperature. The measured values showed that H_2-H_2O equilibrium had not reached. This approach should allow the measurement of catalytic activity of many catalysts at rather low temperatures.

Future Plans

1) To theoretically explore coupled transport in cation and anion conductors, and in single phase and multi-phase conductors. It is generally difficult to realize multi-species transport in a single phase material. However, if one can fabricate multi-phase materials transporting different ions, on a global scale one can still use linear non-equilibrium thermodynamics (Onsager coupling). We will theoretically and experimentally explore mixed cation and anion conductors; examples include Na^+ and O^{2-} ion conductors as well as Li^+ and O^{2-} ion conductors.
2) To synthesize ion conducting materials with dopants added to slightly increase the electronic (electron) conductivity. In predominantly ionic conductors a small increase in electron concentration corresponds to a relatively large increase in the chemical potential of electrons. This leads to a significant lowering of the oxygen chemical potential, thus increasing stability. We will investigate properties of materials removed from thermodynamic equilibrium and specifically study changes in defect chemistry.
3) To measure local thermodynamics of ionic conductors using embedded probes.

References

1) D. Kondepudi and I. Prigogine, 'Modern Thermodynamics: From Heat Engines to Dissipative Structures', John Wiley, New York (1998).
2) S. Kjelstrup and D. Bedeaux, 'Non-Equilibrium Thermodynamics of Heterogeneous Systems', World Scientific, (2008).
3) R. Haase, 'Thermodynamics of Irreversible Processes', Dover Publications, (1990).
4) A. V. Virkar, *J. Electrochem. Soc*., **138** (5) 1481-1487 (1991).
5) A. V. Virkar, *J. Power Sources*, **147** 8-31 (2005).
6) A. V. Virkar, *Int. J. Hyd. Energy*, **35** 9527-9543 (2010).

7) A. V. Virkar, *J. Power Sources*, **196** 5970-5984 (2011).
8) A. V. Virkar, *Int. J. Hyd. Energy*, **37** 12609-12628 (2012).
9) A. V. Virkar, in 'Engineered Ceramics: Current Status and Future Prospects', edited T. Ohji and M. Singh, p. 59-76, Wiley-Am. Ceramic Soc. (2016).
10) M. A. Laguna-Bercero, R. Campana, A. Larrea, J. A. Kilner, and V. M. Orera, *J. Power Sources*, **196** 8942-8947 (2011).
11) J. R. Mawdsley, J. D. Carter, A. J. Kropf, B. Yildiz, and V. A. Maroni, *Int. J. Hyd. Energy*, **34** 4198-4207 (2009).
12) M. H. Hebb, *J. Chem. Phys*. **20** (1) 185-190 (1952).

Publications

1) L. Zhu, L. Zhang and A. V. Virkar, 'A parametric model for solid oxide fuel cells based on measurements made on cell materials and components', *J. Power Sources*, **291** 138-155 (2015). http://dx.doi.org/10.1016/j.jpowsour.2015.04.155

2) L. Zhu, L. Zhang and A. V. Virkar, 'Measurement of ionic and electronic conductivities of yttria-stabilized zirconia by an embedded electrode method', *J. Electrochem. Soc*., **162** (3) F298-F309 (2015). http://dx.doi.org/10.1149/2.0691503jes

3) A. V. Virkar and G. Tao, 'Reversible high temperature cells for power generation and hydrogen production using mixed ionic electronic conducting solid electrolytes', *Int. J. Hyd. Energy*, **40** 5561-5577 (2015). http://dx.doi.org/10.1016/j.jhydene.2015.02.086

4) A. Szendrei, T. D. Sparks and A. V. Virkar, 'Use of yttria-stabilized zirconia for potentiometric measurements at low temperatures', *J. Electrochem. Soc.*, **163** (5) F416-F420 (2016). http://dx.doi.org/10.1149/2.0891605jes

5) L. Zhang, L. Zhu and A. V. Virkar, 'Electronic conductivity measurements of yttria-stabilized zirconia solid electrolytes by a transient technique', *J. Power Sources*, **302** 98-106 (2016). http://dx.doi.org/10.1016/j.jpowsour.2015.10.026

6) L. Zhang, L. Zhu, and A. V. Virkar, 'Nanostructured cathodes for solid oxide fuel cells by a solution spray process', *J. Electrochem. Soc*., **163** (13) F1358-F1365 (2016). http://dx.doi.org/10.1149/2.054163jes

7) L. Zhu, L. Zhang and A. V. Virkar, 'Electroreduction of Zirconia Using Embedded Electrodes', *J. Electrochem. Soc*., **163** (7) F714-F718 (2016). http://dx.doi.org/10.1149/2.1351607jes

Properties, Electrochemical Activity, and Stability of Solid Oxide Cell Materials Under Extreme Conditions

S.A. Barnett
Northwestern University

Program Scope

This project focuses on reversible solid oxide cells (ReSOCs), a technology that can store electricity with high efficiency, reasonable cost, and high storage capacity, and can also be used for renewable (CO_2-neutral) fuel production. A key question is how to make ReSOC electrode materials that provide the requisite performance and efficiency, while at the same time keeping degradation rates very low. Although this is a practical engineering consideration, it motivates fundamental scientific questions about the properties and durability of electrode materials under extreme conditions. Thus, this project aims to develop a comprehensive understanding and mechanistic modeling of ReSOC electrode characteristics and degradation mechanisms. Various effects that contribute to degradation during cell operation will be studied, including particle coarsening, surface segregation, and the extremely high effective oxygen pressures that are present during electrolysis operation. The resulting in-depth understanding of electrode performance and degradation will provide a basis for developing improved materials, and for choosing cell operating conditions that yield desired efficiency and long-term durability.

Recent Progress

The operation of solid oxide cells in electrolysis or reversing-current modes can cause rapid degradation, apparently due to the extremely high effective oxygen pressures that develop at the electrode/electrolyte interface under these conditions. Prior work has focused on the widely used perovskite-oxide (La,Sr)$MnO_{3-\delta}$ and $(La_{0.6}Sr_{0.4})(Co_{0.8}Fe_{0.2})O_{3-\delta}$ (LSCF) oxygen electrodes with typical micron-scale microstructures. There has been no work reported to date on the durability of electrodes with alternate compositions or microstructures. We have studied electrodes based on $La_2NiO_{4+\delta}$ (LNO), a mixed ionically- and electronically-conducting (MIEC) material with the Ruddlesden-Popper structure. The electrodes are formed by infiltration into a $(La_{0.9}Sr_{0.1})(Ga_{0.8}Mg_{0.2})O_{3-\delta}$ (LSGM) scaffold, resulting in an LNO-LSGM composite with nano-scale structure, quite different than the prior micron-scale electrodes. Figure 1 shows the cell resistance measured by impedance spectroscopy versus time for symmetric LNO|LSGM|LNO cells during current-switching life tests (current direction switched abruptly every 6 h) carried out at 1.0 and 2.0 $A \cdot cm^{-2}$. The 1.0 $A \cdot cm^{-2}$ test showed a relatively low resistance degradation of ~ 2.5%/kh. Note that it has been consistently difficult to obtain such low degradation rates at these current densities in prior reports, so these electrodes are quite promising. The degradation is perhaps not related to the cell current/overpotential, but rather to the coarsening or Sr surface segregation effects that we have observed previously. At the higher current density (2.0 $A \cdot cm^{-2}$), the

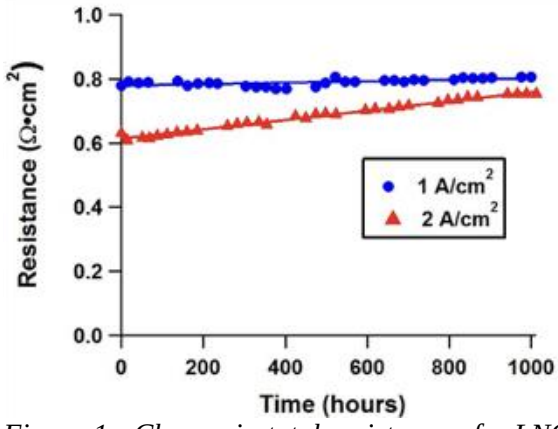

Figure 1. Change in total resistance of a LNO / LSGM / LNO cell during life tests at 650 °C in air at different current densities. Current direction was switched every 6 hours during the test.

degradation rate is ~ 10x higher, prohibitively fast, apparently due to the high effective oxygen potentials under these conditions.

There has been considerable controversy over the effects of atomic-layer deposition (ALD) layers on MIEC oxygen electrodes. Initial reports showed remarkable improvements in performance and long-term stability, but more recently showed that ALD layers can actually hurt performance without benefiting stability. We have studied the effect of ALD ZrO_2 layers on MIEC electrode performance and durability. The results show that 5 or 10 nm thick ZrO_2 layers on infiltrated $(Sm_{0.5}Sr_{0.5})CoO_{3-\delta}$ (SSC) electrodes reduce the initial resistance slightly, and also reduce the degradation rate compared to un-coated SSC (see our prior report), although the effects were not as pronounced as in the initial report. The as-deposited ZrO_2 layer is clearly visible on the SSC surfaces in TEM-EDS measurements, as shown in Figure 2. After ageing for 1500 h at 750C, however, no ZrO_2 layer was visible either by TEM, and EDS measurements showed Zr throughout the nanoparticles. x-ray diffraction measurements indicated that a new phase, $SrZrO_3$, had formed. Furthermore, the amount of segregated Sr present on the SSC surfaces was substantially decreased. These results suggest a surprising new explanation for the effect of ALD ZrO_2 on MIEC electrodes – it appears that the zirconia consumes excess surface Sr in forming the zirconate phase, leaving a pristine SSC surface that can readily exchange oxygen with the gas phase. Apparently, the zirconate phase forms isolated islands that do not block oxygen surface exchange.

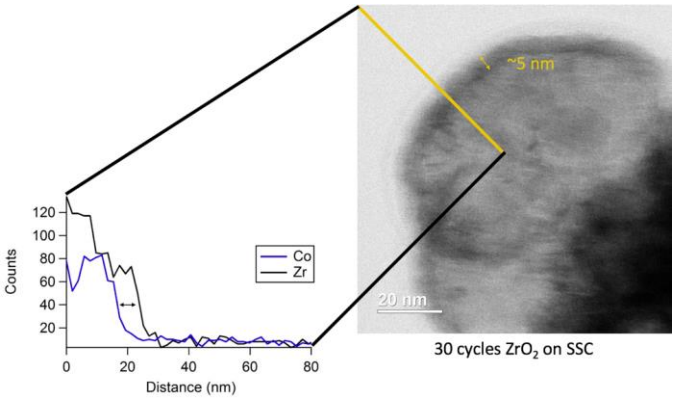

Figure 2. TEM image and EDS line scan showing an ~ 5 nm thick ZrO_2 layer on SSC, prior to ageing.

Our other work has focused on novel conducting-oxide fuel electrodes. Research on oxide fuel electrodes has been underway in many groups for many years, with the aim of replacing the widely-used Ni-YSZ cermet electrodes that have problems with redox cycling, long-term stability, impurity tolerance, and ability to work with hydrocarbon fuels. However, it is only now that our $Sr(Ti,Fe)O_3$ (STF) based electrodes have achieved electrochemical performance that matches Ni-YSZ, as illustrated in Figure 3. STF itself has a somewhat higher resistance than Ni-YSZ, especially at lower temperature. However, the substitution of a small amount of Ni for Fe in STF, producing an oxide with the composition $Sr_{0.95}(Ti_{0.3}Fe_{0.63}Ni_{0.07})O_{3-\delta}$ (STFN), results in resistance as good or better than Ni-YSZ.

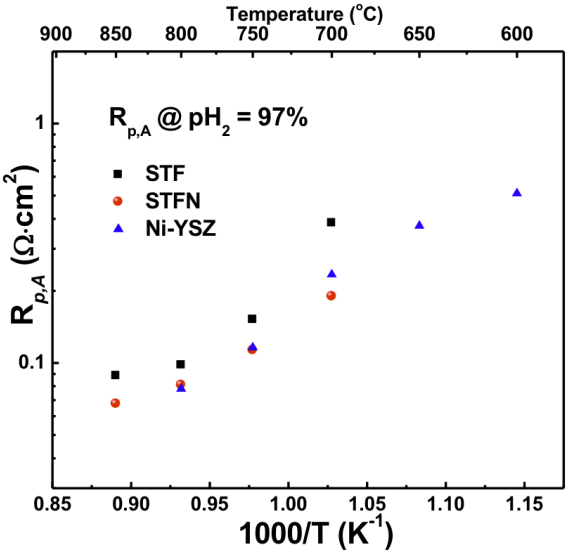

Figure 3. Anode polarization resistances for the STF and STFN anode cells compared with Ni-YSZ anode cell, measured at p_{H_2} = 97%, plotted versus temperature.

While this result has undeniable technological significance, there are also very

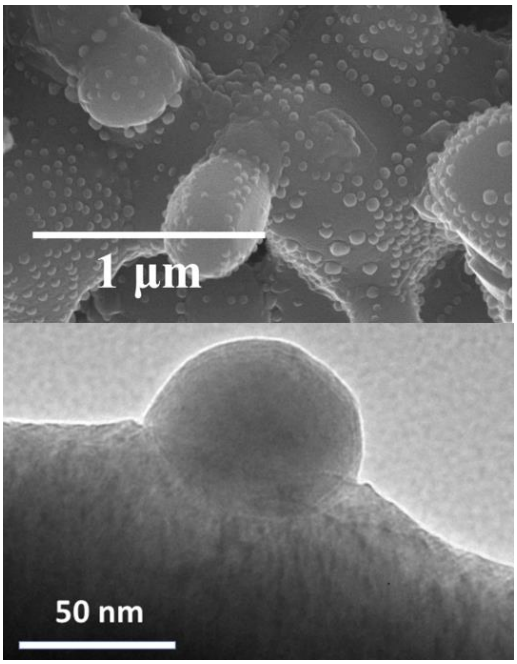

Figure 4. (top) SEM image of the $Sr_{0.95}(Ti_{0.3}Fe_{0.63}Ni_{0.07})O_{3-\delta}$ (STFN) anode microstructure after fuel cell operation. (bottom) TEM image of one of the Ni-Fe alloy nanoparticles have formed on the oxide surface.

interesting basic materials issues related to how the nano-structure in these electrodes develops *in situ* during cell operation, and how this impacts the rate-limiting electrochemical and surface processes. This spontaneous nano-structuring, originally discovered by our group under DoE-BES funding, has recently become a hot topic, with several groups reporting electrodes showing this phenomenon. Figure 4 shows an illustration of the STFN electrode porous structure after fuel cell operation, with the spontaneously-formed nanoparticles decorating the surface. The higher magnification TEM view of an individual particle in Figure 4 shows that it is embedded in the oxide surface, and chemical analysis shows that it is a Ni-Fe alloy.

Figure 5 shows the profound impact the nanoparticles have on the electrode performance. The current-voltage curves show an increase in the solid oxide fuel cell current density, measured at a typical operating voltage of 0.7 V, by a factor of > 3x. There is a corresponding decrease in the electrode resistance by a factor of > 3x, as seen in the impedance spectroscopy data shown in the inset in Figure 5. We have explained the pronounced nanoparticle effect based on an electrochemical model where the fuel (hydrogen) oxidation process is limited by one of two key steps: hydrogen dissociative adsorption or charge transfer. In our prior study of purely oxide electrodes such as STF, the absence of catalytic metal nanoparticles makes adsorption the slow rate-limiting step, especially at low temperature and low hydrogen partial pressure. The addition of metal nanoparticles that promote adsorption, presumably followed by "spillover" of the hydrogen atoms from the metal onto the oxide surface, eliminates this as a rate-limiting step yielding the substantial improvements shown in Figure 5.

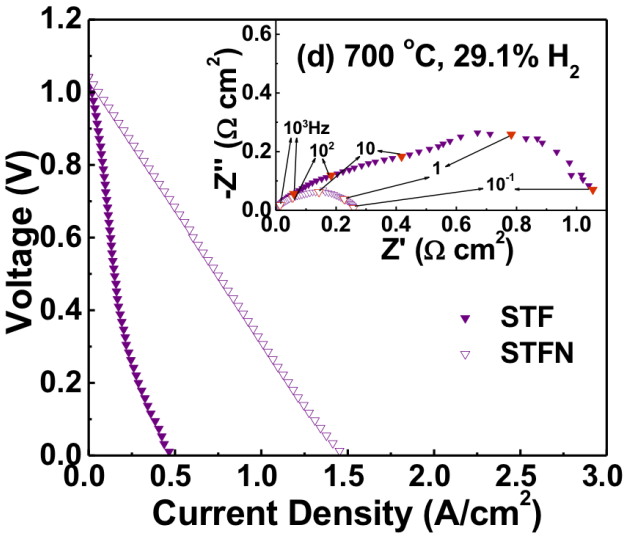

Figure 5. A comparison of j-V curves and EIS data from cells with STF and STFN anodes, measured at 700 °C in 29% humidified hydrogen.

Future Plans

Future work will investigate the basic physical properties and transport kinetics of relevant materials under normal to extreme conditions, probed utilizing pressurization and/or applied electrochemical potentials. The thesis is that an improved understanding will allow "tuning" of properties for use in devices operating under various conditions. This will ultimately allow selection and

development of materials and structures that can achieve the requisite performance and durability in different applications. A main emphasis will be on measurements, *e.g.,* x-ray diffraction and impedance spectroscopy, done under cell operating conditions (*i.e.,* with applied current/potential) on materials in nano-scale electrodes.

Publications

1. Nenning, A., Volgger, L., Miller, E., Mogni, L. V., Barnett, S. & Fleig, J. r. The Electrochemical Properties of Sr(Ti,Fe)O3-δ for Anodes in Solid Oxide Fuel Cells. *Journal of The Electrochemical Society* **164**, F364-F371, doi:10.1149/2.1271704jes (2017). *Partial support by DoE.*
2. Gao, Z., Wang, H., Miller, E. C., Liu, Q., Senn, D. & Barnett, S. A. Tape Casting of High-Performance Low-Temperature Solid Oxide Cells with Thin La0.8Sr0.2Ga0.8Mg0.2O3-delta Electrolytes and Impregnated Nano Anodes. *ACS Appl Mater Interfaces*, doi:10.1021/acsami.6b15224 (2017). *Partial support by DoE.*
3. Duffy, P. K., Beal, R. A., Layton, C. E., Barnett, S. A. & Mason, T. O. Solubility limits and LaGaO3 compatibility in the LaO1.5-GaO1.5-NiO ternary system. *Journal of the American Ceramic Society* **00**, 1-7, doi:10.1111/jace.14702 (2017). *Full DoE support.*
4. Zenou, V. Y., Fowler, D. E., Gautier, R., Barnett, S. A., Poeppelmeier, K. R. & Marks, L. D. Redox and phase behavior of Pd-substituted (La,Sr)CrO3 perovskite solid oxide fuel cell anodes. *Solid State Ionics* **296**, 90-105, doi:10.1016/j.ssi.2016.09.006 (2016). *Full DoE support.*
5. Zhu, T., Fowler, D. E., Poeppelmeier, K. R., Han, M. & Barnett, S. A. Hydrogen Oxidation Mechanisms on Perovskite Solid Oxide Fuel Cell Anodes. *Journal of The Electrochemical Society* **163**, F952-F961, doi:10.1149/2.1321608jes (2016). *Full DoE support.*
6. Duffy, P. K., Barnett, S. A. & Mason, T. O. A Hemispherical Electrolyte Probe for Screening of Solid Oxide Fuel Cell Cathode Materials. *Journal of The Electrochemical Society* **163**, F802-F807, doi:10.1149/2.0341608jes (2016). *Full DoE Support*
7. Wang, H., Yakal-Kremski, K. J., Yeh, T., Rupp, G. M., Limbeck, A., Fleig, J. & Barnett, S. A. Mechanisms of Performance Degradation of (La,Sr)(Co,Fe)O3-δ Solid Oxide Fuel Cell Cathodes. *Journal of The Electrochemical Society* **163**, F581-F585, doi:10.1149/2.0031607jes (2016). *Main support by DoE.*
8. Kennouche, D., Chen-Wiegart, Y.-c. K., Yakal-Kremski, K. J., Wang, J., Gibbs, J. W., Voorhees, P. W. & Barnett, S. A. Observing the microstructural evolution of Ni-Yttria-stabilized zirconia solid oxide fuel cell anodes. *Acta Materialia* **103**, 204-210, doi:10.1016/j.actamat.2015.09.055 (2016). *Partial support by DoE.*
9. Call, A. V., Railsback, J. G., Wang, H. & Barnett, S. A. Degradation of nano-scale cathodes: a new paradigm for selecting low-temperature solid oxide cell materials. *Physical chemistry chemical physics : PCCP* **18**, 13216-13222, doi:10.1039/c6cp02590k (2016). *Main support by DoE.*
10. Gao, Z., Mogni, L. V., Miller, E. C., Railsback, J. G. & Barnett, S. A Perspective On Low-Temperature Solid Oxide Fuel Cells. *Energy & Environmental Science*, doi:10.1039/C5EE03858H (2016). *Main support by DoE.*

Complex Hydrides – A New Frontier for Future Energy Applications

Vitalij K. Pecharsky, Duane D. Johnson, Marek Pruski, L. Scott Chumbley
Ames Laboratory, Iowa State University, Ames, IA 50011-3020, vitkp@ameslab.gov

Program Scope

Hydrogen storage is one of the critical enabling technologies that, when fully developed, is expected to support a gradual transition from internal combustion to much more efficient fuel cell-based power plants in transportation. Although liquid hydrogen is a well-known rocket fuel and it also powers large, stationary fuel cells generating electricity, a real breakthrough would be a broad use of hydrogen as an energy carrier by consumers. Transformative hydrogen storage technology must, however, overcome a number of challenges related to limited space and safety. This program addresses the basic science needs and carries out fundamental research focusing on *materials relevant to hydrogen storage*, which by far is the most viable method known or conceived that can potentially achieve both the volumetric and gravimetric energy density targets set for the year 2020 and beyond [1].

The program is focused on refining, expanding and creating knowledge while addressing materials science issues related to hydrogen rich solids. Our approach has evolved over the years, and utilizes a *unique capability to synthesize and process a range of materials by solvent-free mechanochemistry*, most importantly, under high gas pressures. Synthesis and processing are combined with the state-of-the-art solid-state nuclear magnetic resonance spectroscopy (SS NMR) and other analytical techniques for characterization. A fully validated computational modeling integrated with experiment provides much-needed insights and understanding of the experimentally observed chemical transformations and related phenomena, and in turn, guides the experiments. At the most basic level, the program provides atom and microstructure level understanding of interactions of hydrogen with metals, metalloids, non-metals, and their derivatives. This approach ultimately establishes the (i) underlying reaction mechanisms and pathways, (ii) nature of intermediates, (iii) role of dopants and catalysts and (iv) effects of nanostructuring, confinement and surfaces, all of which are the key components for tailoring kinetic and thermodynamic proprieties, and hydrogen cycling/reversibility in existing and novel solids Another outcome of the project is the continuing development of new synthesis methods, real-time characterization capabilities, and identification of future research needs to accelerate development of new functional materials for hydrogen storage and beyond.

Recent Progress

Alkali metal monohydrides, AH (A = Li, Na, K, Rb, and Cs) were synthesized in quantitative yields at room temperature by reactive mechanochemistry directly from alkali metals under hydrogen gas at 200 bar or less. This newly developed mechanochemical approach eliminates problems associated with the malleability of alkali metals – especially Li, Na, and K – and promotes effective solid-gas reactions, ensuring their completion and, therefore, quantitative yields. This is achieved by incorporating a certain volume fraction of the corresponding hydride powder as a process control agent, which promotes continuous and efficient processing primarily by coating the surface of metal particles, effectively blocking cold welding. Formation of high-purity crystalline monohydrides has been confirmed by X-ray powder diffraction in all cases

(Fig.1 a), by volumetric analyses of reactively desorbed H_2 from as-milled samples (Fig.1b), and SS NMR spectroscopy for LiH (not shown). The proposed synthesis method is scalable and particularly effective for extremely air-sensitive materials, such as alkali and alkaline earth metal hydrides.

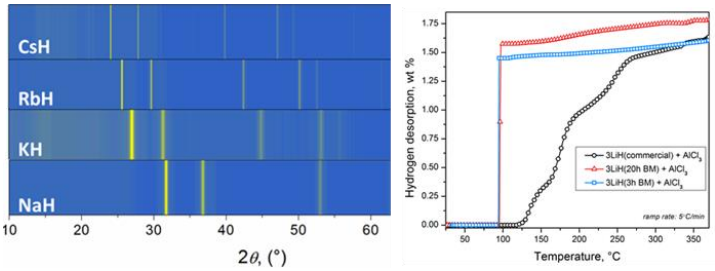

Figure 1(a). X-ray diffraction patterns of as-synthesized AH, and (b) reactive desorption of as-synthesized LiH.

Continuing our work on synthesis of alane, solvent-free mechanochemical metathesis in the $3NaAlH_4$-$AlCl_3$ system has been investigated in detail, showing important differences between this and the $3LiAlH_4$-$AlCl_3$ system. Although both reactions quantitatively yield adduct-free alane (AlH_3) plus the corresponding alkali metal chloride (NaCl or LiCl) byproducts, the reaction proceeds to form alane at *nearly half the critical pressure* required for $3LiAlH_4$-$AlCl_3$ system. We note that under ambient pressure at room temperature, the 3:1 molar mixtures of Li or Na alanate and $AlCl_3$ yield mostly elemental Al and only 30-40 % of alane [2]. The reaction pathway leading to elemental Al can be fully suppressed when a gas pressure above a certain system-specific critical value is applied, which in case of $3NaAlH_4$-$AlCl_3$ is ca. 110 bar.

The time sampled X-ray diffraction analysis suggests that the reaction proceeds via formation of $NaAlCl_4$ during the early stages of reaction, which is analogous to the $LiAlCl_4$ seen in case of $LiAlH_4$. In contrast, a new set of Bragg peaks emerges after about 20 min of milling which clearly indicate a new intermediate not seen in $3LiAlH_4$-$AlCl_3$. Milling beyond 20 min leads to consumption of this new phase and appearance of alane and NaCl. Examination of the reaction pathway studied by x-ray diffraction of products obtained from reactions performed at various stoichiometries shows that the new phase forms predominantly in a reaction mixture in which the molar ratio of $NaAlH_4$ and $AlCl_3$ is close to 1:1. While the complete structural characterization of the phase is ongoing, *a fully quantitative SSNMR approach has been developed* and employed to further establish the composition and local chemical environments of the two quadrupolar nuclei – sodium and aluminum – in the structure.

High-resolution SSNMR studies of metal-hydride systems mostly rely on spectra of half-integer quadrupolar nuclei (*e.g.*, ^{27}Al or ^{23}Na). The quantitative analysis of such spectra is generally complicated by the superposition of powder patterns arising from the central and satellite transitions of each species [3]. Moreover, the (de)hydrogenation products associated with these systems typically involve multiple species with overlapping NMR signals. Compounding the issue of resolution further is the lack of suitable reference materials for many such species. In our recent work, we evaluated, with respect to metal-hydride systems, several possible strategies for the quantification of half-integer quadrupolar nuclei [3]. In particular, we highlighted an important caveat of the most commonly applied method, and proposed an approach that may be employed to avoid such limitations.

Application of this method has proved invaluable for the 3:1 mechanochemical reaction of $NaAlH_4$ and $AlCl_3$, allowing both the identification of *new species, previously unobserved in the solid-state*, as well as the unambiguous elucidation of the reaction pathway. The former was accomplished by a rigorous analysis of the ^{27}Al SS NMR spectra, such as one obtained for the 1:1 reaction of $NaAlH_4$ and $AlCl_3$, shown in Figure 2 (top, black line). In this case, the red line

corresponds to the central transition of the new species and the sharp signal centered around 12 ppm arises from AlH_3. Following normalization of the quantitative contributions with respect to the starting composition, the new species are identified as $NaAlHCl_3$. Based on a similar analysis of the ^{27}Al and ^{23}Na SSNMR spectra obtained for the 3:1 reaction as a function of time (and incorporating the assignment of the new species as $NaAlHCl_3$), the following reaction pathway is suggested:

$0.75NaAlH_4 + 1AlCl_3 \rightarrow 0.75NaAlCl_4 + 1AlH_3$ (1)
$0.25NaAlH_4 + 0.75NaAlCl_4 \rightarrow 1NaAlHCl_3$ (2)
$\underline{2NaAlH_4 + 1NaAlHCl_3 \rightarrow 3NaCl + 3AlH_3}$ (3)
$3NaAlH_4 + 1AlCl_3 \rightarrow 3NaCl + 4AlH_3$ (Overall)

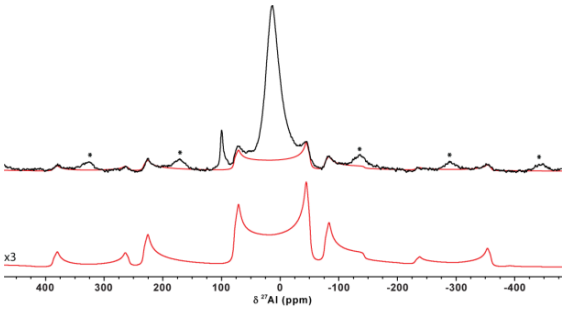

Figure 2. ^{27}Al DPMAS spectrum obtained for the 1:1 reaction of $NaAlH_4$ and $AlCl_3$ (top, black line) and the fitted contribution arising from the new intermediate (red line, top and bottom, where the latter has been expanded by a factor of three). Asterisks denote spinning sidebands arising from AlH_3.

When the relative agreement between the ^{27}Al and ^{23}Na data sets was assessed with respect to the extent of reaction for each step, errors were less than 5% in all cases, which – given the independence of the SS NMR data sets – offers unequivocal support for the elucidation of the 3:1 reaction pathway as indicated above.

Modeling the kinetics of solid-state phase transformation for complex metal hydrides is often critical for understanding of the underlying mechanisms governing hydrogen absorption and desorption properties of complex metal hydrides. While computational modeling of thermodynamic properties is well established, modeling of kinetic properties has lagged. In our recent work, using density functional theory (DFT) calculations, we have addressed this issue by applying the the solid-state nudged elastic band (SSNEB) method [4] co-developed by Ames Lab and UT-Austin, to study the transformation between the polymorphs of complex metal hydrides to reveal the different transformation pathways and the associated kinetic barriers. Choosing a chemically and structurally well characterized MgH_2 as a model system, we have studied the solid-state phase transformation between α- to γ-MgH_2 with a 12-atom unit cell. The α- and γ-MgH_2 phases are very close in energy, with the former being 2 meV per formula unit more stable and having a 2% smaller volume in the DFT-PBE. The α-MgH_2 has a 6-atom per cell tetragonal structure, while the γ-MgH_2 has a 12-atom per cell orthorhombic structure. In both structures, Mg is coordinated by six H atoms and H is coordinated by three Mg atoms, respectively. The structural differences originate from the different networks of the corner- and edge-sharing MgH_6 octahedrons. By doubling the unit cell of α-MgH_2 in the c direction, we have used SSNEB with DFT to study the minimum energy pathway (MEP) for transformation from α- to γ-MgH_2 as shown in Fig.3. The transformation

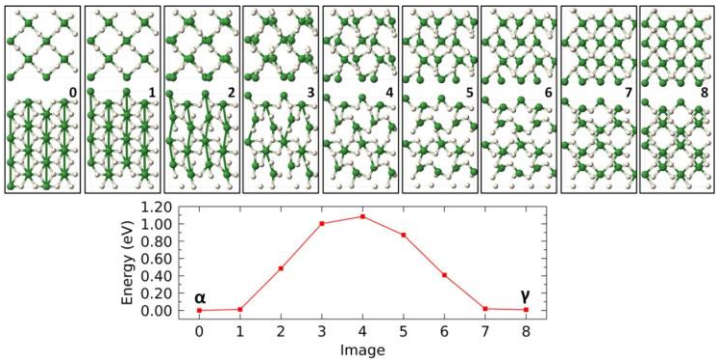

Figure 3. MEP for the α- to γ-MgH_2 transition with a 12-atom unit cell calculated using the SSNEB withiin DFT. (Top panel) Atomic structures along the MEP at each image viewed along *c* (upper) and *a* (lower) directions. Green (white) spheres are for Mg (H) atoms.

involves the shuffling of every other Mg and the associated H atoms (along *c*) in the *a* direction. The transition state with a barrier of 1.08 eV is at Image 4, where the shuffling is half-way complete. The relatively large barrier is because of strong distortion of the MgH_6 octahedron and the broken Mg-H bonds in the transformation.

Future Plans

The program will continue to foster strong integration of advanced and innovative synthesis with the state-of-the art characterization and multi-length and time scale modeling. New paradigms in high-pressure and liquid-assisted mechanochemistry of complex hydrides will be established using the in-situ temperature and pressure and gas monitoring capabilities currently under development. Not only will these new and existing capabilities be used to examine mechanochemical transformations in multi-component hydride systems of increasing complexity, they will be extended to other classes of materials to scrutinize new concepts such as nano-confinement and catalytic effects of surfaces and interfaces. For example, interactions of hydrogen with defect laden hexagonal boronitride (*h*BN) will be examined using hydrogen sorption and advanced SS NMR methods. A variety of other 2D materials including MXenes and transition metal dichalgcogenides will be examined for their effectiveness in catalyzing hydrogen sorption and promoting reversibility in high capacity alanates and borohydrides.

While SS NMR will continually provide routine characterization of samples, we also plan to utilize the game-changing SS NMR capabilities for the studies of unreceptive nuclei in complex hydrides, such as ^{25}Mg or ^{35}Cl, offered by the world's strongest magnet (36 T, 1.5 GHz), which became operable in November of 2016 at the NHMFL facility in Tallahassee, FL. For example, our preliminary ^{25}Mg SS NMR studies of dehydrogenation of $Mg(BH_4)_2$ carried out in Ames Laboratory at 9.4 T and 14.1 T yielded unresolved resonances representing various amorphous products and intermediate species of such transformation. We expect to measure 1D ^{25}Mg and 2D $^{1}H\{^{25}Mg\}$ SSNMR spectra to fully clarify the (de)hydrogenation mechanisms of $Mg(BH_4)_2$ and other Mg-based systems.

Finally, high-level DFT will continue to provide insight and guidance for experiments. In the future, we will include pressure in the SSNEB calculations to investigate the effect of pressure on the transformation pathways and barriers. We will also examine the defect formation and their diffusion kinetics during solid-state transformations under pressure. After the experience gained in polymorphs of MgH_2, we will move to polymorphs of AlH_3, where we have shown surface defects promote alane formation, and other complex metal hydrides.

References

1. U.S. Department of Energy, Energy Efficiency and Renewable Energy. Fuel Cell Technologies Office. Multi-Year Research, Development, and Demonstration Plan. Program Activities for 2011-2020. Section 3.3. Hydrogen Storage, 2012 (Updated October 2014). http://energy.gov/sites/prod/files/2014/11/f19/fcto_myrdd_storage.pdf.
2. S. Gupta, T. Kobayashi, I. Z. Hlova, J. F. Goldston, M. Pruski, and V. K. Pecharsky, "Solvent-free mechanochemical synthesis of alane, AlH3: Effect of pressure on the reaction pathway," Green Chem., **16**, 4378 (2014).
3. C. Fernandez and M. Pruski, "Probing quadrupolar nuclei by solid-state NMR spectroscopy: Recent advances," Top. Curr. Chem., **306**, 119-188 (2012).
4. D. Sheppard, P. H. Xiao, W. Chemelewski, D. D. Johnson, G. Henkelman, "A generalized solid-state nudged elastic band method," J. Chem. Phys., **136**, 074103 (2012).

Publications

1. L.-L Wang, T. L. Tan, and D. D. Johnson, "Nanoalloy electrocatalysis: simulating cyclic voltammetry from configurational thermodynamics with adsorbates" Phys. Chem, Chem Phys., **17**, 28103-28111 (2015).
   http://dx.doi.org/10.1039/c5cp00394f

2. T. L Tan, L.-L Wang, J. Zhang, D. D Johnson, and K. W Bai, "Platinum nanoparticle during electrochemical hydrogen evolution: Adsorbate distribution, active reaction species, and size effect"' ACS Catal., **5**, 2376-2383 (2015).
   http://dx.doi.org/10.1021/cs501840c

3. L.-L. Wang, A. Herwadkar, J. M. Reich, D. D. Johnson, S. D. House, P. Pena-Martin, A. A. Rockett, I. M. Robertson, S. Gupta, and V. K Pecharsky, "Towards direct synthesis of alane: A predicted defect-mediated pathway confirmed experimentally" Chemsuschem **9**, 2358-2364 (2016).
   http://dx.doi.org/10.1002/cssc.201600338

4. I. Z. Hlova, A. Castle, J. F. Goldston, S. Gupta, T. Prost, T. Kobayashi, L. Scott Chumbley, M. Pruski and V. K. Pecharsky "Solvent- and catalyst-free mechanochemical synthesis of alkali metal monohydrides", J. Mater. Chem. A, **4**, 12188-12196 (2016).
   http://dx.doi.org/10.1039/c6ta04391g

5. I. Bigun, V. Smetana, Y. Mudryk, I. Hlova, M. Dzevenko, L. Havela, Y. Kalychak, V. K. Pecharsky, and A. -V. Mudring, "$EuNi_5InH_{1.5-x}$ (x = 0-1.5): hydrogen induced structural and magnetic transitions," J. Mater. Chem. C **5**, 2994 (2017).
   http://dx.doi.org/10.1039/C7TC00121E.
   A figure from this article has been selected as the cover page of Journal of Materials Chemistry C

6. N. K. Singh, S. Gupta, V. K. Pecharsky, and V. P. Balema, "Solvent-free mechanochemical synthesis and magnetic properties of rare-earth based metal-organic frameworks," J. Alloys. Compd. **696**, 118 (2017).
   http://dx.doi.org/10.1016/j.jallcom.2016.11.220

7. J. F. Goldston, T. Kobayashi, S. Gupta, I. Hlova V. K. Pecharsky, and M. Pruski, "Rigorous qantification of quadrupolar nuclei in complex metal hydrides by solid-state NMR", prepared for submission. (2017).

8. I. Z. Hlova, J. F. Goldston, S. Gupta, T. Kobayashi, M. Pruski, and V. K. Pecharsky, "A Benign synthesis of alane by the composition controlled mechanochemical reaction of sodium hydride and aluminum chloride" Under review, J. Mater. Sci. (2017).

9. V. K. Pecharsky, S. Gupta, M. Pruski, I. Hlova, and A. Castle "Method of making alkali metal hydrides" U. S. Patent application 20170022060 A1, Published Jan 26, 2017.

10. S. Gupta, V. K. Pecharsky, T. Kobayashi, M. Pruski, and I. Hlova, “Mechanochemical synthesis of alane” PCT application WO2015123438 A1 Published Aug 20, 2015; U. S. Patent application 20170050846 A1, Published Feb 23, 2017.

Session VII

Quantum Metamaterials

David Awschalom[1,2], Andrew Cleland[1,2], Joseph Heremans[2], Daniel Lopez[2], Leonidas Ocola[2], David Schuster[1], Brian Stephenson[2]

[1]*University of Chicago*

[2]*Argonne National Laboratory*

Program Scope

The past decade has seen an explosion in condensed matter experimentalists' ability to use and control the quantum states of a number of different mesoscopic and macroscopic elements. It is now possible to assert individual quantum control over physical quantities as electron/nuclear spins, microwave/optical photons, and even phonons. Such manipulation and detection is made possible by increasingly sophisticated spin-active optical microscopy techniques, complex superconducting circuits, and photonic and phononic crystals. Based on these recent developments, we believe the field is now poised to develop a new class of engineered structures we term "quantum metamaterials". Loosely defined, this class comprises purpose-designed nanoscale structures integrating materials and active elements that tightly couple electrical signals; phonons; spins; and optical photons, all operating at the quantum coherent level. The directed development of these types of materials would allow the experimental and theoretical exploration of one of the greatest challenges in modern physics: the understanding of quantum many-body interactions, spanning scales from atomic to macroscopic, in systems with many quantized degrees of freedom with strong interactions.

We describe a new program aimed at developing and exploring the first generation of this class of quantum metamaterials. Our basis for engaging in this broad area of research is our proven ability to design and fabricate complex structures that integrate some of these degrees of freedom. In particular, our team combines expertise in color center theory and experiment with expertise in creating and controlling single electron and nuclear spin states in carbon-based semiconductors, superconducting quantum circuits, as well in the design and control of microwave frequency mechanical systems operating in the quantum limit. In addition, we have developed new expertise in structures which strongly couple light (optics) and mechanics, and we are attempting to integrate these optomechanical structures with the quantum control afforded by both color centers and superconducting devices. Cutting across these areas will be a focus on materials growth, characterization, and ab-initio understanding. We intend to advance the state of the art in individual disciplines, and ultimately synthesize these into a single quantum coherent system.

Recent Progress

The quantum metamaterials program has had a number of significant advances during this period, including the hiring of a staff scientist, purchasing optical and growth equipment, as well as several ongoing experiments and published manuscripts. While the facilities and infrastructure are being designed and installed, there are several continuing projects and collaborations associated with the FWP that include using spin defects in diamond, silicon carbide (SiC), and aluminum nitride (AlN) as a qubit for quantum information processing and nanoscale sensing, along with the integration of superconducting qubits, electromagnetic and mechanical structures to create hybrid systems in which to create and explore the physics of entanglement. One experiment focuses on using optical pulse shaping techniques to accelerate and improve quantum state transfer of a diamond NV center defect. The second is a theory collaboration with the Galli group that explores the mechanism behind the unusually long coherence time of the divacancy defects in 4H-SiC. We have also launched a productive collaboration with the SRS (58926) FWP to use their expertise in coherent x-ray diffraction imaging (CXDI) to study the strain distribution in diamond nanoparticles, and explore methods by relaxing this strain for nanoscale sensing applications. Results of an in situ annealing study using CXDI have shown that the diamond nanoparticles reduce in size due to an etching process, and the internal strain is also more homogenized.

Another ongoing project focuses on using surface acoustic waves (SAWs) to couple several distinct quantum systems as part of a collaboration among several members of the FWP. Here, we are working to create strong quantum mechanical coherent coupling between an ensemble of defect spins in SiC and a high-Q mechanical resonator, resulting in mechanical control of the quantum states. We have designed and fabricated SAW resonators on bare SiC as well as an AlN layer on a SiC substrate, and are in the process of characterizing the high-Q resonators. In parallel with these efforts, the groups are working closely together in developing common fabrication and experimental research themes for this effort. Novel coupling schemes for generating remote qubit entanglement are being developed with superconducting qubits, as well as coupling qubits to mechanical and electromagnetic resonant structures. Hybrid quantum systems are being fabricated through coupling electrical and mechanical structures. There are intense design and simulation efforts in all groups to assemble detailed approaches that will form the basis for experiments in the area of quantum metamaterials, as well as the development of the critical fabrication processes in the cleanrooms in order to build the requisite metamaterial patterns.

Superconducting circuits represent the natural electrical counterpart to color centers and high finesse nanomechanical structures. They from DC to microwave frequencies, the same regions in which nanomechanical systems tend to resonate, and have similarly low loss. For these reasons superconductors represent an ideal electrical front-end to study these mechanical and spin based systems.

There have been demonstrations of couplings between superconducting circuits and nanomechanical structures, including FBARs, wires, and drums. The proposed piezoelectric nanomechanical structures developed here will maintain the GHz frequencies and strong coupling but have much higher finesses, enabling a new class of superconducting-nanomechanical hybrid structures. Achieving the highest finesse in both nanomechanical structures and superconducting structures both require complex fabrication protocols and the two procedures are not necessarily compatible with one another. For example, Josephson junctions cannot be heated above 120C without high probability of failure, whereas many MEMS processing techniques require much higher temperatures. We are developing a method by which superconducting circuits can be fabricated on one chip and coupled to a nanomechanical structure fabricated independently. The superconducting chip will be fabricated separately, allowing different substrates to be used and independent processing. Coupling between the two chips is made capacitively, to the piezoelectric transducer, using a flip-chip geometry. This will also facilitate collaboration with superconducting resonators/qubits optimized and separately tested in the Schuster lab, and nanomechanical systems developed in the Cleland lab.

We have completed the design and purchase of a custom UHV deposition system to deposit high-quality aluminum nitride films on a variety of substrates. This system, presently being installed and soon to have initial films grown, will serve as a primary source of high piezoelectric response thin films, enabling coupling of electrical signals to mechanical motion at frequencies from DC to tens of GHz. These films will serve as a fundamental element for mechanical transduction of phonons in the quantum regime, including enabling interfacing high fidelity superconducting qubits to mechanical resonators for fundamental tests of quantum mechanics with acoustic waves. We expect this system to be fully operational in the next 2-3 months, having been received from the vendor in February 2017.

Experimental progress on building systems capable of operating in the quantum regime with phonons, one focus of this project, has been good. We have demonstrated high Q acoustic resonators based on surface acoustic waves in a bulk piezoelectric substrate, with the resonators operating at 4 GHz with quality factors in excess of 104 at mK temperatures. We are developing methods to couple these to superconducting qubits for measurements in the quantum regime.

We have also nearly completed development of parametric amplifiers based on the Josephson effect that should allow quantum limited measurements of photons and phonons in the GHz band; a parallel effort bringing up the superconducting qubit fabrication process in the UC PNF cleanroom has yielded good performance qubits on the first attempt. Measurement facilities in a new lab at UC have also been completely brought up, with mK-capable dilutions refrigerator and two adiabatic demagnetization refrigerators now operating well with full measurement cabling, filters, and custom electronics for time-domain pulsed qubit measurements.

Future Plans

- Install and bring-up AlN sputter tool and diamond CVD growth tool.
- Design and fabrication of materials for hybrid AlN-Si and AlN-SiC optomechanical devices
- Fabricate and test materials for high-Q resonators for coupling to superconducting qubits.
- Integrate high-Q mechanical resonators in SiC with material containing spin defects in SiC to mechanically drive these defect states using surface acoustic waves.
- Explore the interplay between NV centers in nanodiamonds and spin waves in ferromagnetic materials as a platform for hybrid quantum information and sensing systems.
- Continue ongoing collaboration with the SRS FWP to study techniques of minimizing strain distribution in diamond and SiC materials using CXDI.
- Build a broadband confocal spectroscopy laboratory to explore defects.
- Develop efficient SAW device structures on SiC for optomechanical and higher spin coupling
- Improve impedance matching of electronic drives with mechanical modes. Low (mK) operation of SiC SAW devices for extremely high fQ products
- Prepare and test flip chip methodology and devices for coupling across different materials and quantum technologies.

Publications

F. Joseph Heremans, Christopher G. Yale, and David D. Awschalom, "Control of spin defects in wide-bandgap semiconductors for quantum technologies," Proceedings of the IEEE **104**, 2009 (2016).

Hosung Seo, Abram Falk, Paul V. Klimov, Kevin C. Miao, Giulia Galli, and David D. Awschalom, "Quantum decoherence dynamics of divacancy spins in silicon carbide", Nature Communications **7**, 12935 (2016).

Brian B. Zhou, Alexandre Baksic, Hugo Ribeiro, Christopher G. Yale, F. Joseph Heremans, Paul C. Jerger, Adrian Auer, Guido Burkard, Aashish A. Clerk, and David D. Awschalom, "Accelerated quantum control using superadaiabatic driving in a solid-state lambda system", Nature Physics **13**, 330 (2017).

S. O. Hruszkewycz, W. Cha, P. Andrich, C. P. Anderson, A. Ulvestad, R. Harder, P. H. Fuoss, D. D. Awschalom, and F. J. Heremans, "In situ study of annealing-induced strain relaxation in diamond nanoparticles using Bragg coherent diffraction imaging," APL Materials **5**, 026105 (2017).

Probing Coherent States of Light and Matter in Two-Dimensional Semiconductors

Nathaniel P. Stern

Department of Physics and Astronomy, Northwestern University

Program Scope

The ability to enhance light-matter interactions in engineered optical environments is well-established in micro- and nano-photonics. Advances in materials synthesis and preparation have revealed new classes of materials that exhibit rich correlations between spin, momentum, and light polarization. Interfacing these correlations with strong optical interactions in intense optical fields suggests the compelling capability to create hybrid light-matter systems harnessing low-energy and protected properties such as spin and pseudospin. The long-term objective of this program is to investigate the interplay between these properties and light, revealing new coherent phenomena. The materials studied are the monolayer transition metal dichalcogenides (TMDs), which support new properties when reduced to only a single atomic-scale layer thick. In particular, monolayer TMD semiconductors such as MoS_2 exhibit degenerate valleys in momentum space which have topologically distinct Berry curvature [1]. These valleys can be separately addressed by circularly polarized light, providing a tool for selecting distinct regions of momentum space. Integrating this valley pseudospin property of excitons in monolayer TMDs with engineered strong optical excitations to create novel coherent phenomena represents the key goal of this research. Our primary approach in this program is to harness cavity-enhanced optical coupling between photonic resonators and monolayer semiconductors. Valley-sensitive phenomena are also explored using polarized photoexcitation in transport devices.

Recent Progress

Our research program has focused on exploring the interplay of light with the valley degree of freedom in monolayer transition metal dichalcogenides. The primary approach during the last year has been to enhance light-matter interactions using microcavities. We have also investigated methods of enhancing exciton oscillator strength using lateral confinement.

Valley-polarized exciton-polaritons in monolayer semiconductors: Coherent hybrid states of light and matter, exciton-polaritons, have been observed when monolayer TMDs interact with photons in a microcavity [2]. Although exciton-polaritons have been studied for several decades in semiconductors, one feature that sets monolayer TMDs apart from traditional semiconductors is the degenerate valley structure at the band gap that can be selectively excited with circularly

polarized light. We suggested that this valley degree of freedom available in monolayer TMDs can translate to hybrid light-matter states (Fig. 1). To explore this possibility, we embedded monolayer MoS_2 in microcavities made from alternating SiO_2 and SiN dielectric layers. Strongly coupled exciton-polaritons are observed [3], which preserve the valley polarization typical of a bare monolayer evidenced by circularly polarized photoluminescence from the cavity (Fig. 2a). The polarization p from these hybrid MoS_2 microcavities persists to room temperature in contrast to a bare monolayer, indicating the large effect of the microcavity on the depolarization dynamics of strongly-coupled exciton-polaritons.

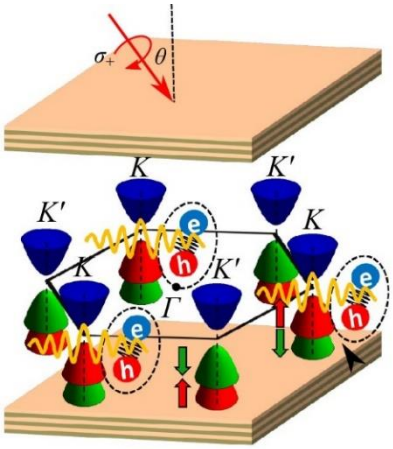

Figure 1: Schematic of valley-polarized exciton-polaritons in a 2D semiconductor embedded in a microcavity. A circularly-polarized pump excites only specific valleys, which couple strongly to the polarized microcavity photon mode.

We explain the temperature behavior of the valley-polarized exciton-polaritons using cavity modeling that incorporate valley-specificity. We show that the strongly-coupled dynamics of these valley-sensitive hybrid light-matter quasiparticles is determined by the relative rates of exciton relaxation and intervalley scattering, which can be highly modified in on-resonant cavities (Fig. 2a). These experimental and modeling results demonstrate that dynamics of valley pseudospin can be controlled by engineering light-matter interactions 2D TMD photonics. The preservation of valley pseudospin and Berry curvature in hybrid light-matter particles in a monolayer semiconductor suggests a material platform for exploring new predicted coherent edge modes in topological polaritons [4].

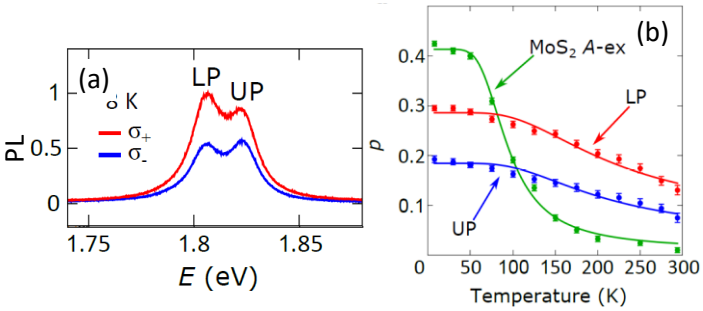

Figure 2: (a) Circularly-polarized emission spectra of monolayer MoS_2 embedded in a microcavity, showing the lower and upper polariton emission peaks. (b) Temperature-dependent valley polarized exciton-polariton emission compared to a bare monolayer, showing distinct dynamics. The lines represent a microcavity rate equation model.

Controlling optical properties of monolayers using lateral confinement: Size-dependent control of semiconductor properties is an important feature for fundamental and technological applications. In 2D TMDs, out-of-plane vertical confinement arises naturally from the layered structure, but because of the small exciton Bohr radius of ~1 nm, size-dependent control using lateral confinement is challenging. Despite the promise of enhanced exciton oscillator strengths, systematic size-dependent control of TMD monolayers is not well established. We have developed nanopatterning for TMD monolayers to achieve laterally confined nanostructures in

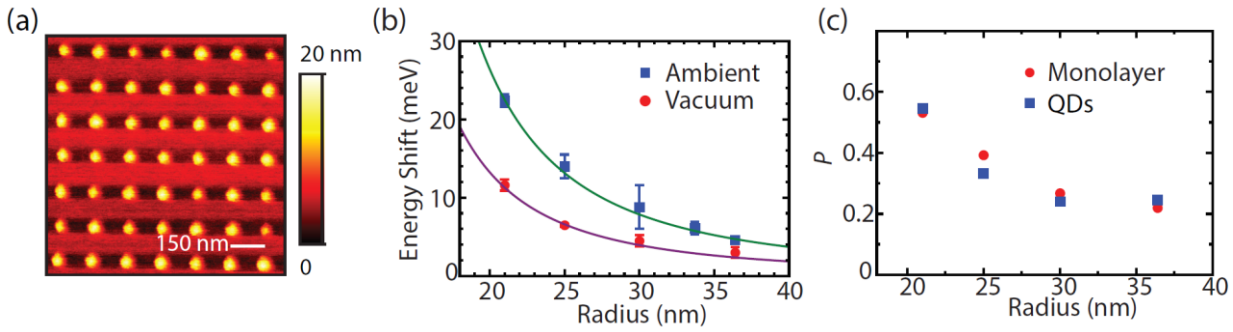

Figure 3: (a) AFM image of MoS_2 nanodots after processing. (b) Shift of the exciton energy as a function of size for MoS_2 nanodots. (c) Polarized emission is nearly identical between MoS_2 flakes and nanodots for all dot sizes, indicating no significant increase in intervalley scattering.

order to control the optical properties and to enhance optical interactions when embedded in microcavity structures. Nanofabrication work was done in collaboration with the Center for Nanoscale Materials at Argonne National Laboratory, a DOE BES facility.

The laterally-confined monolayer TMD semiconductors are created through controlled nanopatterning of single TMD layers into nearly circular nanodots (Fig. 3a). Size-dependent exciton energies are observed in monolayers of MoS_2 and WSe_2 [5]. Lateral confinement is confirmed by the spectral shift of MoS_2 luminescence shown in Fig. 3b. The results are consistent with the expected size scaling of confinement energy in the weak confinement regime. Valley polarization of patterned MoS_2 nanodots was found to be unchanged from that of continuous monolayers, evidenced through low-temperature circularly-polarized emission. This preservation of valley polarization in patterned monolayer TMD nanostructures suggests that valley-polarized exciton-polaritons are also possible in patterned monolayer nanostructures.

Long-term intentions are to integrate these nanodots into microcavities. The need for ever smaller patterned nanodots suggests that lateral confinement will only provide moderate improvements for observing new light-matter phenomena. The strong spin-momentum coupling evident in photoexcitation is a more promising avenue for accessing new coherent effects.

Future Plans

In the next year, we will explore the validity of our modeling of valley-polarized exciton-polariton dynamics using microcavity engineering [3]. We will control photon mode volumes and cavity quality to identify trends in exciton-polariton dynamics. Systematic investigation of depolarization mechanisms and properties of these exciton-polaritons, in particular the new room temperature valley polarization, will lead to understanding of the cavity-modified dynamics of these light-matter quasiparticles. The validity of these models for different material layers, heterostructures, and high-quality hexagonal boron nitride encapsulated layers will be explored.

The ability to shift the energy of a single valley using intense light has received significant attention due to the capability for coherent control of valley excitations [6]. In contrast to the measurements we performed in the last year, the valley Stark shift represents the very weak coupling regime of valley-polarized exciton-polaritons, accessible only with very high optical fluence. We plan to develop a time-resolved Kerr rotation approach to observe valley Stark shifts. We expect this approach to offer a better Stark shift sensitivity compared with absorption-based methods, which may allow the first observation of this effect in Mo-based TMDs.

We also plan to investigate the photoexcitation of valley-polarized currents in monolayer devices. The valley Hall effect and circularly polarized photogalvanic effects have been demonstrated as mechanisms of converting optical polarization to electronic transport due to the intrinsic valley bandstructure of monolayer TMDs [7,8]. These phenomena are not yet investigated with systematic control of the material properties. With our capability to probe materials with scanning microscopy, we will study photoexcitation of spin-valley polarized currents through the circularly-polarized photogalvanic effect. We will fabricate electronic devices with gating control to optimize the conversion efficiency between light and matter. In the long term, we will investigate integrating such electronic devices into microcavities to achieve enhanced opto-electronic effects in the materials.

References

[1] D. Xiao, G.-B. Liu, W. Feng, X. Xu, and W. Yao. "Coupled Spin and Valley Physics in Monolayers of MoS_2 and Other Group-VI Dichalcogenides" *Phys. Rev. Lett.* **108**, 196802 (2012).

[2] X. Liu, T. Galfsky, Z. Sun, F. Xia, E. Lin, Y. Lee, S. Kena-Cohen, and V. M. Menon. "Strong light-matter coupling in two-dimensional atomic crystals." *Nature Photonics* **9**, 20 (2015).

[3] Y.-J. Chen, J. D. Cain, T. K. Stanev, V. P. Dravid, N. P. Stern. "Valley-Polarized Exciton-Polaritons in a Monolayer Semiconductor." *Under review*, arXiv:1701.05579.

[4] T. Karzig, C. Bardyn, N. H. Lindner, and G. Refael. "Topological Polaritons." Phys. Rev. X **5**, 031001 (2015).

[5] G. Wei, D. A. Czaplewski, E. J. Lenferink, T. K. Stanev, I. W. Jung, N. P. Stern. "Valley Polarization in Size-Tunable Monolayer Semiconductor Quantum Dots." *Under review*, arXiv:1510.09135.

[6] Z.Ye, D. Sun, and T. F. Heinz. "Optical manipulation of valley pseudospin." *Nature Phys.* **13**, 26-29 (2017).

[7] K. F. Mak, K. L. McGill, J. Park, and P. L. McEuen. "The valley Hall effect in MoS_2 transistors." *Science* **344**, 1489 (2014).

[8] H. Yuan *et al.* "Generation and electric control of spin–valley-coupled circular photogalvanic current in WSe_2" *Nature Nanotechnol.* **9**, 851 (2014).

Publications

Sponsored by BES 2015 - 2017

1. Y.-J. Chen, J. D. Cain, T. K. Stanev, V. P. Dravid, N. P. Stern. "Valley-Polarized Exciton-Polaritons in a Monolayer Semiconductor." *Under review*, arXiv:1701.05579. Available at: https://arxiv.org/abs/1701.05579

2. G. Wei, D. A. Czaplewski, E. J. Lenferink, T. K. Stanev, I. W. Jung, N. P. Stern. "Valley Polarization in Size-Tunable Monolayer Semiconductor Quantum Dots." *Under review*, arXiv:1510.09135. Available at: https://arxiv.org/abs/1510.09135

3. Y. Jia, T. K. Stanev, E. J. Lenferink, N. P. Stern. "Enhanced Conductivity Along Lateral Homojunction Interfaces of Atomically Thin Semiconductors." *2D Materials* **4**, 021012 (2017). DOI: 10.1088/2053-1583/4/2/021012

4. K. B. Chang, B. W. Edwards, L. Frazer, E. J. Lenferink, T. K. Stanev, N. P. Stern, J. C. Nino, K. R. Poeppelmeier. "Hydrothermal crystal growth, piezoelectricity, and triboluminescence of $KNaNbOF_5$." *Journal of Solid State Chemistry* **236**, 78-82 (2016). DOI: 10.1016/j.jssc.2015.07.011

5. G. Wei, T. K. Stanev, D. A. Czaplewski, I. W. Jung, and N. P. Stern. "Silicon-nitride photonic circuits interfaced with monolayer MoS_2." *Appl. Phys. Lett*. **107**, 091112 (2015). DOI: http://dx.doi.org/10.1063/1.4929779

6. G. Wei, T. K. Stanev, D. A. Czaplewski, I. W. Jung, N. P. Stern. "Interfacing Monolayer MoS_2 with Silicon-Nitride Integrated Photonics." *OSA Technical Digest*, IM4A.3, (2015). DOI: 10.1364/IPRSN.2015.IM4A.3

Spin Transport in group IV materials and 2D membranes

Hanan Dery

Depts. of Electrical and Computer Engineering and of Physics, University of Rochester

Program Scope

This program mainly focuses on two studies. The first one deals with tailoring and quantifying the spin relaxation in *n*-type silicon and germanium due to impurities as a function of strain, temperature and electrical fields. The second study is of charge, spin, and optical properties in two-dimensional semiconductors with emphasis on monolayer transition-metal dichalcogenides (ML-TMDs). While we have made progress in both fronts [see 2-year list of publications supported by BES], I will focus in this short document only on the progress we have made in understanding how many-body interactions affect the optical properties of ML-TMDs.

Recent Progress: optical properties of ML-TMDs

Transition-metal dichalcogenides become direct band-gap semiconductors when thinned to a single atomic monolayer. Stacking such two-dimensional crystals via van der Waals forces alleviates the need to fabricate logic and optoelectronic devices with lattice-matched crystals. Furthermore, the lack of space inversion symmetry in these monolayers lifts the spin degeneracy at the edges of the conduction and valence bands. As a result, time reversal partners the spin and valley degrees of freedom such that spin-up charge carriers populate valleys (low-energy pockets) on one side of the Brillouin zone, while spin-down ones populate valleys on the opposite side. The intense recent research on the spin-valley partnership has led to understanding of optical selection rules and transport phenomena in ML-TMDs [1,2]. What remains an outstanding open question, however, is the origin for the appearance of a distinct optical side band in electron-doped ML-WSe_2 and ML-WS_2 [3]. We have recently addressed this question, revealing an intriguing pairing phenomenon between excitons and plasmons, which has no parallel in other known two-dimensional (2D) systems [4].

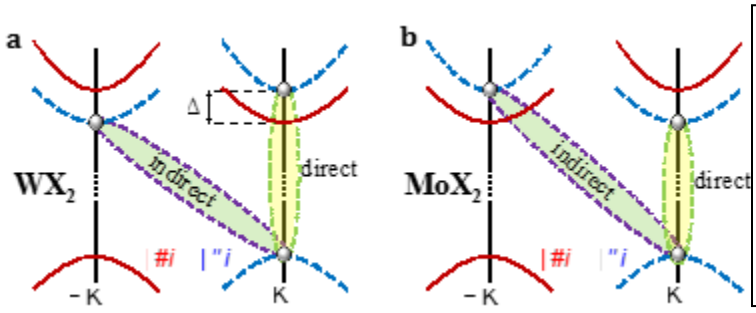

Fig. 1: Direct and indirect excitons in the time-reversed K-point valleys.
a, b, The involved electronic states in tungsten- and molybdenum-based monolayers, respectively. The indirect exciton has lower energy in the former case. Spin of the bands is color coded, and **Δ** is the conduction-band splitting energy.

Before we can explain the coupling between plasmons and excitons, we briefly summarize the relevant properties of each of these quasiparticles separately. Figure 1 shows the valleys pertinent to the formation of low-energy excitons in ML-WX_2 and ML-MoX_2 where X is the chalcogen atom. Only bright excitons are shown, in which the spins of the electron in the conduction band and the missing electron in the valence band are parallel or antiparallel. The

brightest exciton is the direct exciton in which the electron and hole have the same valley index, giving rise to direct-gap optical transitions. The less brighter exciton is the indirect one in which the electron and hole reside in opposite valleys. Optical transitions of indirect excitons in perfect crystals are mediated by external agents such as shortwave phonons, needed to make up for the large momentum mismatch of indirect excitons and photons. As shown in Fig. 1, indirect excitons have lower energy than direct ones in ML-WX_2 and vice versa in ML-MoX_2.

Next, we briefly discuss two plasmon species in ML-TMDs [4]. The first type of plasmons is characterized by their long-wavelength. They originate from the long-range part of the Coulomb potential through which electrons cross the Fermi surface with small crystal momentum transfer (intravalley process). These plasmons are common to all conducting media and are largely independent of the band structure since their wavelength is much longer than the lattice constant. In the context of optical transitions in semiconductors, these plasmons screen the electron-hole attraction and they shrink the band-gap energy by assisting electrons (or holes) of similar spins to avoid each other. The second type of plasmons originates from the short-range Coulomb potential through which electrons transition between valleys. Due to the relatively large spin splitting in the valence band of ML-TMDs, such transitions are mostly relevant in the conduction band wherein the much smaller spin splitting can be comparable to the Fermi energy, as shown in Fig. 2(a). Collective intervalley excitations result in shortwave plasmons, whose charge fluctuations profile is illustrated in Fig. 2(b).

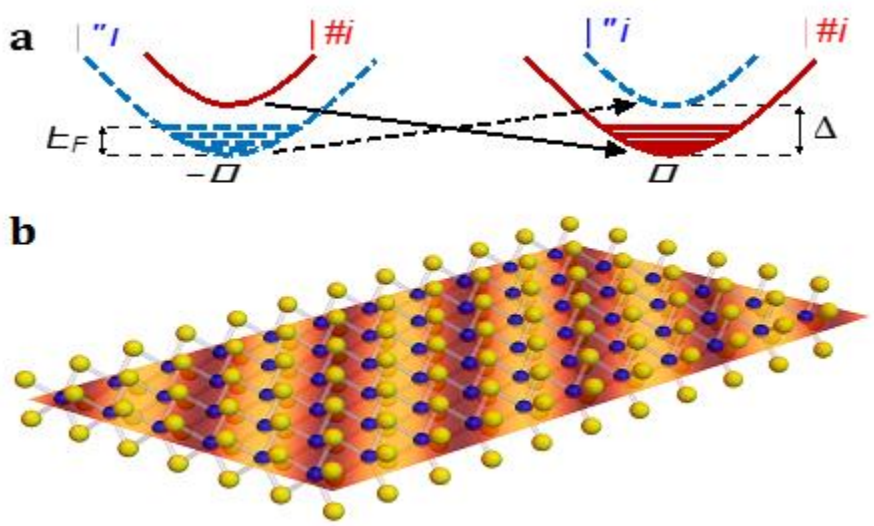

Fig. 2: The intervalley Coulomb interaction in ML- TMDs.
a, Spin-conserving charge excitations from the –K to the K valleys. Electrons need to overcome the spin-splitting energy gap in the conduction band.
b, The resulting shortwave charge fluctuations in the monolayer. The wavelength of the shortwave plasmon is of the order of $2\pi/K_0$ where $K_0 = 4\pi/3a$ is the wavenumber that connect the two valleys (a is the lattice constant).

To study how excitons interact with plasmons, we use the finite-temperature Green's functions formalism, and quantify the optical signature of bright excitons when surrounded by collective charge excitations. The connection to the absorption spectrum is then established via the imaginary part of the electron-hole pair function. The latter is found by solving the two-particle Dyson Equation (starting point for the Bethe-Salpeter Equation). We have solved this equation by employing a dynamically screened Coulomb potential [4]. It includes plasma excitations in addition to static dielectric screening from the environment. While adding dynamical terms in the screened potential renders the solution of the two-particle Dyson Equation evidently more demanding compared with previous studies of excitons in ML-TMDs, it will allow us to simulate the decay of bare electron-hole pairs and the rise of dynamical bands in the spectrum without introducing phenomenological terms.

We begin by evaluating the pair function of direct excitons when we only consider the effect of long-wavelength plasmons. Neglecting shortwave plasmons in the first step allows us to find common attributes between ML-TMDs and conventional semiconductor quantum wells. As mentioned before, the pair function of direct bright excitons is linked with the optical absorption spectrum through its imaginary part. Figure 3 shows the calculated absorption spectrum at T=10 K from which one can clearly notice the screening-induced exciton decay when the background charge density increases. The effective masses for both electrons and holes are $0.36m_0$, where m_0 is the free-electron mass. The dielectric environment is modeled by sandwiching the ML ($\boldsymbol{\varepsilon}$ = 7.25) between thick layers of hexagonal boron-nitride ($\boldsymbol{\varepsilon}$ = 2.7). The arrows in Fig. 3 indicate the continuum redshift due to band-gap renormalization (BGR). Above this energy the excitons are no longer bound. Note that the 2s bound state merges into the continuum already at relatively small densities due to its smaller binding energy. The inset shows that the BGR is strongest when the charge density is ramped up from zero to ~10^{12} cm^{-2}. The continuum redshift is slower at larger densities, and eventually excitons become unbound and merge into the continuum.

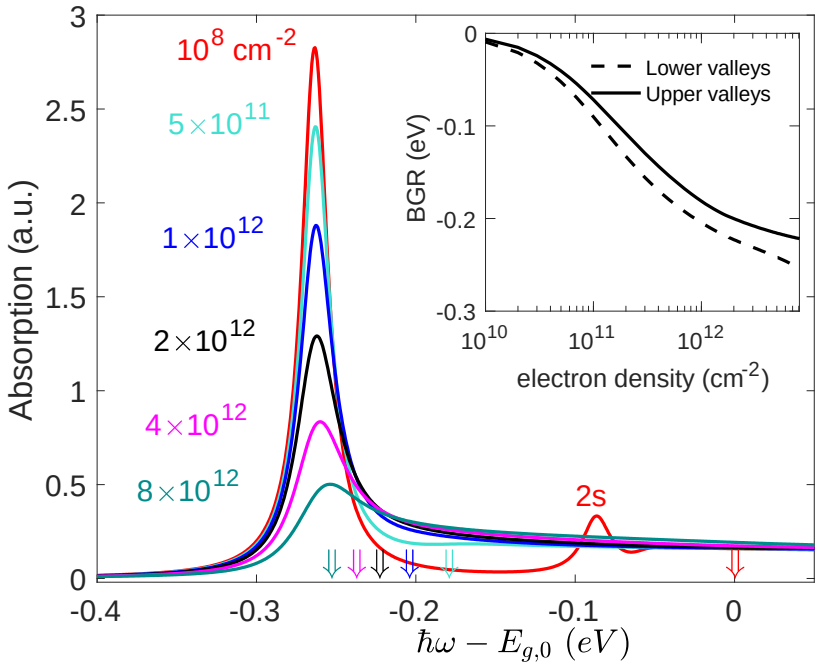

Fig. 3: Characteristic effect of long-wavelength plasmons on the absorption spectrum in ML-TMDs. Increasing the background charge density leads to a decay of the exciton peak. The arrows on the *x*-axis indicate the band-gap renormalization (BGR), showing the redshift for the onset of optical transitions in the continuum (non-interacting electron-hole pairs). **Inset,** BGR of the upper and lower valleys as a function of electron density in the lower valleys. The signatures of dynamical screening and BGR are qualitatively the same when choosing other parameters of effective masses and dielectric constants.

Additional important result in Fig. 3 is that the exciton spectral position is hardly affected by the background charge density. The reason is the mutual offset between BGR and the screening-induced reduction in the binding energy of excitons; the long-wavelength plasmons correspond to both effects. One can therefore realize that the binding energy of excitons in ML-TMDs can be of the order of few hundreds meV only at vanishing charge densities. All in all, long-wavelength plasmons lead to qualitatively similar effects in ML-TMDs and conventional semiconductor quantum wells. The only change is a quantitatively larger effect in ML-TMDs due to reduced dielectric screening and larger electron mass.

In the next step, turning on the coupling between shortwave plasmons and excitons reveals the unique features of ML-TMDs. The energy required to excite a shortwave plasmon at low temperatures is greater than that available thermally. As a result, plasmon signatures in the optical spectrum can be resolved by supplying energy from outside the electron system in amounts greater than the plasmon energy. This is the case when we shakeup the electronic system by exciting electron-hole pairs. Importantly, shortwave charge fluctuations can be

effectively paired up with an exciton in spite of its neutrality; the short-range nature of this coupling allows the hole to act as a spectator while the plasmon interacts with the electron component of the exciton (Fig. 4b). Figure 4a shows the emergence of a dynamical band in electron-doped ML-WX_2. It is absent in ML-MX_2 or hole-doped conditions (Figs. 4c & 4d). For explanations of these important observations, see Ref. [4], where we also make it clear why the optical band is manifested in the spectra of electron-doped ML-WSe_2 and ML-WS_2, while being absent in the hole-doped case or in ML-$MoSe_2$ and ML-MS_2.

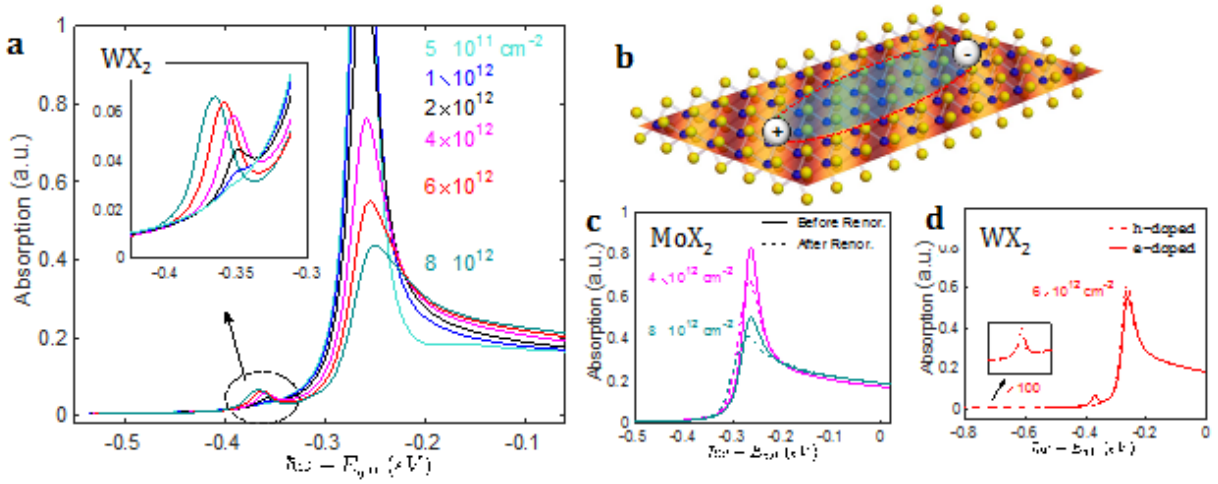

Fig. 4 *The absorption spectrum of direct excitons in ML-TMDs after renormalization due to interaction with shortwave plasmon*s. **a,** The case of electron-doped ML-WX_2. A dynamical band emerges in the low-energy side of the absorption spectrum, as highlighted in the enlarged box. The band initially redshifts and intensifies when the electron density increases, showing saturated behavior at elevated densities. **b,** Cartoon of the exciton and shortwave charge fluctuations. The plasmon wavelength is shorter than the exciton extent, which is further blown-up due to screening. **c,** The case of electron-doped ML-MoX_2 before (solid lines) and after (dashed lines) renormalization. The dynamical band is not seen. **d,** The case of electron-doped (solid line) and hole-doped (dotted line) ML-WX_2. The dynamical band is negligible for hole doping, as highlighted in the magnified box. It emerges ~400 meV below the exciton line due to the large valence-band splitting.

Future Plans

Revealing the exciton-plasmon mechanism and the importance of dynamical screening paves the way to harness unexplored manifestations of spin-valley coupling and the realization of other dynamical bands. For example, we have strong reason to believe that many reports of `trions' or `Fermi polarons' in these polar materials are actually caused by amplification of the exciton-phonon dynamical optical band coupling next to exciton localization centers. Therefore, we plan to study the exciton-phonon coupling in ML-TMDs in the next 12 months.

References

[1] K. F. Mak, K. L. McGill, J. Park, and P. L. McEuen, Science **344**, 1489 (2014).

[2] X. Xu, W. Yao, D. Xiao, and T. F. Heinz, Nature Phys. 10, 343 (2014).

[3] See, e.g., A. M. Jones *et al.* in Nature Nanotechnol. **8**, 634 (2013); J. Shang *et al.* ACS Nano **9**, 647 (2015); You *et al.* in Nature Phys. **11**, 477 (2015); G. Plechinger *et al.* in Nano Lett. **16**,

7899 (2016); Z. Wang *et al.* in Nano Lett. **17**, 740 (2017).

[4] D. V. Tuan, B. Scharf, I. Zutic, and H. Dery, arXiv:1704.01981 (submitted in April 2017).

Publications (2-year list of publications supported by BES)

[1] D. V. Tuan, B. Scharf, I. Zutic, and H. Dery, *Marrying excitons and plasmons in monolayer transition-metal dichalcogenides*, preprint: arXiv:1704.01981 (submitted April 2017)

[2] O. Chalaev, Y. Song, and H. Dery, *Suppressing the spin relaxation of electrons in silicon*, Phys. Rev. B **95**, 035204 (2017).

[3] W. Yan, O. Txoperena, R. Llopis, H. Dery, L. E. Hueso, and F. Casanova, *A two-dimensional spin field-effect switch*, Nat. Commun. **7**, 13372 (2016).

[4] H. Dery, *Theory of intervalley Coulomb interactions in monolayer transition-metal dichalcogenides*, Phys. Rev. B **94**, 075421 (2016).

[5] A. M. Jones, H. Yu, J. Schaibley, J. Yan, D. G. Mandrus, T. Taniguchi, K. Watanabe, H. Dery, W. Yao, X. Xu, *Excitonic luminescence upconversion in a two-dimensional semiconductor*, Nat. Phys. **12**, 323 (2016).

[6] H. Dery and Y. Song, *Polarization analysis of excitons in monolayer and bilayer transition-metal dichalcogenides*, Phys. Rev. B **92**, 125431 (2015). Editors' Suggestion.

Physical Chemistry of Inorganic Halide Perovskite Nanostructures

Peidong Yang, Department of Chemistry, UC Berkeley; Materials Sciences Division, Lawrence Berkeley National Laboratory

A. Paul Alivisatos, Department of Chemistry, UC Berkeley; Materials Sciences Division, Lawrence Berkeley National Laboratory

Stephen R. Leone, Department of Chemistry, UC Berkeley; Materials Sciences Division, Lawrence Berkeley National Laboratory

Eran Rabani, Department of Chemistry, UC Berkeley; Materials Sciences Division, Lawrence Berkeley National Laboratory

Program Scope

Recently, there is a renaissance of halide perovskites as a class of semiconductor materials for a variety of photovoltaics and optoelectronics. Particularly, the inorganic halide perovskites draw more and more attention, owing to their enhanced stability toward moisture, oxygen, and heat, compared to the organic-inorganic hybrid perovskites (e.g. methylammonium lead iodide). The controlled synthesis, detailed structural analysis, optical, and electronic properties are of great fundamental interest. This program currently focuses on the synthesis and theory of inorganic halide perovskites and the characterization of their physical properties to 1) advance synthetic methodology of 0D, 1D, and 2D nanostructures, 2) establish and advance technology and instrumentation to study fundamental nanomaterial properties as well as the physical, chemical, and electronic interactions between them, and 3) apply the extracted knowledge to both develop integrated devices from these nanoscopic building blocks and to feed this knowledge back into the virtuous cycle of design, synthesis, measurement and application.

Recent Progress

1. Synthesis of new nanostructures and related optical properties: Colloidal inorganic nanocrystals (NCs) are a fundamental building block for nanoscience, and the continued development of control over the composition, size, and shape of these building blocks is a central aim of this task. In this program's recent work on the physical chemistry of semiconductor NCs, new synthetic reactions were developed for the synthesis of organic and inorganic lead halide NCs with the perovskite crystal structure. Control has been demonstrated over the resulting shapes and composition of the NCs to obtain high-quality materials with unique photophysical properties. These new strategies have been employed to synthesize 2D perovskite materials (1,2), 1D colloidal wires (3,4), and 0D quantum dots (5).

The reported synthesis of ultrathin two-dimensional (2D) $(C_4H_9NH_3)_2PbBr_4$ organic-inorganic materials developed here represents the first well-controlled ultrathin 2D ionic materials to be created (1). This material consists of ideal quantum wells with monolayers of $PbBr_4^{2-}$ sheets sandwiched between layers of organic chains (Fig. 1a and 1b). This material can be synthesized down to a thickness of a single monolayer (Fig. 1c). The material's blue-shifted photoluminescence and structural relaxation relative to the bulk analog presents a new paradigm for property modulation that can be taken advantage of for fundamental studies and device applications. A related study focused on all-inorganic colloidal $CsPbBr_3$ 2D plates (2). The incorporation of Cs^+ to replace the organic cation increases the melting point and the overall thermal stability of the crystal. Band gap tunability was exhibited through taking advantage of quantum confinement via modulation of 2D plate thickness, with atomic precision.

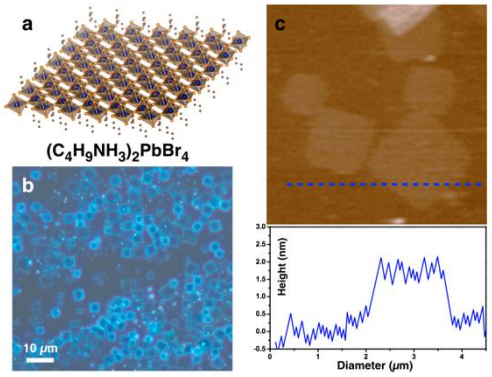

Figure 1. A model of the $(C_4H_9NH_3)_2PbBr_4$ sheet (a), a dark field optical image of the 2D sheets (b), and AFM image of a monolayer.

We have also developed new colloidal chemistry to synthesize $CsPbBr_3$ based nanowires with diameters of around 10 nm. The nanowires show bright photoluminescence (PL) with a peak at the wavelength of 521 nm. A slight quantum confinement was observed in this case, whereas the emission peak locates at 535 nm for the bulk $CsPbBr_3$ crystals. Next, based on this method, a further stepwise purification strategy was developed to obtain ultrathin $CsPbBr_3$ nanowires with a diameter down to ~ 2 nm. Large blue-shifted UV−vis absorption and PL spectra have been observed due to strong quantum confinement in the ultrathin nanowires (see Fig. 2 for the comparison with other nanostructures). The ultrathin NWs have bright photoluminescence with about a 30% photoluminescence quantum yield (PLQY) after purification and surface treatment.

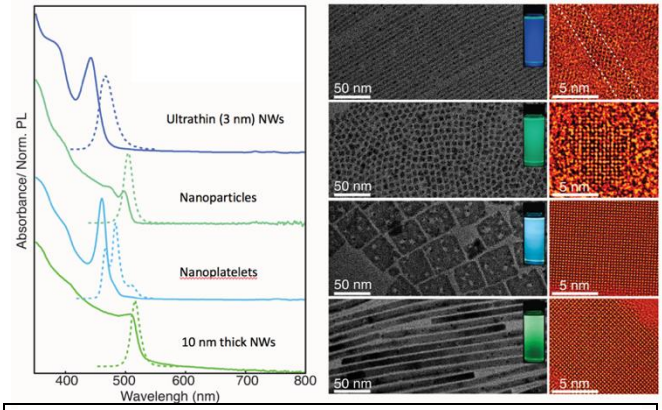

Figure 2. UV−vis absorption and PL spectra of $CsPbBr_3$ nanowires, nanoparticles, and nanoplatelets.

In addition to colloidal chemistry, we demonstrated a low-temperature, solution-phase growth of cesium lead halide nanowires using a substrate-based dissolution-recrystallization method (6). The as-grown nanowires show relatively larger dimensions (200-500 nm in diameter) and clean and sharp end-facets. The nanowires act as high-quality laser cavities and display excellent stability while stored and handled under ambient conditions over the course of weeks. Upon optical excitation using a fs laser, Fabry–Pérot lasing occurs in such $CsPbBr_3$ nanowires with an onset of 5 μJ cm^{-2} with the nanowire cavity displaying a maximum quality factor of 1,009 ± 5.

2. The soft nature of the halide perovskites and anion exchange: Due to the relatively weak bonding in halide perovskites, lattice distortion and atom displacement are common occurrences, even at room temperature. This property directly leads to the unique ability to induce anion exchange transformations which are commonly inaccessible in other semiconductors. In perovskite nanostructures, anion exchange was already demonstrated to occur at room temperature and 1D (7) material with high PLQY even throughout the exchange reaction (Fig. 3), which enabled the study of the exchange kinetics and reaction intermediates. Through our study we were able to resolve clear differences in the exchange kinetics of bromine to iodine, which exhibits a single mono exponential dependence to the bromine to chlorine case and exhibited a more detailed time dependence. This difference was interpreted by us as a surface limited vs diffusion limited exchange mechanisms. These new understandings may help to define an experimental standard for the performance of a given material system, a semiconductor with the ability to gradually tune the composition via anion exchange, while monitoring various photophysical properties, is especially important.

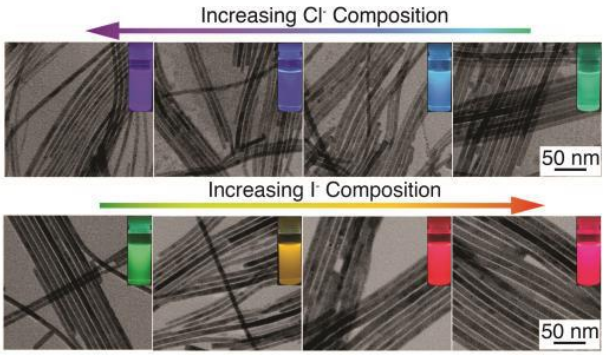

Figure 3. Anion-exchange in CsPbBr3 NWs.

3. Perovskite nanocrystal - polymer composite: The weak bonding nature of the perovskite crystals leads to enhanced sensitivity toward moisture and oxygen. Extending the perovskite stability is of paramount interest. We were able to demonstrate enhanced water and light stability of high surface area colloidal perovskite nanocrystals by encapsulation of colloidal $CsPbBr_3$ quantum dots into matched hydrophobic macroscale polymeric matrices (8). This is achieved by mixing the quantum dots with presynthesized high molecular weight polymers. The photoluminescence quantum yield of the perovskite-polymer nanocomposite films under water-soaking was monitored with no change even after >4 months of continuous immersion in water. Furthermore, photo-stability is greatly enhanced in the macroscale polymer-encapsulated nanocrystal perovskites, which sustain $>10^{10}$ absorption events per quantum dot prior to photo-degradation, a significant threshold for potential device use. Moreover, we achieve a high degree of polarization by alignment of perovskite nanowires in polymeric fibers, further demonstrating that our ligand-passivated perovskite-macroscale polymer composites provide a robust platform for diverse photonic applications.

4. Phase transition behavior: Cesium lead iodide ($CsPbI_3$), in its black perovskite phase, has a suitable bandgap and high quantum efficiency for photovoltaic applications. However, it is known that $CsPbI_3$ tends to crystalize into a yellow non-perovskite phase, which has poor optoelectronic properties. Therefore, controlling the phase transition in $CsPbI_3$ is critical for this material. We showed that the formation of perovskite black phase $CsPbI_3$ nanowires from the non-perovskite yellow phase through a rapid thermal quenching process. The black phase $CsPbI_3$

nanowires exhibit increased photoluminescence emission intensity with a shrinking of the bandgap from 2.78 to 1.76 eV. We also found that the perovskite nanowires are photoconductive and exhibit a fast photoresponse. These promising optical and electrical properties make the perovskite $CsPbI_3$ nanowires attractive for a variety of nanoscale optoelectronic devices.

Future Plans

In the future, we would like to continue pursuing new chemistry to synthesize more advanced halide perovskite nanostructures. The goal is to have better control over the size and shape of the nanostructures. In addition, we will carry out new studies towards a better understanding and better control over the transition behavior in such perovskite nanomaterials. Such transition process not only includes transformation between different crystallographic phases with a certain composition, but also includes chemical transformation of $CsPbX_3$ to other species such as Cs_4PbX_6 and related new compounds under external stimuli. A better understanding these processes will greatly enhance our understanding and control of their optical and electronic properties. Furthermore, the perovskites have also been preliminary measured using transient XUV spectroscopy. The measurements were made possible by controlling the perovskites thermal degradation under the intense laser pulse by using a gas flow cell and deposition on diamond x-ray membranes. The electron and hole dynamics are now being measured using the Pb, Br, and Cs edges.

Referencess

1. L. Dou, A. B. Wong, Y. Yu, M. Lai, N. Kornienko, S. W. Eaton, A. Fu, C. G. Bischak, J. Ma, T. Ding, N. S. Ginsberg, L.-W. Wang, A. P. Alivisatos, P. Yang; Science 2015, 349, 1518–1521.
2. Y. Bekenstein, B. A. Koscher, S. W. Eaton, P. Yang, A. P. Alivisatos; JACS 2015, 137, 16008–16011.
3. D. Zhang, S. W. Eaton, Y. Yu, L. Dou, P. Yang; JACS 2015, 137, 9230–9233.
4. D. Zhang, Y. Yu, Y. Bekenstein, A. B. Wong, A. P. Alivisatos, P. Yang; JACS 2016, 138, 13155–13158.
5. Q. A. Akkerman, V. D'Innocenzo, S. Accornero, A. Scarpellini, A. Petrozza, M. Prato, L. Manna; JACS 2015, 137, 10276–10281.
6. S. W. Eaton, M. Lai, N. Gibson, A. B. Wong, L. Dou, J. Ma, L.-W. Wang, S. Leone, P. Yang; PNAS 2016, 113, 1993–1998.
7. B. A. Koscher, N. D. Bronstein, J. H. Olshansky, Y. Bekenstein, A. P. Alivisatos; JACS 2016, 138, 12065–12068.
8. S.N. Raja, Y. Bekenstein, M.A. Koc, S. Fisher, D. Zhang, L. Lin, R. Ritchie, P. Yang, A. P. Alivisatos; *ACS Appl. Mater. Interfaces* 2016, *8*, 35523–35533.

Publications

1. L. Dou, A. B. Wong, Y. Yu, M. Lai, N. Kornienko, S. W. Eaton, A. Fu, C. G. Bischak, J. Ma, T. Ding, N. S. Ginsberg, L.-W. Wang, A. P. Alivisatos, P. Yang; Science 2015, 349, 1518–1521.
2. Y. Bekenstein, B. A. Koscher, S. W. Eaton, P. Yang, A. P. Alivisatos; JACS 2015, 137, 16008–16011.
3. D. Zhang, S. W. Eaton, Y. Yu, L. Dou, P. Yang; JACS 2015, 137, 9230–9233.
4. D. Zhang, Y. Yu, Y. Bekenstein, A. B. Wong, A. P. Alivisatos, P. Yang; JACS 2016, 138, 13155–13158.
5. S. W. Eaton, M. Lai, N. Gibson, A. B. Wong, L. Dou, J. Ma, L.-W. Wang, S. Leone, P. Yang; PNAS 2016, 113, 1993–1998.
6. B. A. Koscher, N. D. Bronstein, J. H. Olshansky, Y. Bekenstein, A. P. Alivisatos; JACS 2016, 138, 12065–12068.
7. S.N. Raja, Y. Bekenstein, M.A. Koc, S. Fisher, D. Zhang, L. Lin, R. Ritchie, P. Yang, A. P. Alivisatos; *ACS Appl. Mater. Interfaces* 2016, *8*, 35523–35533.
8. Y. Yu, D. Zhang, C. Kisielowski, L. Dou, N. Kornienko, Y. Bekenstein, A. P. Alivisatos, P. Yang; Atomic Resolution Imaging of Halide Perovskites. Nano Letters 2016, 16,7530–7535.
9. M. Lai, Q. Kong, C. G. Bischak, Y. Yu, L. Dou, S. W. Eaton, N. S. Ginsberg, P. Yang; Structural, optical, and electrical study of phase controlled cesium lead iodide nanowires. Nano Research 2016, doi:10.1007/s12274-016-1415-0.
10. A. B. Wong, M. Lai, S. W. Eaton, Y. Yu, E. Lin, A. Fu, L. Dou, P. Yang; Growth and Anion Exchange Conversion of CH3NH3PbX3 Nanorod Arrays for Light-Emitting Diodes. Nano Letters 2015, 15, 5519–5524.
11. Q. Kong, D. Kim, C. Liu, Y. Yu, Y. Su, Y. Li, P. Yang; Directed assembly of nanoparticle catalysts on nanowire photoelectrodes for photoelectrochemical CO_2 reduction. Nano Letters 2016, 16, 5675–5680.
12. D. Zhang, Y. Yang, Y. Bekenstein, Y. Yu, N. A. Gibson, A. B. Wong, S. W. Eaton, N. Kornienko, Q. Kong, M. Lai, A. P. Alivisatos, S. R. Leone, P. Yang; Synthesis of Composition Tunable Cesium Lead Halide Nanowires through Anion-Exchange Reactions. JACS 2016, 138, 7236–7239.
13. S. W. Eaton, A. Fu, A. B. Wong, C. Z. Ning, P. Yang; Semiconductor Nanowire Lasers. Nature Rev. Mater. 2016, 1, 16028.
14. Y. Su, C. Liu, S. Brittman, J. Tang, A. Fu, P. Yang; Single nanowire photoelectrochemistry. Nature Nano. 2016, 11, 609.

Session VIII

Optical, Electrical and Magnetic Studies of Hybrid Organic-Inorganic Perovskite Semiconductors

PI: Z. Valy Vardeny; Physics & Astronomy Department, University of Utah

Program Scope

Spin response of carriers in organic inorganic perovskite semiconductors

(i) During the last year we have launched an investigation of the spin-orbit coupling (SOC) strength in the hybrid organometal trihalide perovskite (OTP) system by employing the method of inverse-spin Hall effect (p-ISHE) that is induced by 'spin-pumping' using pulsed and cw microwave excitation. Also spin-injection has been investigated in perovskite spin-valve devices. (ii) We have also studied the formation of Rashba-splitting in the conduction band of 2D perovskites using optical spectroscopy, including electro-absorption spectroscopy, pump-probe photomodulation in the mid-IR, and cw photomodulation of photocarriers in the mid to far IR.

Recent Progress

The family of OTP, namely $CH_3NH_3PbX_3$ (where X is halogen) has recently revolutionized the photovoltaic field [1], and also has shown promise in a variety of other optoelectronic applications [2,3]. The characteristic spin properties of charge and neutral excitations in the OTP are influenced by the large SOC of the Pb atoms, which may lead to spin-based device applications. We have succeeded in launching 'pure spin-current' and inject spin-aligned carriers in OTP spintronics devices using spin-pumping in FM/OTP bilayers and spin-injection in spin-valve devices, respectively. We have measured a relatively large inverse-spin-Hall effect (ISHE) in $MAPbI_3$ using pulsed microwave excitation in OTP devices at resonance with the ferromagnetic (FM) substrate, from which we derived room temperature spin diffusion length, λ_{sd}~9 nm in $MAPbI_3$. At low temperature we measured giant magnetoresistance in $MAPbI_3$-based spin-valves from which we estimate λ_{sd}~85 nm.

In the following we include two representative figures which show both pulse-ISHE and magnetoresistance measurements in spin-valve devices based on FM/perovskite junctions. **Figure 1** shows pulse-ISHE in FM/perovskite bilayers, whereas **Figure 2** demonstrates magneto-resistance response in a perovskite-based spin-valve device, where the perovskite layer is sandwiched in between two FM electrodes, namely the half metal LSMO and Co.

(i) Spin-pumping into perovskites: Spin-pumping occurs when the magnons in the FM substrate are driven out of equilibrium by absorbing microwaves at ferromagnet resonance [4,5]. The magnons deliver angular momentum to the carriers in the OTP film overlayer through the FM/OTP interface, which aligns the carrier spin ½ sense in the perovskite layer. The spin-aligned carriers in the OTP create an ISHE electric field parallel to the interface that is monitored via an induced ISHE current measured by the Cu electrodes deposited onto the OTP layer. We have demonstrated that the strong SOC in the perovskite layer forms a substantial ISHE current that is only a factor of three smaller than that in Pt metal, which is the standard metal detector for the ISHE. This shows that the perovskites have potential applications in spintronics devices.

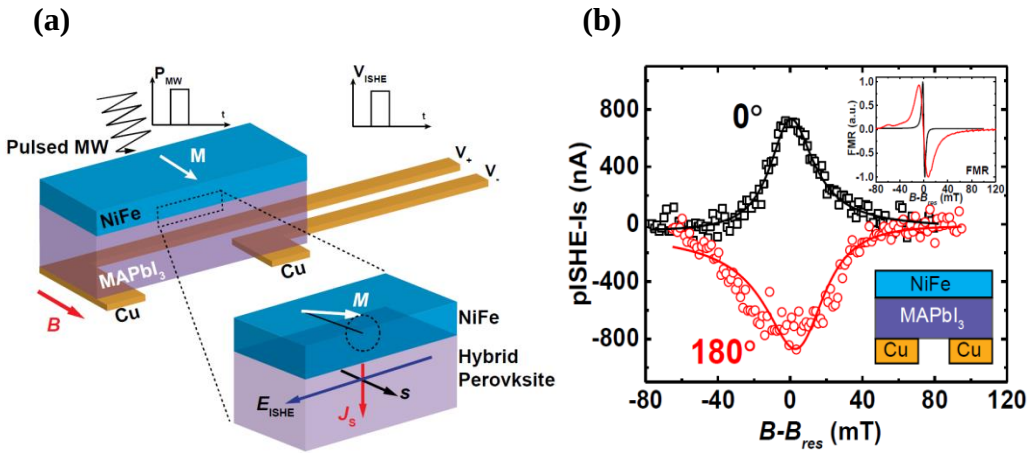

Figure 1: Detection of the pulsed-ISHE response in OTP thin film. a, Schematic illustration of the NiFe/OTP/Cu device used for ISHE measurements (upper panel). **B** and **M** denote, respectively the static external magnetic field and the dynamic magnetization in the NiFe film that precesses around B_0 (lower panel). J_S, S, E_{ISHE}, and I_{pISHE} denote, respectively, the flow of the pulsed spin current in the OTP layer, its spin polarization vector, generated p-ISHE voltage, and detected p-ISHE current. **b,** Typical field response of I_{pISHE} (pISHE-I_S) measured in $MAPbI_3$ perovskite spintronics devices; The black squares and red circles stand for the obtained response using an in-plane magnetic field B at 0º and 180º, respectively. The lines through the data points are fits using a weighted combination of a symmetric ISHE(*B*) function and an asymmetric AHE(*B*) function that represents anomalous Hall effect. The lower inset is schematics of the bilayers device. The upper inset shows the FMR(*B*) response of the NiFe FM film measured without (black) and with (red) the $MAPbI_3$ overlayer, showing spin-pumping into the perovskite layer.

(ii) Spin-injection into perovskites:

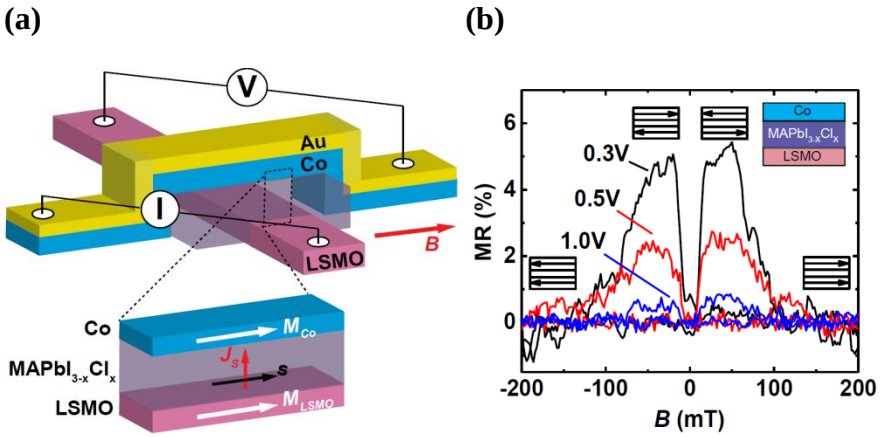

Figure 2: Giant Magnetoresistance in $MAPbI_3$-based spin valve. (a) Schematic of the OPT-based spin-valve. Upper panel: The perovskite layer is positioned in between the LSMO and Co feromagnetic layers having two different cohersive fields (upper panel), where the resistance field-response is measured using 'four probes' geometry. Lower pannel: The LSMO injects spin aligned current, J_S into the OTP layer in a parallel magnetization direction of the two FM electrodes (low resistance). **(b)** Magnetoresistance(*B*) response of $MAPbI_{3-x}Cl_x$ at various bias voltages and *T*=10K. The device schematic is shown in the upper inset. The relative magnetization directions of the FM electrodes are shown for clarity, where the high resistance occurs at antiparallel magnetization configuration.

Figure 2 demonstrates spin aligned carriers injection into OTP film. The measurements were done using a spin-valve device, where the OTP film layer was deposited in between two FM electrodes having two different coercive fields. The MR(*B*) response follows a well-known pattern, where the device resistance, R is higher when the two magnetization direction are antiparallel to each other. We fabricated spin-valves using $MAPbI_{3-x}Cl_x$, as well as other OTP's. Figure 2 shows that the MR(*B*) is strong function of the applied bias voltage; and we also measured a strong MR temperature dependence. These MR responses are very similar to those measured in organic spin-valves [6] indicating similar spin-injection mechanism in both compounds. When the organic moiety in the OTP interacts with the FM metal at the interface, it creates spin-polarized interface states that provide an avenue for more efficient spin-injection into the OTP. This novel spin injection mechanism has been dubbed 'Spinterface' in the organics [7], and we think to use the same definition for interpreting our data here.

(iii) <u>Study of Rashba-splitting in 2D perovskites by optical methods;</u>

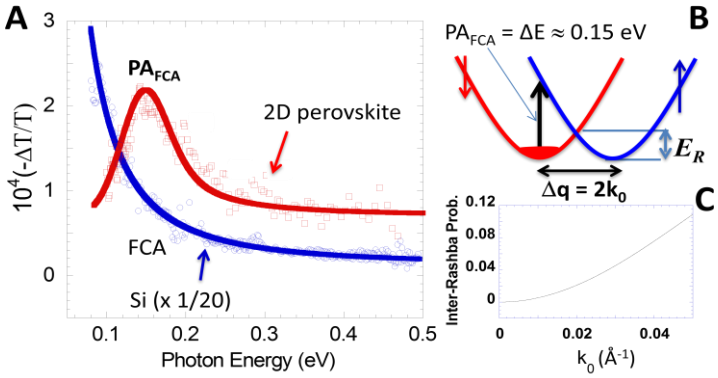

Figure 3: Steady state photomodulation (PM) spectroscopy of 2D OTP film. A: PM spectrum of the 2D OTP film compared to that of a silicon wafer measured at 45K. The PA bands, PA_{FCA} for the 2D OTP and FCA (free carrier absorption) for Si are assigned. The solid lines through the data points are fits using the Drude model in which ($PA \sim \omega^{-2}$) for the Si and another model for the 2D OTP. **B**: Schematic electron energy bands having Rashba-splitting that explains the FCA in the 2D OTP. The Rashba energy (E_R) and momentum offset (k_0 = Δq/2) are assigned. **C**: Probabilities of optical transitions between inter-Rashba-split bands as the function of the Rashba k_0.

The electron dispersion relation, $E(k)$ near the extrema points in the CB and VB of a semiconductor are usually described by the effective-mass approximation, where the electrons and holes are treated as 'free carriers' having an effective mass, m*, that leads to spin-degenerate parabolic dispersion, $E(k)=\hbar^2k^2/2m^*$. However the SOC can split the spin-degenerate bands in non-centrosymmetric compounds. In this case the spin-degenerate parabolic band splits into two spin-polarized bands, where the electron (or/and hole) dispersion relation may be described by the relation $E_{\pm}(k)=(\hbar^2k^2/2m^*)\pm\alpha_R|k|$, where α_R is the Rashba-splitting parameter. This formulation yields new extrema at a momentum offset (k_0) and split energy (E_R) that are related to each other via the relation $\alpha_R = 2E_R/k_0$, see Fig. 3. Importantly, the two Rashba-split branches have *opposite spin sense* that influences the photoexcitations optical and magnetic properties, a situation that may benefit spintronics [8].

Two-dimensional (2D) layered OTP semiconductors form natural 'multiple quantum wells' that possess strong SOC due to the heavy elements in their building block. These may lead to 'Rashba-splitting' close to the extrema in the electron bands. We have employed a plethora of ultrafast transient and nonlinear optical spectroscopies for studying the primary (excitons) and long-lived (free-carriers) photoexcitations in thin films of 2D perovskite, namely $(C_6H_5C_2H_4NH_3)_2PbI_4$. From the photoinduced absorption of excitons and free-carriers (see Fig. 3) we inferred a giant Rashba-splitting in this compound. We have preliminary obtained Rashba-splitting energy of ~40 meV and Rashba parameter of ~2.7 eV•A° in the 2D OTP.

(iv) <u>Electro-absorption (EA) spectroscopy in 2D perovskites;</u>

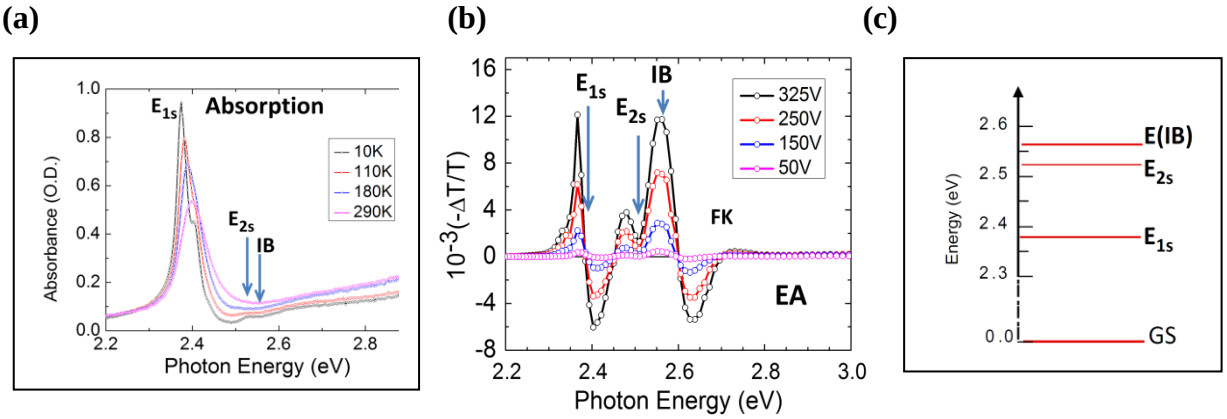

Figure 4: Absorption (a) and electroabsorption (EA) (b) spectra of 2D OTP. The 1s exciton absorption band is clearly seen in (a), but the other absorption features are not discerned. The EA spectrum in (b) clearly shows features associated with the 2s exciton as well as the interband (IB). The energy of these states is summarized in (c).

We have begun measuring the EA spectrum of various 2D OTP's. The exciton binding energy in these compounds is known to be ≈ 200 meV, and this allows the signature of the exciton (Stark shift) and interband transition (Frank Keldish oscillation) to be uniquely separated in the EA spectrum [9]. This is clearly seen in Fig. 4(b) and summarized in Fig. 4(c).

Future Plans

In the 3rd support year of our program we will finish several projects such as spin-pumping in various OTP, spin-injection and importantly also the 'Hanle effect' from which we will obtain the spin relaxation time in these materials. We will also determine the Rashba-splitting energy in various perovskites by optical spectroscopy.

References

<u>[1]</u> Jeon, N. J. *et al*., *Nature* **517**, 476-480 (2015) (Solar Cells); **<u>[2]</u>** Xing, G. et al. *Nat. Mater.* **13**, 476-480 (2014) (Laser action); **<u>[3]</u>** Tan, Z.-K. et al. *Nat. Nano*. **9**, 687-692 (2014) (LEDs).
<u>[4]</u> Ando, K. et al. *Nat. Mater.* **10**, 655-659 (2011) [ISHE discovery]; **<u>[5]</u>** Ando, K. & Saitoh, *Nat. Commun.* **3**, 629 (2012) [ISHE demonstration]. **<u>[6]</u>** Xiong, Z. H. et al., *Nature* **427**, 821-824 (2004) [spin-valve based on organic compounds]. **<u>[7]</u>** Szulczewski, G., et al., *Nat. Mater*. **8**, 693 (2009) [Spinterface]. **<u>[8]</u>** Manchon, *A. et al., Nat. Mater*,**14**, 871-882 (2015) [Rashba splitting]. **<u>[9]</u>** L. Sebastian & G. Weiser, *Phys. Rev. Lett*. **46**, 1156-1159 (1981) [EA spectroscopy].

Publications

[1] "On the role of intrinsic ions accumulation in the photocurrent and photo-capacitive responses of $MAPbBr_3$ photodetectors", E. Lafalce, C. Zhang, X. Liu, and Z. V. Vardeny, ***Applied Materials and Interfaces***, December 2016; 10.1021/acsami.6b11925.

[2] "Multi-Functional Optoelectronic-Spintronics Device Based on Hybrid Organometal Trihalide Perovskites", C. Zhang, D. Sun, Z. V. Vardeny, ***Adv. Electron. Mater.*** **3** DOI: 10.1002/ aelm.201600426 (2017).

[3] "Spin-polarized exciton quantum beats in hybrid organic-inorganic perovskites", P. Odenthal, W. Talmadge, N. Gundlach, R. Wang, C. Zhang, D. Sun, Z.-G. Yu, Z. V. Vardeny, and Y. S. Li, accepted in ***Nature Physics*** (March 2017).

[4] "Reduced lasing thresholds, enhanced emission and increased optical gain of nano-crystalline $MAPbBr_3$ films via anti-solvent treatment", E. Lafalce, C. Zhang, Y. Zhai, D. Sun and Z.V. Vardeny, ***J. Appl. Phys***. **120**, 143101 (2016); doi: 10.1063/1.4964417 2016.

[5] "Giant spin to charge conversion in Organometal Trihalide Perovskites", Dali Sun, Chuang Zhang, Marzieh Kavand, Kipp J. van Schooten, Hans Malissa, Matthew Groesbeck, Ryan McLaughlin, Christoph Boehme, and Z. Valy Vardeny, submitted to ***Nature Commun***. November 2016. http://arxiv.org/abs/1608.00993.

[6] "Novel Spin Physics in Organic-Inorganic Perovskites", Chuang Zhang, Dali Sun, and Z. Valy Vardeny, book chapter on Organic-inorganic Materials and Applications, Willey-VCH, Ed. Dr Sun, August 2016.

[7] "Magnetic field effect in organometal trihalide perovskite", Chuang Zhang, Dali Sun, and Z. Valy Vardeny, book chapter in Spins in Organic, World Scientific, Ed. Markus Wohlgenannt, October 2016.

Coherent control of spin states in organic electronics – spin-spin interaction and collective spin effects on magneto-optoelectronic materials properties

PI: Christoph Boehme, co-PI: John M. Lupton
University of Utah, Department of Physics and Astronomy,
115S 1400E, Salt Lake City, Utah, 84112, boehme@physics.utah.edu
Award # DE-SC0000909

Program Scope

The focus of this program has been on non-polarization related spin-effects that influence material properties of organic semiconductor materials at technologically relevant conditions (room temperature, low magnetic fields). Under these conditions, equilibrium spin-polarization is negligible, yet spin-selection rule-governed phenomena such as spin-dependent charge transport or recombination can nevertheless strongly affect the physical materials behavior under non-equilibrium conditions. Examples for this behavior are revealed by the magnetoresistance experiment of the π-conjugated polymer poly[2-methoxy-5-(2-ethylhexyloxy)-1,4-phenylene-vinylene] (MEH-PPV) that is illustrated in Figure 1(a) and the resulting data that are displayed in panels (b) and (c). These plots show strong, percentage-range room temperature magneto-current changes in the μT to mT-range where spin-polarization is all but vanishing. Moreover, when radio frequency (RF)-range AC magnetic fields are applied in addition to the DC magnetic field, strong magnetic resonance responses of Zeeman split charge carrier states can be observed, as evidenced by the differential magneto-conductance plots shown in (d) and (e), in spite of three orders of magnitude smaller Zeeman energies compared to the thermal equilibrium energy [6].

Given these strong room-temperature/low magnetic field spin-effects, the particular focus of this program is:

(i) To investigate spin-orbit, spin-exchange, spin-dipolar, and spin-hyperfine interactions of and between charge carriers in various organic semiconductor materials with regard to ***how these spin-interactions influence spin-dependent transitions*** and what the physical nature of the spin-dependent transitions is, i.e. to find out which spin manifolds such as charge carriers, excitons, trions, and pairs thereof undergo what kind of spin-dependent electronic transitions, and ***how these spin-dependent processes control the macroscopic electronic and optical properties*** of these materials.

(ii) To study the interplay between hyperfine and spin-orbit interactions over largest experimentally available magnetic field ranges in order to ***determine under which conditions which of the two interaction***

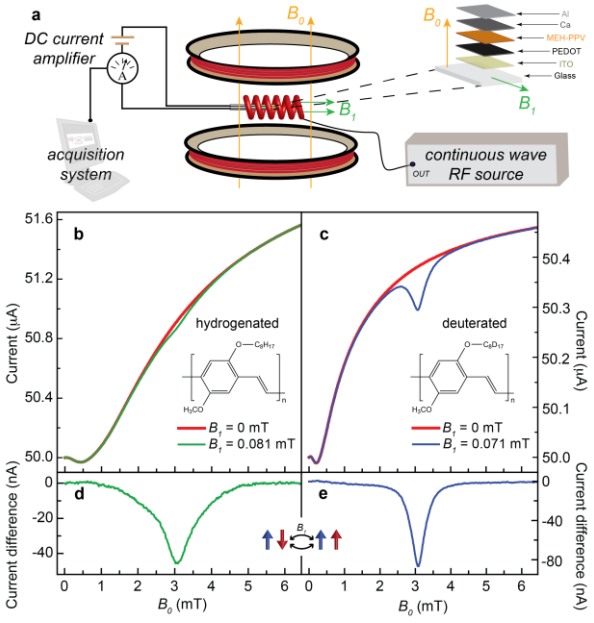

Figure 1: **Magnetoresistance and magnetic resonance in a DC current of a polymer diode at room temperature and low magnetic fields.** a) Experimental setup and sample structure; b,c) magnetoresistance curves for hydrogenated and deuterated MEH-PPV with and without application of RF radiation. d,e) Differential magneto-current. Adapted from Ref. [6].

types is most dominant for the distribution of Larmor frequencies. The results of these activities are not only crucial for the understanding of macroscopic magneto-optoelectronic behavior in general but also for the determination of whether a given material is capable to host electron-hole pair ensembles whose spin states are able to assume a collective state in the so-called spin-Dicke regime. Such spin collectivity has recently been predicted theoretically in organic semiconductors [1] for AC magnetic field drive conditions when the AC amplitude B_1 is equal or larger than a perpendicularly applied DC magnetic field B_0, while the latter must exceed the magnitude of all other random local magnetic fields, including random local hyperfine fields.

(iii) To measure DC magneto-current changes in organic semiconductors at low static magnetic fields (B_0 < 5mT) and the largest technologically achievable range of RF driving field amplitudes (B_1 aimed to exceed 5mT) in order to ***corroborate the existence of the spin-collective behavior of charge carriers and the control of macroscopic material properties (current, optical emissions, etc.) by this effect.*** For this, an experimental approach using a monolithic RF excitation/polymer resistor device system is needed permitting $B_1 > B_0$. Using this device, predictions for the emergence of macroscopic material effects caused due the presence of charge carriers in the Dicke regime can be scrutinized. Furthermore, it is also sought to **independently confirm the Dicke ensemble state** through magnetoresistance effects due to spin-resonantly induced transitions between dressed AC Zeeman states or by observation and quantitative study of an electrically detected Bloch-Siegert shift [1,6]. Once these confirmations were to be made, an ***assessment of whether spontaneously evolving spin-collective domains in organic semiconductors are possible under technological materials operation conditions and whether this can lead to significant influences on opto-electronic materials behavior*** that is not explainable by spin-selective processes of local spin-interacting paramagnetic states (polarons, excitons, trions and pairs thereof).

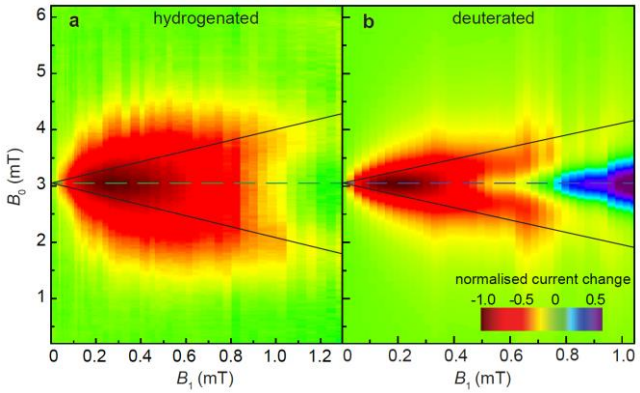

Figure 2: Plots of the magneto-current change in OLEDs with hydrogenated (a) and deuterated (b) MEH-PPV as a function of B_0 and B_1. Both samples magnetic resonant signal for $B_0 \approx$ 3mT. A splitting of the resonance due to the *ac*-Zeeman effect is clearly resolved under weaker hyperfine coupling as provided by the deuterated sample. The deuterated sample also shows a clear inversion of signal amplitude at the onset of the predicted spin-Dicke regime (c). Black lines indicate magnetic field corrections to B_0 arising from B_1-induced Zeeman splitting. Adapted from Ref. [6]

Recent Progress

During the past 24 months, much progress has been made on the simultaneous measurements of spin-orbit induced spin effects (namely, the distribution of effective *g*-factors) and spin-hyperfine coupling induced effects. By means of multi-frequency electrically detected magnetic resonance (EDMR), the two interaction types could be distinguished with excellent accuracy [4], while, by application of simple monochromatic magnetic resonance spectroscopy, they are spectroscopically indistinguishable.

Furthermore, we have expanded our multi-frequency EDMR studies beyond the intensively studied model system MEH-PPV to other materials such as poly(styrene-sulfonate)-doped poly(3,4-ethylene-dioxythiophene) (PEDOT:PSS) [8] or Polyfluorene (PFO) [3]. These studies have revealed values of upper bounds for spin-dipolar and spin-exchange interactions in

PEDOT:PSS and the, so far, strongest electrically detected hyperfine field in a polymer device, which was found in PFO. This progress has been possible because of improvements that have been made on our experimental facilities, most significantly through the development of innovative resonator [4] and magnetic resonance probehead designs [5]. Technological advancements have also been made on the development of high-B_1 AC/low B_0 DC magnetic field facilities and a first demonstration of the emergence of a collective charge carrier state. Spin collectivity is predicted to emerge when all electron-hole pairs within a collective charge carrier spin-ensemble align into triplet states and thus, quench spin-dependent recombination rates [1]. Figure 2 displays the magnetocurrent of two MEH-PPV diodes as functions of B_0 and B_1 with the latter being the amplitude of an 85MHz RF field for hydrogenated (a) and deuterated (b) MEH-PPV [6]. For the hydrogenated sample, a spin resonant change of the recombination current (centered at about 3mT was shown to be negative (indicating a positive recombination rates change) up to the maximally achieved values of B_1 of ~1.2mT. These results are indicative for the presence of spin-dependent recombination but they are not indicative for the presence of a collective regime. In contrast, for the deuterated sample, which has weaker local hyperfine fields, an on-magnetic resonance current increase (a recombination rate quenching, as evidences the blue and purple colors) is seen for $B_1 \approx 0.8$mT and above. We note that for these experiments, B_1 was generated by macroscopic copper coils, which limited B_1 to about 1.2mT due to the extensive heat development of the coils under continuous AC drive. Thus, only the onset of collectivity was observed while the condition $B_1 > B_0$ was not fulfilled yet.

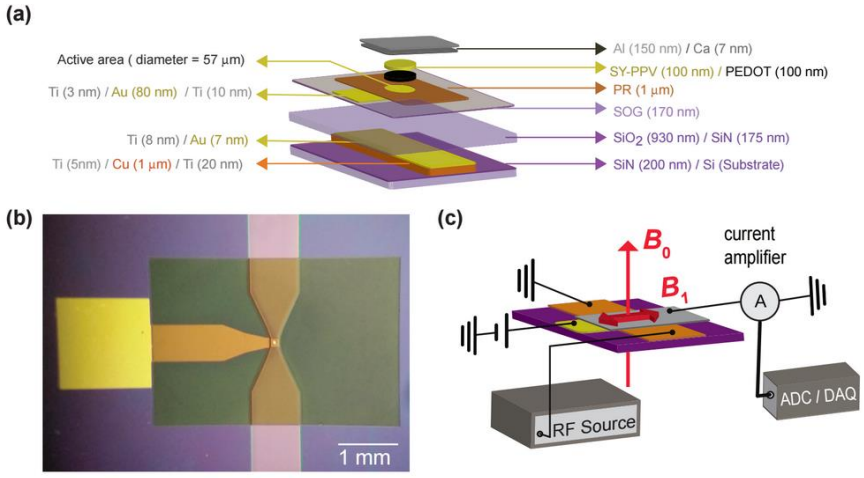

Figure 3: Monolithic polymer diodes with AC drive structures and the used experimental setup needed to measure spin-dependent electric currents. **a)** Layer structure used for the example of a PPV derivative and PEDOT as conducting polymers. **b)** Microscope image of the device with the active device area of 57 µm diameter visible as bright spot, taken prior to spin coating of the electroactive polymer layers and thermal deposition of the cathode. **c)** Sketch of the experimental setup.

Since B_0 must larger than local hyperfine fields and thus, $B_0 \geq 3$mT, a different approach to generate larger values for B_1 had to be found. This was accomplished by developing monolithic polymer/B_1 stripline devices which combine the ability to generate highest RF magnetic driving fields in the vicinity of microscopic conducting polymer-based thin-film devices. The structure of this integrated device concept, as shown in Fig. 3, is based on a thick (~1µm) electrical and thermal insulation layer consisting of silicon nitride/silicon dioxide and spin-on glass (SOG) that separates an approximately equally thick Cu layer which produces the room temperature RF magnetic field oscillations. Due to the use of a crystalline silicon substrate, this design has good heat sinking properties, allowing for high enough AC currents in the Cu stripline to produce $B_1 > B_0$ without causing heat damage to the organic semiconductor layers.

Future Plans

Within the next year, it is planned to carry out magnetic resonance experiments on dressed charge carrier states, i.e. magnetic resonance in the rotating spin reference frame that is defined by the circular component of the driving field B_1. When a collective spin-state appears, charge carrier spin-eigenstates around the oscillating magnetization axis will evolve. An AC magnetic field perpendicular to B_1, i.e. an oscillating magnetic field B_2 that is parallel to the static field B_0 and on-resonance with the dressed AC Zeeman state is then anticipated to magnetic resonantly scramble the collective spin ensemble. By doing this, the spin-Dicke effect will be diminished, causing a disappearance of the recombination current quenching that is seen in Fig.2 (b). This experiment will be a fundamental test of the currently existing description of coherent charge carrier spin dynamics in organic semiconductors.

References

[1] R. C. Roundy, & M. E. Raikh, Organic magnetoresistance under resonant ac Drive, *Phys. Rev. B* **88**, 125206 (2013).

Published Journal Articles of BES sponsored research in 2015-2017

[2] C, Boehme, H. Malissa, Electrically Detected Magnetic Resonance Spectroscopy, *eMagRes* **6**, 83 (2017).
[3] R. Miller, K. J. van Schooten, H. Malissa, G. Joshi, S. Jamali, J. M. Lupton, and C. Boehme, Morphology effects on spin-dependent transport and recombination in polyfluorene thin films, *Phys. Rev. B* **94**, 214202 (2016). https://doi.org/10.1103/PhysRevB.94.214202
[4] G. Joshi, R. Miller, L. Ogden, M. Kavand, S. Jamali, K. Ambal, S. Venkatesh, D. Schurig, H. Malissa, J.M. Lupton, and C. Boehme, Separating hyperfine from spin-orbit interactions in organic semiconductors by multi-octave magnetic resonance using coplanar waveguide microresonators, *Appl. Phys. Lett.* **109**, 103303 (2016). http://dx.doi.org/10.1063/1.4960158
[5] M. Kavand, D. L. Baird, K. J. van Schooten, H. Malissa, J. M. Lupton, C. Boehme, Discrimination between spin-dependent charge transport and spin dependent recombination in π-conjugated polymers by correlated current and electroluminescence-detected magnetic resonance, *Phys. Rev. B* **94**, 075209 (2016). http://dx.doi.org/10.1103/PhysRevB.94.075209
[6] D. P. Waters, G. Joshi, M. Kavand, M. E. Limes, H. Malissa, P. L. Burn, J. M. Lupton, C. Boehme, The spin-Dicke effect in OLED magnetoresistance, *Nature Physics* **11** (11), 910 (2015). http://dx.doi.org/10.1038/nphys3453
[7] W. J. Baker, T. L. Keevers, C. Boehme, and D. R. McCamey, Using coherent dynamics to quantify spin-coupling within triplet-exciton/polaron complexes in organic diodes, *Phys. Rev. B* **92**, *041201(R)*, (2015). http://dx.doi.org/10.1103/PhysRevB.92.041201
[8] K. J. van Schooten, D. L. Baird, M. E. Limes, J. M. Lupton, C. Boehme, Probing quantum entanglement and zero-field splitting in conducting-polymer radical pairs by electrically detected spin-beating, *Nature Communications* **6**, 6688 (2015). http://dx.doi.org/10.1038/ncomms7688

The Mesoscale: A Laboratory for Dynamical Measurements

PI: Raymond L. Orbach
Texas Materials Institute, The University of Texas at Austin

Co-PI's:
E. Dan Dahlberg
School of Physics and Astronomy, University of Minnesota
Gregory G. Kenning
Department of Physics, Indiana University of Pennsylvania

Program Scope

Our Program focuses on the dynamics of random systems at the mesoscale: the dynamical properties of disordered materials with length scales between a few to tens of nanometers. Control of the maximum correlation length of cooperative systems to mesoscale dimensions allows the examination of quasi-equilibrium collective effects within laboratory time scales.

Glassy systems typically are never in equilibrium, so that their dynamics are dependent on measurement times. Nevertheless, there is evidence for a dynamical correlation length in glassy materials.[1] The beauty of mesoscale measurements is that one can examine the nature and growth of a volume with dimensions of the correlation length fixed by the sample size, rather than through fifth-order (!) dielectric susceptibilities.[1]

Our research into glassy properties utilizes the magnetic properties of thin-film spin glasses. Most experimental measurements are analyzed using two competing models ("critical dynamics"[2] and "droplet dynamics"[3]). By thermal quenching a spin glass system, one can initialize the growth of the correlation length, and directly measure the consequences of its growth in time. At the mesoscale, when the correlation length reaches the thin-film thickness, its growth in that direction ceases. In principle, growth continues in the in-plane direction, but it is in two dimensions, which is below the spin glass lower critical dimension of ≈ 2.5.[4] Growth in the in-plane direction is then logarithmic in time,[3] sufficiently slow that it can be ignored on reasonable laboratory time scales. This results in a quasi-equilibrium state, with a three dimensional (d = 3) length scale equal to the thin-film thickness.

We have explored the glassy properties of spin glasses in this regime. Using SQUID susceptometer measurements, we have set limits on the lower critical dimension,[5] and measured the length scale dependence of dynamical properties.[6] This has provided the first direct experimental distinction between the two competing models. We are currently exploring the physics of the growth of the correlation length[7] (compact or fractal); fluctuation properties through noise measurements; and temperature- and magnetic field-induced chaotic behavior.[8] Ultimately, we expect the insights gained through these spin glass dynamical measurements will shed light on the universal properties of glassy materials.

Recent Progress

The systems we have investigated have been thin-film spin glasses, with thicknesses between 4.5 nm and 20 nm. The initial material was a 15.5 nm GeMn layer, formed by ion implantation of Mn into a Ge crystalline substrate. The implantation resulted in an amorphous structure containing magnetic Mn spins at ≈ 11 at. %, displaying spin glass behavior below a spin glass transition temperature $T_g \approx 24$ K. In order to examine different length scales, and to

compare with decades of previous measurements, CuMn thin films of thicknesses between 4.5 nm and 20.0 nm have been grown with a Mn concentration ≈ 11.3 at.%. To insure sufficient measurement signal, multilayer samples were grown with 40 CuMn spin glass layers separated by 60 nm thick Cu layers, sufficiently large to magnetically decouple the spin glass layers.

The experimental procedure is to start with the spin glass system in the paramagnetic state at a temperature well above the spin glass transition temperature T_g. The temperature is then rapidly reduced (10 K/min) to a measurement temperature $T < T_g$. The spin glass correlations nucleate and grow in time in three dimensions until the correlation length reaches the thin film thickness $\mathcal{L}$. At that point, the component of the correlation length in this direction is pinned at $\mathcal{L}$. Further growth in the in-plane direction of the spin glass correlation length is in d = 2, but the lower critical dimension for spin glasses is $d_\ell \approx 2.5$.[4] For $d < d_\ell$, $T_g = 0$ and the in-plane correlation length grows as $\ell n\, t$.[3] Because this growth is slow on laboratory time scales, the spin glass correlated volume is roughly spherical, with a length scale of the order of $\mathcal{L}$. The system is then in a quasi-equilibrium state, and can be "probed" by changes in either magnetic field or temperature. The important point is that it is a d = 3 spin glass, with a maximum length scale given by the film thickness $\mathcal{L}$.

The experimental evidence for this behavior is based on measurements of the thickness dependent activation energy Δ_{max}.[9] The analysis assumed an ultrametric arrangement of metastable states organized by virtue of their overlap q with the initial state. Ultrametricity is a geometry[10] arising from the Parisi solution[11] of the infinite range spin glass model of Sherrington and Kirkpatrick.[12] and pictured as a random "tree,"[13]

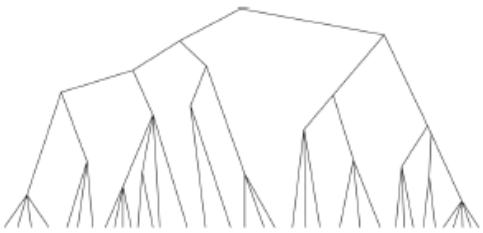

self overlap $q = q_{EA}$ → decreasing overlap q q_{min}

The ultrametric tree

where the tips of the bottom branches represent spin glass states, and the number of vertices traversed between the tips is a measure of the reduction in overlap q. The furthermost state on the left of the tree is the quenched spin glass state with self-overlap q_{EA}, the Edwards-Anderson order parameter. Every bottom tip in the tree has the same energy and magnetization,[14] but its overlap with the initial quenched state is reduced by the number of vertices required to reach that state from the initially quenched state. The last states on the right have the minimum overlap q_{min} with the initial quenched state. Further, the smaller the overlap, the larger the number of pairs of spins that are reversed from the initial quenched state. One can therefore associate a free energy barrier Δ that increases as the overlap diminishes with the initially prepared state.[15] Because the number of states having a given overlap with the initial quenched state increases exponentially as the overlap decreases, dynamics will be controlled by the largest free energy barrier Δ_{max} associated with the states of minimum overlap q_{min}.

Starting at t = 0 after a quench to T, the initial state occupancy diffuses over free energy barriers to states with diminishing overlap q (increasing Δ). The correlation function at time t, ξ(t,T), can be related to the free energy of the highest barrier surmounted in that time:[2]

$$\frac{\Delta_{\max}(T)}{k_B T_g} = \frac{1}{c_2}\left[\ln\left(\frac{\xi(t,T)}{a_0}\right) - \ln c_1\right].$$

Here, c_1 and c_2 are constants of order unity and 0.1, respectively. But $\xi(t,T)$ stops at $\mathcal{L}$ at a time we designate as the crossover time, t_{co}. The time dependence of any parameter, for example the change in magnetization upon a change in magnetic field, will then be dominated by the states with minimum overlap q and maximum barrier height $\Delta_{max}(\mathcal{L})$. The time dependence will be activated, with activation energy $\Delta_{max}(\mathcal{L})$ that is *independent of t and T* and only a function of thin-film thickness $\mathcal{L}$ [see above with $\xi(t,T) = \mathcal{L}$]. This is displayed below in a table from Ref. 6:

$\mathcal{L}$ (nm)	T_f (K)	T_m (K)	$\Delta_{\max}(\mathcal{L})/k_B$ (K)
4.5	25	22.5	907 ± 2
		23	910 ± 7
		23.5	904 ± 2
9	35	31	1243 ± 8
		31.5	1243 ± 13
		32	1252 ± 10
20	46	41	1648 ± 4
		41.5	1650 ± 2
		42	1652 ± 8

Here, T_f is the "freezing" or transition temperature determined by the thickness of the sample, and T_m is the measurement temperature T. An additional "dividend" of this analysis is the dependence of $\Delta_{max}(\mathcal{L})$ on $\mathcal{L}$. Our analysis shows[6] it is consistent with critical dynamics,[2] but not with droplet dynamics;[3] the first clear delineation between the two models.

Future Plans

Now that we have established a "mesoscopic laboratory" for glassy dynamics, we intend to probe its more subtle properties. One such property is chaos. Spin glasses are a superb physical system to examine the nature of chaos, and its dependence on external parameters. We have already observed temperature chaos in the GeMn system.[9] We found that reversible behavior takes place for small temperature changes, with a sharp transition to a chaotic state at large temperature changes. By chaos, we mean that the system "forgets" where it came from. Thus, measuring Δ_{max} for different temperature changes exhibits reversible behavior for small temperature changes (increasing Δ_{max} with decreasing T), but maintains the initial Δ_{max} for large temperature changes.

Very recent theoretical work[8] suggests that temperature chaos is a probabilistic phenomenon, such that both reversible and chaotic states coexist at the same time, their relative magnitudes given by a temperature change probability density. This new insight requires longer measurement times than we have performed previously, and we are currently undertaking steps to explore this interesting possibility.

We also have observed magnetic field induced chaos, and, to this point in time, the absence of *any* reversible behavior. Further, the strength of magnetic field chaos appears to be much larger than for temperature chaos. We believe we understand the nature of the final chaotic state (it can be thought of as "decoupling" the initially occupied states in the ultrametric tree, and then "rejuvenating" the system where each of the uncoupled states now starts diffusing along its own ultrametric tree). The chaotic state seems to occur no matter how small the magnetic field variation, a surprise given the tiny energy associated with small magnetic field variations. This investigation promises significant insight into a topic with only little theoretical guidance.[16]

An exciting new area is to use electronic or resistance noise measurements to probe the fluctuation spectrum of the quasi-equilibrium states when the correlation length $\xi(t \geq t_{co},T) = \mathcal{L}$. Previous researchers have found a significant increase in 1/f fluctuations in the spin glass state.[17] This 1/f noise is a unique probe of the dynamics, and we have already replicated their results as shown in the figure below:

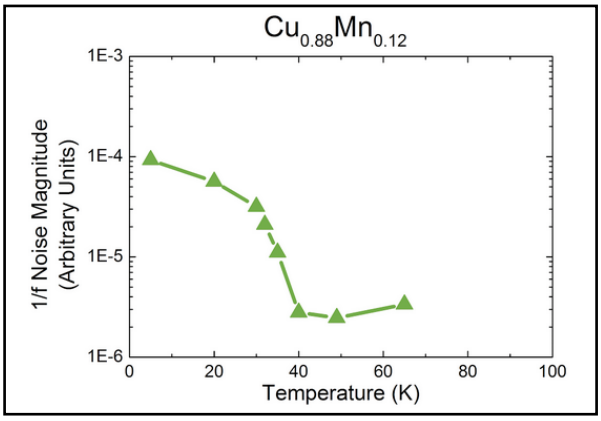

Observed 1/f noise increase by 10^2 in spin glass state

The spectrum is expected to cross over from the 1/f behavior previously observed in spin glass noise fluctuations at times less than t_{co} to an activated form with activation energy $\Delta_{max}(\mathcal{L})$ for times longer than t_{co}. This experiment is crucial because it is independent of any magnetic field or temperature change. Films of different thicknesses, $\mathcal{L}$, are being grown to test this and, if observed, to see if the extracted $\Delta_{max}(\mathcal{L})$ is consistent with the above table.

References

1. S. Albert et al., Science **352**, 1308 (2016).
2. J. Hammann et al., Physica **185A**, 278 (1992).
3. D.S. Fisher and D.A. Huse, Phys. Rev. Lett. **56**, 1601 (1986).
4. L.W. Lee and A.P. Young, Phys. Rev. B **76**, 024405 (2007).
5. S. Guchhait and R.L. Orbach, Phys. Rev. Lett. **112**, 126401 (2014).
6. Q. Zhai et al., Phys. Rev. B **95**, 054304 (2017).
7. F. Belletti et al., J. Stat. Phys. **135**, 1121 (2009).
8. L.A. Fernandez et al., Europhys. Lett. **103**, 67003 (2013).
9. S. Guchhait and R.L. Orbach, Phys. Rev. B **92**, 214418 (2015), plus new $T_q = 20.975$ K point.
10. M. Mézard et al., J. Phys. (Paris) **45**, 843 (1984).
11. G. Parisi, Phys. Lett. A **73**, 203 (1979).
12. D. Sherrington and S. Kirkpatrick, Phys. Rev. Lett. **35**, 1792 (1975).
13. G. Parisi, Proc. Nat. Acad. Sci. **103**, 7948 (2006).
14. M. Mézard and M.A. Virasoro, J. Phys. (Paris) **46**, 1293 (1985).
15. D. Vertechi and M.A. Virasoro, J. Phys. (Paris) **50**, 2325 (1989).
16. I. Kondor, J. Phys. A: Math Gen. **22**, L-163 (1989).
17. N.E. Israeloff et al., Phys. Rev. Lett. **63**, 794 (1989).

Publications supported by and referenced DE-SC0013599

1. S. Guchhait and R.L. Orbach, Temperature Chaos in a Ge:Mn thin-film spin glass, Phys. Rev. B **92**, 214418 (2015). Reference 9 above.

2. D.M. Tennant, Four wave mixing as a probe of the vacuum, Phys. Rev. D **93**, 125032 (2016).

3. Q. Zhai, D.C. Harrison, D. Tennant, E.D. Dahlberg, G.G. Kenning, and R.L. Orbach, Glassy dynamics in CuMn thin-film multilayers, Phys. Rev. B **95**, 054304 (2017). Reference 6 above.

4. P.R.T. Ribeiro, J.M.M. Ramirez, R. Vidyasagar, F.L.A. Machado, S.M. Rezende and E. Dan Dahlberg, Appl. Phys. Lett. **109**, 102404 (2016).

5. S. Guchhait and R.L. Orbach, Magnetic field dependence of spin glass free energy barriers, Phys. Rev. Lett. (in press) (2017).

Session IX

Phase-Field Modeling of Materials Interfaces and Nanostructures

Principal Investigator: Alain Karma
Address: Department of Physics and Center for Interdisciplinary Research on Complex Systems, Northeastern University, 360 Huntington Avenue, Boston, Massachusetts 02115
Email: a.karma@neu.edu

Program Scope

Nanostructured materials offer unique properties for a wide range of energy applications. Liquid metal dealloying (LMD) has recently attracted wide attention in the materials communities as a powerful alternative to electrochemical dealloying to produce topologically complex nanoporous and nanocomposite structures with remarkable properties. Materials applications of LMD range from ultra-high surface area electrolytic capacitors to nanocomposites combining high strength and high ductility to nanoporous Si for battery anodes with high-capacity and very long cycle life. While electrochemical dealloying is limited to a few metallic alloys, LMD can be used to dealloy much more diverse mixtures of both metallic and non-metallic elements, thereby dramatically enhancing the ability to produce novel nanostructures by dealloying. Yet, the fundamental principles that govern structure formation during LMD have just started to be explored. This project exploits the phase-field method to investigate the basic mechanisms that control the morphology and composition of dealloyed nanostructures. This research exploits the unique capability of this method to track simultaneously the geometrically complex evolution of the solid-liquid interface during dealloying and compositional domain formation within the interfacial layer in a thermodynamically consistent way. We are using phase-field simulations to investigate the mechanisms that control the range of alloy and melt compositions yielding nanostructures with desired high-genus connected topologies, the kinetics of dealloying, and the evolution of the structure scale. We are also developing this method to study the formation of nanoporous crystalline Si by dealloying of Si-based alloys (e.g. Si-Mg and Si-Ge) as well as to investigate the chemo-mechanical behavior of nanoporous crystalline Si. The latter study exploits our recently developed phase-field model of chemo-mechanical fracture, which is being extended to include the anisotropic crystalline Si to amorphous Li_xSi alloy phase transformation. This model is being used to address the outstanding question of why nanopourous Si exhibits superior properties as a Li-ion battery anode material.

Recent progress

Nanoporous and nanocomposite structure formation by liquid metal dealloying

Liquid metal dealloying (LMD) is a novel materials processing method that involves placing a precursor A-B alloy with a high enthalpy of mixing in contact with a liquid metal element (C). The miscible element (B) is dissolved selectively in the liquid metal while the immiscible element (A) simultaneously organizes to form a porous structure. After solidification of the liquid metal, a nano/micro-composite of A-rich and B-C solid phases is formed. In a second step, one phase can be etched away to obtain a nanoporous structure with a high specific area. We have recently used phase-field simulations [Geslin et al., 2015] to reproduce for the first time the wealth of structures observed during LMD and to gain

fundamental insights into their formation. Simulations of Ta-Ti alloys dealloyed by a Cu melt revealed that spinodal decomposition confined at the solid-liquid interface at early stages of interfacial pattern formation, and a diffusion-coupled growth mechanism analogous to eutectic growth at later stages, combine in the unique setting of LMD to generate topologically complex structures with varied connectivities.

We have developed a theory of dealloying kinetics and compared the predictions to detailed experimental observations in the Ta-Ti-Cu system [McCue et al., 2016]. In addition, we have extended our phase-field modeling study to investigate how the structure topology, scale, and composition can be controlled by varying the composition of the liquid melt. For this purpose, we simulated dealloying of Ti-Ta alloys by Cu-Ti melts. We simulated microstructural pattern formation as a function of both the concentration C_{Ta}^{s} of Ta in the solid Ta-Ti alloy and the concentration C_{Ti}^{l} of Ti in the liquid Cu-Ti melt. Results of simulations are summarized in Fig. 1. As C_{Ta}^{s} is increased, the dealloyed morphology evolves from disconnected islands to filaments to a connected nanoporous structure to planar dissolution above a critical value of C_{Ta}^{s} beyond which alloy elements cannot be separated. Simulation results also reveal that the scale of the morphology (ligament size) increases with Ti concentration in the melt up to an upper limit beyond which dealloying is no longer possible. This limit corresponds to the thick red line in the upper panel of Fig. 1. To the left of this boundary, spinodal decomposition drives the formation of Ta-rich and Ta-poor regions inside the solid-liquid interfacial layer and, to the right of this boundary, planar dissolution occurs without spinodal decomposition inside the solid-liquid interfacial layer. We further developed a time-dependent analysis of compositional stability within the interfacial layer to predict the occurrence of dealloying. The basic steps of this analysis and its results are shown in the bottom panel of Fig. 1 that distinguishes regions of the (C_{Ta}^{s}, C_{Ti}^{l}) composition plane where spinodoal decomposition occurs (filled yellow circles) or does not occur (blue crosses) during planar front

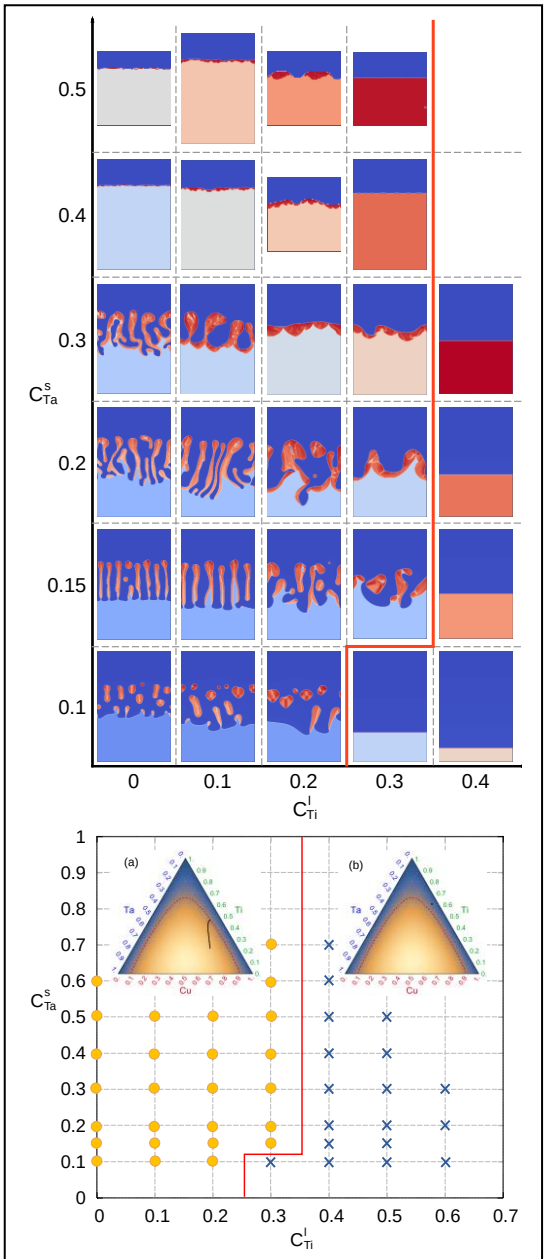

Fig. 1. Results of phase-field simulations of liquid metal dealloying (top panel) as a function of Ta concentration in the base alloy (C_{Ta}^{s}) and Ti concentration in the liquid melt (C_{Ti}^{l}). The red line denotes the boundary between unstable spinodal decomposition and stable planar dissolution that is theoretically predicted by a compositional stability analysis of the interfacial layer (bottom panel).

dissolution. To predict the boundary between those two regions (red line in top and bottom panels), we first compute the range of solid-liquid interfacial compositions that is stable or unstable against compositional modulations, corresponding to regions above and below the spinodal boundary (red dashed line) in a ternary composition plot (insets of the bottom panel of Fig. 1). We then superimpose on the ternary plot the trajectories (solid black lines) of interfacial compositions obtained from phase-field simulations of planar-front dissolution. Dealloying is predicted to occur when a trajectory crosses the spinodal boundary as illustrated in inset (a). In contrast, planar dissolution is stable (no dealloying) when no crossing occurs as illustrated in inset (b). This compositional stability analysis yields predictions in good quantitative agreement with phase-field simulations and provides an efficient method to predict the occurrence of dealloying in more complex alloys.

Chemo-mechanical behavior of Li-ion battery materials

Cyclic volume expansion and contraction associated with Li insertion and removal can cause fracture and ultimately battery failure. As a result, understanding the mechanical behavior of Li-ion battery materials has emerged as a major research topic.

Cathodic particles. We have extended to three dimensions our analysis of the fracture of battery cathodic particles driven by tensile stresses that are generated during the de-lithiation charging cycle. We modeled a spherical cathodic particle with a penny-shaped crack on its surface. Unlike previous investigations, we do not assume any planes of symmetry for these cracks and use instead large scale (~13-15 M tetrahedral elements) finite element phase-field simulations to track geometrically complex fracture paths. Results of those simulations illustrated in Fig. 2 show that penny-shaped cracks tessellate the particle surface but do not penetrate deep inside its interior. Crack propagation releases the tensile stresses generated by de-lithiation and retard their radial propagation. Furthermore, the topology of the created surface patterns changes from a complex network of surface fractures (1st and 2nd images from left in Fig. 2) to a simple fracture ring as the imposed de-lithiation flux increases (3rd and 4th images in Fig. 2). Our simulations further predict that the size of an activated flaw a_0 follows the robust power law $a_0 \sim (t_D/t_C)^{-2}$ for arbitrarily complex crack paths, where t_D is the characteristic Li ion diffusion time scale and t_C is the characteristic charging time.

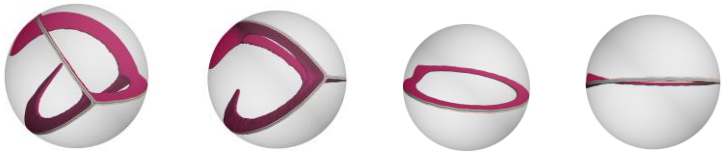

Fig. 2: Fracture topologies generated inside a 10 μm spherical cathodic particles starting from an initial 0.75 μm penny shaped crack for low $t_D/t_C = 10$ (1st and 2nd images from left) and high $t_D/t_C = 15$ (3rd and 4th images from left) de-lithiation flux.

Si anodic particles. We have developed a phase-field model of coupled crystalline to amorphous phase transformation and fracture during lithiation of Si anode particles. We implemented a large deformation Neo-Hookean elastic model and coupled this model to a phase-field formulation of anisotropic crystalline-amorphous interface evolution. The Neo-Hookean model addresses the main shortcomings of previously used St. Venant-Kirchhoff models. Those models assume small strains even in a large deformation framework and do not prohibit an unphysical interpenetration of fracture surfaces under compression. Our

model provides a self-consistent description of both tensile stresses and compressive stresses generated near the particle surface during lithiation. To model the anisotropic crystalline to amorphous phase transformation, we implemented a non-conserved Allen-Cahn dynamics with anisotropic interface mobility [Nguyen et al., Phys. Fluids 22 (2010)] to recover the correct interface dynamics. The anisotropic mobility is modeled using the expression provided in [An et al., Phys. Chem. Chem. Phys. 17 (2015)] where the interface normal direction is expressed in terms of the gradient of the phase-field. Furthermore, as observed experimentally [Liu et al., ACS Nano 7 (2013)], lithiation is limited by the mechanical pressure generated inside the Si structure. To incorporate this effect, we have developed and implemented a thermodynamically consistent phase-field formulation that includes the coupling of mechanical stress to the phase change dynamics.

Future plans

We will extend our phase-field simulation study of liquid metal dealloying to explore the role of faceting of the solid-liquid interface on dealloyed structures. Recent experimental observations in the Si-Mg/Bi and Si-Ge/Bi model systems suggest that coarsening is considerably slower in faceted systems compared to non-faceted metallic systems, thereby yielding smaller ligament sizes in the submicron range. Simulations will explore how faceting affects the dealloyed structure scale and the coarsening kinetics away from the dealloying front.

We will use our phase-field model of coupled phase change and fracture to investigate the mechanical behavior of different Si electrode morphologies varying from nano-pillars to nanoporous crystalline Si structures of different genus created by phase-field simulations of dealloying for the precursor Si-Ge and Si-Mg alloys dealloyed by liquid Bi. Those simulations will investigate which geometrical features of nanoporous Si yield a superior performance for Li ion battery anode applications and explore how to optimize electrode morphology to maximize capacity while minimizing fracture.

References

1. An, Y., Wood, B. C., Ye, J., Chiang, Y. M., Wang, Y. M., Tang, M., & Jiang, H. (2015). *Physical Chemistry Chemical Physics*, *17*(27), 17718-17728.
2. Liu, X. H., Fan, F., Yang, H., Zhang, S., Huang, J. Y., & Zhu, T. (2013). *Acs Nano*, *7*(2), 1495-1503.
3. Nguyen, S., Folch, R., Verma, V. K., Henry, H., & Plapp, M. (2010). *Physics of Fluids*, *22*(10), 103102.
4. Geslin, P. A., McCue, I., Gaskey, B., Erlebacher, J., & Karma, A. (2015). *Nature communications*, *6*, article number 8887.
5. McCue, I., Gaskey, B., Geslin, P. A., Karma, A., & Erlebacher, J. (2016). *Acta Materialia*, *115*, 10-23.

DOE sponsored publications (2015 to 2017)

1. "Topology-generating interfacial pattern formation during liquid metal dealloying", P.-A. Geslin, I. McCue, J. Erlebacher, and A. Karma, *Nature Communications* **6**, 8887 (2015).
2. "Morphological instability of grain boundaries in two-phase coherent solids", P.-A. Geslin, Y. Xu, and A. Karma, *Phys. Rev. Lett.* **114**, 105501 (2015).
3. "Ginzburg-Landau theory of the bcc-liquid interface kinetic coefficient", K.-A. Wu, C.-H. Wang, J.J. Hoyt, and A. Karma, *Phys. Rev.* B **91**, 014107 (2015).
4. "Multiscale cohesive zone model for propagation of segmented crack fronts in mode I+III fracture", J.-B. Leblond, V. Lazarus, and A. Karma, *Int. J. Fracture* **191**, 167-189 (2015).
5. "Three-Dimensional Multiscale Modeling of Dendritic Spacing Selection During Al-Si Directional Solidification", D. Tourret, A.J. Clarke, S.D. Imhoff, P.J. Gibbs, J.W. Gibbs, and A. Karma, *JOM* **67**, 1776-1785 (2015).
6. "Crack Front Segmentation and Facet Coarsening in Mixed-Mode Fracture", C.-H. Chen, T. Cambonie, V. Lazarus, M. Nicoli, A.J. Pons, and A. Karma, *Phys. Rev. Lett.* **115**, 265503 (2015).
7. "Kinetics and morphological evolution of liquid metal dealloying", I. McCue, B. Gaskey, P.A. Geslin, A. Karma, and J. Erlebacher, *Acta Materialia* **115**, 10-23 (2016).
8. Atomistic to continuum modeling of solidification microstructures", A. Karma and D. Tourret, *Current Opinion in Solid State and Materials Science* **20**, 25-36 (2016).
9. "Two-mode Ginzburg-Landau theory of crystalline anisotropy for fcc-liquid interfaces", K.-A. Wu, S.-C. Lin, and A. Karma, *Phys. Rev.* B **93**, 054114 (2016).
10. "Elastically mediated interactions between grain boundaries and precipitates in two-phase coherent solids", Y.-C. Xu, P.-A. Geslin, and A. Karma, *Phys. Rev.* B **94**, 144106 (2016).
11. "Grain growth competition during thin-sample directional solidification of dendritic microstructures: A phase-field study", D. Tourret, Y. Song, A. J. Clarke, and A. Karma, *Acta Materialia* **122**, 220-235 (2017).

Interfaces in Electronic and Structural Materials

Yuri Mishin, PI

Department of Physics and Astronomy
George Mason University, MSN 3F3
4400 University Drive, Fairfax, VA

Phone: 703-993-3984
Fax: 703-993-1269
Email: ymishin@gmu.edu

Program Scope

The objective of this program is to advance the fundamental understanding of interfaces, especially in materials subject to deformations and high temperatures, and to develop new methods for computational prediction of interface properties. The main approach to achieving these goals is based on atomistic computer simulation methods, primarily molecular dynamics and a variety of Monte Carlo techniques. These methods are capable of delivering critical atomic-level information about the interface structures and predicting mechanical, thermodynamic and kinetic properties of interfaces. Over the past two years, the focus has been on two specific topics: (1) Structural phase transformations in materials interfaces, and (2) Effect of interface structure on thermal resistance of grain boundaries and other interfaces.

Recent Progress

1. ***Identification of grain boundary phases and phase transformations.*** Crystallographically, a grain boundary (GB) is fully characterized by five angles describing the lattice misorientation between the grains and the GB plane. In our recent work [1-4], we found that the addition or removal of atoms to/from the GB can lower its excess energy □, creating new stable structures. The newly discovered GB structures behave like two-dimensional phases, existing in certain temperature intervals and reversibly transforming to each other by first-order phase transformations. Such phases and transformations among them have been studied by atomistic simulations for two Σ5 [001] symmetrical tilt GBs in Cu [1-2]. We have now extended the previous studies of the Σ5 GBs to a larger set of [001] symmetrical tilt GBs in order to evaluate the generality of the previous findings. The results provide convincing evidence that the multiplicity of GB phases is not specific to the particular Σ5 GBs; instead, the emergence of new GB structures is a generic phenomenon that must take place in almost every GB. Thus, the atomic density λ in a GB must be considered as an additional thermodynamic parameter whose variation may cause structural transformations. It has also been shown that, for high-angle GBs, both λ and the misorientation angle θ are equally important in comporting the GB energy (Fig. 1).

Each GB contains an array of structural units and follows a systematic behavior that can be rationalized in terms of the structural unit model. There are only three distinct types of structural unit in the series of GBs studied in our work. The GBs are composed of one or two types of structural unit, usually separated by a few perfect-lattice units. This generalizes the structural unit model to the coordinates (θ, λ), not just θ as was known previously.

2. ***An optimized interatomic potential for silicon.*** Large-scale simulations of GBs in Si require the use of an atomistic potential enabling fast evaluations of energy and classical forces on the atoms. An optimized potential has been constructed for Si using a modified Tersoff model. The potential accurately reproduces a wide range of properties of Si and improves over existing potentials with respect to point defect structures and energies, surface energies and reconstructions,

thermal expansion, melting temperature and other properties. For example, the potential accurately predicts the energies and structural parameters of the newly discovered Si allotropes h-Si_6 [5] and Si_{24} [6] without fitting. It also demonstrates a good agreement with first-principles binding energies of small Si_n clusters with n=2-8.

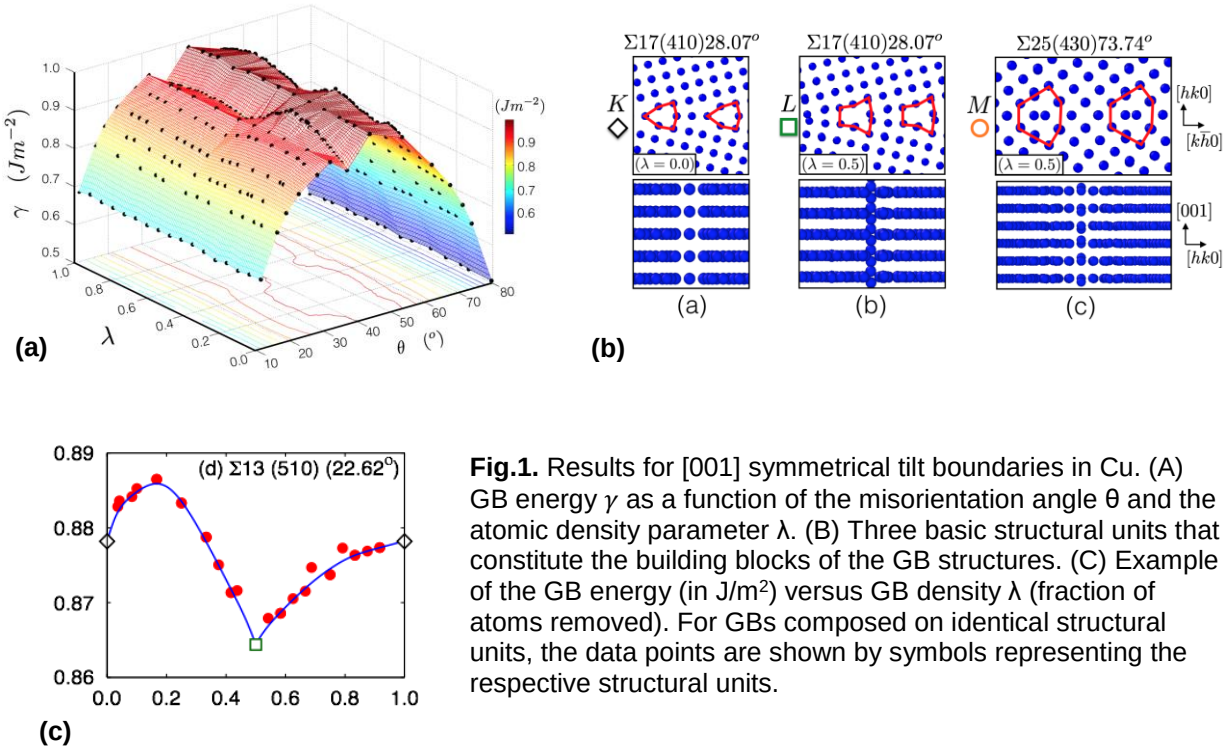

Fig.1. Results for [001] symmetrical tilt boundaries in Cu. (A) GB energy γ as a function of the misorientation angle θ and the atomic density parameter λ. (B) Three basic structural units that constitute the building blocks of the GB structures. (C) Example of the GB energy (in J/m²) versus GB density λ (fraction of atoms removed). For GBs composed on identical structural units, the data points are shown by symbols representing the respective structural units.

The new potential demonstrates reasonable agreement with DFT energies of various structural forms of single-layer and bilayer silicenes. It has been applied to evaluate the thermal stability of free-standing silicenes in the form of nano-ribbons, nano-flakes and nano-tubes (Fig. 2). While single-layer silicene is mechanically stable at zero Kelvin, it becomes unstable and collapses to a nano-cluster at room temperature. The collapse is caused by capillary waves and is due to the chemical reactivity and small bending rigidity of the free-standing structures. This behavior was confirmed for both the bucked and dumbbell single-layer silicenes. By contrast, the bilayer silicene demonstrates a larger bending rigidity and remains stable at and even above room temperature (up to 1000 K). The results suggest that bilayer silicene may exist in a free-standing form at ambient conditions.

3. *Thermal resistance of GBs*. Thermal resistance of GBs can affect heat removal in electronic devices and performance of thermoelectric materials. The Kapitza resistance of a series of [001] tilt GBs in Si has been studied using the new potential and the non-equilibrium MD method. The Kapitza conductance σ_K was found to decrease with the misorientation angle and slightly increase with temperature. For high-angle GBs, σ_K is much lower than the bulk conductivity at low temperatures but the two tend to converge at high temperatures. An interesting effect was found wherein σ_K suddenly decreases when the GB dislocations become disordered due to premelting (Fig.3). Structural phase transformations in GBs have a significant effect on their thermal

conductivity. One of the fundamental issues in nano-scale thermal conductivity is the definition, or even existence, of the local temperature. This issue has been addressed in two publication under this project.

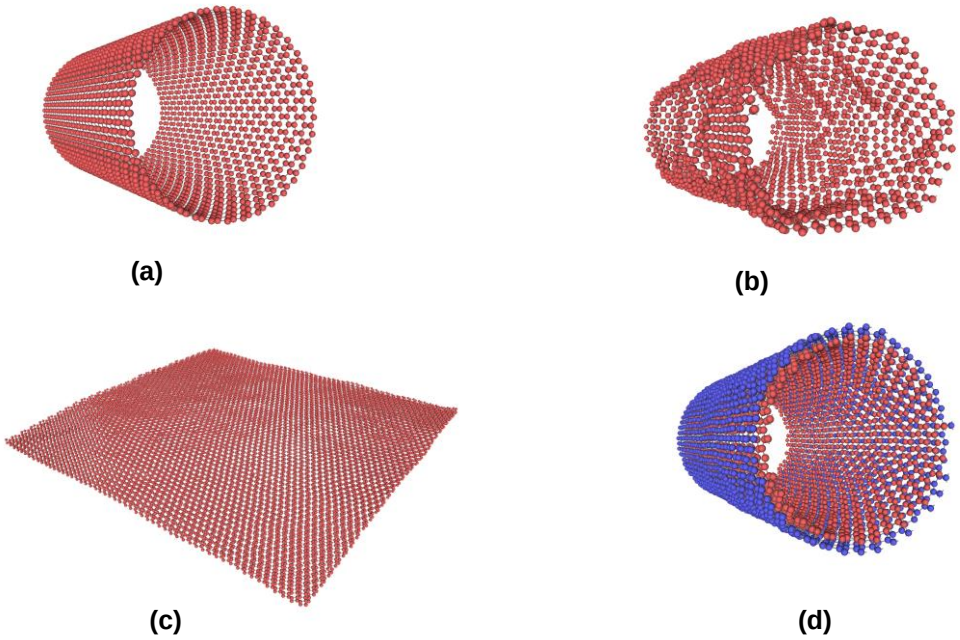

Fig.2. MD simulations of silicene with the new interatomic potential. (a,b) A nanotube of bucked single-layer silicene collapses spontaneously at room temperature. (c,d) A free-standing nano-flake and nanotube of bilayer silicene remain stable at and even above room temperature.

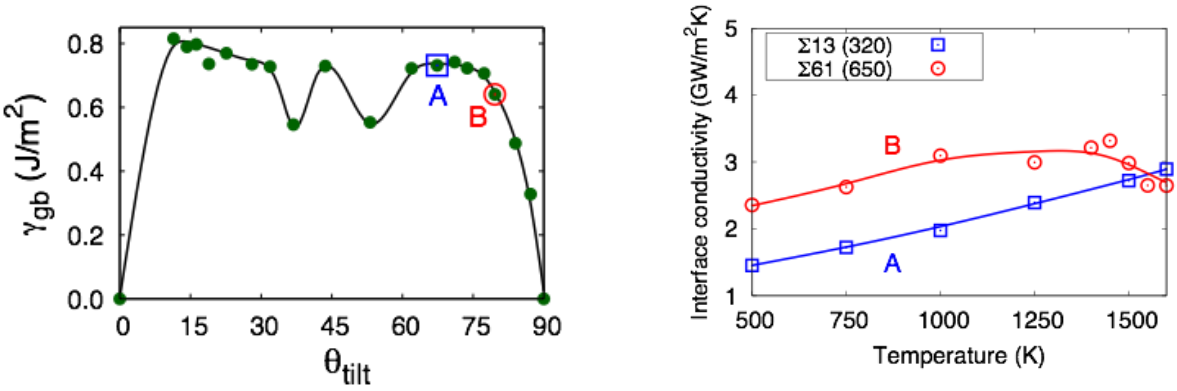

Fig.3. Left: Misorientation dependence of GB energy for tilt GBs in Si. A and B represent a relatively high and a relatively low-angle boundaries. Right: Temperature dependence of the Kapitza conductance of GBs A and B. The sudden decrease in conductance is caused by the disordering transition.

Future Plans

(1) To further improve the reliability of the atomistic simulations, a hybrid machine-learning interatomic potential will be developed for Si and the Si-Ge system using the neural network approach.

(2) The new potential will be applied to study the thermal resistance of interfaces in Si, Ge, and Si-Ge alloys. The interfaces will include individual GBs and heterostructures composed of parallel GBs or alternating Si-Ge layers. The goal will be to establish relations between the phonon scattering and their atomic structure of the interfaces, the feature size (e.g. layer spacing), chemical composition, temperature and other factors.

References cited

1. T. Frolov, S. V. Divinski, M. Asta and Y. Mishin: Effect of interface phase transformations on diffusion and segregation in high-angle grain boundaries, *Physical Review Letters* **111**, 255502 (2013).
2. T. Frolov, D. Olmsted M. Asta and Y. Mishin: Structural phase transformations in metallic grain boundaries *Nature Communications* **4**, 1899 (2013).
3. T. Frolov, M.Asta, Y. Mishin, Segregation-induced phase transformations in grain boundaries, *Physical Review* B **92** (2015) 020103(R).
4. T. Frolov, M. Asta, Y. Mishin, Phase transformations at interfaces: Observations from atomistic modeling, *Current Opinion in Solid State and Materials Science* **20** (2016) 308–315.
5. Y. Guo, Q. Wang, Y. Kawazoe, P. Jena, A new silicon phase with direct band gap and novel optoelectric properties, *Scientific Reports* **5**, 14342 (2015).
6. D. Y. Kim, S. Stefanoski, O. Karakevych, T. A. Strobel, Synthesis of an open-framework allotrope of silicon, *Nature Materials* **14** (2015) 169–173.

Publications of DOE sponsored research (past < 2 years)

1. J. Hickman and Y. Mishin: Energy spectrum of a Langevin oscillator, *Physical Review* E **94**, 062151 (2016).
2. J. Hickman and Y. Mishin: Temperature fluctuations in canonical systems: Insights from molecular dynamics simulations, *Physical Review* B **94**, 184311 (2016).
3. G. P. Purja Pun and Y. Mishin: Optimized interatomic potential for silicon and its application to thermal stability of silicene, *Physical Review* B, with referees.
4. J. Hickman and Y. Mishin: Extra variable in grain boundary description, *Physical Review Letters*, with referees.
5. J. Hickman and Y. Mishin: Thermal resistance of tilt grain boundaries in silicon, in preparation; to be submitted within 2-3 weeks.

Session XI

DOE award # DE-FG02-07ER46426, Stanford University

Nanophotonics-enhanced solar cells

PI: Shanhui Fan, co-PI: Mark Brongersma
Stanford University, Department of Electrical Engineering,
Spilker Building, Room 314, CA 94305, shanhui@stanford.edu

Program Scope or Definition

The overall emphasis of the program is to develop a fundamental understanding of nanophotonic structures for light trapping purposes, and a practical strategy in using nanophotonic structures to enhance solar cell performance. Towards this goal, we are undertaking substantial efforts on understanding the fundamental aspects of both current and voltages in nanophotonic solar cells, on numerical design in seeking to achieve absorption enhancement over the entire solar spectrum, as well as efforts in understanding some of the basic properties of high-index resonant dielectric structures in the context of light-matter interaction at the nanoscale.

Below we review some of the major progress [1-10] made in this report period.

Recent Progress

Opto-electronic analysis of the intrinsic behaviors of nanostructured ultra-thin crystalline silicon solar cells. Nanophotonic designs have been shown to achieve broadband light absorption enhancement as compared to flat cells. Such absorption enhancement can be directly expressed as the increase of the photocurrent. However, in order to understand how nanostructuring influences the efficiency, one would also need to evaluate how the voltage is affected, which requires integrated optoelectronic analysis. We have developed combined electrical and optical analysis of nanostructured solar cells. Our analysis, for a given nanostructured cell, provides an upper theoretical bound on its efficiency, taken into account both its optical properties, and the recombination properties such as Auger recombination and surface recombination. (Figure 1) We also show that the electronic aspects of the solar cell, and in particular, the increase of surface recombination rates due to nanopatterning, can be well accounted for by a simple analytic model. This paper has been published in ACS photonics [1]. The combination of the numerical and analytic results should prove useful in the understanding of the performance of the nanostructured solar cells.

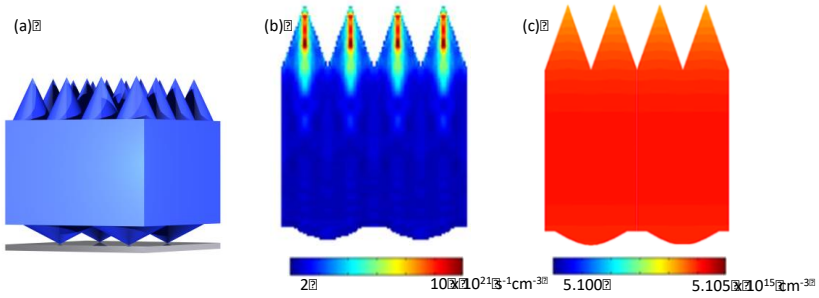

Figure 1. Combined opto-electronic analysis of nanophotonic solar cells. (a) Silicon solar cell geometry consisting of nanocone anti-reflection layer on the front surface and nanocone light scattering layer on the back surface. (b) The carrier generation rate profile for the structure shown in (a). Notice the strong inhomogeneity. (c) The minority carrier density distribution inside the cell. The distribution is almost completely uniform, which enables us to develop a semi-analytic model that accurately accounts for the effects of various non-radiative recombination mechanisms on the open circuit voltage.

Current-voltage enhancement of a single coaxial nanowire solar cell When designing nanostructured solar cells, it is important to reduce the active volume of the cell without any penalty to its absorption. Consequently, there has been considerable recent interest in developing solar cells consisting of single semiconductor nanowires, since the absorption cross section of a nanowire can significantly exceed its geometric cross-section. A properly designed single nanowire can deliver a much higher current in comparison to an equal-volume bulk cell with the same amount of material. Moreover, the strong confinement of light by the single nanowire can also result in an open-circuit voltage that is higher than that of the bulk cell.

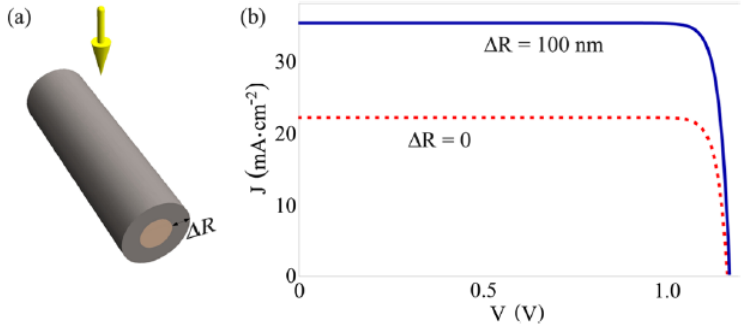

Figure 2. (a) A single nanowire GaAs cell consists of a core GaAs region and a coating layer made of Al_2O_3. (b) The presence of the oxide layer significantly increases the absorption of the nanowire, even though the absorber dielectric volume remains the same. Also, the oxide layer does not affect the ability of the nanowire to achieve a higher open-circuit voltage.

In a paper published in ACS Photonics [3], we show that a coaxial nanowire, in which a transparent dielectric layer is coated around an absorbing nanowire, can have a significantly larger absorption crosssection over a broad bandwidth when compared to a corresponding bare nanowire without the transparent layer. We demonstrate that the absorption enhancement comes from enhanced coupling to incident light in addition to an increased number of resonances supported by the nanowire. Moreover, the use of such a transparent layer also preserves the voltage enhancement capability of the bare nanowire. An illustration of our results is presented in Figure 2, which compares the current−voltage characteristics between an optimized GaAs bare nanowire and the same bare nanowire coated with a ΔR = 100 nm thick Al_2O_3 layer, i.e., a coaxial wire. We can see from Figure 2b that a considerably larger short-circuit current enhancement of ~60% results from just coating the absorbing bare nanowire with this transparent oxide layer. In addition, the coaxial wire has an open-circuit voltage that is similar to that of the bare wire and that is significantly higher than that of a bulk GaAs cell. Our work here points to a new avenue for enhancing the performance of nanowire solar cells.

Broadband Absorption Enhancement in Solar Cells with an Atomically Thin Active Layer. Over the past decade, there has been a growing interest in the optics of atomically thin materials. In particular, the last several years have seen a flurry of studies on the transition metal dichalcogenides (TMDCs) MoS_2 and WSe, which in their monolayer form are direct band gap semiconductors. Having a direct band gap opens up many exciting possibilities for optoelectronic devices with an atomic-scale dimension.

TMDCs can have single-pass absorption of 10−20% in the wavelength range above the band gap. While this is remarkably high for a single atomic layer, for applications such as solar cells and photodetectors this absorption is insufficient for high-performance devices. For solar cell applications, moreover, enhancement of absorption over the entire wavelength range above the band gap is desirable. In a paper published in ACS Photonics [4], we consider the use of multiple

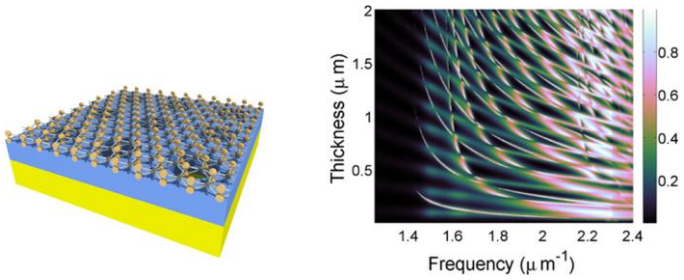

Figure 3. (a) Device geometry consisting of transition metal dichalcogenide (TMDC) placed on top of a photonic crystal slab. (b) The absorption in the TMDC layer as a function of thickness of the photonic crystal slab and frequency. The structure exhibits large numbers of resonances which results in broad-band absorption enhancement.

resonances in photonic crystal slabs for broadband enhancement of above-band-gap absorption in single-layer MoS_2. The schematic of the configuration considered in this paper is shown in Fig. 3a, where a single layer of MoS_2 is placed on top of a photonic crystal slab that sits on a mirror. Here we show that, with proper design, the use of multiple resonances (Fig. 3b) can lead to absorption enhancement over the entire frequency range above the band gap of MoS_2. For normally incident light, our optimal structure shows an average absorption of 51% over the visible spectrum, which is a significant enhancement over the average single-pass absorption of MoS2 of approximately 10% in the same spectral range. This work points to the significant potential of using atomically thin active layers for solar cell applications.

Subwavelength Angle-sensing Photodetectors. The building block of an imaging chip is individual photo-detecting pixels. Current pixels can only detect the intensity of light, but lose other information such as the incident angle. While the intensity information alone is sufficient for traditional application of photography, its limitation starts to show in advanced imaging tasks. For example, a single image of the intensity could not tell the depth of an object in a scene, which however can be calculated from the incident angle of light. Another example is the light field camera, which uses the information of incident angles to refocus even after the image is taken. In order to measure the incident angle, discrete optical components such as lenses or gratings must be used together with photo-detecting pixels. These components are expensive to integrate and degrade the resolution. It has been a great challenge to directly measure the incident angle in a photo-detecting pixel.

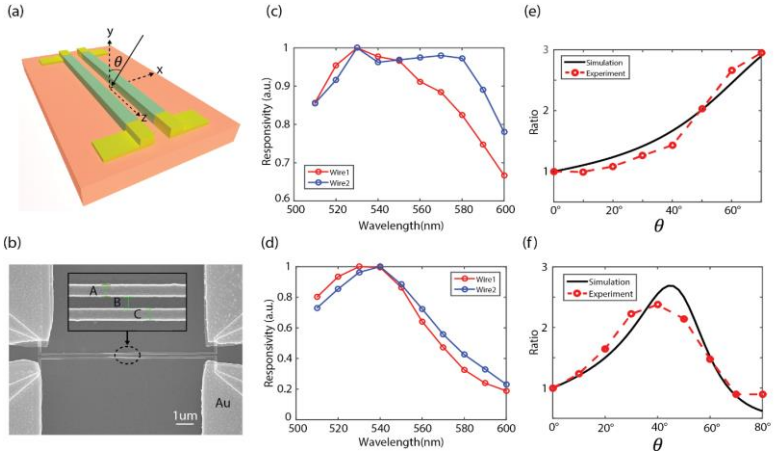

Figure 4. (a)-(b) Schematic and the SEM image of angle-sensing photodetector. Nanowires are 10 um long. Top inset shows a close-up view where A=103nm, B=105nm and C=103nm. (c)-(d) Normalized responsivity of two nanowires, and ratio of photocurrents with electric field polarized in z-direction. The responsivity is defined as $R=\hbar\omega I/P$, where I is the measured photocurrent; P is the incident power. Photocurrent ratio between two nanowires as a function of θ with same polarization as in (b). (e)-(f) Normalized responsivity and ratio of photo-currents of two nanowires with magnetic field polarized in z-direction.

The difficulty lies in the small size of a pixel, which is comparable or even smaller than the optical wavelength λ. Existing methods based on micro lenses or gratings cannot be miniaturized indefinitely. A lens measures the incident

angle by focusing light of different directions to different locations. Its accuracy, measured by the spot size of the focus, scales as $\Delta\theta \sim \lambda/d\cos(\theta)$. Consequently, when the lens' width d decreases below the wavelength λ, the accuracy degrades severely.

In a collaboration between Brongersma and Fan groups [9], we design a subwavelength photodetector that can measure both the intensity and the incident angle of light. It consists of two optical resonators, (Fig. 4a-b). Each resonator is constructed by a subwavelength nano-rod made of a high refractive index material. Both the sizes of resonators and their separation can be much smaller than the optical wavelength. The two resonators while being electrically isolated are optically coupled, which allows angle-sensing based on the inter-resonator difference as shown in Fig. 4c-f. This work highlights the new opportunity of engineering light-matter interactions at nanoscale.

Future Plans

In the near future (the coming year) we plan to focus on continued efforts towards understanding light-matter interaction in dielectric nanophotonic structures in the context of energy applications. In particular, an emerging direction is the possibility for using broad band photonic structures for simultaneous control of both solar absorption and thermal radiation [8], this may open a new avenue in enhancing solar cell efficiency by passive radiative cooling of solar cells.

Journal Publications of DOE Sponsored Research in 2015-2017

[1] I. Karakasoglu, K. X. Wang and S. Fan, "Optical-Electronic Analysis of the Intrinsic Behaviors of Nanostructured Ultrathin Crystalline Silicon Solar Cells", ACS Photonics, vol. 2, pp. 883-889 (2015).
[2] Y. Jia, M. Qiu, H. Wu. Y. Cui, S. Fan, and Z. Ruan, "Theory of half-space light absorption enhancement for leaky mode resonant nanowires", Nano Letters, vol. 15, pp. 5513-5518 (2015)..
[3] S. Sandhu and S. Fan, "Current-voltage enhancement of a single co-axial nanowire solar cell", ACS Photonics, vol. 2, pp. 1698-1704 (2015).
[4] J. Piper and S. Fan, "Broadband Absorption Enhancement in Atomically Thin Solar Cells", ACS Photonics, vol. 3, pp. 571-577 (2016).
[5] J. Zhao, Y. Guo, L. Cai, H. Li, K. X. Wang, I. S. Cho, C. H. Lee, S. Fan, and X. Zheng, "High-Performance Ultrathin $BiVO_4$ Photoanode on Textured Polydimethylsiloxane Substrates for Solar Water Splitting", ACS Energy Letters, vol. 1, pp. 68-75 (2016).
[6] M. L. Brongersma, "Plasmonic Photodetectors, Photovoltaics, and Hot-Electron Devices", Proceedings of IEEE, vol. 104, pp. 2349–2361 (2016).
[7] Z. Zhao, K. Wang, and S. Fan, "Analysis of an anti-reflecting nanowire transparent electrode for solar cells", Journal of Applied Physics, vol. 121, art. No. 113109 (2017).
[8] W. Li, Y. Shi, K. Chen, L. Zhu and S. Fan, "A comprehensive photonic approach for solar cell cooling", ACS Photonics (accepted, 2017).
[9] S. J. Kim, J. –H. Kang, M. Mutlu, J. Park, W. Park, R. Sinclair, S. Fan, P. G. Kik, and M. L. Brongersma, "Anti-Hermitian Photodetector Facilitating Efficient Subwavelength Photon-sorting," Submitted to Nature Nanotechnology (2017).
[10] V. Thareja, M. Esfandyarpour, P. G. Kik, and M. L. Brongersma, "Metamaterial Mirror for Enhancing and Suppressing Raman from Graphene," submitted to Nano Letters (2017).

Directing Charge Transport in Quantum Dot Assemblies.

David H. Waldeck, Chemistry Department, University of Pittsburgh, Pittsburgh PA 15260

Program Scope

This project explores design features for quantum dot nanomaterials that promote efficient transduction of absorbed photons into separated charges. We are identifying features of quantum dots and their assemblies that inhibit charge recombination and operate robustly, *i.e.*, despite structural heterogeneity that can exist in bulk heterojunction films. Our team (comprising experimentalists at the U. Pittsburgh and the Weizmann Institute of Science with theorists at Duke University) has experimentally and computationally explored how to use energy-level gradients, built-in electrostatic potentials, and symmetry/chirality properties to improve the charge-separation efficiency in inorganic-organic hybrid structures.

Recent Progress

Controlling QD Energetics to Affect Charge Transfer: Energy band offsets and energy level gradients affect charge separation efficiencies in quantum dots (QDs). The team has collaborated on both measuring and calculating how the QD's ligand shell affects the energy band positions. We showed that the linker unit, rather than the ligand, plays a dominant role[1] and that attachments of QD films to electrodes can result in Fermi level pinning. Most recently, we showed that the insertion of a thin alumina layer in between a QD layer and an Au substrate can eliminate Fermi level pinning.[2] In this study band edge energies of different sized PbS QD monolayers with different cross-linkers were measured by using ultraviolet photoelectron spectroscopy and electrochemistry. When PbS QDs were immobilized directly on an Au electrode the measured valence band maximum was fixed in energy relative to the Au Fermi level, independent of the QD size or cross-linker. After insertion of a thin film of alumina between the PbS quantum dot monolayer film and the Au substrate, the measured valence band energy position shifts in a way that depends on ligand and QD size. These results identify a general method for eliminating Fermi level for tuning the energetics at QD–metal interfaces.

On a related front we have used Marcus theory and quantum chemistry calculations to examine how the energy band offset and the interfacial chemical contacts between quantum dots (QDs) affect the charge transfer rates.[3] Recently,[4] we measured the electron transfer rate as a function of inter-QD distance and the energy band offset of the QDs (reaction Gibbs energy). The schematic in Figure 1 shows the experimental design in which covalently bound QD dyads are assembled on a colloidal template. The photoinduced charge transfer rates were found to decay exponentially with QD-QD distance (consistent with electron tunneling) and the dependence on energy band offset was consistent with Marcus theory, as long as one performs a sum over final electronic states. These results indicate that our understanding of electron transfer in molecular donor-bridge-acceptor assemblies can be translated to describe nanoparticle-bridge-nanoparticle assemblies.

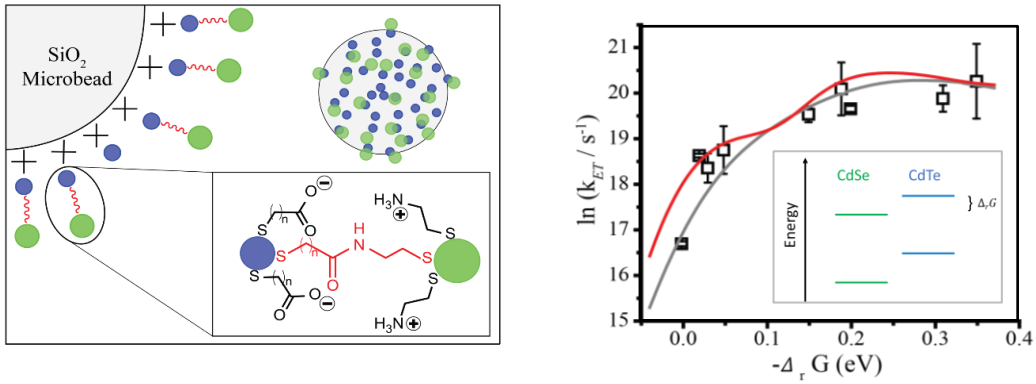

Figure 1. The diagram on the left illustrates the colloidal assembly of NPs and NP dyads onto a silica microbead. The green circles represent the electron donor CdTe NP and the blue circles represent the electron acceptor CdSe NP (< 2.5 nm); the CdTe NPs (~ 4 nm) are covalently bound to the smaller radius CdSe NPs. The graph on the right shows how the electron transfer rate depends on the energy band offset (reaction free energy); the red curve is a fit to semiclassical Marcus theory, and the black curve is a fit that accounts for the size distribution of the NPs. The inset shows the energy band alignment.

Field Effect on Charge Transfer: We explored how to combine donor-acceptor (D-A) energy band offsets and built-in electrostatic fields to affect charge transfer and recombination.[5] Figure 2 shows a system consisting of a conjugated co-polymer (PDPPPV, donor) and CdTe QDs (acceptor). By placing charged functional groups on the polymer side chains (R) and QD surface ligands (L) during synthesis, we obtain positively(+) and negatively(-) charged polymers and QDs. If the oppositely-charged polymer and QD are mixed together in solution, they form electrostatic aggregates in which an internal electrostatic field can be created at the polymer-QD (D-A) interface. In this way, we examined whether the direction of the internal field affects the charge separation driven by the D-A energy offsets (see Fig. 2). The data in Fig. 2 show that a significant difference was observed in photoluminescence decay (Fig. 2C&2D), and it correlates with the different internal field direction between the oppositely charged QD and PDPPPV. For instance, the (+)NP/(-)PDPPPV aggregates has a favorable internal field that drives charge transfer in the same direction as the D-A energy offsets; whereas reversing the surface charge on both QD and PDPPPV inhibits charge separation. These data were corroborated by transient absorption spectroscopy which also showed that the primary event is hole transfer from the QD to the polymer. This work demonstrates a strategy for enhancing charge transfer efficiency by combining the internal field and the energy offsets.

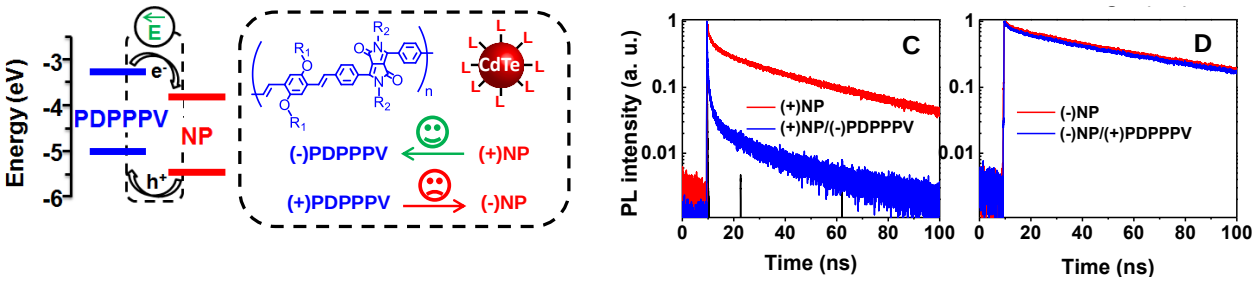

Figure 2. The left panel shows an energy diagram and internal electric field scheme for the two cases of a polyanionic PDPPPV polymer with a cationic CdTe NP and the inverse scheme for a polycationic PDPPPV with an anionic CdTe NP. The panels labeled C and D show the difference in the nanoparticle quenching for the two cases; *i.e.*, the charge transfer in panel C is a few hundred picoseconds and that in panel D is slower than the intrinsic CdTe decay time.

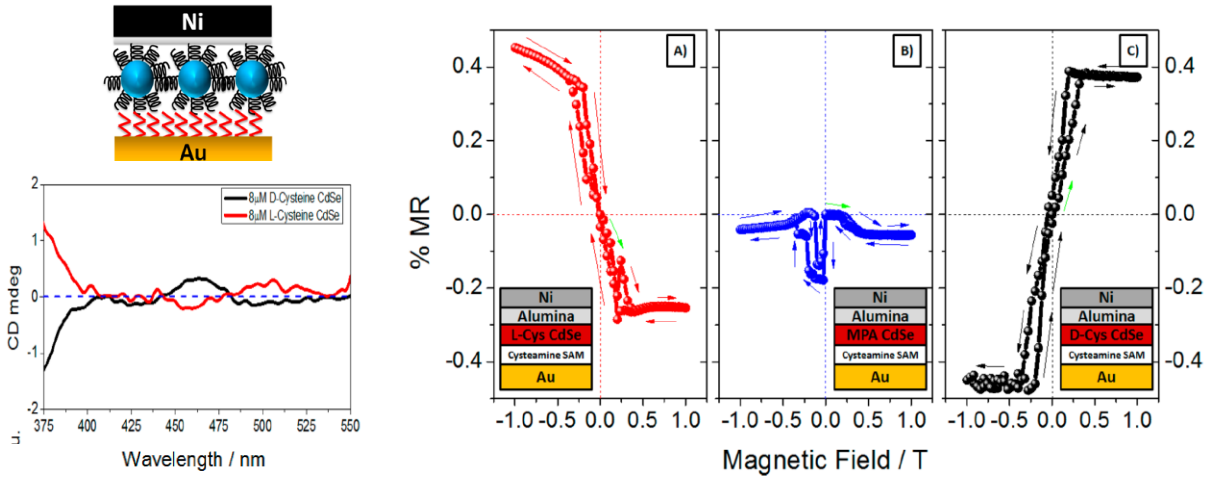

Figure 3: The diagram in the upper left panel shows the device design in which a monolayer of chiral NPs is placed between an Au and Ni electrode, and the spectra in the lower left panel show circular dichroism spectra for the NPs in the exciton region of the NP spectrum. The right panel shows the magnetoresistance data for three different NP films: A) L-CdSe (red), B) achiral CdSe (blue), and C) D-CdSe (black).

Chirality Effect on Charge Transfer: We have developed novel methods to measure spin-selective electron transport, including spin-selective electrochemistry, spin-selective capacitance, and optoelectronic methods, and tested them on chiral molecules to show that they act as electron spin filters.[6]

We have used chiral ligands to imprint chirality on CdSe quantum dots (QDs) and demonstrated that they can act as spin selective filters for charge transport.[7] The spin filtering properties were investigated by magnetic conductive-probe atomic force microscopy (mCP-AFM) measurements and magnetoresistance measurements. Figure 3 shows magnetoresistance measurements which demonstrate that the current through films of chiral QDs correlates with the chiroptical properties of the QD. The panels labeled A), B), and C) show how the magnetoresistance data for these structures change with the chirality of CdSe QDs. Panel A) shows the magnetoresistance for an L-Cys CdSe QD, panel B) shows the case of an achiral QD, and panel C) shows the case of an R-Cys CdSe QD. The asymmetry in the magnetoresistance response with magnetic field, as well as the opposite behavior for the L- and R- enantiomers, arise from the spin filtering of the electrons in the QD layer.

In concert with these device level studies, we recently completed a study of the photoinduced electron transfer between an achiral donor QD, which is excited by circularly polarized light, and a chiral acceptor CdSe QD. We observe order of magnitude effects of chirality on the electron-transfer rates between quantum dots (QDs) in these chiral QD assemblies. Indeed, both the circular polarization of the light that excites an achiral electron donor QD and the imprinted chirality of an acceptor QD affect the dot-to-dot electron-transfer kinetics. Figure 4 shows the QDs luminescence decays under different conditions; panel (A) shows the change in luminescence decay of a CdTe donor QD by electron transfer to an L-cysteine acceptor QD under three different light polarizations and compares it to the case of an achiral acceptor (panel B) for which no change is evident and to the case of a D-cysteine acceptor QD for which the polarization dependence is inverted. Moreover, the magnitude of the lifetime differences correlate with the strength of the acceptor QD circular dichroism spectrum,

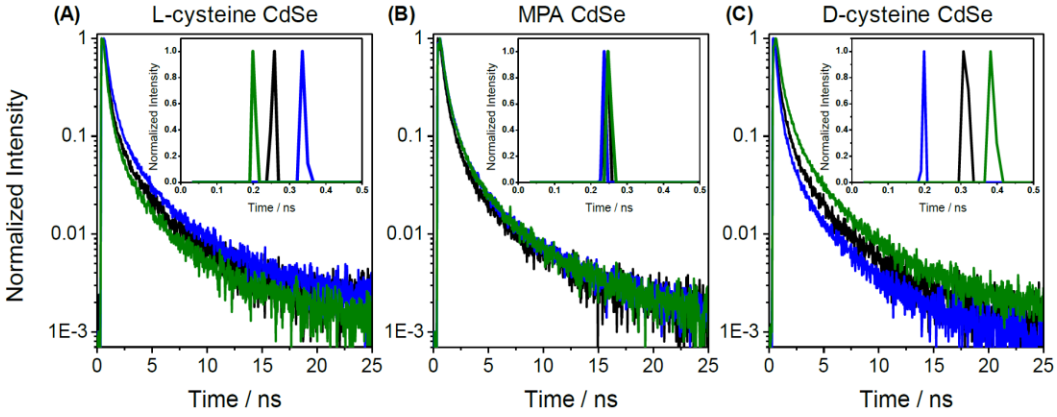

Figure 4. Photoluminescence decays of the donor CdTe NPs are shown as a function of the excitation light polarization when they are bound to CdSe acceptors of different chirality: (A) L-CdSe, (B) achiral CdSe, and (C) D-CdSe. The insets show how the short component of the lifetime distribution shifts with the light polarization. The excitation light polarization is represented by a different color for the plots: linear (black), clock-wise (blue), and counter-clockwise (green).

indicating that chiral imprinting of the QDs lies at the origin of this effect. These studies point toward new approaches to develop nanoscale spintronic and optoelectronic devices.

Future Plans

Currently, we are i) measuring electron transfer rates in QD dyads to validate the theoretical model developed by Beratan, ii) developing Hall probe measurements to quantify directly the electron spin from chiral QDs, and iii) integrating chiral symmetry with energy level gradients and electrostatic fields to promote directional charge flow.

References

1 a) B. P. Bloom, L.-B. Zhao, Y. Wang, D. H. Waldeck, D. N. Beratan, P. Zhang, and R.Liu *J. Phys. Chem. C.* ***117*** (2013) 22401−22411; b) Aleksey E. Kuznetsov, Balamurugan Desinghu, Spiros S. Skourtis, David N. Beratan. *J Phys Chem C* ***116,*** (2012) 6817.

2 B. Bloom, M.N. Mendis, E. Wierzbinski, and D. H. Waldeck *J. Materials Chemistry C* ***4*** (2016)704 – 712.

3 R. Liu, B. Bloom, D. H. Waldeck, P. Zhang, and D. N. Beratan *J Phys Chem C* (2017) submitted.

4 B. M. Graff, B.P. Bloom, E. Wierzbinski, and D. H. Waldeck *J. Am. Chem. Soc.* ***138*** (2016) 13260—13270.

5 Y. Wang, K. Liu, P. Mukherjee, D. A. Hines, P. Santra, H. Y. Shen, P. Kamat, and D. H. Waldeck *Phys. Chem. Chem. Phys.* ***16*** (2014) 5066 – 5070.

6 a) M. Kettner, B. Gohler, H. Zacharias, D. Mishra, V. Kiran, R. Naaman, D. H. Waldeck, S. Sek, J. Pawlowski, and J. Juhaniewicz *J. Phys. Chem. C* ***119*** (2015) 14542-14547; b) R. Naaman and D. H. Waldeck, *Ann. Rev. Phys. Chem.* ***66*** (2015) 263–281.

7 B. P. Bloom, V. Kiran, V. Varade, R. Naaman, D.H. Waldeck *NanoLetters* ***16*** (2016) 4583-4589.

Publications, DOE (2015 –present)

1. R. Liu, B. Bloom, D. H. Waldeck, P. Zhang, and D. N. Beratan *Controlling the electron-transfer kinetics of quantum-dot assemblies* (2017) submitted.

2. B. P. Bloom, B. M. Graff, S. Ghosh, D. N. Beratan, and D. H. Waldeck *Chirality Control of Electron Transfer in Quantum Dot Assemblies* Science (2017) submitted.

3. K. Michaeli, V. Varade, R. Naaman, and D. H. Waldeck *A New Approach towards Spintronics- Spintronics with no Magnets* J. Phys.: Condens. Matter 29 (2017) 103002 (8pp).

4. B. M. Graff, B.P. Bloom, E. Wierzbinski,1 and D. H. Waldeck *Electron Transfer in Nanoparticle Dyads Assembled on Colloidal Template* J. Am. Chem. Soc. 138 (2016) 13260—13270.

5. B. P. Bloom, V. Kiran, V. Varade, R. Naaman, D.H. Waldeck *Spin Selective Charge Transport through Cysteine Capped CdSe Quantum Dots*, NanoLetters ***16*** (2016) 4583-4589.

6. B. Bloom, M.N. Mendis, E. Wierzbinski, and D. H. Waldeck *Eliminating Fermi-Level Pinning in PbS Quantum Dots using an Alumina Interfacial Layer* J. Materials Chemistry C ***4*** (2016)704 – 712.

7. Nirit Kantor-Uriel, Partha Roy, Sergio Saris, Vankayala Kiran, David H. Waldeck, and Ron Naaman, *Evidence for enhanced electron transfer by multiple contacts between self-assembled organic monolayers and semiconductor nanoparticles*, J. Phys. Chem. C ***119*** (2015) 15839–15845.

8. A. Migliore, R. Naaman, D.N. Beratan, "*Sensing of molecules using quantum dynamics"* PNAS, Early Edition 112 (2015) E2419–E2428 .

9. R. Naaman and D. H. Waldeck, *"Spintronics and Chirality: Spin Selectivity in Electron Transport Through Chiral Molecules"* Ann. Rev. Phys. Chem. ***66*** (2015) 263–281.

10. M. Kettner, B. Gohler, H. Zacharias, D. Mishra, V. Kiran, R. Naaman, D. H. Waldeck, S. Sek, J. Pawlowski, and J. Juhaniewicz *"Spin Filtering in Electron Transport through Chiral Oligopeptides"* J. Phys. Chem. C., 119 (2015) 14542-14547.

Probing local, hybrid perovskite photophysics through spatially- and temporally-resolved absorption/emission microscopy

Masaru Kuno and Prashant Kamat, University of Notre Dame, Department of Chemistry and Biochemistry and Notre Dame Radiation Laboratory.

Program Scope

This project focuses on conducting local, spatially- and temporally-resolved absorption/emission microscopy measurements of hybrid perovskite thin films. Motivating this study is the recent discovery that organometal halide perovskites such as methylammonium lead iodide ($MAPbI_3$) possess impressive AM1.5 power conversion efficiencies when used as active layers in thin film solar cells. This is due, in part, to their large, micron-scale carrier diffusion lengths. Hybrid perovskites therefore represent breakthrough materials that transcend limitations of current thin film and sensitized solar cell architectures. Despite impressive performance gains realized in perovskite photovoltaics, much remains to be understood about their fundamental photophysics. To illustrate, little is known about the role compositional and/or morphological disorder plays in the optical and electrical response of these materials. How such disorder can be controlled to enhance performance also remains to be addressed. Consequently, a need exists for detailed microscopic studies of basic hybrid perovskite photophysics as well as spatially-resolved measurements to clarify their disorder-induced optical heterogeneities.

Recent Progress

Effort on this project has progressed along two fronts. The first has entailed investigating local hybrid perovskite photophysics through spatially-resolved optical measurements. By conducting local emission intensity (I_{em}) versus excitation intensity (I_{exc}) measurements, we have established the existence of optical response variations due to electronic disorder stemming from the presence of nonuniform trap densities. Regions of solution-processed $MAPbI_3$ films exhibit effective free carrier recombination while others exhibit emission dynamics strongly influenced by trap states. Through appropriate kinetic modeling of the data, quantitative estimates of local trap densities (N_t) have been made. What results are N_t values between N_t~10^{15}-10^{17} cm^{-3}. We have additionally found that spatially-varying trap densities impact $MAPbI_3$ radiative recombination efficiencies, resulting in local emission quantum yields that range from 5% to ~7% at 1 sun. **Figure 1** illustrates spatially-resolved and correlated maps of $MAPbI_3$ trap densities and emission quantum yields.

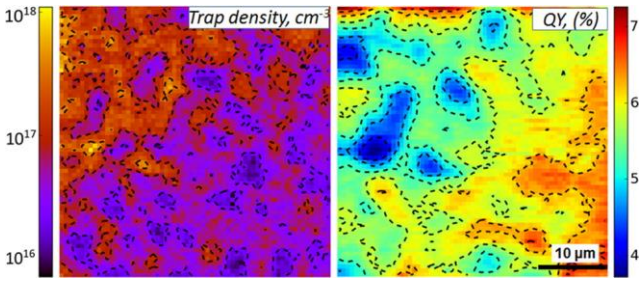

Figure 1. Spatially-resolved/correlated maps of $MAPbI_3$ trap density and emission quantum yield.

To link the above conclusions with corresponding solar cell performance, we have begun to correlate optical response to local solar cell efficiencies. These measurements have entailed I_{em} versus I_{exc}, emission lifetime, and photocurrent measurements on planar (FTO/compact-TiO_2/$MAPbI_3$/Spiro-MeOTAD/Au) ~17% efficiency solar cells. Obtained results confirm that photogenerated electrons are the charge species being trapped in $MAPbI_3$. The fraction of trapped electrons is small and is on the order of 2-3%. An even smaller (~0.2%) fraction undergoes

radiative recombination. What remains available for current generation is ~97-98% of the initially photogenerated carriers. Unfortunately, interface recombination at electron/hole transporting layers significantly suppresses this value, resulting in net power conversion efficiencies below the Shockley limit. Subsequent spatially-resolved measurements (conducted on planar as well as on analogous planar-inverted and mesoporous solar cells) link local power conversion efficiencies to underlying charge trapping/charge injection efficiencies. **Figure 2** shows representative data illustrating spatially-resolved/correlated photocurrent-, emission intensity- and corresponding trap density-maps of a $MAPbI_3$ device.

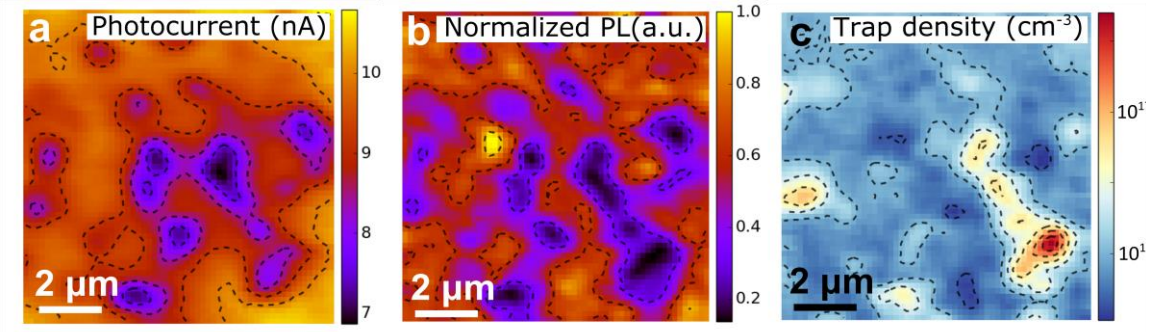

Figure 2. Spatially-resolved/correlated maps of $MAPbI_3$ solar cell photocurrent, emission intensity and corresponding trap density.

On a second front, we have investigated the photophysics of mixed halide perovskites such as $MAPb(I_{1-x}Br_x)_3$. Such mixed halides represent an appealing approach for achieving bandgap (E_g) tuning in perovskite devices given that corresponding E_g values span the range 1.57-2.27 eV.[1] Unfortunately, $MAPb(I_{1-x}Br_x)_3$ exhibits unwanted instabilities under visible light irradiation. What results is I and Br segregation into separate iodide- and bromide-rich domains. While general aspects of photoinduced $MAPb(I_{1-x}Br_x)_3$ phase separation have been established[1-9], unresolved issues remain. They include an explanation of dramatic spectral differences in the emission and absorption of phase-separated perovskites, the I_{exc}-dependent growth of the iodide-rich domain emission, and observed non-linear intensity dependencies of the phase separation rate constant.

Our current efforts have therefore established quantitative insights into the light-induced phase segregation of $MAPb(I_{1-x}Br_x)_3$ thin films. In brief, we have found that bandgap reduction of iodide-rich domains drives phase segregation by overcoming unfavorable iodide- and bromide-rich domain formation energies. Phase-separated domains subsequently undergo self-limited growth to final sizes on the order of 30 nm. The emission properties of $MAPb(I_{1-x}Br_x)_3$ thin films are additionally dictated by nucleated iodide-rich domains due to their favorable band offsets and the existence of large electron/hole diffusion lengths ($l_{e/h}$). Further modeling has revealed that $MAPb(I_{1-x}Br_x)_3$ thin films can be stabilized against phase segregation by reducing carrier diffusion lengths and/or excitation intensities. A corresponding phase stability diagram shown in **Figure 3** has therefore been constructed to reveal complementary I_{exc} and $l_{e/h}$ pairs that yield photostability.

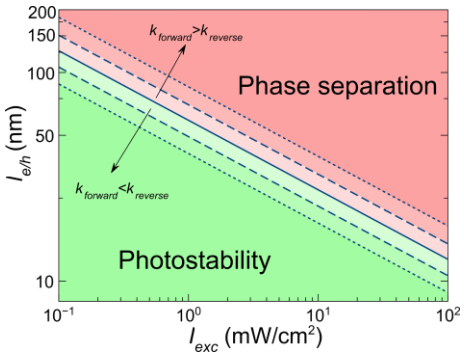

Figure 3. $MAPbI_3$ photostability phase diagram.

Future Plans

Going forward, we propose to conduct detailed studies that link local solar cell performance to underlying charge carrier photophysics. This entails carrying out spatially-resolved carrier time-of-flight measurements to extract local electron/hole drift mobilities on full, high efficiency, hybrid perovskite devices. Extracted mobilities will, in turn, be linked to local charge recombination efficiencies, internal quantum efficiencies, emission quantum yields and trap densities. These measurements will be accompanied by local photothermal heterodyne imaging (PHI) studies to investigate the spatially-resolved subgap absorption of trap states given their impact on device performance. Additional studies will be carried out on mixed halide systems [e.g. $MAPb(I_{1-x}Br_x)_3$] where we will investigate the local evolution of carrier trap densities during photoinduced halide phase segregation. Finally, we will investigate subgap, absorption-induced, emission upconversion in these materials to better elucidate the nature of hybrid perovskite trap states. These studies will include subgap excitation (detuning) measurements to map out local spectra of participating defect states.

References

[1] Noh, J. H., Im, S. H., Heo, J. H., Mandal, T. N. & Seok, S. Il. Chemical management for colorful, efficient, and stable inorganic-organic hybrid nanostructured solar cells. *Nano Lett.* 13, 1764–1769 (2013).

[2] Brivio, F., Caetano, C. & Walsh, A. Thermodynamic origin of photoinstability in the $CH_3NH_3Pb(I_{1-x}Br_x)_3$ hybrid halide perovskite alloy. *J. Phys. Chem. Lett.* **7,** 1083–1087 (2016).

[3] Hoke, E. T. *et al.* Reversible photo-induced trap formation in mixed-halide hybrid perovskites for photovoltaics. *Chem. Sci.* **6,** 613–617 (2015).

[4] Yang, X. *et al.* Light induced metastable modification of optical properties in $CH_3NH_3PbI_{3-x}Br_x$ perovskite films: Two-step mechanism. *Org. Electron.* **34,** 79–83 (2016).

[5] Yoon, S. J. *et al.* Tracking iodide and bromide ion segregation in mixed halide lead perovskite during photoirradiation. *ACS Energy Lett.* **1,** 290-296 (2016).

[6] Sadhanala, A. *et al.* Preparation of single phase films of $CH_3NH_3Pb(I_{1-x}Br_x)_3$ with sharp optical band edges. *J. Phys. Chem. Lett.* **5,** 2501–2505 (2014).

[7] Ruess, R., Benfer, F., Böcher, F., Stumpp, M. & Schlettwein, D. Stabilization of organic-Inorganic perovskite layers by partial substitution of iodide by bromide in methylammonium lead iodide. *ChemPhysChem* **17,** 1505–1511 (2016).

[8] Bischak, C. G. et al. Origin of reversible photoinduced phase separation in hybrid perovskites. *Nano Lett.* **17**, 1028–1033 (2017).

[9] Slotcavage, D. J., Karunadasa, H. I. & McGehee, M. D. Light-induced phase segregation in halide-perovskite absorbers. *ACS Energy Lett*. **1**, 1199–1205 (2016).

Publications

[K1] Connecting efficiency and local charge recombination in 17% planar $CH_3NH_3PbI_3$ solar cells. S. Draguta, J. A. Christians, Y. V. Morozov, A. Mucunguzi, J. S. Manser, P. Kamat, J. M. Luther, M. Kuno (in preparation)

[K2] Shift happens. How halide ion composition can influence photoinduced segregation in mixed halide perovskites. S. J. Yoon, M. Kuno, P. V. Kamat (in preparation)

[K3] Rationalizing the light-induced phase separation of mixed halide organic-inorganic perovskites. S. Draguta, O. Sharia, S. Yoon, M. Brennan, Y. V. Morozov, J. Manser, P. Kamat, W. F. Schneider, M. Kuno (submitted)

[K4] Intriguing optoelectronic properties of metal halide perovskites. J. S. Manser, J. A. Christians, P. V. Kamat, Chem. Rev. **2016**, 116, 12956.
[K5] Tracking iodide and bromide ion movement in mixed halide lead perovskites during photoirradiation. S. J. Yoon, S. Draguta, J. Manser, O. Sharia, W. Schneider, M. Kuno, P. V. Kamat, ACS Energy Lett. **2016**, 1, 290.
[K6] Spatially non-uniform trap state densities in solution-processed hybrid perovskite thin films. S. Draguta, S. Thakur, Y. V. Morozov, Y. Wang, J. S. Manser, P. V. Kamat, M. Kuno, J. Phys. Chem. Lett. **2016**, 7, 715.

Develop On-Demand Nanoplasmonic Device Concepts in a Semiconductor Compatible Hybrid System

Cheng Cen, Department of Physics and Astronomy, West Virginia University

Program Scope

The program focuses on the development of an on-demand nanoplasmonic platform that combines emerging oxide nanoelectronics with a low-loss semiconductor-friendly plasmonic material – graphene. The proposed research is based on a conducting atomic force microscope (c-AFM) based technique that allows conducting nanostructures to be formed and modified on-demand in virtually any desired arrangements at $LaAlO_3$ (LAO)/$SrTiO_3$ (STO) interface with a spatial resolution of only a few nanometers. In a heterostructure of Graphene/LAO/STO, the nanoscale-conducting structures at LAO/STO interface reversibly patterned by c-AFM can spatially modulate the chemical potential in the top graphene layer and provide dynamic confinement and manipulation of plasmon mode in graphene. The completion of this work is expected to demonstrate a series of rewritable nanoplasmonic devices, including waveguides, active modulators, on chip light source and sensors.

Recent Progress

We have recently demonstrated the local control of interface doping mechanisms in 8uc LAO/STO heterostructures. The new method solves the quick decay problem for written 2DEG structures in air, and is able to produce interface nanostructures that are robust even against solvent treatment, which is critical for graphene transfer. Controlling the adsorbates at the surface and oxygen vacancies (OVs) inside the LAO film separately, multiple levels of interface conductance can be flexibly configured at room temperature. At low temperature, interface carrier density is limited by the structurally driven

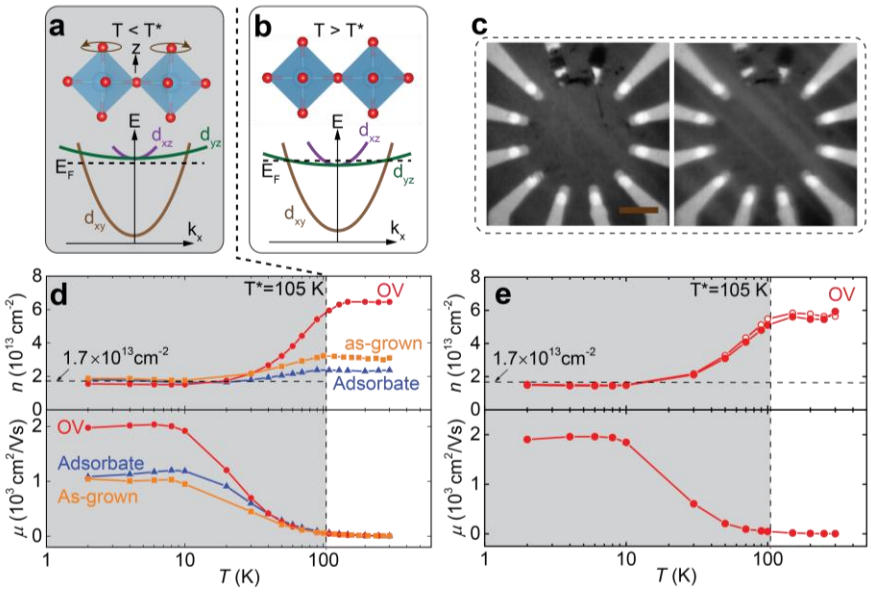

Figure 1 Transport properties of different interface 2DEG states. (a, b) Oxygen octahedral rotations and the shifting of three Ti t2g orbitals in (b) cubic and (a) tetragonal phase. (c) 6 K polarized optical microscopy images taken when focusing (left) at the sample surface and (right) a few microns into the bulk, showing the tetragonal domain pattern formed slightly below the surface. Scale bar indicates 20 μm. (d) Sheet carrier density and mobility measured in 2DEG Hall bars formed from different doping mechanisms. (e) Similar measurements on a OV dominate 2DEG Hall bar patterned in a second sample. The two carrier density curves were measured at the two Hall crosses.

transition from multi-subband conduction to single subband conduction that is independent of the dopant types, while the remote dopants, especially ionized surface adsorbates, have significant influences on the carrier mobility. In addition, the capability of generating non-equilibrium distributions of OVs and surface protons in nanoscale helped revealing the active diffusions of these remote dopants at room temperature.

We also found that graphene transferred to LAO/STO has much lower oxidation resistance comparing to graphene on conventional SiO_2/Si substrate. In the oxidized state, contact friction in graphene can be significantly enhanced by the introduction of vacancies, but is relatively insensitive to the adsorption of add atoms and functional groups. Presence of vacancies can make the graphene sheet more flexible to pucker at the contact edge, which increases the contact area and thus leads to a larger contact friction. Modified graphene in the large fiction state remained a good electrical conductor, making them potentially useful in applications such as triboelectric devices. These samples are also good platforms to study the unique transport behaviors in heavily disordered Dirac system, in which quantum interference effects at room temperature as well as the transition into strong localization regime were observed. Additionally, bilayer graphene, showing much higher oxidation resistance than monolayer graphene, is expected to be a better choice in applications that requires good chemical stability.

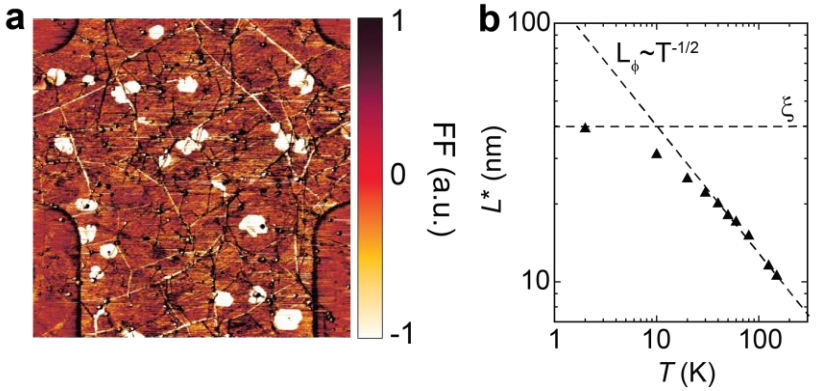

Figure 2 (a) Frictional force image over one junction of a graphene/LAO/STO hall bar treated by shielded oxygen plasma. The islands with low frictional fiorce are bilayer regions which are highly oxidation resistant. At this state, the graphene is highly frictional but still ohmic. Its transport is strongly affected by quantum interference effects even at room temperature. (b) *Temperature dependence of the characteristic length L* of localization effect. At higher temperatures L* is dominated by the phase coherence length* $L_\phi \sim T^{-1/2}$. *As* L_ϕ *increases at low temperatures, L* becomes more significantly affected by the temperature independent localization length* ξ.

Future Plans

Graphene/LAO/STO plasmonic structures will be created by two approaches. In the first approach, with the capability of generating interface 2DEG patterns that are robust in solvents, we are going to first create grating structures in LAO/STO interface without the graphene layer and then transfer graphene on top. This method provides a faster writing speed of interface 2DEG and therefore are suitable for relatively larger periodic structures. After transfer, the plasmon dispersion in the heterostructure is going to be characterized by IR reflectance spectroscopy as a function of grating constant and biases applied to the interface 2DEG. In the second approach, nanoscale plasmonic structures are going to be created and modified with graphene already

transferred. These structures will be characterized by near field optical measurements by the same probe used in c-AFM writing.

Publications

1. Dai, Weitao Dai, Sanjay Adhikari, Andrés Camilo Garcia-Castro, Aldo H. Romero, Hyungwoo Lee, Jung-Woo Lee, Sangwoo Ryu, Chang-Beom Eom and Cheng Cen "Tailoring $LaAlO_3/SrTiO_3$ Interface Metallicity by Oxygen Surface Adsorbates" Nano Letters 16, 2739-2743, (2016)
2. Sanjay Adhikari, Andrés C. Garcia-Castro, Aldo H. Romero, Hyungwoo Lee, Jung-Woo Lee, Sangwoo Ryu, Chang-Beom Eom, and Cheng Cen, "Charge Transfer to $LaAlO_3/SrTiO_3$ Interfaces Controlled by Surface Water Adsorption and Proton Hopping" Advanced Functional Materials 26, 5453-5459, (2016)
3. Cen, Cheng, Yanjun Ma, Qiang Wang, and Chang-Beom Eom. "Surface magnetism and proximity effects in hexaboride thin films." Applied Physics Letters 110, 102404 (2017)
4. Prakash Gajurel, Mina Kim, Qiang Wang, Weitao Dai, Haitao Liu, and Cheng Cen. "Vacancy controlled friction and substrate dependent oxidation resistance in graphene", submitted
5. Weitao Dai, Ming Yang, Hyungwoo Lee, Jung-Woo Lee, Chang-Beom Eom, and Cheng Cen, "Tailoring the subband occupations at oxide interfaces in nanoscale", submitted

Session XIII

Proximity Effects in Charged Oxide Heterostructures

Dillon D. Fong, Jeffrey A. Eastman, Matthew J. Highland, Peter Zapol
Materials Science Division, Argonne National Laboratory

Program Scope: The goal of the PECOH program is to understand and control the behavior of defects in oxide heterostructures, both during synthesis and under applied electrochemical potentials. We employ an approach that exploits our expertise in *in situ* experimentation using synchrotron X-rays in combination with first-principles computational theory. We target the transition metal oxides, materials that exhibit a wide range of fascinating properties. It has become clear that much of the phenomena discovered in the field of complex oxide heterostructures may be related to charged defects and their behavior at interfaces. Such phenomena, however, remain poorly understood due to the inherent difficulties in probing defect-interface interactions at the atomic-level and in the environments relevant to defect evolution. We address this problem by growing heterostructures with excellent sublattice control but variable ionic defect concentrations, enabling the systematic investigation of defect formation and migration behavior both during synthesis and while processing in different electrochemical environments. Throughout this program, the atomic and electronic structure results are fed back to computational theory to gain insight into the mechanisms and energetic processes taking place during defect structure evolution.

Recent Progress: Our program has advanced fundamental understanding in the areas of oxide thin film synthesis and defect interactions at surfaces and heterointerfaces. We explored the functional links between reactivity and stability at oxide surfaces with real-time studies[1], discovered a novel method for modulating electronic properties through reversible vacancy doping[2], and employed first-principles theory to model cation rearrangement in the layered oxides[3], with the results providing insight into the energetics that control ion distributions and the barriers to motion at heterophase boundaries. Efforts using *in situ* synchrotron X-ray techniques to control and monitor epitaxial thin film heterostructure growth revealed remarkable effects of the chemical environment on thin film and surface phase transitions, and allowed an atomic-scale look into the mechanisms governing field-driven oxygen exchange behavior. We briefly describe highlights in two of these areas.

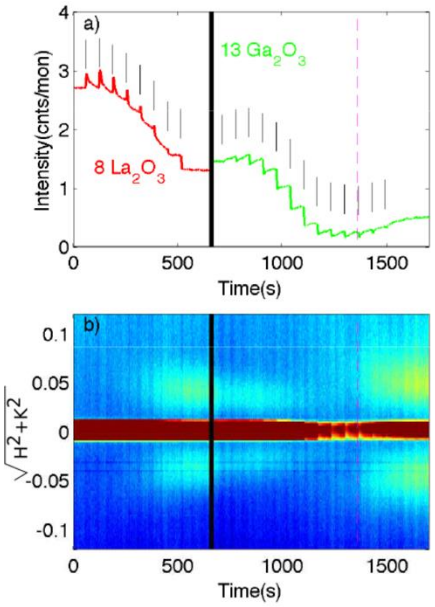

Figure 1 *In situ* X-ray scattering during synthesis of $LaGaO_3$ in a pulsed mode from two sputtering sources. (a) The variation in the specular rod intensity during the application of La_2O_3 pulses (in red) followed by Ga_2O_3 pulses (in green). (b) Diffuse scattering near the specular rod during the same growth.

Stoichiometric control of heterostructures using binary-oxide targets: Magnetron sputter deposition is a versatile growth technique, allowing high growth rates and uniform films even for refractory materials. In the 90° off-axis geometry, with RF powered guns and an oxygen background, it can be used to synthesize complex oxide heterostructures with submonolayer thickness control and atomically sharp

interfaces. However, stoichiometric control of an ABO_3 perovskite can be a major challenge, as cation species often have significantly different masses or volatilities, leading to A/B composition ratios that depend on deposition time as well as other parameters. We have recently constructed a state-of-the-art *in situ* X-ray system for the study of off-axis sputter deposition[4] and focused on pulsed deposition from binary-oxide targets for the stoichiometric growth of ternary complex oxides, permitting MBE-like control over the A/B ratio. Studies were conducted on $LaGaO_3$, a complex oxide comprised of the monovalent cations La^{3+} and Ga^{3+} that has generated much interest due to the appearance of two-dimensional electron gas (2DEG) behavior. As with many perovskites, $LaGaO_3$ has little miscibility with its parent materials, La_2O_3 and Ga_2O_3, and the oxide in excess will appear as a distinct crystalline phase. In work published in Applied Physics Letters[5], we demonstrate that grazing incidence X-ray scattering is highly sensitive to presence of these other phases, providing a simple metric for tuning the overall stoichiometry of the film. Furthermore, we discovered that cation non-stoichiometry can significantly alter the morphology of the film during growth. The diffuse scatter shown in **Fig. 1** indicates that 3D islands form during the deposition of La_2O_3 but disappear once a stoichiometric amount of Ga_2O_3 is added. The ability to precisely control the cation ratio is an essential step toward planned investigations of the growth of cation-deficient materials.

Control of oxygen vacancies at heterointerfaces: Oxygen vacancy concentrations exceeding bulk levels near surfaces and interfaces have been cited as instrumental for controlling a wide range of properties in oxide thin film heterostructures. For example, large changes in conductivity associated with metal-insulator transitions or resistive switching may stem from the formation and migration of oxygen vacancies in thin film heterostructures. As described in a publication in Nature Communications[2], we discovered a means of using a small electric field to induce oxygen ion transport across a thin film heterointerface. The effect is due to the emergence of a contact-resistance-induced electric field component normal to the applied field direction, across the heterointerface between a thin film and a substrate that behaves as a solid electrolyte (see schematic in **Fig. 2(a)**). The cross-interface field component provides a driving force to inject oxygen vacancies from the substrate into the film. As shown in **Fig. 2(b)**, for In_2O_3 films on single crystal Y_2O_3-stabilized ZrO_2 (YSZ), when an in-plane DC field is applied, the conductance increases with time to reach a new steady state value, in some cases more than two orders-of-magnitude larger than the initial sample conductance. While the field-induced doping behavior was demonstrated for In_2O_3/YSZ, similar controllable dynamic doping behavior should be achievable in other systems that combine one material that can be electronically doped with another.

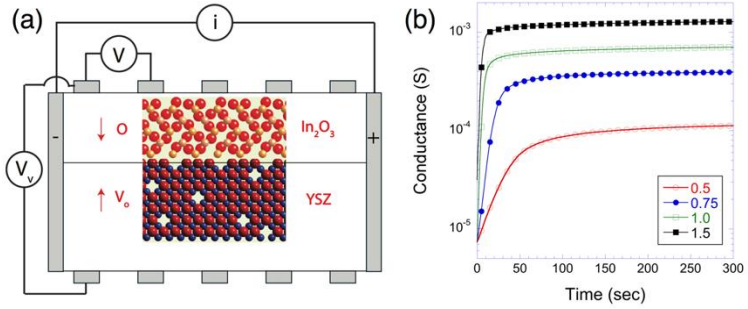

Figure 2 (a) Schematic representation of the In_2O_3/YSZ heterostructure. An in-plane drive current is applied to the end electrodes, which establishes a vertical voltage, V_V, driving oxygen ions from the In_2O_3 to the YSZ substrate. (b) Time-dependent increases in in-plane conductance are shown at different voltages. The voltage was maintained between a pair of pick-off electrodes, while current between the end electrodes at 370°C with the sample equilibrated at pO_2 = 150 Torr.

Future Plans

The goal of future work is determining how to effectively control the cation and oxygen sublattices in oxide heterostructures, both during synthesis and under applied electric fields. We seek ways to manipulate defects and their distributions over multiple length scales, and exploit their coupling with different physical functionalities to arrive at materials with configurable properties. The outcome of this work will be the fundamental scientific understanding that enables advances in ionic- or electronic-based energy storage/conversion devices and information technologies. Here, we describe two areas of interest.

Nanoscale control of oxygen vacancies: Dielectric breakdown in the oxides is often tied to the irreversible formation and flow of defects. With "soft" dielectric breakdown, the material can be partially healed, leading to novel behaviors such as electrical properties that depend sensitively on the voltage history and speed and magnitude of the voltage pulse. For transition metal oxides, these behaviors originate from the formation and dissolution of conducting channels comprised of oxygen vacancies. We plan to gain nanoscale control over these oxygen vacancy channels, allowing direct engineering of the electrical properties: this is an active research area in both resistive switching and memristive computing. We performed test studies with sub-micron resolution on model $WO_{3-\delta}/SrTiO_3$ single crystal heterostructures, using chemical and structural contrast mechanisms in X-ray microscopy to observe the results of vacancy migration under an applied electric field. The 5 μm gap region between two Pt electrodes is shown in **Fig. 3(a)**; the regions above and below the white dashed lines are covered with Pt, but they are invisible in this real-space map, which only shows the oxygen concentration in $WO_{3-\delta}$. The conducting channel extends from top to bottom along the dashed violet curve, which was confirmed with conductive atomic force microscopy. As seen by a quantitative measurement of the $O_{3-\delta}$ profile along this curve (**Fig. 3(b)**), the channel is depleted of much of its oxygen, falling to sub-stoichiometries as low as $WO_{2.15}$. Our aim is to push these *operando* studies toward nanoscale resolution and perform real-time imaging of vacancy migration such that we observe the effects of probe geometry, pulse shape, and pulse timing on vacancy behavior. We will continue studies on $WO_{3-\delta}$, which is of interest for a variety of neuromorphic functionalities, as well as on $LaNiO_{3-\delta}$ and $SrCoO_{3-\delta}$, which also exhibit stoichiometry-driven electronic transitions.

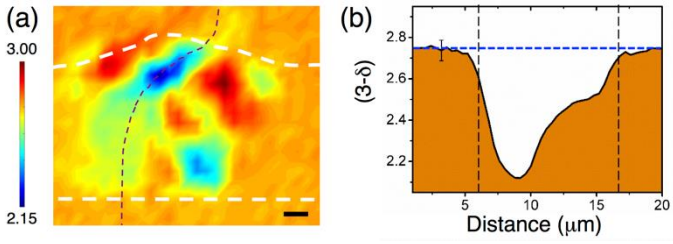

Figure 3 The electroformed region in a 20 nm $WO_{3-\delta}/SrTiO_3(001)$ heterostructure. (a) Chemical map of the $O_{3-\delta}$ distribution; the black line shows 1 μm. The white dashed lines show the edges of the Pt electrodes. (b) The $O_{3-\delta}$ distribution along the curved conducting channel. The blue dashed line at $(3-\delta) = 2.75$ refers to the value of the pristine state.

Stabilizing cation-deficient perovskite heterostructures: Here we focus on cation vacancies on the A-site sublattice, $V_A''^{(\prime)}$, which, given their relatively large effective charge and size difference, can strongly affect material properties as well as perovskite phase stability. We aim to understand what ultimately limits the cation vacancy concentration in epitaxial heterostructures and how vacancy ordering affects cation motion. A-site vacancies can indeed order in systems with a highly charged B-site, leading to structures such as those shown in the top of **Fig. 4**.

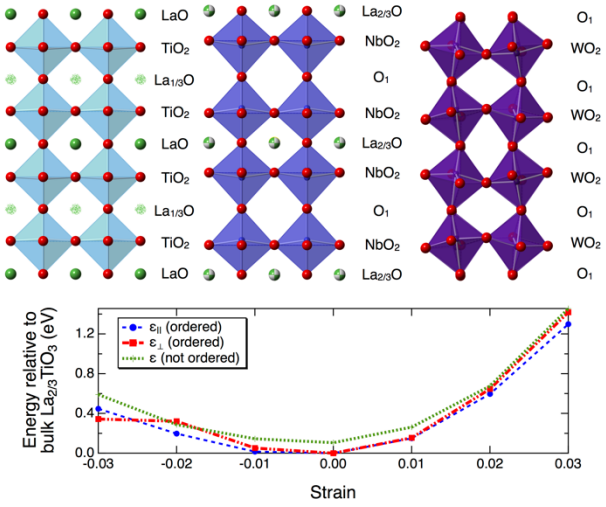

Figure 4 Top: Depictions of (001)-oriented nominal $La_{2/3}TiO_3$ (left), $La_{1/3}NbO_3$ (middle) and WO_3 (right) structures along the pseudocubic [001] axis. Bottom: Calculated relative energies of $La_{2/3}TiO_3$ as a function of biaxial strain.

These efforts will yield the necessary understanding for the design and synthesis of new cation-deficient oxide heterostructures with tailorable electronic and ionic transport properties. Initial studies will be aimed at using two-target sputter deposition to stabilize the $La_{2/3}TiO_3$ and $La_{1/3}NbO_3$ perovskite heterostructures, neither of which have been grown in thin film form. We will determine the range of cation deficiency and the degree of vacancy ordering using X-ray scattering and spectroscopy at the B-site absorption edge, while varying the strain state, the background oxygen potential, and the crystal orientation. The results of a preliminary density functional theory calculation of the relative energies for different $La_{2/3}TiO_3$ structures (bottom of **Fig. 4**) show that cation vacancies prefer long-range ordering over a more random vacancy structure; this furthermore remains true for films with in-plane biaxial strain. However, the degree of cation deficiency may be highly correlated with oxygen non-stoichiometry and vice-versa: for example, Ti^{4+} in $La_{2/3-x}TiO_{3-\delta}$ and Nb^{5+} in $La_{1/3-x}NbO_{3-\delta}$ would favor $x = 2\delta/3$. Our studies will answer a number of important questions concerning the limits of ion deficiency before changing the local and/or long-range order of the crystal structure or the formation of a non-perovskite phase. Following the synthesis of cation-deficient films, we will investigate cation migration, ordering, and phase stability during the deposition of superlattices such as $La_{2/3}TiO_3/SrTiO_3$.

References

1. Chang, S. H., Danilovic, N., Chang, K. C., Subbaraman, R., Paulikas, A. P., Fong, D. D., Highland, M. J., Baldo, P. M., Stamenković, V. R., Freeland, J. W., Eastman, J. A. & Marković, N. M. *Nature Communications* **5,** 4191 (2014).
2. Veal, B. W., Kim, S. K., Zapol, P., Iddir, H., Baldo, P. M. & Eastman, J. A. *Nature Communications* **7,** 11892 (2016).
3. Lee, J. H., Luo, G., Tung, I. C., Chang, S. H., Luo, Z., Malshe, M., Gadre, M., Bhattacharya, A., Nakhmanson, S. M., Eastman, J. A., Hong, H., Jellinek, J., Morgan, D., Fong, D. D. & Freeland, J. W. *Nature Materials* **13,** 879–883 (2014).
4. Folkman, C. M., Highland, M. J., Perret, E., Kim, S. K., Fister, T. T., Zhou, H., Baldo, P. M., Seifert, S., Eastman, J. A., Fuoss, P. H. & Fong, D. D. *Rev. Sci. Instrum.* **84,** 025111 (2013).
5. Highland, M. J., Fong, D. D., Ju, G., Thompson, C., Baldo, P. M., Fuoss, P. H. & Eastman, J. A. *Appl. Phys. Lett.* **107,** 081606 (2015).

Publications

1. M. J. Highland, D. D. Fong, G. Ju, C. Thompson, P. M. Baldo, P. H. Fuoss, and J. A. Eastman, "In-situ x-ray studies of compositional control during synthesis of $LaGaO_3$ by radio frequency-magnetron sputtering," Appl. Phys. Lett. **107,** 081606 (2015), DOI: 10.1063/1.4929753.
2. E.M. Hopper, E. Perret, B.J. Ingram, H. You, K.-C. Chang, P.M. Baldo, P.H. Fuoss, J.A. Eastman, "Oxygen Exchange in $La_{0.6}Sr_{0.4}Co_{0.2}Fe_{0.8}O_{3-\delta}$ Thin Film Heterostructures Under Applied Electric Potential," J. Phys. Chem. C., **119**, no. 34, 19915-19921 (2015), DOI: 10.1021/acs.jpcc.5b05505.
3. C. Liu, B. Yang, E. Tyo, S. Seifert, J. DeBartolo, B. von Issendorf, P. Zapol, S. Vajda, L.A. Curtiss, "Carbon Dioxide Conversion to Methanol over Size-Selected Cu-4 Clusters at Low Pressures," J. Am. Chem. Soc., **137**, 8676-8679 (2015), DOI: 10.1021/jacs.5b03668.
4. X. Zhong, I. Rungger, P. Zapol, O. Heinonen, "Electronic and magnetic properties of Ti_4O_7 predicted by self-interaction-corrected density functional theory," Phys. Rev. B, **91**, 115143 (2015), DOI: 10.1103/PhysRevB.91.115143.
5. C. Cao, R. Tao, D. Ford, R.F. Klie, T. Proslier, L.D. Cooley, A. Dzyuba, P. Zapol, M. Warren, H. Lind, J.F. Zasadzinski, "Giant two-phonon Raman scattering from nanoscale NbC precipitates in Nb," Phys. Rev. B, **91**, 094302 (2015), DOI: 10.1103/PhysRevB.91.094302.
6. D.C. Ford, P. Zapol, L.D. Cooley, "First-Principles Study of Carbon and Vacancy Structures in Niobium," J. Phys. Chem. C., **119**, 14728-14736 (2015), DOI: 10.1021/acs.jpcc.5b00372.
7. A. Ulvestad, M.J. Welland, S.S.E. Collins, R. Harder, E. Maxey, J. Wingert, A. Singer, S. Hy, P. Mulvaney, P. Zapol, O.G. Shpyrko, "Avalanching strain dynamics during the hydriding phase transformation in individual palladium nanoparticles," Nature Communications, **6**, 10092 (2015).
8. B.W. Veal, S.K. Kim, P. Zapol, H. Iddir, P.M. Baldo, J.A. Eastman, "Interfacial control of oxygen vacancy doping and electrical conduction in thin film oxide heterostructures," Nature Communications, **7**, 11892 (2016), DOI: 10.1038/ncomms11892.
9. D. M. Paskiewicz, R. Sichel-Tissot, E. Karapetrova, L. Stan, and D. D. Fong, "Single-Crystalline $SrRuO_3$ Nanomembranes: A Platform for Flexible Oxide Electronics," Nano Lett. 16, 534-542 (2016), DOI: 10.1021/acs.nanolett.5b04176.
10. J. H. Lee, I.C. Tung, S.-H. Chang, A. Bhattacharya, D. D. Fong, J. W. Freeland, and H. Hong, "In Situ Surface / Interface X-ray Diffractometer for Oxide Molecular Beam Epitaxy," Rev. Sci. Instrum. 87, 013901 (2016), DOI: 10.1063/1.4939100.
11. S. Hong, S. M. Nakhmanson, and D. D. Fong, "Screening Mechanisms at Polar Oxide Heterointerfaces," Rep. Prog. Phys. 79, 076501 (2016), DOI: 10.1088/0034-4885/79/7/076501.
12. M.J. Highland, E. Perret, C.M. Folkman, D.D. Fong, Carol Thompson, P.H. Fuoss, J.A. Eastman, "Effect of SrO doping on $LaGaO_3$ synthesis via magnetron sputtering," Cryst. Growth & Design, **16**, 6812-6816 (2016), DOI: 10.1021/acs.cgd.6b00914.
13. R. Gao, Ran; Y. Dong, H. Xu; H. Zhou, Y. Yuan, V. Gopalan, C. Gao, D. Fong, Z. Chen, Z. Luo, and L. Martin, "Interfacial Octahedral Rotation Mismatch Control of the Symmetry and Properties of $SrRuO_3$," ACS Appl. Mater. Int. **8**, 14871-14878 (2016).

14. Y. Zhou, X. Guan, H. Zhou, K. Ramadoss, S. Adam, H. Liu, S. Lee, J. Shi, M. Tsuchiya, D. D. Fong, and S. Ramanathan, "Strongly correlated perovskite fuel cells," Nature **231**, 534 (2016).
15. Z. Feng, W. T. Hong, D. D. Fong, Y.-L. Lee, Y. Yacoby, D. Morgan, and Y. Shao-Horn, "Catalytic Activity and Stability of Oxides: The Role of Near-Surface Atomic Structures and Compositions," Accts. Chem. Res. **49**, 966–973 (2016).
16. R. Mishra, Y. Kim, Q. He, X. Huang, S.K. Kim, M. Susner, A. Bhattacharya, D. D. Fong, S. T. Pantelides, and A. Borisevich, "Towards spin-polarized two-dimensional electron gas at a surface of an antiferromagnetic insulating oxide," Phys. Rev. B. **94**, 045123 (2016).
17. X. Zhong, I. Rungger, P. Zapol, H. Nakamura, Y. Asai, O. Heinonen, "The effect of a Ta oxygen scavenger layer on HfO_2-based resistive switching behavior: thermodynamic stability, electronic structure, and low-bias transport," Physical Chemistry Chemical Physics, **18**, 7502-7510 3 (2016).
18. S. O. Hruszkewycz, Q. Zhang, M. V. Holt, M.J. Highland, P.G. Evans, P.H. Fuoss, "Structural sensitivity of x-ray Bragg projection ptychography to domain patterns in epitaxial thin films," Physical Review A **94**, 043803 (2016).
19. S. Guillemin, R. Parize, J. Carabetta, V. Cantelli, D. Albertini, B. Gautier, G. Brémond, D.D. Fong, H. Renevier, and V. Consonni, Quantitative and simultaneous analysis of the polarity of polycrystalline ZnO seed layers and related nanowires grown by wet chemical deposition, Nanotechnology **28,** 095704 (2017). DOI: 10.1088/1361-6528/aa5657.
20. B.W. Veal, J.A. Eastman, "Conduction in In_2O_3/YSZ heterostructures: Complex Interplay between Electrons and Ions, Mediated by Interfaces," APL Materials, **5** (2017), DOI: 10.1063/1.4977205
21. Q. Zhang, E.M. Dufresne, P. Chen, J. Park, M.P. Cosgriff, M. Yusuf, Y. Dong, D.D. Fong, H. Zhou, Z. Cai, R. Harder, S. Calorie, M. Dawber, P.G. Evans, A.R. Sandy, Thermal fluctuations of ferroelectric nanodomains in a ferroelectric-dielectric $PbTiO_3$/$SrTiO_3$ superlattice, Phys. Rev. Lett. **118,** 097601 (2017).
22. M.-H.Chu, L. Tian, A. Chaker, E. Skopin, V. Cantelli, T. Ouled, R. Boichot, A. Crisci, S. Lay, M.-I. Richard, O.Thomas, J.-L. Deschanvres, H. Renevier, D. Fong, and G. Ciatto, Evaluation of alternative atomistic models for the incipient growth of ZnO by atomic layer deposition, J. Elect. Mater. (2017). DOI:10.1007/s11664-017-5448-2
23. G. Ju, M.J. Highland, A. Yanguas-Gil, Carol Thompson, J.A. Eastman, H. Zhou, S.M. Brennan, G.B. Stephenson, P.H. Fuoss, "An instrument for *in situ* coherent x-ray studies of metal-organic vapor phase epitaxy of III-nitrides," Rev. Sci. Instrum. **88,** (2017), DOI: 10.1063/1.4978656
24. A. Ulvestad, M.J. Welland, W. Cha, Y. Liu, J.W. Kim, R. Harder, E. Maxey, J.N. Clark, M.J. Highland, H. You, P. Zapol, S.O. Hruszkewycz, G.B. Stephenson, "Three-dimensional imaging of dislocation dynamics during the hydriding phase transformation," Nature Mater., published online January 16, 2017, DOI: 10.1038/nmat4842.

Chiral Materials and Unconventional Superconductivity

PI: Qiang Li
Co-PIs: Genda Gu and Tonica Valla
Condensed Matter Physics & Materials Science Division, Brookhaven National Laboratory
e-mail: qiangli@bnl.gov

Program Scope

This program studies relationship between structures and the macroscopic properties of chiral materials and superconductors. A unique feature that makes chiral materials' electronic properties different from all other condensed matter systems is the linear dispersion of their low-energy excitations described by an analog of the relativistic Dirac equation. The spin of three dimensional (3D) Dirac particles has a definitive projection on momentum direction called chirality. The powerful notion of chirality underpins a wide palette of new and useful phenomena, such as non-dissipative charge transport and novel one-way photonic modes. The non-dissipative charge transport in chiral materials is enabled by the newly discovered chiral magnetic effect (Fig. 1).[1,2] The emphasis of this program is now on the investigation of structure and property relationships in chiral materials and chiral charge transport process, shifting from our past emphasis on the investigation of vortex pinning phenomenon and mechanism of superconductivity in high temperature cuprate and iron-based superconducting materials. Our goal is to gain basic understanding and control the chiral fermion transport process, and to explore the power of chirality. In this program, topological superconductors and chiral materials are synthesized in both single crystals and thin film forms, and subsequently characterized via a range of techniques including transport, electron and optical spectroscopy, and transmission electron microscopy. The experimental activities are strongly coupled with a large collaborative effort on theory and computation, providing new strategies for designing robust quantum materials capable of transporting non-dissipative electrical current more efficiently at higher temperature.

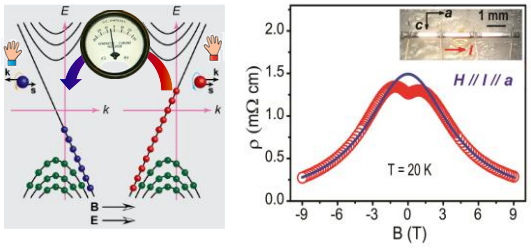

Fig. 1 Left: Chiral magnetic effect is the generation of electric current by chirality imbalance of the Dirac fermions in a magnetic field. Right: negative magneto-resistance observed in Dirac semimetal $ZrTe_5$ (inset) under a parallel magnetic field ($\boldsymbol{B} \parallel \boldsymbol{I}$) exhibits a quadratic field dependence – a signature of the chiral magnetic effect.[1]

Recent Progress

Discovery of chiral magnetic effect in condensed matter systems - Relativistic quantum field theory of chiral fermions in 3D space and time exhibits so-called chiral anomaly,[3,4] which is the non-conservation of chiral charge induced by the external gauge fields with non-trivial topology. A consequence of the chiral anomaly is the chiral magnetic effect – the generation of electric current in an external magnetic field induced by the chirality imbalance (Fig. 1).[5] The recent experimental discovery of Dirac and Weyl semimetals that host chiral fermions has opened unprecedented opportunities to explore the quantum dynamics of relativistic field theory in condensed matter systems.[6] The chiral magnetic effect has the potential of non-dissipative charge transport without any condensates in the ground state.

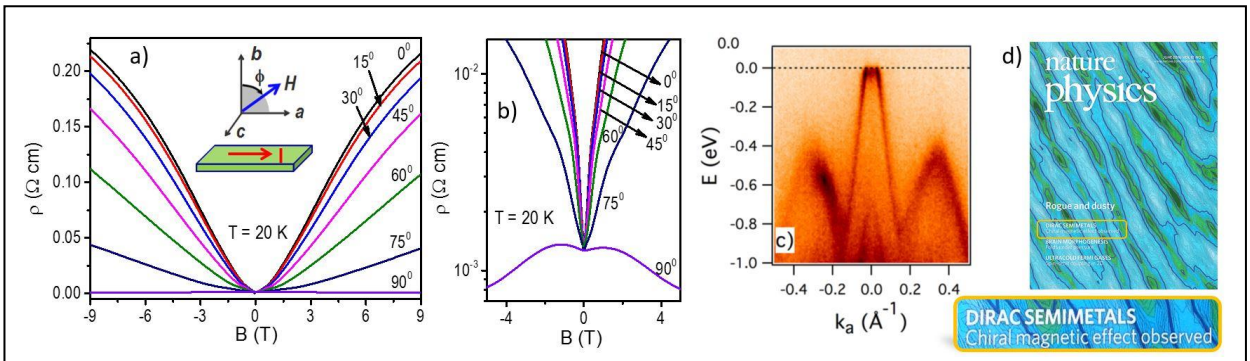

Fig. 2: a) Angular dependent magnetoresistance of $ZrTe_5$ at 20 K, b) The same data as in a), plotted on the logarithmic scale, c) in-plane valence band dispersion of a $ZrTe_5$ single crystal along the $\overline{\Gamma} - \overline{X}$ (chain direction), recorded at $h\nu$ = 63 eV photon energy and T = 20 K, d) Cover of Nature Physics reporting our observation of the chiral magnetic effect in Dirac Semimetals.[1]

We reported angular resolved magneto-transport measurements in zirconium pentatelluride, $ZrTe_5$ (Fig. 2a, b) that provide a strong evidence for the chiral magnetic effect. Our angle-resolved photoemission spectroscopy (ARPES) experiments show that this material's electronic structure is consistent with a 3D Dirac semimetal (Fig. 2c) – a prerequisite for the observation of the chiral magnetic effect. We observed a large longitudinal negative magnetoresistance (4-fold decrease from the zero-field-value at 20 K) when the magnetic field is parallel to the current. The measured quadratic field dependence of the magnetoconductance is a clear indication of the chiral magnetic effect (Fig. 1). We predicted that the chiral magnetic effect may emerge in a wide class of materials that are near the transition between the trivial and topological insulators.[1]

Superconductivity in topological crystal insulators – 3D topological insulators and topological crystalline insulators are predicted to have insulating bulk states and gapless surface states. Experimentally, it has proven difficult to achieve the high bulk resistivity that would allow surface states to dominate the transport properties over a substantial temperature range. We have prepared a series of indium-doped $Pb_{1-x}Sn_xTe$ compounds that show huge bulk resistivity together with transport characteristics consistent with the topological character of the surface states for $x \geq 0.35$.[7]

Due to the small surface-to-bulk ratio in bulk crystals, it is sometimes difficult to conclude whether the topological surface state exists. Thus, low dimensional samples, such as thin films having a much larger surface-to-bulk ratio, are desirable. For integrated device applications like quantum computing, thin films are most desirable. We investigated the superconducting properties of In-doped SnTe thin films. The (100) and (111) oriented thin films were epitaxially grown on (100) and (111) BaF_2 crystalline substrates *for the first time* (Fig. 3). The onset T_cs are about 3.8 K for (100) and 3.6 K for (111) oriented films, respectively,

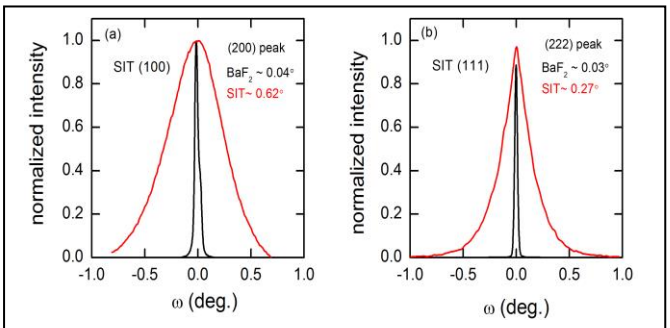

Fig. 3 Rocking curves for (a) (200) peak of $Sn_{0.55}In_{0.45}Te$ film on (100) BaF_2 substrate. (b) (222) peak of SIT film grown on (111) BaF_2.[8]

slightly lower than that of the bulk. These films provide a rich platform for exploring surface states and topological superconductivity.[8]

Fine tuning superconductivity and chiral properties by irradiation – Critical temperatures, T_c, and critical current densities, J_c, of superconducting materials determine the limits of a superconductor in energy applications. The current-carrying capability, measured by J_c, is the ability of defects in superconductors to pin magnetic vortices. Recently, we demonstrated a new route to raise T_c and J_c simultaneously – *the first time this was accomplished in any cuprate- or iron-based superconductors*.[9] By using low-energy proton irradiation, we created cascade defects in $FeSe_{0.5}Te_{0.5}$ films (Fig. 4a). T_c is enhanced due to the nanoscale compressive strain induced by the irradiations and proximity effect, whereas J_c is doubled under zero field at 4.2 K through strong vortex pinning by the cascade defects and surrounding nanoscale strain. At 12 K and above 15 T, one order of magnitude of J_c enhancement is achieved in both parallel and perpendicular magnetic fields to the film surface.[9]

Currently, we are developing the technique of Fermi level tuning in chiral materials by electron irradiation, which will create Frenkel vacancy-interstitial pairs in bulk materials.[10] This approach is based on the difference in the threshold energy E_{th} and cross-section for each element in a specimen. Charge compensation becomes possible by tuning the energy of incident electrons to values lower than E_{th} in one element, but higher in other elements. Topological single crystals and films can be driven from hole-like bulk conductivity to electron-like conductivity, through the Dirac point and back, while preserving the band dispersion and crystal structure. This effort takes advantage of the 2.8 MeV electron irradiation facility at BNL that allows us to change the Fermi level across different bulk bands reversibly in chiral materials.

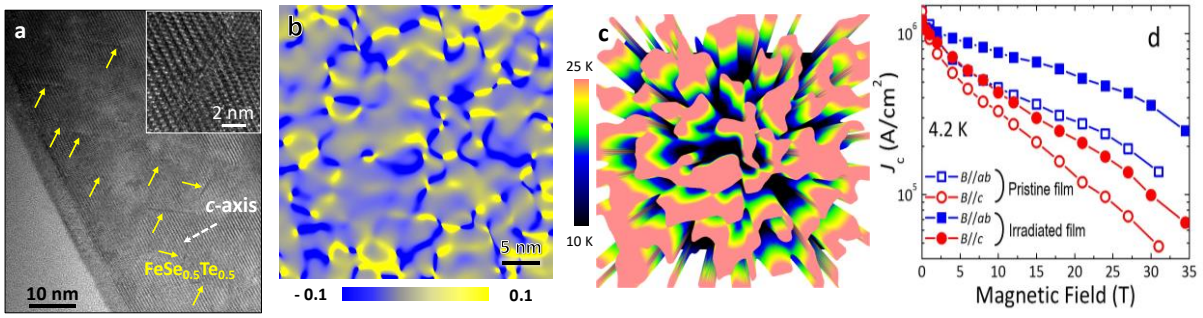

Fig. 4 (a) TEM image of superconducting $FeSe_{0.5}Te_{0.5}$ films irradiated with low-energy protons shows the resulting defects (indicated by yellow arrows). The inset: a zoomed-in view of a typical defect chain. (b) Strain maps of in-plane ε_{xx} in the irradiated film. The color bar indicates the strain value. (c) Perspective view of the spatial distribution of T_c calculated from the local strain; (d) J_c enhancement after irradiation[9]

Future Plans

The physics in 3D Dirac systems is a very active field and results are rapidly produced. However, pieces of information are not well connected, leaving important questions, such as "how does the chiral magnetic effect respond to the change of band topology, Fermi energy, magnetism, strain, spin-orbital coupling, and dimensionality in Dirac/Weyl semimetals?", unanswered. More importantly, a bridge is lacking between the prediction of quantum phenomena and the design of 3D chiral materials. We will bring together theory, computation, materials synthesis, and

characterization of crystal structure, electronic structure, and transport properties to investigate the relationship between crystalline/electronic structure and properties of chiral materials.

While the transport of non-dissipative chiral fermions is protected by chirality conservation, chirality change scattering (chiral flipping) is at play in real chiral materials, which works against the non-dissipative charge transport process. Currently, there is virtually no knowledge on 1) the chirality flipping mechanism in 3D Dirac/Weyl materials; 2) how to harness the power of chirality to achieve non-dissipative charge transport at a practical length scale (for example, size of a typical computer chip), or to use it as a probe to explore other quantum phenomena. We will directly measure the chiral charge relaxation time that determines the limits to non-dissipative transport in chiral materials. We will pursue a new direction of heterostructures made of superconductor and chiral materials, in which we utilize the power of chirality conservation to investigate unconventional superconductivity. This will allow us to experimentally explore a significant recent prediction that odd-parity pairing favored by strong spin-orbit coupling is likely a common underlying mechanism for topological superconductivity.

References

1. Q. Li, D. E. Kharzeev, C. Zhang, Y. Huang, I. Pletikosic1, A. V. Fedorov, R. D. Zhong, J. A. Schneeloch, G. D. Gu and T. Valla. "Chiral magnetic effect in $ZrTe_5$" *Nature Physics* **12** 550 (2016).
2. Q. Li and D. E. Kharzeev "Chiral magnetic effect in condensed matter systems" *Nuclear Physics* A **956** 107-111110 (2016)
3. S. L. Adler, "Axial-vector vertex in spinor electrodynamics" *Physical Review*, **177**, 2426 (1969).
4. J. S. Bell and R. Jackiw "A PCAC puzzle: $\pi^o \rightarrow \gamma\gamma$ in the σ-model" *Il Nuovo Cimento* A, **60**, 47-61 (1969).
5. K. Fukushima, D. Kharzeev, and H. Warringa. "Chiral magnetic effect" *Phys. Rev.* D, **78**, 074033 (2008).
6. H. B. Nielsen and M. Ninomiya. "The Adler-Bell-Jackiw anomaly and Weyl fermions in a crystal" *Physics Letters* B, **130**, 389-396 (1983).
7. R. Zhong, X. He, J. A. Schneeloch, C. Zhang, T. Liu, I. Pletikosi´c, T. Yilmaz, B. Sinkovic, Q. Li, W. Ku, T. Valla, J. M. Tranquada, and G. Gu "Surface-state-dominated transport in crystals of the topological crystalline insulator In-doped $Pb_{1-x}Sn_xTe$" *Phys. Rev*. B **91**, 195321 (2015).
8. W. Si, C. Zhang, L. Wu, T. Ozaki, G. Gu, and Q. Li "Superconducting thin films of (100) and (111) oriented indium doped topological crystalline insulator SnTe" *Appl. Phys. Lett*. **107**, 092601 (2015).
9. T. Ozaki, L. Wu, C. Zhang, J. Jaroszynski, W. Si, J. Zhou, Y. Zhu, and Q. Li, "A route for a strong increase of critical current in nanostrained iron-based superconductors" *Nature Communications* **7**, 13036 (2016).
10. A. Damask, and G. Dienes, "Point Defects in Metals" (Gordon and Breach, 1963).

Publications (2015-present)

1) H. Chi, C, Zhang, G, Gu, D. E. Kharzeev, X. Dai, and Q. Li, "Lifshitz transition mediated electronic transport anomaly in bulk $ZrTe_5$" *New J. Phys*. **19** 015005 (2017);

2) Z. G. Chen, R. Y. Chen, R. D. Zhong, J. A. Schneeloch, C. Zhang, Y. Huang, F. Qu, R. Yu, Q. Li, G. Gu, and N. L. Wang "Spectroscopic evidence for bulk-band inversion and three-dimensional massive Dirac fermions in $ZrTe_5$" *Proc. Natl. Acad. Sci. USA* **114**, 819 (2017)

3) R. D. Zhong, J. A. Schneeloch, Q. Li, W. Ku, J. Tranquada, and G. Gu "Indium substitution effect on the topological crystalline insulator family $(Pb_{1-x}Sn_x)_{1-y}In_yTe$: Topological and superconductivity properties" *Crystals* **7**, 55 (2017)

4) T. Ozaki, L. Wu, C. Zhang, J. Jaroszynski, W. Si, J. Zhou, Y. Zhu, and Q. Li, "A route for a strong increase of critical current in nanostrained iron-based superconductors" *Nature Communications* 7, 13036 (2016)

5) C. Zhang, W. Si, and Q. Li, "Doubling the critical current density in superconducting $FeTe_{0.5}Se_{0.5}$ thin films by low temperature oxygen annealing" *Appl. Phys. Lett*. 109, 202601 (2016)

6) Q. Li and D. E. Kharzeev, "Chiral Magnetic Effect in Condensed Matter Systems" *Nuclear Physics A* **956** 107 (2016)

7) Q. Li, D.E. Kharzeev, C. Zhang, Y. Huang, I. Pletikosic, A. V. Fedorov, R. D. Zhong, J. A. Schneeloch, G. Gu, T. Valla. "Chiral Magnetic Effect in $ZrTe_5$" *Nature Physics* **12**, 550–554 (2016)

8) Y. Zou, X. Q, C. Zhang, S. Ma, W. Zhang, Y. Li, T. Chen, X. Wang, Z. Chen, D. Welch, P. Zhu, B. Liu, Q. Li, T. Cui, and B. Li "Discovery of Superconductivity in Hard Hexagonal ε-NbN" *Sci. Rep*. **6**, 22330 (2016).

9) M. W. Rupich, S. Sathyamurthy, S. Fleshler, Q. Li, V. Solovyov, T. Ozaki, U. Welp, W. K. Kwok, M. Leroux, A. E. Koshelev, D. J. Miller, K. Kihlstrom, L. Civale, S. Eley, and A. Kayani, "Engineered Pinning Landscapes for Enhanced 2G Coil Wire", *IEEE Trans. on Appl. Supercond.* **26** 6601904 (2016)

10) H. Chi, G. Tan, M. G. Kanatzidis, Q. Li, and C. Uher "A low-temperature study of manganese-induced ferromagnetism and valence band convergence in tin telluride" *Appl. Phys. Lett*. **108**, 182101 (2016)

11) W. Si, C. Zhang, L. Wu, T. Ozaki, G. Gu, and Q. Li "Superconducting thin films of (100) and (111) oriented indium doped topological crystalline insulator SnTe" *Appl. Phys. Lett*. **107**, 092601 (2015)

12) W. Si, C. Zhang, X. Shi, T. Ozaki, J. Jaroszynski, and Q. Li "Grain boundary junctions of $FeSe_{0.5}Te_{0.5}$ thin films on $SrTiO_3$ bi-crystal substrates" *Appl. Phys. Lett*. **106**, 032602 (2015);

13) Y. Sun, Y. Tsuchiya, S. Pyon, T. Tamegai, C. Zhang, T. Ozaki, and Q. Li "Magneto-optical characterizations of $FeTe_{0.5}Se_{0.5}$ thin films with critical current density over 1 $MA.cm^{-2}$" *Supercond. Sci. Technol*. **28** 015010 (2015)

14) R. Y. Chen, S. J. Zhang, J. A. Schneeloch, C. Zhang, Q. Li, G. Gu, and N. L. Wang "Optical spectroscopy study of the three-dimensional Dirac semimetal $ZrTe_5$" Phys. Rev. B **92**, 075107 (2015)

15) I. K. Dimitrov, X. Zhang, V. F. Solovyov, O. Chubar, and Q. Li "Rapid and Semi-analytical Design and Simulation of a Toroidal Magnet Made With YBCO and MgB_2 Superconductors" *IEEE Trans. on Appl. Supercond.* **25** 5701208 (2015)

16) R. Zhong, X. He, J. A. Schneeloch, C. Zhang, T. Liu, I. Pletikosi´c, T. Yilmaz, B. Sinkovic, Q. Li, W. Ku, T. Valla, J. M. Tranquada, and G. Gu "Surface-state-dominated transport in crystals of the topological crystalline insulator In-doped $Pb_{1-x}Sn_xTe$" *Phys. Rev*. B **91**, 195321 (2015)

17) A. Tiano, G. C. Papaefthymiou, C. S. Lewis, J. Han, C. Zhang, Q. Li, C. Shi, A. M. Abeykoon, S. J. L. Billinge, E. Stach, J. Thomas, K. Guerrero, P. Munayco, J. Munayco, R. B. Scorzelli, P. Burnham, A. J. Viescas, and S. S. Wong, "Correlating Size and Composition-Dependent Effects with Magnetic, Mössbauer, and Pair Distribution Function Measurements in a Family of Catalytically Active Ferrite Nanoparticles", *Chem. Mater*., **27**(10), 3572–3592 (2015).

18) X. Shi, J. Yang, L. Wu, J. R. Salvador, C. Zhang, W. L. Villaire, D. Haddad, J. Yang, Y. Zhu, and Q. Li "Band Structure Engineering and Thermoelectric Properties of Charge-Compensated Filled Skutterudites" *Sci. Rep*. **5**, 14641(2015)

19) J. Wang, R. Zhong, S. Li, Y. Gan, Z. Xu, C. Zhang, T. Ozaki, M. Matsuda, Y. Zhao, Q. Li, G. Xu, G. Gu, J. M. Tranquada, R. J. Birgeneau, and Jinsheng Wen, "Substitution of Ni for Fe in superconducting $Fe_{0.98}Te_{0.5}Se_{0.5}$ depresses the normal-state conductivity but not the magnetic spectral weight" *Phys. Rev*. B **91**, 014501 (2015)

Project Title: Complex magnetism and emergent phenomena in correlated electron oxide materials

Principal Investigator: Prof. Hari Srikanth
University of South Florida, Department of Physics, PHY 114
4202 East Fowler Ave, Tampa, FL 33620
E-mail: sharihar@usf.edu

Co-Principal Investigator: Dr. Manh-Huong Phan
University of South Florida, Department of Physics, PHY 114
4202 East Fowler Ave, Tampa, FL 33620
E-mail: phanm@usf.edu

Project Participants (USF): Eleanor Clements (Ph.D. student), Vijaysankar Kalappattil (Ph.D. student), Dr. Raja Das (Postdoctoral fellow).

Project Collaborators: Prof. Sang-Wook Cheong (Rutgers University), Prof. David Mandrus (The University of Tennessee)

Other Collaborators: Dr. Xavier Moya (Cambridge University, UK), Prof. Hung T. Diep (Universite de Cergy-Pontoise, France)

Program Scope:

Complex magnetic oxides represent a class of materials that blend fascinating physical phenomena and potential technological importance originating from interplay between structural, electronic and magnetic degrees of freedom. The overall goal of our DOE funded project is to investigate the impacts of reduced dimensionality, strain, and anisotropy on the exotic magnetic properties and their inter-relationship with emerging phenomena, such as magnetoresistive effect (MRE), magnetoelectric effect (MEE), electroresistive effect (ERE), electrocaloric effect (ECE), magnetocaloric effect (MCE), and spin Seebeck effect (SSE). We have demonstrated the importance of combining DC and AC magnetic susceptibility measurements, neutron diffraction, synchrotron X-ray diffraction with relatively unconventional RF transverse susceptibility (TS) and magnetocaloric effect (MCE) to yield new insights into the ground state magnetism in a wide variety of complex oxides, including quasi-one-dimensional (1D) spin chain compounds of $Ca_3Co_{2-x}T_xO_6$ (T = Mn or Fe, x=0, 0.05, ...1), multicaloric $EuTi_{1-x}Nb_xO_3$ (x=0, 0.05, …0.2) single crystals and films, and strain-mediated $La_{0.7}R_{0.3}MnO_3/BaTiO_3$ (R=Ca and Sr) heterostructured films. Other research efforts include the exploration of exotic magnetism in other strongly coupled systems, such as core/shell $Fe/\gamma\text{-}Fe_2O_3$ nanoparticles, hollow $\gamma\text{-}Fe_2O_3$ nanoparticles, multiferroic CrO_2 nanoparticles, $Pb(Zr_{0.52}Ti_{0.48})O_3/La_{0.7}Sr_{0.3}MnO_3$ multiferroic heterostructures, a ferromagnetic insulator $Y_3Fe_5O_{12}$ (YIG), and a monoaxial chiral helimagnet $Cr_{1/3}NbS_2$ that share some common and novel phenomena.

We present here selective results from $Ca_3Co_{2-x}T_xO_6$ (single crystalline, polycrystalline, and nanocrystalline), $EuTi_{1-x}Nb_xO_3$ (single crystalline and thin film) and $La_{0.7}R_{0.3}MnO_3/BaTiO_3$ (R = Ca or Sr) thin films, highlighting the important effects of reduced dimensionality, strain and anisotropy in correlated electron oxide materials.

Recent Progress:

1. Frozen dynamics and new magnetic phase diagrams of 1D spin chain $Ca_3Co_{2-x}T_xO_6$

Quasi-one-dimensional (1D) spin chain $Ca_3Co_2O_6$, which combines geometric frustration with intrinsic low-dimensionality giving rise to complex magnetism, continues to attract a great deal of interest [1,2]. Although the question of the true magnetic ground state of this complex spin chain system and its temperature- and time-variation have been highly scrutinized, less work has been undertaken on the evolution of the magnetic state under the influence of a field.

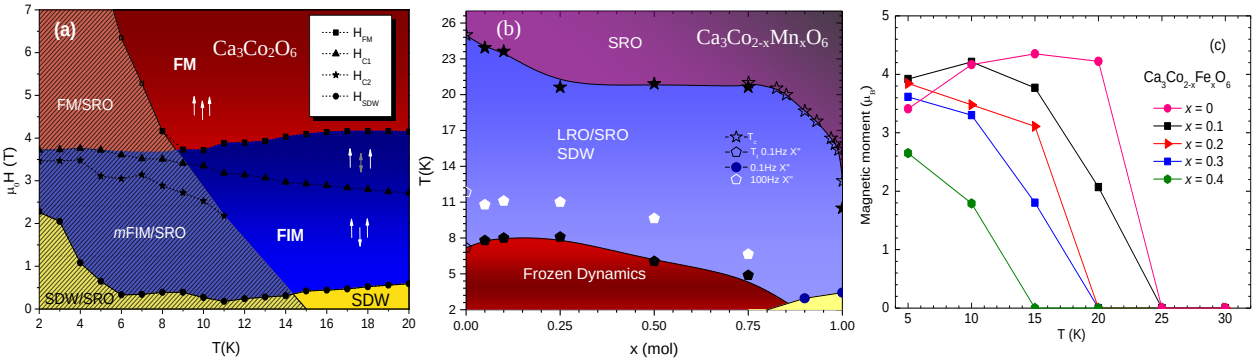

Figure 1: Magnetic phase diagrams including ferromagnetic (FM), ferrimagnetic (FIM), metastable FIM (*m*FIM), short-range-order (SRO), and spin-density wave (SDW) phases for (a) $Ca_3Co_2O_6$ and (b) $Ca_3Co_{2-x}Mn_xO_6$. Dashed lines represent locations of the magnetization steps taken from *M*(*H*) curves; (c) Temperature dependence of magnetic moment at the 6a site for $Ca_3Co_{2-x}Fe_xO_6$.

Our MCE study has established a new and comprehensive magnetic phase diagram for a single crystal of $Ca_3Co_2O_6$ (grown and provided by Prof. Cheong's group at Rutgers University) consistent with recently identified spin-density wave and short-range order phases [3]. In addition to extending previous phase boundaries to below 10 K, new sub-features of the ferrimagnetic phase are identified. A systematic magnetic study of $Ca_3Co_2O_6$ nanocrystaline samples synthesized by an advanced sol-gel method in our laboratory at USF has shown that grain size reduction to just below the maximum correlation length has no significant effect on the appearance of the low-temperature magnetization steps but the low temperature magnetization dynamics change (Fig. 1a). Our finding indicates that correlations in the *ab*-plane are more important than correlations along the *c*-axis in the appearance of the plateaus, resolving issues that remained unexplained in the literature. Recent neutron diffraction measurements on nanocrystaline $Ca_3Co_2O_6$ under high presssure (up to 6.8 GPa) evidence the enhanced AFM coupling and emergence of a new magnetic ordering at low temperature. When Co ions are replaced with Mn or Fe in $Ca_3Co_2O_6$, the new, emerging magnetic features are also observed. In case of $Ca_3Co_{2-x}Mn_xO_6$ ($0.05 \leq x \leq 1.0$), the exotic spin glass-like behavior is enhanced for a modest doping range of $x<0.25$ (Fig. 1b). Beyond this limit the frozen electron dynamics is suppressed as perfect ionic order is approached at the $x=1.0$ composition. A new magnetic phase is emerging which competes with the frozen electron dynamics. Magnetization and neutron diffraction studies on $Ca_3Co_{2-x}Fe_xO_6$ evidence the presence of incommensurate magnetic structures with an amplitude modulation of the moments along the *c*-axis, and that the Fe doping breaks the ferromagnetically ordered linear spin chain along the *c*-axis (Fig. 1c). A manuscript featuring these important findings is being written targeted to Nature Physics. We are currently investigating the effects of reduced dimentionality and Fe substitution on the low-temperature spin dynamics and related magnetization relaxation processes in $Ca_3Co_2O_6$.

2. New ferromagnetic order, ferromagnetic clusters, and complex magnetic phase diagram of multicaloric $EuTi_{1-x}Nb_xO_3$

Among the rare earth titanates ($RTiO_3$, where R is a rare earth ion), $EuTiO_3$ is emerging as a novel class of multicaloric materials exhibiting giant magnetoelectric (GME), giant electrocaloric (GEC), and giant magnetocaloric (GMC) effects [4,5]. While the exact nature of the structural and magnetic transitions, cluster dynamics, and their association with these effects has remained elusive, a thorough understanding of which may provide a pathway for designing new multicaloric materials for use in spintronics and solid-state refrigeration.

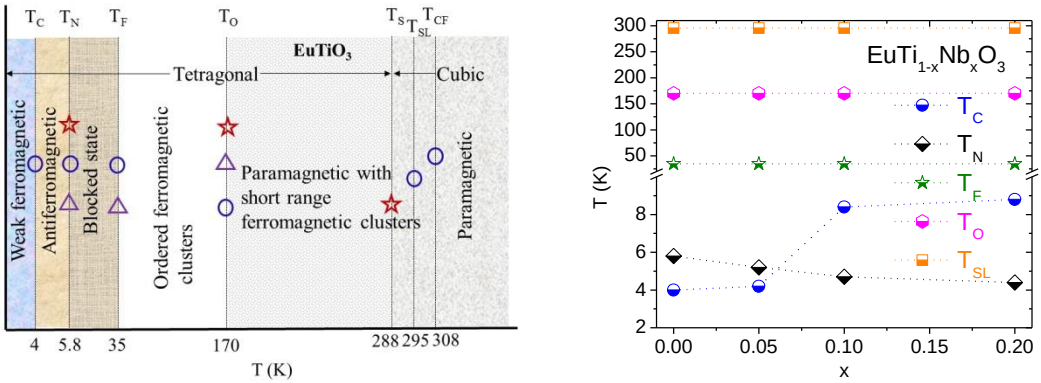

Figure 2: (Left panel) Magnetic phase diagram including structural transition determined from RUS (red star), Monte Carlo simulation (purple triangle), and AC, DC magnetic susceptibility data (blue circle) for $EuTiO_3$; (Right panel) Magnetic phase diagram for $EuTi_{1-x}Nb_xO_3$ (x = 0-0.2) derived from AC, DC magnetic susceptibility data.

Our DC/AC magnetization, synchrotron X-ray diffraction, specific heat, MCE, and resonant ultrasound spectroscopy (RUS) measurements and Monte Carlo simulations on high quality $EuTi_{1-x}Nb_xO_3$ (x = 0, 0.05, 0.1, and 0.2) single crystals (grown and provided by Prof. Mandrus' group at the University of Tennessee) uncover the nature of the field-independent cubic-to-tetragonal phase transition, ordering and freezing of ferromagnetic clusters, inter- and intra-cluster interactions, and a new ferromagnetic order just below the Néel temperature that were not observed or identified previously, leading to the first comprehensive phase diagram that accounts for the puzzling questions as posed in the literature (Fig. 2). This hidden, new ferromagnetic order originates from the ferromagnetic interaction between localized Eu 4*f* spins and is enhanced by Nb substitution, giving rise to the giant magnetocaloric effect in $EuTi_{1-x}Nb_xO_3$. Strain is also shown to enhance the GMC effect in a $EuTiO_3$ thin film relative to its bulk counterpart. Our study provides a new pathway for designing novel multicaloric materials for use in oxide-based spintronics and solid-state cooling technology. One manuscript featuring these findings has been submitted to Nature Communications (under review). We are currently investigating the magnetic properties of $EuTi_{1-x}B_xO_3$ (B=Nb, Zr, Cr) single crystals and thin films.

3. Strain-mediated magnetic anisotropy in $La_{0.7}R_{0.3}MnO_3/BaTiO_3$ heterostructures

Recently, the use of the structural phase transitions of $BaTiO_3$ (BTO) to manipulate lattice strain of $La_{0.7}Sr_{0.3}MnO_3$ (LSMO) and $La_{0.7}Ca_{0.3}MnO_3$ (LCMO) thin films has resulted in many fascinating physical properties, including the new discovery of a giant reversible extrinsic MCE in the LCMO film due to strain-mediated feedback from BTO substrate near its first-order structural phase transition [6]. These heterostructures are interesting model systems for studying the substrate strain-mediated magnetic anisotropy and its variation with respect to temperature across the magnetic and structural transitions.

Our RF transverse susceptibility measurements on $La_{0.7}R_{0.3}MnO_3/BaTiO_3$ (R=Ca, Sr) films (grown and provided by Dr. Moya's group at University of Cambridge) provide the first direct evidence for the enhancement of magnetic anisotropy due to strain as a result of the structural transition of BTO (Fig. 3). The strong spin-lattice coupling is shown to contribute to the GMC effect observed around the orthohombic to rhombohedral structural transtion of BTO. These findings offer new possibilities for manipulating magnetic anisotropy and novel effects such as MEE, MCE, ECE and SSE. A manuscript is being written for publication in Physical Review Letters. We are currently investigating effects of film thickness (LCMO or LSMO) on the magnetic anistropy and its association with MCE and SSE in $La_{0.7}R_{0.3}MnO_3/BaTiO_3$ films.

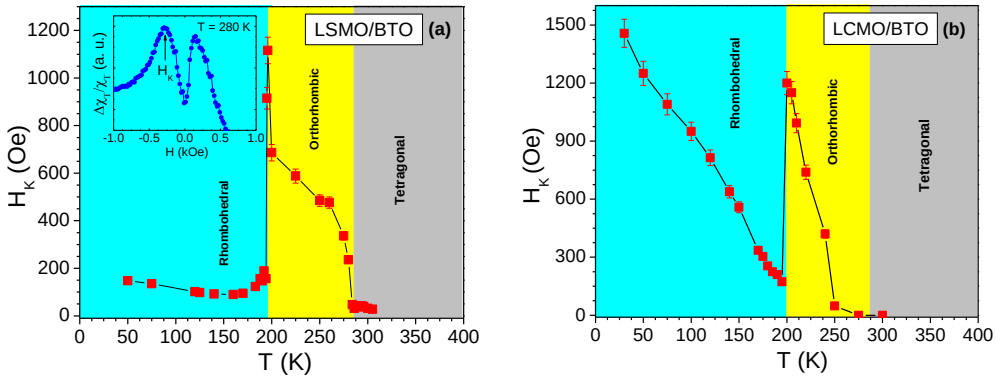

Figure 3: Temperature dependence of magnetic anisotropy field (H_k) determined from TS spectrum (inset) for (a) LSMO and (b) LCMO films grown on BTO. The structural transitions of BTO had strong impacts on the magnetic anisotropy of LSMO and LCMO films in the ferromagnetic regime.

Future plans:

In addition to continuing our studies on the ground state magnetic properties of bulk, thin film, and nanoparticles of complex oxides, including spin chain compounds of $Ca_3Co_{2-x}T_xO_6$ (T=Fe or Mn or Fe and Mn; x = 0-1), multicaloric $EuTi_{1-x}B_xO_3$ (B=Nb, Zr, Cr; x = 0, 0.05, 0.1, and 0.2), $La_{0.7}R_{0.3}MnO_3/BaTiO_3$ (R=Ca, Sr) heterostructured films, and the chiral helimagnet $Cr_{1/3}NbS_2$ we will also extend our efforts to address some of the outstanding issues in rare-earth cobalt arsenides (RCo_2As_2), rare-earth pyrochlores ($R_2Ti_2O_7$), magnetic semiconductors (GaV_4S_8) with skyrmion lattice, and thin films of $VTiO_3$. Each of these systems is of topical interest with unresolved issues that we are well-suited to address through our unique combination of DC and AC magnetization, TS and MCE studies coupled with neutron diffraction and other local structural probes. We would also utilize the SSE as a new probe of thermally induced magnetic ordering in complex oxides. Our research efforts over the next year will be targeted towards elucidating these emergent aspects of correlated magnetic oxide physics.

References:

[1] Y. Kamiya et al., *Phys. Rev. Lett.* **109**, 067204 (2012).
[2] J.A. M. Paddison et al., *Phys. Rev. B* **90**, 014411 (2014).
[3] P. Lampen et al., *Phys. Rev. B* **89**, 144414 (2014).
[4] T. Katsufuji et al., *Phys. Rev. B* **64**, 054415 (2001).
[5] A. Midya et al., *Phys. Rev. B* **93**, 094422 (2016).
[6] X. Moya et al., *Nature Materials* **12**, 52 (2013).

Publications:

List of papers acknowledging DoE grant support during the 2-year period (2015-2016):

(Students and postdocs' names are italicized, PI and co-PI names are in bold)

1. "Exchange bias effects in iron oxide based nanoparticle systems" (Feature Review Article), **M.H. Phan**, ***J. Alonso***, ***H. Khurshid***, *P. Lampen-Kelley*, *S. Chardra*, *K. Stojak*, *Z.N. Porshokouh*, ***R. Das***, Ò. Iglesias, and **H. Srikanth**, ***Nanomaterials*** 6, 221 (2016)
2. "Spin-glass-like freezing of inner and outer surface layers in hollow γFe_2O_3 nanoparticles" - ***H. Khurshid***, *P. Lampen-Kelley*, Òscar Iglesias, ***J. Alonso***, **M.H. Phan**, M.L Saboungie, Chengjun Sun, and **H. Srikanth**, ***Nature: Scientific Reports*** 5, 15054 (2015)
3. "From core/shell to hollow Fe/γ-Fe_2O_3 nanoparticles: Evolution of the magnetic behavior" - *Z. Nemati*, ***H. Khurshid***, ***J. Alonso***, **M.H. Phan**, P. Mukherjee, and **H. Srikanth**, ***Nanotechnology*** 26, 405705 (2015)
4. "Simultaneous enhancements of polarization and magnetization in epitaxial $Pb(Zr_{0.52}Ti_{0.48})O_3/La_{0.7}Sr_{0.3}MnO_3$ multiferroic heterostructures enabled by ultrathin $CoFe_2O_4$ sandwich-layers" - D. Mukherjee, M. Hordagoda, *P. Lampen*, **M.H. Phan**, **H. Srikanth**, S. Witanachchi, and P. Mukherjee, ***Physical Review B*** 91, 054419 (2015)
5. "Superparamagnetic properties of carbon nanotubes filled with $NiFe_2O_4$ nanoparticles" - *K. Stojak Repa*, D. Israel, J. Alonso, **M.H. Phan**, E.M. Palmero, M. Vazquez, and **H. Srikanth**, ***Journal of Applied Physics*** 117, 17C723 (2015)
6. "Disclosure of double exchange bias effect in chromium (III) oxide nanoparticles" - N. Rinaldi, P. Gorria, A.B. Fuertes, D. Blanco, L. Olivi, I. Puente Orench, ***J. Alonso***, **M.H. Phan**, **H. Srikanth**, X. Marti, and J. A. Blanco, ***IEEE Transactions on Magnetics*** 53, 2300204 (2017)
7. "Mössbauer spectroscopy studies of phase evolution in $SrFe_{12}O_{19}/La_{0.5}Ca_{0.5}MnO_3$ composites" - *P. Lampen-Kelley*, A.S. Kamzin, K.E. Romachevsky, D.T.M. Hue, H. D. Chinh, **H. Srikanth**, and **M.H. Phan**, ***Journal of Alloys and Compounds*** 636, 323 (2015)
8. "Impacts of nanostructuring and magnetic ordering of Nd^{3+} on the magnetic and magnetocaloric response in $NdMnO_3$" - *S. Chandra*, ***A. Biswas***, **M.H. Phan** and **H. Srikanth**, ***Journal of Magnetism and Magnetic Materials*** 384, 138 (2015)
9. "Enhanced refrigerant capacity in Gd-Al-Co microwires with a biphase nanocrystalline/amorphous structure" - H.X. Shen, D.W. Xing, J.L. Sánchez Llamazares, C.F. Sánchez-Valdés, H. Belliveau, H. Wang, F.X. Qin, Y.F. Liu, J.F. Sun, **H. Srikanth**, and **M.H. Phan**, ***Applied Physics Letters*** 108, 092403 (2016)
10. "Enhanced magnetic hyperthermia and biodetection of functional manganese ferrite/graphene oxide nanocomposites" - A.T. Le, C.D. Giang, V.N. Phan, ***J. Alonso***, *J. Devkota*, **H. Srikanth**, and **M.H. Phan**, ***Nanotechnology*** 27, 155707 (2016)
11. "Superparamagnetic nanoparticles encapsulated in lipid vesicles for advanced magnetic hyperthermia and biodetection" - ***J. Alonso***, ***H. Khurshid***, *J. Devkota*, Nawal K. Khadka, **H. Srikanth**, J.J. Pan, and **M.H. Phan**, ***Journal of Applied Physics*** 119, 083904 (2016)
12. "Formation of tree-like and vortex magnetic domains of nanocrystalline α-(Fe,Si) in La-Fe-Si ribbons during rapid solidification and subsequent annealing" - X.L. Hou, Y. Tian, Y. Xue, C.Y. Liu, W.X. Xia, H. Xu, *P. Lampen-Kelley*, **H. Srikanth**, and **M.H. Phan**, ***Journal of Alloys and Compounds*** 669, 205 (2016)
13. "Formation mechanisms of NaZn13-type phase in giant magnetocaloric La-Fe-Si compounds

during rapid solidification and annealing" - X.L. Hou, *P. Lampen*, Y. Xue, C. Liu, H. Xu, N. Han, C. Ma, **H. Srikanth**, and **M.H. Phan**, ***Journal of Alloys and Compounds*** 646, 503 (2015)

14. "Anisotropy effect in magnetic hyperthermia: A comparison between spherical and cubic exchange-coupled FeO/Fe_3O_4 nanoparticles" - ***H. Khurshid***, *Z. Nemati*, ***J. Alonso***, **M.H. Phan**, P. Mukherjee, M. L. Fdez-Gubieda, J. M. Barandiarán, and **H. Srikanth**, ***Journal of Applied Physics*** 117, 17A337 (2015)

15. "Enhanced cryogenic magnetocaloric effect in $Eu_8Ga_{16}Ge_{30}$ clathrate nanocrystals" - ***A. Biswas***, *S. Chandra*, S. Stefanoski, J.S. Blázquez, J.J. Ipus, A. Conde, **M.H. Phan**, V. Franco, G.S. Nolas, and **H. Srikanth**, ***Journal of Applied Physics*** 117, 033903 (2015)

16. "Improving mechanical and magnetocaloric responses of amorphous melt-extracted Gd-based microwires via nanocrystallization" - *H. F. Belliveau*, Y. Y. Yu, Y. Luo, F. X. Qin, H. Wang, H. X. Shen, J.F. Sun, S.C. Yu, **H. Srikanth**, and **M.H. Phan**, ***Journal of Alloys and Compounds*** 692, 658 (2017)

17. "Ferromagnetic glass-coated microwires with excellent inductive heating properties for magnetic hyperthermia" - A. Talaat, ***J. Alonso***, V. Zhukova, E. Garaio, J. A. García, **H. Srikanth**, **M.H. Phan**, and A. Zhukov, ***Nature: Scientific Reports*** 6, 39300 (2016)

18. "Tailoring circular magnetic domain structure and high frequency magneto-impedance of melt-extracted $Co_{69.25}Fe_{4.25}Si_{13}B_{13.5}$ microwires through Nb doping" - *T. Eggers*, *O. Thiabgoh*, S. D. Jiang, H. X. Shen, J. S. Liu, J.F. Sun, **H. Srikanth**, and **M.H. Phan**, ***AIP Advances*** 7, 056643 (2017)

19. "Correlation between domain structure, surface anisotropy and high frequency magneto-impedance in Joule annealed CoFe-based melt-spun ribbons" - *T. Eggers*, A. Leary, M. McHenry, J. Martin, I. Skorvanek, **H. Srikanth**, and **M.H. Phan**, ***Journal of Alloys and Compounds*** 682, 799 (2016)

20. "Cooling achieved by rotating an anisotropic superconductor in a constant magnetic field: A new perspective" - **M.H. Phan** and D. Mandrus, ***AIP Advances*** 6, 125022 (2016)

21. "Tunable High Aspect Ratio Iron Oxide Nanorods for Enhanced Hyperthermia" – R. Das, J. Alonso, Z.N. Porshokouh, V. Kalappattil, D. Torres, **M.H. Phan**, E. Garayo, J.A. García, J.Luis Sanchez Llamazares, and **H. Srikanth**, ***The Journal of Physical Chemistry C*** 120, 10086 (2016)

22. "Core/shell iron/iron oxide nanoparticles: Are they promising for magnetic hyperthermia?" - *Z. Nemati*, ***J. Alonso***, ***H. Khurshid***, **M.H. Phan**, and **H. Srikanth**, ***RSC Advances*** 6, 38697 (2016)

23. "Iron Oxide Nano-Octopods with Tunable Sizes for Enhanced Hyperthermia " - *Z. Nemati*, ***J. Alonso***, L. M. Martinez, ***H. Khurshid***, E. Garaio, J.A. Garcia, **M.H. Phan**, and **H. Srikanth**, ***The Journal of Physical Chemistry C*** 120, 8370 (2016)

24. "Ag@Fe_3O_4 nanoflowers as dual agents for magnetic hyperthermia and photo-thermal therapy" - *R. Das*, *N. Rinaldi-Montes*, ***J. Alonso***, Z. Amghouz, P. Gorria, J.A. Blanco, **M.H. Phan**, and **H. Srikanth**, ***ACS Applied Materials and Interfaces*** 8, 25162 (2016)

25. "Relating surface roughness and magnetic domain structure to giant magneto-impedance of Co-rich melt-extracted microwires" - S.D. Jiang, *T. Eggers*, *O. Thiabgoh*, D.W. Xing, W. D. Fei, H. X. Shen, J. S. Liu, J.R. Zhang, W.B. Fang, J.F. Sun, **H. Srikanth**, and **M.H. Phan**, ***Nature: Scientific Reports*** 7, 46235 (2017)

Session XIV

Energy Carrier Transport in Functionalized Two-Dimensional Layered Chalcogenides

Principal Investigator: Steve Cronin, University of Southern California

Collaborator: Li Shi, University of Texas at Austin

Program Scope

The goal of this collaborative project is to study two-dimensional (2D) layered chalcogenide materials and tune and improve the electrical, optical, thermal and thermoelectric properties of this class of functional materials. Building on the progress made in our study of phonon and electron transport in pristine 2D layered heterostructures, we investigate both in-plane and cross-plane thermal and thermoelectric transport properties of 2D chalcogenide materials and develop tools and techniques for studying thermal and thermoelectric transport over smaller length scales and larger spectral ranges than was previously possible.

Recent Progress

The major findings from the in-plane and scanning probe measurements are summarized below.

(i) Cross-Plane Seebeck Coefficient Measurement of Misfit Layered Compounds $(SnSe)_n(TiSe_2)_n$ (n = 1,3,4,5)

We report cross-plane thermoelectric measurements of misfit layered compounds $(SnSe)_n(TiSe_2)_n$ (n = 1,3,4,5), approximately 50 nm thick. Metal resistance thermometers are fabricated on the top and bottom of the $(SnSe)_n(TiSe_2)_n$ material to measure the temperature difference and heat transport through the material directly. By varying the number of layers in a supercell, n, we vary the interface density while maintaining a constant global stoichiometry. The Seebeck coefficient measured across the $(SnSe)_n(TiSe_2)_n$ samples was found to depend strongly on the number of layers in the supercell (n). When n decreases from 5 to 1, the cross-plane Seebeck coefficient decreases from −31 to −2.5 μV/K, while the cross-plane effective thermal conductivity decreases by a factor of 2, due to increased interfacial phonon scattering. The cross-plane Seebeck coefficients of the $(SnSe)_n(TiSe_2)_n$ are very different from the in-plane Seebeck coefficients, which are higher in magnitude and less sensitive to the number of layers in a supercell, n. We believe this difference is due to the different carrier types in the n-SnSe and p-$TiSe_2$ layers and the effect of tunneling on the cross-plane transport.

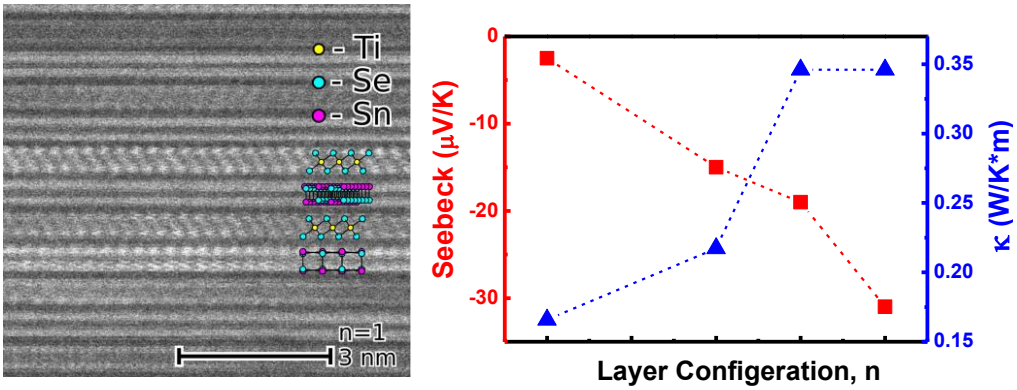

Figure 1. (left) Cross-sectional TEM image of the n=1 thin film illustrating the turbostratic disorder between the layers. Schematic structures overlaid on the n=1 image highlight various orientations. (right) Cross-plane Seebeck coefficient and thermal conductivity with different layer configuration n. The Seebeck coefficient is increased from -2.5 to -31 μV/K as n varies from 1 to 5, and the thermal conductivity is increased from 0.17 to 0.34 W/K·m.

(ii) Effects of Basal-plane Thermal Conductivity and Interface Thermal Conductance on the Hot Spot Temperature in Graphene Electronic Devices

In this work, electrostatic force microscopy (EFM) and scanning thermal microscopy (SThM) have been employed to investigate electric transport and localized heating around defects introduced during transfer of graphene grown by chemical vapor deposition (CVD) to an oxidized Si substrate. Numerical and analytical models are developed to explain the results based on reported basal-plane thermal conductivity, κ, and interfacial thermal conductance, G, of graphene and to investigate their effects on the peak temperature. Irrespective of the κ values, increasing G beyond 4×10^7 W m^{-2} K^{-1} can reduce the peak temperature effectively for graphene devices made on sub-10 nm thick gate dielectric, but not for the measured device made on 300-nm-thick oxide dielectric, which yields a cross-plane thermal conductance (G_{ox}) much smaller than the typical G of graphene. For typical G values reported for graphene, in comparison, increasing κ from 300 W m^{-2} K^{-1} toward 3000 W m^{-2} K^{-1}is effective in reducing the hot spot temperature for the 300-nm-thick oxide devices but not for the sub-10 nm gate dielectric case, because the heat spreading length (l) can be increased to be appreciable compared to the micron scale localized heat generation spot size (r_0) around the defect so as to increase vertical heat transfer area through the gate dielectric only for the thick dielectric case. In all cases considered, the hot spot temperature is sensitive to varying G and κ only when the G/G_{ox} ratio and r_0/l ratio are below about 5, respectively.

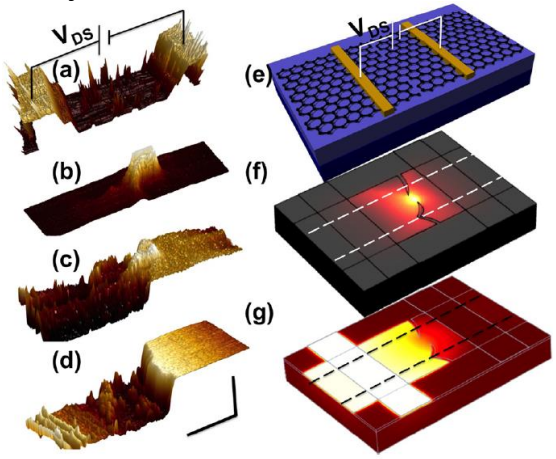

Figure 2. Measured (a-d) and calculated (f-g) topographic (a), thermal (b, f), and electrical potential profiles (c, d, g) of the graphene channel, which is illustrated in a schematic (e). (a) Three-dimensional (3D) AFM image showing the topography of device. (b) SThM image showing a localized hot spot. (c) EFM image showing a steep potential drop at the location where the hot spot is shown by the SThM image. (d) EFM image after the constriction is destroyed by ESD, showing a step change in the surface potential that spans the entire channel signifying an open circuit. Horizontal scale bar is 5 μm and the vertical scale bar is 50 nm, 160 K, 4° and 10° phase shift for images a, b, c, and d, respectively.

(iii) Charge Neutral MoS_2 Field Effect Transistors Through Oxygen Plasma Treatment

Lithographically fabricated MoS_2 field effect transistors suffer from several critical imperfections, including low sub-threshold swings, large turn-on gate voltages (V_T), and wide device-to-device variability. The large magnitude and variability of V_T stems from unclean interfaces, trapped charges in the underlying substrate, and sulfur vacancies created during the mechanical exfoliation process. In this study, we demonstrate a simple and reliable oxygen plasma treatment, which mitigates the effects of unintentional doping created by surface defect sites, such as *S* vacancies, and surface contamination. This plasma treatment restores charge neutrality to the MoS_2 and shifts the threshold turn-on voltage towards 0 V. Out of the 10 devices measured, all exhibit a shift of the FET turn-on voltage from an average of -18 V to -2 V. The oxygen plasma treatment passivates these defects, which reduces surface scattering, causing increased mobility and improved subthreshold swing. For as-prepared devices with low mobilities (0.01 cm^2 /V s), we observe up to a 190-fold increase in mobility after exposure to the oxygen plasma. Perhaps the

most important aspect of this oxygen plasma treatment is that it reduces the device-to-device variability, which is a crucial factor in realizing any practical application of these devices.

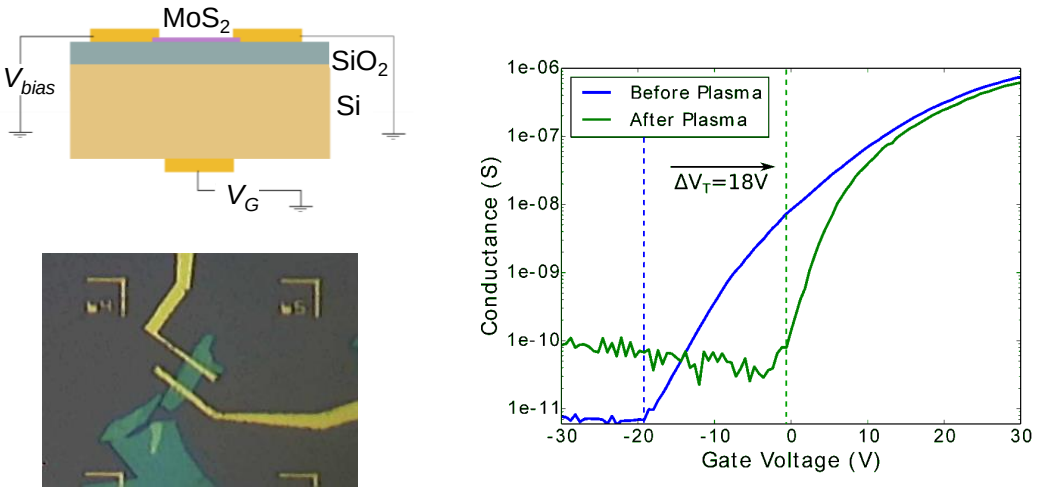

Figure 3. (a) Schematic diagram and (b) optical microscope image of a back-gated MoS_2 FET device. (c) A log-linear plot of the source-drain current as a function of the applied gate voltage.

(iv) Highly Efficient, High Speed Vertical Photodiodes based on Few-layer MoS_2

During this funding period, we reported highly efficient photocurrent generation from vertical MoS_2 devices fabricated using asymmetric metal contacts, exhibiting an external quantum efficiency of up to 7%. Compared to in-plane MoS_2 devices, the vertical design of these devices has a much larger junction area, which is essential for achieving highly efficient photovoltaic devices. Photocurrent and photovoltage spectra are measured over the photon energy range from 1.25 to 2.5 eV, covering both the 1.8 eV direct K-point optical transition and the 1.3 eV Σ-point indirect transition in MoS_2. Photocurrent peaks corresponding to both direct and indirect transitions are observed in the photocurrent spectra and exhibit different photovoltage–current characteristics. Compared to previous in-plane devices, a substantially shorter photoresponse time of 7.3 μs is achieved due to fast carrier sweeping in the vertical devices, which exhibit a −3 dB cutoff frequency of 48 kHz.

Future Plans

We plan to measure the in-plane and cross-plane thermal and thermoelectric properties of 2D materials using a combination of electrical, optical, and electron microscopy techniques, and to collaborate with the Shi group measuring the in-plane transport properties of 2D materials using microbridge devices.

Publications

1. Li, Z., S.R. Bauers, N. Poudel, D. Hamann, X.M. Wang, D.S. Choi, K. Esfarjani, L. Shi, D.C. Johnson and S.B. Cronin, *Cross-Plane Seebeck Coefficient Measurement of Misfit Layered Compounds (SnSe)(n)(TiSe2)(n), (n=1,3,4,5).* Nano Letters, **17**, 1978-1986 (2017).
2. Choi, D., N. Poudel, S.B. Cronin and L. Shi, *Effects of basal-plane thermal conductivity and interface thermal conductance on the hot spot temperature in graphene electronic devices.* Applied Physics Letters, **110**, 073104 (2017).
3. Chen, C.C., Z. Li, L. Shi and S.B. Cronin, *Thermoelectric transport across graphene/hexagonal boron nitride/graphene heterostructures.* Nano Research, **8**, 666-672 (2015).
4. Dhall, R., Z. Li, E. Kosmowska and S.B. Cronin, *Charge neutral MoS_2 field effect transistors through oxygen plasma treatment.* Journal of Applied Physics, **120**, 195702 (2016).
5. Li, Z., S.S. Yang, R. Dhall, E. Kosmowska, H.T. Shi, I. Chatzakis and S.B. Cronin, *Layer Control of WSe_2 via Selective Surface Layer Oxidation.* ACS Nano, **10**, 6836-6842 (2016).
6. Gamage, S., Z. Li, V.S. Yakovlev, C. Lewis, H. Wang, S.B. Cronin and Y. Abate, *Nanoscopy of Black Phosphorus Degradation.* Advanced Materials Interfaces, **3**, 1600121 (2016).
7. Dhall, R., K. Seyler, Z. Li, D. Wickrarnaratne, M.R. Neupane, I. Chatzakis, E. Kosmowska, R.K. Lake, X.D. Xu and S.B. Cronin, *Strong Circularly Polarized Photoluminescence from Multilayer MoS2 Through Plasma Driven Direct-Gap Transition.* Acs Photonics, **3**, 310-314 (2016).
8. Abate, Y., S. Gamage, Z. Li, V. Babicheva, M.H. Javani, H. Wang, S.B. Cronin and M.I. Stockman, *Nanoscopy reveals surface-metallic black phosphorus.* Light-Science & Applications, **5**, e16162 (2016).
9. Mason, B.J., S.W. Chang, J.H. Chen, S.B. Cronin and A.W. Bushmaker, *Thermoacoustic Transduction in Individual Suspended Carbon Nanotubes.* ACS Nano, **9**, 5372-5376 (2015).
10. Dhall, R., M.R. Neupane, D. Wickramaratne, M. Mecklenburg, Z. Li, C. Moore, R.K. Lake and S. Cronin, *Direct Bandgap Transition in Many-Layer MoS_2 by Plasma-Induced Layer Decoupling.* Advanced Materials, **27**, 1573 (2015).
11. Chatzakis, I., Z. Li, A.V. Benderskii and S.B. Cronin, *Broadband terahertz modulation in electrostatically-doped artificial trilayer graphene.* Nanoscale, **9**, 1721-1726 (2017).
12. Li, Z., J. Chen, R. Dhall and S.B. Cronin, *Highly efficient, high speed vertical photodiodes based on fewlayer MoS_2.* 2D Materials, **4**, 015003 (2016).
13. Chen, J.H., R. Dhall, B.Y. Hou, S.S. Yang, B. Wang, D. Kang and S.B. Cronin, *Enhanced photoluminescence in air-suspended carbon nanotubes by oxygen doping.* Applied Physics Letters, **109**, 153109 (2016).
14. Bushmaker, A.W., V. Oklejas, D. Walker, A.R. Hopkins, J.H. Chen and S.B. Cronin, *Single-ion adsorption and switching in carbon nanotubes.* Nature Communications, **7**, 10475 (2016).
15. Chang, S.W., J. Theiss, J. Hazra, M. Aykol, R. Kapadia and S.B. Cronin, *Photocurrent spectroscopy of exciton and free particle optical transitions in suspended carbon nanotube pn-junctions.* Applied Physics Letters, **107**, 053107 (2015).
16. Amer, M.R., S.W. Chang and S.B. Cronin, *Competing Photocurrent Mechanisms in Quasi-Metallic Carbon Nanotube pn Devices.* Small, **11**, 3119-3123 (2015).
17. Chang, S.W., J. Hazra, M. Amer, R. Kapadia and S.B. Cronin, *A Comparison of Photocurrent Mechanisms in Quasi-Metallic and Semiconducting Carbon Nanotube pn-Junctions.* Acs Nano, **9**, 11551-11556 (2015).

Measurements of near-field thermal radiation between flat plates for energy conversion applications

Project Title: Tailoring thermal radiative properties with doped-silicon nanowires

Principle Investigator: Zhuomin Zhang
George W. Woodruff School of Mechanical Engineering
Georgia Institute of Technology, Atlanta, GA 30332

Program Scope

Aligned doped-silicon nanowire (D-SiNW) arrays form a hyperbolic metamaterial in the mid-infrared and have unique thermal radiative properties, such as broadband omnidirectional absorption, low-loss negative refraction, etc. A combined theoretical and experimental investigation will be performed to characterize D-SiNW arrays and other metamaterials for tailoring thermal radiative properties. Near-field thermal radiation between anisotropic materials with hyperbolic dispersions will also be predicted for potential application in energy harvesting. This project will allow the measurement data to be confirmed by additional verifications and detailed uncertainty analysis for archival publication. This project aims at realizing D-SiNW-based metamaterials for thermal radiation control as well as for near-field imaging in the mid-infrared region. Other metamaterials, such as graphene, multilayered structures, and gratings or the combination will also be considered.

The activities and findings summarized below focus on the recent experimental results obtained for near-field radiative heat transfer between parallel doped-silicon plates at a spacing down to approximately 200 nm, as well as a theoretical analysis and prediction of nanoscale electroluminescent refrigeration concept.

Recent Progress

The study of near-field radiative heat transfer between closely spaced objects and the electromagnetic wave interactions with micro/nanostructured materials has become an emerging multidisciplinary field due to its importance in advanced energy systems, manufacturing, local thermal management, and high spatial resolution thermal sensing and mapping [1,2]. For energy harvesting applications, increasing the surface area and shrinking the gap spacing are both critical in order to achieve high radiative heating rates. While tremendous progress has been made in recent years toward experimental realization, measurements between planar surfaces with square-centimeter-sized areas at deep submicron gap distances are still quite challenging due to difficulties in controlling the gap spacing. We have recently measured greatly enhanced near-field radiative heat transfer between doped silicon plates [3].

A heat flux measurement system is developed to measure the near-field radiation in vacuum as shown in Fig. 1a. The sample is placed in the middle and consists of two 1 cm^2 doped-silicon pieces separated by a sparse array of SiO_2 micropillars. The pillars fabricated on one plate support the other to maintain the necessary gap spacing, as shown in Fig. 1b.

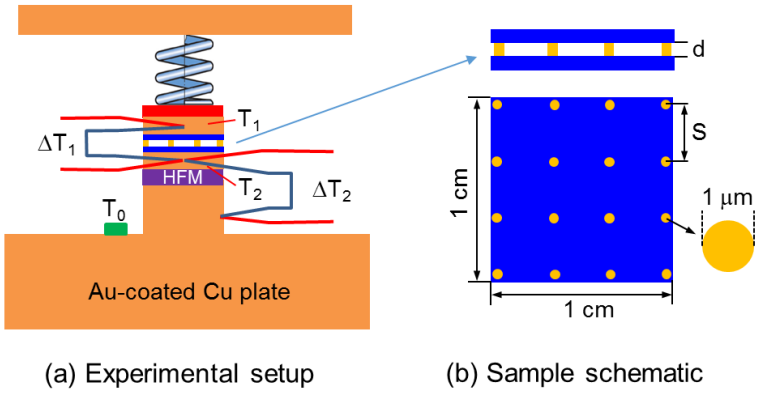

Fig. 1. Schematics of the experimental setup for measuring near-field radiative heat transfer between flat plates and the structure of the sample. (a) The measurement stage that contains a stack of layers below the spring, namely, a heater, a Cu plate, the sample containing two doped-Si plates separated by a gap, another Cu plate, and a heat flux meter (HFM) mounted on a Cu heat sink. (b) The sample made of two doped-Si pieces separated by a submicron gap using SiO_2 posts, where S is the distance between adjacent posts. Detailed can be found in [3].

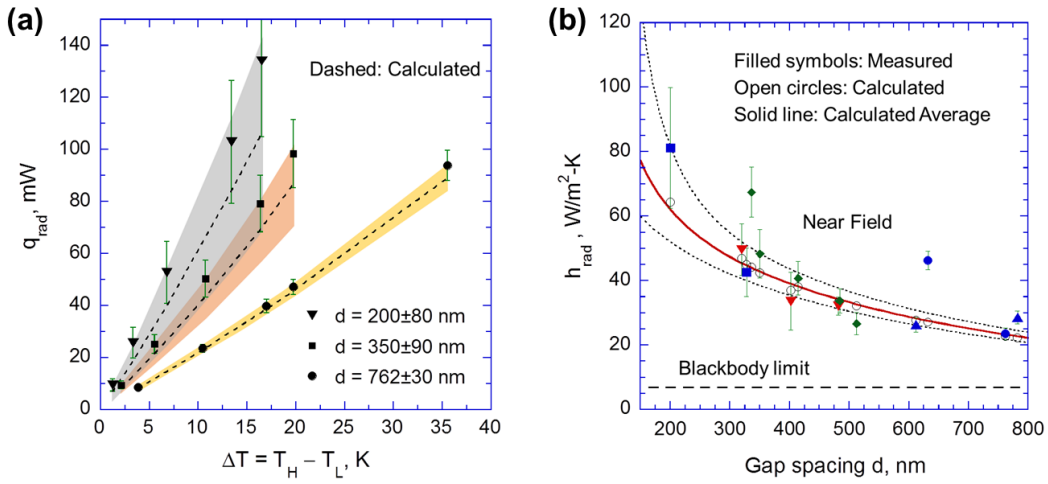

Fig. 2. (a) Radiative heat transfer rate for three different gap spacings as a function of the temperature difference. (b) Radiative heat transfer coefficient for 14 measurements at different gap spacings with ΔT ranging from 15.2 K to 19.2 K. Each symbol is for the same sample under different applied pressures. The results show about one order of magnitude enhancement of near-field radiative transfer down to 200 nm spacing [3].

Figure 2a displays the radiative heat transfer rate q_{rad} for three different gap spacings versus the temperature difference between the two doped-Si plates (ΔT). The isolated solid symbols represent the measured results with uncertainty bounds indicated by the error bars. The dashed lines are from the fluctuational electrodynamic calculation with the shaded region indicating the uncertainty bounds. The large enhancement in nanoscale thermal radiation is attributed to the excitation of coupled surface plasmon polaritons (SPPs). The uncertainty of the

theoretical calculation is mainly due to the determination of the gap spacing. Different ΔT is created by controlling the power provided by the DC power supply. However, due to radiation from the top of the heater and conduction through the spring, not all the heating power flows down across the sample. For example, with a 265 mW power provided by the DC power supply, about 191 mW (134 mW due to radiation and 57 mW due to conduction) passes through the sample, creating a ΔT = 16.5°C across its 200 nm gap. Figure 2b illustrates the results for radiative heat transfer coefficient h_{rad} for 14 measurements at different gap spacings. The measured data are presented as filled symbols with error bars, while the calculated values at the same temperature and gap spacings are shown as open circles. Each shape of the solid symbols represents a different sample under specified applied forces. The solid (red) line represents the calculated results using the average T_{H} and T_{L} (i.e., 318.5 K and 302.3 K, respectively) of all measurements and plotted as a function of gap spacing. The two dotted lines represent the calculation uncertainty bounds. The horizontal dashed line is the blackbody limit using the average T_{H} and T_{L}. Note that h_{rad} increases as d decreases, reaching a value of 81.2 W/m^2·K that is about 11 times that of the blackbody limit at the same emitter and receiver temperatures. The experience gained and the facilities mentioned can be employed with modifications to study near-field energy conversion devices.

When two or more bodies at different temperatures are brought sufficiently close to each other with vacuum gap spacing smaller than the characteristic thermal wavelength, near-field radiative heat flux can exceed the far-field blackbody limit, governed by the well-known Stefan-Boltzmann law, by orders of magnitude. As a result, new routes for efficient thermal management and energy harvesting are opened. Electroluminescent refrigeration, though theoretically proposed half a century ago, is rarely reported due to the lower refrigeration power per unit area and the requirement of extremely low nonidealities. Recently, our group [4] has developed a model that can take into account the position dependence of the chemical potential of photons in the diode based on fluctuation-dissipation theory combined with dyadic Green's function approach for a multilayered system. The system is schematically shown in Fig. 3a, where the lower portion is a p-i-n junction that is biased with a voltage V. As a result, the photons emitted, including propagating waves, evanescent waves, and ultrahigh wavevector (k) modes, have a nonzero chemical potential of qV at frequencies higher than the bandgap. Subsequently, more energy is emitted from the intrinsic region even though its temperature is lower than the top plate (T_2). By employing dedicated choices of materials, we show that both near- and far-field refrigeration can be achieved for certain range of temperature differences and the refrigeration rate can be improved by orders of magnitude by operating at the nanoscale. As shown in Fig. 3b, by operating the device in the near-field regime with a vacuum gap down to 10 nm, the refrigeration rate may be enhanced by 2000-fold over the far-field scenario. Furthermore, photon tunneling through evanescent waves can increase the tolerance of non-intrinsic nonradiative recombination to 31.6%. Thus, the lowest achievable cooling temperature against the ambient condition of T_2 = 300 K extends from 284.2 K to 270.6 K. Note that for 470 nm < d < 830 nm, as shown in Fig. 3b, the conventional thermal radiation at longer wavelengths from the Ge plate to the diode that overwhelms the luminescent refrigeration, resulting in a loss of the refrigeration effect. This study opens a route to greatly enhance electroluminescent refrigeration for solid-state noncontact thermal management. Future experiments are needed to demonstrate the advantages of electroluminescent refrigeration operating in the near-field regime.

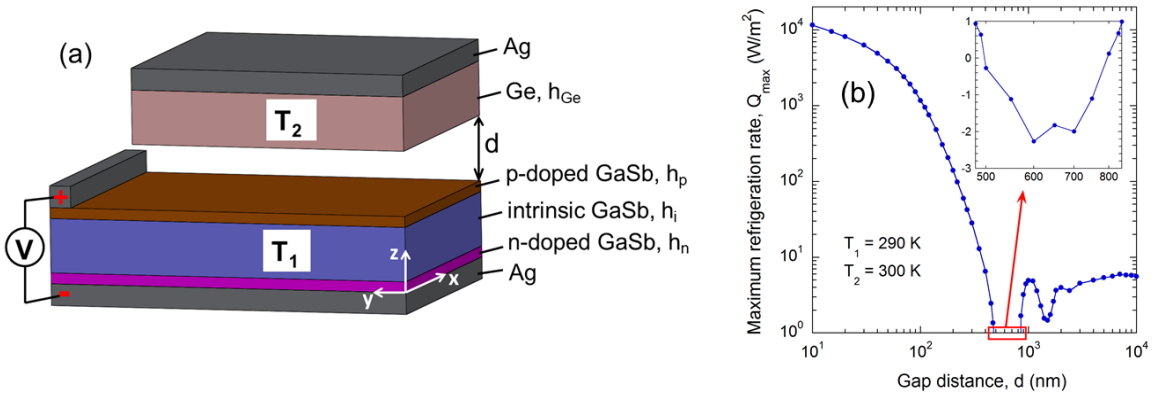

Fig. 3. (a) Schematic of a forward-biased *p-i-n* GaSb diode separated with a Ag substrate with Ge deposited on top with a gap distance of *d*. The temperature of the diode is T_1, and is assumed to be lower than that of the top object. In all calculations, $h_p = h_n = 0.1$ μm, $h_i = 1$ μm, $h_{Ge} = 500$ μm, $T_2 = 300$ K. Unless specified, $T_1 = 290$ K. (b) The maximum refrigerate rate from the biased diode versus the gap distance *d*. Significant enhanced refrigeration rate can be achieved at nanometer distances. Detailed can be found in [4].

Future Plans

The PI has submitted a new proposal to DOE on Near-Field Thermoradiative Energy Harvesting and Electroluminescent Refrigeration. It leverages the extensive expertise and resources developed through the past DOE supports. The objective is to demonstrate luminescent refrigeration and thermoradiative energy generation at distances down to a few hundred nanometers. A unified model for photon entropy under nonequilibrium conditions will be developed. The results will lead to a deeper understanding of nonequilibrium radiation entropy, especially when the photons have a nonzero chemical potential. The findings will facilitate the design of novel energy conversion devices based on near-field thermal radiation.

References

1. X.L. Liu, L.P. Wang, and Z.M. Zhang, "Near-field thermal radiation: Recent progress and outlook," Nanoscale Microscale Thermophys. Eng. **19**, 98 (2015).
2. J.I. Watjen, X.L. Liu, B. Zhao, and Z.M. Zhang, "A computational simulation of using tungsten gratings in near-field thermophotovoltaic devices," J. Heat Transfer **139**, 052704 (2017).
3. J.I. Watjen, B. Zhao, and Z.M. Zhang, "Near-field radiative heat transfer between doped-Si parallel plates separated by a spacing down to 200 nm," Appl. Phys. Lett. **109**, 203112 (2016).
4. X.L. Liu and Z.M. Zhang, "High-performance electroluminescent refrigeration enabled by photon tunneling," Nano Energy **26**, 353 (2016).

Publications 2015-2017 (with support by the DOE-BES grant)

1. X.L. Liu, B. Zhao, and Z.M. Zhang, "Blocking-assisted infrared transmission of subwavelength metallic gratings by graphene," J. Opt. **17**, 035004 (2015).
2. R.Z. Zhang, X.L. Liu, and Z.M. Zhang, "Near-field radiation between graphene-covered carbon nanotube arrays," AIP Advances **5**, 053501 (2015).
3. R.Z. Zhang and Z.M. Zhang, "Negative refraction and self-collimation in the far infrared with aligned carbon nanotube films," J. Quant. Spectrosc. Radiat. Transfer **158**, 91 (2015).
4. R.Z. Zhang, X.L. Liu, and Z.M. Zhang, "Modeling the optical and radiative properties of vertically aligned carbon nanotubes in the infrared region," J. Heat Transfer **137**, 091009 (2015).
5. X.L. Liu, L.P. Wang, and Z.M. Zhang, "Near-field thermal radiation: Recent progress and outlook," Nanoscale Microscale Thermophys. Eng. **19**, 98 (2015).
6. X.L. Liu and Z.M. Zhang, "Near-field thermal radiation between metasurfaces," ACS Photonics **2**, 1320 (2015).
7. X.L. Liu and Z.M. Zhang, "Giant enhancement of nanoscale thermal radiation based on hyperbolic graphene plasmons," Appl. Phys. Lett. **107**, 143114 (2015).
8. X.L. Liu, B. Zhao, and Z.M. Zhang, "Enhanced near-field thermal radiation and reduced Casimir stiction between doped-Si gratings," Phys. Rev. A **91**, 062510 (2015).
9. B. Zhao and Z.M. Zhang, "Strong plasmonic coupling between graphene ribbon array and metal gratings," ACS Photonics **2**, 1611 (2015).
10. X.L. Liu and Z.M. Zhang, "Tunable stable levitation based on Casimir interaction between nanostructures," Phys. Rev. Appl. **5**, 034004 (2016).
11. B. Zhao, A. Skurai, and Z.M. Zhang, "Polarization dependence of the reflectance and transmittance of anisotropic metamaterials," J. Thermophys. Heat Transfer **30**, 240 (2016).
12. X.L. Liu and Z.M. Zhang, "High-performance electroluminescent refrigeration enabled by photon tunneling," Nano Energy **26**, 353 (2016).
13. J.I. Watjen, B. Zhao, and Z.M. Zhang, "Near-field radiative heat transfer between doped-Si parallel plates separated by a spacing down to 200 nm," Appl. Phys. Lett. **109**, 203112 (2016).
14. J.I. Watjen, X.L. Liu, B. Zhao, and Z.M. Zhang, "A computational simulation of using tungsten gratings in near-field thermophotovoltaic devices," J. Heat Transfer **139**, 052704 (2017).
15. X.L. Liu and Z.M. Zhang, "Silicon metamaterials for infrared applications," *Silicon Nanomaterials Sourcebook*, K.D. Sattler (ed.), CRC Press, Taylor & Francis Group, Boca Raton, Vol. II, Chap. 14, pp. 345-369 (2017, in press).
16. B. Zhao and Z.M. Zhang, "Design of optical and radiative properties of solids," *Handbook of Thermal Science and Engineering: Radiative Heat Transfer*, F.A. Kulachi (ed.), Springer Nature (accepted for publication, 2017).

Poster Sessions

Physical Behavior of Materials Principal Investigators' Meeting

POSTER SESSION I

Tuesday, May 2, 2017

1) **Metamaterials as a Platform for the Development of Novel Materials for Energy Applications**
   Willie J. Padilla, Duke University

2) **Tailoring Electron-Photon Interaction in Active 3D Photonic-Crystal Architecture**
   Shawn-Yu Lin, Rensselaer Polytechnic Institute

3) **Photonic Systems**
   Joseph Shinar, Ames Laboratory

4) **Electronic Materials Program**
   Daryl C. Chrzan, Lawrence Berkeley National Laboratory

5) **Electronic Materials Program**
   Joel Ager, Lawrence Berkeley National Laboratory

6) **Characterization of Functional Nanomachines**
   Michael Crommie, Lawrence Berkeley National Laboratory

7) **Electronic and Optical Processes in Novel Semiconductors for Energy Applications**
   Angelo Mascarenhas, National Renewable Energy Laboratory

8) **Light-Stimulated Epitaxy of Novel Semiconductor Alloys and Heterostructures**
   Kirstin Alberi, National Renewable Energy Laboratory

9) **Harnessing Order Parameter in Ternary II-IV-V_2 Semiconductors**
   Adele Tamboli, National Renewable Energy Laboratory

10) **Elucidation of Hydrogen Interaction Mechanisms with Metal-Doped Carbon Nanostructures**
    Ragaiy Zidan, Savannah River National Laboratory

11) **Uncovering and Surmounting Loss Mechanisms in Light Emitters**
    Chris Van de Walle, University of California, Santa Barbara

12) **Electronics without Semiconductors by Functionalized Boron Nitride Nanotubes**
    Yoke Yap, Michigan Technological University

13) **Actinide Materials under Extreme Conditions**
Krzysztof Gofryk, Idaho National Laboratory

14) **Fundamental Piezotronic and Piezo-phototronic Effects in Nanowires**
Zhong Lin Wang, Georgia Institute of Technology

15) **High Performance Thermoelectric Materials and Flexible Transparent Electrodes**
Zhifeng Ren, University of Houston

16) **Extraordinary Responsive Magnetic Rare Earth Materials**
Vitalij Pecharsky, Ames Laboratory

17) **Magnetostructural Phase Transitions and Multicaloric Materials**
Shane Stadler, Louisiana State University

18) **Interfacial Design for Aqueous Photoelectrochemical Cells and Solar Flow Batteries**
Yiying Wu, The Ohio State University

19) **Polymeric Multiferroics**
Shenqiang Ren, Temple University

20) **Tuning Morphology, Packing and Electrical Performance of Semiconducting Polymer through Solution Processing**
Zhenan Bao, Stanford University

21) **Energy Carrier Transport in Functionalized Two-Dimensional Layered Chalcogenides**
Li Shi, University of Texas at Austin

22) **Bare, Coated, and Supported Clusters**
Puru Jena, Virginia Commonwealth University

23) **Mesoscale Design of Magnetoelectric Heterostructures and Nanocomposites**
Dwight Viehland, Virginia Polytechnic Institute and State University

Physical Behavior of Materials Principal Investigators' Meeting

POSTER SESSION II

Wednesday, May 3, 2017

1) **Thermoelectric Effects and Spin-Mediated Thermal Properties of Oxide Conductors and Insulators**
   Joshua Cohn, University of Miami

2) **Superconductivity in Quasi-One-Dimensional $BaNbS_3$**
   John Neumeier, Montana State University

3) **Tailoring Exchange and Spin-Orbit Interactions in Graphene by Proximity Coupling**
   Jing Shi, University of California, Riverside

4) **Pure Spin Current Phenomena**
   Chia-Ling Chien, Johns Hopkins University

5) **Electron Spin Polarization in Large Electric Fields**
   Vanessa Sih, University of Michigan, Ann Arbor

6) **Quantum Nanoplasmonics Theory**
   Mark Stockman, Georgia State University Research Foundation

7) **Plasmon and Photon Excitations in Two-Dimensional and Layered Materials**
   Harry Atwater, California Institute of Technology

8) **Optical, Plasmonic, and Excitonic Phenomena in Nanostructures Described within a Theoretical Framework for Dissipative Quantum Electronic Transport**
   Irena Knezevic, University of Wisconsin, Madison

9) **Three-Dimensional Plasmonic Light Concentrators for Efficient Terahertz Generation**
   Mona Jarrahi, University of California, Los Angeles

10) **Energy and Photon Conversion with Nanocrystals and Optically Active Media**
    Anton Malko, University of Texas, Dallas

11) **One-Dimensional Carrier Confinement in Semiconductor Excitonic Nanoshells**
    Mikhail Zamkov, Bowling Green State University

12) **Nanocrystal-Based Diodes for Solar to Electric Energy Conversion**
    David Beratan, Duke University

13) **Plasmon-Mediated Electrochemical Reactions: Using Optical Readouts to Probe Plasmonic Nanoparticle Activity**
Katherine A. Willets, Temple University

14) **Nanostructured Colloidal Self-Assembly and Controlled Alignment of Anisotropic Nanoparticles**
Ivan I. Smalyukh, University of Colorado, Boulder

15) **Atomic and Mesoscopic Study of Metallic Glasses**
Takeshi Egami, Oak Ridge National Laboratory

16) **Universal Parameter to Quantitatively Predict Metallic Glass Properties**
Evan Ma, Johns Hopkins University

17) **Spectrally-Tunable Far-Field Thermal Radiation Extraction from Micro and Nanostructures**
Gang Chen, Massachusetts Institute of Technology

18) **Driven Morphological Evolution and Patterning of Crystal Surfaces, Epitaxial Thin Films, and Two-Dimensional Materials**
Dimitrios Maroudas, University of Massachusetts

19) **Prediction of Thermal Transport Properties of Materials with Microstructural Complexity**
Youping Chen, University of Florida, Gainesville

20) **Tuning Spin Functionality at Interfaces through Complex Oxide Heteroepitaxy**
Yuri Suzuki, Stanford University

21) **Zinc Oxide and Its Alloys**
Matthew McCluskey, Washington State University

22) **Combined Coherent Manipulation and Single-Shot Measurement of an Electron Spin in a Quantum Dot**
Edward Flagg, West Virginia University

23) **Non-equilibrium Dynamics of Interacting Light-Matter Systems**
Hakan Tureci, Princeton University

24) **Enhancement of Spin-Lattice Coupling in Nanoengineered Oxide Films and Heterostructures by Laser MBE**
Xiaoxing Xi, Temple University

Poster Abstracts

Light-Stimulated Epitaxy of Novel Semiconductor Alloys and Heterostructures

PI: Kirstin Alberi
National Renewable Energy Laboratory

Project Scope

Synthesis of semiconductor alloys and heterostructures often requires growth conditions that are far from equilibrium, yet such conditions can also enhance the incorporation of defects. The objective of this project is to explore light stimulation of growth surfaces as a means to selectively manipulate processes that enhance adatom kinetics and enable the epitaxy of new semiconductor material systems. Studies specifically focus on exploring the basic mechanisms through which photons and photogenerated carriers affect adatom mobility, doping processes, defect populations and interface formation at low growth temperatures. This information is used to tailor the growth of new semiconductor alloys and heterostructures that are difficult to synthesize by traditional techniques.

Recent Progress

Our research into the mechanisms of light-stimulated epitaxy has largely revealed that it affects growth processes through electronic rather than thermal effects.[1,2] The studies detailed below explore the different ways in which excess photogenerated carriers can be used to tailor growth.

Suppression of Compensating Native Defects with Photogenerated Carriers

Native defect populations are well known to adversely impact the performance and properties of a wide range of semiconductor materials. Various methods have been explored over the years to control them. Because their formation energy is linked to the Fermi level, compensating native defects tend to form in greater densities in doped semiconductors, imposing doping limits.[3,4] Controlling the growth temperature or chemical potential (i.e. through atomic or molecular fluxes) alone will not overcome this driving force. However, Fermi level splitting induced by the injection of excess photogenerated carriers may provide another parameter with which to alter defect formation energies. In collaboration with Mike Scarpulla at the University of Utah, we have developed a rigorous theoretical framework that can be used to determine defect concentrations produced during growth under steady-state illumination. This model accounts for changes to the formation energy due to quasi-Fermi level (QFL) splitting and self-consistently solves for the excess carrier concentrations.

In preliminary work, we applied this framework to narrow bandgap n-type GaSb because it is a relatively simple system with two dominant native defects (Ga_{Sb}^{-2} and Sb_{Ga}^{+2}).[5] We found that QFL splitting led to a substantial reduction on compensating Ga_{Sb}^{-2} defects, which would improve the overall free electron concentration and mobility.[6] This analysis yielded a set of guidelines for applying light-stimulated epitaxy or processing techniques to suppress native compensating defects.

Since defect formation involves the real exchange of carriers between the defect and their reservoirs (i.e. conduction and valence bands), the model weights the relative contribution of the electron and hole QFLs to the overall Fermi level term based on carrier emission and capture rates (see Fig. 1). These rates can vary significantly in wide bandgap semiconductors depending on the position of the defect charge transition levels in the bandgap. To understand the range of possible responses to excess carriers, we have investigated the behavior of a single donor-like defect as functions of extrinsic doping and energy of the charge transition level in a generic wide bandgap semiconductor.[7] Our results indicate that the position of the charge transition level relative to the conduction or valence bands, and thus the bandgap energy itself, impacts the defect formation energy through the carrier capture and emission rates. Compensating defect concentrations can usually be lowered through the injection of excess carriers during growth or annealing, but defects with the same charge polarity as the majority dopant may remain unchanged or even increase under such conditions. This has important implications for the use of photo-assisted processing techniques for controlling defects in wide bandgap semiconductors, which are among those materials that suffer most from doping limits.

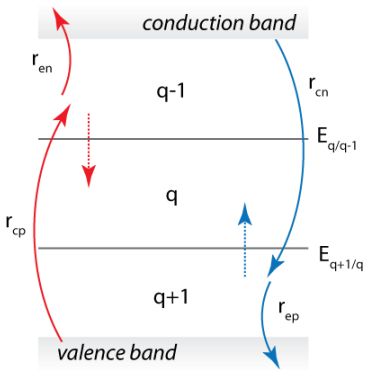

Figure. 1 *Schematic of the electron and hole (n or p) emission and capture (e or c) rates involved in creating a defect with charge q from defects with charges q+1 or q-1.*

Experimentally, our group has demonstrated improved p-type doping of ZnSe epilayers with nitrogen using light-stimulated molecular beam epitaxy (MBE) and a broadband Xe lamp (see Fig. 2). Improvements are on the order of 2-5x and increase with lamp power. An increase in the doping efficiency may be due to a decrease in compensating defects, and we are currently applying our generalized model to the ZnSe:N system to determine the magnitude of change that might be possible. It is also understood that photogenerated holes enhance Se desorption, which would make more sites available for N incorporation. We are presently investigating which one of these scenarios is responsible for the improved p-type doping we have measured.

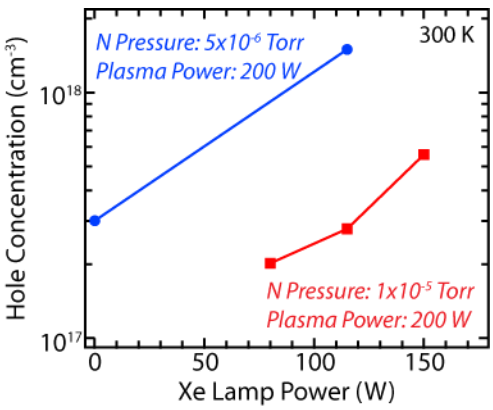

Figure. 2 *Hole concentration in N-doped ZnSe epilayers as a function of lamp power.*

Modification of Heterovalent ZnSe/GaAs Interface Properties

Combining III-V and II-VI semiconductors into an optoelectronic device provides access to a wider range of material properties and creates new opportunities for overcoming existing performance limitations in III-V devices. For example, high bandgap II-VI semiconductors could provide greater carrier confinement potentials and act as better window or cladding layers for III-V solar cells and light emitters. The prospect of developing such next generation devices critically depends on the ability to fabricate high quality III-V/II-VI heterovalent interfaces and preserve the optical and electrical

properties of the III-V and II-VI materials on either side. However, the charge imbalance at the interface is well known to drive atomic inter-diffusion and secondary phase formation. The conditions under which interface growth is initiated therefore play an important role in the bonds that are formed and the resulting properties. Electronic effects introduced by light-stimulated epitaxy, such as enhanced anion desorption or charge screening, may provide a way to modify these conditions.

To understand the growth parameters that most influence the resulting ZnSe/GaAs interface properties, we first explored the effect surface pre-treatment conditions without light-stimulation. While a substantial amount of work has already been performed on ZnSe/GaAs interface growth[8,9], most of that research was motivated by growing II-VI devices on passive GaAs substrates and therefore was focused on improving the optical properties of the ZnSe epilayer. The optical properties of the underlying GaAs substrate have not been substantially explored. ZnSe epilayers were grown on GaAs substrates at 300 °C after the application of a Zn or Se flux. Our investigation focused on understanding the how the surface pre-treatment affects the optical properties of both layers.[10] We found that Zn exposure of an As-rich surface promotes Zn and Se diffusion into the GaAs layer. Alternatively, Se exposure of an As-rich surface may be better for maintaining the high optical quality of the GaAs. These results consequently provide a set of guidelines for III-V/II-VI heterovalent interface initiation depending on whether the optical properties of the III-V or II-VI layer is more important to the application.

Building on these preliminary results, we then investigated how those interface initiation conditions change when the growth surface is irradiated with broadband light from a Xe lamp.[11] The interface was initiated with a Zn flux pre-treatment, and the ZnSe growth temperature was lowered to 200 °C to prevent excessive intermixing at the interface. Light irradiation only during the ZnSe epilayer growth produced abrupt interfaces and improved the free exciton emission from the ZnSe epilayer to that of epilayers grown at 300 °C (see Fig 3). Light irradiation during growth of the interface and the ZnSe epilayer led to depletion of the As-terminated GaAs surface and allowed more Ga-Se bonding. This approach appears to provide some passivation at the interface and improve free exciton emission from the underlying GaAs. The ZnSe optical properties were also similar to those obtained with light-stimulation only during ZnSe growth. These results suggest that light-stimulated As desorption may be used to regulate the mixture of bonds at the ZnSe/GaAs interface.

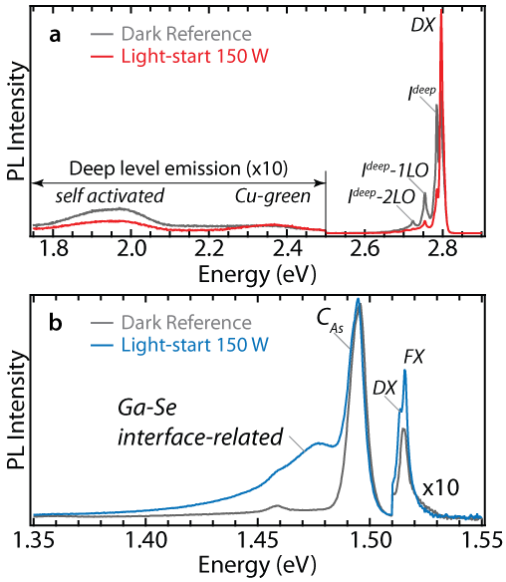

Figure. 3 *PL spectra of the (a) ZnSe and (b) GaAs layers of a ZnSe/GaAs heterostructure grown under light-stimulation at 200 °C.*

Future Work

Ongoing research will continue to explore the light-stimulated growth mechanisms identified above with a combination of *in-situ* and *ex-situ* measurement techniques. Work will include the identification of the mechanism by which light-

stimulation produces an improvement in the p-type doping efficiency of ZnSe and the regulation of defects in II-VI epilayers and at heterovalent interfaces.

References

1. D.A. Beaton, C. Sanders and K. Alberi, *J. Crystal Growth*, **413**, 76 (2015).
2. C.E. Sanders, D.A. Beaton, R.C. Reedy and K. Alberi, *Appl. Phys. Lett.*, **106**, 182105 (2015).
3. W. Walukiewicz, *Phys. Rev. B*, **37**, 4760-4763 (1988).
4. S.B. Zhang, S.-H. Wei, and A. Zunger, *Phys. Rev. Lett.*, **84**, 1232-1235 (2000).
5. V. Virkkala, V. Havu, F. Tuomisto and M.J. Puska, *Phys. Rev. B*, **86**, 144101 (2012).
6. K. Alberi and M.A. Scarpulla, *Scientific Reports*, **6**, 27954 (2016).
7. K. Alberi and M.A. Scarpulla, *submitted* (2017).
8. J. Qiu, Q.-D. Qian, R.L. Gunshor, M. Kobayashi, D.R. Menke, D. Li and N. Otsuka, *Appl. Phys. Lett.*, **56**, 1272 (1990).
9. S. Miwa, L.H. Kuo, K. Kimura, T. Yasuda, A. Ohtake, C.G. Jin and T. Yao, *Appl. Phys. Lett.*, **73**, 939 (1998).
10. K. Park, D.A. Beaton, K.X. Steirer and K. Alberi, *Appl. Surf. Sci.*, **405**, 247 (2017).
11. K. Park and K. Alberi, *submitted* (2017)

Publications

1. C.E. Sanders, D.A. Beaton, R.C. Reedy and K. Alberi, Fermi energy tuning with light to control doping profiles during epitaxy, *Appl. Phys. Lett.*, **106**, 182105 (2015)
2. D.A. Beaton, A. Mascarenhas and K. Alberi, Insight into the epitaxial growth of high optical quality $GaAs_{1-x}Bi_x$, *J. Appl. Phys.*, **118**, 235701 (2015)
3. K. Alberi and M.A. Scarpulla, Suppression of compensating native defect formation during semiconductor processing via excess carriers, *Scientific Reports*, **6**, 27954 (2016)
4. P.M. Mooney, M. Tarun, D.A. Beaton, A. Mascarenhas and K. Alberi, Deep level defects in dilute $GaAs_{1-x}Bi_x$ alloys grown under intense UV illumination, *Semicond. Sci. Technol.*, **31**, 085014 (2016)
5. K. Park, D.A. Beaton, K.X. Steirer and K. Alberi, Effect of ZnSe/GaAs interface treatment in ZnSe quality control for optoelectronic device applications, *Appl. Surf. Sci*., **405**, 247 (2017).

Plasmon and Photon Excitations in Two-Dimensional and Layered Materials

Harry A. Atwater, California Institute of Technology

Program Scope

The control of the flow of light and heat is fundamental to the performance of optical materials in energy applications. Study of light-matter interactions in layered and two-dimensional materials represents a method to both achieve extreme optical confinement, approaching the atomic scale, and also a tool for observing and exploring new materials phenomena. Layered narrow bandgap and zero bandgap materials such as bismuth antimony telluride, black phosphorus, and graphene support unusual and intriguing quantum-confined electronic states in thin layers and topological surface electronic states. Our research project seeks to understand the nature of plasmon excitations in layered materials. In topological insulators, such as ultrathin bismuth antimony telluride heterostructures the conducting surface states give rise to spin-charge coupling affecting plasmons and other optical excitations.

The incomplete screening of applied electrostatic fields in ultrathin materials permits the exploration of matter at high electric fields and carrier densities, enabling interrogation of materials properties over a wide range of electrochemical potential conditions in a single sample. This enables us explore the relationship between the electrochemical potential and the optical and plasmonic properties of ultrathin and layered materials.

Recent Progress

Our major focus is investigation of light matter-interactions in layered materials whose complex permittivity can be modulated under electrochemical potential control, and new light-induced electrochemical potential generation phenomena. The scope of this effort included exploration of the interplay of light and potential in the behavior of layered materials such as bismuth antimony telluride and black phosphorus, as well as electrochemically doped graphene and conducting oxides.

Highlights of recent progress include:

- Determination of contribution of intraband and interband optical processes to absorption in epitaxial bismuth antimony telluride topological insulator samples.
- Observation of interband and intraband absorption processes of quantum-confined states in <10 nm thick phosphorene (black phosphorus) as a function of Fermi level position (NanoLetters 2017).
- Demonstration of mid-infrared phase modulation in resonant graphene/gold plasmonic antenna arrays; we observed phase modulation of up to 237° at an operating wavelength of 8.50 μm(Arxiv 2017).[21]
- Observation of thermoelectric potentials in resonantly excited subwavelength thermoelectric nanostructures designed for spectrally selective absorption. Resonant thermoelectric nanophotonic structures supported on low heat capacity membranes create large localized temperature gradients, even with unfocused spatially-uniform illumination, giving rise to easily measureable thermoelectric voltages. We investigated both resonant nanophotonic bismuth telluride – antimony telluride structures and chromel – alumel structures as examples of a broad class of nanophotonic thermoelectric structures(Nature Nanotechnology, in press).[23]

- Demonstration of tunable enhanced absorption in graphene plasmonic nanostructures using a Salisbury screen geometry (Phys. Rev.B 2014),[19] and tunable extraordinary optical transmission in graphene (Nature Communications 2016).[20]
- Realization of tunable 'perfect' (up to 97%) absorption in graphene plasmonic nanostructures (ArXiv 2017). By variation of the graphene Fermi level, we were able to tune absorption in a patterned graphene layer with a coverage of 0.07 monolayers from 2.9% (the non-resonant interband absorption value) up to >95%. This was achieved using careful analysis of the impedance matching between the nanostructured graphene surface and free space.
- Demonstration of near-infrared phase modulation in plasmonic antenna arrays with tunable permittivity in indium tin oxide; by Fermi level modulation, we observed phase modulation of >180° at an operating wavelength of 1.55 μm (NanoLetters 2016).[22]

Bismuth Antimony Telluride Topological Insulator Structures

Three-dimensional electronic topological insulators are band insulators with Dirac semimetallic surface states in which carrier spins are locked in plane, orthogonal to their crystal momentum. These surface states are remarkably robust; they span the entire bulk band gap, and are topologically protected against material defects and reconstructions that do not break time reversal symmetry. In addition, back-scattering events – in which both momentum and spin

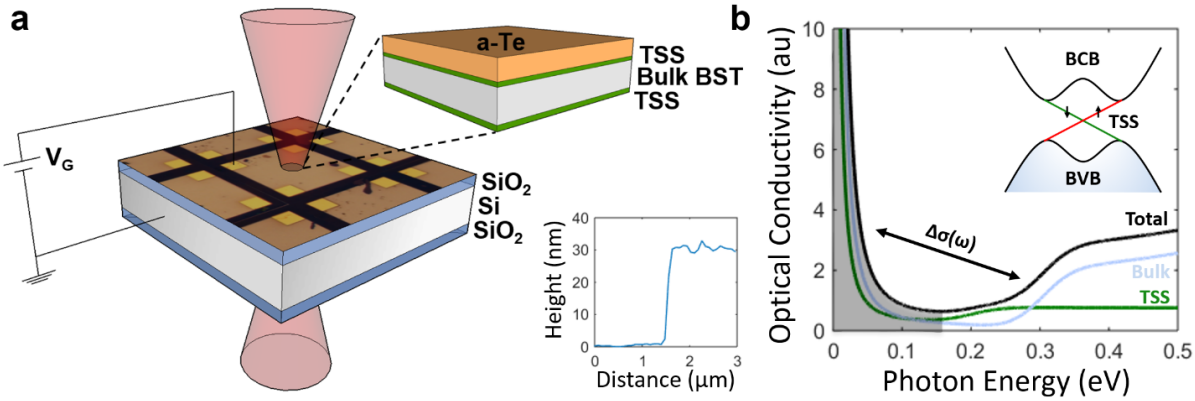

Figure 1: (a) Schematic of the optical measurement configuration. The sample structure consists of a 10 nm a-Te layer atop a 20 nm $(Bi_{1-x}Sb_x)_2Te_3$ (BST) film on 285 nm thermal oxide on silicon. The metallic topological surface states in the BST film penetrate 1-2 nm into the insulating bulk. The transmittance and reflectance of this stack are probed by an FTIR spectrometer coupled to an infrared microscope as the gate voltage is modulated. Inset: AFM cross-sectional profile of transferred BST film, showing a 30 nm total height for a-Te and BST. (b) Schematic of observed behavior. The optical response of the BST consists of contributions from bulk and topological surface carriers39. With changing gate voltage, spectral weight is transferred between both bulk (blue) and topological surface (green) channels and between interband (unshaded region) and intraband (shaded region) channels, as indicated by the arrow. Inset: Schematic band structure of BST, with bulk valence and conduction bands, topological surface states and 0.3 eV band gap indicated.

directions must flip – are strongly suppressed [1-3]. Recently, we began investigating the infrared reflectance and transmittance of ultrathin $(Bi_{1-x}Sb_x)_2Te_3$ (x = 0.94) topological insulator (TI) films while modulating the Fermi level via an applied gate voltage; typical experimental conditions are illustrated in Fig. 1. To enable Fermi level-dependent transmittance measurements, we developed

an epitaxial lift-off method for large-area transfer of TI films from the infrared-absorbing $SrTiO_3$ substrates, used for $(Bi_{1-x}Sb_x)_2Te_3$ growth, to thermal oxidized silicon substrates.

Our approach is to combine optical measurements with Fermi level-dependent transport measurements and angle-resolved photoemission spectroscopy (ARPES) to identify the mechanism for the observed light-matter interactions and their spectral modulation. We perform infrared spectroscopy to explore inter- and intra-band optical transitions in transmittance and reflectance. At lower photon energies, transmittance is increased as the Fermi level is increased. At higher photon energies, transmittance is decreased as the Fermi level is increased. Between these features is an isosbestic point that sees no modulation, suggesting a cross-over between two competing phenomena. Given the identified Fermi level position of the film, we suggest that the optical response at higher photon energies is driven by Fermi level modulation of interband transitions via population of bulk valence band states with holes.

Black Phosphorus Quantum-Confined Structures

The isolation of atomically thin black phosphorus in recent years has opened scientific exploration of two-dimensional and layered materials with energy gaps between graphene and transition metal dichalcogenides, as black phosphorus is an emerging two-dimensional semiconductor material with an infrared energy gap and typical carrier mobilities between those of graphene and transition metal dichalcogenides [4-6].

Recently, we began a first experimental initiative to observe the infrared optical response of ultrathin BP samples under field effect modulation. In measurements performed to date, we have demonstrated experimentally that ultra-thin black phosphorus exhibits widely tunable, quantum well-like optical properties at mid-infrared wavelengths. Our results indicate that BP is

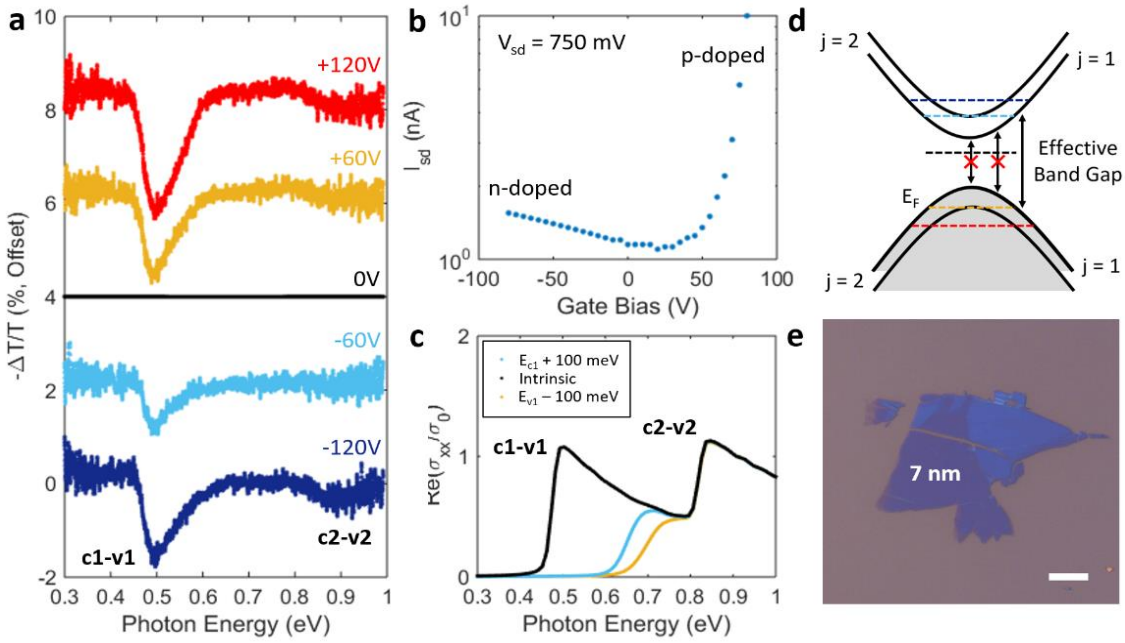

Figure 2: Gate modulation of lightly doped 7 nm sample. **(a)** FTIR transmission extinction vs photon energy normalized to zero bias **(b)** Source-drain current vs gate voltage. Ambipolar conduction is seen. **(c)** Calculated optical conductivity of a 4.5 nm thick BP sample at different carrier concentrations, normalized to the universal conductivity of graphene. No field effects included. **(d)** Schematic of electronic band structure and allowed interband transitions at different voltages. **(e)** Optical microscope image of sample. Scale bar is 10μm.

both an interesting system for exploring the fundamental behavior of quantum-confined carriers in two-dimensional semiconductors under field-effect modulation, and a promising candidate for tunable mid-infrared heterostructures. The extinction modulation results are shown in Fig. 2a, and we observe two major features in this sample at energies of 0.5 eV (I) and 0.9 eV (II). The dip in extinction at 0.5 eV is present for both positive and negative gate voltages, as the sample is increasingly hole or electron doped, respectively. It grows in strength as the doping is further increased at larger gate-biases. The same trend is true for the feature at 0.9 eV. We can interpret our spectroscopic results in light of a Burstein-Moss shift, a well-known phenomenon in chemically doped narrow-band gap semiconductor materials. This effect, which results from band filling, changes the effective optical band gap of a semiconductor. As the charge carrier density is increased and the Fermi level moves into the conduction or valence band, there are fewer unoccupied electronic states available, and optical transitions to the occupied states are disallowed. This results in a decrease in the optical conductivity of the material at the energy of the transition, and is manifest in measurements as a decrease in absorption. Because this sample exhibits ambipolar transport behavior, we can explain both features (I) and (II) as arising from an ambipolar Burstein-Moss effect. This ambipolar, gate-modulated Burstein-Moss shift is the first observed in a two-dimensional semiconductor, to the best of our knowledge.

Future Plans

Our research project seeks to understand the nature of plasmon excitations in the conducting surface states of topological insulators, such as ultrathin bismuth antimony telluride heterostructures and how spin-charge coupling affects plasmons and other optical excitations in topological insulators, including a plasmonic Berry phase, as well as a novel gapless infrared photoresponse for nanostructured samples. We will investigate optical interband and plasmon excitations in narrow bandgap layered semiconductors such as phosphorene (black phosphorus), and explore how strong electrostatic fields alter the band occupancy and electronic structure of thin narrow bandgap semiconductors. The anisotropic in-plane crystal structure of black phosphorus as well as it optical and electronic properties allow polarization-tunable light-matter interactions. We anticipate that field effect control of electrochemical potential control in black phosphorus may enable creation of materials that undergo a band inversion transition from a massive-band narrow gap semiconductor to a topological insulator, and which may also be characterized by in-plane hyperbolic optical dispersion, for certain Fermi level positions.

References

1. X.-L. Qi and S.-C. Zhang, Rev. Mod. Phys. **83** (4), 1057-1110 (2011).
2. M. Z. Hasan and C. L. Kane, Rev. Mod. Phys. **82** (4), 3045-3067 (2010).
3. D. Kong and Y. Cui, Nat. Chem. **3** (11), 845-849 (2011).
4. A. Castellanos-Gomez, The Journal of Physical Chemistry Letters 6 (21), 4280-4291 (2015).
5. L. Li, Y. Yu, G. J. Ye, Q. Ge, X. Ou, H. Wu, D. Feng, X. H. Chen and Y. Zhang, Nat. Nanotechnol. 9 (5), 372-377 (2014).
6. T. Low, A. S. Rodin, A. Carvalho, Y. Jiang, H. Wang, F. Xia and A. H. Castro Neto, Phys. Rev. B 90 (7), 075434 (2014).

Publications

1. Gate-Variable Mid-Infrared Optical Transitions in a $(Bi_{1-x}Sb_x)_2Te_3$ Topological Insulator William S. Whitney, Victor W. Brar, Yunbo Ou, Yinming Shao, Artur R. Davoyan, D. N. Basov, Ke He, Qi-Kun Xue, and Harry A. Atwater, *Nano Letters*, 17, 255−260 (2017).
2. Field Effect Optoelectronic Modulation of Quantum-Confined Carriers in Black Phosphorus, William S. Whitney, Michelle C. Sherrott, Deep Jariwala, Wei-Hsiang Lin, Hans A. Bechtel, George R. Rossman, and Harry A. Atwater, *Nano Letters*, 17, 78−84 (2017).
3. Resonant Thermoelectric Nanophotonics, Kelly W. Mauser, Slobodan Mitrovic, Seyoon Kim, Dagny Fleischman, and Harry A. Atwater, *Nature Nanotechnology*, in press (2017).
4. Experimental Demonstration of >230° Phase Modulation in Gate-Tunable Graphene-Gold Reconfigurable Mid-Infrared Metasurfaces, Michelle C. Sherrott, Philip W.C. Hon, Katherine T. Fountaine, Juan C. Garcia, Samuel M. Ponti, Victor W. Brar, Luke A. Sweatlock, Harry A. Atwater, *Nano Letters*, in press (2017).
5. Electronically tunable extraordinary optical transmission in graphene plasmonic ribbons coupled to subwavelength metallic slit arrays, Seyoon Kim, Min Seok Jang, Victor W. Brar, Yulia Tolstova, Kelly W. Mauser and Harry A. Atwater, *Nature Communications*, 7:12323, DOI: 10.1038/ncomms12323 (2016).
6. Gate-Tunable Conducting Oxide Metasurfaces, Yao-Wei Huang, Ho Wai Howard Lee,Ruzan Sokhoyan, Ragip A. Pala, Krishnan Thyagarajan, Seunghoon Han, Din Ping Tsai, and Harry A. Atwater, *Nano Letters*, 16, 5319−5325 (2016).
7. Thermodynamic theory of the plasmoelectric effect, Jorik van de Groep, Matthew T. Sheldon, Harry A. Atwater and Albert Polman, *Scientific Reports*, 6:23283 DOI: 10.1038/srep23283 (2016).
8. Field-effect induced tunability in hyperbolic metamaterials, Georgia T. Papadakis and Harry A. Atwater, *Physical Review B* 92, 184101 (2015).
9. Electrochemical Tuning of the Dielectric Function of Au Nanoparticles, Ana M. Brown, Matthew T. Sheldon, and Harry A. Atwater, *ACS Photonics,* 2, 459−464 (2015).

Tuning morphology, packing and electrical performance of semiconducting polymer through solution processing

Zhenan Bao, Department of Chemical Engineering, Stanford University

Program Scope

Solution-processed organic electronics presents great potential for the development of transparent, large-area and flexible/stretchable electronic devices at low cost. Semiconducting (SC) polymers can be tailored to be soluble in common solvents so that they can be solution-processed as thin films. Furthermore, these films often present different phases that influence dramatically the electrical behavior of the SC polymer. Understanding and controlling the occurrence of these polymer phases is paramount for the development of performing electronic devices based on organic materials.

The aim of this program is to explore the different packing and morphologies available in thin films of SC polymers when processed from solutions at different conditions. For that purpose, we are developing innovative processing methods, based on the solution-sheared (SS) technique, which will allow us to have a tight control in the structure of the films. Moreover, we will evaluate the impact of this morphology in their electrical performance of the SC films, particularly in their field effect transistor (FET) mobility. The controlled alignment of solution-sheared SC polymer chains will be tackled either by utilizing a micro-structured blade for fluid dynamics control; by combining SS with the application of electric fields to polarize SC molecules; or by blending SC polymers with dielectric polymers to induce innovative phase-separated structures with unprecedented mechanical and electrical properties.

Recent Progress

1. Controlling molecular packing using electric field: The solution shearing (SS) is a versatile method previously developed in the Bao group to prepare thin-films of organic materials with high alignment [1]. In this method, a solution is spread on a substrate by a sliding top blade. A variety of processing parameters, such as shearing speed, substrate temperature and gap between substrate and blade, can be independently controlled. Patterning the surface of blade with different topologies has also been proved to create a “brush” effect that improves film morphology and material alignment by modifying the fluid dynamics of the process [2]. On top of that, another new functionality has been recently added to the SS method by applying a voltage between the blade and the substrate. This voltage subjects the SC molecules to an electric field during the forming of the film and alters its packing motif [3] (Fig. 1). This strategy is currently being investigated for long molecules of semiconducting polymer with the intention of enhance

their alignment and FET mobility. Utilizing concepts of dielectrophoresis (DEP) theory, a tight control of the polymer morphology can be potentially achieved by selecting the right solvent and frequency of the electric field. Fig. 2 shows the differences in surface morphology (images obtained with AFM), bulk polymer chains alignment (results from UV-Vis absorption) and crystalline packing direction (diffraction pattern obtained from grazing incidence X-ray diffraction, GIXD) of two films of the polymer poly(2,5-bis(2-octyldodecyl)- 3,6-di(thiophen-2-yl)diketopyrrolo[3,4-c]pyrrole- 1,4-dione-alt-thieno[3,2-b]thiophen) (DPPT-TT) with Mn = 10kDa. The polymer films were fabricated from p-xylene by SS at low speed (80 µm/s) in absence (reference) and presence of electric field. Whilst the polymer fibers at the surface of the reference film align mostly perpendicular to shearing direction, vortices appear on the surface of the film sheared under the influence of electric field (Fig.2 a). This observation suggest a tendency of the field to align the polymer fibers along its own direction (the shearing direction). Electric field-induced alignment along shearing direction occurs also in the bulk of the film. This fact is supported by a decrease in the dichroic ratio obtained with UV-Vis (Fig.2 b). On the other hand, GIXD measurements indicate that the field affects the crystalline packing as well. The direction of the π-π stacking is oriented along the shearing direction (the corresponding diffraction rod appears when probing the samples in the direction perpendicular to shearing) in a reference sample sheared in absence of field. However, the diffraction rod corresponding to the π-π stacking is no longer visible when the film is sheared under electric field (Fig.2 c).

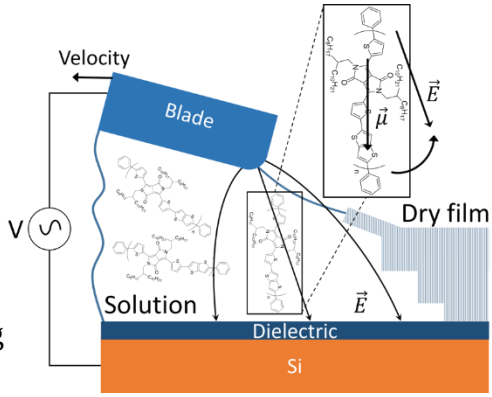

Figure 1. Sketch of the experimental set-up used for applying electric field to SC polymers during solution-shearing to modify their packing and morphology.

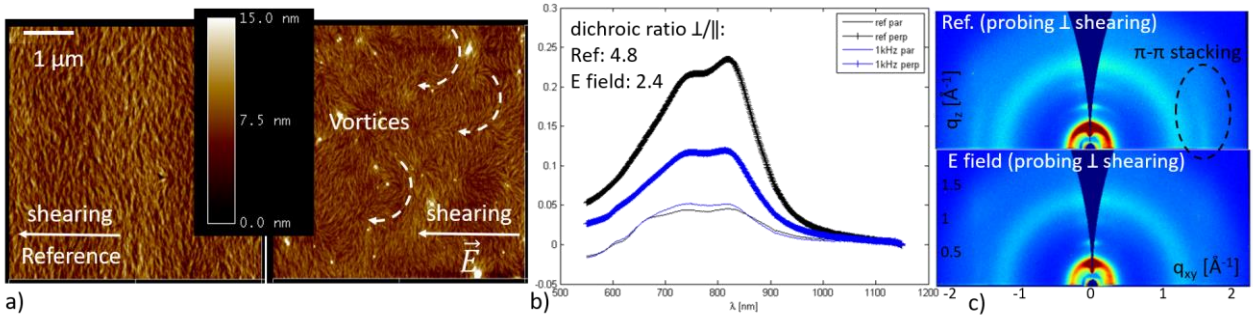

Figure 2. Comparison of the morphology of a DPP-DTT polymer solution-sheared in absence and presence of electric field (150 V at 1 kHz): a) Image of the film surface obtained with AFM; b) absorption spectrum obtained with UV-Vis; c) GIXD pattern.

2. Controlled molecular packing and mechanical properties using non-equilibrium processing of polymer blends: Another route that we are exploring to induce novel morphologies in solution-processed polymer films consists of polymer semiconductor/insulator blends. These blends have been shown to be a great approach for the fabrication of

semiconducting layers with high electrical performance, in which the semiconducting polymer forms nanofibril structures as a result of phase separation [4]. Recently, we developed a new concept based on a polymer physics effect—the nanoconfinement—to largely increase the mechanical ductility of the conjugated polymer (Fig.3 a). This is experimentally realized by a new physical engineering approach, the CONjugated-polymer-elastomer PHase-separation INduced Elasticity (termed CONPHINE). This is a one-step process, which involves direct coating of the solution of conjugated polymer and the compatible elastomer to spontaneously form the nanoconfined structures (Fig.3 b). We first investigated DPPT-TT as the high-mobility semiconducting polymer and polystyrene-block-poly(ethylene-ranbutylene)-block-polystyrene (SEBS) as the soft elastomer. Their comparable surface energies should ensure a nanoscale mixed morphology. As observed by the atomic force microscopy (AFM) phase images, the CONPHINE film showed the desired fiber network with smaller nanofiber diameters at higher SEBS concentrations. At 70 weight % of SEBS, the nanofiber diameter became small enough (<50 nm) to give a strong nanoconfinement effect at both the top and bottom surfaces (Fig.3 c). In the case of DPP-based polymers, we found that the polymer chains preferably align along the nanofiber directions due to space confinement. GIXD measurements show a suppressed crystallization of DPPT-TT in this nanostructured films (Fig.3 d). However, because of the better aggregation of DPPT-TT in the nanofibers, the electrical performance can maintain or become even better than the original neat film (Fig.3 e). Such blend systems not only have the advantages of improved mechanical ductility from the nanoconfinement effect from our recent study [5], but aligned polymer chains in the nanofibers due to the space confinement and much reduced amount of semiconducting polymer usage for films fabrication.

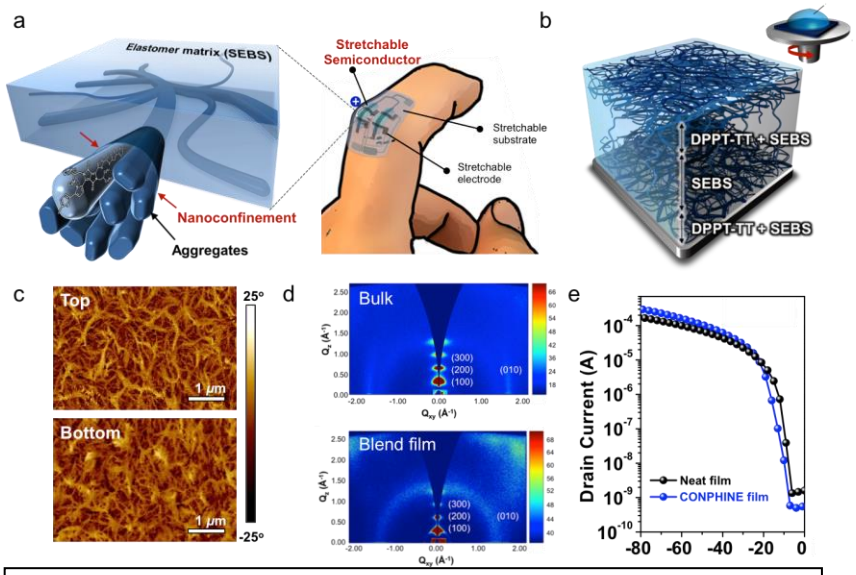

Figure 3. (a) A 3D schematic of the desired morphology composed of embedded nanoscale networks of polymer semiconductor, which can be used to construct a highly stretchable and wearable TFT. (b) A 3D illustration of the morphology of the CONPHINE film. (c) AFM phase images of the top and bottom interfaces of the CONPHINE film with 70 wt%SEBS. (d) GIXD images of bulk neat and CONPHINE films. (e) Transfer curves (drain voltage = −80 V) obtained from the CONPHINE and the neat film in its original condition.

Future Plans

Whilst our preliminary results show different methods able to modify the morphology and packing of SC polymer, a better understanding of these processes would allow us to pinpoint the configuration that best suit electrical performance:

1. For SS coupled with electric field, a theoretical model based on DEP will be developed to gain understanding of the process. This will permit us to select the most favorable alignment and packing of the polymer using as main parameters the solvent and the frequency of the applied AC field. Also, different SS conditions will be explored leading to a synergistic effect between shearing forces and electric field for maximized polymer alignment. For this purpose, we will consider the combination of a blade patterned with different geometries and the application of electric field. Finally, we will correlate the attained polymer morphologies with their electrical performance. The configuration yielding the highest FET mobility will be pointed out.

2. In the CONPHINE method, spin-coated films yield nanofibers with isotropic orientations, which creates a large number of junctions and therefore limits the charge transport mobility. Since it is generally easier to align nanofibers than to directly align entangled polymer chains, we propose to use the SS method to induce a high degree of polymer chain alignment from such blending systems, to significantly investigate its impact on charge transport. During the SS process, the alignment of the nanofibers is mainly determined by the driving force from the shear blade and the speed of freezing of the formed film. By using the shearing blades with patterned nano/micro-structures, the degree of alignment can be enhanced. We will perform a set of systematic studies on the influence of the nano-pattern geometries (such as lines, dots and squares) with varied densities, pattern layout, and the shearing conditions (such as shearing speed, temperature, solvent, gap distance and substrate surface treatment). Through this, both the condition for the best polymer chain alignment and a deeper understanding of the solution-shearing process will be obtained. The charge transport of the fabricated semiconducting film will also be measured for the fundamental investigation for the influence of the polymer chain alignment on the charge transport behavior.

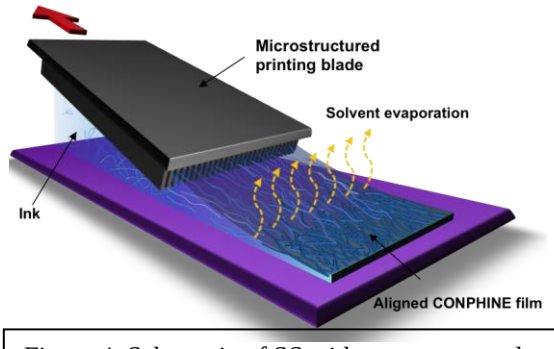

Figure 4. Schematic of SS with nanostructured blade to align the nanofibers in CONPHINE film.

References

[1] G. Giri, E. Verploegen, S. C. B. Mannsfeld, S. Atahan-Evrenk, D. H. Kim, S. Y. Lee, H. a Becerril, A. Aspuru-Guzik, M. F. Toney, Z. Bao, *Nature* **2011**, *480*, 504.

[2] Y. Diao, B. C.-K. Tee, G. Giri, J. Xu, D. H. Kim, H. a Becerril, R. M. Stoltenberg, T. H. Lee, G. Xue, S. C. B. Mannsfeld, Z. Bao, *Nat. Mater.* **2013**, *12*, 665.

[3] F. Molina-Lopez, H. Yan, X. Gu, Y. Kim, M. F. Toney, Z. Bao, *Adv. Funct. Mater.* **2017**, *27*, 1605503.

[4] S. Wang, S. Fabiano, S. Himmelberger, S. Puzinas, X. Crispin, A. Salleo, M. Berggren, *Proc. Natl. Acad. Sci. U. S. A.* **2015**, *112*, 10599.

[5] J. Xu, Z. Bao *et al.*, *Science (80-.).* **2017**, *355*.

Publications

[1] F. Molina-Lopez, H. Yan, X. Gu, Y. Kim, M. F. Toney, and Z. Bao, "Electric Field Tuning Molecular Packing and Electrical Properties of Solution-Shearing Coated Organic Semiconducting Thin Films," *Adv. Funct. Mater.*, vol. 27, no. 8, p. 1605503, Feb. 2017.

[2] J. Xu, S. Wang, G.-J. N. Wang, C. Zhu, S. Luo, L. Jin, X. Gu, S. Chen, V. R. Feig, J. W. F. To, S. Rondeau-Gagné, J. Park, B. C. Schroeder, C. Lu, J. Y. Oh, Y. Wang, Y.-H. Kim, H. Yan, R. Sinclair, D. Zhou, G. Xue, B. Murmann, C. Linder, W. Cai, J. B.-H. Tok, J. W. Chung, and Z. Bao, "Highly stretchable polymer semiconductor films through the nanoconfinement effect," *Science*, vol. 355, no. 6320, p. 59, 2017.

[3] X. Gu, Y. Zhou, K. Gu, T. Kurosawa, Y. Guo, Y. Li, H. Lin, B. C. Schroeder, H. H. Yan, F. Molina-Lopez, C. J. Tassone, C. Wang, S. C. B. Mannsfeld, H. H. Yan, D. Zhao, M. F. Toney, Z. Bao, F. Molina-Lopez, C. J. Tassone, C. Wang, S. C. B. Mannsfeld, H. H. Yan, D. Zhao, M. F. Toney, and Z. Bao, "Roll-to-Roll Printed Large-Area All-Polymer Solar Cells with 5% Efficiency Based on a Low Crystallinity Conjugated Polymer Blend," *Adv. Energy Mater.*, p. 1602742, Mar. 2017.

Nanocrystal-Based Diodes for Solar to Electric Energy Conversion

David N. Beratan
Departments of Chemistry, Physics, and Biochemistry
Duke University, Durham, NC 27708

Program Scope

This project explores design features that promote efficient charge transfer in nanoparticle-based bulk heterojunction materials. Our goal is to identify properties of the charge-transfer elements and their assemblies that form by self-assembly, that are robust, and that affect transduction of the absorbed photons into separated charges. Using a staggered band energy alignment of the nanoparticles is critical to the device function. As well, it is important to inhibit charge recombination so that electrons and holes are extracted efficiently. Our theoretical research program, conducted in close collaboration with the experimental programs of Profs. Waldeck and Naaman [1-7], is identifying essential features of nanoparticles, and their assemblies, to promote effective charge separation, to inhibit charge recombination, and to operate robustly. We intend for the structures under development to operate effectively in spite of structural heterogeneity that will exist in bulk heterojunction films. Research at Duke focuses on theoretical modeling and simulation of charge separation reaction mechanisms and kinetics in the NP assemblies.

Recent Progress

In the last three years, our collaborative project has demonstrated that one can use energy-level gradients, built-in electrostatic potentials, and symmetry/chirality properties to improve charge-separation efficiency in inorganic-organic hybrid structures. Moreover, we have developed theoretical principles that are providing significant design and interpretive tools that can be leveraged in the experimental program.

We used Marcus theory and quantum chemistry calculations to examine how the energy band offset and the interfacial chemical contacts between quantum dots (QDs) influence the charge transfer rates. In a recent experimental studies our collaborators measured the electron transfer rate as a function of inter-QD distance and the energy band offset of the QDs (reaction Gibbs free energy). The experimental design includes covalently bound QD dyads assembled on a colloidal template. The photo-induced charge transfer rates were found to decay exponentially with QD-QD distance (consistent with an electron tunneling mechanism) and the dependence on energy band offset was consistent with Marcus theory, as long as one performs a sum over final electronic states of the QDs. These results indicate that our understanding of electron transfer in molecular donor-bridge-acceptor assemblies can be translated to describe nanoparticle-bridge-nanoparticle assemblies. While we and others have shown how the ligand shell can be used to manipulate the band-edge energetics and the thus the free energy for charge transfer, less is known about other important parameters, such as the electronic coupling and its dependence on the NP radius and the medium between the donor/acceptor NPs.

We have used theory to examine how the electronic coupling between QDs depends on their size, separation distance, linking molecules, and surrounding dielectric environment. The electronic coupling between two QDs was analyzed using tight-binding models. Depending on the QD size, the coupling interactions can be dominated either by through-solvent or through-bond interactions. We have derived analytical expressions for the QD radius and distance

dependent couplings. Parameterizing the QD models (for CdSe and CdTe), we find that both the through-solvent and through-bond couplings decrease as the radii of the QDs grow. The dominance of through-solvent and through-bridge coupling mechanisms switches as the QD size increases. We have tested these predictions using tight-binding models, and some comparisons can be made with our earlier DFT analysis. We have used the charge transfer characteristics found in these studies to explore strategies to maximize charge transfer yields in coupled QD pairs.

Intimately related to the size dependence of the electronic coupling between QDs is the change in the density of electronic states with QD size, which can profoundly alter the electron transfer rates. For example, our experimental studies of dyads show that the Marcus inverted region for electron transfer can be masked by the growth in the number of electronic accepting states with increasing band-edge offset, causing a systematic increase in electron transfer rate with increasing driving force. This effect is captured in the theoretical studies as well. Because the band edge and density of states determine the free energy and Franck-Condon overlaps for charge transfer between QDs, understanding and controlling their size dependence is important for manipulating the dependence of charge transfer rates on the QD chemistry and their assembly. We have used our models to evaluate the band-edge energy and density of states of QDs, and the resulting QD electron/hole transfer kinetics for type II assemblies. In the typical size range of QDs used experimentally, the computed band edge energetics are consistent with those measured by photoemission spectroscopy, and the computed densities of states agree well with those calculated using DFT.

In addition to the studies described above, we have also explored the possibility of using intrinsically quantum mechanical phenomena for coherent sensing, by combining the full analytical description of electronic relaxation processes with mass diffusion and charge transport models. This theory produces molecular-scale design criteria for sensors. For example, we analyzed sensing schemes based on charge transfer and polarization (electronic relaxation) processes, and we showed that the detector sensitivity can increase with decreased coupling between the molecular binding sites and the sensor substrate. This counterintuitive response and other quantum features give these devices favorable characteristics, such as enhanced sensitivity and selectivity. As well, we have developed theories for multi-electron coherent transport.

Future Plans

1. **Exploring transitions between through-bond and through-solvent coupling between NPs**

In our previous studies, we found that the relative dominance of through-solvent and through-bridge coupling switches as the QD radius grows. In the next stage of our studies, we will examine the sensitivity of these two coupling mechanisms to solvent and to QD chirality. Dissymmetry can arise from the QD chirality and also from chiral ligands. The chiral imprint can significantly modify the donor-acceptor interaction strength, their QD size dependence, the donor-acceptor coupling dependence on distance, the coupling pathway interferences, and the charge-transfer efficiency. Similarly, the solvent ionic strength and charged groups on the molecular linker are expected to modify the dependence of the two coupling mechanisms on QD size and distance. Our preliminary analysis finds that charged groups on the molecular linker can modify the through-bond and through-solvent coupling decay exponent by more than 20%.

Additionally, we plan to investigate the magnetic field dependence of these two coupling mechanisms in the case of coupling via multiple molecular linkers.

2. Higher-order NP assemblies: NP triads

In preliminary studies, we have used kinetic modeling to explore the current-voltage, power-voltage and power conversion efficiency characteristics of quantum dot dyads and triads as light absorption and charge separation engines for quantum dot solar cells. Open-circuit voltages appear to be about 10% larger for triads than for dyads, and short-circuit currents for triads are more than double those of dyads when charge the recombination rates are larger than the charge separation rates. These apparent advantages indicate potential opportunities to develop multi QD assemblies for solar energy harvesting and conversion, and we plan to explore enhanced performance that can be generated with higher order assemblies of this kind.

3. QD chirality effects on charge transfer

In the last phase of the project, Prof. Waldeck discovered order of magnitude kinetic effects on spin dependent charge transfer in chiral ligand coated CdSe QDs. The photoinduced charge transfer from states with a well defined spin orientation was realized by photoexciting with circularly polarized light (CPL). We propose to investigate the underpinning ET mechanism for this phenomenon. The possible mechanism may be analogous to a mechanism for chirality control of electron transfer proposed earlier [8]. The spin dependence may also be related to a Rashba spin-orbit coupling effect that induces different interactions with up and down spins in different chiral environments. As well, the electron-nuclear hyperfine interactions may modify the electronic couplings of different spin states. The hyperfine interactions arise from the interactions of nuclear magnetic moments of the QD, and this could be different for QDs of different chiralities. The observed order of magnitude CT rate changes may well have contributions from several chirality and magnetic moment effects, and we intend to rank the magnitudes of the various effects at play.

References

1. B. P. Bloom, L.-B. Zhao, Y. Wang, D. H. Waldeck, D. N. Beratan, P. Zhang, and R.Liu *J. Phys. Chem. C.* ***117*** (2013) 22401−22411; b) Aleksey E. Kuznetsov, Balamurugan Desinghu, Spiros S. Skourtis, David N. Beratan. *J Phys Chem C* ***116,*** (2012) 6817.
2. B. Bloom, M.N. Mendis, E. Wierzbinski, and D. H. Waldeck *J. Materials Chemistry C* ***4*** (2016)704 – 712.
3. R. Liu, B. Bloom, D. H. Waldeck, P. Zhang, and D. N. Beratan *J Phys Chem C* (2017) submitted.
4. B. M. Graff, B.P. Bloom, E. Wierzbinski, and D. H. Waldeck *J. Am. Chem. Soc.* ***138*** (2016) 13260—13270.
5. Y. Wang, K. Liu, P. Mukherjee, D. A. Hines, P. Santra, H. Y. Shen, P. Kamat, and D. H. Waldeck *Phys. Chem. Chem. Phys.* ***16*** (2014) 5066 – 5070.
6. a) M. Kettner, B. Gohler, H. Zacharias, D. Mishra, V. Kiran, R. Naaman, D. H. Waldeck, S. Sek, J. Pawlowski, and J. Juhaniewicz *J. Phys. Chem. C* ***119*** (2015) 14542-14547; b) R. Naaman and D. H. Waldeck, *Ann. Rev. Phys. Chem.* ***66*** (2015) 263–281.
7. B. P. Bloom, V. Kiran, V. Varade, R. Naaman, D.H. Waldeck *NanoLetters* ***16*** (2016) 4583-4589.
8. S.S. Skourtis, D.N. Beratan, A. Nitzan, D.H. Waldeck, *Phys. Rev. Lett*., **101 (**2008) 238103.

Publications

1. R. Liu, B. Bloom, D. H. Waldeck, P. Zhang, and D. N. Beratan *Controlling the electron-transfer kinetics of quantum-dot assemblies* J. Phys. Chem. C (2017) submitted. Acknowledgement Excerpt: "This work was funded by the U.S. Department of Energy (Grant No. ER46430 and SC0010662/ER46952)."
2. B. P. Bloom, B. M. Graff, S. Ghosh, D. N. Beratan, and D. H. Waldeck *Chirality Control of Electron Transfer in Quantum Dot Assemblies* Nature Chem. (2017) submitted. Acknowledgement Excerpt: "This work was funded by the U.S. Department of Energy (Grant No. ER46430 and SC0010662/ER46952)."
3. A. Migliore, R. Naaman, D.N. Beratan, "*Sensing of molecules using quantum dynamics"* Proc. Natl. Acad. Sci., 112 (2015) E2419–E2428 DOI:0.1073/pnas. 1502000112. Acknowledgement excerpt: '*We thank the US Department of Energy for support of this research (Grant SC0010662).*' Erratum submitted: "This research is supported by the U.S. Department of Energy, Office of Basic Energy Sciences, Division of Materials Sciences and Engineering under Award ER46430."
4. J. Lin, D. Balamurugan, P. Zhang, S.S. Skourtis, and D.N. Beratan, *"Two electron transfer pathways,"* J. Phys. Chem. B 119 (2015) 7589-7597DOI: 10.1021/jp511429z). Acknowledgment excerpt (a 2-way collaboration): '*We thank the U.S. Department of Energy (SC0010662) and the People Programme (Marie Curie Actions) of the European Union's Seventh Framework Programme (FP7/2007-2013) under REA Grant Agreement No. [609305]*.' Erratum submitted: "This research is supported by the U.S. Department of Energy, Office of Basic Energy Sciences, Division of Materials Sciences and Engineering under Award ER46430 (Duke University) and by the People Programme (Marie Curie Actions) of the European Union's Seventh Framework Programme (FP7/2007-2013) under REA Grant Agreement No. [609305] (University of Cyprus and University of Freiburg)."
5. A.E. Kuznetsov and D.N. Beratan, *"Structural and electronic $Cd_{33}Se_{33}$ and $Cd_{33}Te_{33}$ quantum dots,"* J. Phys. Chem. C, 118, 7094-7109 (2014). Acknowledgment excerpt: '*This work was supported by DOE Grant ER 46430.*'
6. B. P. Bloom, L.-B. Zhao, Y. Wang, D. H. Waldeck, D. N. Beratan, P. Zhang, and R.Liu "*Ligand Induced Changes in the Characteristic Size Dependent Electronic Energies of CdSe Nanoparticles"* J. Phys. Chem. C. (2013) 22401−22411. Acknowledgment excerpt:*' This work was funded by the U.S. Department of Energy (Grant No. ER46430).'*

Spectrally-tunable far-field thermal radiation extraction from micro & nanostructures

Gang Chen (PI) and Svetlana V. Boriskina (co-PI), Department of Mechanical Engineering, Massachusetts Institute of Technology, Cambridge, MA, USA

Program Scope

The overall goal of this project is to explore new approaches towards radiative heat extraction from the near field to the far field via morphology-mediated thermal emission. We seek to develop a general understanding and specific design rules for morphology-mediated radiative heat extraction. In particular, we investigate mechanisms of manipulating far-field thermally-emitted photons via engineering of local electromagnetic potentials, and probe limits of thermal radiation from (or via coupling to) micron and nanoscale structures into the far field. We also explore possibilities to convert low energy photons into high energy phonons via phonons in low-dimensional thermal absorbers/emitters.

Recent Progress

We focused on combining fundamental understanding and exploration of new application areas for the spectral shaping of emittance, absorptance, and transmittance via micro- and nano-scale engineering of the local photon density of states [1,2]. Confined quantized photon states in optical nanostructures can be used to enhance and tailor energy extraction via photon emission in both near and far field regimes. These photon states include guided modes in thin films[3–5] as well as trapped modes and localized polariton modes in optical fiber [6] and micro-/nano-cavities[6–8]. To achieve the required level of photon confinement, the dimensions of the radiating objects should be on the order of either incoming wavelength of light (for photon absorbers and filters) or of the thermal wavelength predicted by Planck's law at a given temperature (for thermal emitters). Emission spectra of low-dimensional objects deviate from Planck's law predictions both in the near- and the far field, expanding their application range.

As one example of using this concept of photon spectrum shaping, we predicted a new way to improve performance of thermophotovoltaic energy converters. TPV conversion platforms harvest thermal radiation from hot emitters and convert it into electrical current in a photovoltaic (PV) cell. However, the broad thermal emission spectrum is not optimally matched to the PV cell absorption window (Fig. 1a). Ideally, emission of long-energy photons that cannot be utilized by the PV cell needs to be suppressed, and emission of photons with the energies just above the PV cell bandgap enhanced. Our proposed new TPV system design consisted of a thin-film thermal emitter and a thin-film PV cell, which both support quantized optical modes trapped inside the material by total internal reflection. Dispersion characteristics of these confined modes lead to resonant enhancement of their photon density of states (Fig. 1b), which in turn modifies their thermal emission and absorption, both in the near- and far-field (Fig. 1a). Most importantly, these confined modes exhibit cut-off frequencies at longer wavelengths, enabling suppression of emission of photons with energies smaller than the band gap of the PV cell. Simultaneously, in a thin PV cell, photo-excited electrons and holes need to travel shorter distances, which reduces their bulk recombination losses and yields a lower saturation current in the PV cell.

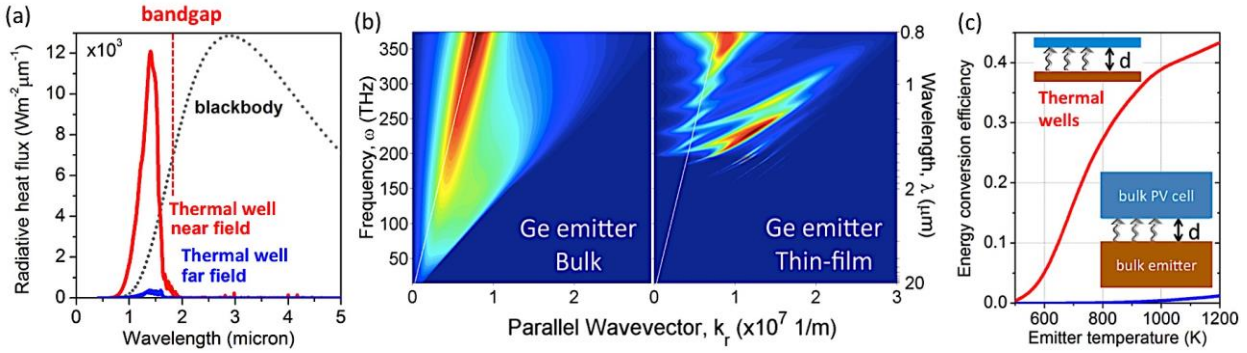

Figure 1. Spectral shaping of thermal emission and absorption via optical confinement in thin-film 'thermal wells'. (a) Spectral radiative heat flux between a thin-film 'thermal well' emitter and a thin-film absorber in both near-field (10nm vacuum gap, solid red line) and far-field (solid blue line) regimes with respect to a blackbody heat flux at the same temperature (grey dotted line). (b) Modal dispersion of the bulk emitter and a thermal well emitter. (c) Thermal well TPV efficiency improvement over that of its bulk counterpart.

By improving the spectral selectivity and reducing the saturation current, the 'thermal well' effect theoretically offers enhancement of the TPV system energy conversion efficiency by over an order of magnitude compared to both the bulk limit and the Shockley Queisser limit for a blackbody emitter at the same temperature. For a thin-film Ge emitter and a thin-film GaSb PV cell, the maximum TPV energy conversion efficiency was predicted to be as high as 38.7% at an emitter temperature of 1000 K and gap separation of 100 nm (Fig. 1c). In the far-field limit, this efficiency decreases to 31.5%; however, this is still significantly higher than the Shockley Queisser limit even for a blackbody emitter at a temperature of 2000 K[3]. These predictions offer a significant improvement in the TPV system performance over prior designs based on the use of surface polariton modes coupling in the near field, which are challenging to realize in a practical system. The new thermal emitter design also does not require nanoscale patterning, and thus offers a simple low-cost solution to improve the performance of thermal emitters not only for TPV systems but also for improved incandescent lightbulbs and infrared spectroscopy.

To approach the extreme limit of shaping the emission spectra of the ultra-thin planar emitters/absorbers, we developed theoretically and realized experimentally the conjugate-impedance matching approach to achieve perfect absorption with tunable narrow-band spectral lines. Typically, large mismatch between optical and electron length scales in thin films weakens light-matter interactions and reduces the emittance/absorptance (see e.g. Fig. 1a, far field spectrum). To alleviate this limitation, we designed and demonstrated spectrally-selective perfect absorbers based on topologically-protected interfacial optical states in planar multi-layered thin-film materials. These structures have tunable absorption lines, are easy to fabricate, and can incorporate ultra-thin and even 2D materials as absorbers. One example of a planar structure that exhibits an interfacial (Tamm) state is a thin-film metal absorber integrated with a finite-length 1D photonic crystal (Fig. 2a). The existence of Tamm states on the interface between the metal layer and the dielectric PhC is topologically protected provided the surface impedance of the bottom surface of the PhC facing the metal is tuned to match that on the metal surface. We further proved that perfect absorption can be achieved if the impedance of the absorber layer is conjugate-matched to the optical filter, which does not necessarily have to be a periodic PhC. The topological protection is achieved because the optical surface impedance is directly related

to the bulk topological properties of the bulk material through the geometrical (Zak) phases of its photonic bands. We demonstrated performance of fabricated Tamm structures as absorbers and singular-phase optical sensors[9], and are exploring their applications as thermal emitters.

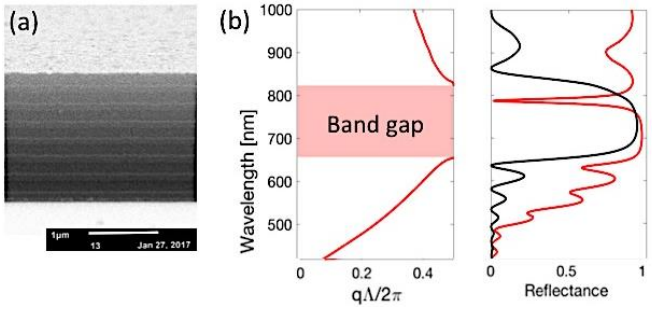

Figure 2. Ultrathin narrowband perfect emitters/absorbers with topologically-protected interfacial Tamm states. (a) SEM image of the fabricated Tamm structure. (b) Narrow-band absorption line resulting from the conjugate impedance matching between finite 1D PhC and a thin metal absorber.

TPV cells discussed above offer the opportunity to improve the energy efficiency over the conventional PV cells via better tailoring of the thermal radiation that minimizes entropy generation in the PV engine. Instead of looking for further improvements in the spectral shaping of the thermal radiation from the terrestrial emitter that is used to photo-excite charge carriers in the PV cell, we asked the question what could be the most efficient engine that makes use of radiative heat flux as the mechanism to either receive or reject energy and entropy. An ideal engine should receive energy in the form that carries the lowest entropy content, and dump entropy in the form that carries the highest entropy content. To find the ideal engine, we performed detailed theoretical analysis of the entropy content of radiation with various energy spectra. We found that heat conduction or high frequency radiation carry the lowest entropy content, and thus are the most favorable forms of energy for the engine input. In turn, best form of energy to maximize the entropy removal from the engine is low frequency emission.

Based on the above insights, a thermoradiative (TR) cell – a PN junction working under the reverse bias due to enhanced thermal radiation at elevated temperatures – was identified as an excellent candidate for high-efficiency engine (Fig. 3a). It receives energy through heat conduction and dumps entropy through radiation, which carries higher entropy content than conduction. If a PV cell is heated by an external terrestrial heat source, the system is driven out of the equilibrium with the environment, and its emission rate increases. This process also creates a potential difference, albeit of an opposite polarity from that of a photo-excited solar cell, which can drive electric current through the load. We proposed a new way to increase the efficiency of TR cells via spectrally selective thermal emission with the major contribution from long-wavelength photons. As predicted via the entropy analysis, the TR cell efficiency can be enhanced in the situation when its emission is highly spectrally selective, narrowband, and dominated by low frequency photons. When low frequency photons dominate the emission spectrum, the maximum efficiency is increased and approaches the Carnot limit (Fig. 3b), which significantly exceeds the limiting efficiency of an ideal solar PV cell made of the same material.

Ideally, an engine should provide high efficiency and high power density. However, maximum power generation of the TR cell does not occur at the cell highest efficiency point, forcing to compromise between efficiency and power density. To resolve this dilemma, we showed via simulation that not only the conversion efficiency but also the power generation density of the TR cell can be increased via the near-field photon extraction. In the near-field extraction scheme, the TR cell is integrated with a heat sink, which is separated from the cell by a nanoscale gap. If

the heat sink material supports electromagnetic surface modes, the radiative photon flux from the TR cell to the heat sink can be dramatically enhanced, which translates into high power generation density. Our calculations show that the radiative power flux can be increased within a narrow spectral range by orders of magnitude if the emitter and the heat sink are electromagnetically coupled through the near-field[4]. We also predicted that an ideal InSb TR cell that dumps entropy via the near-field narrow-band emission into a heat sink can achieve a maximum efficiency and power density up to 20.4 % and 327 Wm^{-2}, respectively, between a hot source at 500K and a cold sink at 300K. However, sub-bandgap and non-radiative losses will significantly degrade the cell performance[4].

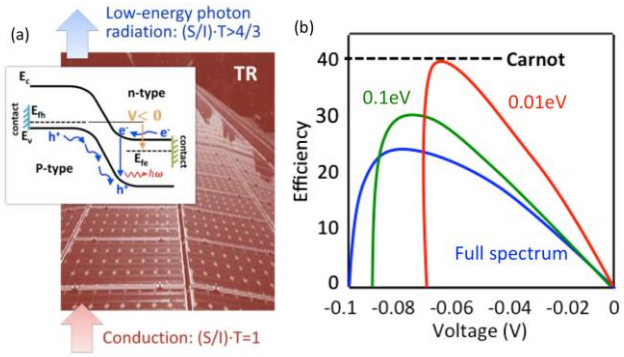

Figure 3. (a) TR cell principle of operation. (b) Efficiency improvement via emission spectrum narrowing.

Future Plans

We plan to further investigate manipulation of radiation and absorption via photon confinement effects as well as development of nanostructures with topologically-protected interfacial photon states. This will achieve perfect absorption and tailored thermal emission in ultra-thin or even 2D materials, and will ultimately allow studying light-matter interactions in these systems both in steady state and on the ultrafast timescale. We will continue exploring thermal up- and down-conversion of photon energy by combining morphological effects with non-equilibrium excitation/emission processes such as photoluminescence.

References

1. Boriskina, S. V. *et al.* Heat meets light on the nanoscale. *Nanophotonics* **5,** 134 (2016).
2. Boriskina, S. V *et al.* Roadmap on optical energy conversion. *J. Opt.* **18,** 73004 (2016).
3. Tong, J. K., Hsu, W.-C., Huang, Y., Boriskina, S. V. & Chen, G. Thin-film 'Thermal Well' emitters and absorbers for high-efficiency TPV. *Sci. Reports* **5,** 10661 (2015).
4. Hsu, W.-C. *et al.* Entropic and near-field improvements of thermoradiative cells. *Sci. Rep.* **6,** 34837 (2016).
5. Boriskina, S. *et al.* Enhancement and tunability of near-field radiative heat transfer mediated by surface plasmon polaritons in thin plasmonic films. *Photonics* **2,** 659 (2015).
6. Boriskina, S. V. *et al.* Hybrid optical-thermal devices and materials for light manipulation and radiative cooling. in *Proc. SPIE 9546*, (2015). doi:10.1117/12.2189679
7. Boriskina, S. V. *et al.* Thermal emission shaping and radiative cooling with thermal wells, wires and dots. in *Adv. Photonics 2015* IT2A.3 (OSA, 2015).
8. Boriskina, S. V., Weinstein, L. A., Tong, J. K., Hsu, W.-C. & Chen, G. Hybrid optical–thermal antennas for enhanced light focusing and local temperature control. *ACS Photonics* 3(9), 1714–1722 (2016).
9. Boriskina, S. V. *et al.* Topological darkness of Tamm plasmons for high-sensitivity singular-phase optical detection. *Front. Opt. 2016*, FW2E.2 (2016).

Two-year publications list

1. Boriskina, S. V., Weinstein, L. A., Tong, J. K., Hsu, W.-C., and Chen, G. Hybrid optical–thermal antennas for enhanced light focusing and local temperature control. *ACS Photonics* 3(9), 1714–1722 (2016).
2. Boriskina, S.V., Tong, J. K., Hsu, W.-C., Liao, B., Huang, Y., Chiloyan, V., Chen, G. Heat meets light on the nanoscale. *Nanophotonics* 5, 134–160 (2016).
3. Hsu, W.-C., Tong, J.K., Liao, B., Huang, Y., Boriskina, S.V., Chen, G. Entropic and near-field improvements of thermoradiative cells. *Sci. Rep*. 6, 34837 (2016).
4. Boriskina, S.V., Green, M.A., Catchpole, K., Yablonovitch, E., Beard, M.C., Okada, Y., Lany, S., Gershon, T., Zakutayev, A., Tahersima, M., Sorger, V.J., Naughton, M.J., Kempa, K., Dagenais, M., Yao, Y., Xu, L., Sheng, X., Bronstein, N.D., Rogers, J.A., Alivisatos, A.P., Nuzzo, R.G., Wu, D.M., Wisser, M.D., Salleo, A., Dionne, J., Gordon J.M., Bermel, P., Greffet, J.-J., Celanovic, I., Soljacic, M., Manor, A., Rotschild, C., Raman, A., Zhu, L., Fan, S., Chen G. Roadmap on optical energy conversion. *J. Opt*. 18, 73004 (2016).
5. Tong, J. K., Hsu, W.-C., Huang, Y., Boriskina, S. V. & Chen, G. Thin-film “thermal well” emitters and absorbers for high-efficiency thermophotovoltaics. *Sci. Reports* 5, Article no. 10661 (2015).
6. S.V. Boriskina, J.K. Tong, Y. Huang, J. Zhou, V. Chiloyan, and G. Chen, "Enhancement and tunability of near-field radiative heat transfer mediated by surface plasmon polaritons in thin plasmonic films," *Photonics*, 2(2), 659-683 (2015).
7. S.V. Boriskina, L.A. Weinstein, W.-C. Hsu, J.K. Tong, and G. Chen, "Hybrid optical-thermal devices and materials for light manipulation and radiative cooling," *Proc. SPIE 9546*, Active Photonic Materials VII, 95461U (September 1, 2015); doi:10.1117/12.2189679.
8. Chiloyan, V., Garg, J., Esfarjani, K. & Chen, G. Transition from near-field thermal radiation to phonon heat conduction at sub-nanometre gaps. *Nat. Commun*. **6**, 6755 (2015).

Prediction of Thermal Transport Properties of Materials with Microstructural Complexity

Youping Chen, University of Florida, Gainesville, Florida

Program Scope

The project has led to the development of a concurrent atomistic-continuum (CAC) methodology for simulations of mechanical and thermal transport properties of materials with microstructural complexity. The CAC methodology includes a theoretical formulation that extends Irving-Kirkwood's statistical mechanical theory of transport processes to a concurrent two-level material description, and a computational tool that simulates non-equilibrium processes that take place in materials, with no empirical rule or parameter other than Newton's law and the interatomic potential. Its efficacy has been tested with simulations of dislocations, fracture, and thermal transport in single and polycrystalline SrTiO3 and through demonstration of the nature of phonon-dislocation and phonon-grain boundary interactions.

Recent Progress

(1) A new formalism for deriving atomistic formulas for momentum and heat flux

Our recent theoretical work has examined existing formalisms for the derivation of atomistic formulas for momentum and heat fluxes. Using both analytical and simulation results, we have shown that the flux formulas that are widely used in literature and available in LAMMPS are invalid for transient transport processes or inhomogeneous systems[1, 2]. A new formalism is developed for deriving atomistic momentum and heat fluxes from the integral form of conservation laws. The resulting flux formulas, expressed as the flow of a physical quantity across a surface per unit area and time, are shown to be fully consistent with the physical concepts of momentum and heat fluxes and applicable to transient processes in atomically inhomogeneous systems with general many-body interactions. Shown in Fig. 1 is the molecular dynamics (MD) simulation result of the local heat flux at the interface of a superlattice under pulsed heating. The overlap of the results from the new formula and that obtained from the Continuity Equation indicates the validity of the new flux formula.

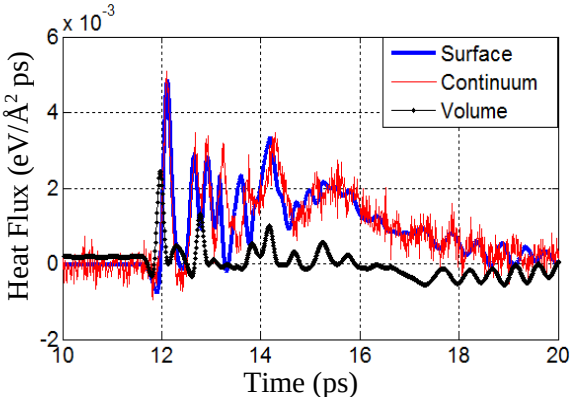

FIG.1 MD simulation result of the heat flux at an interface of a superlattice under pulsed laser heating, where *Surface* denotes the new heat flux formula, *Volume* the volume-averaged formula, which is the most popular heat flux formulas in literature, *Continuum* the energy flux obtained from the *Continuity Equation* through relating the change of the total energy in a region to the flow of energy across the surface enclosing the region.

(2) Demonstration of the nature of phonon-GB scattering

A CAC simulation of the propagation of a heat pulse across ∑19 grain boundaries (GBs) has provided a clear-cut demonstration of a simultaneous ballistic and diffuse phonon transport, as well as a co-existence of coherent and incoherent phonon scattering by GBs, as shown in Fig.2. The results also provide a visual observation of the formation of phonon-focusing caustics (cf. Fig. 2b and c) as well as the GB thermal resistance (Fig. 2e).

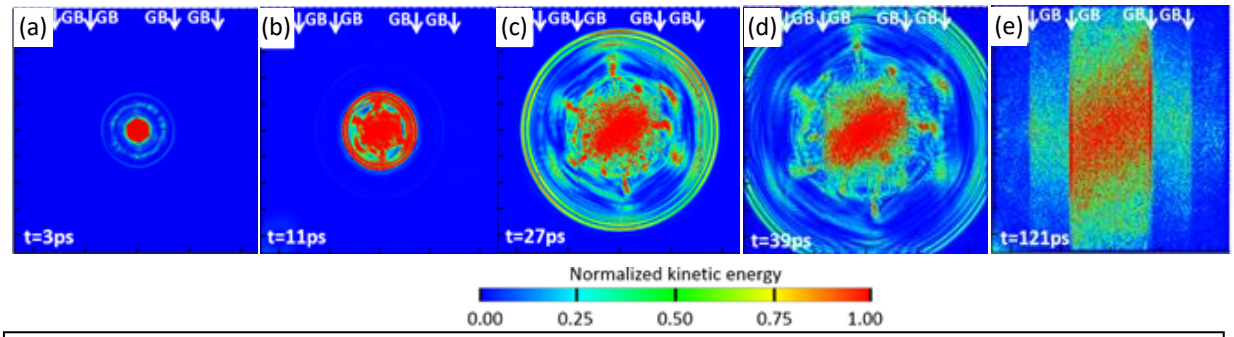

Fig.2. Time sequences of normalized kinetic energy obtained from CAC simulations of a heat pulse (with Bose-Einstein distribution of phonons) propagation across ∑19 GBs (the location of GBs are indicated by white arrows), showing simultaneous ballistic and diffuse transport, a co-existence of coherent and incoherent phonon scattering by GBs, energy caustics as a result of phonon focusing, and GB thermal resistance.

(3) Demonstration of wavelength-dependent GB-scattering and energy transmission

CAC simulations have demonstrated the phonon wavelength (λ)-dependent GB scattering and energy transmission. Shown in Fig. 3a is ballistic transport with 100% energy transmission for λ=20nm; Fig.3b shows dominant ballistic transport with partial spectral scattering by the GBs and 95% energy transmission for λ=10nm. Fig.3c shows non-ballistic transport with coherent GB scattering up to t = 60ps, phonon mode conversion, and 50% energy transmission for λ=5nm. Fig.3d exemplifies that, at t =620ps, phonon transport for λ=5nm becomes diffusive as a result of the phonon-GB scattering; this leads to temperature rise, which in turn gives rise to anharmonic phonon-phonon scattering. Note that the phonon-focusing caustics are very clear in Fig.3c.

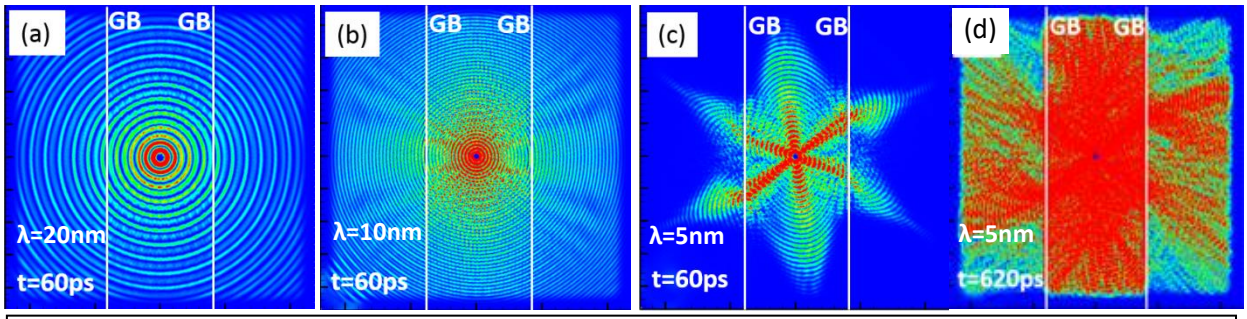

Fig. 3 Kinetic energy plots obtained from CAC simulations of phonon with different wavelength. Note that in (c) energy caustics phonon focusing is clearly observed, which change their directions after across the GBs

(4) Demonstration of the nature of phonon-dislocation scattering

The CAC simulation results of the phonon-dislocation interaction during the propagation of a heat pulse in a single crystal specimen of 5x5 μm demonstrate that (1) the motion of the dislocation is accompanied by radially-shaped wavefronts of phonons ahead of the moving dislocation, and V-shaped wave tails in the wake of the dislocation; (2) there is a co-existence of coherent and incoherent phonon scattering by the dislocations; (3) a dislocation has a very long-range strain field; (4) a moving dislocation emits phonons which indicates multiple phonon scattering mechanisms for phonon-dislocation interaction, including phonon scattering by phonons emitted from moving dislocations.

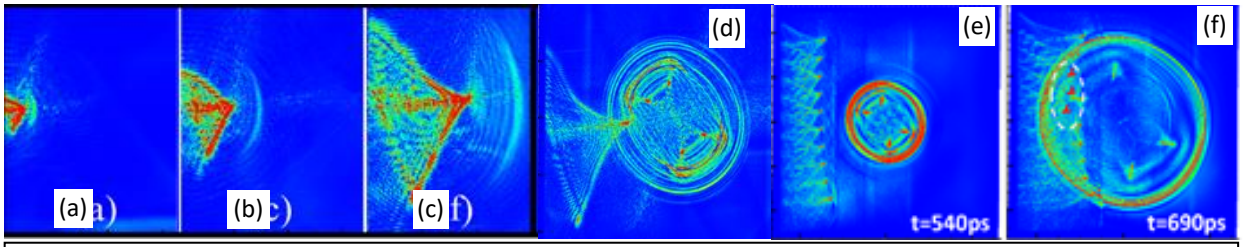

Fig. 4 (a-f) Normalized kinetic energy distribution in CAC simulations of the propagation of dislocations and a heat pulse: (a-c) a moving dislocation before meeting a heat pulse; (d) the dislocation meeting with a propagation heat pulse; (e-f) an array of moving dislocations meeting with a propagation heat pulse, showing partially coherent partially diffuse scattering of the phonons by the array of moving dislocations.

Future Plans

With the support of the DOE Physical Behavior of Materials Program, this research has led to the development of a space- and time-resolved simulation methodology that unifies defect dynamics and phonon transport; the method assumes no mechanisms for phonon transport or criteria for defect nucleation & propagation. CAC simulations can provide a visualization of the fundamental process of wave interference or phonon-defect interaction. It can also be used to study phenomena such as the collective behavior of dislocations, interfaces, and phonons. Our future plan is to further expand the capability of CAC to enable larger-scale simulation for the visualization and understanding of emergent phenomena from complex materials systems.

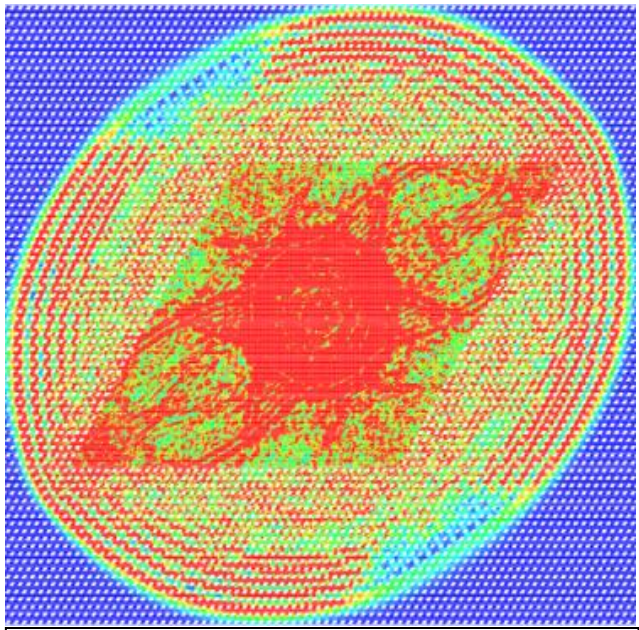

Fig. 5 CAC simulation of heat pulse propagation in a defect-free Si phononic crystal, showing wave interference and coherent-incoherent phonon transport

Publications (03/2015-04/2017) [1-16]

1. Chen, Y. and A. Diaz, *Local momentum and heat fluxes in transient transport processes and inhomogeneous systems.* Physical Review E, 2016. **94**(5): p. 053309.
2. Chen, Y., *The origin of the distinction between microscopic formulas for stress and Cauchy stress.* EPL (Europhysics Letters), 2016. **116**(3): p. 34003.
3. Xiong, L., J. Rigelesaiyin, X. Chen, S. Xu, D.L. McDowell, and Y. Chen, *Coarse-grained elastodynamics of fast moving dislocations.* Acta Materialia, 2016. **104**: p. 143-155.
4. Xiong, L., S. Xu, D.L. McDowell, and Y. Chen, *Concurrent atomistic–continuum simulations of dislocation–void interactions in fcc crystals.* International Journal of Plasticity, 2015. **65**: p. 33-42.
5. Li, W., X. Chen, Z. Zheng, and Y. Chen, *Minimum thermal conductivity in periodically twinned SrTiO 3.* Computational Materials Science, 2016. **112**: p. 107-112.
6. Chen, X., A. Chernatynskiy, L. Xiong, and Y. Chen, *A coherent phonon pulse model for transient phonon thermal transport.* Computer Physics Communications, 2015.
7. Pluchino, P.A., X. Chen, M. Garcia, L. Xiong, D.L. McDowell, and Y. Chen, *Dislocation migration across coherent phase interfaces in SiGe superlattices.* Computational Materials Science, 2016. **111**: p. 1-6.
8. Yang, S. and Y. Chen, *Concurrent Atomistic-Continuum Simulation of Defects in Polyatomic Ionic Materials*, in *Multiscale Materials Modeling for Nanomechanics*2016, Springer International Publishing. p. 261-296.
9. Yang, S., N. Zhang, and Y. Chen, *Concurrent atomistic–continuum simulation of polycrystalline strontium titanate.* Philosophical Magazine, 2015. **95**(24): p. 2697-2716.
10. Yang, S. and Y. Chen, *Concurrent atomistic and continuum simulation of bi-crystal strontium titanate with tilt grain boundary.* Proceedings of the Royal Society A: Mathematical, Physical & Engineering Sciences, 2015. **471**(2175).
11. Xu, S., L. Xiong, Y. Chen, and D.L. McDowell, *Shear stress-and line length-dependent screw dislocation cross-slip in FCC Ni.* Acta Materialia, 2017. **122**: p. 412-419.
12. Xu, S., L. Xiong, Y. Chen, and D.L. McDowell, *Edge dislocations bowing out from a row of collinear obstacles in Al.* Scripta Materialia, 2016. **123**: p. 135-139.
13. Xu, S., L. Xiong, Y. Chen, and D.L. McDowell, *An analysis of key characteristics of the Frank-Read source process in FCC metals.* Journal of the Mechanics and Physics of Solids, 2016. **96**: p. 460-476.
14. Xu, S., L. Xiong, Y. Chen, and D.L. McDowell, *Sequential slip transfer of mixed-character dislocations across Σ3 coherent twin boundary in FCC metals: a concurrent atomistic-continuum study.* npj Computational Materials, 2016. **2**: p. 15016.
15. Xu, S., R. Che, L. Xiong, Y. Chen, and D.L. McDowell, *A quasistatic implementation of the concurrent atomistic-continuum method for FCC crystals.* International Journal of Plasticity, 2015.
16. Xu, S., L. Xiong, Q. Deng, and D.L. McDowell, *Mesh refinement schemes for the concurrent atomistic-continuum method.* International Journal of Solids and Structures, 2016. **90**: p. 144-152.

Pure Spin Current Phenomena

C. L. Chien, Johns Hopkins University

Program Scope

Exploration of pure spin current phenomena and devices, including generation, detection, and amplifications of pure spin currents in ferromagnetic metals, antiferromagnetic insulators, and heavy metals with strong spin orbit coupling.

Recent Progress

Recent advents in spintronics have led to the exploitation of pure spin current, which efficiently transports spin angular momentum accompanied by a minimal of Joule heating and no Oersted field due to the absence of net charge flow. Pure spin current phenomena, such as spin pumping, spin Hall effect and spin Seebeck effect, have been explored in heterostructures of normal metal (NM) and ferromagnetic (FM) metals and insulators. Recently, the exploration of spin current phenomena has been extended also to antiferromagnetic (AF) materials [1].

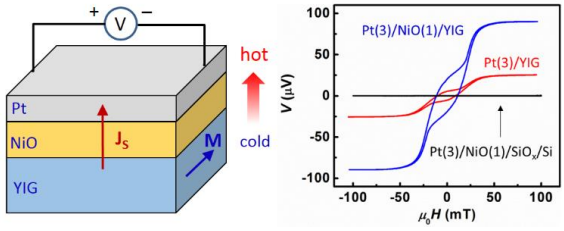

(Left) Schematic of pure spin current injection via the longitudinal spin Seebeck effect and detection by inverse spin Hall effect, (Right) Typical experimental results of thermal spin transport in Pt/NiO/YIG and Pt/YIG, and the null results in Pt/NiO.

Insulators (e.g., SiO_2) usually greatly attenuate, if not completely block, the transport of carriers of charge and spin. However, certain AF insulators, not only transmit, actually enhance pure spin current. We show by inserting a thin AF insulating layer of NiO (also CoO) between the ferrimagnetic insulator yttrium iron garnet (YIG) and the NM, the thermally injected spin current can be enhanced by as much as one order of magnitude.

We use longitudinal spin Seebeck effect [2] in Pt/NiO/YIG to inject pure spin current from ferromagnetic insulator YIG, passing through NiO, into Pt, where the inverse spin Hall effect (ISHE) reveals the enhanced pure spin current [3]. The spin current enhancement is negligible at low temperatures but increasing with temperature and exhibiting a maximum near the Néel temperature of the thin AF layers. The enhancement varies greatly among various *3d*, *4d*, and *5d* metals when NiO is inserted between YIG and these NMs. The enhancement, unrelated to the spin Hall angle of these NMs, has been found to scale linearly with the spin-mixing conductance at the NM/YIG interface measured by spin pumping [4]. The large enhancement and temperature dependence have been accounted for by our theoretical studies [3, 5].

We also show enhanced spin Hall magnetoresistance (SMR) in Pt/NiO/YIG heterostructures with characteristics very different from those in Pt/YIG [6]. This phenomenon indicates that spin current generated by the spin Hall effect in Pt, passing through the insulating NiO, reflected from the NiO/YIG interface, passing through NiO again, and finally detected in Pt via SMR. The SMR in Pt/NiO/YIG shows strong temperature dependence dominated by spin conductance, due to AF magnons and spin fluctuation. Inverted SMR has been observed below a characteristics temperature, which increases with the NiO thickness, suggesting spin-flip reflection from the AF NiO exchange coupled with the YIG [3].

Our results demonstrate the attributes of AF insulator for highly efficient transmission and large amplification of magnon spin current. The employment of AF materials provides a new route for advancing spin physics and devices.

Future Plans

We plan to use Andreev reflection spectroscopy to detect pure spin current in Pt/YIG and Pt/NiO/YIG. We also plan to study the effect of competing spin currents.

References

[1] H. Wang, C. Du, P. C. Hammel, and F. Yang, *Phys. Rev. Lett.* **112**, 197201 (2014).

[2] D. Qu, S. Y. Huang, J. Hu, R. Wu, and C. L. Chien, "Intrinsic spin Seebeck effect in Au/YIG." *Phys. Rev. Lett.* 110, 067206 (2013).

[3] W. Lin, K. Chen, S. Zhang, and C. L. Chien. Enhancement of thermally injected spin current through an antiferromagnetic insulator. *Phys. Rev. Lett.* **116**, 186601 (2016).

[4] C. Du, H. Wang, F. Yang, and P. C. Hammel, *Phys. Rev. Appl.* **1**, 044004 (2014); *Phys. Rev. B* **90**, 140407(R) (2014).

[5] Kai Chen, Weiwei Lin, C. L. Chien, and Shufeng Zhang, "Temperature dependence of angular momentum transport across interfaces," *Phys. Rev. B* ***94***, 054413 (2016).

[6] W. Lin and C. L. Chien. Electrical detection of spin backflow from an antiferromagnetic insulator/$Y_3Fe_5O_{12}$ interface. *Phys. Rev. Lett.* **118**, 067202 (2017).

Publications

[1] D. Qu, S. Y. Huang, and C. L. Chien. Inverse spin Hall effect in Cr: Independence of antiferromagnetic ordering. *Phys. Rev. B* **92**, 020418(R) (2015).

[2] B. F. Miao, S. Y. Huang, D. Qu, and C. L. Chien. Absence of anomalous Nernst effect in spin Seebeck effect of Pt/YIG. *AIP Adv.* **6**, 015018 (2016).

[3] W. Lin, K. Chen, S. Zhang, and C. L. Chien. Enhancement of thermally injected spin current through an antiferromagnetic insulator. *Phys. Rev. Lett.* **116**, 186601 (2016).

[4] W. Lin and C. L. Chien. Electrical detection of spin backflow from an antiferromagnetic insulator/$Y_3Fe_5O_{12}$ interface. *Phys. Rev. Lett.* **118**, 067202 (2017).

Thermoelectric Effects and Spin-Mediated Thermal Properties of Oxide Conductors and Insulators

PI: Joshua L. Cohn, Department of Physics, University of Miami, P.O. Box 248046, Coral Gables, FL 33124

Contact: (305) 284-7123; cohn@physics.miami.edu

Program Scope

This program involves experimental transport studies of low-dimensional, bulk oxide conductors and insulators exhibiting extreme thermoelectric behavior and/or spin-mediated thermal conduction. The thermoelectric investigations were motivated by observations of a giant Nernst effect [1] and very large Seebeck anisotropy above room temperature in quasi-one-dimensional (Q1D) $Li_{0.9}Mo_6O_{17}$ ("Li-purple bronze" or LiPB). Current efforts are focused on understanding its unusual magnetic field-suppressed metallic state below its superconducting transition [2] (T_c=2K). Also an active target of research efforts is the insulating ferrimagnet Cu_2OSeO_3. We have discovered a record-high magnon thermal conductivity at T<10 K in this compound that exceeds that of all known ferro- and ferrimagnets by nearly two orders of magnitude. This work is expected to inform the understanding of long-wavelength magnons and their interactions (e.g. with other magnons, phonons), relevant to the spin-Seebeck effect and the burgeoning field of spin caloritronics.

Recent Progress

Electronic transport in the ground state of the quasi-one-dimensional metal $Li_{0.9}Mo_6O_{17}$:unusually small carrier density

[Manuscript in preparation]

Ongoing investigations of electronic transport in the superconducting ground state of $Li_{0.9}Mo_6O_{17}$ reveal intriguing results. The increasing normal-state resistivity upon approaching the superconducting transition at T_C=2K (Fig. 1) and in the field-suppressed metallic state evident at the lowest T remain poorly understood. Our thermopower (S) measurements (lower panel, Fig. 1) show a saturation in S/T as $T \to 0$ for the field-suppressed metal, as expected for carrier diffusion, $S = \frac{\pi^2}{3}\frac{k_B}{e}\frac{T}{T_F}$, but imply a *very low* Fermi temperature: $T_F \approx 17K$. Both the Nernst signal and Hall resistivity are nonlinear in magnetic field (Fig. 2), demonstrating the two-carrier nature of transport. This supports our previous proposal that LiPB is a compensated metal, based on Nernst data alone[1] at higher T, and extends it to the low-T state. Self-consistent fits to the Hall resistivity and magnetoresistance data using a two-band model yield mobilities and carrier densities shown in Fig. 3. Two-band superconductors pose potentially interesting physics, e.g. different order parameters for electrons and holes or proximity-induced superconductivity for one group of are carriers due to inter-band transitions. Most notable, and consistent with the thermopower data,

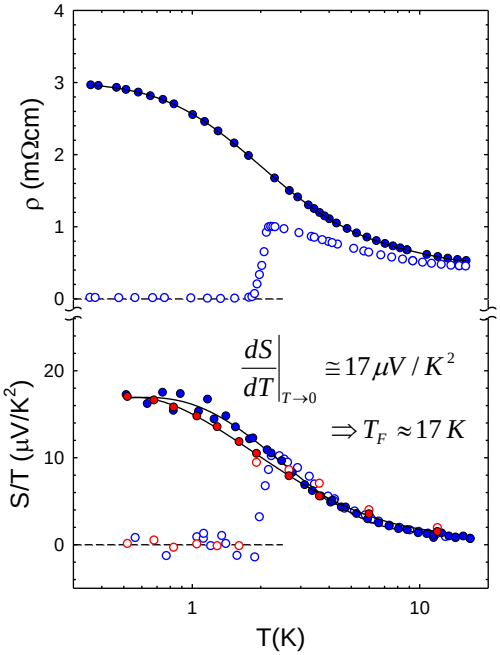

Fig. 1 Resistivity and thermopower divided by T for $Li_{0.9}Mo6O_{17}$ crystals along the quasi-1D chain axis. Red and blue symbols correspond to different crystals.

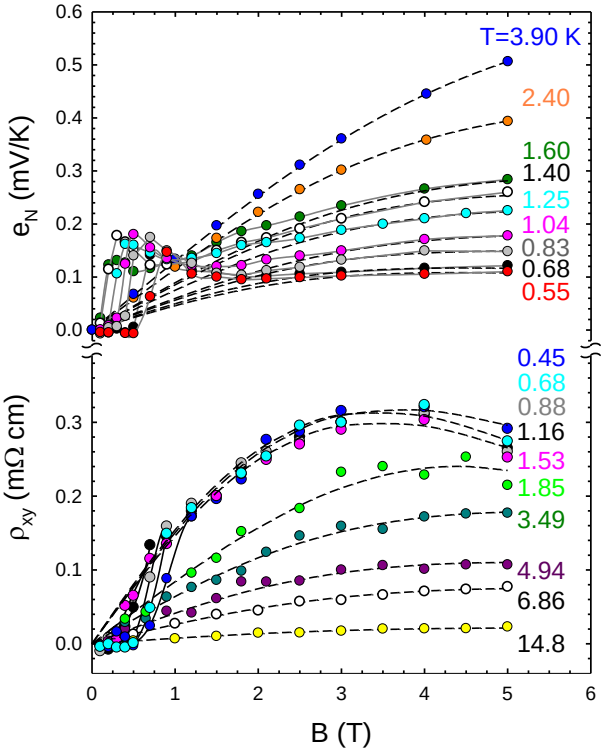

Fig. 2 Nernst signal and Hall resistivity as functions of magnetic field measured for a $Li_{0.9}Mo6O_{17}$ crystal along the quasi-1D chain axis, at various T's through its superconducting transition at 2K.

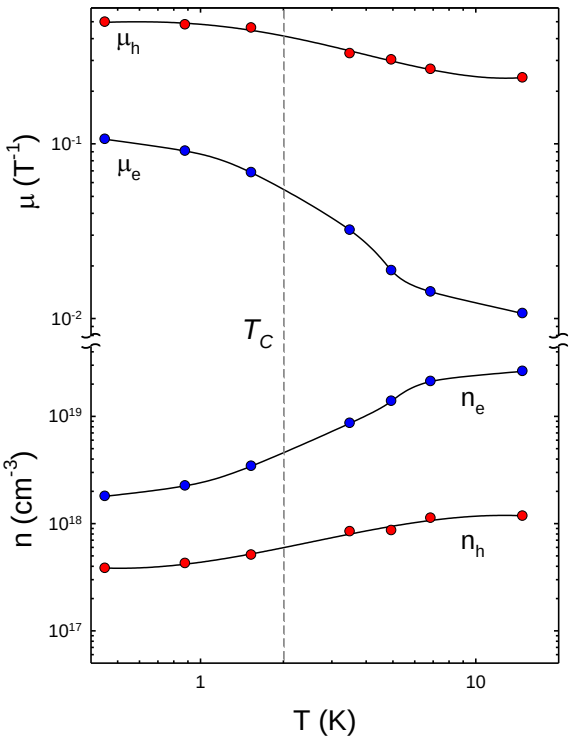

Fig. 3 Carrier mobilities and densities determined from fitting the Hall and magnetoresistance data. The vertical dashed line marks the superconducting transition temperature, T_c=2 K.

the very low carrier densities: (at T_C=2K) ~5 ×10^{18} cm^{-3} (electrons) and 7 ×10^{17} cm^{-3} (holes). These values are among the lowest known for any superconductor.[3] The low carrier densities also underlie the very large Nernst signals observed (e_N, Fig. 2). Note also very large vortex Nernst signals attributable to voltages induced by thermally driven magnetic vortices at low fields in the mixed state.

Such low carrier densities are at odds with the large measured electron-like Fermi surface determined from photoemission. A novel density-wave state[4,5] of electronic origin may suppress all but very small portions of the Fermi surface, but the nature of this competing order and its relation to strong correlations associated with low dimensionality remain unexplained and are a subject of continuing investigation.

Ballistic magnon heat conduction and possible Poiseuille flow in the helimagnetic insulator Cu_2OSeO_3 [Submitted to PRB, *Rapid Communications*]

We have identified a remarkably large magnon thermal conductivity (κ_m) at T<10K in single crystals of the ferromagnetic insulator Cu_2OSeO_3 (Fig. 4) – **the largest ever observed for any known ferro- or ferromagnetic material** — and nearly two orders of magnitude larger than for yttrium-iron garnet (YIG),[6] the best studied system to date. Spin-mediated heat conduction in ferromagnetic materials has been of interest for decades, but a dearth of suitable ferro- or ferrimagnetic insulators exhibiting magnonic heat conduction has limited investigation.

Cu_2OSeO_3 is a cubic material, consisting of a three-dimensional distorted pyrochlore lattice of corner-sharing Cu tetrahedra. Inequivalence of copper sites and strong magnetic interactions within tetrahedra lead to a 3-up-1-down, spin S=1 magnetic state [7,8] that persists above the long-

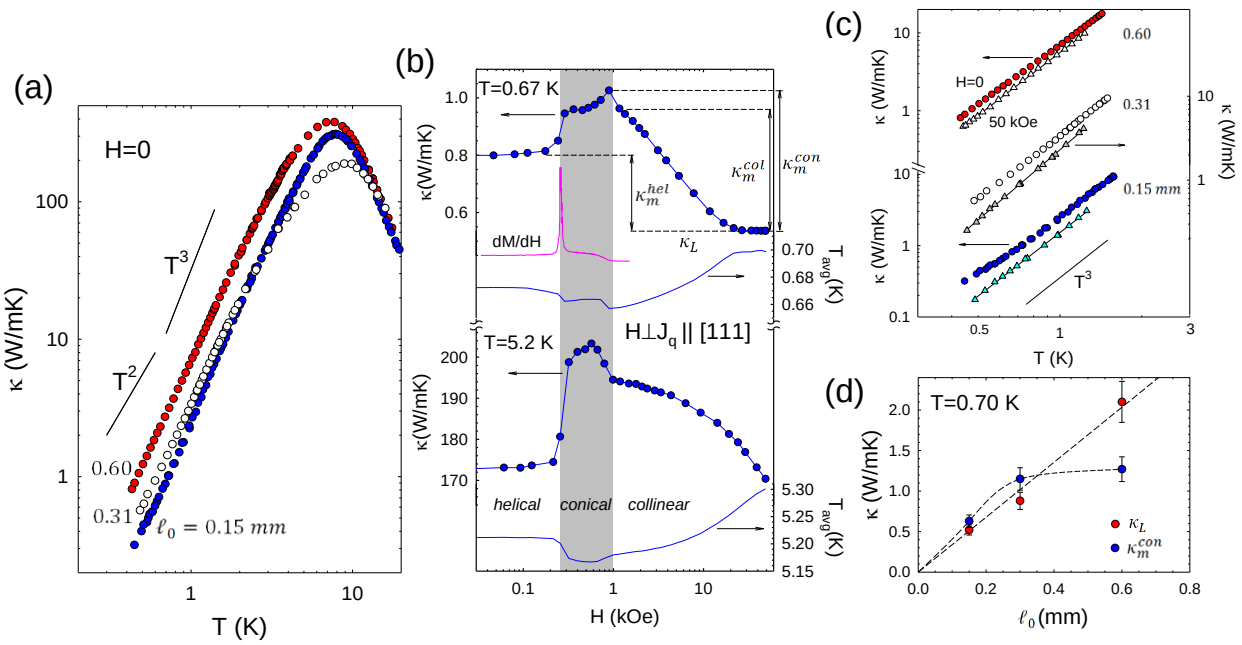

Fig. 4 (a) Thermal conductivity measured along [111] for three specimens (at $H = 0$) labeled by their transverse dimensions ℓ_0. (b) $\kappa(H)$ (left ordinates) and average specimen temperature (right ordinates) at two temperatures for $\ell_0 = 0.15\ mm$. Also shown in the upper panel is dM/dH at 1.9 K. Here H is the internal field, i.e. corrected for demagnetization. The gray shading delineates the different spin phases. The lattice contribution κ_L is identified as the high-field saturation value of κ for $= 0.67\ K$, and κ_m in the helical, conical, and collinear phases as differences (vertical arrows and dashed lines). (c) Low-T data for the same three specimens from (a) at $H = 0$ (circles) and $H = 50\ kOe$ (triangles). The solid lines are linear-least-squares fits. (d) κ_L and κ_m *vs.* ℓ_0 at $T = 0.70\ K$ for the three specimens from (a).

range magnetic ordering temperature $T_C \approx 58\ K$. Dzyaloshinsky-Moriya interactions induce a long-wavelength, incommensurate helical spin structure. At low temperatures, the low-field state is helimagnetic wherein the atomic spins rotate within a plane perpendicular to the helical axis with a wavelength of 62 nm; multiple domains with helices aligned along ⟨100⟩ directions characterize this phase. At $H \geq 300\ Oe$ the helices of individual domains rotate along the field to form a single-domain, conical phase in which spins rotate on the surface of a cone. Further increasing the field narrows the conical angle until $H \geq 1\ kOe$ where the ferrimagnetic, collinear-spin state emerges.

Figure 4 shows the thermal conductivity, $\kappa(T, H)$, for three crystals of Cu_2OSeO_3 oriented with the heat flow along [111] and field perpendicular (along$[1\bar{1}0]$). At low T and high field, a gap is induced for spin waves (when $g\mu_B H \gg k_B T$), thereby suppressing κ_m and allowing for a separation of magnon and lattice contributions [Fig. 4 (b) and (c)]. Figure 5 shows $\kappa_m(T)$ in the conical phase for several crystals compared to that of YIG. A striking feature of data for the least defective specimens (blue and green circles, Fig. 5): κ_m increases faster than $\propto T^2$ such that the magnon mean-free path (mfp) substantially exceeds

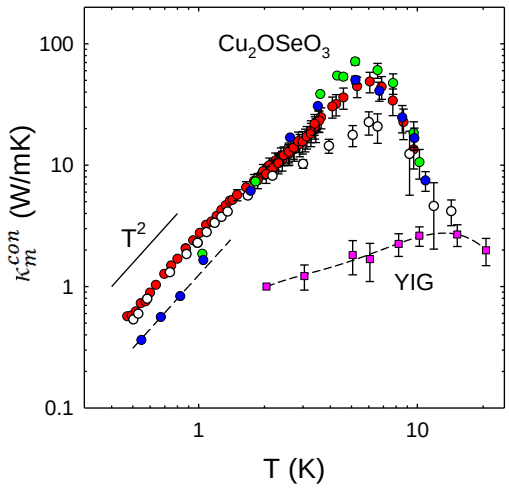

Fig. 5 Conical-phase magnon thermal conductivity for four Cu_2OSeO_3 single crystals. The data for YIG are from Ref. 6.

their transverse dimensions (ℓ_0). We hypothesize that this behavior is associated with Poiseuille flow of magnons, predicted 50 years ago for both phonons and magnons,[9,10,11] but observed only for phonons and only in exceptionally clean materials (e.g. crystalline ^{4}He). When the mfp for normal scattering (ℓ_N) is much shorter than both the transverse dimension (ℓ_0) and the mfp for bulk resistive scattering processes (ℓ_R), quasiparticles undergo many momentum-conserving scattering events before losing their momentum at the specimen boundaries. Under the stringent condition, $\ell_N < \frac{\ell_0}{2} < (\ell_N \ell_R)^{1/2}$, the effective mfp approaches that of a particle undergoing random walk with step size ℓ_N, mfp $\sim \ell_0^2/4\ell_N \gg \ell_0$.

Future Plans

Further investigations of magnetotransport transport in LiPB to 0.3 K with current and heat flow perpendicular to the quasi-1D chains are an immediate priority to clarify the nature of its low carrier density and effective Fermi temperature.

We have begun measurements of the spin-Seebeck effect on Cu_2OSeO_3 crystals to explore the role of the spin phases on interfacial spin current transfer and to test spin-Seebeck models by exploiting the unprecedentedly large and calibrated spin currents available in this compound.

References

1. J. L. Cohn, B. D. White, C. A. M. dos Santos, and J. J. Neumeier, *Giant Nernst Effect and Bipolarity in the quasi-one-dimensional metal, $Li_{0.9}Mo_6O_{17}$,* Phys. Rev. Lett. **108**, 056604 (2012).
2. J.-F. Mercure, A. F. Bangura, X. Xu, N. Wakeham, A. Carrington, P. Walmsley, M. Greenblatt, and N. E. Hussey, *Upper Critical Magnetic Field far above the Paramagnetic Pair-Breaking Limit of Superconducting One-Dimensional Single Crystals*, Phys. Rev. Lett. **108**, 187003 (2012).
3. Xiao Lin, Zengwei Zhu, Benoît Fauqué, and Kamran Behnia, *Fermi Surface of the Most Dilute Superconductor*, Phys. Rev. X **3**, 021002 (2013).
4. C. A. M. dos Santos, B. D. White, Y. K. Yu, J. J. Neumeier,and J. A. Souza, *Dimensional Crossover in the Purple Bronze*, $Li_{0.9}Mo_6O_{17}$ Phys. Rev. Lett. **98**, 266405 (2007).
5. Xiaofeng Xu, A. F. Bangura, J. G. Analytis, J. D. Fletcher, M. M. J. French, N. Shannon, J. He, S. Zhang, D. Mandrus, R. Jin, and N. E. Hussey, *Directional Field-Induced Metallization of Quasi-One-Dimensional $Li_{0.9}Mo_6O_{17}$*, Phys. Rev. Lett. **102**, 206602 (2009).
6. S. R. Boona and J. P. Heremans, *Magnon thermal mean free path in yttrium iron garnet*, Phys. Rev. B **90**, 064421 (2014).
7. Jan-Willem G. Bos, C. V. Colin, and T. T. M. Palstra, *Magnetoelectric coupling in the cubic ferrimagnet Cu_2OSeO_3*, Phys. Rev. B **78**, 094416 (2008).
8. M. Belesi, I. Rousochatzakis, H. C. Wu, H. Berger, I. V. Shvets, F. Mila, and J. P. Ansermet, *Ferrimagnetism of the magnetoelectric compound Cu_2OSeO_3 probed by ^{77}Se NMR*, Phys. Rev. B **82**, 094422 (2010).
9. R. N. Gurzhi, *Thermal Conductivity Of Dielectrics And Ferrodielectrics At Low Temperatures*, Sov. Phys. JETP **19**, 490 (1964).
10. R. A. Guyer and J. A. Krumhansl, *Thermal Conductivity, Second Sound, and Phonon Hydrodynamic Phenomena in Nonmetallic Crystals*, Phys. Rev. **148**, 778 (1966).
11. J.-J. Forney and J. Jäckle, *Second Sound and Heat Conduction of Magnons in the Ferromagnetic Eu-Chalcogenides*, Phys. Kondens. Materie **16**, 147 (1973).

Publications 2015-2017

1. S. Moshfeghyeganeh, A. N. Cote, J. J. Neumeier and J. L. Cohn, *Anisotropic transport in the quasi-one-dimensional semiconductor* $Li_{0.33}MoO_3$, J. Appl. Phys. **119**, 095105 (2016).
2. S. H. Masunaga, A. Rebello, A. T. Schye, N.Prasai, J. J. Neumeier, and J. L. Cohn, Heat capacity, thermal expansion and heat transport in the Han Blue ($BaCuSi_4O_{10}$): Observation of structural phase transitions, J. Phys. Chem. Sol. **85**, 69 (2015).
3. N. Prasai, A. Rebello, A. B. Christian, J. J. Neumeier, and J. L. Cohn, *Phonon-spin scattering and magnetic heat transport in the quasi-one-dimensional spin-1/2 antiferromagnetic chain compound* $CuSb_2O_6$, Phys. Rev. B **91**, 054403 (2015).

Manuscripts submitted or to be submitted in 2017

1. N. Prasai, B. A. Trump, G. G. Marcus, A. Akopyan, S. X. Huang, T. M. McQueen, and J. L. Cohn, *Ballistic magnon heat conduction and possible Poiseuille flow in the helimagnetic insulator* Cu_2OSeO_3, submitted to Phys. Rev. B, Rapid Communications.
2. J. L. Cohn and J. J. Neumeier, *Magnetotransport in the ground state of the low-dimensional superconductor* $Li_{0.9}Mo_6O_{17}$, in preparation.
3. N. Prasai, B. A. Trump, G. G. Marcus, A. Akopyan, S. X. Huang, T. M. McQueen, and J. L. Cohn, *Spin-Seebeck effect and spin transitions in the helimagnetic insulator* Cu_2OSeO_3, in preparation.
4. N. Prasai, A. Rebello, S. H. Masunaga, J. J. Neumeier, and J. L. Cohn, *Phonon-spin resonant scattering and magnetic heat transport in the frustrated spin-1/2 ladder compound,* $BiCu_2PO_6$, in preparation.

Characterization of Functional Nanomachines

PI: Michael F. Crommie
Co-investigators: A. P. Alivisatos, C. Bustamante, M. L. Cohen, S. G. Louie, A. Zettl
UC Berkeley, Physics Department, 366 LeConte Hall #7300, Berkeley, CA 94720
Materials Sciences Division, Lawrence Berkeley National Laboratory
e-mail: crommie@berkeley.edu

Program Scope: The overarching goal of this program is to explore the fundamental science of nanomachines engineered at the atomic scale that have the ability to control energy and information through mechanical transduction processes. We are following two paths toward this goal. First, we are exploring naturally occurring biomotors that take advantage of the molecular mechanisms provided by Nature. Second, we are purposefully designing new synthetic molecular machines in a molecule-by-molecule fashion. This research helps to clarify the mechanisms by which nanomachines convert different forms of energy into directed mechanical activity, as well as how these processes are affected by different environmental dissipation mechanisms. The program is aimed at creating new categories of functional nanomachines, such as bottom-up fabricated synthetic molecular machines that operate on surfaces, top-down fabricated carbon-based nanomachines that exploit the electromechanical properties of nanotubes and graphene, and hybrid nanomachines composed of integrated synthetic and biological components.

This program has six co-investigators whose expertise span physics, chemistry, and biology. The experimental tools utilized by our collaboration range from synthetic chemistry, electron microscopy, and scanned probe techniques (**Alivisatos** and **Crommie**), to photolithography, wet biology, and laser tweezers (**Zettl** and **Bustamante**). **Cohen** and **Louie** provide theoretical support through the use of *ab initio* density functional techniques and molecular dynamics calculations.

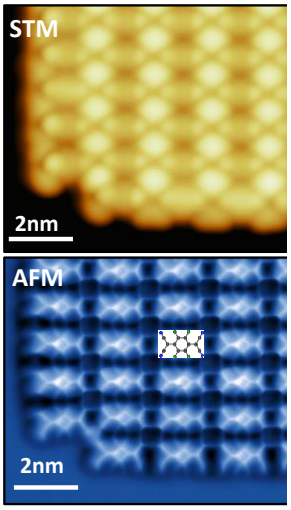

Fig. 1: Top: STM image of close-packed F_4TCNQ island. Bottom: nc-AFM image of same island.

Recent Progress: Here I will highlight our activities within the following subtask of our overall program: *Exploration of Coulomb-driven electromechanical behavior of charged molecules on nanodevice surfaces.* This subtask involves single-molecule-level interrogation of molecular machine systems in four different stages, as follows: Stage 1 - Observation of a new self-assembly mechanism for molecular islands, Stage 2 - Controlling single molecule charging, Stage 3 - Observation of charge alternation in linear molecular arrays, and Stage 4 - Mechanical manipulation of molecular charge configurations in linear arrays.

Stage 1* - *New molecular island self-assembly mechanism: We have discovered a new electromechanically driven self-assembly mechanism for highly charged molecules at the surface of poorly screened materials. For most cases the driving forces when molecules self-assemble are relatively short ranged, such as hydrogen-bonding-like interactions, covalent bonding, metallic bonding, and van der Waals coupling. Like-charged adsorbates typically repel one another at a surface unless these attractive interactions can overcome the Coulomb repulsion. We have discovered a new self-assembly mechanism driven by long-range electrostatic interactions that

causes adsorbates to self-assemble even when "standard" short range forces add up to a net repulsive force between adsorbates.[1]

The system that we have studied involves the use of F_4TCNQ molecules (see sketch, Fig. 1) adsorbed onto a graphene substrate positioned on top of a BN crystal. F_4TCNQ molecules are strongly electronegative and have been shown to repel each other at the surface of graphene supported by a metal.[2] Indeed, we have shown theoretically via *ab initio* techniques that in environments without long-range charge heterogeneity then F_4TCNQ molecules repel each other and do not form close-packed islands.[1] Our experimental investigations, however, show that these molecules do readily self-assemble. F_4TCNQ molecules deposited onto graphene/BN at room temperature were seen to form close-packed island structures that are not commensurate with the underlying graphene lattice (Fig. 1). Single-bond-resolved non-contact AFM images with CO-functionalized tips show that the F_4TCNQ molecules form a rectangular lattice with no signs of covalent bond formation (Fig. 1).

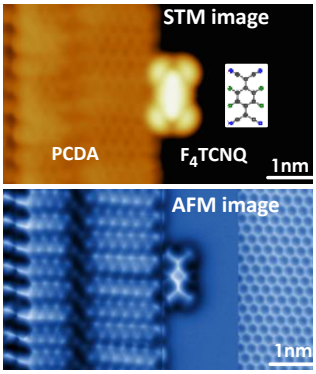

Fig. 2: Top: STM image of single F_4TCNQ molecule adjacent to PCDA island. Bottom: nc-AFM image of same molecule.

This counterintuitive experimental result is explained by long-range electrostatic interactions that are not significant in highly screened environments and that also do not play a role for uniform adsorbate coverages. Our experiment differs from the previously simulated conditions in that the adsorbate distribution is not uniform, thus leading to heterogeneous charge distributions that induce heterogeneity in the work function. Because the molecules carry negative charge, they cause a local work function enhancement when they cluster. Grounded graphene has a uniform electrochemical potential and so charge must then flow into the regions where the molecules cluster, causing them to bind even more strongly to the graphene surface (and thus lowering their overall energy). This novel assembly mechanism was confirmed by *ab initio* calculations which show that increased molecular density on graphene causes an increase in surface work function and also that increased charge density within molecular adsorbate complexes causes enhanced binding energy.[1]

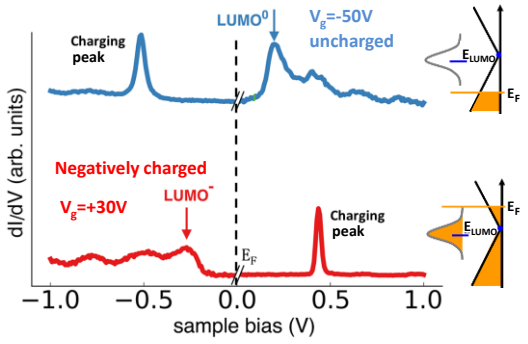

Fig. 3: STS spectra show charge state for molecule back-gated into neutral state (blue curve) and negative state (red curve).

Stage 2 **– Controlling single-molecule charging:** Our exploration of molecular island formation (Stage 1) showed that novel electromechanical effects can occur at the nanoscale when molecules are placed in poorly screened environments. However, we were unable to control molecular behavior at the single molecule level in that study. In order to gain better direct control over molecular electronic behavior, we placed F_4TCNQ molecules onto the surface of gated field-effect transistors (FETs). The idea here is to control the charge on each molecule by electrostatically controlling the surface chemical potential.

We found that isolated molecules on graphene/BN surfaces are often too mobile for high-resolution STM spectroscopy, and so we anchored them at the edge of PCDA islands. PCDA is an inert alkyl chain that is already known to grow well-ordered islands on graphene.[3] Fig. 2 shows an image of a single F_4TCNQ molecule anchored at the edge of a PCDA island at the

surface of a graphene/BN-based FET device. Single-bond-resolved non-contact AFM imaging (lower panel, Fig. 2) shows that F_4TCNQ molecules do not covalently bond with the PCDA chains, thus preserving essential F_4TCNQ electronic properties.[4]

The electronic charge on individual molecules was tuned using the back gate of the graphene/BN FET substrate. Fig.3 shows dI/dV spectra taken at the site of the F_4TCNQ molecule shown in Fig. 2. For negative back gate voltage (V_G = -50 V) the molecular LUMO (lowest unoccupied molecular orbital) is pushed up above the Fermi energy (E_F) (see sketch, upper right side of Fig. 3). Since $E_{LUMO} > E_F$ in this case, the LUMO orbital remains empty and the molecule is charge-neutral. This can be seen in the blue curve of Fig. 3 which shows the LUMO state clearly above the V = 0 point that marks E_F (satellite peaks near the LUMO state are due to phonon-induced excitations). For positive back gate voltage, however, the LUMO state is pulled down in energy below E_F (see sketch, lower right) and so the LUMO fills with an electron and becomes negatively charged.[4] This is seen in the red curve of Fig. 3 where the LUMO state is clearly below E_F.

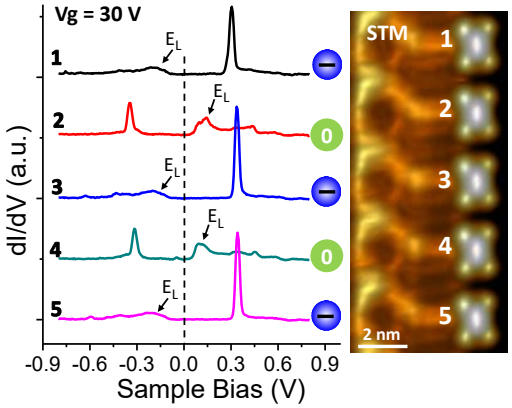

Fig. 4: Right: F_4TCNQ 1D array anchored at PCDA island edge. Left: STS shows charge state of each molecule resulting in alternating charge configuration.

Stage 3 **- Charge alternation in linear arrays:** In order to explore electromechanical behavior at the single-molecule level in a controlled system, we arranged F_4TCNQ molecules into atomically-precise 1D arrays at the straight edges of PCDA islands. Regular molecular arrays form at these edges due to the attraction of F_4TCNQ molecules to maxima in the moiré pattern that arises from the interaction of PCDA islands with graphene (Fig. 4, Fig. 5). By placing the molecules so close to each other in a regular array we were able to precisely control the Coulomb interaction between adjacent molecules (i.e., the repulsive energy felt between molecules when they are charged).

The Coulomb response of the 1D molecular charge array was measured directly for different gate voltages using STM spectroscopy. The charge on individual molecules was determined by the energy location of the molecular LUMO level. If the LUMO level is above E_F then the LUMO for that molecule is empty and it is charge-neutral. On the other hand, if the LUMO level is below E_F then that molecule is negatively charged by one electron. For high positive gate voltage (V_G = 60V) the molecular LUMO levels are pulled down in energy below E_F, and all molecules in the linear arrays under this condition become negatively charged. Similarly, for low gate voltages ($V_G \leq 0$ V) the LUMO levels are pushed above E_F and the linear arrays are completely uncharged (charge-neutral). For "medium" gate voltages ($V_G \approx 30$V), however, we observed novel intermediary charging configurations along molecular arrays. Fig. 4 shows one such array. The LUMO level (marked by "E_L" on spectroscopic curves) is seen to alternate in its location from one side of E_F to the other for each adjacent molecule as the array is traversed. This indicates that molecular charge alternates between q = -e (odd molecules) and q = 0 (even molecules), thus leading to an alternating molecular charge array configuration.

Stage 4 **- Mechanical manipulation of molecular array charge configuration:** We mechanically manipulated the charge configuration of molecular arrays by individually sliding molecules at the end of an array by one moiré unit cell using the tip of an STM. Fig. 5(a) shows

the array before sliding the end molecules. The spatially alternating charge states of the array molecules are labeled to the right of the array ("0" for q = 0, "-" for q = -e) (the charge on the last molecule is not shown because end molecules are always too mechanically unstable to measure directly via STS). We observed that the charge alternation pattern always configures itself so that the last molecule (the end molecule) is negative (this is inferred by extrapolating the charge periodicity). A likely reason for this is that the LUMO wavefunction at the end is less confined by nearest neighbors and so it slightly expands, thus reducing electronic kinetic energy and electron-electron interactions for the end molecule.

Fig.5 (b) shows the same array after sliding the top two molecules of the array up by one moiré unit cell, thus disengaging them from the array below. Because this leaves the new end molecule of the array in a negatively charged state (the low-energy configuration), we expect that this will cause no change in the charge configuration of the molecular array. This was confirmed by subsequent measurement of the molecular charge states along the array, as shown by the charge labels to the right of the array (the red dashed line shows how the same molecule in the array of Fig. 5(a) and Fig. 5(b) retains the same charge state after this manipulation).

Very different behavior is seen when only a *single* additional molecule is disengaged from the end of the array. Fig.5(c) shows the same array after shifting just one molecule from the array's end up by a single moiré unit cell. This exposes a neutral molecule ("0") at the array's end which creates frustration due to the fact that this places the array in a higher-energy electronic configuration. This causes the entire charge configuration of the molecular array to alter so that all previously neutral molecules become charged and vice versa. This is seen experimentally via STS as indicated by the charge labels to the right of the molecular array in Fig. 5(c). The dashed red line shows explicitly that a previously negatively charged molecule has switched to the neutral state. This demonstrates a new mechanism for controlling the long-range charge-state configuration of an entire molecular array via mechanical switching of just one molecule. The information encoded in the end-molecule mechanical state thus propagates through the entire molecular array via highly correlated charge-hopping.

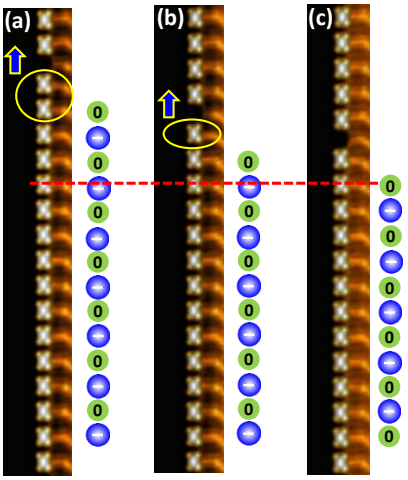

Fig. 5: (a) 1D array charge state before moving end molecules. (b) Charge state after moving two end molecules is the same. (c) Charge state after moving just one end molecule is altered.

Future Plans: A future goal for this subtask is to create synthetic, controllable nanomachines at surfaces by coupling together chemically-designed molecular building blocks. We intend to synthesize these on either graphene or insulating substrates in order to control them via photonic and/or electronic actuation. To accomplish this we will integrate new covalent coupling techniques with photo-active (azobenzene, spiropyran) and electrically active (F_4TCNQ) molecular building blocks on electrostatically gated device surfaces. We will use combinations of photonic and gate-induced actuation to mechanically control the resulting nanomachines, and we will characterize them at the single-molecule level. We will additionally explore the use of metallic nanostructures to both control surface electrostatic potentials and to focus light via plasmonic coupling to better control the mechanical response of surface-bound molecular machines.

References:

[1] H.Z. Tsai, A.A. Omrani, S. Coh, H. Oh, S. Wickenburg, Y.W. Son, D. Wong, A. Riss, H.S. Jung, G.D. Nguyen, G.F. Rodgers, A.S. Aikawa, T. Taniguchi, K. Watanabe, A. Zettl, S.G. Louie, J. Lu, M.L. Cohen, and M.F. Crommie, *ACS Nano* **9**, 12168 (2015).

[2] D. Stradi, M. Garnica, C. Díaz, F. Calleja, S. Barja, N. Martín, M. Alcamí, A. L. Vazquez de Parga, R. Miranda, and F. Martín, *Nanoscale* **6**, 15271 (2014).

[3] J. M. P. Alaboson, C.H. Sham, S. Kewalramani, J.D. Emery, J.E. Johns, A. Deshpande, T. Chien, M.J. Bedzyk, J.W. Elam, M.J. Pellin, and M.C. Hersam, *Nano Lett.* **13**, 5763 (2013).

[4] S. Wickenburg, J. Lu, J. Lischner, H.-Z. Tsai, A. Omrani, A. Riss, C. Karrasch, A. Bradley, H.S. Jung, R. Khajeh, D. Wong, K. Watanabe, T. Taniguchi, A. Zettl, A. Castro Neto, S. Louie, and M. F. Crommie, *Nature Commun*. **7,** 131553 (2016).

DOE Publications Relevant To This Subtask:

[1] Q. Zhou, J. Zhenga, S. Onishia, M.F. Crommie, and A.K. Zettl, *PNAS* 112, 8942 (2015).

[2] R.R. Cloke, T. Marangoni, G.D. Nguyen, T. Joshi, D.J. Rizzo, C. Bronner, T. Cao, S.G. Louie, M.F. Crommie, and F.R. Fischer, *J. Am. Chem. Soc.* **137**, 8872 (2015).

[3] H.Z. Tsai, A.A. Omrani, S. Coh, H. Oh, S. Wickenburg, Y.W. Son, D. Wong, A. Riss, H.S. Jung, G.D. Nguyen, G.F. Rodgers, A.S. Aikawa, T. Taniguchi, K. Watanabe, A. Zettl, S.G. Louie, J. Lu, M.L. Cohen, and M.F. Crommie, *ACS Nano* **9**, 12168 (2015).

[4] G. D. Nguyen, F. Toma, T. Cao, Z. Pedramrazi, C. Chen, D. J. Rizzo , T. Joshi, C. Bronner, Y. C. Chen, M. Favaro, S. G. Louie, F. R. Fischer, M. F. Crommie, *J. Phys. Chem. C,* **120**, 2684 (2016).

[5] A. Riss, A. Pérez Paz, S. Wickenburg, H.-Z. Tsai, D. G. de Oteyza, A. J. Bradley, M. Moreno Ugeda, P. Gorman, H. S. Jung, M. F. Crommie, A. Rubio, and F. R. Fischer, *Nature Chemistry* **8**, 678 (2016).

[6] Dan Lehnherr, Chen Chen, Zahra Pedramrazi, Catherine R. DeBlase, Joaquin M. Alzola, Ivan Keresztes, Emil B. Lobkovsky, Michael F. Crommie and William R. Dichtel, *Chem. Sci.* **7**, 6357 (2016).

[7] D. G. de Oteyza, A. Pérez Paz, Y.-C. Chen, Z. Pedramrazi, A. Riss, S. Wickenburg, H.-Z. Tsai, F. R. Fischer, M. F. Crommie, and A. Rubio, *J. Am. Chem. Soc.* **138**, 10963 (2016).

[8] S. Wickenburg, J. Lu, J. Lischner, H.-Z. Tsai, A. Omrani, A. Riss, C. Karrasch, A. Bradley, H.S. Jung, R. Khajeh, D. Wong, K. Watanabe, T. Taniguchi, A. Zettl, A. Castro Neto, S. Louie, and M. Crommie, *Nature Commun*. **7,** 131553 (2016).

[9] M. M. Ugeda, A.J. Bradley, L. Rodrigo, M. Yu, W. Liu, P. Doak, A. Riss, J. B. Neaton, T. D. Tilley, R. Pérez, and M.F. Crommie, *J. of Phys. Chem. C* **120**, 26448 (2016).

[10] J. Cho, I. V. Pechenezhkiy, L. Berbil-Bautista, S. K. Meier, K. P. C. Vollhardt, and M. F. Crommie, *J. of the Korean Phys. Soc.* **70**, 586 (2017).

Atomic and Mesoscopic Study of Metallic Glasses

T. Egami (egami@utk.edu)
Joint Institute for Neutron Sciences, University of Tennessee, Knoxville, TN 37996
Oak Ridge National Laboratory, Oak Ridge, TN 37831

Program Scope

The primary goal of this project is to gain a fundamental understanding of metallic liquids and glasses that will enable the development of new bulk metallic glasses (BMG) with superior properties. Metallic glasses have exceptionally high strength and have excellent potential for improving the efficiency of energy production, storage and utilization when applied as structural materials. However, the basic science of metallic glasses at the atomistic level remains poorly developed. In this program we establish a fundamental understanding of atomistic mechanisms which control the structural and dynamic properties of metallic liquids and glasses through combination of tightly coupled simulation, theory and experiment. We use a novel approach, based upon the concept of atomic-level stresses and fluctuations in the local topology of atomic connectivity network. The computational effort includes classical and first-principles molecular dynamics (MD) simulation. Experimental studies include neutron and synchrotron x-ray scattering with data processed in novel ways. Based upon our recent breakthrough in understanding the properties of liquids and glasses we develop a general atomistic theory of deformation, dynamics and the glass transition in metallic glasses, which will guide us to the development of metallic glasses with superior properties. We have also successfully applied our approach to the study of superfluidity in ^{4}He and viscosity in water and in interacting colloid. Our long-range goal is to ultimately contribute to the development of the general physics of liquids and glasses.

Recent Progress

1. Time Evolution and Energy Landscape of Metallic Glass

The properties of glass are strongly dependent on thermal history, such as the cooling rate to obtain glass from liquid. Glass is in a non-equilibrium state, and evolves with time, albeit very slowly below the glass transition. Its energy may decrease (structural relaxation) or increase (rejuvenation) with time, depending where it starts from. General description of such time-evolution in the energy landscape has been a very difficult task. Based upon the results of computer simulation using the molecular dynamics (MD) and the activation-relaxation technique (ART) we derived an equation which successfully describes such time-evolution [P23]. The glass state is characterized by the energy of its inherent structure, the state attained by removing the kinetic energy, E_{IS} [1]. The phase diagram of

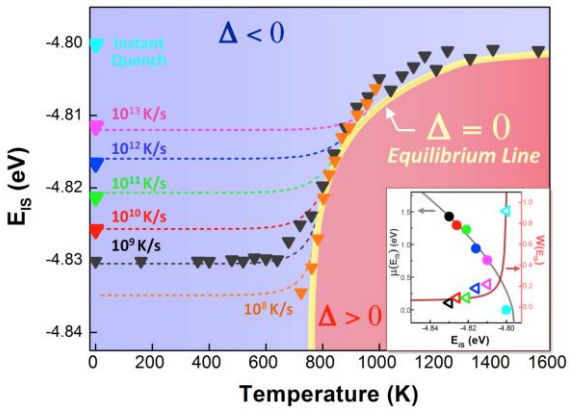

Fig. 1 2D diagram of the energy of the inherent structure, E_{IS}, and temperature. The field shows the structural relaxation regime ($\Delta = E_{IS,final} - E_{IS,initial} < 0$) and the rejuvenation regime ($\Delta > 0$) are separated by the equilibrium line ($\Delta = 0$) [P23].

E_{IS} and temperature (Fig. 1) shows the structural relaxation regime ($\Delta < 0$) and the rejuvenation regime ($\Delta > 0$) are separated by the equilibrium line ($\Delta = 0$), where Δ is the energy difference between the final and initial states. This scheme is based upon the realization that the process of activation from the initial state to the saddle point and the subsequent process of relaxation to the final state are essentially *decoupled*. In other words, when the system is in the high energy saddle point, it is for a brief time in the liquid state, and loses the memory of its history.

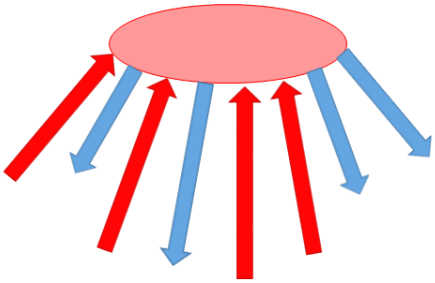

Fig. 2 New perspective of the energy landscape. The saddle point is shared by many minima, and is like the communal assembly point or plaza.

This realization has an enormous impact on our understanding of the potential energy landscape (PEL). The conventional one-dimensional picture of the PEL is extremely misleading. The PEL is highly connected through the common saddle point, as in Fig. 2. The full implication of this discovery, including the explanation of the Kauzmann paradox, will be published soon.

2. Atomic Mechanism of Superfluidity in Liquid ^{4}He

Superfluidity of ^{4}He was discovered in 1938 by Kapitza, and was first explained by Fritz London in terms of the Bose-Einstein condensation (BEC). But ^{4}He liquid is not gas, but is condensed matter with strong atomic correlation. Lev Landau proposed the celebrated roton model without invoking BEC. Both roton and BEC were later confirmed by neutron scattering, but the interplay between BEC and atomic interaction has long been the subject of study. Also, although Landau explained superfluidity from the energy dissipation side, the real-space atomic mechanism of superfluidity has not been known. We used inelastic neutron scattering at the CNCS of the Spallation Neutron Source (SNS) to observe the real-space atom-atom correlation in liquid helium [P22]. Usually the inelastic neutron scattering data are presented in the momentum (Q) and energy

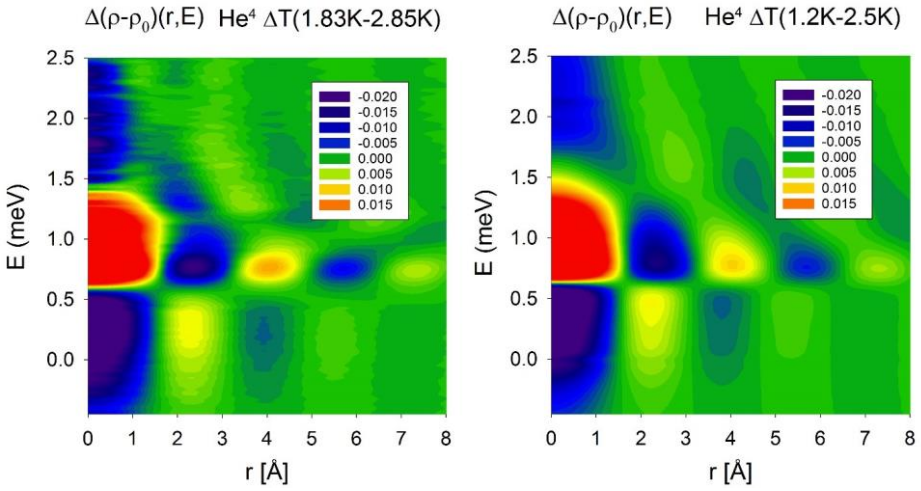

Fig. 3 Difference in the DPDF between the superfluid state and the normal state, (left) determined by inelastic neutron scattering, and (right) calculated by quantum Monte-Carlo method [P22]. They are in excellent agreement.

(E) space as $S(Q, E)$, but it can be brought to real space through the Fourier transformation, in the form of the dynamic pair-density function (DPDF), $g(r, E)$. Fig. 3 shows the difference in the DPDF between the superfluid state and the normal state, determined by neutron scattering (Fig. 3 left) and by quantum Monte-Carlo simulation (Fig. 3 right). The experimental results are in excellent agreement with those of the simulation. The peak discovered in the DPDF at 2.3 Å and 0.3 meV indicates the length-scale and the energy-scale of the real-space mechanism of superfluid. The intensity of this peak is proportional to the superfluid density, indicating that it is directly related to the dynamics of superfluid. This correlation is due to coherent tunneling action of superfluid, and provides the atomistic mechanism of flow in superfluid.

3. Molecular Mechanism of Viscosity in Water

Earlier we identified the atomic origin of viscosity in liquid to be the local topological excitation in the atomic connectivity network; the Maxwell relaxation time, $\tau_M = \eta/G_\infty$ (η: viscosity, G_∞: high frequency shear modulus), is equal to τ_{LC}, the time to lose or gain the neighbor, changing the local topology [2]. To prove this equality we carried out an inelastic x-ray scattering (IXS) measurement of water at the Spring-8 facility in Harima, Japan. The result of IXS was double Fourier-transformed to obtain the van Hove function, $g(r, t)$ [3]. The van Hove function has been known for a long time, but was hardly used, because $S(Q, E)$ has to be determined over wide ranges of Q and E to obtain $g(r, t)$. The result in Fig. 4 [4] shows that the first and second peaks merge, indicating the exchange of the nearest and next nearest neighbors. From this we can determine τ_{LC} to be 0.4 ps, whereas τ_M = 0.32 – 0.4 ps as determined from viscosity. Thus we have proven the equality, $\tau_M = \tau_{LC}$, for the first time. We also made similar measurement for water with NaCl to study the effect of ions on water dynamics.

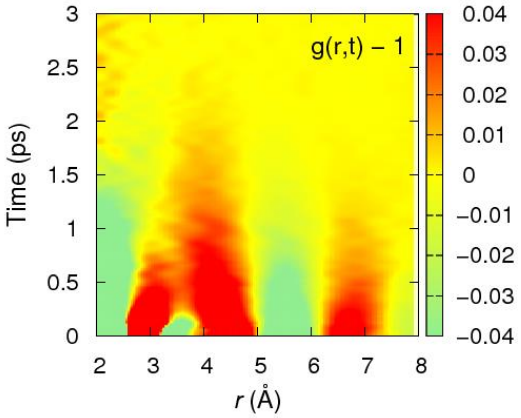

Fig. 4 The van Hove function of water at room temperature [4].

4. Origin of Viscosity in Interacting Colloid

By MD simulation we found that the structure of shear driven metallic liquid is not homogeneous, but is characterized by transient elastic zone (TEZ). The elastic stress generated by TEZ balances the applied stress, thus generates viscosity [5]. The reduction in its size with increasing shear rate explains shear thinning. To prove this mechanism we studied the system of charged silica colloid under shear using small-angle neutron scattering (SANS) [6]. The SANS results were Fourier-transformed to the anisotropic PDF, and confirmed the formation of TEZ. The size of TEZ is reduced with increasing shear rate as predicted (Fig. 5). The behavior is quite different in hard-sphere colloids,

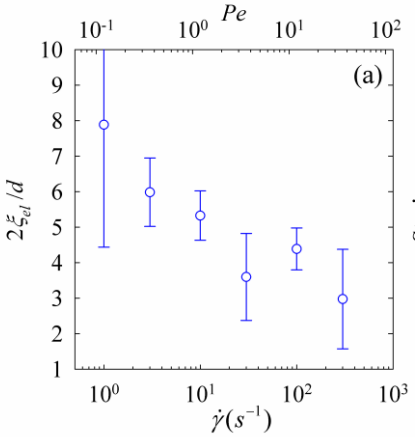

Fig. 5 Dependence of the size of TEZ on shear rate. d is the particle-particle separation. The reduction explains shear-thinning [6].

suggesting that the electro-static interaction among charged colloids is responsible for high viscosity in this system, raising doubts against the popular idea to explain the behavior of interacting colloids in terms of the hard-sphere colloids with appropriately chosen effective particle density.

Future Plans

We have shown that the van Hove function can be experimentally determined by inelastic x-ray or neutron scattering. With this approach we now can directly observe real-space, real-time atomic dynamics which can be compared with the results of molecular dynamics simulation. We are currently working on determining the van Hove function by inelastic neutron scattering of super-cooled liquid metal alloys electro-statically levitated to avoid the contact with a container. By simulation we found that the decay rate of the van Hove function of liquid with time is not uniform as widely assumed, but is dependent on distance between atoms, *r*. At high temperatures the decay rate is linearly dependent on *r*. At low temperatures, however, the *r* dependence is weaker, and with deeper supercooling the TEZ is formed.

Thus the *r*-dependence of the decay rate is deeply related to the non-linear, glassy nature of the supercooled liquid, and the deviation from linearity is an excellent signature of the crossover from the high-temperature gas-like liquid to the low-temperature cooperative liquid [2]. We plan to extend this approach to a wide class of liquids, including colloids. For colloids we should be able to identify the crossover from non-interacting hard-sphere-like colloid at low particle volume fraction to interacting viscous colloid at high particle volume fraction. Currently the philosophy of the field of colloid is that every colloid behavior can be described by the hard-sphere colloid with the appropriate effective volume fraction. Our analysis suggests that such an approach is too simplistic, and will not work. Interacting colloids behave similar to the cooperative supercooled liquid below the crossover temperature, and cannot be modeled by hard-sphere systems.

Our long-range plan is to use our approach as the basis to activate the field of "liquid-state-physics" as the basis for "glass physics". It will be an important effort by itself, but may also be very useful to soft-matter physics and eventually to bio-medical fields.

References

1. S. Sastry, P. G. Debenedetti, and F. H. Stillinger, "Signatures of distinct dynamical regimes in the energy landscape of a glass-forming liquid", *Nature* **393,** 554 (1998).
2. T. Iwashita, D. M. Nicholson and T. Egami, "Elementary Excitations and Crossover Phenomenon in Liquids", *Phys. Rev. Lett.*, **110,** 205504 (2013).
3. L. Van Hove, "Correlations in space and time and Born approximation scattering in systems of interacting particles", *Phys. Rev*. **95,** 249-262 (1954).
4. T. Iwashita, B. Wu, W.-R. Chen, S. Tsutsui, A.Q. R. Baron and T. Egami, "Seeing Real-Space Dynamics of Liquid Water through Inelastic X-Ray Scattering", *unpublished*.
5. T. Iwashita and T. Egami, "Atomic Mechanism of Flow in Simple Liquids under Shear", *Phys. Rev. Lett.*, **108,** 196001 (2012).
6. Zhe Wang, Takuya Iwashita, Lionel Porcar, Yangyang Wang, Yun Liu, Luis E. Sánchez-Díaz, William A. Hamilton, Takeshi Egami and Wei-Ren Chen, "Structure of Viscous Colloid under Shear by Neutron Scattering", *unpublished*.

Publications ('15 - '17)

P1. W. Dmowski, Y. Tong, T. Iwashita, Y. Yokoyama and T. Egami, "Universal Mechanism of Thermo-Mechanical Deformation in Metallic Glasses", *Phys. Rev. B,* **91** 060101(R) (2015).

P2. Y. Fan, T. Iwashita and T. Egami, "Crossover from Localized to Cascade Relaxations in Metallic Glasses", *Phys. Rev. Lett.*, **115,** 045501 (2015).

P3. Y. Wu, H. Bei, Y. L. Wang, Z. P. Lu, E. P. George, Y. F. Gao, "Deformation-induced spatiotemporal fluctuation, evolution and localization of strain fields in a bulk metallic glass", *International J. of Plasticity,* **71,** 136 (2015).

P4. J. S. Langer, "Shear-Transformation-Zone Theory of Yielding in Athermal Amorphous Materials", *Phys. Rev. E* **92,** 012318 (2015).

P5. J. S. Langer, "Statistical Thermodynamics of Strain Hardening in Polycrystalline Solids", *Phys. Rev. E* **92,** 032125 (2015).

P6. T. Egami, M. Ojha, O. Khorgolkhuu, D. M. Nicholson and G. M. Stocks, "Local Electronic Effects and Irradiation Resistance in High-Entropy Alloys", *J. of Metals,* **67,** 2345 (2015).

P7. A. Jaiswal, T. Egami and Yang Zhang, "Atomic-Scale Dynamics of a Model Glass-Forming Metallic Liquid: Dynamical Crossover, Dynamical Decoupling, and Dynamical Clustering", *Phys. Rev. B,* **91,** 134204 (2015).

P8. O. Haruyama, K. Yoshikawa, R. Wada, Y. Yamazaki, Y. Yokoyama and T. Egami, "Pre-Annealing Effects on Structural Relaxation in $Zr_{55}Cu_{30}Ni_5Al_{10}$ Bulk Metallic Glasses just below the Glass Transition", *Mater. Trans. JIM,* **56,** 648 (2015).

P9. A. Jaiswal, A. Podlesynak, G. Ehlers, R. Mills, S. O'Keeffe, J. Stevick, J. Kempton, G. Jelbert, W. Dmowski, K. Lokshin, T. Egami and Y. Zhang, "Coincidence of Collective Relaxation Anomaly and Specific Heat Peak in a Bulk Metallic Glass-Forming Liquid", *Phys. Rev. B,* **92,** 024202 (2015).

P10. M. E. Blodgett, T. Egami, Z. Nussinov and K. F. Kelton, "Proposal for Universality in the Viscosity of Metallic Liquids", *Nature Sci. Rep.* **5,** 13837 (2015)

P11. Ling Li, James Morris, Michael Koehler, Zhiling Dun, Haidong Zhou, Jiaqiang Yan, David Mandrus, Veerle Keppens, "Structural and Magnetic Phase Transitions in $EuTi_{1-x}Nb_xO_3$", *Phys. Rev. B* **92**, 024109 (2015)

P12. "Local Structures of High-Entropy Alloys (HEAs) on Atomic Scales: An Overview", H. Diao, L. J. Santodonato, Z. Tang, T. Egami and P. K. Liaw, *J of Metals,* **67,** 2321 (2015)

P13. B. Wu, T. Iwashita and T. Egami, "Anisotropy of Stress Correlations in Two-Dimensional Liquids and a Pseudospin Model", *Phys. Rev. E*, **92,** 052303 (2015).

P14. Y. Wu, A. D. Stoica, Y. Ren, D. Ma, Y. F. Gao and H. Bei, "Direct Synchrotron X-ray Measurements of Local Strain Fields in Elastically and Plastically Bent Metallic Glasses", *Intermetallics* **67,** 132 (2015).

P15. W. Li, Y. F. Gao and H. Bei, "On the Correlation between Microscopic Structural Heterogeneity and Embrittlement Behavior in Metallic Glasses", *Nature Sci. Rep.* **5,** 14786; doi: 10.1038/srep14786 (2015).

P16. T. Egami, Y. Tong and W. Dmowski, "Deformation in Metallic Glasses Studied by Synchrotron X-Ray Diffraction", *Metals,* **6,** 22 (2016).

P17. T. Egami, "How to Characterize Disorder", *Nucl. Instrum. Method B,* **374,** 2 (2016).

P18. M. L. Johnson, M. E. Blodgett, K. A. Lokshin, N. A. Mauro, J. Neuefeind, C. Pueblo, D. G. Quirinale, A. J. Vogt, T. Egami, A. I. Goldman and K. F. Kelton, "Measurements of Structural and Chemical Order in $Zr_{80}Pt_{20}$ and $Zr_{77}Rh_{23}$ Liquids", *Phys. Rev. B,* **93,** 054203 (2016).

P19. T. Egami, Y. Fan and T. Iwashita, "Mechanical Deformation in Metallic Liquids and Glasses: From Atomic Bond Breaking to Avalanches", in *Avalanches in Functional Materials and Geophysics*, ed. E. Salje, A. Saxena and A. Planes (Springer Verlag, Berlin, 2016) Chapt. 10, pp. 199-225.

P20. W. D. Li, Y. F. Gao and H. Bei, "Instability Analysis and Free Volume Simulations of Shear Band Directions and Arrangements in Notched Metallic Glasses", *Nature Sci. Rep.* **6,** 34878 (2016).

P21. W. D. Li, H. Bei and Y. F. Gao, "Effects of Geometric Factors and Shear Band Patterns on Notch Sensitivity in Bulk Metallic Glasses", *Intermetallics* **79,** 12-19 (2016).

P22. W. Dmowski, S. O. Diallo, K. Lokshin, G. Ehlers and T. Egami, "Observation of Dynamic Atom-Atom Correlation in Liquid Helium in Real Space", *Nature Communications,* **8,** 15294 (2017); DOI: 10.1038/ncomms15294.

P23. Yue Fan, T. Iwashita, and T. Egami, "Energy Landscape-Driven Nonequilibrium Evolution of Inherent Structure in Disordered Material", *Nature Communications, in press.*

Combined Coherent Manipulation and Single-Shot Measurement of an Electron Spin in a Quantum Dot

PI: Edward B. Flagg
West Virginia University, Department of Physics and Astronomy
Morgantown, WV 26506

Program Scope

We are pursuing a scheme to measure the spin-state of a single electron trapped in an optically active quantum dot via a cycling transition induced by the AC Stark effect. The spin degree of freedom of an electron in a quantum dot (QD) is a candidate system to act as a quantum bit. The necessary capabilities of a single quantum bit are initialization, manipulation, and measurement of its quantum state. Optical spin initialization and manipulation are allowed by a magnetic field in the Voigt configuration that modifies the polarization selection rules of the transitions [1]. The lack of a cycling transition in the Voigt configuration, however, makes a single-shot measurement of the spin-state very difficult. Spin-state measurement can be accomplished in the Faraday magnetic field configuration [2], but the optical selection rules preclude spin manipulation. Therefore, there is a critical need for a method to perform a single-shot measurement of the electron spin-state while maintaining the initialization and manipulation capabilities of the Voigt configuration. Achievement of this measurement is an important problem because without the ability to perform all three operations, optically active QDs will not be viable quantum bits.

The central hypothesis driving the proposal is that the AC Stark effect is capable of modifying the optical transitions to allow a spin-preserving cycling transition, which can be used for a single-shot measurement. The hypothesis was formulated based on published evidence that the AC Stark effect of an off-resonant laser can both modify the transition energies of a QD [3,4] and manipulate the electron spin [1,5]. The rationale for the proposed research is that successful completion of the objective would result in all the prerequisite single-qubit operations for quantum computation using QDs. We have performed preliminary simulations of the proposed experimental situations indicating that the single-shot measurement scheme can be successfully accomplished [6].

We propose to test our central hypothesis and thereby achieve the overall objective of this project by addressing the following specific objectives:

Objective #1: Characterize the cycling transitions induced by the AC Stark effect on a QD in a Voigt configuration magnetic field. Our working hypothesis is that an AC Stark shift much larger than the Zeeman splitting in a Voigt configuration will result in a "pseudo-Faraday" configuration with spin-preserving cycling transitions.

Objective #2: Demonstrate single-shot measurement of the electron spin-state using spin-preserving cycling transitions. Our working hypothesis is that the cycling transitions will be sufficiently spin-preserving so as to be suitable for a high-fidelity measurement of the spin-state faster it is disturbed by the measurement back-action.

Objective #3: Demonstrate spin initialization and manipulation in the Voigt configuration, with single-shot spin measurement under AC Stark shift. Our working hypothesis is that the system can be reconfigured more rapidly than the electron spin lifetime and that the reconfiguration does not additionally disturb the spin-state.

Recent Progress

Funding for this project began at the end of 2016. In the following four months we have arranged and aligned the optical equipment to prepare it for the required experiments.

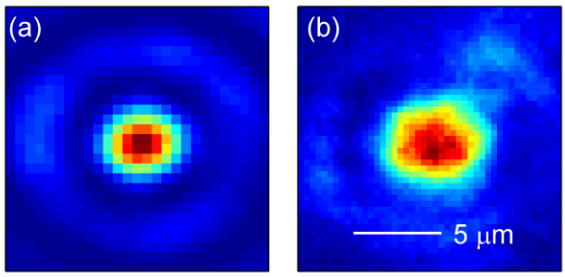

Figure 1. Fluorescence images of resonantly excited quantum dots. (a) Excitation via a waveguide mode. (b) Confocal excitation with cross-polarized detection.

The AC Stark laser that switches between Voigt and pseudo-Faraday configurations must be circularly polarized, which requires that it be applied normal to the sample surface and have a fully controllable polarization. In order to accomplish this experimental requirement, we have combined the two major resonant excitation techniques used in quantum dot experiments: cross-polarized confocal excitation [7], and side excitation in a waveguide mode [8,9]. Each of these techniques has its own advantages and disadvantages. Cross-polarized excitation allows any polarization to be used for excitation, but restricts the detection to an orthogonal polarization. It will be used to apply the AC Stark laser to the quantum dot since it allows the necessary circular polarization. In comparison, side excitation preserves complete freedom in the detection polarization by utilizing the orthogonality between the propagation modes of excitation and detection beams to suppress the laser scattering. However, only one linear polarization is allowed for the excitation laser. Side excitation will be used to resonantly excite the cycling transitions in the pseudo-Faraday configuration. Since those transitions will be circularly polarized, the restricted linear polarization of side excitation will still be sufficient for excitation. Figure 1 shows resonantly excited fluorescence from a single QD in both cases: side excitation through a waveguide mode and cross-polarized confocal excitation.

In addition to specific requirements on excitation, we must also be able to measure the spectral and polarization properties of the fluorescence. This requires recording high resolution emission spectra of the fluorescence in the pseudo-Faraday configuration. A spectrometer by itself does not have sufficient spectral resolution and must be preceded by a tunable narrow-band filter like a Fabry-Perot interferometer (FPI). One difficulty of tunable FPIs is that they must be stabilized. This often requires an additional tunable laser to which the FPI is locked by an optical feedback mechanism. The laser itself must be stable and can be very expensive – in the range of tens of thousands of dollars. We have developed an alternative active stabilization scheme which uses a relatively inexpensive fixed-wavelength stabilized HeNe laser, and detectors and electronics based on the Arduino platform. The mirrors in the FPI are mechanically linked to mirrors in a shearing interferometer, which produces a spatial interference pattern from a monochromatic laser, so there is no tuning of the laser required. Rapid measurement and analysis

of the interference pattern allows determination of the spacing between the mirrors, which can be used as feedback to a piezoelectric actuator that controls the spacing. We have been able to stabilize the mirror spacing of the interferometer to less than 0.30 nm RMS variation over about an hour. Such precision is suitable for the necessary high-resolution measurements of the quantum dot emission spectrum. Figure 2 shows the variation in the separation of the FPI mirrors using this optical feedback method. The cavity length is stable to within 0.14 nm.

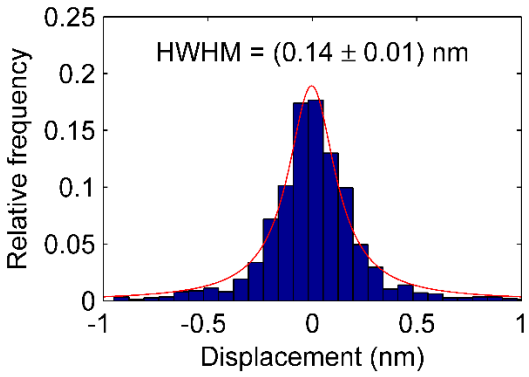

Figure 2. Variation of the relative displacement of the Fabry-Perot mirrors with optical feedback. The red curve is a Lorentzian fit with a half-width at half-max of 0.14 nm.

Now that the required capabilities in both excitation and detection have been combined in our experimental setup, we are prepared to finish the experiments comprising Objective 1.

Future Plans

The next step in this project is to measure the energy level shift caused by an AC Stark laser in a Voigt field. To change the polarization selection rules to produce cycling transitions, the AC Stark shift must be greater than the Zeeman splitting caused by the Voigt magnetic field. In order to determine over what range of magnetic field amplitude the reconfiguration from Voigt to pseudo-Faraday is feasible, we must measure the maximum AC Stark shift we can induce. We will measure the emission spectrum of the QD both in a Voigt field and with the application of the AC Stark laser. The shift in the QD energy states will be extracted from the spectra and recorded as a function of the AC Stark laser intensity. This will be accomplished via confocal excitation of the QD sample by both the AC Stark laser and a laser tuned to the energy of the QD wetting layer simultaneously. The circularly-polarized, red-detuned AC Stark laser will induce a shift of the QD energy states, while the wetting layer excitation laser will populate those states, causing fluorescence. The fluorescence will be spectrally distinguished from the laser scattering by a spectrometer, and high-resolution spectra will be recorded using a combination of the spectrometer and a scanning Fabry-Perot interferometer. At the conclusion of this study we expect to have measured the magnitude of the AC Stark shift that can be induced in the QD energy levels in a Voigt configuration magnetic field.

References

1. Berezovsky, J., Mikkelsen, M. H., Stoltz, N. G., Coldren, L. A., and Awschalom, D. D. "**Picosecond Coherent Optical Manipulation of a Single Electron Spin in a Quantum Dot**" *Science* 320, no. 5874 (2008): 349–352. doi:10.1126/science.1154798
2. Delteil, A., Gao, W., Fallahi, P., Miguel-Sanchez, J., and Imamoğlu, A. "**Observation of Quantum Jumps of a Single Quantum Dot Spin Using Submicrosecond Single-Shot Optical Readout**" *Physical Review Letters* 112, no. 11 (2014): 116802. doi:10.1103/PhysRevLett.112.116802

3. Unold, T., Mueller, K., Lienau, C., Elsaesser, T., and Wieck, A. D. "**Optical Stark Effect in a Quantum Dot: Ultrafast Control of Single Exciton Polarizations**" *Physical Review Letters* 92, no. 15 (2004): 157401. doi:10.1103/PhysRevLett.92.157401
4. Muller, A., Fang, W., Lawall, J., and Solomon, G. S. "**Emission Spectrum of a Dressed Exciton-Biexciton Complex in a Semiconductor Quantum Dot**" *Physical Review Letters* 101, no. 2 (2008): 027401. doi:10.1103/PhysRevLett.101.027401
5. Press, D., Ladd, T. D., Zhang, B., and Yamamoto, Y. "**Complete Quantum Control of a Single Quantum Dot Spin Using Ultrafast Optical Pulses**" *Nature* 456, no. 7219 (2008): 218–221. doi:10.1038/nature07530
6. Flagg, E. B. and Solomon, G. S. "**Optical Spin Readout Method in a Quantum Dot Using the AC Stark Effect**" *Physical Review B* 92, no. 24 (2015): 245309. doi:10.1103/PhysRevB.92.245309
7. Kuhlmann, A. V., Houel, J., Brunner, D., Ludwig, A., Reuter, D., Wieck, A. D., and Warburton, R. J. "**A Dark-Field Microscope for Background-Free Detection of Resonance Fluorescence from Single Semiconductor Quantum Dots Operating in a Set-and-Forget Mode**" *Review of Scientific Instruments* 84, no. 7 (2013): 073905. doi:10.1063/1.4813879
8. Muller, A., Flagg, E. B., Bianucci, P., Wang, X. Y., Deppe, D. G., Ma, W., Zhang, J., Salamo, G. J., Xiao, M., and Shih, C. K. "**Resonance Fluorescence from a Coherently Driven Semiconductor Quantum Dot in a Cavity**" *Physical Review Letters* 99, no. 18 (2007): 187402. doi:10.1103/PhysRevLett.99.187402
9. Flagg, E. B., Muller, A., Robertson, J. W., Founta, S., Deppe, D. G., Xiao, M., Ma, W., Salamo, G. J., and Shih, C. K. "**Resonantly Driven Coherent Oscillations in a Solid-State Quantum Emitter**" *Nature Physics* 5, no. 3 (2009): 203–207. doi:10.1038/nphys1184

Publications

KC, R., Lander, G., Chen, D., Nichols, C., Flagg, E.B., "Tunable Fabry-Perot Interferometer Optically Stabilized using Fixed-Wavelength Reference Laser" *in preparation.*

Actinide Materials Under Extreme Conditions

Krzysztof Gofryk, Idaho National Laboratory, Idaho Falls, ID 83415

Program Scope

The goal of this project is to understand phonon, spin and charge transport in actinide materials by investigating the interactions between lattice vibrations, spins and carriers. These couplings are probed by extensive transport, thermodynamic, and spectroscopic measurements performed under extreme conditions such as high-pressure, low temperatures, and high magnetic fields. The characteristic responses of these materials to extreme experimental conditions will help to elucidate the underlying transport mechanisms, provide decisive data for theoretical models, and have broad implications across actinide materials science generally.

Recent Progress

Thermoelectric properties of $PuCoGa_5$: in order to advance the fundamental understanding of actinide materials and their thermophysical properties, all aspects of the so-called 5*f*-electron challenge have to be addressed. This problem is well emphasized in the first plutonium based superconductor, $PuCoGa_5$ (T_c = 18.5 K) [1]. After a decade of investigation, the mechanism responsible for Cooper pair formation remains unknown, as does the role of 5*f*-electrons. By measuring its thermoelectric properties we show that Seebeck coefficient of $PuCoGa_5$ is strongly enhanced and its magnitude and temperature dependence is characteristic of intermediate valence systems, indicating the presence of the 5*f*-band in close proximity to the Fermi level (see Fig.1a). The results obtained point to the itinerant nature of the 5*f*-electrons in $PuCoGa_5$ and their importance for unconventional superconductivity. The electronic structure parameters for $PuCoGa_5$ obtained from the thermoelectric measurements are shown to be related to those obtained from photoemission and this relation can be extended to other valence fluctuating correlated systems. The proposed correlation between photoemission and thermoelectric power opens up new possible approaches to research on the electronic structure of correlated actinide materials.

Piezomagnetism and magnetoelastic memory in uranium dioxide: uranium dioxide (UO_2) is a prime nuclear fuel and perhaps the most thoroughly studied actinide material to date. Its thermal and magnetic properties remain, however, a puzzle resulting from strong couplings between magnetism and lattice vibrations. The magnetic state of this cubic material is characterized by a non-collinear antiferromagnetic structure [2] and multidomain Jahn-Teller distortions [3] that could be behind novel thermal properties [4]. We show that single crystals of UO_2, subjected to magnetic fields up to 95 T in the magnetic state, exhibit the abrupt appearance of positive linear magnetostriction leading to a trigonal distortion (see Fig.1b). Upon reversal of the field the linear term also reverses sign, a hallmark of piezomagnetism. The switching

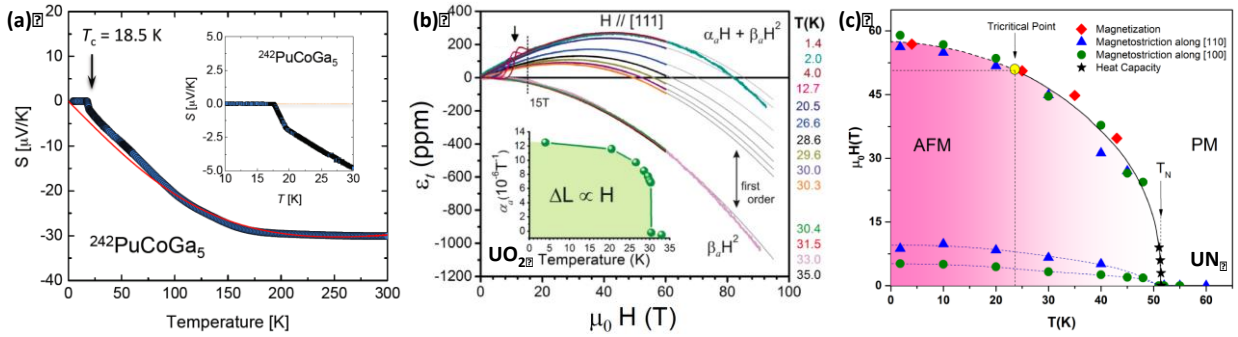

Figure 1 (a) The temperature dependence of the thermoelectric power of $PuCoGa_5$. A superconducting transition is clearly visible as a sharp transition to zero at 18.5 K (see the inset). In the normal state, the temperature dependence of S(T) is characteristic of intermediate valence systems; (b) Isothermal axial strain ε_a vs. H||[111] at different temperatures. Grey lines are fits to the expression $\alpha_a H+\beta_a H^2$. Linear magnetoelastic coefficient $\alpha_a(T)$ vs. T (inset); (c) The magnetic phase diagram of UN. A solid yellow circle marks the tricritical point at T_{tri}~24 K and H_{tri}~52 T. The dashed and solid lines mark lines of first and second order transition, respectively and serve as a guide to the eye.

phenomenon occurs at 18 T and persists during subsequent field reversals, demonstrating robust magneto-elastic memory. This is the first example of piezomagnetism in an actinide spin system and the magneto-elastic memory loop here is nearly an order of magnitude wider in field than those previously observed [5], making UO_2 the hardest piezomagnet known. To account for the observed phenomena we propose a model including a strong magnetic anisotropy, elastic, Zeeman, Heisenberg exchange, and magnetoelastic contributions to the total energy.

Tricritical point from high-field magnetoelastic and metamagnetic effects in UN: uranium nitride (UN) is one of the most studied actinide materials as it is a promising fuel for the next generation of nuclear reactors. UN crystalizes in a face center cubic crystal structure and orders antiferromagnetically below the Neel temperature T_N = 52 K. Despite large experimental and theoretical efforts, some of the fundamental questions such as degree of 5*f*–electron localization/delocalization and its relationship to magneto-vibrational properties are not resolved yet. We show that the magnetostriction of UN measured in pulsed magnetic fields up to 65 T and below the Neel temperature is large and exhibits complex behavior with two transitions. While the high field anomaly is a field-induced metamagnetic-like transition and affects both magnetisation and magnetostriction, the low field anomaly does not contribute to the magnetic susceptibility. Our data suggest a change in the nature of the metamagnetic transition from first to second order like at a tricritical point at T_{tri}~24 K and H_{tri}~52 T (see Fig.1c). Using the results obtained here we have constructed a magnetic phase diagram of UN. These studies demonstrate that dilatometry in high fields is an effective method to investigate the magneto structural coupling in actinide materials.

Kondo lattice behavior in antiferromagnetic NpPdSn: while the effect of electronic correlations is relatively well studied in Ce, Yb and U based materials, there is still lack of knowledge on how these collective phenomena impact magnetic and transport properties in transuranium intermetallics. We show, by performing extensive magnetic, transport, thermodynamic and neutron diffraction measurements that the low temperature magnetic and transport properties of NpPdSn are governed by a competition between Ruderman-Kittel-Kasuya-Yosida and Kondo interactions leading to partial delocalization of 5*f*-states,

characteristic of dense Kondo systems. The energy scale of Kondo interactions, T_K ~20 K, has been estimated to be similar to its Neel temperature, T_N = 19 K. Neutron diffraction and ^{237}Np Mossbauer spectroscopy confirm antiferromagnetic ordering in NpPdSn at 19 K with an ordered moment of about 2.2(2) μ_B/Np along the *c*-axis. All the results indicate that NpPdSn can be classified as a new Np-based antiferromagnetic dense Kondo lattice.

Future Plans

During the next year of the project we plan to:

(a) continue with the low temperature high-field magnetostriction and magnetization studies on selected actinide crystals.
(b) perform low temperature synchrotron crystallography studies under pressure and pulsed magnetic fields on selected actinide single crystals.
(c) perform thermal conductivity measurements under magnetic field and pressure on various actinide materials.

References

[1] J. L. Sarrao et al., Nature 420, 297 (2002).
[2] P. Burlet et al., J. L. Comm. Met. 121, 121 (1986).
[3] D. Ippoliti et al., Phys. Rev. B 71, 064419 (2005).
[4] K. Gofryk et al., Nature Comm. 5, 264 4551 (2014).
[5] A.S. Borovik-Romanov, JETP 11, 786 (1960).

Publications

K. Gofryk, J-C. Griveau, P. S. Riseborough, and T. Durakiewicz, *Thermoelectric power as a probe of density of states in correlated actinide materials: the case of $PuCoGa_5$ superconductor*, Physical Review B 94, 195117 (2016).

M. Jaime, A. Saul, M. Salamon, V.S. Zapf, N. Harrison, T. Durakiewicz, J.C. Lashley, D.A. Andersson, C. Stanek, J.L. Smith, and K. Gofryk, *Piezomagnetism and magnetoelastic memory in uranium dioxide*, Nature Communications – accepted.

K. Shrestha, D. Antonio, M. Jaime, N. Harrison, D. S. Mast, D. Safarik, T. Durakiewicz, J.-C. Griveau, and K. Gofryk, *Tricritical point from high-field magnetoelastic and metamagnetic effects in UN*, Nature Scientific Reports – under review.

K. Shrestha, D. Antonio, J-C. Griveau, K. Prokes, P. Gaczynski, E. Colineau, R. Caciuffo, and K. Gofryk, *Kondo lattice behavior in antiferromagnetic NpPdSn*, Physical Review B – under review.

Three-Dimensional Plasmonic Light Concentrators for Efficient Terahertz Generation

Mona Jarrahi, University of California Los Angeles

Program Scope

The objective of this research program is to conduct fundamental physical studies on interaction of optical waves with plasmonic photoconductive nanostructures for high power terahertz wave generation. Optical-to-terahertz wave conversion through photoconduction is not restricted by the Manley-Rowe limit and, therefore, has a great promise for high efficiency terahertz wave generation. This is because each absorbed pump photon can generate one electron-hole pair, which can emit several terahertz photons upon reaching a terahertz radiating element. However, the main obstacle of these devices that prevents high power terahertz generation has been the inherent tradeoff between high quantum efficiency and ultrafast operation in conventional photoconductors as well as device thermal breakdown at high optical pump power levels. During this research program we plan to investigate unique capabilities of plasmonic nanostructures and light concentrators to address the quantum efficiency limitation of ultrafast photoconductors. Utilizing plasmonic contact electrodes and light concentrators enables manipulating the intensity of the incident optical pump beam and focusing it tightly next to the device contact electrodes. By enhancing the number of photocarriers in close proximity to the device contact electrodes, the number of the photocarriers drifted to the contact electrodes and routed to the terahertz radiating elements within a terahertz oscillation cycle is increased and significantly higher quantum efficiency levels are achieved. Toward this goal, we plan to explore novel high aspect-ratio, three-dimensional plasmonic contact electrodes embedded inside the photo-absorbing semiconductor substrate to confine up to ~100% of the photo-generated carriers within nanoscale distances from the contact electrodes to efficiently contribute to terahertz radiation generation. We plan to conduct an extensive study on various geometries of three-dimensional plasmonic electrodes and investigate the tradeoffs between plasmonic losses and quantum efficiency enhancements as a function of electrode depth for different designs. We plan to use the results of this study to determine the fundamental physical limitations of optical-to-terahertz conversion efficiency in photoconductive terahertz sources based on three-dimensional plasmonic electrodes.

Recent Progress

During the first four months of this research program, we have explored the use of three-dimensional plasmonic light concentrators formed by combining plasmonic contact electrodes with reflecting substrates to enhance quantum efficiency of ultrafast photoconductors for efficient optical-to-terahertz conversion. When a femtosecond optical pump beam is incident on an ultrafast photoconductor, photocarriers are generated and routed to the terahertz radiating element to generate pulsed terahertz radiation. Only the photocarriers that are routed to the terahertz radiating element within a sub-picosecond time-scale can contribute to efficient terahertz generation. The slower photocarriers would heat the device without a considerable contribution to terahertz generation. In order to prevent thermal failures, short carrier lifetime semiconductor substrates are usually used in conventional ultrafast photoconductors. These substrates are usually obtained by introducing high concentration of defects inside a semiconductor lattice. This degrades carrier mobility and drift velocity, which negatively impact optical-to-terahertz conversion efficiency.

We have addressed this problem by a novel photoconductive terahertz emitter architecture that suppresses slow photocarriers through three-dimensional light confinement near terahertz radiating elements. The emitter is fabricated on a low-defect photo-absorbing semiconductor substrate with an embedded optical reflector layer. The geometric characteristics of the emitter and optical reflector layer are chosen to tightly confine most of the incident optical pump beam within nanometer-scale distances from the terahertz radiating elements. This leads to an efficient photocarrier generation and drift to the terahertz radiating elements with high mobility. As a result, significantly higher optical-to-terahertz conversion efficiencies are achieved compared to conventional terahertz emitters based on short carrier lifetime semiconductors. Additionally, by suppressing the slow photocarriers and mitigating thermal breakdown, the presented terahertz emitter architecture offers a robust operation even at high optical pump powers.

Schematic diagram of the presented terahertz emitter is shown in Fig. 1a. A 190 nm-thick epitaxially grown GaAs film on a distributed Bragg reflector (DBR) layer is used as the low-defect photo-absorbing substrate. The DBR structure consists of 25 pairs of 60 nm-thick AlAs and 55 nm-thick $Al_{0.33}Ga_{0.67}As$. A 262 nm-thick $Al_{0.31}Ga_{0.69}As$ buffer layer separates the photo-absorbing GaAs layer from the DBR. Arrays of plasmonic nano-antennas fabricated on top of the GaAs layer are used as the terahertz radiating elements. The nano-antenna arrays are biased such that the photo-generated electrons, which have much higher mobilities compared to holes, would be the dominant photocarriers contributing to terahertz generation. A Si_3N_4 anti-reflection coating layer covers the plasmonic nano-antennas to further enhance optical pump transmission into the GaAs layer. The gaps between adjacent nano-antenna arrays are shadowed by depositing metal stripes on top of the Si_3N_4 layer. This prevents photocurrent generation in the opposite direction to the photocurrent coupled to the nano-antenna arrays. The geometry of the plasmonic nano-antennas and DBR is selected to offer enhanced optical absorption inside the top GaAs layer in response to a TM-polarized optical pump beam at ~770 nm wavelength. For this purpose, Au gratings with 100 nm width, 200 nm periodicity, and 80 nm thickness, covered by a 360 nm-thick Si_3N_4 anti-reflection coating layer are used. The length of the plasmonic nano-antennas (5 μm) is chosen to offer broadband terahertz radiation.

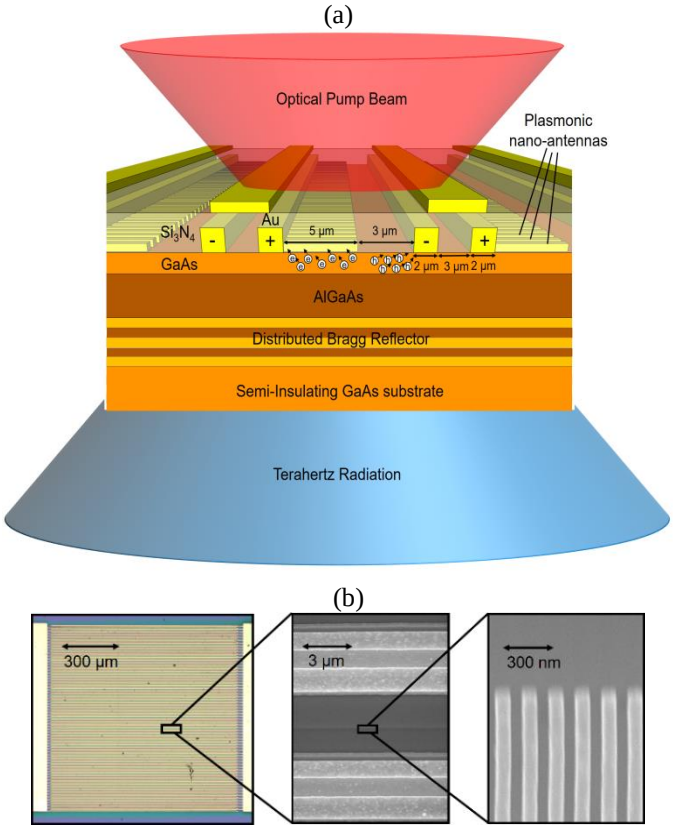

Fig.1. (a) Schematic of the terahertz emitter with 3D plasmonic light concentrators, (b) Optical microscope image of a fabricated terahertz emitter prototype and the scanning electron microscope image of the bias lines, shadow metals, and plasmonic nano-antennas.

Figure 1b shows the top view of a fabricated terahertz emitter prototype with a 1×1 mm^2 active area. Fabrication process starts with epitaxial growth of the DBR, buffer, and GaAs layers on a semi-insulating GaAs substrate using molecular beam epitaxy. The plasmonic nano-antennas are formed by electron beam lithography followed by metal deposition and liftoff. The Si_3N_4 anti-reflection coating layer is deposited by plasma-enhanced vapor deposition. The bias lines and shadow metals are formed by optical lithography followed by metal deposition and liftoff.

A Ti:sapphire laser is used to characterize the fabricated terahertz emitter prototype. First, the Ti:sapphire laser beam is focused on the plasmonic nano-antennas, while operating in continuous-wave mode. The beam polarization is set to be normal to the plasmonic gratings and its wavelength is swept between 740 nm and 820 nm. Figure 2 shows the reflected optical spectrum (blue curve), confirming a low optical reflection at ~770 nm wavelength, which indicates a high optical absorption inside the top GaAs active layer at this wavelength. Next, the Ti:sapphire laser beam is defocused to illuminate the entire device active area and the induced photocurrent is measured at a bias voltage of 5 V and optical pump power of 8 mW. Figure 2 shows the induced photocurrent as a function of the optical wavelength (red curve), indicating that the maximum photocurrent is induced at ~770 nm due to the high optical absorption inside the top GaAs active layer.

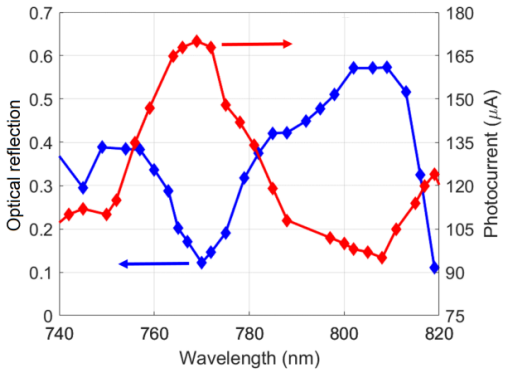

Fig 2. Optical reflection and photocurrent spectra at an optical pump power of 8 mW and bias voltage of 5 V are shown in blue and red curves, respectively.

In the next phase of experiments, the operation mode of the Ti:sapphire laser is switched to mode-locked, the center wavelength is set to 770 nm, and 135 fs-wide pulses with 76 MHz repetition rate are generated. In order to evaluate the impact of three-dimensional light confinement on emitter performance, a comparable photoconductive terahertz emitter with optimum plasmonic nano-antenna geometry is fabricated on a 1 μm-thick low temperature (LT) grown GaAs layer with a carrier lifetime of

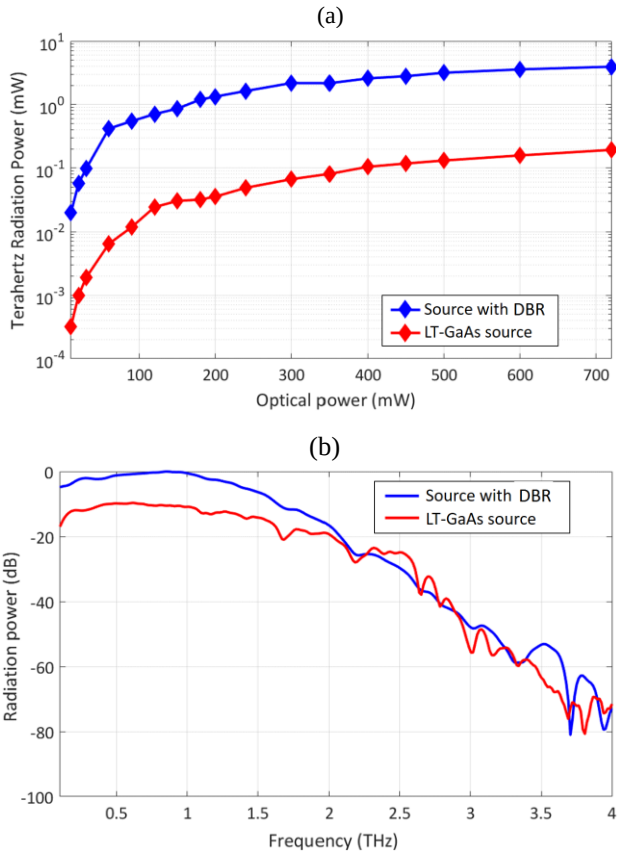

Fig.3. The measured terahertz radiation powers and radiation spectra for the emitter fabricated on the DBR substrate and the LT-GaAs emitter are shown in (a) and (b), respectively.

0.3 ps, which is grown on a semi-insulating GaAs substrate. As illustrated in Fig. 3a, the presented emitter fabricated on the DBR substrate offers significantly higher optical-to-terahertz conversion efficiencies compared to the LT-GaAs emitter. Up to 62 times enhancement in the optical-to-terahertz conversion efficiency is offered by the presented emitter fabricated on the DBR substrate at an optical pump power of 10 mW. The optical-to-terahertz conversion efficiency enhancement factor is reduced at higher optical pump power levels due to the carrier screening effect. Despite this reduction, a record-high terahertz radiation power of 4 mW is achieved at a 720 mW optical pump power. The radiation spectra of the fabricated terahertz emitters are characterized in a time-domain terahertz spectroscopy setup with electro-optic detection in a 0.5 mm-thick ZnTe crystal. As illustrated in Fig. 3b, significantly higher power levels are generated by the presented terahertz emitter fabricated on the DBR substrate below 2 THz. This is due to the tighter light confinement near the plasmonic nanoantenna arrays and the use of a higher-mobility semiconductor substrate. However, since only the photocarriers generated within few tens of nanometers distance from the nanoantenna arrays contribute to the radiated power at frequencies above 2 THz and the carrier concentration in this region is similar for both emitters, similar terahertz power levels are radiated by the two emitters at frequencies above 2 THz.

Future Plans

For the next steps of this research program, we plan to investigate novel configurations of large area plasmonic photoconductive sources integrated with nanoscale terahertz radiating elements to mitigate the thermal breakdown limitation of conventional photoconductive terahertz sources while achieving high terahertz power levels. We will investigate the radiation bandwidth-efficiency tradeoff for each design to determine the physical limitations of optical-to-terahertz conversion for both continuous-wave and pulsed operation. We will also conduct theoretical and experimental studies on the induced thermal heating for various two/three dimensional plasmonic contact electrodes and light concentrators with various configurations and photo-absorbing substrates including GaAs, InGaAs, and graphene. Our motivation for using graphene as the photo-absorbing layer of photoconductive terahertz sources is its high in-plane thermal conductivity and robust high temperature operation accompanied by its high carrier mobility levels. To that end, we plan to investigate various graphene-based photoconductive terahertz sources based on different types of three-dimensional plasmonic light concentrators and radiating elements as well as different metal contacts and gating mechanisms for maximizing optical-to-terahertz conversion efficiency and terahertz radiation powers.

Publications (Jan 2017- April 2017)

[1] N. T. Yardimci, S. Cakmakyapan, S. Hemmati, M. Jarrahi, “A High-Power Broadband Terahertz Source Enabled by Three-Dimensional Light Confinement in a Plasmonic Nanocavity,” in review

[2] D. Turan, S. C. Corzo-Garcia, N. T. Yardimci, E. Castro-Camus, M. Jarrahi, “Impact of the Metal Adhesion Layer on the Radiation Power of Plasmonic Photoconductive Terahertz Sources,” in review

[3] S. Cakmakyapan, P. K. Lu, A. Navabi, M. Jarrahi, “Gold-Patched Graphene Nanoribbons for High-Responsivity and Ultrafast Photodetection from Visible to Infrared Regimes,” in review

Electronic Materials Program

Joel W. Ager,[1,2] Daryl C. Chrzan,[1,2] Oscar D. Dubon,[1,2] Wladek Walukiewicz,[1,2] Junqiao Wu,[1,2] and Ali Javey[1,3]
[1]Materials Sciences Division, Lawrence Berkeley National Laboratory, Berkeley, CA
[2]Materials Science and Engineering, University of California, Berkeley, CA
[3]Electrical Engineering and Computer Science, University of California, Berkeley, CA

Program Scope

LBNL's Electronic Material Program (EMAT) discovers and creates semiconductors of novel composition and morphology for energy applications by *removing chemical and physical constraints* that limit materials performance and growth. Emphasis is placed on exploration of single-crystalline semiconductors that are not epitaxially coupled with the underlying substrates, thus expanding the utility of semiconductors for new applications while enabling study of new material properties. In the case of monolayer semiconductors, elimination of the difference between the surface and the bulk allows us to control defects (including fixing/creating them) via surface treatments. In parallel, we utilize a toolbox of physical and chemical approaches to implement extreme control of band structures in both low dimensional and 3D materials using surface/interface effects. Finally, by exploiting new insights into the process of templated liquid-phase nucleation and growth, we synthesize high-quality single-crystal semiconductors on amorphous substrates.

Recent Progress

Discovery that chemical defect passivation of 2D semiconductor can produce near-unity photoluminescence quantum efficiency.

While there has been intense research interest in the optical properties of monolayer transition metal dichalcogenides (TMDs) such as MoS_2, their intrinsic optical properties had remained unknown. For example, the observed quantum efficiency for light emission for direct gap TMDs was low, on the order of 1% or less,[1,2] which would rule out their use in important energy-related applications such as photovoltaics or light emitting diodes.[3–5] *This limitation has been essentially eliminated* by our discovery that treatment of monolayers of MoS_2 with an organic superacid eliminates all defect related non-radiative recombination, resulting in near unity quantum efficiency at low pump powers, as shown in Fig. 1.[6] The treatment is air-stable and the monolayers remain essentially opto-electronically perfect for weeks. Our ability to obtain optoelectronic monolayers with near-perfect properties opens the door for the development of highly efficient light-emitting diodes, lasers, and solar cells based on monolayer materials.

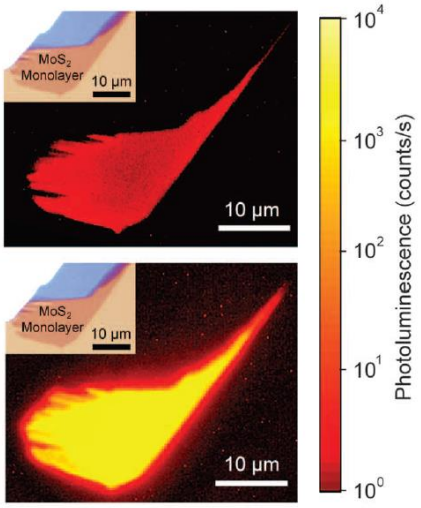

Figure 1. The photoluminescence from a monolayer of MoS_2 is increased by orders of magnitude by treatment with an organic superacid. The photoluminescence quantum efficiency is essentially 100% at low carrier generation rates. From Amani *et al.*, *Science*, 2015.[6]

Transistor with 1 nm gate length

Scaling of silicon (Si) transistors is predicted to fail below 5 nm gate lengths because of severe short channel effects. As an alternative to Si, certain 2D layered semiconductors are attractive because of their atomically uniform thickness down to a monolayer, lower dielectric constants, larger band gaps, and heavier carrier effective mass. Here, we demonstrate molybdenum disulfide (MoS_2) field effect transistors (FETs) with a 1-nm physical gate length using a 1D single-walled carbon nanotube (SWNT) as the gate electrode.[7] The 1D2D FETs exhibit excellent switching characteristics with near ideal subthreshold swing of ~65 millivolts per decade and an On/Off current ratio of ~10^6 when the MoS_2 approaches 1 nm in thickness.

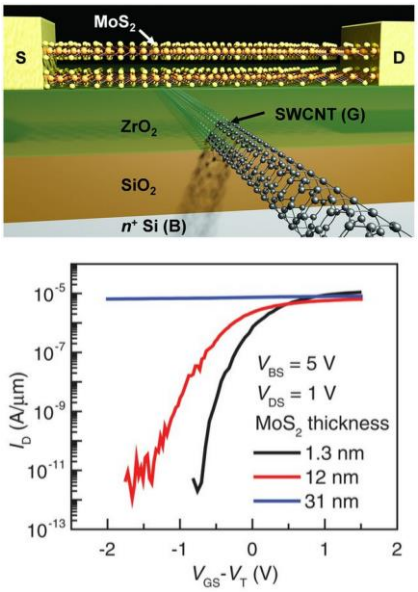

Fig. 2 (top) Schematic of 1D2D-FET with a MoS_2 channel and SWCNT gate. (bottom) For thin MoS2 channels the subthreshold swing (SS) is near-ideal at ~65 mV per decade at room temperature Adapted from Desai *et al., Science*, 2016.[7]

Grown of high-quality single-crystal III-V semiconductors on amorphous substrates.

The program has focused on controlling phase transitions at the nanoscale with an eye towards developing processing routes that enable the growth of a broad range of materials. The scientific genesis of this work is our discovery that control of nucleation can allow III-V semiconductors to be grown with very large grain sizes on amorphous substrates.[8] The key innovation is the use of a semi-permeable capping layer to control the flux of the group V in such a way as to control the nucleation rate. The growth mechanism can produce single crystalline materials if only a single nucleation site is allowed in a given volume. We have shown that templated liquid-phase crystal growth (TLPCG) is capable of growing high-quality (nominally) *single crystalline* III-V semiconductors on *amorphous* substrates.[9] In the prototypical process we synthesized InP in (nominally) single-crystal form in a variety of shapes (Fig. 3). The approach has been demonstrated for GaP and InSb, and even extended to the synthesis of multilayers.

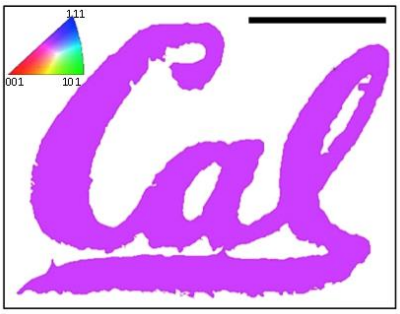

Fig. 3. *Orientation image map of single crystal InP* grown on an amorphous substrate (SiO_2) using TLPCG. Scale bar is 3 μm. Adapted from Chen *et al., Nature Comm.*, 2016.[9]

Dopant-free heterojunction solar cells.

A salient characteristic of solar cells is their ability to subject photo-generated electrons and holes to pathways of asymmetrical conductivity—"assisting" them towards their respective contacts. All commercially available crystalline silicon (c-Si) solar cells achieve this by making use of doping in either near-surface regions or overlaying silicon-based films. Despite being commonplace, this approach is hindered by several optoelectronic losses and technological

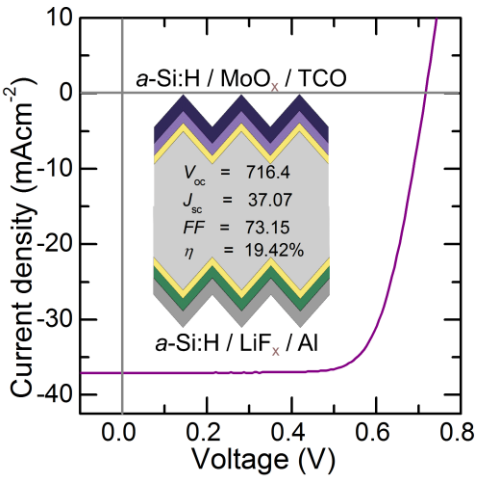

Fig. 4. Light JV characteristic and schematic of the dopant-free asymmetric heterocontact (DASH) silicon solar cell that uses moly oxide and lithium fluoride as hole and electron-selective contacts, respectively. TCO refers to a Transparent Conductive Oxide stack. Adapted from Bullock *et al.*, *Nature Energy*, 2016.[10]

limitations specific to doped silicon. *EMAT made a major breakthrough in the discovery of alternative materials that can form "carrier-selective" interfaces on c-Si.*[10] The work successfully interfaced both dopant-free electron and hole carrier-selective heterocontacts using alkali metal fluorides and metal oxides, respectively (Fig. 4). Cells fabricated with this approach had high open circuit voltages over 710 mV, demonstrating the quality of the interfaces, and power conversion efficiencies approaching 20%. The new interface approach allows for a simplification in architecture and for lower temperature processing, both of which will improved the cost-to-performance ratio of c-Si photovoltaics.

Future Plans

Our discovery that certain monolayer TMDs can be made to be optically "perfect," with their luminescence dynamics appearing to be controlled only by intrinsic processes, allows us to use these materials as a starting point for incisive studies of intrinsic and extrinsic defects.[6,11] The overall strategy will involve manipulation and chemical surface treatment of TMDs, controlled defect introduction, optical characterization, and electronic structure calculations**.** Initial work in this area is promising. We have discovered a method to retain the near-unity quantum efficiency of MoS_2 monolayers while they undergo exposure to conditions typical of semiconductor processing such as solvent and vacuum treatments.

In the next three years, we will employ a systematic and rational approach to engineer band structure of low-dimensional materials by modulating their interactions with the environment, and by doing so, we will stabilize new phase, states and properties needed for applications in energy production, conversion and transport. Two general approaches will be employed: physical modulation and chemical modulation. In an initial demonstration of the former approach, we have demonstrated strain engineering during the growth of WSe_2, showing that strains on the order of 1% can be achieved even in the case of non-epitaxial growth. For bilayer WSe_2, the strain can be sufficient to drive the indirect

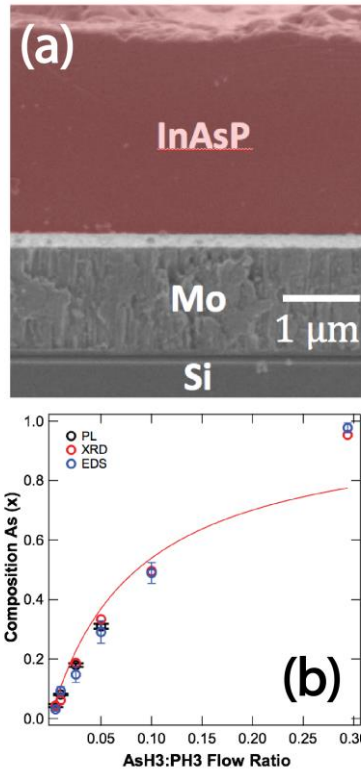

Fig. 5. Growth of single crystal $InAs_xP_{1-x}$ using TLPCG. (a) SEM image of $InAs_xP_{1-x}$ film. (b) Composition of the film as a function of growth conditions.

to direct phase transition which we had previously observed by the application of mechanical strain.[12]

It is clear that a broad range of semiconductor technologies would be impacted by the ability to inexpensively grow one material upon any other. Therefore we are continuing our efforts to grow high quality, single crystal semiconductor films of any desired thickness upon any substrate. At present, we have demonstrated non-epitaxial growth of high quality single crystal materials with lateral dimensions much larger than the film thickness. Recently, we have shown that growth of *ternary* III-V single crystal material is possible using TLPCG (Fig. 5). However, a remaining challenge is control of the orientation of the resultant single crystals grown via TLPCG. We are exploring a number of nucleation strategies to address this remaining challenge in non-epitaxial growth.

References

(1) Yuan, L.; Huang, L. *Nanoscale* **2015**, *7* (16), 7402–7408.

(2) Wang, H.; Zhang, C.; Rana, F. *Nano Lett.* **2015**, *15* (1), 339–345.

(3) Miller, O. D.; Yablonovitch, E.; Kurtz, S. R. *IEEE J. Photovoltaics* **2012**, *2* (3), 303–311.

(4) Tran, T.-T. D.; Sun, H.; Ng, K. W.; Ren, F.; Li, K.; Lu, F.; Yablonovitch, E.; Chang-Hasnain, C. J. *Nano Lett.* **2014**, *14* (6), 3235–3240.

(5) Sutter-Fella, C. M.; Li, Y.; Amani, M.; Ager, J. W.; Toma, F. M.; Yablonovitch, E.; Sharp, I. D.; Javey, A. *Nano Lett.* **2016**, *16* (1), 800–806.

(6) Amani, M.; Lien, D.-H.; Kiriya, D.; Xiao, J.; Azcatl, A.; Noh, J.; Madhvapathy, S. R.; Addou, R.; KC, S.; Dubey, M.; Cho, K.; Wallace, R. M.; Lee, S.-C.; He, J.-H.; Ager, J. W.; Zhang, X.; Yablonovitch, E.; Javey, A. *Science (80-.).* **2015**, *350* (6264), 1065–1068.

(7) Desai, S. B.; Madhvapathy, S. R.; Sachid, A. B.; Llinas, J. P.; Wang, Q.; Ahn, G. H.; Pitner, G.; Kim, M. J.; Bokor, J.; Hu, C.; Wong, H.-S. P.; Javey, A. *Science (80-.).* **2016**, *354* (6308), 99–102.

(8) Kapadia, R.; Yu, Z.; Wang, H.-H. H.; Zheng, M.; Battaglia, C.; Hettick, M.; Kiriya, D.; Takei, K.; Lobaccaro, P.; Beeman, J. W.; Ager, J. W.; Maboudian, R.; Chrzan, D. C.; Javey, A. *Sci. Rep.* **2013**, *3*, 2275.

(9) Chen, K.; Kapadia, R.; Harker, A.; Desai, S.; Seuk Kang, J.; Chuang, S.; Tosun, M.; Sutter-Fella, C. M.; Tsang, M.; Zeng, Y.; Kiriya, D.; Hazra, J.; Madhvapathy, S. R.; Hettick, M.; Chen, Y.-Z.; Mastandrea, J.; Amani, M.; Cabrini, S.; Chueh, Y.-L.; Ager III, J. W.; Chrzan, D. C.; Javey, A. *Nat. Commun.* **2016**, *7*, 10502.

(10) Bullock, J.; Hettick, M.; Geissbühler, J.; Ong, A. J.; Allen, T.; Sutter-Fella, C. M.; Chen, T.; Ota, H.; Wolf, S. De; Schaler, E. W.; Ballif, C.; Cuevas, A.; Javey, A. *Nat. Energy* **2016**, *1* (January), 15031.

(11) Amani, M.; Taheri, P.; Addou, R.; Ahn, G. H.; Kiriya, D.; Lien, D.-H.; Ager, J. W.; Wallace, R. M.; Javey, A. *Nano Lett.* **2016**, *16* (4), 2786–2791.

(12) Desai, S. B.; Seol, G.; Kang, J. S.; Fang, H.; Battaglia, C.; Kapadia, R.; Ager, J. W.; Guo, J.; Javey, A. *Nano Lett.* **2014**, *14* (8), 4592–4597.

Publications primarily supported by DOE Physical Behavior of Materials 2015-2017

(1) Rembert, T.; Battaglia, C.; Anders, A.; Javey, A. Room Temperature Oxide Deposition Approach to Fully Transparent, All-Oxide Thin-Film Transistors. *Adv. Mater.* **2015**, *27*, 6090–6095.

(2) García-Hemme, E.; Yu, K. M.; Wahnon, P.; González-Díaz, G.; Walukiewicz, W. Effects of the D-Donor Level of Vanadium on the Properties of $Zn_{1-x}V_xO$ Films. *Appl. Phys. Lett.* **2015**, *106*, 182101.

(3) Wełna, M.; Kudrawiec, R.; Nabetani, Y.; Tanaka, T.; Jaquez, M.; Dubon, O. D.; Yu, K. M.; Walukiewicz, W. Effects of a Semiconductor Matrix on the Band Anticrossing in Dilute Group II-VI Oxides. *Semicond. Sci. Technol.* **2015**, *30*, 85018.

(4) Jaquez, M.; Yu, K. M.; Ting, M.; Hettick, M.; Sánchez-Royo, J. F.; Wełna, M.; Javey, A.; Dubon, O. D.; Walukiewicz, W. Growth and Characterization of $ZnO_{1-x}S_x$ Highly Mismatched Alloys over the Entire Composition. *J. Appl. Phys.* **2015**, *118*, 215702.

(5) Amani, M.; Lien, D.-H.; Kiriya, D.; Xiao, J.; Azcatl, A.; Noh, J.; Madhvapathy, S. R.; Addou, R.; KC, S.; Dubey, M.; Cho, K.; Wallace, R. M.; Lee, S.-C.; He, J.-H.; Ager, J. W.; Zhang, X.; Yablonovitch, E.; Javey, A. Near-Unity Photoluminescence Quantum Yield in MoS_2. *Science* **2015**, *350*, 1065–1068.

(6) Hsu, W.; Sutter-Fella, C. M.; Hettick, M.; Cheng, L.; Chan, S.; Chen, Y.; Zeng, Y.; Zheng, M.; Wang, H.-P.; Chiang, C.-C.; Javey, A. Electron-Selective TiO_2 Contact for $Cu(In,Ga)Se_2$ Solar Cells. *Sci. Rep.* **2015**, *5*, 16028.

(7) Francis, C. A.; Detert, D. M.; Chen, G.; Dubon, O. D.; Yu, K. M.; Walukiewicz, W. NixCd1−xO: Semiconducting Alloys with Extreme Type III Band Offsets. *Appl. Phys. Lett.* **2015**, *106*, 22110.

(8) López, N.; Yu, K. M.; Tanaka, T.; Walukiewicz, W. Multicolor Electroluminescence from Intermediate Band Solar Cell Structures. *Adv. Energy Mater.* **2015**, 1501820.

(9) Baranowski, M.; Kudrawiec, R.; Luce, A. V.; Latkowska, M.; Yu, K. M.; Misiewicz, J.; Tu, C. W.; Walukiewicz, W.; Kuang, Y. J. Temperature Evolution of Carrier Dynamics in $GaN_xP_yAs_{1-y-x}$ alloys. *J. Appl. Phys.* **2015**, *117*, 175702.

(10) Liu, K.; Hsin, C.-L. L.; Fu, D.; Suh, J.; Tongay, S.; Chen, M.; Sun, Y.; Yan, A.; Park, J.; Yu, K. M.; Guo, W.; Zettl, A.; Zheng, H.; Chrzan, D. C.; Wu, J. Self-Passivation of Defects: Effects of High-Energy Particle Irradiation on the Elastic Modulus of Multilayer Graphene. *Adv. Mater.* **2015**, *27*, 6841–6847.

(11) Ting, M.; dos Reis, R.; Jaquez, M.; Dubon, O. D.; Mao, S. S.; Yu, K. M.; Walukiewicz, W. Electronic Band Structure of ZnO-Rich Highly Mismatched $ZnO_{1-x}Te_x$ Alloys. *Appl. Phys. Lett.* **2015**, *106*, 92101.

(12) Kiriya, D.; Zhou, Y.; Nelson, C.; Hettick, M.; Madhvapathy, S. R.; Chen, K.; Zhao, P.; Tosun, M.; Minor, A. M.; Chrzan, D. C.; Javey, A. Oriented Growth of Gold Nanowires on MoS_2. *Adv. Funct. Mater.* **2015**, *25*, 6257–6264.

(13) Roy, T.; Tosun, M.; Hettick, M.; Ahn, G. H.; Hu, C.; Javey, A. 2D-2D Tunneling Field-Effect Transistors Using $WSe_2/SnSe_2$ Heterostructures. *Appl. Phys. Lett.* **2016**, *108*, 83111.

(14) Amani, M.; Taheri, P.; Addou, R.; Ahn, G. H.; Kiriya, D.; Lien, D.-H.; Ager, J. W.; Wallace, R. M.; Javey, A. Recombination Kinetics and Effects of Superacid Treatment in Sulfur- and Selenium-Based Transition Metal Dichalcogenides. *Nano Lett.* **2016**, *16*, 2786–2791.

(15) Sutter-Fella, C. M.; Li, Y.; Amani, M.; Ager, J. W.; Toma, F. M.; Yablonovitch, E.; Sharp, I. D.; Javey, A. High Photoluminescence Quantum Yield in Band Gap Tunable Bromide Containing Mixed Halide Perovskites. *Nano Lett.* **2016**, *16*, 800–806.

(16) Wang, H.-P.; Sutter-Fella, C. M.; Lobaccaro, P.; Hettick, M.; Zheng, M.; Lien, D.-H.; Miller, D. W.; Warren, C. W.; Roe, E. T.; Lonergan, M. C.; Guthrey, H. L.; Haegel, N. M.; Ager, J. W.; Carraro, C.; Maboudian, R.; He, J.-H.; Javey, A. Increased Optoelectronic Quality and Uniformity of Hydrogenated P-InP Thin Films. *Chem. Mater.* **2016**, *28*, 4602–4607.

(17) Xu, X.; Bullock, J.; Schelhas, L. T.; Stutz, E. Z.; Fonseca, J. J.; Hettick, M.; Pool, V. L.; Tai, K. F.; Toney, M. F.; Fang, X.; Javey, A.; Wong, L. H.; Ager, J. W. Chemical Bath Deposition of P-Type Transparent, Highly Conducting $(CuS)_x:(ZnS)_{1-X}$ Nanocomposite Thin Films and Fabrication of Si Heterojunction Solar Cells. *Nano Lett.* **2016**, *16*, 1925–1932.

(18) Alarcón-Lladó, E.; Brazzini, T.; Ager, J. W. Surface Origin and Control of Resonance Raman Scattering and Surface Band Gap in Indium Nitride. *J. Phys. D. Appl. Phys.* **2016**, *49*, 255102.

(19) Tosun, M.; Chan, L.; Amani, M.; Roy, T.; Ahn, G. H.; Taheri, P.; Carraro, C.; Ager, J. W.; Maboudian, R.; Javey, A. Air-Stable N-Doping of WSe_2 by Anion Vacancy Formation with Mild Plasma Treatment. *ACS Nano* **2016**, *10*, 6853–6860.

(20) Desai, S. B.; Madhvapathy, S. R.; Amani, M.; Kiriya, D.; Hettick, M.; Tosun, M.; Zhou, Y.; Dubey, M.; Ager, J. W.; Chrzan, D.; Javey, A. Gold-Mediated Exfoliation of Ultralarge Optoelectronically-Perfect Monolayers. *Adv. Mater.* **2016**, *28*, 4053–4058.

(21) Amani, M.; Burke, R. A.; Ji, X.; Zhao, P.; Lien, D.-H.; Taheri, P.; Ahn, G. H.; Kirya, D.; Ager, J. W.; Yablonovitch, E.; Kong, J.; Dubey, M.; Javey, A. High Luminescence Efficiency in MoS_2 Grown by Chemical Vapor Deposition. *ACS Nano* **2016**, *10*, 6535–6541.

(22) Chen, K.; Kapadia, R.; Harker, A.; Desai, S.; Seuk Kang, J.; Chuang, S.; Tosun, M.; Sutter-Fella, C. M.; Tsang, M.; Zeng, Y.; Kiriya, D.; Hazra, J.; Madhvapathy, S. R.; Hettick, M.; Chen, Y.-Z.; Mastandrea, J.; Amani, M.; Cabrini, S.; Chueh, Y.-L.; Ager III, J. W.; Chrzan, D. C.; Javey, A. Direct Growth of Single-Crystalline III–V Semiconductors on Amorphous Substrates. *Nat. Commun.* **2016**, *7*, 10502.

(23) Zhou, Y.; Kiriya, D.; Haller, E. E.; Ager, J. W.; Javey, A.; Chrzan, D. C. Compliant Substrate Epitaxy: Au on MoS_2. *Phys. Rev. B* **2016**, *93*, 54106.

(24) Chen, Y.; Zhang, S.; Gao, W.; Ke, F.; Yan, J.; Saha, B.; Ko, C.; Suh, J.; Chen, B.; Ager, J. W.; Walukiewicz, W.; Jeanloz, R.; Wu, J. Pressure-Induced Structural Transition of $Cd_xZn_{1-x}O$ Alloys. *Appl. Phys. Lett.* **2016**, *108*, 152105.

(25) Kiriya, D.; Lobaccaro, P.; Nyein, H. Y. Y.; Taheri, P.; Hettick, M.; Shiraki, H.; Sutter-Fella, C. M.; Zhao, P.; Gao, W.; Maboudian, R.; Ager, J. W.; Javey, A. General Thermal Texturization Process of MoS_2 for Efficient Electrocatalytic Hydrogen Evolution Reaction. *Nano Lett.* **2016**, *16*, 4047–4053.

(26) Bullock, J.; Hettick, M.; Geissbühler, J.; Ong, A. J.; Allen, T.; Sutter-Fella, C. M.; Chen, T.; Ota, H.; Schaler, E. W.; De Wolf, S.; Ballif, C.; Cuevas, A.; Javey, A. Efficient Silicon Solar Cells with Dopant-Free Asymmetric Heterocontacts. *Nat. Energy* **2016**, *1*, 15031.

(27) Ristova, M. M.; Francis, C.; Toma, F. M.; Yu, K. M.; Walukiewicz, W. Electrochemical Modification of the Optical and Electrical Properties of Cd-Rich $Ni_xCd_{1-x}O$ Alloys. *Sol. Energy Mater. Sol. Cells* **2016**, *147*, 127–133.

(28) Roy, T.; Tosun, M.; Hettick, M.; Ahn, G. H.; Hu, C.; Javey, A. 2D-2D Tunneling Field-Effect Transistors Using WSe_2/$SnSe_2$ Heterostructures. *Appl. Phys. Lett.* **2016**, *108*, 83111.

(29) Desai, S. B.; Madhvapathy, S. R.; Sachid, A. B.; Llinas, J. P.; Wang, Q.; Ahn, G. H.; Pitner, G.; Kim, M. J.; Bokor, J.; Hu, C.; Wong, H.-S. P.; Javey, A. MoS_2 Transistors with 1-Nanometer Gate Lengths. *Science* **2016**, *354*, 99–102.

(30) Yu, K. M.; Detert, D. M.; Chen, G.; Zhu, W.; Liu, C.; Grankowska, S.; Hsu, L.; Dubon, O. D.; Walukiewicz, W. Defects and Properties of Cadmium Oxide Based Transparent Conductors. *J. Appl. Phys.* **2016**, *119*, 181501.

(31) Ristova, M. M.; Zhu, W.; Yu, K. M.; Walukiewicz, W. Semiempirical Modeling of a Three Sublayer Photoanode for Highly Efficient Photoelectrochemical Water Splitting: Parameter and Electrolyte Optimizations. *Sol. Energy Mater. Sol. Cells* **2016**, *157*, 190–199.

(32) Fonseca, J. J.; Tongay, S.; Topsakal, M.; Chew, A. R.; Lin, A. J.; Ko, C.; Luce, A. V.; Salleo, A.; Wu, J.; Dubon, O. D. Bandgap Restructuring of the Layered Semiconductor Gallium Telluride in Air. *Adv. Mater.* **2016**, *28*, 6465–6470.

(33) Gao, W.; dos Reis, R.; Schelhas, L. T.; Pool, V. L.; Toney, M. F.; Yu, K. M.; Walukiewicz, W. Formation of Nanoscale Composites of Compound Semiconductors Driven by Charge Transfer. *Nano Lett.* **2016**, *16*, 5247–5254.

(34) Chen, Y.; Ke, F.; Ci, P.; Ko, C.; Park, T.; Saremi, S.; Liu, H.; Lee, Y.; Suh, J.; Martin, L. W.; Ager, J. W.; Chen, B.; Wu, J. Pressurizing Field-Effect Transistors of Few-Layer MoS_2 in a Diamond Anvil Cell. *Nano Lett.* **2017**, *17*, 194–199.

PROJECT TITLE: "Bare, Coated, and Supported Clusters"

PI: Jena, Purusottam
Department of Physics, Virginia Commonwealth University, Richmond, VA 23284-2000
pjena@vcu.edu

PROGRAM SCOPE:

The objective of this project is to provide a fundamental understanding of the structure-property relationships of isolated atomic clusters and how they are affected when clusters are coated or supported on a substrate. We focus primarily on clusters that mimic the chemistry of halogen atoms. These species termed as super-halogens are then used to synthesize a novel class of super-salts with applications as electrolytes in Li, Na, and Mg-ion batteries and as components of hybrid perovskite-based solar cells. We are also studying fundamental properties of matter at the atomic scale such magnetism and stability of multiply charged species, and two-dimensional materials with unique electronic properties.

The project exploits the unique size and composition specific properties of clusters and how they are affected by interaction with ligands and support. Using first-principles theory our goal is to design atom-by-atom a new class of negative ions suitable for forming salts with unusual properties, validate our predictions by working closely with experimentalists, and guide experiments in focused discovery of new materials. The project deals with three interrelated thematic areas: (1) Design unconventional super-halogen clusters whose electron affinities far exceed those of halogen atoms. Most super-halogens known thus far are composed of inorganic species. Our goal is to design super and hyper-halogens composed of organic species as well as metallo-fullerenes encapsulating rare-earth and actinide elements. Stability of a new class of Zintl ions composed of transition metal atoms embedded in Au cages is explored. Fundamental chemistry of the electrolytes in Li-ion batteries (LIBs) is studied with a view to creating halogen-free LIBs. (2) Study the effect of ligands on the magnetic properties of coated transition metal clusters. We focus on Mn based systems as the coupling between Mn atoms is very sensitive to inter-atomic distances and charge state. (3) Provide a fundamental understanding of cluster support interaction by focusing on bare superatom clusters and those supported on metal oxide, Au(111), and graphene substrates. The objective is to see if cluster-assembled materials composed of earth-abundant elements can mimic the properties of scarce or costly elements. We also explore the possibility of creating low-dimensional materials with unusual stoichiometry and properties. The choice of the above systems is motivated not only by their rich physical and chemical properties, but also by a wealth of supporting experimental and theoretical data.

RECENT PROGRESS:

Research over the past two years has resulted in 47 publications, two of which are featured on the cover of journals [1,2]. These are given in Figs. 1and 2. Some of the papers are published in high-impact journals such as Nano Letters, Proceedings of the National Academy of Sciences, Angew. Chem. Int. Ed, and J. Phys. Chem. Letters. The papers cover a wide range of topics involving structure-property relationships of zero-dimensional systems (clusters), one-dimensional systems (nano-wires and nano-ribbons), two-dimensional systems (graphene oxide,

functionalized graphene, C-N sheets, MoS_2, and organic monolayers), three-dimensional metallic carbon and boron nitride as well as topological insulators. The works on clusters involve the design and synthesis of super- and hyper-halogen clusters whose electron affinities far exceed those of halogen atoms as well as studies of the interaction between two like charges: In defiance of the Coulomb's law, two like charges are found to attract [3]. The work on nano-wires and mono-layers involve unusual magnetic and electronic properties. Also published during this period are four invited papers, perspectives, and viewpoints [4-7]. Four of our papers are published jointly with experimentalists [8-11].

J. Mater. Chem. A,
4, 4621 (2016)

Phys. Chem. Chem. Phys.,
18, 8755 (2016)

Figs. 1-2 Covers of Journals-J. Materials Chemistry A, Phys. Chem. Chem. Phys.

It is impossible to cover in detail the basic science addressed in all the papers published in the past two years. The presentation, therefore, focuses on one paper [12] dealing with a new carbon allotrope, penta-graphene. Composed of only pentagons, this new two-dimensional (2D) metastable carbon allotrope resembles the Cairo pentagonal tiling. This paper was highlighted "In This Issue" of the proceedings of the National Academy of Sciences (Fig. 3).

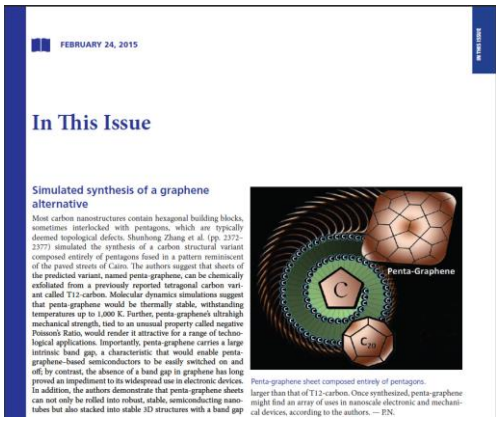
FEBRUARY 24, 2015

In This Issue

Simulated synthesis of a graphene alternative

Most carbon nanostructures contain hexagonal building blocks, sometimes interlocked with pentagons, which are typically deemed topological defects. Shunhong Zhang et al. (pp. 2372–2377) simulated the synthesis of a carbon structural variant composed entirely of pentagons fused in a pattern reminiscent of the paved streets of Cairo. The authors suggest that sheets of the predicted variant, named penta-graphene, can be chemically exfoliated from a previously reported tetragonal carbon variant called T12-carbon. Molecular dynamics simulations suggest that penta-graphene would be thermally stable, withstanding temperatures up to 1,000 K. Further, penta-graphene's ultrahigh mechanical strength, tied to an unusual property called negative Poisson's Ratio, would render it attractive for a range of technological applications. Importantly, penta-graphene carries a large intrinsic band gap, a characteristic that would enable penta-graphene–based semiconductors to be easily switched on and off; by contrast, the absence of a band gap in graphene has long proved an impediment to its widespread use in electronic devices. In addition, the authors demonstrate that penta-graphene sheets can not only be rolled into robust, stable, semiconducting nanotubes but also stacked into stable 3D structures with a band gap larger than that of T12-carbon. Once synthesized, penta-graphene might find an array of uses in nanoscale electronic and mechanical devices, according to the authors. — EN.

Penta-graphene sheet composed entirely of pentagons.

Fig. 3, Penta-graphene

First-principles calculations based on density functional theory confirm that the new carbon polymorph is not only dynamically and mechanically stable, but also can withstand temperatures as high as 1000 K. Due to its unique atomic configuration penta-graphene has an unusual negative Poisson's ratio (NPR) and ultra-high ideal strength that can even outperform graphene. Furthermore, unlike graphene that needs to be functionalized for opening a band gap, penta-graphene possesses an intrinsic quasi-direct band gap as large as 3.25 eV - close to that of ZnO and GaN. Equally important, penta-graphene can be exfoliated from T12-carbon. When rolled up, it can form pentagon-based nanotubes which are semiconducting, regardless of their chirality. When stacked in different patterns, stable 3D twin structures of T12-carbon are generated with band gaps even larger than that of T12-carbon. The versatility of penta-graphene and its derivatives are expected to have broad applications in nano-electronics and nano-mechanics. The paper has generated considerable excitement in the scientific community and has been cited nearly 100 times since its publication in 2015.

FUTURE PLANS

Our future plans are to make use of the unique properties of clusters to rationally design materials for energy applications and for the synthesis of magnetic materials with uncommon properties. We also plan to study the minimum size a particle can have to accommodate multiple charges without the benefit of counter-ions or solvents and use such particles in the design of new salts. The project deals with three interrelated thematic areas: (1) *Super-ions as building blocks of energy materials:* Realizing that electrolytes in metal-ion batteries and hybrid perovskites solar cell materials are salts composed of complex cations and anions, we will study a wide range of super-alkalis and super-halogens as building blocks of these salts and tailor their properties by choosing their size and composition. To address environmental concern, we will also study the role of super-alkalis in CO_2 activation. (2) *Stability of multiply charged clusters:* While multiply charged clusters are stabilized in solutions and in the solid phase by compensating cations, they often fragment or auto-eject the extra electron(s) in the gas phase. Although doubly charged anions are well studied, very little is known about the stability of tri-anions. Using various electron-counting rules we will study the size and composition of tri-anions that are stable in the gas phase and explore their potential as building blocks of electrolytes in Al-ion batteries. (3) *Mn_2^+ as a building block of low-dimensional magnetic materials:* Our focus on Mn-based systems is based on the fact that magnetic coupling between Mn atoms is sensitive to inter-atomic distance and charge state. While Mn_2 dimer is antiferromagnetic, removal of a single electron makes it ferromagnetic with a magnetic moment of 11 μ_B. We will study magnetic properties of clusters, nanowires, and two-dimensional arrays composed of Mn_2Au cluster which, due to charge transfer from Mn_2 to Au, also has a moment of 11 μ_B. Our studies not only complement recent experiments but also are aimed at guiding experiments in discovery of new materials.

REFERENCES:

1. Fang, H. and Jena, P.: "Super-ion Inspired Colorful Hybrid Perovskite Solar Cells", J. Mat. Chem. A **4**, 4728 (2016)
2. Liu, J., Sun, Q., Y. Kawazoe, K., and Jena, P.: "Exfoliating biocompatible ferromagnetic Cr-trichalcogenide monolayers", Phys. Chem. Chem. Phys. **18**, 8777 (2016)
3. Zhao, T., Zhou, J., Wang, Q., and Jena, P.: "Like Charges Attract?", J. Phys. Chem. Letters **7**, 2689 (2016)
4. Jena, P., and Castleman, A. W.: "Mass spectrometry and its role advancing cluster science", Int. J. Mass Spectrometry, **377**, 235 (2015) (invited Retrospective)
5. Jena, P.: "Superhalogens: A Bridge Between Complex Metal Hydrides and Li-ion Batteries", J. Phys. Chem. *Letters* **6**, 1119 (2015) (invited Perspective)
6. Jena, P.: "Atomic Clusters: Opportunities in the face of challenges", J. Phys. Chem. *Letters* **6**, 1549 (2015) (invited Viewpoint)
7. Mohtadi, R., Remhof, A., and Jena, P.: "Complex Metal Borohydrides: Multifunctional Materials for Energy Storage and Conversion", J. Phys. Cond. Mat. **28**, 353001 (2016) (invited topical review)

8. Jena, P., and Castleman, A. W.: "Mass spectrometry and its role advancing cluster science", Int. J. Mass Spectrometry, **377**, 235 (2015) (invited Retrospective)
9. O'Neal, K. R., Zhou, J., Cherian, J. G., Turnbull, M. M., Landee, C. P., Jena, P., Liu, Z., and Musfeldt, J. L.: "Pressure-induced structural transition in copper pyrazine dinitrate and implications for quantum magnetism", Phys. Rev. B **93**, 104409 (2016)
10. Islamoglu, T., Behera, S., Kahveci, Z., Tessema, T-D., Jena, P., El-Kaderi: "Enhanced Carbon Dioxide Capture from Landfill Gas using Bifunctinalized Benzimidazole-Linked Polymers", ACS Applied Materials & Interfaces **8**, 14648 (2016)
11. Mohtadi, R., Remhof, A., and Jena, P.: "Complex Metal Borohydrides: Multifunctional Materials for Energy Storage and Conversion", J. Phys. Cond. Mat. **28**, 353001 (2016) (invited topical review)
12. Zhang, S., Zhou, J., Wang, Q., Chen, X., Kawazoe, Y., and Jena, P.: "Penta-graphene: A New Carbon Allotrope", Proc. Nat. Acad. Sci. **112**, 2372 (2015)

PUBLICATIONS in 2015-2017:

1. Zhou, J., Zhang, S., Wang, Q., Sun, Q., Kawazoe, Y., and Jena, P.: "Self-assembly of Metal Atoms (Na, K, Ca) on Graphene", Nanoscale **7**, 2352 (2015)
2. Jena, P., and Castleman, A. W.: "Mass spectrometry and its role advancing cluster science", Int. J. Mass Spectrometry, **377**, 235 (2015) (invited Retrospective)
3. Zhang, S., Zhou, J., Wang, Q., Chen, X., Kawazoe, Y., and Jena, P.: "Penta-graphene: A New Carbon Allotrope", Proc. Nat. Acad. Sci. **112**, 2372 (2015)
4. Jena, P.: "Superhalogens: A Bridge Between Complex Metal Hydrides and Li-ion Batteries", J. Phys. Chem. *Letters* **6**, 1119 (2015) (invited Perspective)
5. Jena, P.: "Atomic Clusters: Opportunities in the face of challenges", J. Phys. Chem. *Letters* **6**, 1549 (2015) (invited Viewpoint)
6. Zhou, J. Wang, Q., Sun, Q., Kawazoe, Y., and Jena, P.: "Giant Magnetocrystalline Anisotropy of 5*d* Transition Metal-based Phthalocyanine Sheet", Phys. Chem. Chem. Phys. **17**, 17182 (2015)
7. Giri, S., Child, B., Zhou, J., and Jena, P.: "Unusual Stability of Multiply Charged Organo-Metallic Complexes", RSC Advances **5**, 44003 (2015)
8. Gutsev, G. L., Belay, K. G., Weatherford, C. W., Ramachandran, B. R., Gutsev, L. G., and Jena, P.: "Structure and Properties of Polyfluorides F_n^- Clusters (n = 3 – 29)", J. Phys. Chem. A. **119**, 6483 (2015)
9. Zhou, J., Wang, Q., Sun, Q., and Jena, P.: "High-temperature superconductivity in heavily N-(B-) doped graphene", Phys. Rev. B **92**, 064505 (2015)
10. Li, Y., Zhang, S., Yu, J., Wang, Q., Sun, Q., and Jena, P.: "A new C=C embedded porphyrin sheet with superior oxygen reduction performance", Nano Research, **8(9)**, 2901-2912 (2015)
11. Kandalam, A. K., Kiran, B., and Jena, P.: "Superhalogens beget Superhalogens: A case study with $(BO_2)_n$ oligomers", Phys. Chem. Chem. Phys. **17**, 26589 (2015)
12. Guo, Y., Wang, Q., Kawazoe, Y., and Jena, P.: "A New Silicon Phase with Direct Band Gap and Novel Optoelectronic Properties", Sci. Reports **5**, 14342 (2015)
13. Liu, J., Guo, Y., Zhang, S., Wang, Q., Kawazoe, Y. and Jena, P.: "New Phosphorene Allotropes Containing Ridges with 2- and 4- Coordination", J. Phys. Chem. C **119**, 24674 (2015)
14. Wu, F., Huang, C., Wu, H., Lee, C., Deng, K., Kan, E., and Jena, P.: "High-temperature Ferromagnetism and Half-metallicity in Flat Two-dimensional Transition-metal Dinitrides", Nano Letters. **15**, 8277 (2015)

15. Tao, K., Guo, Q., Jena, P., Xue, D., and Stepanyuk, V." "Tuning Magnetic Properties of Antiferromagnetic Chains with Exchange Interactions: *ab initio* Studies", Phys. Chem. Chem. Phys. **17**, 26302 (2015)
16. Mukherjee, P., Gupta, B., and Jena, P.: "Catalytic activities of Pt nanotubes: A density functional study", E. Phys. J. B **88**, 247 (2015)
17. Zhao, H., Zhou, J., Fang, H., and Jena, P.: "From Halogen to Superhalogen Behavior of Organic Molecules Created by Functionalizing Benzene", Chem. Phys. Chem. **17**, 184 (2016)
18. Zhang, S., Zhou, J., Wang, Q., and Jena, P.: "Beyond graphitic carbon nitride: Nitrogen-rich penta-CN2 sheet", J. Phys. Chem. C **120**, 3993 (2016)
19. Chen, Y., Kan, M., Sun, Q., and Jena, P.: "Structure and properties of Egyptian Blue monolayer family: $XCuSi_4O_{10}$ (X = Ca, Sr and Ba)", J. Phys. Chem. Letters **7**, 399 (2016)
20. Zhao, H., Zhou, J., and Jena, P.: "Stability of $B_{12}(CN)_{12}^{2-}$: Implications for Lithium and Magnesium Ion Batteries", Angew. Chem. Int. Ed. (*VIP*) **55**, 3704 (2016)
21. O'Neal, K. R., Zhou, J., Cherian, J. G., Turnbull, M. M., Landee, C. P., Jena, P., Liu, Z., and Musfeldt, J. L.: "Pressure-induced structural transition in copper pyrazine dinitrate and implications for quantum magnetism", Phys. Rev. B **93**, 104409 (2016)
22. Fang, H. and Jena, P.: "Super-ion Inspired Colorful Hybrid Perovskite Solar Cells", J. Mat. Chem. A **4**, 4728 (2016)
23. Liu, J., Sun, Q., Y. Kawazoe, K., and Jena, P.: "Exfoliating biocompatible ferromagnetic Cr-trichalcogenide monolayers", Phys. Chem. Chem. Phys. **18**, 8777 (2016)
24. Giri, S., Reddy, G.N., and Jena, P.: "Organo-Zintl Clusters $[P_7R_4]$: A New Class of Superalkalis", J. Phys. Chem. Lett. **7**, 800 (2016)
25. Fang, H. and Jena, P.: "Molecular Origin of the properties of organic-inorganic hybrid perovskites: The Big Picture from Small Clusters", J. Phys. Chem. Lett. **7**, 1596−1603 (2016)
26. Huang, C., Zhou, J., Wu, H., Deng, K., Jena, P., Kan, E.: "Quantum Phase Transition in Germanene and Stanene Bilayer: From Normal Metal to Large-gap Topological Insulator", J. Phys. Chem. Letters **7**, 1919 (2016)
27. Zhou, J., Wang, Q., Sun, Q., and Jena, P.: "Strain and Carrier-Induced Coexistence of Topologically Insulating and Superconducting Phase in iodized Si (111) Films", Nano Research **9**, 1578 (2016)
28. Mukherjee, P., Gupta, B. C., Jena, P.: "Magnetic Properties of Bimetallic Clusters Composed of Gd and transition metals", J. Appl. Phys. **119**, 074301 (2016)
29. Zhou, J. Sun, Q., Q. Wang, Q., Kawazoe, Y., and Jena, P.: "Intrinsic quantum spin Hall and quantum anomalous Hall effect in *h*-Sb/Bi epitaxial growth on ferromagnetic MnO_2 thin film", Nanoscale **8**, 11202 (2016)
30. Zhao, T., Wang, Q., and Jena, P.: "Cluster Inspired Design of High Capacity Anode for Li-Ion Batteries", ACS Energy Letters **1**, 202 (2016)
31. Wang, F. Q., Yu, J., Wang, Q., Kawazoe, Y., and Jena, P.: "Lattice thermal conductivity of penta-graphene", Carbon **105**, 424 (2016)
32. Zhou, J., Zhang, S., Wang, Q., Sun, Q., Jena, P.: "Integrating superconducting phase and topological crystalline quantum spin Hall effect in hafnium intercalated gallium film", Appl. Phys. Lett. **108**, 253102 (2016)
33. Zhao, T., Zhou, J., Wang, Q., and Jena, P.: "Like Charges Attract?", J. Phys. Chem. Letters **7**, 2689 (2016)
34. Zhu, G., Liu, J., Sun, Q., and Jena, P.: "Assembling bi-coordinated Cr complex for ferromagnetic nanorings: Insight from first-principles calculations", Phys. Chem. Chem. Phys. **18**, 17868 (2016)

35. Chen, Y., Sun, Q., and Jena, P.: "SiTe Monolayers: Si-Based Analogues of Phosphorene", J. Mat. Chem. C **4**, 6353 (2016)
36. Zhou, J., Huang, C., Kan, E., and Jena, P.: "Valley contrasting in epitaxial growth of In/Tl homoatomic monolayer with large anomalous Nernst conductance", Phys. Rev. B. **94**, 035151(2016)
37. Zhao, H., Zhou, J., and Jena, P.: "Substituent-stabilized Organic Dianions in the Gas Phase- and Their Potential for Electrolytes in Li-Ion Batteries, Chem. Phys. Chem. **17**, 2992 (2016)
38. Zhao, T., Zhou, J., Wang, Q., Kawazoe, Y., and Jena, P.: "Ferromagnetic and half-metallic FeC_2 monolayer containing C_2 dimers", ACS Applied Materials and Interfaces **8**, 26207 (2016)
39. Yao, Q., Fang, H., Deng, K., Kan, E., and Jena, P. "Superhalogens as Building Blocks of Two-Dimesional Organic-Inorganic Hybrid Perovskites for Optoelectronic Applications, Nanoscale **8**, 17836 (2016)
40. Islamoglu, T., Behera, S., Kahveci, Z., Tessema, T-D., Jena, P., El-Kaderi: "Enhanced Carbon Dioxide Capture from Landfill Gas using Bifunctinalized Benzimidazole-Linked Polymers", ACS Applied Materials & Interfaces **8**, 14648 (2016)
41. Yu, J., Sun, Q., and Jena, P.: "Assembling π-conjugated molecules with negative Gaussian curvature for efficient metal-free organic thermoelectric material", J. Phys. Chem C **120**, 27829 (2016)
42. Jena, P. and Kandalam, A.: "Proceedings of the International Symposium on Clusters and Nanomaterials" held in Richmond, VA, 2015. SPIE Digital Library, 2016
43. Mohtadi, R., Remhof, A., and Jena, P.: "Complex Metal Borohydrides: Multifunctional Materials for Energy Storage and Conversion", J. Phys. Cond. Mat. **28**, 353001 (2016) (invited topical review)
44. Huang, C., Zhou, J., Wu, H., Deng, K., Jena, P., Kan, K.: "Quantum Anomalous Hall Effect in Ferromagnetic Transition Metal Halides", Phys. Rev. B **95**, 045113 (2017)
45. Cheng, Y., Feng, X., Cao, X., Wen, B., Wang, Q., Kawazoe, Y., and Jena, P.: "Body-Centered Tetragonal C_{16} : A Novel Topological Node-Line Semi-Metallic Carbon Composed of Tetrarings", Small 1602894 (2017)
46. Zhou, J. and Jena, P.: "Two-dimensional Topological Crystalline Quantum Spin Hall Effect in Transition Metal Intercalated Compounds", Phys. Rev. B. **95**, 081102 (R) (2017)
47. Zhao, T., Wang, Q., and Jena, P.: "Rational Design of Superalkalis and Their Role in CO_2 Activation", Nanoscale (in press)

Optical, plasmonic, and excitonic phenomena in nanostructures described within a theoretical framework for dissipative quantum electronic transport

PI: Irena Knezevic, University of Wisconsin – Madison, irena.knezevic@wisc.edu

Program Scope

The objective of this project is to develop versatile theoretical models and computational tools for accurate predictive simulation of the far-from-equilibrium and time-dependent quantum electronic transport in realistic semiconductor nanostructures interacting with electromagnetic fields. A key challenge in simulating nonequilibrium time-dependent transport is that one must capture the interaction between electrons, phonons and other sources of dissipation, as well as electromagnetic fields in the same simulation, simultaneously and self-consistently.

Recent Progress

Dielectric function and plasmons in graphene. The challenge of understanding the optical response and plasmon behavior in nanostructured materials, such as graphene and its nanoribbons, lies in describing screening in the presence of several concurrent electron scattering mechanisms. We developed a technique for calculating the dielectric function of a dissipative electronic system with an arbitrary band dispersion and Bloch wave functions: a self-consistent-field approach within a Markovian master-equation formalism (SCF–MMEF) coupled with full-wave electromagnetic equations. This technique accurately captures interband electron-hole pair generation, as well as both interband and intraband electron scattering with phonons and impurities. We employ the SCF–MMEF to calculate the dielectric function, complex conductivity, and loss function for supported graphene (Fig. 1). From the loss-function maximum, we obtain plasmon dispersion and propagation length for different substrate types [nonpolar diamondlike carbon (DLC) and polar SiO_2 and hBN], impurity densities, carrier densities, and temperatures. Plasmons on the two polar substrates are suppressed below the highest surface phonon energy, while the spectrum is broad on the nonpolar DLC. Plasmon propagation lengths are comparable on polar and nonpolar substrates and are on the order of tens of nanometers, considerably shorter than previously reported. They improve with fewer impurities, at lower temperatures, and at higher carrier densities.

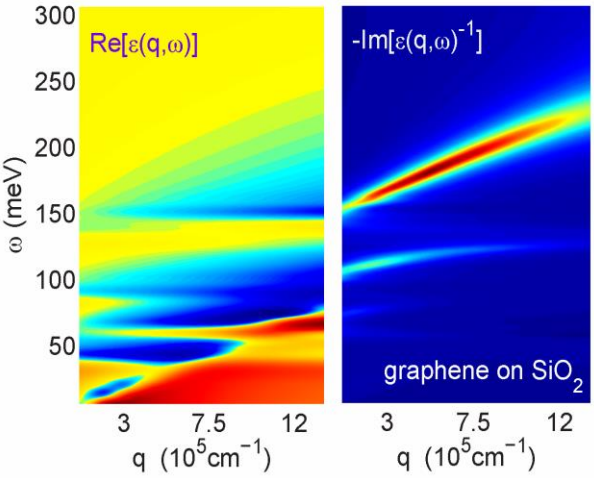

Fig. 1: Real part of the dielectric function (left panel) and the loss function (right) for graphene on SiO_2 with impurities in the substrate. The peak of the loss function gives the plasmon dispersion while the peak width gives information about dissipation due to scattering with phonons (graphene and substrate) and substrate impurities [1].

Exciton energy transfer in carbon nanotube composites. Photovoltaics based on aggregates of single-wall carbon nanotubes (CNTs) are promising candidates for cost-effective solar-energy harvesters. Understanding and controlling the diffusion of excitons (bound electron–hole pairs) through CNT aggregates are key to achieving high efficiencies in the photovoltaics based on CWT aggregates. However, experiments report a very wide range of typical times for ET rates between tubes, which makes it hard to understand the limiting mechanisms. Here, we computed the exciton transfer (ET) rate between semiconducting single-wall CNTs (Fig. 2) for different chiralities, orientations, lengths, as well as different temperatures, dielectric properties of the surrounding medium, and confinement due to disorder in the environment. We showed that the main reasons for the wide range of measured ET rates reported in the literature are (1) exciton confinement in local quantum wells stemming from disorder in the environment and (2) exciton thermalization between dark and bright states due to intratube scattering.

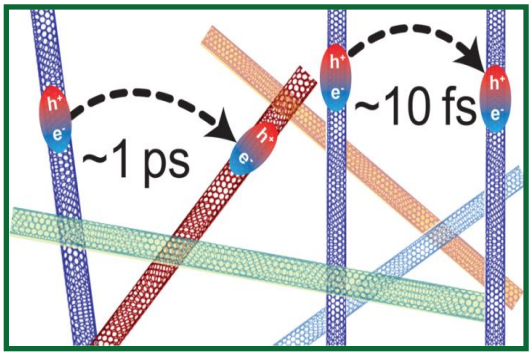

Fig. 2: Illustration of the exciton transfer process between single-wall carbon nanotubes. Based on our calculation, typical transfer between bundled parallel tubes is very fast (~10 fs) while it is roughly 2 orders of magnitude slower between misoriented tubes or tubes of different chirality (~ 1 ps). Due to disorder in the environment this difference vanishes, so most measurements will report exciton transfer lifetime on the order of 1 ps regardless of tube orientation of chirality (~0.1 ps if significant thermalization with the optically inactive dark states takes place) [2].

The SWNT excitonic states were calculated by solving the Bethe−Salpeter equation using tight-binding basis functions and the GW approximation. The ET rates due to intertube Coulomb interaction were computed via Fermi's golden rule. In pristine samples, the ET rate between parallel (bundled) CNTs of similar chirality is very high ($\sim 10^{14}$ s^{-1}), while the ET rate for dissimilar or nonparallel tubes is considerably lower ($\sim 10^{12}$ s^{-1}). Exciton confinement reduces the ET rate between same-chirality parallel CNTs by two orders of magnitude but has little effect otherwise. Consequently, the ET rate in most measurements will be on the order of 10^{12} s^{-1}, regardless of the tube relative orientation or chirality. Exciton thermalization between bright and dark states further reduces the ET rate to $\sim 10^{11}$ s^{-1}. The ET rate also increases with increasing temperature and decreases with increasing dielectric constant of the surrounding medium.

Density-matrix technique for modeling quantum cascade lasers. We derived a Markovian master equation for the single-electron density matrix, applicable to quantum cascade lasers (QCLs). The equation conserves the positivity of the density matrix, includes off-diagonal elements (coherences) as well as in-plane dynamics, and accounts for electron scattering with phonons and impurities. We used the model to simulate terahertz and midinfrared QCLs, and compared the results with both experiment and simulation via nonequilibrium Green's functions (NEGF). We obtained very good agreement with both experiment and NEGF when the QCL is biased for optimal lasing. For the considered devices, we show that the magnitude of coherences can be a significant fraction of the diagonal matrix elements (Fig. 3), which demonstrates their

importance when describing QCLs. We showed that the in-plane energy distribution deviated far from a heated Maxwellian distribution, which suggests that the assumption of thermalized subbands in simplified density-matrix models is inadequate. We also showed that the current density and subband occupations relax toward their steady-state values on very different time scales.

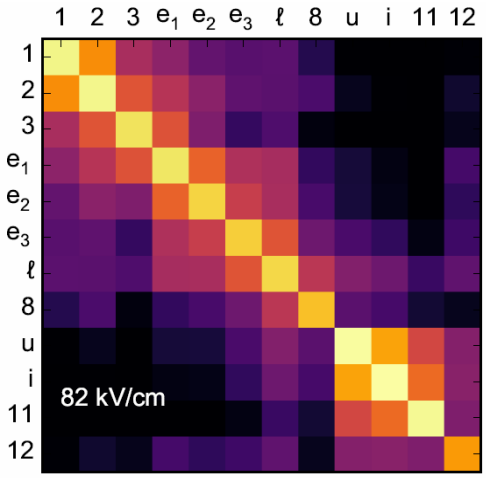

Fig. 3: A color map showing the absolute value of the density matrix elements on the log10 scale for a 4.6 μm quantum cascade laser from our density matrix calculation [4]. Bright color is high, dark is low. Upper (u), lower (l), and three extractor states (e1, e2, e3), the most efficient injector state (i) and other injector and extractor states are depicted. The results are at the operating field of 82 kV/cm, far above threshold.The off-diagonal terms of the density matrix are appreciable, so a quantum transport formalism is necessary [3,4].

Future Plans

On the front of calculating the dielectric response and plasmons in nanostructures, we are currently working on graphene nanoribbons (they show interesting features owing to their quasi-1D nature) and other two-dimensional materials, such as MoS_2 and phosphorene. We are also analyzing nonlinear response based on the same formalism.

On the front of exciton energy transfer in CNT composites, we are continuing the work on exciton hopping in carbon nanotube composites, specifically a) second-order phonon-assisted exciton transfer and b) the development of a full Monte Carlo simulation of exciton transfer process through a realistic real-space network of carbon nanotubes.

On the front of transport simulation in quantum cascade lasers, we are working on coupling full wave-electrodynamics with quantum transport to obtain a self-consistent picture of coherent light emission from these devices.

References

[1] F. Karimi, A. H. Davoody, and I. Knezevic, "Dielectric function and plasmons in graphene: a self-consistent-field theory within a Markovian master-equation formalism," *Phys. Rev. B* 93, 205421 (2016).

[2] A. H. Davoody, F. Karimi, M. S. Arnold, and I. Knezevic, "Theory of Exciton Energy Transfer in Carbon Nanotube Composites," *J. Phys. Chem. C* **120**, 16354−16366 (2016).

[3] O. Jonasson, F. Karimi, and I. Knezevic, "Partially coherent electron transport in terahertz quantum cascade lasers based on a Markovian master equation for the density matrix," *J. Comput. Electron.* 15, 1192 (2016).

[4] O. Jonasson, S. Mei, F. Karimi, J. D. Kirch, D. Botez, L. J. Mawst, and I. Knezevic, "Quantum transport simulation of high-power 4.6-μm quantum cascade lasers," *Photonics* 3, 38 (2016).

Publications

a) Journal publications

1. F. Karimi, A. H. Davoody, and I. Knezevic, "Dielectric function and plasmons in graphene: a self-consistent-field theory within a Markovian master-equation formalism," *Phys. Rev. B* 93, 205421 (2016). << Editors' suggestion
2. A. H. Davoody, F. Karimi, M. S. Arnold, and I. Knezevic, "Theory of Exciton Energy Transfer in Carbon Nanotube Composites," *J. Phys. Chem. C* **120**, 16354−16366 (2016).
3. Y. B. Shi, S. Mei, O. Jonasson, and I. Knezevic, "Modeling quantum cascade lasers: Coupled electron and phonon transport far from equilibrium and across disparate spatial scales," *Fortschritte der Physik - Progress of Physics*, 1600084 (2016) / DOI 10.1002/prop.201600084 (2016) (2016). http://arxiv.org/abs/1609.08717
4. O. Jonasson, F. Karimi, and I. Knezevic, "Partially coherent electron transport in terahertz quantum cascade lasers based on a Markovian master equation for the density matrix," *J. Comput. Electron.* 15, 1192 (2016).
5. L. N. Maurer, S. Mei, and I. Knezevic, "Rayleigh waves, surface disorder, and phonon localization in nanostructures," *Phys. Rev. B* **94**, 045312 (2016). << Image chosen for PRB Kaleidoscope
6. O. Jonasson, S. Mei, F. Karimi, J. D. Kirch, D. Botez, L. J. Mawst, and I. Knezevic, "Quantum transport simulation of high-power 4.6-μm quantum cascade lasers," *Photonics* 3, 38 (2016).
7. O. Jonasson and I. Knezevic, "Dissipative transport in superlattices within the Wigner function formalism," *J. Comput. Electron.* 14, 879-887 (2015).
8. L. N. Maurer, Z. Aksamija, E. B. Ramayya, A. H. Davoody, and I. Knezevic, "Universal features of phonon transport in nanowires with rough correlated surfaces," *Appl. Phys. Lett.* 106, 133108 (2015).

b) Full-length papers in conference proceedings

1. A. H. Davoody, A. J. Gabourie, and I. Knezevic, "Simulation of Resonance Energy Transfer in Carbon Nanotube Composites for Photovoltaic Applications," SISPAD 2015, Washington, DC, USA, September 9-11, 2015. http://dx.doi.org/10.1109/SISPAD.2015.7292267
2. A. H. Davoody and I. Knezevic, "Study of the Förster resonance energy transfer in composite films of carbon nanotubes," Proc. SPIE 9358, Physics, Simulation, and Photonic Engineering of Photovoltaic Devices IV, 93580T (March 16, 2015). http://dx.doi.org/10.1117/12.2079832
3. K. J. Willis, N. Sule, S. C. Hagness, and I. Knezevic, "Coupled simulation of carrier transport and electrodynamics: the EMC/FDTD/MD technique," Proc. SPIE 9357, Physics and Simulation of Optoelectronic Devices XXIII, 935706 (2015). http://dx.doi.org/10.1117/12.2083396

Tailoring Electron-Photon Interaction in Active 3D Photonic-Crystal Architectures

Shawn-Yu Lin[1] and Sajeev John[2], (1) Rensselaer Polytechnic Institute, Troy, NY 12180; (2) University of Toronto, Toronto, Canada

Program Scope Our research program is focused on the study of active 3D photonic-crystal (PC) architecture. Our first program is the study of ultra-thin solar cells, to be realized in 3D conical PC-architectures. The scientific goal is to implement this design concept, to accomplish a complete light-trapping over broad solar spectrum and to achieve power conversion efficiency of 25-30% for a silicon of only t=10μm thick. Our second program is to study metal- oxide 3D PC, operating in the visible and ultra-violate wavelengths. The scientific goal is to realize TiO_2 PC at wafer-scale, to study its ability to trap light with an effectively infinite optical path-length and to use it to form a new type of quantum cavity for a strong exciton-photon coupling.

Recent Progress Here, we will describe two recent advances in 3D visible PC-architectures. The first is the successful demonstration of a conical (teepee) silicon photonic-crystal. The spectral-average absorption over λ=400-1000nm is <Abs.>=98.5% for a t=500μm thick silicon and <Abs.>=95% for a t=10μm thick silicon [1, 2]. The accomplishment is shown in Figure.1 below.

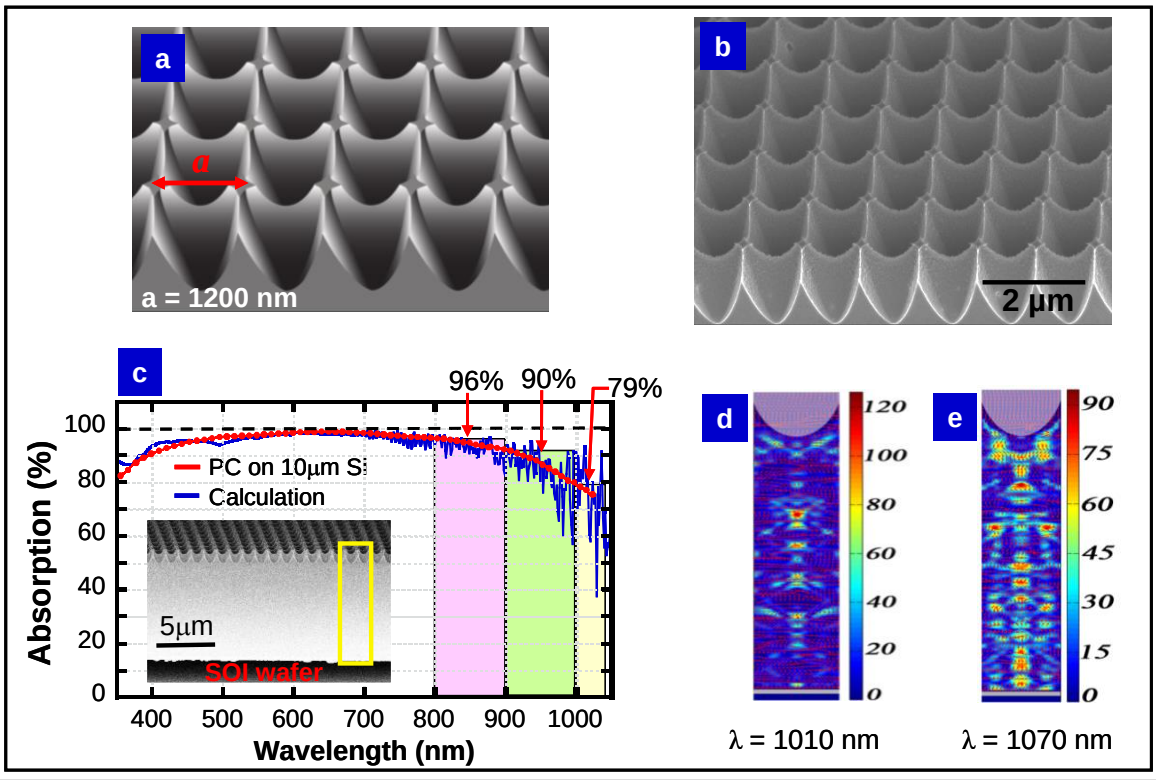

Figure.1 Teepee PC structure on 10μm thick silicon for near-unity solar absorption. (a) a schematic drawing of a Teepee-like PC; (b) a SEM image of a fabricated Teepee PC with a Gaussian index profile; (c) an absorption spectrum of Teepee PC on 10μm thick silicon; orthogonal slice plots for resonance at (d) λ=1010 nm and (e) λ~=1070 nm, for Poynting vector and energy density distribution, showing Vortex-like high field concentration (red color regions) of ~100 times in the PC 10-μm silicon structure.

The second is the realization of TiO_2 PC to experimentally validate a newly-discovered mechanism for extreme light-bending [3]. This absorption enhancement was observed extending 1-2 orders of magnitude over that of a reference TiO_2 film [4]. These results are not dependent on the material used, and can be applied to any future light trapping applications such as phosphor-converted white light generation, water-splitting, or thin-film solar cells, where increased response in areas of weak absorption is desired. A brief description of accomplishment is shown in Figure.2 below.

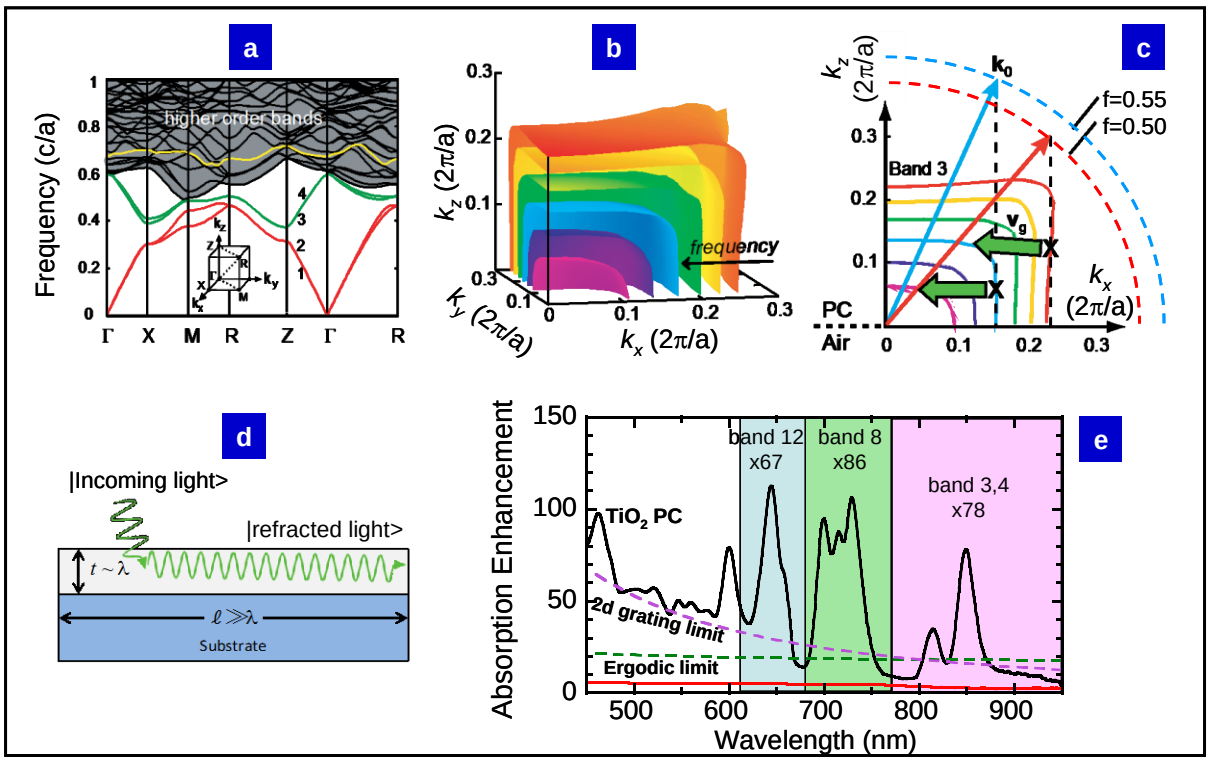

Figure.2 Dispersion, iso-frequency surfaces and absorption enhancement of a TiO_2 photonic crystal. (a) Photonic bandstructure of the simple cubic PC. The inset shows the first Brillouin zone of the simple cubic lattice. (b) Iso-frequency surfaces for frequencies in band 3. (c) Cross-section of the band 3 iso-frequency surfaces demonstrating parallel-to-interface refraction, PIR, (green arrows). (d) a schematic illustration of PIR refraction of light . (e)) Absorption Enhancement for PC at $\theta=18^0$ (black). Also shown are theoretical limits for absorption enhancement in an ergodic system (Lambertian Limit), and in the diffraction grating on absorbing layer scheme.

References

1. Kuang et al, "Achieving an accurate surface profile of a photonic crystal for near-unity solar absorption in a super thin-film architecture, ***ACS Nano*** 10, 6116 (2016).
2. S. Eyderman et al, "Light-trapping optimization in wet-etched silicon photonic crystal solar cells", ***J. Appl. Phys.*** 118, 23103 (2015).
3. A. Chutinan et al, "Light trapping and absorption optimization in certain thin-film photonic crystal architectures", ***Phys. Rev. A*** 78, 23825 (2008).
4. Frey et al, "Effectively infinite optical path length created using a simple cubic photonic crystal for extreme light trapping", ***Nature Scientific Reports*** (under revision), April 2017.

Future Plans The future research plan will be focused on:

(i) ***Greater than 30% efficient 10-μm thick crystalline silicon solar-cells using photonic-crystal*** We will continue to make advances in crystalline silicon PC photovoltaics (photo-current density I>42mA/cm^2), and crystalline silicon passivation (surface recombination velocity ~2cm/s). We will address the above mentioned challenges and realize the potential of practically approaching 30% plus photovoltaic conversion efficiency using an ultra-thin (~10 micron) crystalline silicon PC architecture.

(ii) ***100 times enhancement of optical path-length in a simple-cubic TiO_2 PC architecture*** In light of our recent success in realizing a visible TiO2 PC, capable of enhancing optical absorption by two-order-of-magnitudes, we will start to explore its potential applications in white light generation, water-splitting, or thin-film solar cells. Particularly, we will evaluate photo-activity of the TiO_2 photonic-crystal and characterize their redox properties (i.e. to determine density of states DOS). To test photo-activity, we have also decided to begin testing photocurrents generated by the PC materials.

(iii) ***Input-output characteristics of "quasi-thermal" radiation from a cavity/PC filament.*** Our recent experiment indicates a strong threshold behavior in the input-output characteristic of quasi-equilibrium thermal radiation from an integrated cavity-PC filament. We will continue to confirm the observation and to formulate a theoretical framework for it. We will also implement a new setup to provide a direct confirmation of super-Planckian radiation by near-infrared imaging.

(iv) ***Theoretical roadmap for approaching the Shockley-Queisser limit*** We plan to develop a full theoretical roadmap for approaching the Shockley-Queisser power conversion limit for crystalline silicon solar cells. Unlike all previous strategies to achieve world record efficiency using thick (100-400 μm) silicon, we will use light-trapping in 10-μm thick silicon to absorb 98% of all available sunlight in the 300-1100 nm wavelength range. Our future study will focus on the detailed interplay between this remarkable light-trapping in a thin film and electronic properties such as carrier diffusion lengths, surface recombination velocities and location of the P-N junction and contacts. Our preliminary finding is that if the minority carrier diffusion length is at least 50 times the cell thickness and the surface recombination velocity is in the range of 1-10 cm/sec, a power conversion efficiency of 30% is achievable with thin-film silicon.
We also plan to fabricate and experimentally test inverted-pyramid photonic-crystal silicon structures that fulfill the required optical and electronic properties for nearly 30% power conversion efficiency.

(v) ***Roadmap for GaAs/ 3D photonic-crystal sructure for room temperature Bose-Einstein Condensation (BEC)*** We plan to complete our theoretical roadmap for GaAs-based quantum-well structures, sandwiched by 3-D photonic band gap structures (woodpile and slanted pore) for realizing room-temperature, long-lifetime, equilibrium, BEC of exciton-polaritons. This involves careful balancing of exciton energy detuning from the photonic modes for appropriate polariton composition, choice of exciton densities within the quantum wells, and choice of the photonic architecture.
Preliminary studies suggest one or more routes to achieving room temperature BEC with experimentally realizable material parameters.
We also plan to study the nature of exciton-exciton interactions in these systems to determine if novel quantum many-body ground states (apart from the coherent-state BEC) can be realized under suitable circumstances.

Publications supported by DOE-BES Award (May 2015-May 2017)

1. "Effectively infinite optical pathlength created by simple-cubic photonic crystal for extreme light trapping", B. Frey, P. Kuang, M-L Hsieh, J.-H. Jiang, Sajeev John and Shawn-Yu Lin, ***Nature Scientific Report*** (under revision), April 2016.
2. "Achieving an Accurate Surface Profile of a Photonic-Crystal for Near-Unity Solar Absorption in a Super Thin-Film Architecture", Ping Kuang, S. Eyderman, M.-L. Hsieh, A. Post, Sajeev John, and Shawn-Yu Lin, ***ACS Nano* 10,** 6116-1624 (2016).
3. " Probing the Intrinsic Optical Bloch-Mode Emission from a Three-Dimensional Photonic Crystal", Mei-Li Hsieh, James A. Bur, Qingguo Du, Sajeev John, and Shawn-Yu Lin, ***Nanotechnoogy* 27,** 415204 (2016).
4. "Experimental observation of unusual thermal radiation from a 3D metallic photonic-crystal", Mei-Li Hsieh, Shawn-Yu Lin, J. Bur and R. Shenoi, ***Nanotechnology* 26**, 234002 (2015).
5."Integrated three-dimensional photonic nanostructures for achieving near-unity solar absorption and superhydrophobicity", P. Kuang, M.L. Hsieh and Shawn-Yu Lin, ***J. Appl. Phys* 117**, 215309 (2015).
6. "Lens-less bending and concentration of light by volume hologram", M.L. Hsieh, H Y Chen, C.T. Peng and Shawn-Yu Lin, ***Optics Communications* 365**, p. 12-16 ***(***2015).
7. "Light-trapping and recycling for extraordinary power conversion in ultra-thin gallium-arsenide solar cells," Sergey Eyderman and Sajeev John, ***Nature Scientific Reports* 6** 28303 (2016).
8. "Light-trapping in perovskite solar cells," Qing Guo Du, Guansheng Shen and Sajeev John, ***AIP Advances* 6,** 065002 (2016).
9."Light-trapping for room temperature Bose-Einstein condensation in InGaAs quantum wells," Pranai Vasudev, Jian-Hua Jiang and Sajeev John, ***Optics Express* 24** No.13, 14010 (2016).
10. "Light-trapping design for thin-film silicon-perovskite tandem solar cells," Stephen Foster and Sajeev John, ***Journal of Applied Physics* 120**, 103103 (2016).
11. "Light-trapping optimization in wet-etched silicon photonic crystal solar cells," Sergey Eyderman, Sajeev John, M. Hafez, S. S. Al-Ameer, T. S. Al-Harby, Y. Al-Hadeethi and D. M. Bouwes, ***Journal of Applied Physics* 118**, 023103 (2015).
12. "Waveguide-mode polarization gaps in square spiral photonic crystals," Rong-Juan Liu, Sajeev John and Zhi-Yuan Li, ***EPL*, 111** 54001 (2015).

Universal Parameter to Quantitatively Predict Metallic Glass Properties

E. Ma

Department of Materials Science and Engineering, Johns Hopkins University, Baltimore, MD 21218 ema@jhu.edu

Program Scope

Identifying the microscopic mechanisms that control the behavior of glasses is one of the most challenging unresolved problems in physical sciences. Structure-property relationship, in particular, is a central tenet of materials science. For metallic glasses (MGs), the *amorphous* nature of their structures poses major challenges, to a quantitative prediction of the properties. This project is designed to establish "flexibility (volume)" as a universal indicator of the state the MG structure is in, as well as a *quantitative* property correlation derived and confirmed for all MGs.

The flexibility volume will be demonstrated to be universally applicable across various MGs and lengscales from atomic level and up, using molecular dynamics (MD) simulations and synchrotron X-ray experiments, for MGs of all compositions and processing history, enabling a direct comparison of different MG systems to explain the composition dependence often observed for properties. We will illustrate the advantages of flexibility volume over previous phenomenological structural descriptors, such as free volume, liquid-like regions, soft spots and local atomic packing topology.

The advances are expected to help explain the much lowered and variable elastic modulus of MGs with respect to their conventional crystalline counterpart. The availability of a single indicator for a robust property correlation should be of widespread interest to both experimentalists and modelers, particularly useful for formulating mathematical equations about the behavior of the MGs.

Recent Progress

During the past year, we have studied ~32 MGs in 13 alloy systems, using MD simulations. The results have been reported in Ref. 1. The new indicator, termed "flexibility volume" (υ_{flex}), is defined as

$$\upsilon_{flex} = f \cdot \Omega_a , \qquad (1)$$

where $f = \frac{\langle r^2 \rangle}{a^2}$ brings in the critical dynamics information from the vibrational mean square displacement (MSD), via the Lindemann ratio, where $a = \sqrt[3]{\Omega_a}$ (Ω_a is atomic volume) is the average atomic spacing. Starting from the Debye model, we derived that υ_{flex} universally and deterministically controls the shear modulus, *G*, at any given temperature (*T*),

$$G = C\frac{k_B T}{\langle r^2 \rangle \cdot a} = C\frac{k_B T}{\upsilon_{flex}}, \qquad (2)$$

where *C* is predicted to be a universal constant. Our data suggest that for MGs at temperatures well below glass transition, the flexibility volume has advantages over previous structural descriptors, as summarized below in eight respects. First, the υ_{flex} is

clearly defined, from the atomic level and up, making it a simple and yet quantitative parameter. Second, the absolute value of υ_{flex} is measurable both computationally and experimentally, incorporating the readily known atomic volume and the familiar vibrational MSD (not either one alone). Third, υ_{flex} is indeed a universal indicator that enables comparison of various MG states (and properties) at different compositions and processing conditions, mapping all of them onto a common metric and reference. This is shown in Fig. 1, which quantitatively validates the correlation derived and predicted in Eq. (2), for a wide range of υ_{flex} and shear modulus *G* for over 30 MGs.

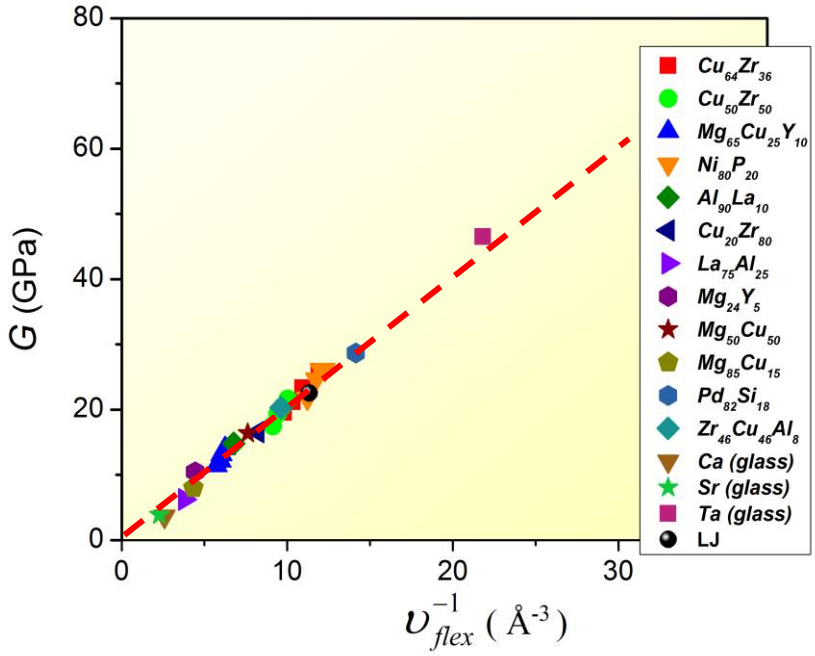

Figure 1 Universal and quantitative correlation between the shear modulus and the flexibility volume in metallic glasses. The values of *G* and υ_{flex} are computed for 32 different MGs at 300 K. The dashed straight line is not a fit, but the prediction derived in Eq. (2).

Fourth, the effects of anisotropic distribution of the accessible volume, as well as of local packing environment and chemical interaction between neighboring atoms, are all included in, or reflected by, the flexibility volume. Fifth, as an advance over static structural descriptors it also incorporates dynamics survey information obtained from probing the landscape, akin to Debye-Waller parameter used before for viscosity and dynamic heterogeneity in liquids. From these latter two aspects, a collection of factors is now replaced by a single workable metric υ_{flex}, which is then expected to connect strongly to MG behavior, as indeed seen in the next three areas. Sixth, υ_{flex} is actually the "tell-tale" structural parameter deterministic of shear modulus, Eq. (2). Such a quantitative correlation was not possible for all standard structural parameters, including free volume and fictive temperature (and even the MSD alone, which was hypothesized but not demonstrated). Specifically, our extensive and systematic data set establish that MGs can be treated as normal Debye solid, with υ_{flex} as the proper variable to quantitatively link the vibrational behavior with elastic constants. Moreover,

through G and its correspondence with other state variables, υ_{flex} serves to provide a common underpinning that predicts the various properties originating from the configurational state. For example, increasing the quench rate or aging temperature around T_g of an MG would impart a higher υ_{flex}, which then quantitatively predicts a lowered G that reduces the barrier for shear flow, and hence an exponentially increased participation probability in shear transformations and consequently fracture toughness. Seventh, υ_{flex} exhibits strong correlation with the participation in low-frequency soft vibrational modes (soft spots), and more usefully with slow dynamics such as (energy barrier for) thermally activated β relaxation, and with (propensity for) stress-activated shear transformations. The latter correlation is illustrated in Fig. 2 below.

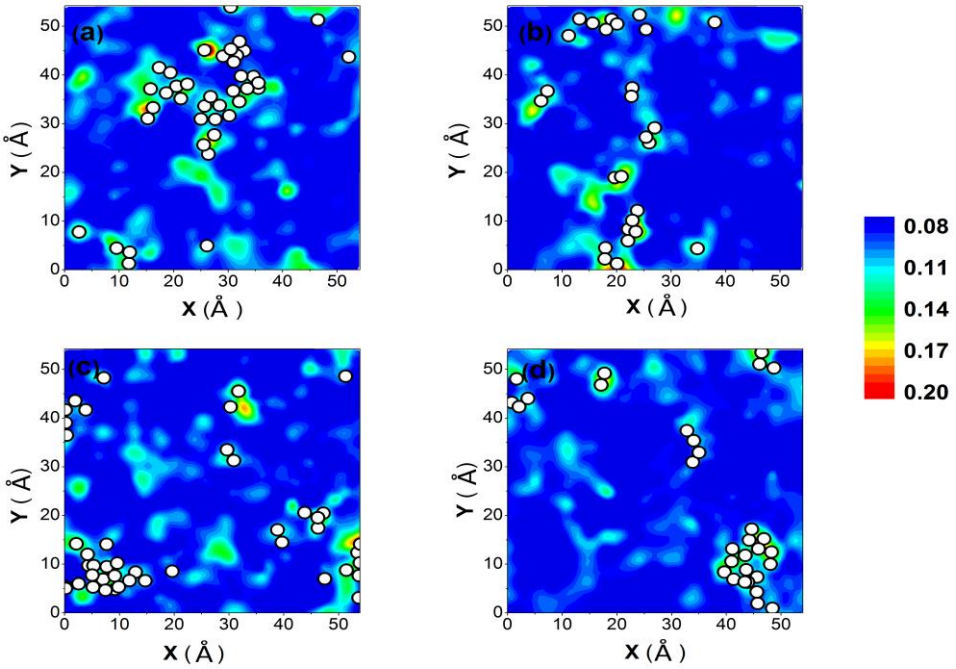

Figure 2 Strong correlation between $\upsilon_{flex,i}$ and shear transformations. Contoured maps show the spatial distribution of flexibility volume $\upsilon_{flex,i}$ (see sidebar: high flexibility corresponds to brighter colors) in the $Cu_{64}Zr_{36}$ metallic glass. Four slabs (a-d) are sampled for illustration purposes and each has a thickness of 2.5 Å. White spots superimposed in the maps mark the locations of atoms that have experienced the most (top 5%) accumulative non-affine displacement (D^2_{min}), upon athermal quasi-static shear of the simulation box to a global strain of 5%. Note that not all such regions would undergo shear transformation for a particular loading. This is reasonable because apart from the intrinsic flexibility of the local configurations, the stress field (tensor) is another (extrinsic) factor that will influence the response of the atoms.

Eighth and finally, on the one hand the $\upsilon_{flex,i}$ of atoms is directly determined by local topological and chemical environment, making the local average a prognostic parameter in monitoring the inherent structural inhomogeneity distributed inside an MG, and on the other hand υ_{flex} exhibits robust correaltions with local dynamic properties, signaling a structural mechanism to connect with the spatial elastic or plastic

heterogeneity. As such, the flexibility volume also serves as a quantitative benchmark for explaining the mechanical heterogeneities in MGs. All these attributes make υ_{flex} a useful property-revealing indicator of the structural state. In comparison, the frequently invoked free volume (or Ω_a) is deficient in each of these respects, as confirmed again in our simulated systems. In the meantime, the simple υ_{flex} is particularly convenient for integration into mathematical equations for theory and modeling, to represent the structural state from local atomic configurations all the way to the global MG sample (system average). All these justify our introduction of the flexibility volume for dealing with MG problems, and incentivize the adoption of this new structural parameter, in lieu of the widely cited but ambiguous **"**free volume", to explain the effective atomic flexibility beyond the traditional space-centric view.

The flexibility parameter builds a bridge between the structure and properties of MGs, making the correlation universally quantitative with no fitting parameters, which was not possible with any of the previous structural indicators. The ability to predict and compare the properties of various MGs based on a single parameter will be interesting to experimentalists who take an MG to different configurational states via thermomechanical processing, in particular intentional rejuvenation of the MG structure, as well as to modelers that need such a quantitative indicator to represent the state the MG is in (as well as the distribution of inhomogeneity inside the glass structure) when writing mathematical equations. Our findings thus address a pressing challenge facing materials scientists in the field of amorphous metals, *i.e*., the lack of robust, causal and mathematically derivable relationships that link the MG structure with properties [1].

Future Plans

In the second year of this project, we will measure the flexibility volume experimentally, in addition to the computational analyses reported above. The flexibility volume υ_{flex} can be obtained from the MSD, $\langle r^2 \rangle$, or Debye temperature θ_D, both of which can be measured in the laboratory via Inelastic Neutron Scattering (INS) and X-ray/neutron diffraction. We are in the process of applying for beam time at ORNL, and are making MG samples in 5 selected alloy systems. We will first experimentally determine their shear modulus using ultrasound velocity measurements, and then measure the flexibility in these very same samples, such that we can quantitatively validate the correaltion in Eq. (2).

Another issue that remains to be examined is if this flexibility parameter is useful for other types of glasses with bonding characteristics, atomic packing structures as well as properties that are distinctly different from metallic glasses. In the second year, we will tackle this issue through systematic MD simulations of amorphous silicon (a-Si) models produced with different cooling rates, as a-Si is a prototypical covalently bonded network glass whose structure and properties cannot be characterized using structural parameters such as free volume used for metallic and polymeric glasses. This will help establish the universality of flexibility volume, applicable across amorphous materials with different chemical bonding and atomic packing structures.

[1] Ding, Jun; Cheng, Y.-Q.; Sheng, Howard; Asta, M; Ritchie, R.; Ma, Evan; *Universal structural parameter to quantitatively predict metallic glass properties*, **Nature Communications** Volume: 7 No: 13733 Published: DEC 12 2016 DOI: 10.1038/ncomms13733

Publications

The most recent (~ past 2 years) papers are listed below.

1. Meng Li, De-Gang Xie, Evan Ma, Ju Li, Xi-Xiang Zhang & Zhi-Wei Shan, *Effect of hydrogen on the integrity of aluminum oxide interface at elevated temperatures*, **Nature Communications** 8 (2017) 14564.

2. E. Ma and J. Ding, *Tailoring structural inhomogeneities in metallic glasses to enable tensile ductility at room temperature*, review in **Materials Today** 19 (2016) 568-579.

3. Ding, Jun; Cheng, Yong-Qiang; Sheng, Howard; Asta, Mark; Ritchie, R.; Ma, Evan; *Universal structural parameter to quantitatively predict metallic glass properties*, **Nature Communications** Volume: 7 No: 13733 Published: DEC 12 2016 DOI: 10.1038/ncomms13733

4. Li, Qing-Jie; Li, Ju; Shan, Zhi-Wei; Ma, Evan; *Strongly correlated breeding of high-speed dislocations*, **Acta Materialia** Volume: 119 Pages: 229-241 Published: OCT 15 2016 DOI: 10.1016/j.actamat.2016.07.053

5. Li, Qing-Jie; Li, Ju; Shan, Zhi-Wei; Ma, Evan, *Surface Rebound of Relativistic Dislocations Directly and Efficiently Initiates Deformation Twinning*, **Physical Review Letters** 117 (16) 165501 Published: OCT 11 2016 DOI: 10.1103/PhysRevLett.117.165501

6. Ding, Ming-Shuai; Tian, Lin; Han, Wei-Zhong; Li, J; Ma, Evan; Shan, Zhi-Wei; *Nanobubble Fragmentation and Bubble-Free-Channel Shear Localization in Helium-Irradiated Submicron-Sized Copper*, **Physical Review Letters** Volume 117 (21) 215501 Published: NOV 16 2016 DOI: 10.1103/PhysRevLett.117.215501

7. D. G. Xie, M. Li, E. Ma, J. Li and Z. W. Shan, *Hydrogenated Vacancies Lock Dislocations in Aluminum*, **Nature Communications**, 7 (2016) 13341.

8. Wang, Yue-Cun; Zhang, Wei; Wang, Li-Yuan; Zhuang, Z; Ma, Evan; Li, J; Shan, Zhi-Wei; *In situ TEM study of deformation-induced crystalline-to-amorphous transition in silicon*, **NPG Asia Materials** Volume 8 Published: JUL 2016 DOI: 10.1038/am.2016.92

9. Zhang, B, Zhang, W, Shen, ZJ, Chen, YJ, Li, JX, Zhang, SB, Zhang, Z, Wuttig, M, Mazzarello, R, Ma, E, Han, XD, *Element-resolved atomic structure imaging of rocksalt Ge2Sb2Te5 phase-change material*, **Applied Physics Letters** 108 (2016) 191902.

10. Ding, MS, Du, JP, Wan, L, Ogata, S, Tian, L, Ma, E, Han, WZ, Li, J, Shan, ZW, *Radiation-Induced Helium Nanobubbles Enhance Ductility in Submicron-Sized Single-Crystalline Copper*, **Nano Letters** Volume 16 Pages: 4118-4124 Published: JUL 2016.

11. Yang, MX, Yuan, FP, Xie, QG, Wang, YD, Ma, E and Wu, XL, *Strain hardening in Fe-16Mn-10Al-0.86C-5Ni high specific strength steel*, **Acta Materialia** Volume: 109 Pages: 213-222 Published: MAY 1 2016.

12. N.C. Wu, L. Zuo, J.Q. Wang and E. Ma, *Designing aluminum-rich bulk metallic glasses via electronic-structure-guided microalloying*, **Acta Mater.** 108 (2016) 143-151.

13. Zhen-Qiang Song, Evan Ma and Jian Xu, *Mode III fracture toughness of the Zr61Ti2Cu25Al12 bulk metallic glass*, **Acta Mater**. 109 (2016) 275-285.

14. X. G. Wang, K. Chen, Y. Q. Zhang, J. C. Wan, O. L. Warren, J. Oh, J. Li, E. Ma and Z. W. Shan, *Growth Conditions Control the Elastic and Electrical Properties of ZnO Nanowires*, **Nano Letters**, Volume:15 Issue:12 Pages:7886-7892 DOI:10.1021/acs.nanolett.5b0285 Published: DEC 2015.

15. Z. J. Wang, Q. J. Li, Y. N. Cui, Z. L. Liu, E. Ma, J. Li, J. Sun, Z. Zhuang, M. Dao, Z. W. Shan, and Subra Suresh, *Cyclic deformation leads to defect healing and strengthening of small-volume metal crystals*, **Proceedings of the National Academy of Sciences of the United States of America**, Volume:112 Issue:44 Pages:13502-13507 DOI:10.1073/pnas. 1518200112 Published: NOV 2015.

16. Song, ZQ; He, Q; Ma, E; Xu, J, *Fatigue endurance limit and crack growth behavior of a high-toughness Zr61Ti2Cu25Al12 bulk metallic glass*, **Acta Mater.**, Volume: 99 Pages:165-175 DOI:10.1016/j.actamat.2015.07.071 Published: OCT 2015.

17. W. Zhang, V. L. Deringer, R. Dronskowski, R. Mazzarello, E. Ma and M. Wuttig, *Density functional theory guided advances in phase-change materials and memories*, **MRS Bulletin,** Volume:40 Issue:10 Pages:856-869 DOI:10.1557/mrs.2015.227 Published: OCT 2015.

18. D. G. Xie, Z. J. Wang, J. Sun, J. Li, E. Ma and Z. W. Shan, *In situ study of the initiation of hydrogen bubbles at the aluminium metal/oxide interface*, **Nature Materials**, Volume:14 Issue:9 Pages:899-903 DOI:10.1038/NMAT4336 Published: SEP 2015.

19. X.L. Wu, F.P. Yuan, E. Ma, *Nanodomained Ni Unites Nanocrystal Strength with Coarse-Grain Ductility*, **Scientific Reports** 5 (2015) 11728.

20. Mao, YW; Li, J; Lo, YC; Qian, XF; Ma, E, *Stress-driven crystallization via shear-diffusion transformations in a metallic glass at very low temperatures*, **PHYSICAL REVIEW B**, Volume:91 Issue: 21 Art No. 214103 DOI:10.1103/PhysRevB.91.214103 Published: JUN 2015.

21. Ma, E, *Tuning order in disorder*, **Nature Materials**, Volume:14 Issue:6 Pages: 547-552 DOI:10.1038/nmat4300 Published: JUN 2015.

Energy and Photon Conversion with Nanocrystals and Optically Active Media

(Project # DE-SC0010697)

PIs: Anton Malko, Yves Chabal, and Yuri Gartstein (The University of Texas at Dallas)

Program Scope

Photon management and exciton conversion represent transformative opportunities for improved operational and functional performances, providing the fields of optoelectronics, nanophotonics and energy materials with new functionalities. This project explores the underlying scientific questions for such opportunities arising in hybrid nanostructures comprised of different materials components that are coupled via near-field electromagnetic interactions mediating radiative and nonradiative energy transfer (ET) [1-3]. We specifically focus on structures that would contain hierarchically ordered nanocrystal solids and various semiconductors such as crystalline Si, two-dimensional transition metal dichalcogenides (TMDCs) and strongly absorbing organic-inorganic perovskites. We explore applications of different nanocrystal quantum dots (NQDs): from well-known smaller-size CdSe/ZnS dots to novel "giant" nanocrystals (gNQDs) that have reduced Auger recombination rates and support multiexcitonic (MX) states.

Recent Progress

<u>*Towards "designer" NQD solids*</u> [4]. Many applications could benefit from dense NQD assemblies with precise control over the composition and location of NQDs. Such assemblies *would constitute an essential part of the overall photonic environment, where the interconversion between photons and NQD excitons and resulting energy flows take place in an application-*oriented way. As a step toward production of macroscopically thick, high-quantum-yield NQD solids with controlled layered configurations, we succeeded at using the sequential assembly method to deposit multilayer NQD structures on different substrates (Figure 1a). The stepwise approach enabled precise placement of each layer a discrete distance from the substrate and allowed us to observe the spectroscopic evolution of NQD excitons upon addition of individual discrete layers. The observed spectroscopic signatures agree well with theoretical expectations (Figure 1b).

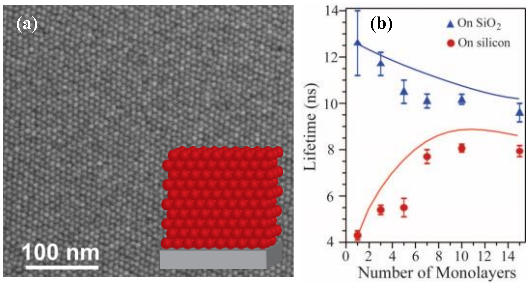

Figure 1. (a) SEM image and schematic of dense multilayers of CdSe/ZnS NQDs. (b) Measured PL lifetimes for multilayers deposited on Si (red circles) and SiO_2 (blue triangles) substrates. Solid lines show modeling results.

<u>*Nanocrystals with efficient multiexcitonic properties*</u> [5,6]. Exciton thermalization via phonon emission is a major contributor to the Shockley-Queisser (SQ) photovoltaic limit. Multiexcitonic

(MX) photoexcited states may help alleviate this effect. Novel types of core/shell gNQDs with suppressed Auger recombination and much longer multiexciton lifetimes are the candidates to support such states. In collaboration with Dr. Hollingsworth at LANL, we designed, synthesized and characterized several types of core/shell CdSe/CdS nanocrystals with efficient emission from charged exciton and multiexciton states. With silica-coated CdSe/CdS gNQDs, e.g., we observed and studied the emergence of up to 8 emissive states in a single gNQD's emission (Figure 2c). Furthermore, we demonstrated the possibility to exploit the shape *asymmetry* in core/shell nanostructures (nanorods, tetrapods) to enhance the opportunities for MX states. Figure 2a illustrates the CdSe/CdS tetrapod realization, where eneregtically distinct emissions arise from a CdSe core (Figure 2b, red) and an elongated CdS shell/arm (green). The properties of dual emission and photostability were found to depend on different structural parameters—arm length and arm diameter, respectively—but both properties can be realized in the same nanostructure.

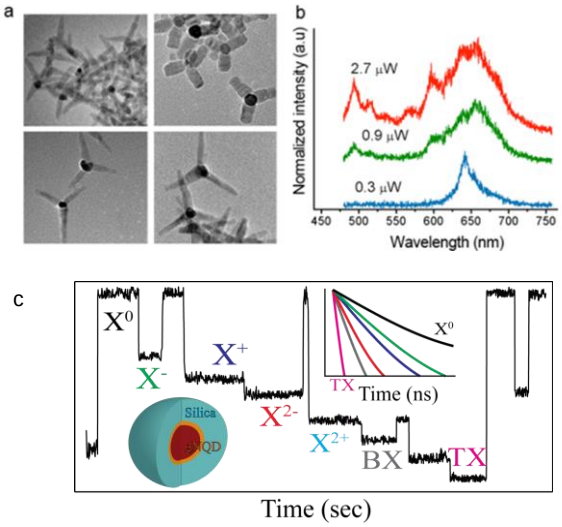

Figure 2. (a) TEM images and (b) PL spectra of individual CdSe/CdS tetrapod showing evolution of MX lines from core and arms as the function of excitation power. (c) Several excitonic complexes in a blinking trace of a single silica-coated gNQD.

Energy transfer from trions and biexcitons into semiconducting substrates [7,8]. We provided experimental evidence for efficient ET from higher-order photoexcited gNQD states (trions and biexcitons) into two very different types of semiconducting substrates that are mediated by physically distinct mechanisms. Nonradiative ET (NRET) was demonstrated from charged excitons (trions) into proximal monolayer MoS_2 (Figure 3). A macroscopic electrodynamics model for the decay of electric-dipole emitters in the vicinity of an ultrathin semiconducting layer with a strong in-plane excitonic polarizability confirmed the viability of observed high NRET efficiencies from >95% to 85% for dots with diameters from 10 to 20 nm. This demonstration opens new possibilities for studies of ET between zero-dimensional emitters and the whole class of novel two-dimensional absorbers, potentially enabling new avenues for multiexciton harvesting and utilization. We further employed gNQDs in the vicinity of crystalline Si substrates and conducted collection of massive amount of photoluminescence (PL) decay traces that were compared to analogous data on reference (glass) substrates. The statistical

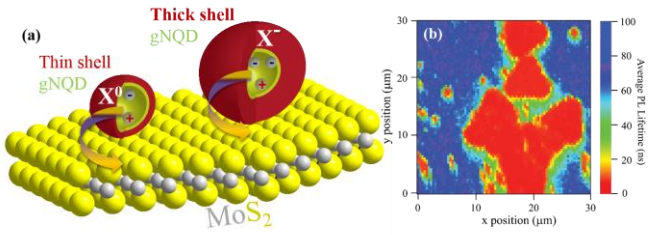

Figure 3. (a) Schematics of nonradiative ET from excitons and trions found in gNQDs to monolayer MoS_2 domain. (b) PL lifetime surface scan of MoS_2 domains grown on sapphire substrate and covered with gNQDs. Blue areas - lifetimes of gNQDs on sapphire, red - on MoS_2.

analysis of PL lifetimes clearly shows the acceleration of PL decay taking place on Si substrates for all three types of excited species that were clearly identifiable: ordinary neutral excitons, trions and biexcitons. The representative ET efficiencies were respectively estimated at ~ 75%, 55% and 45%. Detailed analysis of the MX decay rates demonstrate that in this case it is the radiative ET mechanism that plays the crucial role in maintaining high overall transfer efficiency (Figure 4).

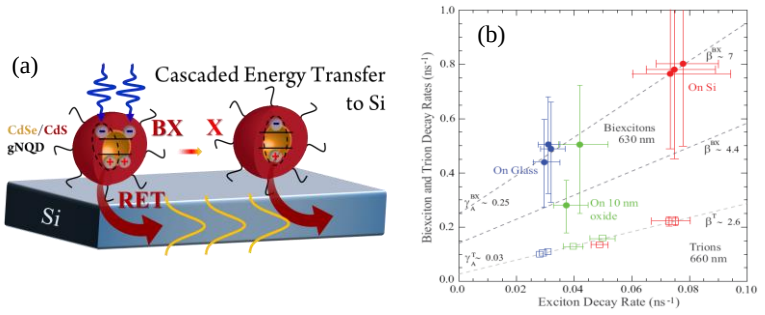

Figure 4. (a) Schematics of radiative ET from excitons and biexcitons found in gNQDs into Si substrate. (b) The interdependence of trion and biexciton decay rates vs exciton's collected from different samples.

Enhancement of monolayer MoS_2 photoluminescence due to ET from nanocrystals [9]. Monolayer TMDCs like MoS_2 constitute a new class of two-dimensional direct-gap semiconductors widely believed to be promising candidates for various optoelectronic applications. The typical photoluminescence (PL) of monolayer MoS_2 is however known to suffer very low quantum yields. We demonstrated that a nearly 10-fold increase of MoS_2 excitonic PL (Figure 5c) can be enabled by NRET from adjacent NQD films. We also applied transient absorption (TA) spectroscopy to monitor the energy influx into the monolayer MoS_2 in the process of ET from photoexcited CdSe/ZnS nanocrystals (Figure 5b) and registered an order of magnitude enhancement of the MoS_2 excitonic TA signatures in hybrid structures with NQDs. The appearance of ET-induced nanosecond-scale kinetics in TA features is consistent with PL dynamics of energy-accepting MoS_2 (Figure 5a) and PL quenching data of the energy-donating NQDs. The observed enhancement was attributed to the reduction of recombination losses for excitons gradually transferred via ET into MoS_2 under quasi-resonant conditions.

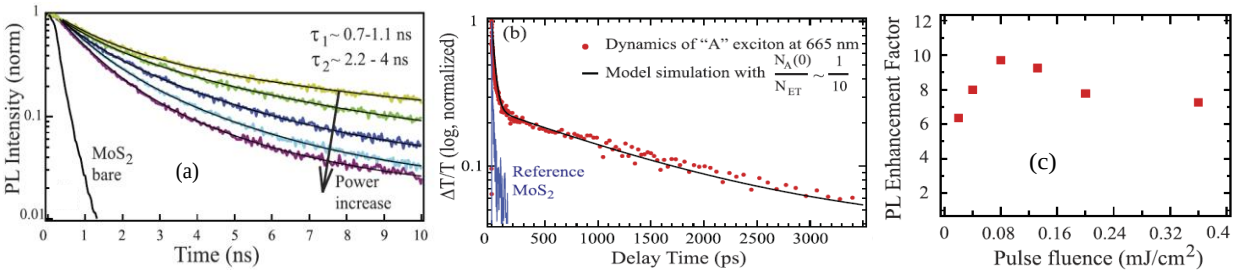

Figure 5. Comparison of reference bare monolayer MoS_2 and hybrid MoS_2/NQDs samples in: (a) PL lifetime, (b) transient absorption, (c) PL magnitude.

Future Plans

Our future plans are several-fold. We will continue studying ways to fabricate well-ordered dense NQD solids, in particular via conformal dip-coating assisted by Atomic Layer Deposition (ALD) to passivate, protect and stabilize the NQD layers. We will continue synthesis and development of nanocrystals of different dimensionalities and spectral signatures for ET applications, in particular NQDs with enhanced MX-bearing abilities and gNQDs for the NIR range. The ET interactions will be explored between NQDs and various representatives of atomically flat 2D materials beyond MoS_2, including heterostructures thereof that can feature not only intraplane (both charges reside within the same TMDC layer) but also interplane (charges separated into different TMDC layers) excitons. These studies will include extensions to low-temperature as well as to electrical measurements. We also plan to start exploration of more involved hybrid structures that can take advantage of enhanced near-field interactions in plasmonic, waveguiding and microcavity configurations.

References

[1] Agranovich, V. M.; Gartstein, Y. N.; Litinskaya, M. *Chem. Rev.* **2011**, 111, 5179.

[2] Peng, W.; Rupich, S. M.; Shafiq, N.; Gartstein, Y. N.; Malko, A. V.; Chabal, Y. J. *Chem. Rev.* **2015**, 115, 12764.

[3] Guzelturk, B.; Demir, H. V. *Adv. Funct. Mater*. **2016**, 26, 8158.

[4] Rupich, S. M.; Gartstein, Y. N.; Chabal, Y. J.; Malko, A. V. *Adv. Opt. Mat.* **2016**, 4, 378.

[5] Sampat, S.; Karan, N. S.; Guo, T.; Htoon, H.; Hollingsworth, J. A.; Malko, A. V. *ACS Photonics* **2015**, 2, 1505.

[6] Mishra, C. N.; Orfield, N. J.; Wang, F.; Hu, Z.; Krishnamurthy, S.; Malko, A. V.; Casson, J. L.; Htoon, H.; Sykora, M.; Hollingsworth, J. A. *Nat. Commun.* **2017**, 8, 15083.

[7] Sampat, S.; Guo, T.; Zhang, K.; Robinson, J.A.; Htoon, H.; Hollingsworth, J. A.; Gartstein, Y. N.; Malko, A. V. *ACS Photonics* **2016**, 3, 708.

[8] Guo, T.; Sampat, S.; Rupich, S.M.; Hollingsworth, J.A.; Htoon, H.; Chabal, Y.J.; Gartstein, Y.N.; Malko, A.V. *ACS Nano* **2017** (submitted).

[9] Guo, T.; Sampat, S.; Zhang, K.; Robinson, J. A.; Rupich, S. M.; Chabal, Y. J.; Gartstein, Y. N.; Malko, A. V. *Sci. Rep.* **2017**, 7, 41967.

All Project Publications (2015-2017)

1. S. Sampat, N. S. Karan, T. Guo, H. Htoon, J. A. Hollingsworth, and A. V. Malko, *"Multistate blinking and scaling of the recombination rates in individual silica-coated CdSe/CdS nanocrystals*", ***ACS Photonics* 2 (10)**, 1505-1512 (2015).
2. J. Wang, L. Xu, Y.-J. Lee, M. De Anda Villa, A. V. Malko and J. W. P. Hsu, "*Effects of Contact-induced Doping on the Behaviors of Organic Photovoltaic Devices*", ***Nano Letters* 15 (11)**, 7627–7632 (2015).
3. N. S. Karan, A. M. Keller, S. Sampat, O. Roslyak, A. Arefin, C. J. Hanson, J. L. Casson, A. Desireddy, A. Piryatinski, R. Iyer, H. Htoon, A. Malko and J. A. Hollingsworth, "*Plasmonic Giant Quantum Dots: Hybrid Nanostructures for Truly Simultaneous Optical Imaging, Photothermal Effect and Thermometry*", ***Chem. Science* 6**, 2224-2236 (2015).
4. W. Peng, S. Sampat, S. M. Rupich, B. Anand, H. M. Nguyen, D. Taylor, B. E. Beardon, Y. N. Gartstein, Y. J. Chabal and A. V. Malko, "*Hybrid light sensor based on ultrathin Si nanomembranes sensitized with CdSe/ZnS colloidal nanocrystal quantum dots*", ***Nanoscale* 7**, 8524-8530 (2015).
5. W. Peng, S. M. Rupich, N. Shafiq, Y. N. Gartstein, A. V. Malko, and Y. J. Chabal, "*Silicon surface modification and characterization for emergent photovoltaic applications based on energy transfer*", ***Chem. Reviews* 115 (23),** 1264-12796 (2015).
6. S. M. Rupich, Y. N. Gartstein, Y. J. Chabal, and A. V. Malko, "*Controlled Deposition and Spectroscopic Signatures of Ordered Multilayer Nanocrystal Assemblies for Optoelectronic Applications", **Adv. Opt. Mat.* 4,** 378-383 (2016).
7. H. T. Yi, Y. N. Gartstein, and V. Podzorov, "*Charge carrier coherence and Hall effect in organic semiconductors*", ***Sci. Rep***. **6**, 23650 (2016).
8. S. Sampat, T. Guo, K. Zhang, J. A. Robinson, H. Htoon, J. A. Hollingsworth, Y. N. Gartstein and A. V. Malko, "*Exciton and Trion Energy Transfer from Giant Semiconductor Nanocrystals to MoS_2 Monolayers", **ACS Photonics* 3,** 708-715 (2016).
9. B. Anand, S. Sampat, E. Danilov, W. Peng, S. M. Rupich, Y. N. Gartstein, Y. J. Chabal and A. V. Malko, "*Broadband transient absorption study of photoexcitations in lead halide perovskites: towards a multi-band picture*", ***Phys. Rev. B: Rapid Comm.* 93**, 161205(R) (2016).
10. L. Xu, J. Wang, M. De Anda Villa, T. Daunis, Y.-J. Lee, A. V. Malko, and J. W. P. Hsu, "*Quantitative Analyses of Competing Photocurrent Generation Mechanisms in Fullerene-Based Organic Photovoltaics*", ***J. Phys. Chem.* C 120,** 16470-16477 (2016).
11. W. Peng, B. Anand, L. Liu, S. Sampat, B. E. Bearden, A. V. Malko and Y. J. Chabal, "*Influence of growth temperature on bulk and surface defects in hybrid lead halide perovskite films*", ***Nanoscale* 8**, 1627-1634 (2016).
12. Y. Chen, H. T. Yi, X. Wu, R. Haroldson, Y. N. Gartstein, Y. I. Rodionov, K. S. Tikhonov, A. Zakhidov, X.Y. Zhu and V. Podzorov, "*Extended carrier lifetimes and diffusion in hybrid perovskites revealed by steady-state Hall effect and photoconductivity measurements*", ***Nat. Commun.* 7**, 12253 (2016).

13. T. Guo, S. Sampat, K. Zhang, J. A. Robinson, S. M. Rupich, Y. J. Chabal, Y. N. Gartstein, and A. V. Malko, "*Order of magnitude enhancement of monolayer MoS_2 photoluminescence due to near-field energy influx from nanocrystal films", **Sci. Rep***. 7, 41967 (2017).
14. C. N. Mishra, N. J. Orfield, F. Wang, Z. Hu, S. Krishnamurthy, A. V. Malko, J. L. Casson, H. Htoon, M. Sykora, J. A. Hollingsworth, "*Using shape to turn off blinking for two-colour multiexciton emission in CdSe/CdS tetrapods*", ***Nat. Commun.* 8**, 15083 (2017).
15. C. J. Hanson, N. F. Hartmann, W. De Benedetti, X. Ma, J. L. Casson, J. K. Grey, Y. J. Chabal, A.V. Malko, H. Htoon, and J. A. Hollingsworth, "*Giant PbSe/CdSe quantum dots: Stable single-nanostructure photoluminescence toward blinking suppression*", ***JACS*** (submitted).
16. T. Guo, S. Sampat, S.M. Rupich, J.A. Hollingsworth, H. Htoon, Y.J. Chabal, Y.N. Gartstein, and A.V. Malko, "Biexciton and Trion Energy Transfer from CdSe/CdS Giant Nanocrystals to Si Substrates", ***ACS Nano*** (submitted).

Driven Morphological Evolution and Patterning of Crystal Surfaces, Epitaxial Thin Films, and Two-Dimensional Materials

Dimitrios Maroudas (maroudas@ecs.umass.edu)
Department of Chemical Engineering, University of Massachusetts, Amherst, MA 01003

Program Scope

This work is part of our research program on *Surface Engineering by Simultaneous Action of Multiple External Fields* (**Award No. DE-FG02-07ER46407**). This program aims at enabling surface engineering strategies based on the fundamental understanding and predictive modeling of the surface morphological response of solid materials subjected to the combined action of multiple external forces. We focus on the surface morphological evolution and stability of electrically conducting and semiconducting solids under the simultaneous application of mechanical stresses, electric fields, and temperature gradients; materials of interest include metals, such as Cu, Ag, and Al, and semiconductors, such as Si and chemically functionalized or defect engineered graphene-based metamaterials. We emphasize on: identifying the conditions under which the driven surface morphology is stable, exploring the complexity of the corresponding various morphologically stable surface patterns, and generating and controlling nanoscale patterns on surfaces. Specifically, we investigate the morphological response to the combined action of multiple external forces of bulk solid surfaces, surfaces of thin films grown epitaxially on thick or thin substrates, as well as nanoscale surface features such as coherently strained epitaxial islands on substrate surfaces. The analysis of complex pattern formation as a result of the driven evolution of surface features (directed assembly), including single-layer epitaxial islands and quantum dots on epitaxial films, offers new paradigms of driven nanopatterning. The research is based on a modeling approach that combines theoretical analyses of surface/feature morphological stability with self-consistent dynamical simulations of driven surface/feature evolution based on properly parameterized continuum and multi-scale surface transport models that we develop and systematic exploration of the models' parameter space.

Recent Progress

Current-Driven Nanowire Formation on Surfaces of Crystalline Conducting Substrates – We have conducted a theoretical study on formation of nanowires with precisely controlled widths, starting from single-layer conducting islands on crystalline conducting substrates under the controlled action of macroscopic forcing provided by an externally applied electric field that drives island edge electromigration [1]. Numerical simulations based on an experimentally validated model and supported by linear stability theory show that large-size islands undergo a current-induced fingering instability, leading to nanowire formation after finger growth [1]. Depending on the substrate surface crystallographic orientation, necking instabilities after fingering lead to the formation of multiple parallel nanowires per island. In all cases, the axis of the formed nanowires is aligned with the direction of the externally applied electric field. The nanowires have constant widths, on the order of 10 nm, which can be tuned by controlling the externally applied electric field strength [1]. Our findings have important implications for developing future lithography-free nanofabrication and nanoelectronic patterning techniques.

Surface Nanopattern Formation Due to Current-Induced Homoepitaxial Nanowire Edge Instability – Using an externally applied electric field as a precisely controlled macroscopic force, we have carried out a computational study on the formation of surface nanopatterns consisting of single-layer homoepitaxial islands; these nanopatterns form as a result of a morphological instability that can occur under edge electromigration conditions on the straight edge of a single-layer nanowire grown epitaxially on a crystalline substrate [2]. Direct dynamical simulations based on a model that has been validated experimentally for the Ag/Ag system show that the current-induced nanowire edge instability causes the breakup of the nanowire and leads to the formation of uniformly distributed islands, arranged in linear or V-shaped arrays, which are uniformly sized with nanoscale dimensions [2]. The simulation results are supported by linear stability theory and demonstrate that the geometrical features of the island patterns and the island sizes can be controlled precisely by controlling the electric field direction with respect to the nanowire axis and the electric field strength [2]. Our findings have important implications for developing physical nanopatterning approaches toward enabling future nanofabrication technologies.

Complex Pattern Formation from Current-Driven Dynamics of Single-Layer Epitaxial Islands on Crystalline Conducting Substrates – We have conducted a systematic study of complex pattern formation resulting from the driven dynamics of single-layer homoepitaxial islands on surfaces of face-centered cubic (FCC) crystalline conducting substrates under the action of an externally applied electric field [3]. The analysis has been based on an experimentally validated nonlinear model of mass transport via island edge atomic diffusion, which also accounts for edge diffusional anisotropy. We have analyzed the morphological stability and simulated the field-driven evolution of rounded islands for an electric field oriented along the fast edge diffusion direction. For larger-than-critical island sizes on {110} and {100} FCC substrates, we have found that multiple necking instabilities generate complex island patterns, including not-simply-connected void-containing islands, mediated by sequences of breakup and coalescence events and distributed symmetrically with respect to the electric field direction [3]. We have analyzed the dependence of the formed patterns on the original island size and on the duration of application of the external field. Starting from a single large rounded island, we have characterized the dynamics of the number of daughter islands and their average size and uniformity. The evolution of the average island size follows a universal power-law scaling relation and the evolution of the total edge length of the islands in the complex pattern follows Kolmogorov-Johnson-Mehl-Avrami kinetics [3]. Our study makes a strong case for the use of electric fields, as precisely controlled macroscopic forcing, toward forming complex nanoscale patterns on conducting solid surfaces.

Theory of Multiple Quantum Dot Formation in Strained-Layer Heteroepitaxy – We have developed a theory for the experimentally observed formation of multiple quantum dots (QDs) in strained-layer heteroepitaxy based on surface morphological stability analysis of a coherently strained epitaxial thin film on a crystalline substrate [4]. Using a fully nonlinear model of surface morphological evolution that accounts for a wetting potential contribution to the epitaxial film's free energy as well as surface diffusional anisotropy, we have demonstrated the formation of multiple QD patterns in self-consistent dynamical simulations of the evolution of the epitaxial film surface perturbed from its planar state [4]. The simulation predictions are supported by weakly nonlinear analysis of the epitaxial film surface morphological stability. We have found that, in addition to the Stranski-Krastanow instability, long-wavelength perturbations from the planar film

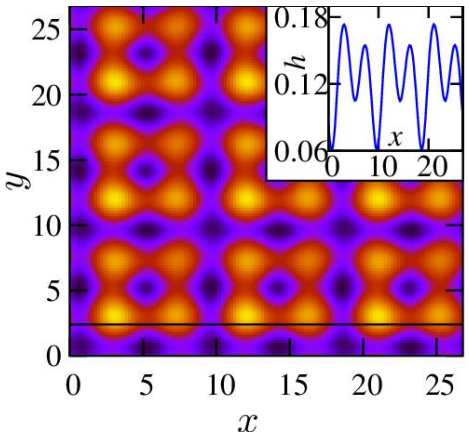

FIG. 1. 2D contour map of simulated surface morphology, $h(x,y,t)$, of coherently strained epitaxial film on a patterned substrate. The 1D surface profile $h(x; y,t)$ along the black solid line marked on the 2D map is plotted in the inset. For most material systems of interest, 1 unit of length ≈ 5-10 nm.

surface morphology can trigger a nonlinear instability, resulting in the splitting of a single QD into multiple QDs of smaller sizes, and predicted the critical wavelength of the film surface perturbation for the onset of the nonlinear tip-splitting instability. The theory provides a fundamental interpretation for the observations of "QD pairs" or "double QDs" and other multiple QDs reported in experimental studies of epitaxial growth of semiconductor strained layers, such as the multiple QD patterns on the surface of an epitaxial film grown on a patterned substrate as shown in Fig. 1. The theory also sets the stage for precise engineering of tunable-size nanoscale surface features in strained-layer heteroepitaxy by exploiting film surface nonlinear, pattern forming phenomena [4].

Current-Induced Surface Roughness Reduction in Conducting Thin Films – Thin film surface roughness is responsible for various materials reliability problems in microelectronics and nanofabrication technologies, which requires the development of surface roughness reduction strategies. Toward this end, we have conducted a modeling and simulation study that established the electrical surface treatment of conducting thin films as a viable physical processing strategy for surface roughness reduction [5]. We have developed a continuum model of surface morphological evolution that accounts for the residual stress in the film, surface diffusional anisotropy and film texture, the film's wetting of the layer that is deposited on, and surface electromigration. Supported by linear stability theory, self-consistent dynamical simulations based on the model have demonstrated that the action over several hours of a sufficiently strong and properly directed electric field on a conducting thin film can reduce its nanoscale surface roughness and lead to an atomically smooth planar film surface, as shown in Fig. 2. The modeling predictions are in agreement with experimental measurements on copper thin films deposited on silicon nitride layers [5].

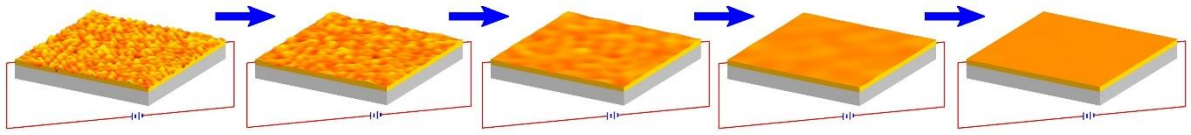

FIG. 2. Sequence of snapshots from a computer simulation of electric-field-driven surface morphological evolution of a copper thin film on a silicon nitride layer, demonstrating current-induced surface smoothening.

Edge Patterning in Defect-Engineered Graphene Nanoribbons and its Impact on Their Electronic Band Structure – We have conducted a systematic analysis of pore-edge interactions in graphene nanoribbons (GNRs) using first-principles density functional theory (DFT) calculations and molecular-statics computations based on reliable interatomic potentials, which has revealed strongly attractive interactions for nanopores in the vicinity of GNR edges [6]. These attractive interactions provide the thermodynamic driving force for nanopore migration toward the GNR edge, leading to its coalescence with the GNR edge through a sequence of carbon ring reconstructions. We have studied nanopore dynamics near GNR edges in detail through molecular-

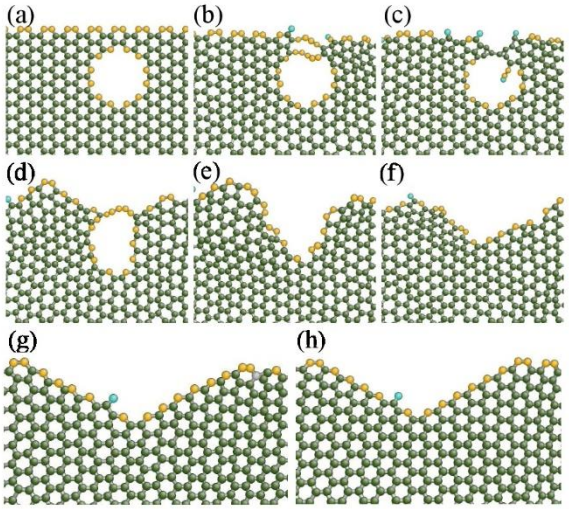

FIG. 3. (a-g) Sequence of configurations from a MD trajectory capturing the coalescence of a 24-vacancy pore with the edge of an armchair GNR and the resulting faceting and V-shape zigzag-edged pattern formation. The configuration shown in (h) is the quenched configuration of (g). Atoms are colored according to their atomic coordination, *Z*: green, gold, and light-blue spheres denote atoms with $Z = 3$, 2, and 1, respectively.

dynamics (MD) simulations at high temperature [6]. We have constructed the optimal kinetic pathways of the mechanisms mediating the coalescence of the nanopore and the GNR edge, as identified by the MD simulations, using climbing-image nudged elastic band calculations. The post-coalescence morphological evolution of an armchair GNR edge leads to the formation of a V-shaped edge pattern consisting of zigzag linear segments (facets), as shown in Fig. 3. DFT calculations of the electronic band structure of such patterned GNRs show that the zigzag segments formed at the armchair edges can be used to tune the bandgap of the GNR. The bandgap of the patterned GNRs exhibits a linear dependence on the density of the zigzag edge atoms, which is controlled by the size and concentration of the pores introduced in the defect-engineered GNR [6].

Future Plans

Our future research plans include: (1) Continuum-level analysis, simulation, and parametric exploration of driven dynamics of single-layer islands and vacancy islands and their assemblies toward developing systematic strategies for *physical nanopatterning of surfaces*. (2) Targeted atomic-scale computations of surface/edge properties and their dependence on temperature and stress for further incorporation of atomistic information into continuum-level predictive models. (3) Development and optimization of physical processing strategies for surface roughness reduction in thin films. (4) Development of multi-scale models of driven surface morphological evolution involving kinetic Monte Carlo simulations for atomic-scale modeling of surface/feature propagation for physically driven nanopattering. (5) Atomic-scale studies of driven evolution and physical patterning of graphene-based structures. (6) Development of experimental protocols to continue the validation of our models and test the modeling predictions for driven evolution of epitaxial film surfaces, epitaxial islands, and graphene-based nanomaterials.

References

1. A. Kumar, D. Dasgupta, C. Dimitrakopoulos, and D. Maroudas, *Applied Physics Letters* **108**, 193109/1-5 (2016).
2. A. Kumar, D. Dasgupta, and D. Maroudas, *Applied Physics Letters* **109**, 113106/1-4 (2016).
3. A. Kumar, D. Dasgupta, and D. Maroudas, submitted to *Physical Review Applied* (2017).
4. L. Du and D. Maroudas, *Applied Physics Letters* **109**, 023103/1-4 (2016).
5. L. Du and D. Maroudas, *Applied Physics Letters* **110**, 103103/1-5 (2017).
6. L. Du, T. Nguyen, A. Gilman, A. R. Muniz, and D. Maroudas, in preparation for submission to *Physical Review Letters* (2017).

Publications Resulting from Work Supported by this DOE Grant over the Past Two Years

1. M. A. Bevan, D. M. Ford, M. A. Grover, B. Shapiro, D. Maroudas, Y. Yang, R. Thyagarajan, X. Tang, and R. M. Sehgal, "Controlling Assembly of Colloidal Particles into Structured Objects: Basic Strategy and a Case Study," *Journal of Process Control* **27**, 64-75 (2015).

2. L. Du, D. Dasgupta, and D. Maroudas, "Weakly Nonlinear Theory of Secondary Rippling Instability in Surfaces of Stressed Solids," *Journal of Applied Physics* **118**, Article No. 035303, 14 pages (2015).

3. R. M. Sehgal and D. Maroudas, "Equilibrium Shape of Colloidal Crystals," *Langmuir* **31**, 11428-11437 (2015).

4. A. Kumar, D. Dasgupta, C. Dimitrakopoulos, and D. Maroudas, "Current-Driven Nanowire Formation on Surfaces of Crystalline Conducting Substrates," *Applied Physics Letters* **108**, Article No. 193109, 5 pages (2016).

5. L. Du and D. Maroudas, "Theory of Multiple Quantum Dot Formation in Strained-Layer Heteroepitaxy," *Applied Physics Letters* **109**, Article No. 023103, 4 pages (2016).
   - **Editor's pick**; one of five articles highlighted on the journal homepage for the week of 7/17/2016.

6. A. Kumar, D. Dasgupta, and D. Maroudas, "Surface Nanopattern Formation Due to Current-Induced Homoepitaxial Nanowire Edge Instability," *Applied Physics Letters* **109**, Article No. 113106, 4 pages (2016).

7. L. Du and D. Maroudas, "Current-Induced Surface Roughness Reduction in Conducting Thin Films," *Applied Physics Letters* **110**, Article No. 103103, 5 pages (2017).
   - **Editor's pick**; one of five articles highlighted on the journal homepage for the week of 3/6/2017
   - American Institute of Physics (AIP) **press release** for this article posted on 3/7/2017 (news articles also appeared in most physics and science news websites): https://publishing.aip.org/publishing/journal-highlights/reducing-conducting-thin-film-surface-roughness-electronics

8. A. Kumar, D. Dasgupta, and D. Maroudas, "Complex Pattern Formation from Current-Driven Dynamics of Single-Layer Epitaxial Islands on Crystalline Conducting Substrates," submitted to *Physical Review Applied* (2017).

9. D. Dasgupta, A. Kumar, and D. Maroudas, "Effects of Edge Diffusional Anisotropy on the Current-Driven Complex Oscillatory Dynamics of Single-Layer Epitaxial Islands," submitted to *Physical Review E* (2017).

10. L. Du, T. Nguyen, A. Gilman, A. R. Muniz, and D. Maroudas, "Tuning the Bandgap of Graphene Nanoribbons through Edge Patterning Induced by Pore-Edge Interactions," in preparation for submission to *Physical Review Letters* (2017).

Electronic and Optical Processes in Novel Semiconductors for Energy Applications

Principal Investigator: Angelo Mascarenhas
Co-Investigators: Brian Fluegel, Dan Beaton, Kirstin Alberi
National Renewable Energy Laboratory
15013 Denver West Parkway, Golden, CO 80401-3305, angelo.mascarenhas@nrel.gov

Program Scope

The overarching and longstanding objective of this project is to develop novel approaches for understanding and controlling the electronic properties of semiconductor alloys for energy applications. To this end, we have proposed to investigate two classes of phenomena that are described by two fundamental science Goals and their technological relevance:

Goal 1) Transformation of the electronic properties of semiconductors through co-doping with isoelectronic impurities.

Goal 2) Control of semiconductor optical properties induced by interacting electron systems.

Recent Progress: Goal 1

Bi Pair and Cluster States in $GaAs_{1-x}Bi_x$

Isoelectronic Bi impurities form resonant states in the valence band of GaAs and induce a modification to the band structure, leading to a significant reduction in the bandgap energy (~88 meV/% Bi) and an almost equal increase in the spin orbit splitting energy.[1,2] At the same time, Bi impurities can also form pair and cluster states that introduce bound states above the valence band edge. The role of these localized states on the material properties and their influence on the broader band structure remain outstanding questions in understanding the evolution of $GaAs_{1-x}Bi_x$ alloys. Our recent improvements in the molecular beam epitaxy (MBE) of $GaAs_{1-x}Bi_x$ have allowed us to spectrally resolve excitonic transitions associated with Bi pair and cluster states.[3,4] We find that the energies of these transitions, labeled T_3 and T_4 in Fig. 1, exhibit a weaker dependence on Bi concentration than the band gap energy, E_g. We have used the difference in the energy shifts to gain information about the relative movement of the valence and conduction bands with alloy composition.

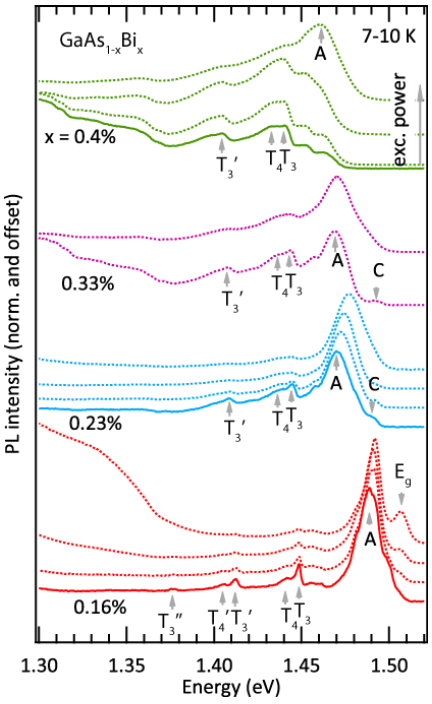

Figure 1. Low temperature PL spectra of dilute $GaAs_{1-x}Bi_x$. Bi pair transitions T_3 and T_4 and their phonon replicas, T_3', T_3'' and T_4' are marked.

Bound Bi pair and cluster states strongly localize holes. This is analogous to electron localization at N pair and cluster states bound below the conduction band of $GaAs_{1-x}N_x$ alloys. However, the radiative lifetime of the localized holes is much longer than that of the electrons. Figure 2 shows the low temperature PL spectrum of a $GaAs_{1-x}Bi_x$ sample with 0.46% Bi and the corresponding PL decay curves from several spectral regions. Recombination from the T_2 and T_3 Bi pair states is much longer than the shallow acceptor-bound exciton transition, labeled *A* in Fig. 2a, and reaches well over one hundred nanoseconds. The non-exponential behavior of the PL decay from the spectral regions containing the T_2 and *A* transitions is indicative of energy transfer through these states to the lower-lying T_3 states.

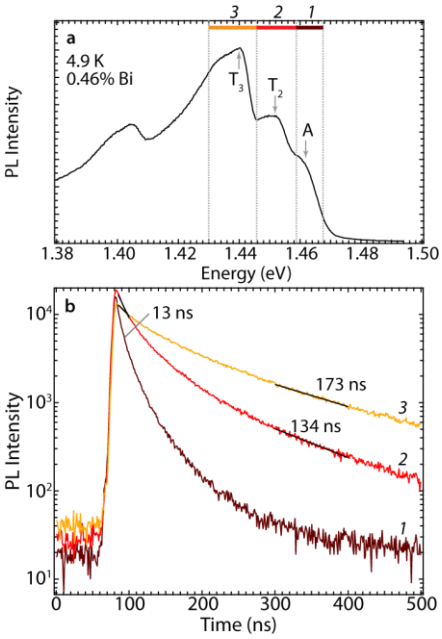

Figure 2. (a) PL spectrum of $GaAs_{1-x}Bi_x$ with 0.46% Bi and (b) PL decay curves from the spectral regions marked in (a).

We have also investigated the behavior of the Bi pair states under high magnetic fields up to 60 T. The spectra of a $GaAs_{1-x}Bi_x$ sample with 0.46% Bi is shown in Fig. 3. The diamagnetic shifts of the T_2, T_3 and T_4 transitions are similar to each other but are slower than that of the *A* transition. Assuming that the hole is completely localized at the Bi pairs and behaves as though it has infinite mass, the diamagnetic shift is determined only by the electron mass. The corresponding electron masses extracted from the Bi pair states is m_e ~0.071-0.075m_0. Correspondingly, the exciton reduced mass for the *A* transition was only $\mu_{ex} = 0.062m_0$ and is close to that of GaAs. The larger m_e measured in relation to the Bi pair transitions is likely due to high compressive strain in the immediate area around the Bi pairs in the lattice, which acts on the electron orbiting the trapped hole. These results indicate that Bi pairs can strongly affect electrons as well as holes.

Absence of Bi Cluster State PL in GaPBi

We have also incorporated Bi into GaP.[5] In this case, isolated Bi impurities form bound states above the valence band edge. PL spectra from two $GaP_{1-x}Bi_x$ epilayers with 0.1 and 1% Bi are displayed in Fig. 4. They exhibit excitonic recombination from bound Bi impurity states, labeled *A*, as well as several phonon replicas. Unlike $GaAs_{1-x}Bi_x$, no evidence of recombination from Bi pair states is observed, even though the Bi concentrations are relatively high. We attribute the absence of Bi pair recombination in $GaP_{1-x}Bi_x$ to suppression of energy transfer from the band edge and bound isolated Bi states to

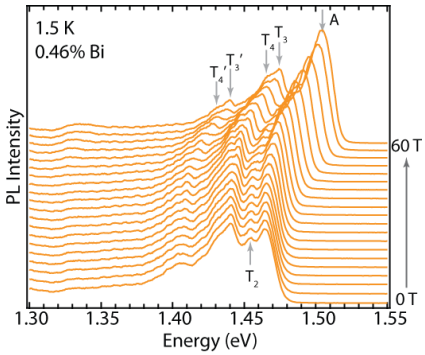

Figure 3. Magneto-PL spectra from a $GaAs_{1-x}Bi_x$ sample with 0.46% Bi.

lower-lying states. Since facile energy transfer to low energy states can strongly influence carrier transport and recombination behavior, these findings have interesting implications for using dilute bismide alloys in a variety of technological applications.

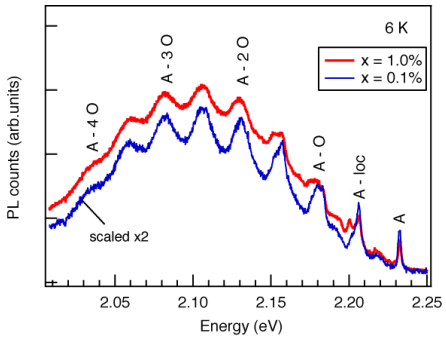

Figure 4. PL spectra of $GaP_{1-x}Bi_x$ epilayers with 0.1 and 1% Bi.

Recent Progress: Goal 2

We have demonstrated that a proper set of conditions—encompassing sample quality, trapping method, and pumping techniques—can reduce the onset threshold of polariton condensation by over an order of magnitude compared to previous demonstrations. Microcavity exciton-polaritons are routinely used as an accessible system to study quantum many-body phenomena[6], and the system has been proposed as a candidate for optical logic[7] or as a low-threshold coherent light source[8]. Our results, along with an assessment of which excitation conditions were so favorable to reducing the condensation onset, inspire future work on the system both for the study of fundamental quantum and optical phenomena and as a low-power source of highly coherent light.

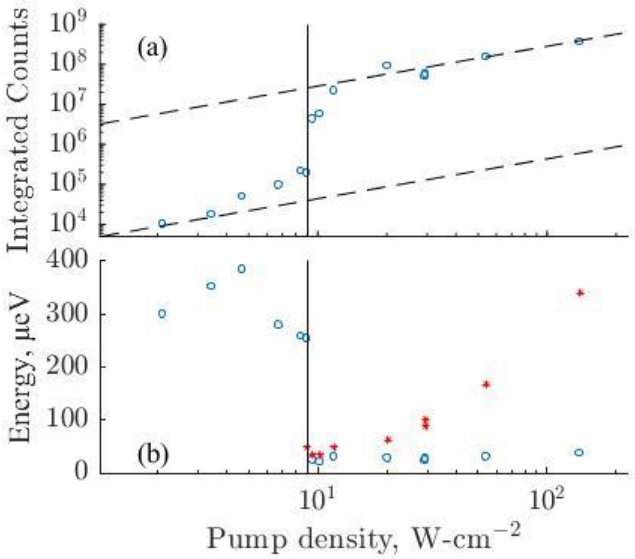

Figure 5. The onset of polariton condensation is seen as a superlinear increase in the emitted intensity from the lower polariton (frame (a)) and a sharp decrease in the spectral full-width at half-maximum (blue circles in frame (b)). Unlike less stable systems or those farther out of thermal equilibrium, our results show negligible broadening and blueshift for over an order of magnitude increase in density above condensation onset.

Future Plans

Having demonstrated the capability of doping isoelectronic bismuth in GaAs and GaP to yield single as well as pair and cluster signatures, we now plan to incorporate them concomitantly and search for the signatures of isoelectronic codoping, i.e evidence of Bi-N pairs as opposed to Bi-Bi and N-N pairs. We have also completed the design of dielectric Bragg gratings and are in the final stage of work with a company to fabricate them. This will enable demonstration of room temperature polariton condensates and the search for Bogulibov modes in light scattering. The main experiments that we will do are:

1) We will use high resolution confocal optical PL measurements to look for single impurity pairs of Bismuth in GaAs and GaP. This will identify and confirm our assignments of PL transitions as well as demonstrate that GaAsBi is an analog of GaAsN with respect to behavior of hole traps versus electron traps.

2) We plan to look for signatures of isoelectronic co-doping using 1) macroscopic studies such as SdH transport and 2) microscopic studies such as spatially resolved Near-Field optical spectroscopy.

3) We are currently designing dielectric mirrors for a microcavity based on ZnCdSe active layers to demonstrate room temperature polariton condensates. If successful, this will enable near 100% light extraction from polariton based LED devices.

4) We have also begun to search for Bogoliubov modes in GaAs microcavity polariton condensates using inelastic light scattering.

References

1. S. Francoeur, M.-J. Seong, A. Mascarenhas, S. Tixier, M. Adamcyk and T. Tiedje, *Appl. Phys. Lett.*, **82**, 3874 (2003).
2. B. Fluegel, S. Francoeur, A. Mascarenhas, S. Tixier, E.C. Young and T. Tiedje, *Phys. Rev. Lett.*, **97**, 067205 (2006).
3. D.A. Beaton, A. Mascarenhas, and K. Alberi, *J. Appl. Phys.*, **118**, 235701 (2015).
4. T.M. Christian, K. Alberi, D.A. Beaton, B. Fluegel and A. Mascarenhas, *Jpn. J. Appl. Phys.*, **56**, 035801 (2017).
5. T.M. Christian, D.A. Beaton, K. Alberi, B. Fluegel and A. Mascarenhas, *Appl. Phys. Express*, **8**, 061202 (2015).
6. H. Deng, H. Haug, and Y. Yamamoto, Rev. Mod. Phys. **82**, 1489 (2010).
7. T. C. H. Liew, A. V. Kavokin, T. Ostatnický, M. Kaliteevski, I. A. Shelykh, R. A. Abram, Phys. Rev. B **82**, 033302 (2010)
8. H. Deng, G. Weihs, D. Snoke, J. Bloch, and Y. Yamamoto, Proc. Natl. Acad. Sci. **100**, 15318 (2003).

Publications

1. "Ferroelastic lattices and the Bloch Formalism", A. Mascarenhas, B. Fluegel, L. Bhusal. To be published in *Science Advances.*
2. "Spectrally resolved localized states in $GaAs_{1-x}Bi_x$", T.M. Christian, K. Alberi, D.A. Beaton, B. Fluegel, A. Mascarenhas. *Jpn. J. Appl. Phys*. **56**, 035801 (2017).
3. "Ultra-low threshold polariton condensation", M. Steger, B. Fluegel, K. Alberi, A. Mascarenhas, D.W. Snoke, L. N. Pfeiffer, K. West. *Optics Letters* **42**, 1165 (2017).
4. "Consequences of spatial antisymmetry on light", A. Mascarenhas and B. Fluegel, *Proc. SPIE* 10174, International Symposium on Clusters and Nanomaterials, 101740E (December 21, 2016).
5. "Bismuth Incorporation into Gallium Phosphide", T.M. Christian, D.A. Beaton, A. Mascarenhas, K. Alberi, *Proc. SPIE* 10174, International Symposium on Clusters and Nanomaterials, 101740F (December 21, 2016).
6. "Magnetic field stabilized electron-hole liquid in indirect-band-gap $A l_x G a_{1-x}As$". K. Alberi, B. Fluegel, S.A. Crooker, A. Mascarenhas. *Phys. Rev. B*. **93**, 075310 (2016).
7. "Bismuth-induced Raman modes in $GaP_{1-x}Bi_x$" T.M. Christian, B. Fluegel, D.A. Beaton, K. Alberi, A. Mascarenhas. *Jpn. J. Appl. Phys*. **55**, 108002 (2016).
8. "Insight into the epitaxial growth of high optical quality GaAsBi", D.A. Beaton, A. Mascarenhas and K. Alberi, *J. Appl. Phys*. **118**, 235701 (Dec. 2015).
9. "Direct observation of the E_- resonant state in $GaAs_{1-x}Bi_x$". K. Alberi, D.A. Beaton and A. Mascarenhas. *Phys. Rev. B. Rapid Comm.* **92**, 241201(R) (Dec. 2015).
10. "Anharmonicity in light scattering by optical phonons in $GaAs_{1-x}Bi_x$", R.S. Joshya, V. Rajaji, Chandrabhas Narayana, A. Mascarenhas and R.N. Kini. *J. Appl. Phys.* **119**, 205706 (2016).
11. "THz generation mechanisms in the semiconductor alloy, $GaAs_{1-x}Bi_X$", C.P. Vaisakh, A. Mascarenhas and R.N. Kini, *J. Appl. Phys.* **118**, 165702 (Oct. 2015).
12. "Mysterious absence of pair luminescence in gallium phosphide bismide", Theresa M. Christian, Daniel A. Beaton, Kirstin Alberi, and Angelo Mascarenhas, *Appl. Phys. Express* 8, 061202 (2015).
13. "Electronic Raman Scattering as an Ultra-Sensitive Probe of Strain Effects in Semiconductors". B. Fluegel, A.V. Mialitsin, D. A. Beaton, J. L. Reno, and A. Mascarenhas. *Nature Comm*. 6, 7136 (2015).
14. "Spectroscopic determination of the bandgap crossover composition in MBE-grown $Al_xGa_{1-x}As$". Brian Fluegel, Kirstin Alberi, John Reno, and A. Mascarenhas, *Jpn. J. Appl. Phys.* 54 042402 (2015).

Zinc oxide and its alloys

Matthew D. McCluskey, Washington State University (WSU), Pullman, WA

Leah Bergman, University of Idaho (UI), Moscow, ID

Program Scope

This project investigates the fundamental physical properties of oxide semiconductors. This class of materials has a range of potential energy applications, including light emission, photovoltaics, hydrogen production, and fuel cells. In general, oxide semiconductors are *n*-type or insulating as grown. Reliable *p*-type doping, necessary for high-performance devices, has proved to be an elusive goal [1-3]. The achievement of reproducible, consistent *p*-doping in oxide semiconductors would have a major impact on science and technology.

To address this challenge, we are performing systematic studies on ZnS_xO_{1-x} and $ZnSe_xO_{1-x}$ alloys. By alloying with chalcogens (S and Se), the valence band is pushed upward in energy, making deep acceptors shallow. We have summarized this approach as "if you can't bring the level to the band, bring the band to the level." We are actively overcoming materials challenges such as phase segregation and have succeeded in growing high-quality thin films. To complement this growth program, the stability of $Mg_xZn_{1-x}O$ with deep-UV band gaps is also studied. Through a systematic program of growth and characterization, we aim to produce high-quality alloys with *p*-type doping, and obtain a basic energy-level picture for these dopants. Additionally, we will gain insight into fundamental optical phenomena in semiconductor alloys, which could be important for future solar cell and light emission technologies.

To achieve the project goals, we are pursuing a coordinated program of synthesis and optical characterization at WSU and UI (only 8 miles apart). Our fruitful bi-state collaboration takes advantage of resources at both institutions and provides students with excellent research opportunities. Complementary experiments are performed at the Advanced Light Source (ALS), Lawrence Berkeley National Laboratory (LBNL), where we have an active user proposal.

Recent Progress

<u>Li-diffused ZnO:</u> In the prior project, we established that Li is a deep (0.8 eV) acceptor that can yield weakly *p*–type material [4]. In the present work (Corolewski et al., 2016), hydrogen-related complexes in Li-diffused ZnO single crystals were investigated. In addition to the well-known Li-OH complex, we discovered several new hydrogen defects. When a mixture of Li_2O and ZnO is used as the dopant source, zinc vacancies are suppressed and the bulk Li concentration is very high ($>10^{19}$ cm^{-3}). In that case, the predominant hydrogen complex has a

vibrational frequency of 3677 cm^{-1}, which we attribute to an unknown hydrogen donor. When a zinc-poor precursor (Li_2CO_3) is used, positron annihilation measurements indicate a high concentration of zinc vacancies near the surface (Fig. 1). Along with this, a structured blue luminescence band and O-H mode at 3327 cm^{-1} are observed at 10 K (Fig. 2). These observations suggest a zinc vacancy – hydrogen complex. The zero-phonon line (ZPL) indicates an acceptor level ~0.3 eV above the valence-band maximum. This relatively shallow acceptor could be beneficial for *p*-type ZnO.

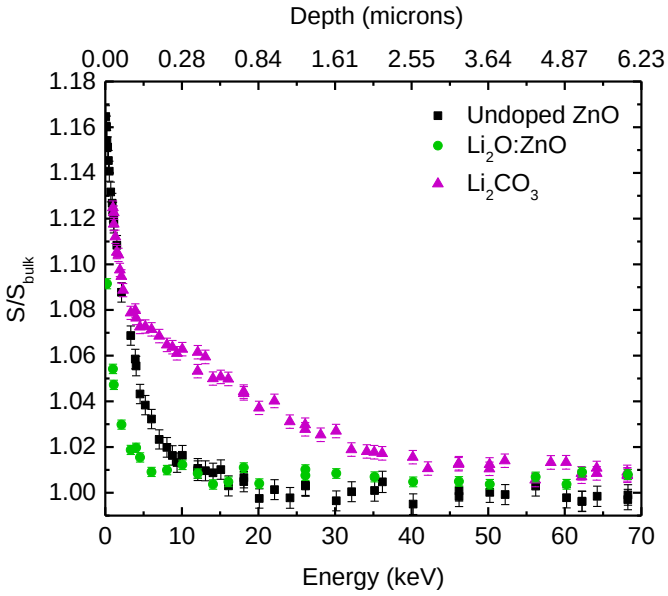

Fig. 1. Positron annihilation spectroscopy *S* parameter before and after Li diffusion. The high near-surface *S* value for samples annealed with Li_2CO_3 is a signature for zinc vacancies.

MgZnO: A fundamental understanding of the stability of crystal phases in mismatched alloys is essential to incorporate these materials into devices [5]. Toward that end, we are investigating the metastability of alloy films as a function of composition and temperature. Preliminary work on the effect of post-growth annealing is discussed by Thapa et al. (2017).

Additionally, we have investigated two films: $Mg_{0.17}Zn_{0.83}O$ (low Mg) with a band gap of 3.45 eV, and $Mg_{0.8}Zn_{0.2}O$ (high Mg) with a deep UV band gap of 5.6 eV. X-ray diffraction (XRD) shows that the low-Mg sample is highly stable, retaining its wurtzite crystal structure up to 1000°C. The high-Mg sample, in contrast, phase separates into cubic and wurtzite phases after annealing at 750°C (Fig. 3). The ZnO-rich wurtzite phase gives rise to a band-gap absorption peak near 3.5 eV (Fig. 4). This process is important because the formation of ZnO clusters may also occur in other semiconductor alloys such as ZnS_xO_{1-x}.

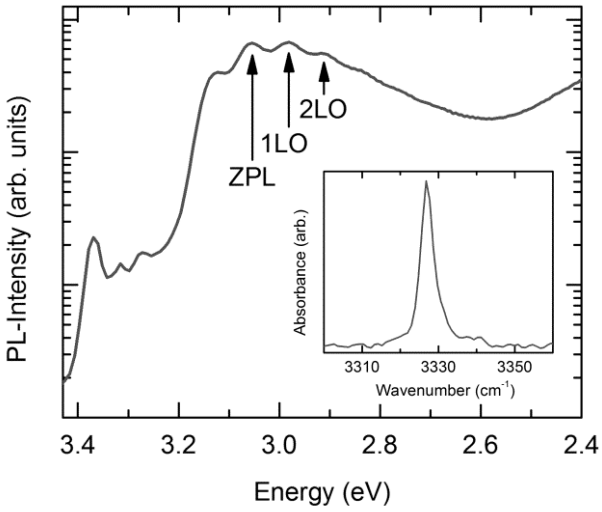

Fig. 2. The "blue band" has a ZPL of 3.05 eV and LO phonon replicas on the low-energy side. Inset: IR absorption spectrum, showing an O-H peak attributed to a zinc vacancy – hydrogen complex.

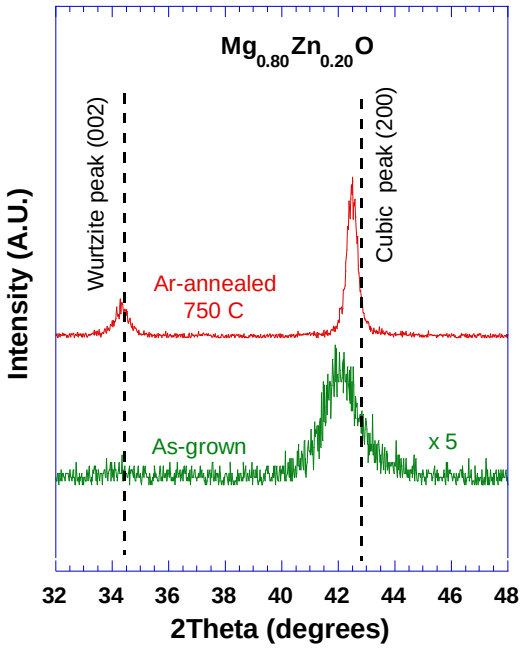

Fig. 3. XRD spectrum of the high-Mg film, showing phase separation after annealing.

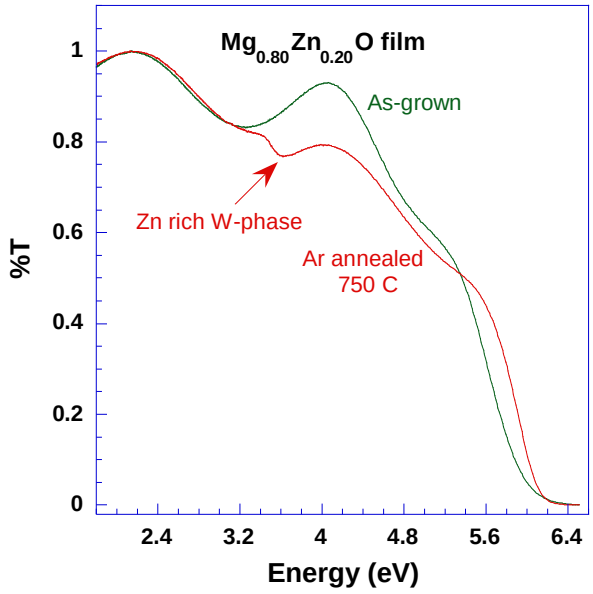

Fig. 4. Transmission spectrum of the high-Mg film. The peak at 3.5 eV is due to a ZnO-rich wurtzite (W) phase.

ZnSO: By systematically varying sputtering growth conditions, we have developed a reliable method for growing ZnS_xO_{1-x} semiconductor alloys at the ZnS-rich end. This composition range is important because the high valence band enables *p*-type doping. Using optimized parameters, we grew ZnS_xO_{1-x} from $x = 1.0$ to 0.6, where composition was determined by Rutherford backscattering spectrometry (RBS) and energy dispersive spectroscopy (EDS).

Raman spectroscopy reveals an O local vibrational mode (LVM) at 420 cm^{-1} for $x = 1.0$ (Fig. 5). The frequency exhibits a strong, nonlinear shift with composition (Fig. 6). We attribute this unusual nonlinear behavior to a local-to-extended defect transition. At the dilute-oxide limit, the vibrational motion is highly localized, as the O acts as a point defect. With increasing O concentration, O clusters begin to form and the mode becomes more phonon-like.

This phenomenon is important because ZnO-rich clusters could serve as centers that provide near-UV (3.2 eV) luminescence. In principle, one could exploit the *p*-dopability of ZnS while retaining the desirable optical properties of ZnO. Understanding the local versus extended character of these O centers is especially relevant in this regard.

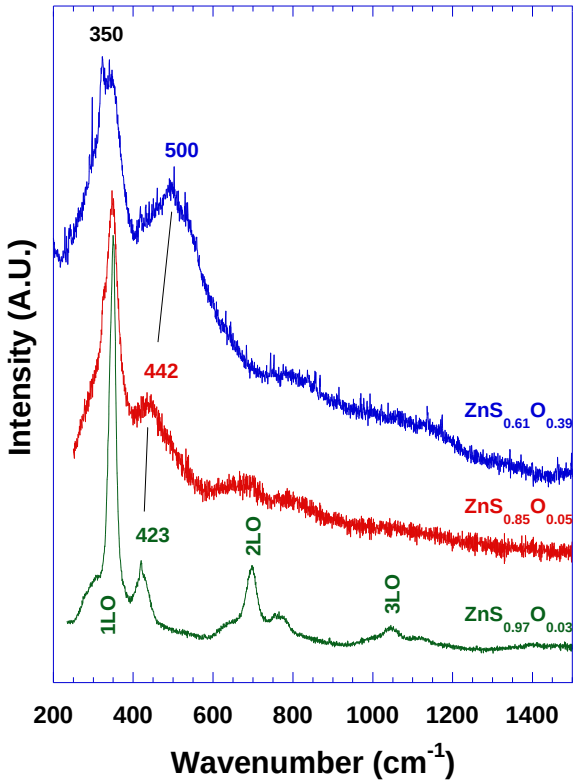

Fig. 5. Resonant Raman spectra of ZnS_xO_{1-x} alloys. The O LVMs are indicated by the numbers.

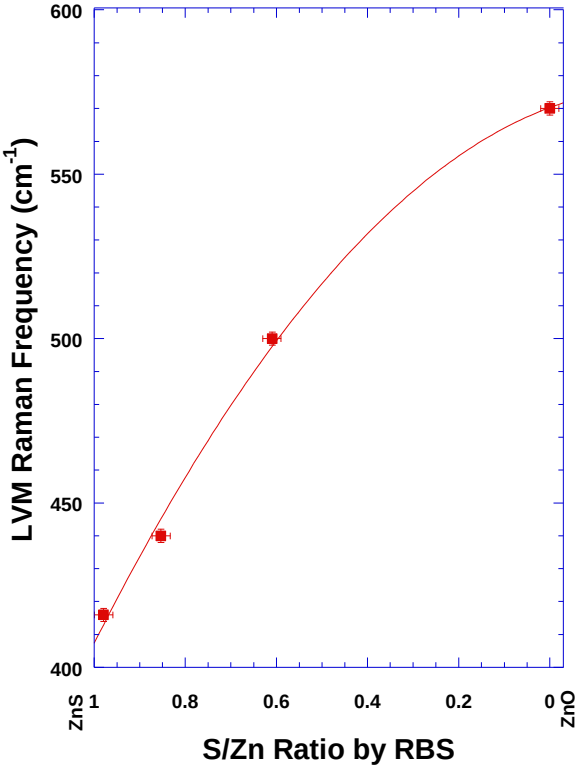

Fig. 6. Plot of the O vibrational frequency versus composition, showing nonlinear behavior.

Future Plans

In collaboration with a theorist, Zhi-Gang Yu, we are investigating clustering of ZnO phases in ZnS_xO_{1-x} alloys. We will begin growth of Li-doped ZnS_xO_{1-x} alloys at the ZnS-rich composition range, toward *p*-type doping. The luminescence properties of these materials will be studied. High-pressure synchrotron XRD experiments on ZnS_xO_{1-x} will begin this year.

References

1. M.D. McCluskey and S.J. Jokela, "Defects in ZnO," J. Appl. Phys. **106**, 071101 (2009).
2. M.D. McCluskey, "Point defects in ZnO," in *Semiconductors and Semimetals* **91**, ed. C. Jagadish, V. Privitera, and L. Romano (Elsevier, 2015), 279.
3. M.C. Tarun, M. Zafar Iqbal, and M.D. McCluskey, "Nitrogen is a deep acceptor in ZnO," *AIP Advances* **1**, 022105 (2011).
4. M.D. McCluskey, C.D. Corolewski, J. Lv, M.C. Tarun, S.T. Teklemichael, E.D. Walter, M.G. Norton, K.W. Harrison, and S. Ha, "Acceptors in ZnO," *J. Appl. Phys.* **117**, 112802 (2015).

5. J. Huso, H. Che, D. Thapa, J.L. Morrison, M.G. Norton, and L. Bergman, "Phonon dynamics and anharmonicity in phase segregated structural domains of MgZnO films," *Appl. Phys. Lett.* **104**, 031908 (2014).

Publications

D. Thapa, J. Huso, K. Miklos, P.M. Wojcik, D.N. McIlroy, J.L. Morrison, C. Corolewski, M.D. McCluskey, T.J. Williams, M.G. Norton, and L. Bergman, "UV-luminescent MgZnO semiconductor alloys: Nanostructure and optical properties," *J. Mater. Sci.:Mater. Electron.* **28**, 2511–2520 (2017).

C.D. Corolewski, N.S. Parmar, K.G. Lynn, and M.D. McCluskey, "Hydrogen-related complexes in Li-diffused ZnO single crystals," *J. Appl. Phys.* **120**, 035702:1–5 (2016).

A. Alkauskas, M.D. McCluskey, and C.G. Van de Walle, "Tutorial: Defects in semiconductors–Combining experiment and theory," *J. Appl. Phys.* **119**, 181101:1–11 (2016).

D. Thapa, J. Huso, J.L. Morrison, C.D. Corolewski, M.D. McCluskey, and Leah Bergman, "Achieving highly-enhanced UV photoluminescence and its origin in ZnO nanocrystalline films," *Optical Materials* **58**, 382–389 (2016).

V.M. Poole and M.D. McCluskey, "Large persistent photoconductivity in strontium titanate single crystals," *Proc. SPIE* **9749**, DOI: 10.1117/12.2207714 (2016).

M.D. McCluskey and S.T. Teklemichael, "A very shallow acceptor in Cu-diffused Si," in The 7th International Symposium on Advanced Science and Technology of Silicon Materials (JSPS Si Symposium), Nov. 21-25, 2016, Kona, Hawaii, USA, pp. 159–62.

V.M. Poole, C.D. Corolewski, and M.D. McCluskey, "*P*-type conductivity in annealed strontium titanate," *AIP Advances* **5**, 127217:1–4 (2015).

K.W. Harrison, C.D. Corolewski, M.D. McCluskey, J. Lindemuth, S. Ha, and M.G. Norton, "Electronic transport in molybdenum dioxide thin films," *J. Mater. Sci.: Mater. Electron.* **26**, 9717–20 (2015).

J. Huso, H. Che, D. Thapa, A. Canul, M.D. McCluskey, and L. Bergman, "Phonon dynamics and Urbach energy studies of MgZnO alloys," *J. Appl. Phys.* **117**, 125702:1–8 (2015).

N.S. Parmar, C.D. Corolewski, M.D. McCluskey, and K.G. Lynn, "Potassium acceptor doping of ZnO crystals," *AIP Advances* **5**, 057107:1–7 (2015).

V.M. Poole, J. Dashdorj, M.E. Zvanut, and M.D. McCluskey, "Large persistent photoconductivity in strontium titanate at room temperature," *MRS Proceedings* **1792**, DOI: 10.1557/opl.2015.531 (2015).

Superconductivity in Quasi-One-Dimensional $BaNbS_3$

John J. Neumeier and M. G. Smith, Physics Department, Montana State University.

Program Scope

Some of the most amazing physical properties in condensed matter occur only in compounds with dimension that is effectively lower than three. These are bulk, three dimensional in form, but with two-dimensional structural elements such as planes, or one-dimensional elements such as chains. Coupling between the neighboring elements plays a subtle, significant, and maybe even a dominant role in determining the bulk physical properties. Related to this is the fact that restriction of fermions to one dimension (1D) amplifies quantum effects and destroys the discontinuity at the Fermi energy that is normally present for a gas of fermions. This leads to boson-like properties in the collective excitations, and is known as Luttinger-liquid behavior. The proposed research will investigate compounds with crystal structures that dimensionally-constrain the fermions to develop a better understanding of 1D physics.

Recent Progress

For this extended abstract, the PI will focus on some recent investigations of $BaNbS_3$. Some transition-metal chalcogenides are known to possess quasi-1D structural elements and also exhibit high electrical conductivity. For example, $BaNbS_3$ has a hexagonal crystal structure with space group $P6_3/mmc$ (Fig. 1) that is composed of Nb-Nb chains along the crystallographic *c*-direction, which are surrounded by face-sharing sulfur octahedra [1-3]. The Nb atoms in the chains form metallic bonds, with bond length [2] of 2.87 Å; the interchain distances are much longer, at 6.84 Å. As a result, $BaNbS_3$ is a compound where the physics of one-dimensional metallic chains with weak interchain coupling can be investigated. The recent discovery [4] of superconductivity in hydrogen sulfide near 200 K is further reason for devoting research into studying the physical properties of sulfide compounds.

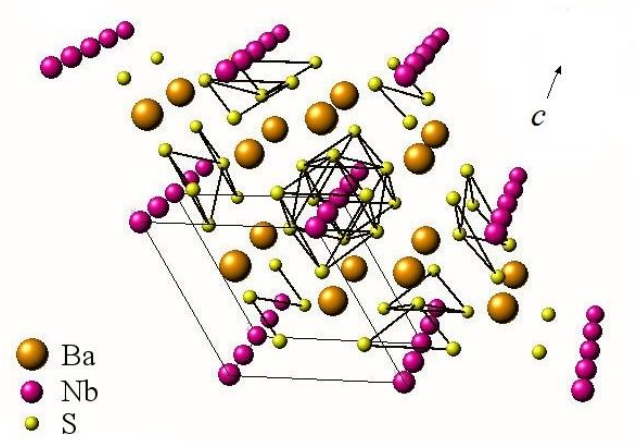

Fig. 1. The hexagonal crystal structure of $BaNbS_3$, with space group $P6_3/mmc$. The Nb-Nb chains (in red) run parallel to the *c* axis.

Samples of $BaNbS_3$ were synthesized from stoichiometric amounts of $BaCO_3$ and Nb_2O_5 using CS_2. The CS_2-laden nitrogen was sent through the quartz tube of a tube furnace containing the sample at about 20 cm^3/min. The sample was heated in 1 h to 500 ˚C, held there for 2 h, heated in 2 h to 800 ˚C, held there for 12 h followed by cooling over a period of 1 h to room temperature. The sample was reground, pressed into pellets, and reacted a second time under the same conditions. Subsequently, the sample was reground for 5 min, pressed into pellets, and placed in a 14 mm i.d. quartz tube with 10.66 mg of sulfur. The tube's volume was chosen to provide approximately 2 atm of pressure at 800 ˚C. The tube was evacuated to ~10^{-6} mbar over a period of 20 h, sealed, heated in 3 h to 800 ˚C, held there for 20 h, and cooled over a period of 12 h to room temperature. X-ray powder diffraction revealed the expected crystal structure. The sample's mass density was 3.93 g/cm^3, which is 84% of the expected density from published lattice parameters [2].

Electrical resistivity was measured with a four-probe dc method using current densities of about 3 mA/cm^2; when magnetic field was present, the current direction was perpendicular to the field. Hall effect measurements utilized a five-probe configuration on a sample of thickness 0.427 mm with an ac excitation current density of 1.14 A/cm^2. The Hall coefficient was measured with positive and negative magnetic fields to eliminate the voltage component associated with displacement of the voltage leads. Magnetic susceptibility was measured using a vibrating sample magnetometer. Specific heat measurements used a standard heat-pulse method.

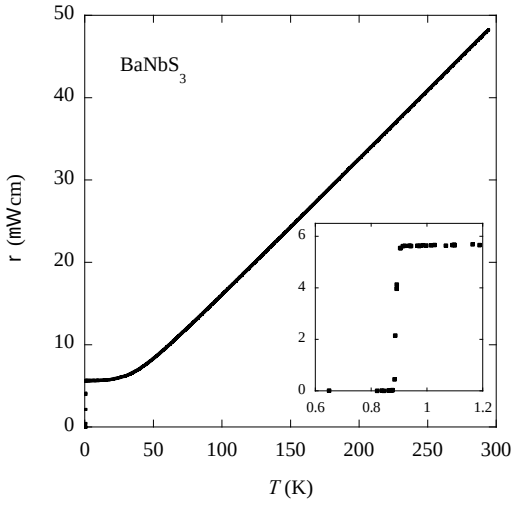

Fig. 2. Electrical resistivity versus temperature for $BaNbS_3$. The inset shows the region near the transition to the superconducting state.

The electrical resistivity ρ versus temperature T of $BaNbS_3$ is shown in Fig. 2. The temperature dependence is metallic with ρ(295 K)/ρ(1 K) = 57.6 and linear in T above 75 K. The inset of Fig. 2 reveals a transition to the superconducting state at T_c = 0.89 K. The transition is sharp, with a width of under 0.01 K. Prior work [3] presented measurements of ρ(T) to the lowest temperature of 2 K, and did not report superconductivity. The overall magnitude of ρ is small, with a value at 295 K that is only about 29 times larger than copper.

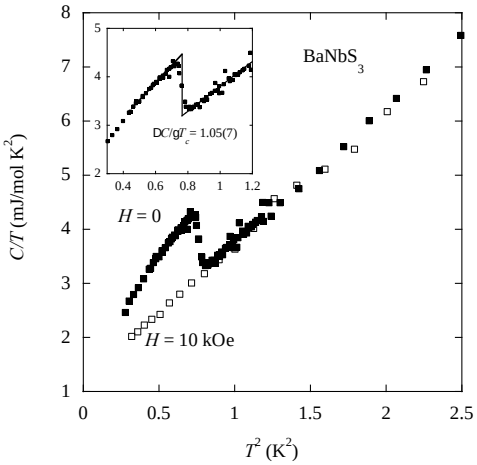

Fig. 3. Specific heat C/T versus T^2 for $BaNbS_3$. Inset shows the region near T_c and the entropy-conserving construction for estimating the jump due to the superconducting phase transition.

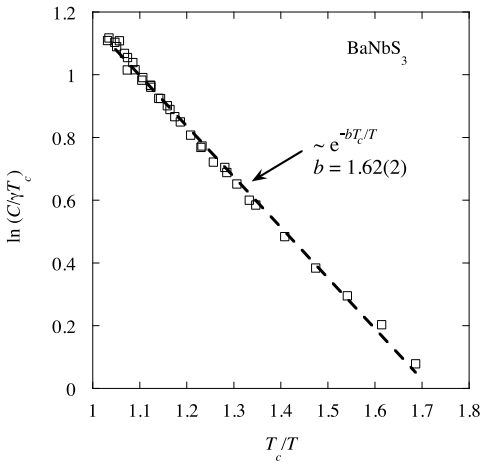

Fig. 4. Plot of $\ln(C/\gamma T_c)$ versus T_c/T for $BaNbS_3$ below T_c. The dashed line is a fit to Equation (1).

Measurements of the specific heat at constant pressure are shown in Fig. 3 at $H = 0$ and 10 kOe. Fitting the $H = 0$ data to $C/T = \gamma + \beta T^2$ in the range $0.9 < T^2/K^2 < 16$ yielded $\gamma = 1.35(9)$ mJ/mol K^2 and $\beta = 2.54(1)$ mJ/mol K^4. The Debye temperature θ_D was calculated from β with the result $\theta_D = 91.4(1)$ K. It is comparable [5] to the values of elements such as Bi, Ba, Hg and K. The $H = 0$ data reveal a jump at T_c associated with the second-order phase transition to the superconducting state. The jump is shown in more detail in the figure's inset, where an entropy-conserving construction for estimating the magnitude of the jump is shown. The value $(C_s - C_n)/\gamma T_c = \Delta C/\gamma T_c = 1.05(7)$ was found. Here, C_s and C_n are the specific heats in the superconducting and normal states, respectively, near T_c. The midpoint of the bulk phase transition to the superconducting state observed in $C(T)$ is 0.87 K, and is close to the value determined from ρ of 0.89 K. The narrow transition (~45 mK) suggests good compositional homogeneity.

The jump in the specific heat for a conventional superconductor is expected [6] to be $\Delta C/\gamma T_c = 1.43$. Our value of 1.05 suggests that about 74% of the sample's available electronic states are involved in superconductivity, assuming that this is a BCS superconductor. The data were plotted as $\ln(C/\gamma T_c)$ versus T_c/T to investigate the presence of an energy gap below T_c, and to compare to the prediction from BCS theory

$$C = a\gamma T_c e^{-bT_c/T}. \qquad (1)$$

The resulting fit is shown in Fig. 4 as the dashed line. The values $a = 2.77(2)$ and $b = 1.62(2)$ were found. BCS theory [7] predicts $a = 8.5$ and $b = 1.44$. The smaller value of a is attributed to the involvement of 74% of available electronic states in the superconductivity, as suggested by $\Delta C/\gamma T_c$. The exponential factor is related to the energy gap E_g using [5] $E_g = 2bT_c$, which yields

E_g = 2.84(3) K or 0.245(3) meV. This compares well with the expected value from BCS theory [6,7] of $E_g = 3.528 k_B T_c$ = 0.274 meV.

In summary, bulk superconductivity was observed in $BaNbS_3$ at 0.89 K. Although the crystal structure is quasi-one dimensional, with interchain Nb-Nb distances about 1.4 times larger than the intrachain distances, the superconductivity appears to be isotropic on the scale of tens of Nb-Nb spacings, and BCS like. This is due to the large coherence lengths perpendicular and parallel to the chains, as determined from critical magnetic field measurements (not shown), which allow coherence over 30 to 340 Nb-Nb spacings, respectively. Measurements on single crystals would provide information on the anisotropies of its physical properties, and additional insight into possible quasi-1D behavior.

Future Plans

We are presently studying the phase relationships among various Nb sulfides. At present, we have discovered superconductivity near 1 K in two other Nb sulfides. Attempts to grow single crystals are currently in progress. Plans are also underway to investigate additional physical properties, such as the crystal structures with neutron diffraction, and thermal transport.

References

[1] J. Yan, K. V. Ramanujachary, and M. Greenblatt, Mat. Res. Bull., **30**, 463 (1995).

[2] S.-J. Kim, H.-S. Bae, K.-A. Yee, J.-H. Choy, and D.-K. Kim, J. Solid State Chem., **115**, 427 (1995).

[3] T. Ohtani, H. Sawada, and M. Chikamori, Mat. Res. Bull., **39**, 561 (2004).

[4] A. P. Drozdov, M. I. Eremets, I. A. Troyan, V. Ksenofontov, and S. I. Shylin, Nature, **525**, 73 (2015).

[5] C. Kittel, *Introduction to Solid State Physics* (John Wiley, New York, NY, 1996).

[6] M. Tinkham, *Introduction to Superconductivity* (Robert E. Krieger, Malabar, FL, USA, 1985).

[7] J. Bardeen, L. N. Cooper, and J. R. Schrieffer, Phys. Rev., 108, 1175 (1957).

Publications

[1] *Superconductivity in quasi-one-dimensional $BaNbS_3$,* J. J. Neumeier and M. G. Smith, submitted to Phys. Rev. B.

[2] *Local and long-range order and the influence of applied magnetic field on single-crystalline $NiSb_2O_6$*, A. B. Christian, C. D. Hunt, and J. J. Neumeier, submitted to Phys. Rev. B.

[3] *The Magnetic and Thermal Properties of Low-Dimensional Single-Crystalline Transition-Metal Antimonates and Tantalates,* Aaron B. Christian, Ph. D. thesis, Montana State University, 2017.

Metamaterials as a Platform for the Development of Novel Materials for Energy Applications

Willie J. Padilla, Duke University

Program Scope

The program is focused on exploration of the fundamental properties of metamaterials (MMs) / metasurfaces and their potential for control of energy at the sub-wavelength scale in support of the mission of the Department of Energy and the office of Basic Energy Sciences. Electromagnetic metamaterials provide a platform for the discovery and design of new materials with novel structures, functions, and properties. The program will advance the knowledge base of these materials through fundamental investigations of the experimental and theoretical properties of metamaterials for the discovery, prediction and design of new materials with novel structures, functions, and properties. The proposed research activities emphasize a complete basic research program including the conceptual / computational design, fabrication / synthesis of the materials, and the characterization and analysis of their electromagnetic properties.

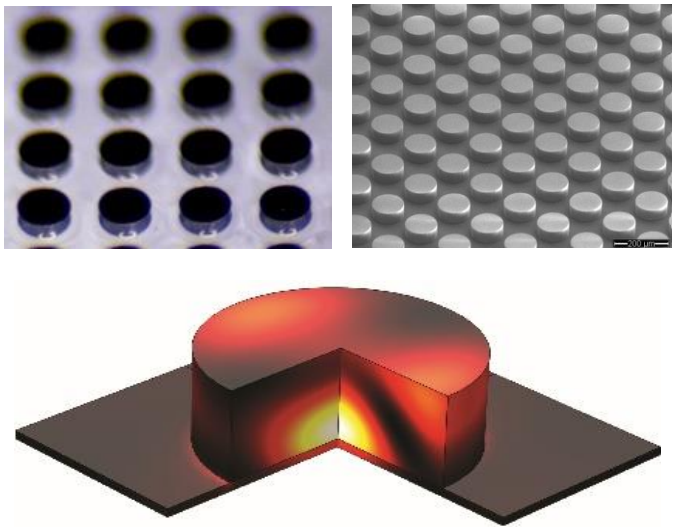

Figure 1. Top left shows an all-dielectric silicon terahertz metamaterial absorber fabricated on a polymer substrate. Top right shows a different all-dielectric terahertz metamaterial absorber. Bottom shows isometric cutaway view of a simulation of the power loss density of the absorber.

Recent Progress

We have recently proposed and demonstrated an all-dielectric absorber operating at terahertz frequencies. Our computational and experimental results are supported by theory which shows that the absorption process is well described as hybrid electric and hybrid magnetic modes that are supported and determined by the geometry of the cylindrical shapes – see Figure 1. Much like metallic based metamaterials, all-dielectric metamaterials support magnetic and electric modes, [1] and these modes may be tuned independently. Figure 2 shows experimental and

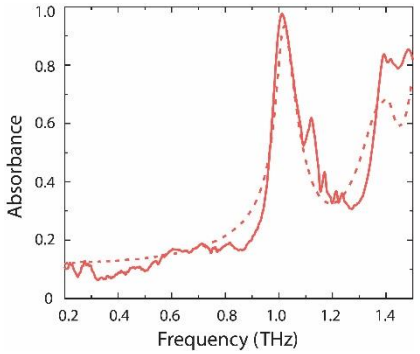

Figure 2. Frequency dependent absorptivity for the fabricated (solid curve) and simulated (dashed curve) all-dielectric absorber.

simulated absorbance in the terahertz range of the electromagnetic spectrum, for the metasurface shown on the top right of Figure 1. As can be observed we obtain a high absorbance near 1 terahertz and find good agreement with simulation.

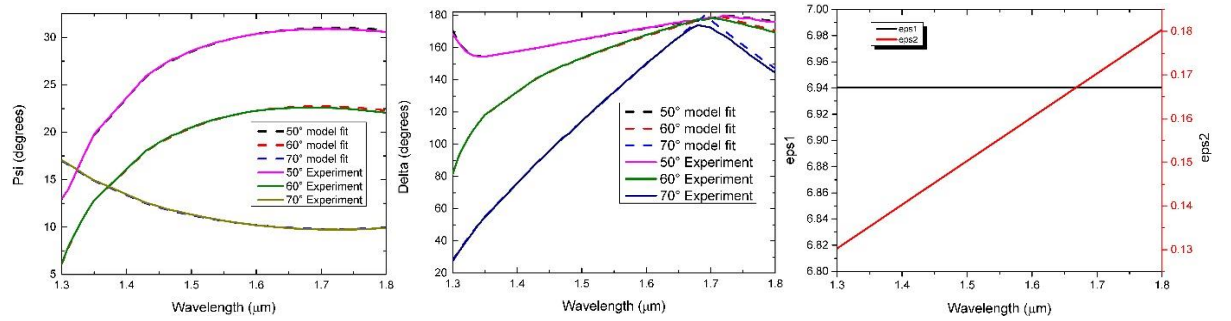

Figure 3. Results from infrared ellipsometric measurements of sputtered silicon carbide films from 1.3μm to 1.8μm. Left and middle show measured Ψ and Δ, respectively, both as a functions of wavelength for a number of different incidence angles (solid curves) and the dashed curves are fits for each angle. The right plot shows the resulting real (left axis) and imaginary (right axis) permittivity as a function of wavelength.

In related work we have designed and fabricated an all-dielectric metasurface emitter intended for operation in the infrared portion of the electromagnetic spectrum. We have chosen an operational wavelength of 1.5μm and the following constituent materials – quartz (SiO_2) substrate and dielectric metasurfaces fashioned from silicon carbide (SiC). We choose these materials owing to their high melting temperatures, silicon carbide (2730 °C) and quartz (1713 °C). Additionally, SiC has good oxidation resistance up to 1200 °C and a high refractive index with reasonable absorption coefficient at 1.5μm wavelength. However, it is important to directly characterize the material parameters of each of our constituent materials, owing to the variation that may result from using different vendors or alternate fabrication methods. In Figure 3 we show results of our spectroscopic ellipsometry measurements on silicon carbide across the range of interest. We measured three angles of 50°, 60° and 70° incidence both for S and P polarizations, in order to calculate the ellipsometric parameters given by, $\rho = \frac{r_p}{r_s} = \tan(\Psi)e^{i\Delta}$. As can be observed from Figure 3, we find that a value of ε_1=6.94 and $\varepsilon_2(\lambda=1.5\mu m)$=0.15, fits all of the data sets good. We have simulated some all-dielectric materials based on the results of our ellipsometric measurements. Based on simulation results we fabricated and measured some initial samples, as shown in Figure 4. Results are modes and some optimization still needs to be performed, as we find a maximum absorptivity of 70% at a wavelength of 1.31μm.

In other work we demonstrated an infrared spatio-temporal metamaterial emitter which realized the capability to tailor the emissivity of a surface, which operates at room temperature. When viewed with an infrared camera, the modification of the emissivity appears as a nearly 20 °C

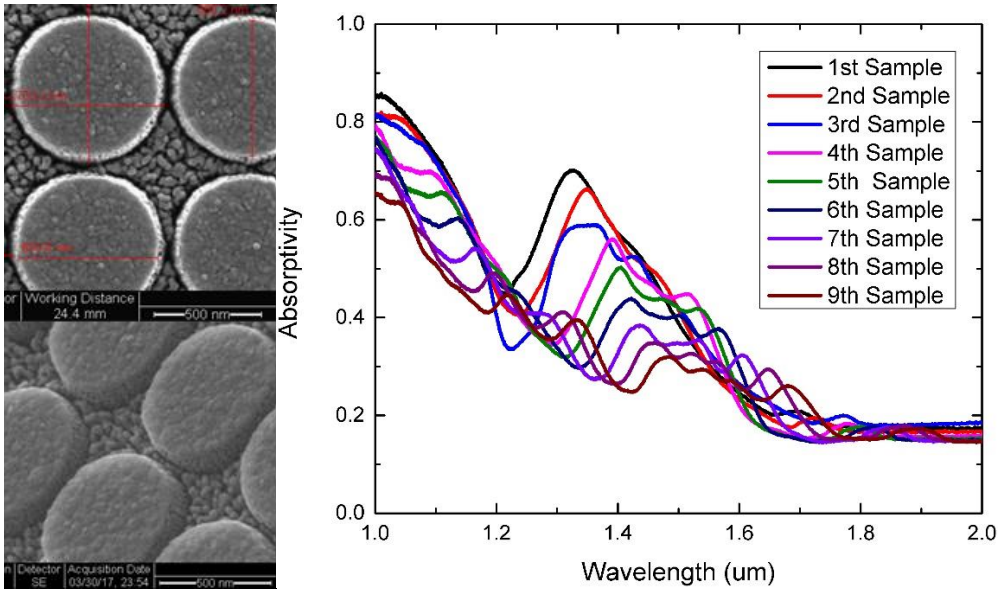

Figure 4. Left two panels show SEM images of IR emitters designed for 1.5μm wavlength made from silicon carbide on quartz. Right shows absorptivity measurements of nine different samples in the IR.

change. Further our emitter is able to modulate to speed up to 110 kHz – a speed approximately 10^4 times faster than that possible with a thermal-based approach. Our emitter realizes a modulation index of 23.7% at thermal infrared wavelengths, and what we have shown is general and not limited to the case experimentally demonstrated, but our procedure may be replicated to achieve nearly any desired tunable emissivity at nearly any wavelength.

Future Plans

We will continue to develop the theory of all-dielectric metasurface absorbers and emitters. This will include their description as waveguides, but also we will also reconcile our approach with Mie scattering theory. Our all-dielectric absorbers are similar to fiber optics, and thus we will leverage the extensive body of fiber literature in order to inform our future work. One example is the use of the cladding layer, which may allow us to incorporate additional modes, such as absorptive, or scattering channels.

We will also continue our computational, and fabricational realization of high temperature all-dielectric metasurface emitters. Although we have demonstrated high absorption of radiation at THz frequencies, and have some initial results in the NIR, we will continue to simulate and fabricate metasurfaces for IR wavelengths – including long and mid-wave frequencies. The angular performance has yet to be characterize and we would additionally like to understand the basic physics governing the dependence. We will also investigate the ability of all-dielectric metasurface emitters to achieve multi-band absorption.

Another area of investigation involves achieving dynamic infrared emission. Although we have shown dynamic IR emission in the long-wave infrared, we would like to realize such reconfigurability in the mid and short-wave infrared as well.

References

1. E. Snitzer, "Cylindrical dielectric waveguide modes," J. Opt. Soc. Amer. **51**, 491–498 (1961).

Publications

1. X. Liu and W.J. Padilla, *Reconfigurable room temperature metamaterial infrared emitter*, Accepted for publication in Optica, (2017).

2. X. Liu, K. Fan, I.V. Shadrivov, and W.J. Padilla, *Experimental realization of a terahertz all-dielectric metasurface absorber*, Optics Express **25**, 191-201 (2017).

3. K. Fan, J. Suen, X. Wu and W.J. Padilla, *Graphene metamaterial modulator for free-space thermal radiation*, Optics Express **24**, 25189-25201 (2016).

4. X. Liu and W.J. Padilla, *Thermochromic Infrared Metamaterials*, Advanced Materials **28**, 871 (2016).

5. Wen-Chen Chen, Andrew Cardin, Machhindra Koirala, Xianliang Liu, Talmage Tyler, Kevin G. West, Christopher M. Bingham, Tatiana Starr, Anthony F. Starr, Nan M. Jokerst and Willie J. Padilla, *Role of surface electromagnetic waves in metamaterial absorbers*, Optics Express **24**, 6783 (2016).

Extraordinary Responsive Magnetic Rare Earth Materials

Vitalij K. Pecharsky, Durga Paudyal, Yaroslav Mudryk, L. Scott Chumbley, and Thomas A. Lograsso

Ames Laboratory of US DOE, Iowa State University, Ames, Iowa, 50011-3020

Program Scope

Rare earth elements play a critical role in numerous technological applications, including permanent magnets, sensors, actuators, and solid state cooling, among other. Knowledge of the mechanisms of phase transformations driven by a minor stimulus, followed by a major perturbation of properties is of interest for understanding nonlinear relationships in the free energy, and is crucial for guiding the discovery of advanced energy materials. It is the latter that is the focus of this research, building upon the state-of-the-art synthesis, processing and characterization integrated with theory, modeling and computations gauged against reliable experimental data.

The goal of this research is to uncover the underlying electronic, atomic, and microscopic interactions that are magnetically and structurally anisotropic and result in an extraordinarily strong coupling between the magnetic and crystal lattices. The result is a remarkable responsiveness of selected rare earth intermetallic materials to temperature, pressure, and magnetic field. Such materials exhibit a number of unique properties associated with magnetic ordering alone, magneto-volume, itinerant electron metamagnetic, and magnetostructural transformations, which may be precisely controlled by chemistry, taloring reversible or irreversible breaking and reforming of specific chemical bonds. The overarching objective is to both understand and manipulate the responsiveness of materials that are sufficiently complex to facilitate control at length scales ranging from electronic interactions to atomic, nano- and microstructural scales and establish a playground to develop and employ predictive theoretical and computational modeling. Experiments and predictive modeling, when properly coupled, lead to subtle yet precise control of crystallography, electronic structure, and magnetic properties of compounds in focus. All of the model systems (R_5T_4, RM_2, RM, R_3M, RScT, $R_{117}M_{52\pm x}T_{112\pm y}$, and $RM_{13-x}T_x$), selected for this research, contain rare earth (R), transition metals, aluminum or magnesium (M), and Group 14 (T) elements.

Recent Progress

We have made significant progress in achieving the stated goal and objectives. We have refined and employed our synthesis, characterization, and computational tools to (a) understand the mechanism(s) by which the magnetism of rare earth sublattices, where the indirect 4f-5d-4f exchange interactions and magneto-crystalline anisotropy are dominant, can be affected by the introduction of non-rare earth elements, (b) quantify chemistry-structure-magnetic property relationships in rare-earth intermetallics, (c) build a foundation towards predicting most favorable adjustments of the chemical and physical parameters critical in controlling the responsive behavior of magnetic materials, (d) discover and develop cluster science beyond traditional physical or chemical heterogeneity, and (e) delineate pathways to ensure impact on energy-related technologies in the future. A few major achievements are highlighted below:

Modeling magnetism in rare-earth intermetallic materials: Rare-earth compounds are increasingly important in the development of novel materials for high-tech applications. Creating robust models predicting their properties and coupling the models with experimental validation is, therefore, vital for future reduction to practice. Our modeling followed by experiments have led to a key development in understanding of complex magnetic properties in a series of rare earth-intermetallic materials where gadolinium – an element from the middle of the rare earth series – was combined with magnesium, zinc, or cadmium [1]. We have developed disordered local moment theory explaining how the localized 4f electrons of gadolinium fluctuate with temperature and correlate. The localized 4f electrons fluctuate slowly compared to the mobile valence and conduction electrons. These mobile electrons not only act as communicators between the 4fs, but unexpectedly play a greater role in particular magnetic patterns displayed by each intermetallic compound (Fig. 1).

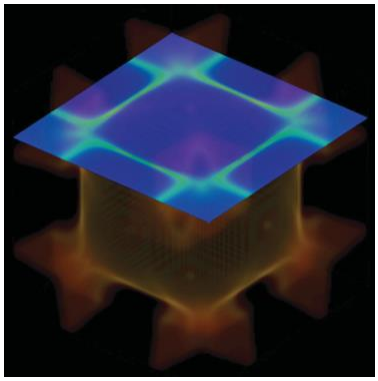

Fig. 1. Three-dimensional Fermi surface of paramagnetic GdMg. A constant-k_z slice through the Fermi surface is highlighted in blue. *This figure from* [1] *is featured on the cover of the PRL issue*.

Evolution of localized and itinerant magnetism: The evolution of magnetism and crystallography through a sequence of coupled magnetic and structural transformations has been examined in $HoCo_2$ – a model low-temperature magneto-responsive compound [2]. In the magnetically ordered state the unexpected increase of magnetization at the tetragonal to orthorhombic transformation is coupled with the lattice contraction. The low-temperature transition that occurs simultaneously with the change in magnetic anisotropy leads to a reduction of Co moment via rearrangement of both Co 3d and Ho 5d states. This complex process suppresses the role of itinerant magnetism in the orthorhombic $HoCo_2$. The materials responds strongly to the external magnetic field: suppression of the structural distortions both at T_C and at spin reorientation transition temperature (T_{SR}), a change in the nature of the transition at T_C from first to second order, and the enhancement of the low-temperature Schottky anomaly are all observed in moderately high magnetic fields.

Unexpected Co/Ni ordering in a magnetic rare-earth intermetallic compound: Synthesis and characterization experiments assisted by theoretical modeling revealed unique crystallographic ordering of two neighboring transition elements – nickel and cobalt – in a new gadolinium compound - Gd_3NiCo [3]. In the $Gd_3Ni_{2-x}Co_x$ solid solution, the cobalt atoms preferentially occupy only one of the two available transition metal sites avoiding direct Co-Co interactions. This is the first example of a rare earth intermetallic phase showing a clear preferrence in site occupacy by metallurgically very similar Co and Ni. The increased itinerant (mainly d-electron) magnetism acts as a key to enhance magnetic transitions in the Co-substituted Gd_3Ni_2 [3].

Tunable magnetic and structural transformations in mixed light and heavy-lanthanide dialuminides: Structural behaviors, specific heat, and magnetism of $Pr_{1-x}Er_xAl_2$ have been studied by means of temperature-dependent x-ray powder diffraction, heat capacity, magnetization, and first-principles calculations [4]. Although the cubic lattice of $PrAl_2$ distorts tetragonally at the Curie temperature, T_C, the distortion is rhombohedral in $ErAl_2$, creating a potential for instability in the pseudobinary $PrAl_2$–$ErAl_2$ system. The pseudobinary compounds with $0.05 \leq x \leq 0.5$ show complex magnetization behaviors, including metamagnetic transitions and short range magnetism. Unique among other mixed-lanthanide dialuminides, the substitution

of Er for Pr in $Pr_{1-x}Er_xAl_2$ results in an unexpected ferrimagnetic behavior, and the ferrimagnetic interactions become strongest around x = 0.25, where the compound shows unusual metamagnetic like transitions. The electronic structure calculations, including exchange interactions and crystal field splitting, magnetic moments, anisotropic 4f energy density, and magnetic surface potentials rationalize the interesting physics observed experimentally [4].

Future Plans

We will focus on (1) precise control of magnetic and/or structural transformations at the electronic level, (2) underlying correlations between magnetic anisotropy and magnetostructural transformations, (3) science of crystallographic and magnetic clustering, and short-range magnetism, (4) understanding of 4f-nd interactions that lead to structural and magnetic instabilities, and (5) advancing the basic science of responsive materials for impact by expanding the availability of model systems. We are in a strong position to take advantage of advanced synthesis (both polycrystals and single crystals), characterization, and theoretical and computational modeling tools. Our theoretical and computational results are always verified and refined against reliable experimental data obtained while examining a broad range of structure-property relationships at different length scales and as functions of multiple stimuli. With this we expect to reach a high accuracy and consistency of calculations of the electronic and crystal structures, in addition to correct predictions of both ground states and finite temperature properties of rare earth intermetallic compounds with the ever increasing complexity. The expected outcome is the development of a clear picture revealing relationships among chemical composition; crystal, magnetic, and microscopic structures; and physical properties of rare earth materials that are poised for breakthroughs in materials science, chemistry and physics of intermetallic phases. New materials with potentially functional physics are expected to emerge from various rare-earth intermetallic systems, and the science of responsive materials will, therefore, be elevated to a new high, where validated computations become refined enough for prediction-based engineering of energy-relevant materials. Advanced experimental characterization of these materials (such as neutron and Mössbauer) will help to further explain the nature of responsive phenomena. Following are a few specific examples, work on which is in progress.

Nonmagnetic 3d metal - induced ferromagnetism in gadolinium-based materials: Preliminary results show that the replacement of the strongly magnetic gadolinium atoms with non-magnetic scandium strongly enhances ferromagnetic (FM) interactions in $(Gd_{1-x}Sc_x)_5Ge_4$ (Fig. 2). This counterintuitive experimental observation can be explained by a unique role 3d electrons of scandium play in mediating magnetic interactions between the gadolinium atoms from the neighboring layers in the peculiarly layered crystal lattice. At 20% concentration and below, scandium substitutions effectively increase the Curie temperature, T_C, remove both the kinetic arrest and hysteresis, and drastically improve reversibility of the magnetostructural transformation observed in the parent Gd_5Ge_4. In agreement with first principles predictions, Sc concentrations higher than 20% lead to a formation of a closely related Pu_5Rh_4-type structure where first order magnetostructural transformation is replaced by a second-order magnetic ordering that too is

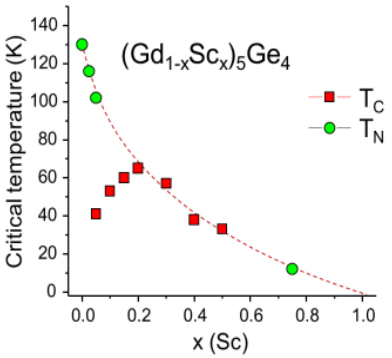

Fig. 2. The ferromagnetism in $Gd_{5-x}Sc_xGe_4$ rises when a strongly magnetic element, Gd, is replaced by a nominally non-magnetic Sc.

accompanied by a structural distortion. This work will demonstrate how theory can guide experiments by predicting anomalous physical behaviors in a series of alloys where conventional wisdom suggests a rather trivial continuous solid solubility and uninteresting magnetism.

Role of 4f electrons in crystallographic and magnetic complexity: Mastering basic science of compounds that undergo multiple phase transformations without major hysteresis losses is critical for intelligent design of functional materials. An unusually rich mix of structurally and magnetically distinct phases in $Er_{1-x}Dy_xCo_2$ can be judiciously controlled via tuning of 4f states, where Er and Dy – two neighboring lanthanides – each play a distinct role in defining phase stability. The surprising complexity can be attributed to the interplay of two different 4f electron energy landscapes, even though it has been commonly assumed that 4f electrons have little, if any, participation in the chemical bonding in intermetallic compounds. Unlike the parent binaries that exhibit lone distortions at their respective Curie temperatures, T_C, $Er_{0.75}Dy_{0.25}Co_2$ undergoes two magnetostructural transitions: a first order at T_C, followed by a second order below T_C. Surprisingly, the ground state phase adopts *Imma* symmetry instead of the *Fddd* observed in $HoCo_2$. Supported by first principles calculations, our results are expected to offer new insights into the role of 4f electrons in controlling chemistry and physics of responsive alloys and compounds containing rare earths.

Tuning RScT materials to the edge of stability: The equiatomic RScT compounds exhibit non-trivial magnetic behaviors: despite the low concentration of the magnetic lanthanide (R) and high overall concentration of non-magnetic Sc and T = Si, Ge, Sb, their T_Cs are comparable to or higher than that of pure Gd [5]. RScT adopt two different, yet closely related layered crystal lattices: CeScSi-type is stable for the light R, CeFeSi-type structure is stable for the heavy R. Advanced *ab-initio* calculations confirmed by experiment show that the CeScSi-type structure favors FM, while the CeFeSi-type structure supports antiferromagnetic (AFM) ground state. Calculations also show a lateral shift of spin-split bands toward lower energy and away from the Fermi level as the exchange-split FM CeScSi-type changes to the AFM CeFeSi-type structure in RScSb. A preliminary experimental investigation of the structural and physical properties in the $Gd_{1.02}Sc_{0.98}Ge_{1-x}Sb_x$ series indeed reveals that Sb substitution leads to a gradual conversion from FM CeScSi to AFM CeFeSi-type structure. We will continue tailoring band shifts by modeling chemical substitutions on the R (Gd) and T (Sb) sites to establish the most promising combinations of Gd and R′, Sb and T′, and ranges of concentrations (x) to realize instability. As the modeling work progresses, promising compounds will be prepared and fully characterized.

References

1. L. Petit, D. Paudyal, Y. Mudryk, K. A. Gschneidner, V. K. Pecharsky, M. Luders, Z. Szotek, R. Banerjee, and J. B. Staunton, Phys. Rev. Lett. **115**, 207201 (2015).
2. Y. Mudryk, D. Paudyal, A. K. Pathak, V. K. Pecharsky, and K. A. Gschneidner Jr., J. Mater. Chem. C **4**, 4521 (2016).
3. A. Provino, V. Smetana, D. Paudyal, K. A. Gschneidner, A. V. Mudring, V. K. Pecharsky, P. Manfrinetti, and M. Putti, J. Mater. Chem. C **4**, 6078 (2016).
4. A. K. Pathak, D. Paudyal, Y. Mudryk, K. A. Gschneidner, and V. K. Pecharsky, Phys. Rev. B **94**, 224406 (2016).
5. C. Ritter, S. K. Dhar, R. Kulkarni, A. Provino, D. Paudyal, P. Manfrinetti, and K. A. Gschneidner Jr, J. Phys.: Condens. Matter **26**, 366001(2014) and references therein.

Publications

1. L. Petit, D. Paudyal, Y. Mudryk, K. A. Gschneidner, V. K. Pecharsky, M. Luders, Z. Szotek, R. Banerjee, and J. B. Staunton, "Complex magnetism of lanthanide intermetallics and the role of their valence electrons: Ab initio theory and experiment," Phys. Rev. Lett. **115**, 207201 (2015).
   https://doi.org/10.1103/PhysRevLett.115.207201
   A figure from this article has been selected as the cover page of Physical Review Letters.

2. Y. Mudryk, D. Paudyal, T. Prost, L. S. Chumbley, V. K. Pecharsky, and K. A. Gschneidner Jr., "Correlations between magnetism, microstructure, crystallography, and phase stability in $GdNi_{1-x}Co_x$ alloys," Acta Mater. **92**, 18 (2015).
   http://dx.doi.org/10.1016/j.actamat.2015.03.049

3. A. Provino, K. A. Gschneidner, Jr., S. K. Dhar, C. Ferdeghini, Y. Mudryk, P. Manfrinetti, D. Paudyal, and V.K. Pecharsky, "The nano-microfibrous $R_{11}Ni_4In_9$ intermetallics: New compounds and extraordinary anisotropy in $Tb_{11}Ni_4In_9$ and $Dy_{11}Ni_4In_9$," Acta Mater. **91**, 128 (2015).
   http://dx.doi.org/10.1016/j.actamat.2015.03.003

4. J. Liu, V.K. Pecharsky, and K.A. Gschneidner, Jr., "Metamagnetic transition and magnetothermal properties of $ErCo_4Ge_2$," J. Appl. Phys. **118**, 013904 (2015).
   http://dx.doi.org/10.1063/1.4923414

5. V. I. Zverev, A. M. Tishin, M. Zou, Ya. Mudryk, K. A. Gschneidner, Jr., and V. K. Pecharsky, "Magnetic and magnetothermal properties, and the magnetic phase diagram of single crystal holmium along the easy magnetization direction," J. Phys: Condens. Matter **27**, 146002 (2015).
   http://dx.doi.org/10.1088/0953-8984/27/14/146002

6. R. L. Hadimani, S. Gupta, S. M. Harstad, V. K. Pecharsky, and D. C. Jiles, "Investigation of room temperature ferromagnetic nanoparticles of Gd_5Si_4," IEEE Transactions on Magnetics **51**, 2504104 (2015).
   http://dx.doi.org/10.1063/1.4923414

7. X. C. Zhong, Z. W. Liu, J. X. Min, H. C. Tian, K. A. Gschneidner, Jr., and V. K. Pecharsky, "Magnetic properties and magnetic entropy changes of MRE_2Co_7 compounds," China Phys. Mech. Astron. **58**, 597501 (2015).
   http://dx.doi.org/10.1007/s11433-015-5656-9

8. C. Ritter, A. Provino, P. Manfrinetti, V. K. Pecharsky, K. A. Gschneidner, and S. K. Dhar, "Magnetic Structures of $R_5Ni_2In_4$ and $R_{11}Ni_4In_9$ (R = Tb and Ho): Strong hierarchy in the temperature dependence of the magnetic ordering in the multiple rare-earth sublattices," J. Phys: Condens. Matter **27**, 476001 (2015).
   http://dx.doi.org/10.1088/0953-8984/27/47/476001

9. W. Xie, J. Liu, V. K. Pecharsky, and G. J. Miller, "γ-Brasses with spontaneous magnetization: Atom site preferences and magnetism in the Fe-Zn and Fe-Pd-Zn phase spaces," Z. Anorg. Allg. Chem **641**, 270 (2015).
http://dx.doi.org/10.1002/zaac.201400539

10. V. Smetana, S. Steinberg, Y. Mudryk, V. Pecharsky, G. J. Miller, and A.-V. Mudring, "Cation-poor complex metallic alloys in Ba(Eu)–Au–Al(Ga) systems: Identifying the keys that control structural arrangements and atom distributions at the atomic level," Inorg. Chem. **54**, 10296-10308 (2015).
http://dx.doi.org/10.1021/acs.inorgchem.5b01633

11. Y. Mudryk, D. Paudyal, A. K. Pathak, V. K. Pecharsky, and K. A. Gschneidner Jr, "Balancing structural distortions via competing 4f and itinerant interactions: A case of polymorphism in magnetocaloric $HoCo_2$," J. Mater. Chem. C **4**, 4521 (2016).
http://dx.doi.org/10.1039/C6TC00867D

12. V. K. Pecharsky, J. Cui, and D. D. Johnson, "(Magneto)caloric refrigeration: Is there light at the end of the tunnel?" Phil. Trans. R. Soc. A **374**, 20150305 (2016).
http://dx.doi.org/10.1098/rsta.2015.0305

13. A. Provino, V. Smetana, D. Paudyal, K. A. Gschneidner, A. V. Mudring, V. K. Pecharsky, P. Manfrinetti, and M. Putti, "Gd_3Ni_2 and $Gd_3Co_xNi_{2-x}$: Magnetism and unexpected Co/Ni crystallographic ordering," J. Mater. Chem. C **4**, 6078 (2016).
http://dx.doi.org/10.1039/c6tc01035k

14. C. L. Wang, J. Liu, Y. Mudryk, K. A. Gschneidner, Y. Long, and V. K. Pecharsky, "The effect of boron doping on crystal structure, magnetic properties and magnetocaloric effect of $DyCo_2$," J. Magn. Magn. Mater. **405**, 122 (2016).
http://dx.doi.org/10.1016/j.jmmm.2015.12.062

15. A. K. Pathak, D. Paudyal, Y. Mudryk, K. A. Gschneidner, and V. K. Pecharsky, "Tunable magnetism and structural transformations in mixed light- and heavy-lanthanide dialuminides," Phys. Rev. B **94**, 224406 (2016).
https://doi.org/10.1103/PhysRevB.94.224406

16. J. Logan, R. Harder, L. X. Li, D. Haskel, P. Chen, R. Winarski, P. Fuesz, D. Schlagel, D. Vine, C. Benson, and I. McNulty, "Hard X-Ray polarizer to enable simultaneous three-dimensional nanoscale imaging of magnetic structure and lattice strain," J. Synchrotron Rad. **23**, 1210 (2016).
https://doi.org/10.1107/S1600577516009632

17. S. K. Dhar, A. Provino, P. Manfrinetti, R. Kulkarni, N. Goyal, and D. Paudyal, "Ti_3CrCu_4: A possible 2-D ferromagnetic spin fluctuating system," AIP Advances **6**, 055817 (2016).
http://dx.doi.org/10.1063/1.4943922

18. A. Maurya, R. Kulkarni, A. Thamizhavel, D. Paudyal, and S. K. Dhar, "Kondo lattice and antiferromagnetic behavior in quaternary $CeTAl_4Si_2$ (T = Rh, Ir) single crystals," J. Phys. Soc. Jpn. **85**, 034720 (2016).
http://dx.doi.org/10.7566/jpsj.85.034720

19. S. K. McCall, N. Nersessian, G. P. Carman, V. K. Pecharsky, D. L. Schlagel, and H. B. Radousky, "Temperature and field induced strain measurements in single crystal $Gd_5Si_2Ge_2$," JOM **68**, 1589 (2016).
http://dx.doi.org/10.1007/s11837-016-1895-0

20. A. Provino, N. S. Sangeetha, S. K. Dhar, V. Smetana, K. A. Gschneidner, Jr., V. K. Pecharsky, P. Manfrinetti, and A. -V. Mudring, "New R_3Pd_5 compounds (R=Sc, Y, Gd-Lu): Formation and stability, crystal structure and antiferromagnetism," Crystal Growth and Design **16**, 6001 (2016).
http://dx.doi.org/10.1021/acs.cgd.6b01045

21. T. E. Prost, L. S. Chumbley, Y. Mudryk, and V. K. Pecharsky, "Crystallographic and compositional contributions to the breakdown of the $GdNi_{1-x}$ Co_x solid solution," J. Alloys. Compd. **696**, 382 (2017).
http://dx.doi.org/10.1016/j.jallcom.2016.11.312

22. M. Khan, A. K. Pathak, Y. Mudryk, K. A. Gschneidner, Jr., and V. K. Pecharsky, "Anisotropy induced anomalies in $Dy_{1-x}Tb_xAl_2$," J. Mater. Chem. C **5**, 896 (2017).
http://dx.doi.org/10.1039/C6TC05384J

23. S. Harstad, N. D'Souza, N. Soin, A. A. El-Gendy, S. Gupta, V. K. Pecharsky, T. Shah, E. Siores, and R. L. Hadimani, "Enhancement of $\boldsymbol{\beta}$-phase in PVDF films embedded with ferromagnetic Gd_5Si_4 nanoparticles for piezoelectric energy harvesting," AIP Advances **7**, 056411 (2017).
http://dx.doi.org/10.1063/1.4973596

24. D. Prodius, V. Smetana, S. Steinberg, M. Wilk-Kozubek, Y. Mudryk, V. K. Pecharsky and A. -V. Mudring, "Breaking the paradigm: record quindecim charged magnetic ionic liquids," Mater. Horiz. **4**, 217 (2017).
http://dx.doi.org/10.1039/C6MH00468G.
A figure from this article has been selected as the cover page of Materials Horizons

25. C. Ritter, A. Provino, P. Manfrinetti, and A.K. Pathak, "Tetragonal to triclinic transition in the prototypical CeScSi induced by a two-step magnetic ordering: a temperature-dependent neutron diffraction study of CeScSi, CeScGe, amd LaScSi," J. Phys. Condens. Matter. **29**, 045802 (2017).
http://dx.doi.org/10.1088/1361-648X/29/4/045802

26. I. Bigun, S. Steinberg, V. Smetana, Y. Mudryk, , Y. Kalychak, L. Havela, V. K. Pecharsky, and A.-V. Mudring, "Magnetocaloric behavior in ternary europium indides EuT_5In: Probing

the design capability of first-principles-based methods on the multifaceted magnetic materials," Chem. Mater. **29**, 2599 (2017). http://dx.doi.org/10.1021/acs.chemmater.6b04782

27. A.L. Pires, J.H. Belo, I.T. Gomes, R.L. Hadimani, D.L. Schlagel, T.A. Lograsso, D.C. Jiles, A.M.L. Lopes, J.P. Araujo, and A.M. Pereira, "Suppression of magnetostructural transition on GdSiGe thin film after thermal cycling," Thin Solid Films **621**, 247 (2017). http://dx.doi.org/10.1016/j.tsf.2016.09.013

Polymeric Multiferroics

Shenqiang Ren, Temple University

Program Scope

The goal of this project is to investigate room temperature magnetism and magnetoelectric coupling of polymeric multiferroics. A new family of molecular charge-transfer crystals has been emerged as a fascinating opportunity for the development of all-organic electrics and spintronics due to its weak hyperfine interaction and low spin-orbit coupling; nevertheless, direct observations of room temperature magnetic spin ordering have yet to be accomplished in organic charge-transfer solids. Furthermore, room temperature magnetoelectric coupling effect hitherto known multiferroics, is anticipated in organic donor-acceptor complexes because of magnetic field effects on charge-transfer dipoles, yet this is also unexplored. The PI seeks to fundamental understanding of the control of organic crystals to demonstrate and explore room temperature multiferroicity.

Recent Progress

***Finding 1: A free-standing molecular spin-charge converter for ubiquitous magnetic-energy harvesting* (Advanced Materials, 29, 8, 2016)**

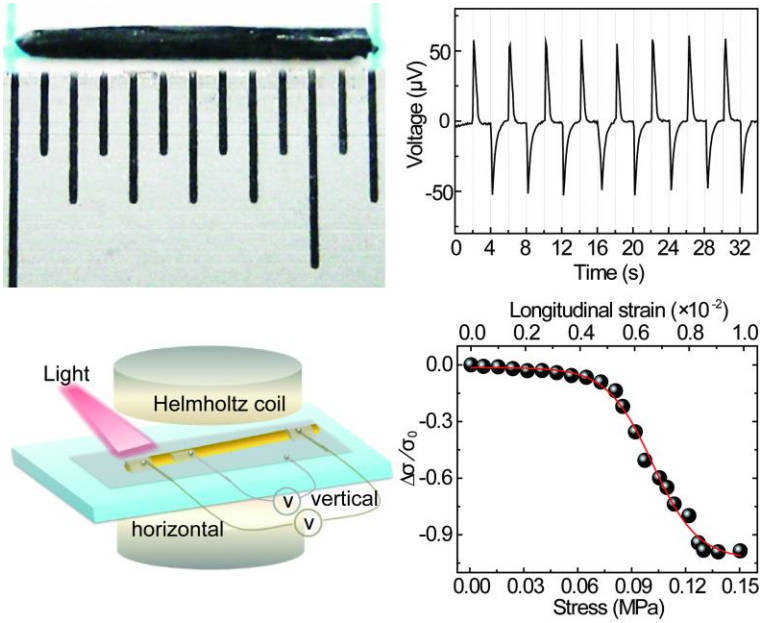

Figure 1. The centimeter-sized molecular charge-transfer crystals, as a new spin-charge converter, for magnetic energy harvesting and sensing.

Self-powered organic conjugated materials with multiple sensing ability are of vital importance for the development of micro/nanosystems for next-generation, flexible, and fully-integrated energy, sensing, personal healthcare systems, and artificial intelligence technologies. [1] Among them, the most rapidly developing technologies is energy harvesting and sensing from the ubiquitous distributed magnetic field of the earth, human brain and heart, and high-voltage power lines. Compared with inorganic materials, the lightweight, flexible, solution processable ability endows organic materials with multiple freedom for flexible electronics. However, it still remains a great challenge to converts magnetic energy into electrical energy, and transduces multiple stimuli into a coupled signal in non-integrated organic semiconductors. In this work, we demonstrate magnetic energy harvesting ability from centimeter-sized free-standing organic single crystal semiconductor prepared by solution process (Fig. 1). The largest output voltage and current reaches ~67 μV and ~62 pA at a magnetic field of 2000 Oe. The functional properties of these crystals are then rationalized through the nature of their charge transfer process using experimental measurements and quantum mechanical density functional theory (DFT) calculations. The simulation confirms the strong intermolecular charge transfer interaction. By controlling the intrinsic intermolecular charge transfer state and carrier transport

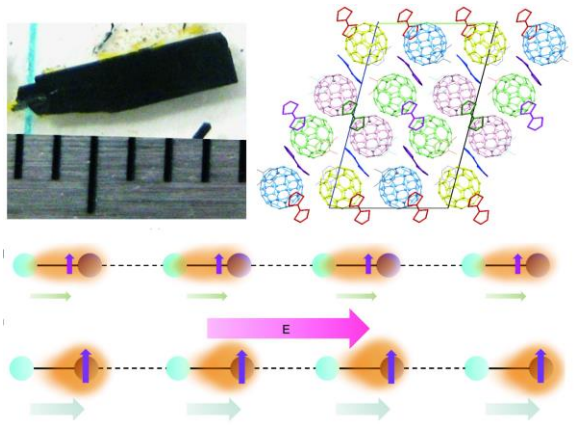

Figure 2. Centimeter-sized segregated stacking TTF-C_{60} single crystals are crystallized by mass-transport approach combined with solvent vapor evaporation for the first time. The intermolecular charge transfer interaction in the long-range ordered superstructure enables the crystals to demonstrate external stimuli-controlled multifunctionalities and angle/electrical potential dependent luminescence.

through external magnetic field, heat and strain, the capacitance and conductivity can be modulated in a large scale, enabling the semiconductor with sensitive optical, thermal, mechanical sensing ability. The crystal shows an excellent temperature sensitivity of < 0.01 K as well as good photoresponse. Moreover, the anisotropic molecular stacking enables the crystals with obvious anisotropy. The self-powered sensing performance, together with its solution processability and flexibility, endow it with the capability to drive a new generation of non-contact magnetic energy harvesting and sensing technologies.

Finding 2: Multifunctional charge-transfer single crystals through supramolecular assembly **(Advanced Materials, 28, 26, 2016)**

Organic molecular charge-transfer solids have attracted tremendous interest in contemporary materials science, where the charge, spin and lattice degrees of freedom are all strongly entangled to promote new properties (superconductivity, ferroelectricity, quantum spin liquid state, etc.) for flexible and lightweight multifunctional materials.[2, 3] There is a great deal of interest and excitement recently in understanding the role of charge transfer and stacking arrangement in multifunctional supramolecular assembly networks for efficient optoelectronics and molecular electronics.[4] Historically, the invention of each new kind of organic charge-transfer (CT) complex initiates a technological revolution. Here, we report external stimuli-controlled multifunctionalities of molecular charge-transfer single crystals, in which electron donor tetrathiafulvalene (TTF) and acceptor fullerene (C_{60}) build a charge-transfer network in the crystalline lattice solid (Fig. 2). The intermolecular contacts between asymmetric TTFs and multi-orientational C_{60} molecules lead to spin and charge order within the crystal structure. These crystals are found to exhibit spontaneous and hysteretic polarization, potential-dependent luminescence, and magnetoelectric properties owing to the presence of spin-charge composite ferroic ordering in the long-range ordered TTF-C_{60} lattice solids. In combination with their relatively simple crystallization process and broad chemical flexibility, molecular charge-transfer crystals promote the material-by-design paradigm towards the development of multifunctional all-organic nanoferronics. This work provides, for the first time, the evidence that molecular stacking and orientational ordering regulate the charge, spin and photonic orders within organic molecular CT single crystals. In this work, we report on the observation of the centimeter-sized three-dimensional supramolecular assembly of alternating π-electron tetrathiafulvalene donor and fullerene acceptor as the prototypical π-conjugated supramolecular charge-transfer single crystal, which is solved by high resolution synchrotron diffraction.

Finding 3: All-polymeric control of nanoferronics **(Science Advance, e1501264, 2015)**

In the search of light and flexible nanoferronics, a significant research effort is geared towards discovering the coexisting magnetic and electric orders in crystalline charge-transfer complexes.

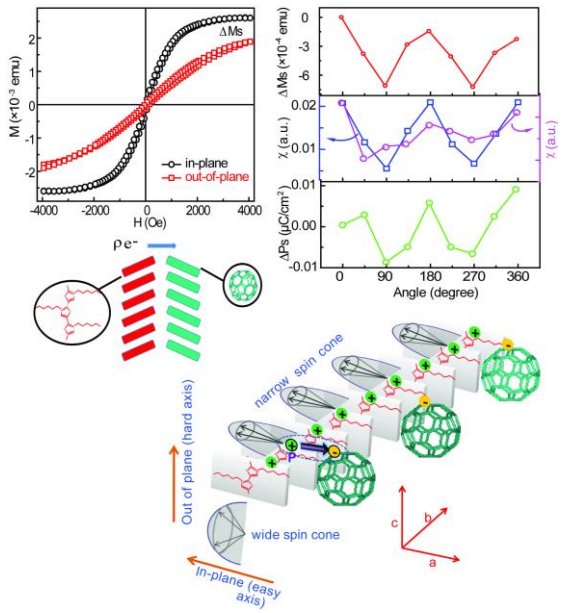

Figure 3. Magnetic hysteresis loops of polymeric nanoferronics in the in-plane and out-of-plane directions. Angle dependent saturation magnetization (above), experimental (middle left) and calculated spin susceptibility (middle right), and saturation polarization (below). The spin cone distribution along the long axis (b axis) of the CTTC and the polarization induced by charge ordering and charge transfer at the interface. The direction and width of the spin cone depend on the spin direction and the charge-lattice coupling extent.

Here, we report the first example of multiferroicity in the centimeter-sized crystalline polymeric charge-transfer superstructures that grow at the liquid-air interface and are controlled by the regioregularity of the polymeric chain. The charge-order-driven ferroic mechanism reveals spontaneous and hysteretic polarization and magnetization at the donor-acceptor interface. The charge transfer and ordering in the ferroic assemblies depends critically on self-organizing and molecular packing of electron donor and acceptor. Charge transfer and ordering at interfaces enables the appearance of simultaneous room temperature anisotropic ferroic orders and their coupling along the stacking axis of the crystalline CT superstructures. The giant anisotropic behavior is largely resulted from packing structure along different crystal growth direction, which leads to the unique optical properties, extraordinary anisotropic electric and magnetoelectric coupling behaviors. Theoretical simulation uncovers a structural and interfacial mechanism on the crystal structure, energy level fluctuation and wavefunction distribution of CT superstructures. The invention described here not only represents a new coupling mechanism of magnetic and electric ordering, but also stands for a new class of the emerging all-organic nanoferronics. The large-sized freestanding charge-transfer crystals will constitute a new direction for solution-processable all organic ferroic devices. In this respect, this work defines a research avenue for alternative materials to those studied extensively in recent years such as inorganic multiferroic oxides and organic spintronics, and opens a search for suitable carbon-based charge transfer materials with yet untapped potential for efficient ferroic devices. The principal of using crystalline CT compounds offers a broad design flexibility, which leads to a great potential for the development of room temperature organic magnetoelectric multiferroics.

Finding 4: Chemically driven interfacial coupling in charge-transfer mediated functional superstructures **(Nano Letters, 16, 2851, 2016)**

The mixing of conductivity and ferroic orders in functional materials could lead to numerous technological advances, such as ferroic field-effect transistors and magnetoelectric tunnel junctions.[5, 6] However, the ferroic orders are related to the interaction of localized electrons while the conduction is determined by the movement of electrons; thus, simultaneous conducting and ferroic orders remains challenging in conventional materials. Materials-by-design and assembly principle provides a unique and exciting opportunity, as it allows us to design novel multifunctional organic materials that combine two or more physical properties in the same crystal lattice, which are difficult or impossible to achieve in continuous inorganic crystalline solids. In this work, we shed light on the impact of chemically driven side-chain engineering on correlated

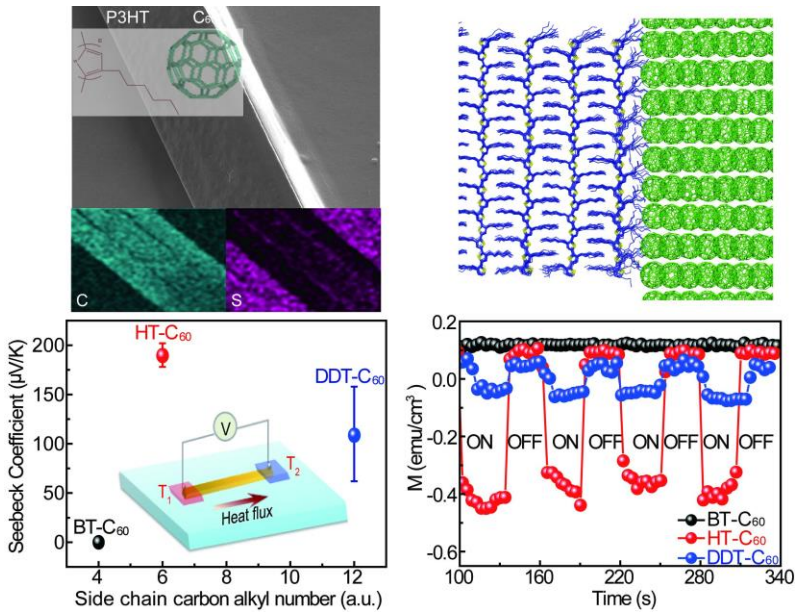

Figure 4. The control of organic crystallization and interfacial electron coupling are keys to dictate external stimuli responsive behaviors in organic charge-transfer superstructures. The integrated experimental and computational study reveals the importance of chemically driven interfacial coupling in organic charge-transfer superstructures.

optical, thermal, electric and magnetic properties of CT superstructures using a combined experimental and theoretical approach (Fig. 4). The CT superstructures with crystallization between fullerene (C_{60}) acceptor and polythiophene donor with varying alkyl side chains were chosen as prototype systems since exceptional optoelectronic response and optical characteristics have been observed in these π-conjugated systems. Our results suggest that the essential strategy for side-chain design to dictate external stimuli responsive behavior is control over polymer crystallization and interfacial electron coupling. Moreover, the Seebeck coefficients observed in such CT superstructures are among the highest reported for polymeric thermoelectric materials.

Future Plans

The current program ends on Feb. 2017, and the future plan focuses on the multiferroic orders of molecular charge transfer solids, consisting of electron donor and acceptor building blocks with the control of their dimension, charge states and charge-transfer degrees. The detailed experimental and computational modeling plan includes:

1) High quality molecular crystal growth with in-situ operando monitoring capabilities;
2) Exploration of exotic and emergent physical properties;
3) Mechanistic understanding of CT controlled physical properties in molecular crystals.

References

1.Wang, Z. L.; Wu, W. *Angewandte Chemie International Edition* **2012,** 51, (47), 11700-11721.
2.Allemand, P. e. a. *Science* **1991,** 253, (5017), 301-302.
3.Hebard, A. F.; Rosseinsky, M. J.; Haddon, R. C.; Murphy, D. W.; Glarum, S. H.; Palstra, T. T. M.; Ramirez, A. P.; Kortan, A. R. *Nature* **1991,** 350, (6319), 600-601.
4.Lunkenheimer, P.; Muller, J.; Krohns, S.; Schrettle, F.; Loidl, A.; Hartmann, B.; Rommel, R.; de Souza, M.; Hotta, C.; Schlueter, J. A.; Lang, M. *Nature materials* **2012,** 11, (9), 755-8.
5.Bibes, M. *Nature materials* **2012,** 11, (5), 354-357.
6.Naber, R. C. G.; Tanase, C.; Blom, P. W. M.; Gelinck, G. H.; Marsman, A. W.; Touwslager, F. J.; Setayesh, S.; de Leeuw, D. M. *Nature materials* **2005,** 4, (3), 243-248.

Publications (2015~ 2016)

1) B. Xu, H. Chakraborty, Z. Zhang, M. L. Klein and S. Ren, Tunable two-dimensional interfacial coupling in molecular heterostructures, ***Nature Communications***, ASAP (2017).
2) B. Xu, H. Chakraborty, R. C. Remsing, M. L. Klein, and S. Ren, A free-standing molecular spin-charge converter for ubiquitous magnetic-energy harvesting and sensing, ***Advanced Materials***, 29, 8 (2017)
3) Z. Zhang, B. Xu, B. Xu, L. Jin, H. Dai, Y. Rao and S. Ren, External stimuli responsive two-dimensional charge transfer polymers, ***Advanced Materials Interfaces***, 4, 2 (2016)
4) Z. Zhang and S. Ren, Colloidal Excimer Superstructures, ***Angewandte Chemie International Edition***, 10.1002/anie.201608845 (2016)
5) S. Han, L. Yang, K.Gao, S. Xie, W. Qin, and S. Ren, Spin Polarization of Excitons in Organic Multiferroic Composites, ***Scientific Reports***, 6, doi:10.1038/srep28656 (2016).
6) B. Xu and S. Ren, Integrated charge transfer in organic ferroelectrics for flexible multisensing materials, ***Small***, 12, 33 (2016). * Accepted as the Frontispiece Cover Art for ***Small.***
7) Z. Zhang, B. Xu, L. Zhang and S. Ren, Hybrid chalcopyrite-polymer magnetoconducting materials, ***ACS Applied Materials & Interfaces***, 10.1021/acsami.6b0336 (2016)
8) B. Xu, Z. Luo, A. J. Wilson, K. Chen, W. Gao, G. Yuan, H. Chopra, X. Chen, K. A. Willets, Z. Dauter, and S. Ren, Multifunctional charge-transfer single crystals through supramolecular assembly, ***Advanced Materials***, 28, 26 (2016)
9) B. Xu, H. Li, H. Li, A. J. Wilson, L. Zhang, K. Chen, K. A. Willets, F. Ren, J. C. Grossman, S. Ren, Chemically driven interfacial coupling in charge-transfer mediated functional superstructures, ***Nano Letters***, 10.1021/acs.nanolett.6b00712 (2016)
10) B. Xu, Z. Luo, W. Gao, A. J. Wilson, C. He, X. Chen, G. Yuan, H. Dai, Y. Rao, K. Willets, Z. Dauter, and S. Ren, Solution-processed molecular opto-ferroic crystals, ***Chemistry of Materials***, 10.1021/acs.chemmater.6b00836 (2016)
11) B. Xu, H. Li, A. Hall, W. Gao, M. Gong, G. Yuan, J. Grossman and S. Ren, All-polymeric control of nanoferronics, ***Science Advances***, 1, e1501264 (2015)
12) W. Qin, X. Chen, J. Lohrman, M. Gong, G. Yuan, M. Wuttig and S. Ren, External Stimuli Controlled Multiferroic Charge Transfer Crystals, ***Nano Res***, 10.1007/s12274-015-0975-8 (2015)
13) W. Qin, X. Chen, H. Li, M. Gong, G. Yuan, J. C. Grossman, M. Wuttig and S. Ren, Room temperature multiferroicity of charge transfer crystals, ***ACS Nano***, 9, 9373 (2015) Feature on Youtube: https://www.youtube.com/watch?v=ugM9XVlJtT4, and ACS Nano Podcast.
14) M. Gong, T. A. Shastry, Q. Cui, R. R. Kohlmeyer, K. A. Luck, A. Rowberg, T. J. Marks, M. F. Durstock, H. Zhao, M. C. Hersam, and S. Ren, Understanding Charge Transfer in Carbon Nanotube–Fullerene Bulk Heterojunctions, ***ACS Appl. Mater. Interfaces***, 7, 7428 (2015).
15) W. Qin, B. Xu and S. Ren, An Organic Approach for Nanostructured Multiferroics, ***Nanoscale***, 10.1039/C5NR01435B (2015). **Invited Minireview Article**.
16) Y. Xie, J. Lohrman and S. Ren, Phase Aggregation and Morphology Effects on Nanocarbon Optoelectronics, ***Nanotechnology***, 25, 485601 (2014).

High Performance Thermoelectric Materials and Flexible Transparent Electrodes

Zhifeng Ren
University of Houston

Program Scope

In this program, we aim to discover new thermoelectric materials with higher thermoelectric figure-of-merit (ZT) and power factor (PF) and flexible transparent electrodes with higher flexibility, transparency, and electrical conductivity.

Recent Progress

During the last two years since 2015, we have focused on studying 1) thermoelectric materials and their applications, 2) flexible transparent electrodes, plus exciting work on 3) nanostructures for enhanced oil recovery, and 4) catalysts for enhanced hydrogen evolution reaction and oxygen evolution reaction in water splitting electrochemically. We have achieved lots of unexpected exciting results. These results have been published in 43 peer-reviewed papers in which 30 is on thermoelectric materials, 8 on flexible transparent electrodes, 2 on enhanced oil recovery, 1 on hydrogen evolution reaction, and 2 on other topics. In this presentation, I will present some of the exciting results in the four areas we have studied.

Future Plans

We plan to discover new thermoelectric materials and further improve the thermoelectric performance of the existing thermoelectric materials. We will also continue the study on enhanced oil recovery and new catalysts for efficient full water splitting.

Publications in years from 2015 to 2017

2017

1. Dan Luo, Feng Wang, Md Kamrul Alam, Fang Yu, Ishwar Kumar Mishra, Jiming Bao, Richard C. Willson, and Zhifeng Ren, "Colloidal Stability of Graphene-based Amphiphilic Janus Nanosheet Fluid", *Chemistry of Materials* (2017, in press).
2. Keshab Dahal, Qian Zhang, Ran He, Ishwar Mishra, and Zhifeng Ren, "Thermal Conductivity of $(VO_2)_{1-x}Cu_x$ Composites across the Phase Transition Temperature", *J. of Applied Physics* (2017, in press).
3. J. de Boor, T. Dasgupta, U. Saparamadu, E. Müller, and Zhifeng Ren, "Recent progress in p-type thermoelectric magnesium silicide based solid solutions", *Materials Today Energy* (2017, in press).
4. Yuan Liu, Jianming Zhang, Heng Gao, Yang Wang, Qingxian Liu, Siya Huang, Chuan Fei Guo, and Zhifeng Ren, "Capillary force induced cold welding in silver-nanowire-based flexible transparent electrodes", *NanoLetters* **17**, 1090-1096 (2017).
5. Siya Huang, Yuan Liu, Chuanfei Guo, and Zhifeng Ren, "A Highly Stretchable and Fatigue-free Transparent Electrode Based on In-Plane Buckled Au Nanotrough Network", *Advanced Electronic Materials* **3**, 1600534 (2017).
6. Hee Seok Kim, Weishu Liu, and Zhifeng Ren, "The bridge between the materials and devices of thermoelectric power generators", *Energy and Environmental Science* **10**, 69-85 (2017).

7. Zihang Liu, Yumei Wang, Weihong Gao, Jun Mao, Huiyuan Geng, Jing Shuai, Wei Cai, Jiehe Sui, and Zhifeng Ren, "The influence of doping sites on achieving higher thermoelectric performance for nanostructured α-MgAgSb", *Nano Energy* **31**, 194-200 (2017).
8. Zihang Liu, Weihong Gao, Xianfu Meng, Xiaobo Li, Jun Mao, Yumei Wang, Jing Shuai, Wei Cai, Zhifeng Ren, and Jiehe Sui, "Mechanical properties of nanostructured thermoelectric materials α-MgAgSb", *Scripta Materialia* **127**, 72-75 (2017).

2016

9. Jun Mao, Hee Seok Kim, Jing Shuai, Zihang Liu, Ran He, Udara Saparamadu, Fei Tian, Weishu Liu, Zhifeng Ren. "Thermoelectric properties of materials near the band crossing line in Mg_2Sn-Mg_2Ge-Mg_2Si system", *Acta Materialia* **103**, 633-642 (2016).
10. Haiqing Zhou, Fang Yu, Jingying Sun, Hangtian Zhu, Ishwar Kumar Mishra, Shuo Chen, and Zhifeng Ren, "Highly efficient hydrogen evolution from edge-oriented $WS_{2(1-x)}Se_{2x}$ particles on three-dimensional porous $NiSe_2$ foam", *NanoLetters* **16**, 7604-7609 (2016).
11. Jun Mao, Zihang Liu, and Zhifeng Ren, "Size Effect in Thermoelectric Materials", *NPJ Quantum Materials* **1**, 16028 (2016).
12. Ran He, Daniel Kraemer, Jun Mao, Qing Jie, Yucheng Lan, Chunhua Li, Jing Shuai, Hee Seok Kim, David Broido, Gang Chen, and Zhifeng Ren, "Achieving high power factor and output power density in p-type half-Heuslers $Nb_{1-x}Ti_xFeSb$", *PNAS* **113**, 13576-13581 (2016).
13. Zihang Liu, Huiyuan Geng, Jun Mao, Jing Shuai, Ran He, Chao Wang, Wei Cai, Jiehe Sui, and Zhifeng Ren, "Understanding and manipulating the intrinsic point defect in α-MgAgSb for higher thermoelectric performance", *J. of Materials Chemistry A* **4**, 16834-16840 (2016).
14. J. de Boor, U. Saparamadu, J. Mao, K. Dahal, E. Müller, Zhifeng Ren, "Thermoelectric performance of Li doped, p-type Mg_2(Ge,Sn) and comparison with Mg_2(Si,Sn)", *Acta Materialia* **120**, 273-280 (2016).
15. Jing Shuai, Huiyuan Geng, Yucheng Lan, Zhuan Zhu, Chao Wang, Zihang Liu, Jiming Bao, Ching-Wu Chu, Jiehe Sui, and Zhifeng Ren, "Higher thermoelectric performance of Zintl phases $(Eu_{0.5}Yb_{0.5})_{1-x}Ca_xMg_2Bi_2$ by band engineering and strain fluctuation", *PNAS* **113**, E4125-E4132 (2016).
16. Jun Mao, Yumei Wang, Binghui Ge, Qing Jie, Zihang Liu, Udara Saparamadu, Weishu Liu, and Zhifeng Ren, "Thermoelectric performance enhancement of Mg_2Sn based solid solutions by band convergence and phonon scattering via Pb and Si/Ge substitution for Sn", *Physical Chemistry Chemical Physics* **18**, 20726-20737 (2016).
17. Dan Luo, Feng Wang, Jingyi Zhu, Feng Cao, Yuan Liu, Xiaogang Li, Richard C. Willson, Zhaozhong Yang, Ching-Wu Chu, and Zhifeng Ren, "Nanofluid of graphene-based amphiphilic Janus nanosheets for tertiary or enhanced oil recovery: High performance at low concentration", *PNAS* **113**, 7711-7716 (2016).
18. Jun Mao, Weishu Liu, and Zhifeng Ren, "Carrier Distribution in Multi-Band Materials and Its Effects on Thermoelectric Properties", *J Materiomics* **2**, 203-211 (2016).
19. Zhuan Zhu, Jiangtan Yuan, Haiqing Zhou, Jonathan Hu, Jing Zhang, Chengli Wei, Fang Yu, Shuo Chen, Yucheng Lan, Yao Yang, Yanan Wang, Chao Niu, Zhifeng Ren, Jun Lou, Zhiming Wang, and Jiming Bao, "Excitonic Resonant Emission−Absorption of Surface Plasmons in

Transition Metal Dichalcogenides for Chip-Level Electronic−Photonic Integrated Circuits", *ACS Photonics* **3**, 869-874 (2016).

20. Hee Seok Kim, Tianbao Wang, Weishu Liu, and Zhifeng Ren, "Engineering thermal conductivity for balancing between reliability and performance of bulk thermoelectric generators", *Adv. Func. Mater*. **26**, 3678-3686 (2016).
21. Ran He, Lihong Huang, Yumei Wang, Georgy Samsonidze, Boris Kozinsky, Qinyong Zhang, and Zhifeng Ren, "Enhanced thermoelectric properties of n-type NbCoSn half-Heusler by improving phase purification", *APL Materials* **4**, 104804 (2016).
22. Zihang Liu, Yumei Wang, Jun Mao, Huiyuan Geng, Jing Shuai, Yuanxu Wang, Ran He, Wei Cai, Jiehe Sui, and Zhifeng Ren, "Lithium doping to enhance thermoelectric performance of MgAgSb with weak electron-phonon coupling", *Adv. Energy Mater.* **6**, 1502269 (2016).
23. Jing Shuai, Yumei Wang, Zihang Liu, Hee Seok Kim, Jun Mao, Jiehe Sui, and Zhifeng Ren, "Enhancement of thermoelectric performance of phase pure Zintl compounds $Ca_{1-x}Yb_xZn_2Sb_2$, $Ca_{1-x}Eu_xZn_2Sb_2$, and $Eu_{1-x}Yb_xZn_2Sb_2$ by mechanical alloying and hot pressing", *Nano Energy* **25**, 136-144 (2016).
24. Hao Zhang, Yumei Wang, Keshab Dahal, Jun Mao, Lihong Huan, Qinyong Zhang, and Zhifeng Ren, "Thermoelectric properties of n-type half-Heusler compounds $(Hf_{0.25}Zr_{0.75})_{1-x}Nb_xNiSn$", *Acta Materialia* **113**, 41-47 (2016).
25. Jing Shuai, Hee Seok Kim, Zihang Liu, Ran He, Jiehe Sui, and Zhifeng Ren, "Thermoelectric Properties of Zintl Compound $Ca_{1-x}Na_xMg_2Bi_{1.98}$", *Appl. Phys. Lett*. **108**, 183901 (2016).
26. Yuan Liu, Xiuzhang Wang, Yumei Wang, Zhongjia Tang, Tatyana Makarenko, Arnold Guloy, Qinyong Zhang, and Zhifeng Ren, "Ultra-low thermal conductivities of hot-pressed attapulgite and its potential as thermal insulation material", *Appl. Phys. Lett*. **108**, 101906 (2016).
27. Jing Shuai, Zihang Liu, Hee Seok Kim, Yumei Wang, Jun Mao, Ran He, Jiehe Sui, and Zhifeng Ren, "Thermoelectric properties of Bi-based Zintl compounds $Ca_{1-x}Yb_xMg_2Bi_2$", *J. Materials Chemistry A* **4**, 4312-4320 (2016).
28. Chuan Fei Guo, Yan Chen, Lu Tang, Feng Wang, and Zhifeng Ren, "Enhancing the Scratch Resistance by Introducing Chemical Bonding in highly Stretchable and Transparent Electrodes", *NanoLetters* **16**, 594-600 (2016).
29. Hao Zhang, Yumei Wang, Lihong Huang, Shuo Chen, Keshab Dahal, Dezhi Wang, and Zhifeng Ren, "Synthesis and thermoelectric properties of n-type half-Heusler compound VCoSb with valence electron count of 19", *Journal of Alloys and Compounds* **654**, 321-326 (2016).
30. Zihang Liu, Jing Shuai, Jun Mao, Yumei Wang, Zhengyun Wang, Wei Cai, Jiehe Sui, and Zhifeng Ren, "Effects of Antimony content in $MgAg_{0.97}Sb_x$ on output power and energy conversion efficiency", *Acta Materialia* **102**, 17-23 (2016).

2015

31. Shuai Dong, Jun-Ming Liu, Sang-Wook Cheong, and Zhifeng Ren, "Multiferroic materials and magnetoelectric physics: symmetry, entanglement, excitation, and topology", *Advances in Physics* **64**, 519-626 (2015).
32. Siya Huang, Chuanfei Guo, X. Zhang, Wei Pan, Xi Luo, Chunsong Zhao, Jianghong Gong, X. Li, Zhifeng Ren, and Hui Wu, "Buckled Tin Oxide Nanobelt Webs as Highly Stretchable and Transparent Photosensors", *Small* **11**, 5712-5718 (2015).

33. Dandan Li, Huaizhou Zhao, Shanming Li, Beipei Wei, Jing Shuai, Chenglong Shi, Xuekui Xi, Peijie Sun, Sheng Meng, Lin Gu, Zhifeng Ren, Xiaolong Chen, "Atomic disorders induced by silver and magnesium ion migrations favor high thermoelectric performance in α-MgAgSb based materials", *Advanced Functional Materials* **25**, 6478-6488 (2015).
34. Chuan Fei Guo, Qihan Liu, Guohui Wang, Yecheng Wang, Zhengzheng Shi, Zhigang Suo, Ching-Wu Chua, and Zhifeng Ren, "Fatigue-free, superstretchable, transparent, and biocompatible metal electrodes", *PNAS* **112**, 12332-12337 (2015).
35. Zihang Liu, Huiyuan Geng, Jing Shuai, Zhengyun Wang, Jun Mao, Dezhi Wang, Qing Jie, Wei Cai, Jiehe Sui, and Zhifeng Ren, "The effect of nickel doping on electron and phonon transport in the n-type nanostructured thermoelectric material CoSbS", *J. Mater. Chem. C* **3**, 10442-10450 (2015).
36. Hee Seok Kim, Weishu Liu, and Zhifeng Ren, "Efficiency and output power of thermoelectric module by taking into account corrected Joule and Thomson heat", *Journal of Applied Physics* **118**, 115103 (2015).
37. Hee Seok Kim, Weishu Liu, Gang Chen, Ching-Wu Chu, and Zhifeng Ren, "Relationship between Thermoelectric Figure of Merit and Energy Conversion Efficiency", *PNAS* **112**, 8205-8210 (2015).
38. Jing Shuai, Yumei Wang, Hee Seok Kim, Zihang Liu, Jingying Sun, Shuo Chen, Jiehe Sui, and Zhifeng Ren, "Thermoelectric properties of Na-doped Zintl compound: $Mg_{3-x}Na_xSb_2$", *Acta Materialia* **93**, 187–193 (2015).
39. Yuan Liu, Chuan-Fei Guo, Siya Huang, Tianyi Sun, Yumei Wang, and Zhifeng Ren, "A new method for fabricating ultrathin metal films as scratch resistant flexible transparent electrodes", *J Materiomics* **1**, 52-59 (2015).
40. Chuan Fei Guo and Zhifeng Ren, "Flexible transparent conductors based on metal nanowire networks", *Materials Today* **18**, 143-154 (2015).
41. Weishu Liu, Qing Jie, Hee Seok Kim, and Zhifeng Ren, "Current progress and future challenges in thermoelectric power generation: from materials to devices", *Acta Materialia* **87**, 357-376 (2015).
42. Jiehe Sui, Jing Shuai, Yucheng Lan, Yuan Liu, Ran He, Dezhi Wang, Qing Jie, and Zhifeng Ren, "Effect of Cu concentration on the thermoelectric properties of nanostructured p-type $MgAg_{0.97-x}Cu_xSb_{0.99}$", *Acta Materialia* **87**, 266-272 (2015).
43. Jing Shuai, Hee Seok Kim, Yucheng Lan, Shuo Chen, Yuan Liu, Huaizhou Zhao, Jiehe Sui, and Zhifeng Ren, "Study on thermoelectric performance by Na doping in nanostructured $Mg_{1-x}Na_xAg_{0.97}Sb_{0.99}$", *Nano Energy* **11**, 640-646 (2015).

Tailoring exchange and spin-orbit interactions in graphene by proximity coupling

Jing Shi, Department of Physics & Astronomy, University of California, Riverside

Program Scope

We plan to explore novel interface phenomena in heterostructures of graphene and other materials for tailoring desired interactions such as exchange and spin-orbit coupling which standalone graphene does not have. These interactions are crucial for realizing quantum states including quantum anomalous Hall effect and quantum spin Hall effect in nanodevices. We will also study similar spin-dependent effects in topological surface states.

Recent Progress

By taking advantage of proximity coupling with atomically flat yttrium iron garnet films grown with pulsed laser deposition, we have demonstrated the anomalous Hall effect in graphene up to 300 K (ref. A and other unpublished results). The anomalous Hall conductivity reaches ¼ of the quantum anomalous Hall conductance value. In order to increase the size of the exchange gap near the Dirac point which is determined by the strength of both exchange and spin-orbit coupling, we need to increase the spin-orbit coupling strength in graphene. Therefore we have investigated the proximity coupling (ref. B) between graphene and transition metal

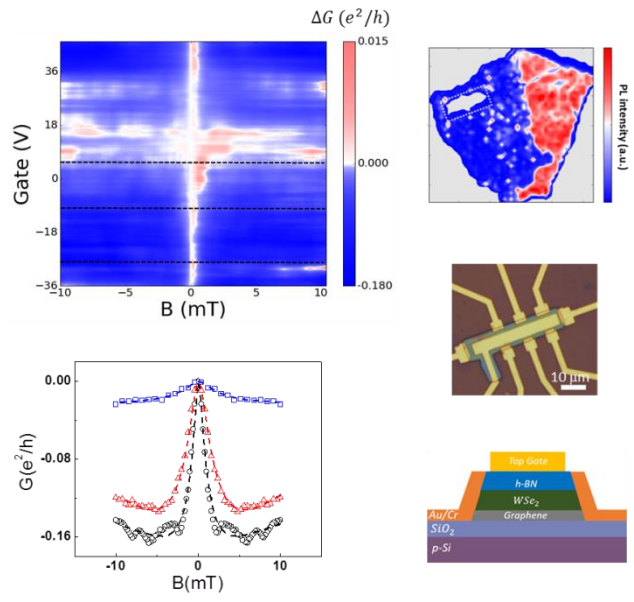

Figure 1. Magneto-conductance as a function of gate voltage and magnetic field: 2D plot (upper left) and line traces at three densities marked by dash lines in the 2D plot (lower left). Photoluminescence (PL) mapping of heterostructure of graphene with WSe_2 (upper right). Red region has WSe_2 only, but blue regon has both graphene and WSe_2. Quenching of PL in the blue region indicates strong coupling between the two materials. Transport device carved out of the blue region shown in the PL map by dry etching (central right). It has a top gate metal separated by hexagonal boron nitride right above the channel. Side view of the transport device with one-dimensional side contacts (lower right).

dichalcogenides such as MoS_2 and WSe_2 fabricated by either exfoliation or chemical vapor deposition. Both single-layer and multi-layer MoS_2 and WSe_2 have been incorporated in the heterostructures stack. In graphene/single-layer WSe_2 heterostructure devices fabricated with a

recently developed pickup-transfer technique, we have demonstrated strong Rashba spin-orbit coupling (~1.5 meV) extracted from pronounced weak anti-localization effects in low-field magnetoresistance (Figure 1) (ref. C). This is at least two orders of magnitude larger than the intrinsic spin-orbit coupling strength in standalone graphene. In both types of heterostructures, the distance between graphene and yttrium iron garnet films or transition metal dichalcogenides is critical to the coupling strength of the proximity effects. We are currently studying the distance effect by applying a hydrostatic pressure while performing transport measurements at low temperatures and in external magnetic fields. Another interesting spin-dependent effect in yttrium iron garnet/topological insulator heterostructures that we are currently investigating is the dramatic modification of spin dynamics of the magnetic insulator by the presence of the surface states of the topological insulator (ref. D). We have found that the spin-momentum locking in the surface states generates a much large spin current flow compared with any heavy metals with strong spin-orbit coupling.

Future Plans

We will continue the pressure dependence study to systematically tune both proximity induced interactions. New garnet films with perpendicular magnetic anisotropy will be used to generate anomalous Hall loops. Stronger proximity induced interactions are expected in heterostructures under pressure. We aim to demonstrate sufficiently strong interactions for quantum anomalous Hall effect at high temperatures. In addition, we will continue the spin dynamics study in magnetic insulator/topological insulator heterostructures in collaboration with theorists.

References

A. Z.Y. Wang, C. Tang, R. Sachs, Y. Barlas, and Jing Shi, Proximity-Induced Ferromagnetism in Graphene Revealed by the Anomalous Hall Effect, Phys. Rev. Lett. **114**, 016603 (2015).

B. B.W. Yang, M.-F. Tu, J.W. Kim, Y. Wu, H. Wang, J. Alicea, R.Q. Wu, M. Bockrath and Jing Shi, Tunable Spin–Orbit Coupling and Symmetry-Protected Edge States in Graphene/WS_2, 2D Materials **3**, 031012 (2016).

C. B.W. Yang, M. Lohmann, and Jing Shi, Strong Induced Rashba Spin-Orbit Coupling in Heterostructures of Graphene and Chemical Vapor Deposition Grown Single-Layer WSe_2 and $MoSe_2$ (under preparation).

D. C. Tang, Q. Song, C.Z. Chang, J. Moodera, S. Maekawa, D.J. Smith, W. Han, and Jing Shi, Dramatically Modified Spin Dynamics in Magnetic Insulators by Spin-Momentum Locked Surface States of Topological Insulators (to be submitted).

Publications

1. Y.D. Xu, B.W. Yang, C. Tang, Z.L. Jiang, M. Schneider, R. Whig, and Jing Shi, Heat-Driven Spin Transport in a Ferromagnetic Metal, Appl. Phys. Lett. **105**, 242404 (2014).
2. Z.Y. Wang, C. Tang, R. Sachs, Y. Barlas, and Jing Shi, Proximity-Induced Ferromagnetism in Graphene Revealed by the Anomalous Hall Effect, Phys. Rev. Lett. **114**, 016603 (2015).
3. Z.L. Jiang, C.-Z. Chang, C. Tang, P. Wei, J. S. Moodera, and Jing Shi, Independent Tuning of Electronic Properties and Induced Ferromagnetism in Topological Insulators with Heterostructure Approach, Nano Letters **15**, 5835 (2015).
4. B.W. Yang, M.-F. Tu, J.W. Kim, Y. Wu, H. Wang, J. Alicea, R.Q. Wu, M. Bockrath and Jing Shi, Tunable Spin–Orbit Coupling and Symmetry-Protected Edge States in Graphene/WS_2, 2D Materials **3**, 031012 (2016).

Energy Carrier Transport in Functionalized Two-Dimensional Layered Chalcogenides

Principal Investigator: Li Shi, University of Texas at Austin

Collaborator: Steve Cronin, University of Southern California

Program Scope

The goals of this collaborative project is to study two-dimensional (2D) layered chalcogenide materials functionalized with various interstitial species to tune and improve the electrical, optical, thermal and thermoelectric properties of this class of functional materials. Building on the progress made in our study of phonon and electron transport in pristine 2D layered heterostructures, we investigate both in-plane and cross-plane thermal and thermoelectric transport properties of functionalized 2D chalcogenide materials and develop tools and techniques for studying thermal and thermoelectric transport over smaller length and time scales and larger spectral ranges than was previously possible.

Recent Progress

During the past year, we have employed our new four-probe thermal transport measurement method to investigate the intrinsic in-plane thermal and thermoelectric transport properties of several 2D layered materials including surface-functionalized bismuth telluride, germanane, and black phosphorous. In addition, we have collaborated with the Cronin group to probe energy dissipation in graphene electronic devices and cross-plane thermoelectric transport in misfit-layered compounds. The major findings from the in-plane and scanning probe measurements are summarized below.

(i) Thermoelectric Transport in Surface- and Antimony-doped Bismuth Telluride Nanoplates

It was predicted that quantum confinement of electrons in 2D Bi_2Te_3 layers can result in enhanced thermoelectric power factor of bismuth telluride (Bi_2Te_3), which is a commonly used thermoelectric material. Recent experimental observations of surface electronic states protected by time-reversal symmetry in bismuth chalcogenides have also led to theoretical predictions of enhancement of the thermoelectric performance in ultrathin layers of these so-called topological insulators. The enhancement is predicted in ultrathin bismuth chalcogenides with a precise control of the Fermi level and carrier concentration. However, bismuth chalcogenides synthesized by different methods often suffer from chalcogen vacancies in the bulk crystal and surface doping from exposure to the air environment, both of which make these materials degenerate *n*-type semiconductors with reduced thermoelectric power factor.

In this work, we have tuned and measured the in-plane thermoelectric properties of thin $(Bi_{1-x}Sb_x)_2Te_3$ nanoplates with x ranging from 0.07 to 0.95. The carrier concentration in the nanoplates is varied by antimony substitution, while the surface potential is tuned by direct deposition of a hole-injecting molecule, F_4-TCNQ, onto all surfaces of individually measured suspended nanoplates. The individual $(Bi_{1-x}Sb_x)_2Te_3$ nanoplates ranging in thickness from 9 to 42 nm exhibit a maximum Seebeck coefficient and thermoelectric figure of merit (zT) for the x = 0.5 sample (Fig. 1). Antimony substitution is found to alter the majority carrier type from electrons for $x \leq 0.07$ to holes for $x \geq 0.25$. The addition of a highly electronegative organic molecule is found to dope the surface of the nanoplates to approach *p*-type even with a very thin coating of only a few nm, and increase the maximum zT further. Additionally, we find that the lattice thermal conductivity is reduced compared to a diffuse surface-phonon scattering model

indicating the potentially important role of alloy scattering and defect scattering in the samples. These results indicate that both chemical alloying and surface potential modification can play important roles in optimizing the thermoelectric properties in ultrathin $(Bi_{1-x}Sb_x)_2Te_3$ nanoplates.

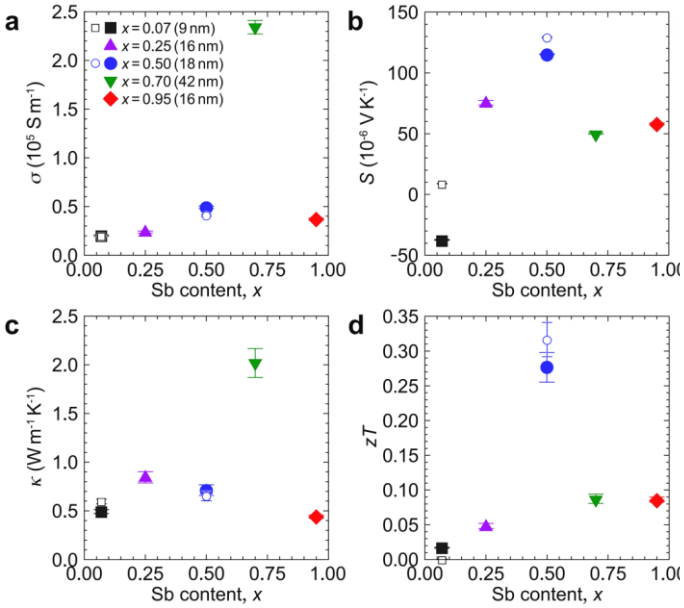

Fig. 1. Measured room temperature thermoelectric properties of $(Bi_{1-x}Sb_x)_2Te_3$ nanoplates. (a) Electrical conductivity, σ, (b) Seebeck coefficient, S, (c) thermal conductivity, κ, and (d) thermoelectric figure of merit, $zT = (S^2\sigma/\kappa)T$, as a function of antimony content, x, for as-grown samples (filled symbols) and after deposition and removal of excess F_4-TCNQ (open symbols). The nanoplate thicknesses are listed in parentheses of the legend shown in (a), which also applies to panels (a–d).

(ii) Basal-plane Thermal Conductivity of Nanocrystalline and Amorphized Thin Germanane

Germanane (GeH), a hydrogen-terminated layered germanium structure, has recently been synthesized for potential applications as an electronic and thermoelectric material. The thermal transport properties of 2D Si and Ge, including silicene, germanene, and germanane, are mostly unknown. Besides relevance to device applications, the lattice thermal conductivity can serve as an indicator of the crystallinity of these 2D materials that have been synthesized by different methods. In this work, we have employed our newly invented four-probe thermal transport measurement method to obtain the basal-plane thermal conductivity of thin exfoliated GeH flakes and correlated the measurement results with the crystal structure. The obtained thermal conductivity increases with increasing temperature, suggesting that extrinsic grain boundary and defect scattering dominate over intrinsic phonon-phonon scattering. Annealing a polycrystalline GeH sample at 195°C caused it to become amorphous, reducing the room-temperature thermal conductivity from 0.53 ± 0.09 W m^{-1} K^{-1}, which is close to the value calculated for 16 nm grain size, to 0.29±0.05 W m^{-1} K^{-1}, which approaches the calculated amorphous limit in the basal plane thermal conductivity. The results indicates that further control of defect concentrations and grain size can be utilized to further tune the thermal conductivity in this 2D material near and above the amorphous regime.

(iii) Temperature and Thickness Dependences of the Anisotropic In-Plane Thermal Conductivity of Black Phosphorus

Few-layer phosphorene has recently been exfoliated from black phosphorus (BP). The 2D layered phosphorene structure exhibits a thickness-dependent direct bandgap and relatively high electron mobility. The unique properties give rise to considerable interest in the use of this 2D material as the active layer in electronic and optoelectronic devices. Compared to other 2D materials, BP and phosphorene exhibit distinct orthogonal electrical and thermal transport anisotropies arising from their puckered structure. Past first-principles-based theoretical

calculations have yielded different values of the anisotropic thermal conductivities in monolayer phosphorene and bulk BP. Meanwhile, recent measurements have obtained different thermal conductivity results in thin BP flakes.

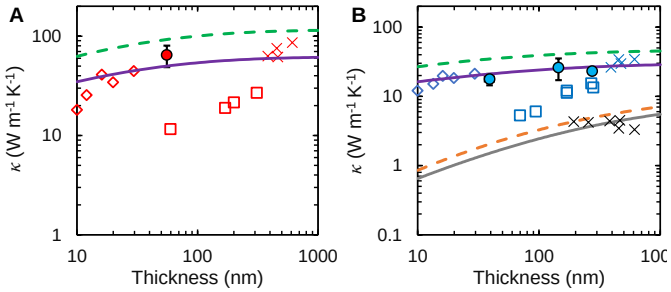

Fig. 2. Thickness dependence of the room-temperature thermal conductivities of the BP samples measured in this work (filled circles), and by Luo et al. with micro-Raman thermometry (unfilled diamond symbols), by Lee et al. with a two-probe method (unfilled square symbols), and by Jang et al. using TDTR (crosses) for the zigzag (A, red symbols) direction and the armchair (B, blue symbols) and through-plane direction (B, black crosses) directions. The dashed and solid lines are the calculation results for defect-free samples and samples with 0.1% point vacancies, respectively.

In this work, we have carried out a combined experimental and theoretical investigation of anisotropic thermal transport in thin BP flakes. The four-probe thermal transport measurements have yielded considerably higher thermal conductivity values than those from prior two-probe measurements of etched BP samples in the entire temperature range, and show much more pronounced low-temperature peaks and higher anisotropic ratio in the basal-plane thermal conductivity. Additionally, the four-probe experiment and first principles calculation have observed a weak thickness dependence of the basal-plane thermal conductivities of the thin BP flakes due to a phonon focusing effect in the anisotropic 2D layered material (Fig. 2). Even the higher thermal conductivity measured in this work is still lower than the first principles calculation results for defect-free BP samples of a similar thickness. The theoretical analysis elucidates the importance of point defect scattering of phonons in the BP samples measured in this and prior works, especially in thin BP samples exposed to air or extensive sample preparation steps, which are responsible for the relatively insensitive temperature dependence and pronounced thickness dependence observed previously. Moreover, the theoretical calculation has revealed a higher thermal conductivity in bulk BP than in monolayer phosphorene due to its lack of the reflection symmetry that causes the opposite behavior in graphene and graphite and some other flat 2D systems. These findings are not only relevant to evaluating thermal behaviors of devices made from thin BP and phosphorene but also important for establishing a comprehensive understanding of the complicated phonon transport and thermal properties of existing and emerging 2D materials.

(iv) Effects of Basal-plane Thermal Conductivity and Interface Thermal Conductance on the Hot Spot Temperature in Graphene Electronic Devices

Physical defects such as rips, tears, and wrinkles are often introduced during the fabrication of graphene electronic devices and can potentially result in local hot spots during operation. Such hot spots in turn can significantly degrade performance and reliability. It remains elusive whether the high basal plane thermal conductivity of graphene can lead to an added benefit of enhanced heat removal and reduced peak temperatures during operation despite its atomic scale thickness. Because of the high surface to volume ratio of graphene, it is unclear whether the hot spot temperature is more sensitive to the thermal interface conductance (G) between the 2D atomic layer and the substrate than to the in-plane thermal conductivity (κ).

In this work, electrostatic force microscopy (EFM) and scanning thermal microscopy (SThM) have been employed to investigate electric transport and localized heating around

defects introduced during transfer of graphene grown by chemical vapor deposition (CVD) to an oxidized Si substrate (Fig. 3). Numerical and analytical models are developed to explain the results based on reported κ and G of graphene and to investigate their effects on the peak temperature. In all cases considered, the hot spot temperature is sensitive to varying G and κ when the G/G_{ox} ratio and r_0/l ratio are below about 5, respectively, where G_{ox} is the cross-plane thermal conductance of the underlying dielectric, l is the heat spreading length, and r_0 is the localized heat generation spot size.

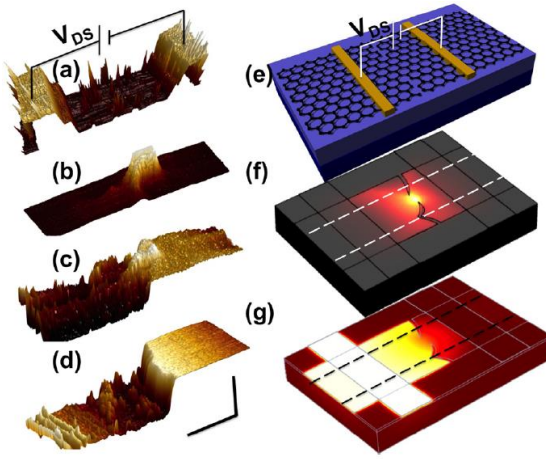

Fig. 3. Measured (a-d) and calculated (f-g) topographic (a), thermal (b, f), and electrical potential profiles (c, d, g) of the graphene channel, which is illustrated in a schematic (e). Horizontal scale bar is 5 μm and the vertical scale bar is 50 nm, 160 K, 4° and 10° phase shift for images a, b, c, and d, respectively.

Future Plans

We plan to pursue in-plane thermal and thermoelectric property measurements of 2D materials using micro-bridge devices under electric and magnetic fields, and collaborate with the Cronin group in cross-plane and inelastic light scattering measurements of transport properties of 2D materials.

Publications

Z. Li, S. R. Bauers, N. Poudel, D. Hamann, X. Wang, D. S. Choi, K. Esfarjani, L. Shi, D. C. Johnson, S. B. Cronin, "Cross-Plane Seebeck Coefficient Measurement of Misfit Layered Compounds (SnSe)n(TiSe2)n (n = 1,3,4,5)," Nano Letters 17, 1978–1986 (2017)

D. Choi, N. Poudel, S. Cronin, L. Shi, "Effects of Basal-plane Thermal Conductivity and Interface Thermal Conductance on the Hot Spot Temperature in Graphene Electronic Devices," Applied Physics Letters 110, 073104 (2017)

B. Smith, B. Vermeersch, J. Carrete, E. Ou, J. H. Kim, N. Mingo, D. Akinwande, L. Shi, "Temperature and Thickness Dependences of the Anisotropic In-Plane Thermal Conductivity of Black Phosphorus," Advanced Materials 29, 1603756 (2017)

M. T. Pettes, J. Kim, W. Wu, K. C. Bustillo, and L. Shi, "Thermoelectric Transport in Surface- and Antimony-doped Bismuth Telluride Nanoplates," APL Materials 4, 104810 (2016)

G. Coloyan, N. D. Cultrara, A. Katre, J. Carrete, M. Heine, E. Ou, J. H. Kim, S. Jiang, L. Lindsay, N. Mingo, D. Broido, J. Heremans, J. Goldberger, L. Shi, "Basal-plane Thermal Conductivity of Nanocrystalline and Amorphized Thin Germanane," Applied Physics Letters 109, 131907 (2016)

J. Kim, D. A. Evans, D. P. Sellan, O. M. Williams, E. Ou, A. H. Cowley, and L. Shi, "Thermal and Thermoelectric Transport Measurements of an Individual Boron Arsenide Microstructure," Applied Physics Letters 108, 201905 (2016)

I. Kholmanov, J. H. Kim, E. Ou, R. S. Ruoff, and L. Shi, "Continuous Carbon Nanotube–Ultrathin Graphite Hybrid Foams for Increased Thermal Conductivity and Suppressed Subcooling in Composite Phase Change Materials," ACS Nano 9, 11699-11707 (2015)

Ames Laboratory Photonic Systems FWP

Lead PI: Joseph Shinar. PIs: Kai-Ming Ho, Rana Biswas, Costas Soukoulis, Thomas Koschny, Vagharsh Mkhitaryan, and Jigang Wang,

Project Title: Intrinsic Photodegradation Processes in Polymer:Fullerene Blends and Bulk Heterojunction Solar Cells

Rana Biswas and Joseph Shinar

Ames Laboratory and Physics & Astronomy Department, Iowa State University

Ruth Shinar

Microelectronics Research Center and Electrical & Computer Engineering Department, Iowa State University

Program Scope

Advances in photonic sciences critically impact the mission of DOE in efficient energy conversion and utilization. Hence the Ames Laboratory established the study of such systems as one of its central missions. In line with the BES mission, this FWP was created to address that outstanding DOE mission through fundamental studies of photonic materials, primarily luminescent & photovoltaic organic semiconductors (OSs) and methyl ammonia lead halide and other Perovskites (MAPs) (e.g., carrier dynamics, exciton quenching processes) and photonic crystals (PCs: beaming, control, & low-threshold lasing), and, in particular, materials and structures that combine them (e.g., science underlying outcoupling of light from organic LEDs (OLEDs)). Recently theoretical & experimental verification efforts in quantum dynamics & control of spins in OSs & structures were added to the FWP. Most recently a collaboration with the Ames Laboratory's Critical Materials Institute (CMI) on light-emitting electrochemical cells was established.

The science drivers of our effort, which is to explore the basic science underlying challenges in OLED and organic photovoltaic (OPV) efficiency & stability (BES Mission) are exciton and carrier dynamics (e.g., polarons & bipolarons), carrier spin dynamics (relevant for organic spintronics), exciton quenching processes, the various fundamental degradation processes, and the basic science underlying PCs and PC-inspired novel optical structures (e.g., their coupling to OLEDs & OPVs, and structures yielding beaming & low threshold lasing).

Recent Progress

Intrinsic photodegradation of organic solar cells, theoretically attributed to C-H bond rearrangement/breaking [1-5], remains a key commercialization barrier. Our recent work presented, via dark electron paramagnetic resonance (EPR), the first experimental evidence for metastable C dangling bonds (DBs) formed by blue/UV irradiation of poly[4,8-bis(5-(2-ethylhexyl) thiophen-2-yl)benzo[1,2-b;4,5-b']dithiophene-2,6-diyl-alt-(4-(2-ethylhexyl)-3-fluorothieno[3,4-b]thiophene-)-2-carboxylate-2-6-diyl)] (PBDTTT-EFT):$PC_{70}BM$ blend films in nitrogen (Fig. 1) [6]. This system was chosen since the PBDTT-EFT:$PC_{70}BM$ bulk heterojunction solar cells exhibit a high (>9%) power conversion efficiency but degrade rapidly even in an inert N_2 atmosphere. We therefore explored the EPR of pristine and photodegraded PBDTT-EFT: $PC_{70}BM$ blend films. The DB density increased with irradiation and decreased ~4 fold after 2 weeks in the dark. The dark EPR also showed increased densities of other spin-active sites in photodegraded polymer, fullerene, and polymer:fullerene blend films, consistent with broad electronic measurements of fundamental properties, including defect/gap state densities. The EPR and electronic measurements enabled identification of defect states, whether in the polymer, fullerene, or at the donor/acceptor (D/A) interface. Importantly, the EPR results indicate that the DBs are at the D/A interface, as they were present only in the blend films. The role of polarons in interface DB formation was also explored, specifically the possible role of polarons that become highly energetic hot polarons following absorption of a blue or UV photon.

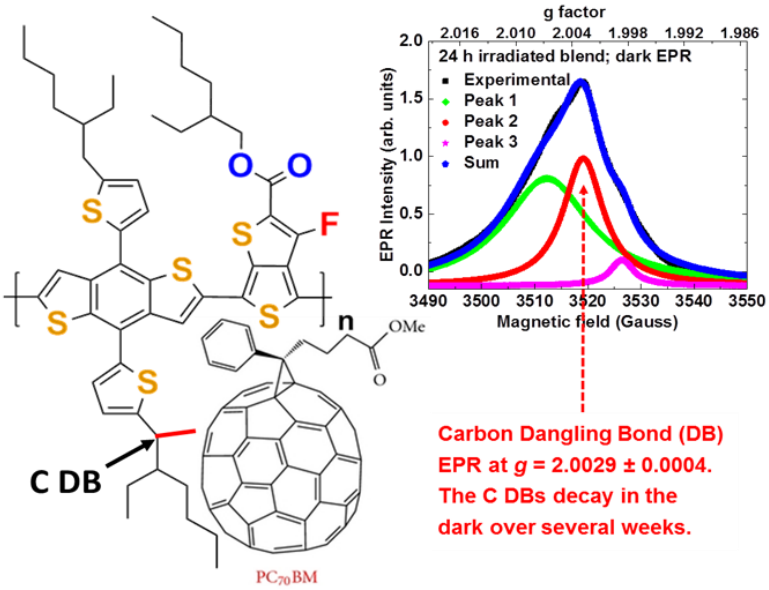

Fig. 1. X-band EPR of PBDTTT-EFT:C_{70} blend films photodegraded in N_2 for 24 h.

In a closely related modeling effort [5], we explored atomic pathways underlying light-induced changes in polymer: fullerene BHJ solar cells. We identified atomic pathways, involving local O and H motion, which underlie intrinsic light-induced changes of organic materials, utilizing ab initio simulations. Light exposure generates prolonged intrinsic degradation of organic solar cells, when moisture and oxygen are absent. We considered polythieno[3,4-b]-thiophene-co-benzodithiophene (PTB7):$PC_{71}BM$, common for higher efficiency cells, as well as the archetypal poly(3-hexylthiophene) (P3HT):$PC_{71}BM$. Local motion of O from the C−O−C bridge to a C=O bond in the aromatic backbone, creates a C-dangling bond defect, with an energy of 2.1 eV. The energy barrier of ≤2.65 eV can be surmounted with

blue photons. Local H motion from βC to αC within the alkyl, also generates a C-dangling bond, a similar rebonding of bridging-O, and cleaving of PTB7. Bridging O creates instability. Defect energies are lowered by ~0.5 eV by excited electronic states. Defects can anneal reversibly or irreversibly to distorted configurations. We identified why certain organic materials are more stable, and pathways to design more stable materials.

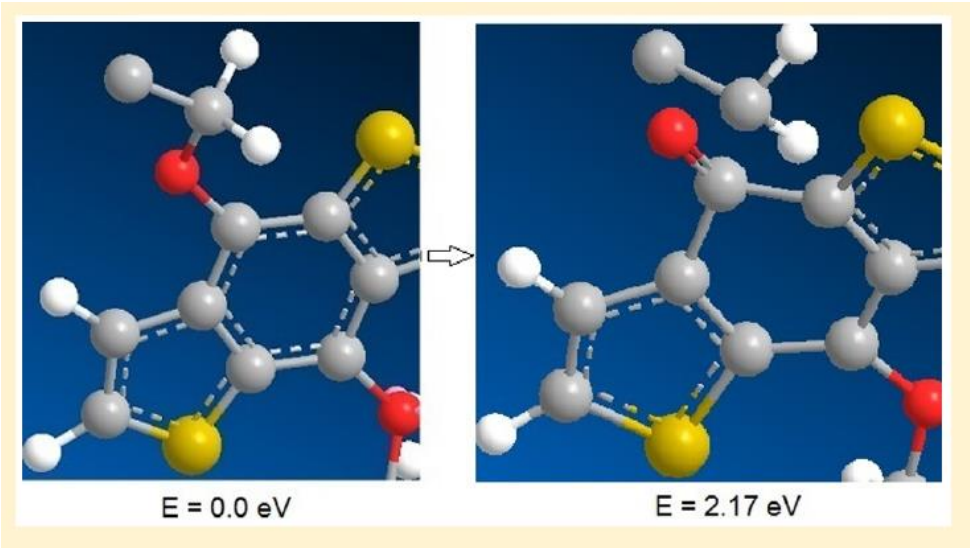

Fig. 2. Results of *ab initio* simulations showing the photoinduced rearrangement of an H atom in PTB7: $PC_{71}BM$ blend films that breaks the conjugation on a phenylene ring and generates a dangling bond on the adjacent αC.

Future Plans

Understanding of the degradation processes in organic electronic materials remains a significant challenge. Our initial results indicate that H-induced π conjugation breaks and C dangling bonds may be playing a pivotal role, similar to Si dangling bonds in hydrogenated amorphous Si and related materials. We will therefore continue to explore the mechanisms for H atom rearrangement that results in π conjugation breaks and C dangling bonds. We will utilize infrared spectroscopy to identify bonding changes occurring during illumination of organic materials, and correlate these with ab-initio simulations and measurements of spin-active defects. We will also explore the role of hot polarons in this bond rearrangement, which was alluded to but not established in our recent work [6]. We will also attempt to identify alternative structures where this bond rearrangement process is minimized or even eliminated altogether. In parallel, we will also try to identify the other defects that exhibited an EPR signature but whose nature is all but unknown.

Other projects that we continue to pursue include spin relaxation in OSs, which has a critical role in organic spintronics as well as in OLED and OPV performance. Indeed, we have discovered intriguing quantum dynamics resulting from back action of nuclear spins [7].

In another area mentioned above we have discovered that strongly anisotropic lossy dielectric composites can form effective media where moderate dissipative loss in the constituents can actually improve propagation length and coupling [8]. This demonstrated a realistic implementation and enables energy collimations and simultaneous impedance match at the all-important 1.5μm communications ban, and we explore this low-loss approach to lasing at this band. We will also investigate the photoluminescence of quantum dots in photonic metasurfaces, that can tailor the densities of photonic states to be very high.

Finally, we have recently completed an ultrafast ultrabroadband study that yielded the Rydberg states of excitons in MAPs and established their low exciton binding energy [9]. We will continue to explore the dynamics of excitons and polarons, including spin dynamics, in these highly promising novel materials to establish the physics underlying their behavior.

References

1. R. A. Street, K. W. Song, J. E. Northrup, and S. Cowan, "Photoconductivity measurements of the electronic structure of organic solar cells," Phys Rev. B 83, 165207 (2011)

2. R. A. Street, A. Krakaris, and S. R. Cowan, "Recombination Through Different Types of Localized States in Organic Solar Cells," Adv. Func. Mater. (2012).

3. R. A. Street and D. M. Davies, "Kinetics of light induced defect creation in organic solar cells," Appl. Phys. Lett. **102**, 043305 (2013).

4. J. E. Northrup, "Radiation induced hydrogen rearrangement in poly(3-alkylthiophene)," Appl. Phys. Express **6**, 121601 (2013).

5. Satvik Shah and Rana Biswas, "Atomic Pathways Underlying Light-Induced Changes in Organic Solar Cell Materials," J. Phys. Chem. C **119**, 20265−20271 (2015).

6. F. Fungura, W. R. Lindemann, J. Shinar, and R. Shinar, "Carbon dangling bonds in photodegraded polymer:fullerene solar cells," Adv. Energy Mater **7**, 1601420 (2017).

7. V. V. Mkhitaryan and V. V. Dobrovitski, "Quantum dynamics of nuclear spins and spin relaxation in organic semiconductors," arXiv:1607.01640 (submitted to PRB)

8. Nian-Hai Shen, Peng Zhang, Thomas Koschny, and Costas M. Soukoulis, "Metamaterial-based lossy anisotropic epsilon-near-zero medium for energy collimation," Phys. Rev. B **93**, 245118 (2016).

9. L. Luo, L. Men, Z. Liu, Y. Mudryk, X. Zhao, Y. Yao, J. Vela, K. M. Ho, I. E. Perakis, R. Shinar, J. Shinar, and J. Wang, "Ultrafast Terahertz Snapshots of Excitonic Rydberg States and

Electronic Coherence in an Organometal Halide Perovskite," Nature Communications (accepted).

Publications

1. L. Luo, L. Men, Z. Liu, Y. Mudryk, X. Zhao, Y. Yao, J. Vela, K. M. Ho, I. E. Perakis, R. Shinar, J. Shinar, and J. Wang, "Ultrafast Terahertz Snapshots of Excitonic Rydberg States and Electronic Coherence in an Organometal Halide Perovskite," Nature Communications (accepted).

2. Fadzai Fungura, William R. Lindemann, Joseph Shinar, and Ruth Shinar, "Carbon Dangling Bonds in Photodegraded Polymer:fullerene Solar Cells," Adv. Energy Mater. 7, 1601420 (2017). DOI: 10.1002/aenm.201601420

3. J. Bhattacharya, P. Joshi, R. Biswas, V. Dalal, Pathway for recovery of photo-degraded polymer solar cells by post degradation thermal anneal, Solar Energy and Materials **164**, 70-79 (2017).

4. P. Pathi, A. Peer and R. Biswas, Nano-photonic structures for light trapping in ultra-thin crystalline silicon solar cells, Nanomaterials **7**, 17 (2017). Special issue on "Nanostructured solar cells" ; AL/ DOE-NERSC News release

5. A. Peer and R. Biswas, Extraordinary Optical Transmission in Nanopatterned Ultrathin Metal Film without Holes, Nanoscale **8**, 4657 - 4666 (2016)

6. Nian-Hai Shen, Peng Zhang, Thomas Koschny, and Costas M. Soukoulis, "Metamaterial-based lossy anisotropic epsilon-near-zero medium for energy collimation," Phys. Rev. B **93**, 245118 (2016).

7. Ying Chen, Min Cai, Emily Hellerich, Ruth Shinar, and Joseph Shinar, "Origin of the Positive Spin 1/2 Photoluminescence-Detected Magnetic Resonance in π-Conjugated Materials and Devices," Phys. Rev. B **92**, 115203 (2015).

8. Emily S. Hellerich, Robert Heise, Eeshita Manna, Rana Biswas, Ruth Shinar, and Joseph Shinar, Deep blue/ultraviolet microcavity OLEDs based on solution-processed PVK:CBP. Organic Electronics **24**, 246-253 (2015).

9. Eeshita Manna, Fadzai Fungura, Rana Biswas, Joseph Shinar, and Ruth Shinar, "Tunable Near UV Microcavity OLED Arrays: Characterization and Analytical Applications," Adv. Func. Mater. **25**, 1226–1232 (2015).

10. Satvik Shah and Rana Biswas, "Atomic Pathways Underlying Light-Induced Changes in Organic Solar Cell Materials," J. Phys. Chem. C **119**, 20265−20271 (2015).

11. R. S. Gebhardt, P. Du, A. Peer, M. Rock, M. R. Kessler, R. Biswas, B. Ganapathy-subramanian, and S. Chaudhary ; Utilizing Wide Band Gap, High Dielectric Constant Nanoparticles as Additives in Organic Solar Cells, J. Phys. Chem. C, Vol. **119**, Issue 42, pp 23883–23889 (2015).

Electron Spin Polarization in Large Electric Fields

Vanessa Sih, Department of Physics, University of Michigan, Ann Arbor

Program Scope

This research program will investigate the response of electron spin polarization in semiconductors to large accelerating electric fields. The goals of this research are to understand the mechanism for the electrical generation of spin polarization in non-magnetic materials and the role of spin-orbit effects and spin scattering in a strongly driven regime and to determine whether a high-electric field regime that preserves or even amplifies spin polarization can be experimentally realized. The expectation is that this research will improve our understanding of the fundamental processes that cause the electrical generation of spin polarization and contribute to spin dephasing. This knowledge will aid the development of robust spin-based devices for information processing, storage and communication.

Recent Progress

We have investigated how electric fields affect electron spin dynamics and how changing sample parameters, such as spin-orbit field, mobility, and carrier density, affect electrical spin generation efficiency. Electrically-contacted gallium arsenide and indium gallium arsenide samples were fabricated and characterized.

Time- and spatially-resolved optical pump-probe measurements were used to excite spin polarization and monitor its drift and decay. Data for three applied electric fields are shown in the figure, along with fits to determine the spin precession frequency and decay time. We observe that the spin lifetime decreases with increasing electric field in this sample, consistent with previous work performed using steady-state spin drift measurements [1,2].

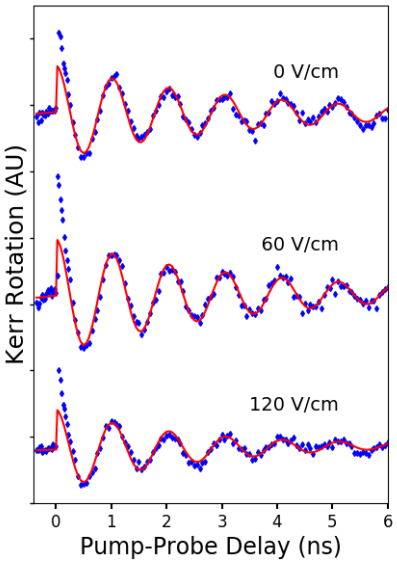

Time-resolved Kerr rotation measured on an n-GaAs epilayer with B = 160 mT and T = 30 K. The red lines are fits to a decaying cosine. There is an additional fast decay related to photocarrier recombination that is not included in these fits.

An accelerating in-plane electric field has also been shown to generate spin polarization [3], but the mechanism and how this effect depends on material properties have been unclear. In earlier work, we found that, when comparing the strength of the spin-orbit field with the electrical spin generation efficiency for electric fields applied along different in-plane crystal directions, the direction with the largest electrical spin generation efficiency was the direction with the smallest

spin-orbit splitting [4]. This finding was not explained by existing models, which either predicted that the electrical spin generation should be proportional to the spin-orbit splitting or only considered an isotropic spin-orbit field [5]. Therefore, we have measured a set of samples to study how the electrical spin generation efficiency depends on strain, indium concentration, carrier density, mobility and spin lifetime and to determine whether intrinsic or extrinsic effects dominate.

Future Plans

The current measurements have been conducted with modest electric fields to check for the effects of spin drift and heating. The next step is to conduct measurements at larger electric fields and with varying voltage pulse duration and duty cycle.

References

[1] M. Furis, D. L. Smith, S. A. Crooker, and J. L. Reno, Appl. Phys. Lett **89**, 102102 (2006).

[2] M. Beck, C. Metzner, S. Malzer, and G. H. Dohler, Europhys. Lett. **75**, 597 (2006).

[3] Y. K. Kato, R. C. Myers, A. C. Gossard, and D. D. Awschalom, Phys. Rev. Lett. **93**, 176601 (2004).

[4] B. M. Norman, C. J. Trowbridge, J. Stephens, A. C. Gossard, D. D. Awschalom, and V. Sih, Phys. Rev. B **82**, 081304(R) (2010).

[5] A. G. Aranov, Y. B. Lyanda-Geller, and G. E. Pikus, Sov. Phys. JETP **73**, 537 (1991).

Nanostructured colloidal self-assembly and controlled alignment of anisotropic nanoparticles

Ivan I. Smalyukh, University of Colorado at Boulder

Program Scope

Self-assembly of nano-sized functional units is an exceptionally promising way of designing inexpensive artificial composite materials with new macroscopic physical behavior and properties. The main objective of this project is to explore self-organization of anisotropic nanoparticles into colloidal composites with tunable ordered structures. The research focuses on understanding and control of self-assembly of metal and semiconductor nanoparticles, as well as on material behavior arising from their ordered self-organization and alignment. Fundamental studies of shape-dependent colloidal interactions and ordering of quantum dots and plasmonic metal nanoparticles will reveal underpinning physical mechanisms that guide mesoscale morphology and ultimately determine material properties of the self-assembled composites. These properties are characterized and correlated with hierarchical structures and composition. Analytical and numerical modeling of colloidal interactions and material properties provides important insights. This research may lead to new, cheaper, and more efficient renewable energy technologies, a new breed of energy-efficient information displays and consumer devices, as well as a fertile ground for new basic science.

Recent Progress

Within two years since the previous DOE BES workshop, we have developed triclinic colloidal crystals with facile switching of photon up-converting properties [1,2], introduced a method of patterning mesostructured materials through laser reduction of graphene oxide colloidal dispersions [3], developed nematic dispersions gold nanoparticles covered with silica shells and dye molecules that enable switching of luminescence lifetimes through plasmon-exciton interactions [4,5], developed ferromagnetic molecular-colloidal biaxial liquid crystals [6], as well as explored the role of geometry and chirality in driving self-assembly at the mesoscale [7-9]. The net total of published peer-reviewed articles emerging from this project is 20 [1-20]. Considering the page limitations, below I will focus on conveying the advances related to colloidal composites formed by photon up-converting nanoparticles [1,2].

Since the works of Einstein and Perrin showed how particles in colloidal dispersions obey the same statistical thermodynamics as atoms, the colloidal atom paradigm has provided insights into physics of atomic and molecular systems through probing dynamics of colloidal crystals and glasses. This colloidal atom paradigm has inspired the development of colloidal self-assembly to reproduce or exceed the diversity of atomic systems. However, experimental realization of colloidal architectures with low crystallographic symmetry remained challenging. We recently demonstrated [1] that low-symmetry triclinic colloidal crystals can self-assemble in liquid crystal (LC) dispersions as a result of competition between the highly anisotropic elastic

interactions and (more conventional) electrostatic repulsive forces. Realization of this triclinic colloidal crystal (Fig. 1) suggests that the large crystallographic diversity previously established for atomic and molecular crystals can now be accessible in LC colloids. The triclinic colloidal crystal serves as an illustration of how competition of long-range electrostatic and anisotropic quadrupolar elastic interactions in nematic colloids can lead to self-assembly of colloidal particles with long-range orientational and positional ordering (Fig. 1) [1]. The long-range electrostatic repulsions arise from weakly screened Coulomb-type forces in a low-ionic-strength nonpolar LC with a large (500 nm and larger) Debye screening length. Since the elasticity-mediated interactions are also long-ranged, colloidal crystal assemblies with micrometer-range lattices emerging from the competition of these electrostatic and elastic forces can be an order of magnitude larger than the size of constituent colloidal particles (Fig. 1*a*-*d*).

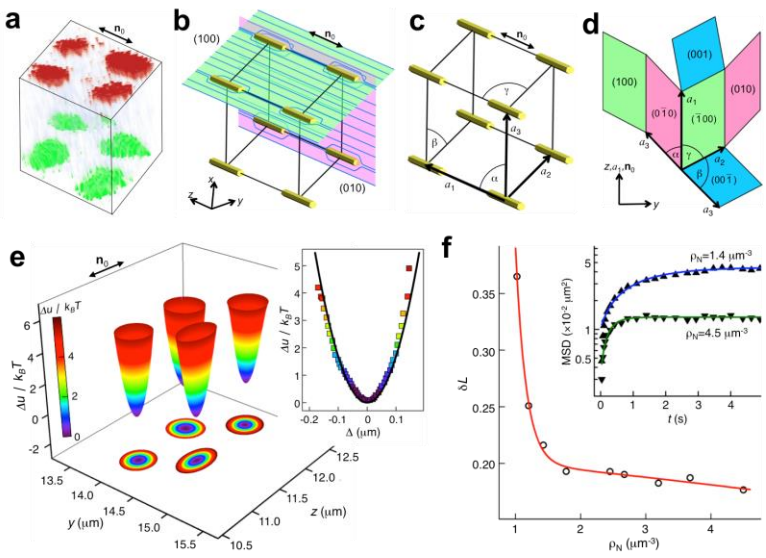

Fig. 1. Triclinic colloidal crystals. (*a*) 3D micrograph showing a primitive unit cell of a triclinic colloidal crystal, which was reconstructed on the basis of confocal imaging. It shows spatial arrangements of colloidal particles as they explore potential energy landscape near their minimum-energy triclinic lattice sites. (*b*-*d*) Schematics (not to scale) of a primitive cell of a triclinic colloidal crystal, (*b*) showing director field **n**(**r**)-distortions (blue lines) induced by nanorods, (*c*) defining parameters of a triclinic lattice, and (*d*) showing it unfolded. Crystallographic planes, axes, and angles are marked on the schematics. (*e*) The potential energy Δu landscape corresponding to four lattice sites in the (100) crystallographic plane of a triclinic crystal. The inset shows a local distance Δ dependence of the relative Δu experienced by colloidal particles. (f) Lindemann parameter δL versus ρ_N of nanorods, characterizing the crystallization-melting transition. Inset shows the MSD of particles versus time at ρ_N=1.4 μm^{-3} (▲) and 4.5 μm^{-3} (▼). For more details, see Ref. [1].

The crystallographic axes of the triclinic lattices and colloidal nanorods within them tend to follow the director **n**(**r**), which can be controlled on large scales via approaches used to manufacture LC displays. Triclinic crystallization of particles at packing factors <<1% shows a potential for fabricating mesostructured composites through self-assembly on device scales, tuned by weak external stimuli, such as low voltages [1,2]. From a fundamental science standpoint, it is interesting that the thermal fluctuations of particles within the lattice and the melting and crystallization transitions (Fig. 1*e*,*f*) are consistent with what is expected for their atomic counterparts [1]. Mean square displacement (MSD) exhibited by colloidal particles within these dispersions saturates with time when in crystal but continues growing when in a colloidal fluid state (inset of Fig. 1*f*). Characterization of MSD $\langle \Delta r^2(t) \rangle$ relative to the crystal lattice, quantified by the dependence of the Lindemann parameter $\delta L=[3\langle \Delta r^2(t\to\infty)\rangle/(4R^2)]^{1/2}$ on the

nanorod number density ρ_N, provides a means of demonstrating how low-symmetry positional ordering (Fig. 1*f*) emerges from the interplay of weakly screened electrostatic and elasticity-mediated interactions in a nematic host. The triclinic pinacoidal lattices of orientationally ordered nanorods are the lowest symmetry 3D colloidal crystals achieved so far (Fig. 1*a-e*) and may prompt realization of colloidal architectures with other symmetries, from cubic to triclinic pedial. Though demonstrated only for elastic quadrupoles and electrostatic monopoles so far, the use of competition of elastic, electrostatic and other (e.g. magnetic) interactions to guide symmetry and density of colloidal crystals can be extended to other nematic colloidal multipoles. Considering the intrinsic anisotropy and diversity of elastic multipoles, one can expect a large variety of low-symmetry colloidal architectures emerging from such interactions. The combination of the facile response of LC & the unique up-converting properties of nanoparticles enables ~1V electric switching of the up-conversion by the ensuing composite materials [2].

Future Plans

The PI and his research group are conducting in-depth studies of how this mesoscale self-organization, which can yield centimeter-large mono-crystals of colloidal nanoparticles with tunable center-to-center separations, leads to new physical behavior and material properties arising from a combination of unique properties of nanoparticles as well as structural organization at nanometer to macroscopic scales. The PI is also planning to develop LC co-dispersions of quantum and plasmonic nanoparticles. In these systems, he will probe how plasmon-exciton interactions can lead to new physical behavior when the nanoparticle-scale interactions are combined with different forms of long-range orientational and positional ordering that can be tuned by weak external stimuli applied to soft matter host media. More broadly, by exploiting unique properties of solid nanostructures in the forms of their colloidal dispersions and by combining them with the facile response of soft matter to external stimuli, the PI intends to develop a new breed of composites with novel physical behavior, pre-engineered properties, and facile response to external fields. Recent preliminary studies in the PI's group (unpublished) show that perovskite nanoparticles dispersed in thermotropic LCs can self-assemble into colloidal crystals with different symmetries and voltage- and light-tunable lattices.

References (articles acknowledging the DOE award):

1. H. Mundoor, B. Senyuk, and I. I. Smalyukh. "Triclinic colloidal crystals from competing elastic and electrostatic interactions." ***Science*** 352, 69-73 (2016).
2. H. Mundoor and I. I. Smalyukh. "Electrically tunable nematic colloidal dispersions of upconversion nanorods." ***Small*** 11, 5572–5580 (2015).
3. B. Senyuk, N. Behabtu, A. Martinez, T. Lee, D. E. Tsentalovich, G. Ceriotti, J. M. Tour, M. Pasquali and I. I. Smalyukh. "Three-dimensional patterning of solid microstructures through laser reduction of colloidal graphene oxide in liquid-crystalline dispersions" *Nature Communications* 6, 7157 (2015).

4. L. Jiang, H. Mundoor, Q. Liu, and I. I. Smalyukh. “Surface Plasmon Mediated Electric Switching of Fluorescence Decay in Gold-Silica-Dye Nematic Nanocolloids.” ***ACS Nano*** 10, 7064-7072 (2016).
5. Y. Zhang, Q. Liu, H. Mundoor, Y. Yuan, and I. I. Smalyukh. “Metal nanoparticle dispersion, alignment and assembly in nematic liquid crystals for applications in switchable plasmonic color filters and E-polarizers.” *ACS Nano* 9, 3097-3108 (2015).
6. Q. Liu, P.J. Ackerman, T. C. Lubensky and I. I. Smalyukh. “Biaxial ferromagnetic liquid crystal colloids.” *Proc. Natl. Acad. Sci. U.S.A.* 113, 10479–10484 (2016).
7. B. Senyuk, Q. Liu, E. Bililign, P. D. Nystrom, and I. I. Smalyukh. “Geometry-guided colloidal interactions and self-tiling of elastic dipoles formed by truncated pyramid particles in liquid crystals.” ***Phys. Rev. E*** 91, 040501 (2015).
8. M.B. Pandey, P.J. Ackerman, A. Burkart, T. Porenta, S. Žumer, and Ivan I. Smalyukh. “Topology and Self-Assembly of Defect-Colloidal Superstructure in Confined Chiral Nematic Liquid Crystals.” *Phys Rev E* 91, 012501 (2015).
9. A. Martinez and I.I. Smalyukh. “Light-driven dynamic Archimedes spirals and periodic oscillatory patterns of topological defects in anisotropic soft matter.” *Optics Express* 23, 4591-4604 (2015).
10. Q. Liu, Y. Yuan, and I. I. Smalyukh. “Electrically and Optically Tunable Plasmonic Guest-Host Liquid Crystals.” ***Nano Lett.*** 14, 4071–4077 (2014).
11. Q. Liu, J. Tang, Y. Zhang, A. Martinez, S. Wang, S. He, T. J. White, and I. I. Smalyukh. “Shape-dependent dispersion and alignment of non-aggregating plasmonic gold nanoparticles in lyotropic and thermotropic liquid crystals.” ***Phys Rev E*** 89, 052505 (2014).
12. B. Senyuk, D. Glugla, and I. I. Smalyukh. “Rotational and translational diffusion of anisotropic gold nanoparticles in liquid crystals controlled by varying surface anchoring.” ***Phys. Rev. E*** 88, 062507 (2013).
13. Q. Liu, M. Campbell, J.Evans, I.I. Smalyukh. “Orientationally Ordered Co-Dispersion of Gold Nanorods & Cellulose Nanocrystals.” ***Adv. Mater.*** 26, 7178–7184 (2014).
14. M. Campbell, Q. Liu, A. Sanders, J. S. Evans, I.I. Smalyukh. “Preparation of Nanocomposite Plasmonic Films Made from Cellulose Nanocrystals or Mesoporous Silica Decorated with Unidirectionally Aligned Gold Nanorods.” ***Materials*** 7, 3021-3033 (2014).
15. A. Martinez and I.I. Smalyukh. “Light-driven dynamic Archimedes spirals and oscillatory patterns of topological defects in anisotropic soft matter.” ***Opt. Exp.*** 23, 4591-4604 (2015).
16. M.B. Pandey, P.J. Ackerman, A. Burkart, T. Porenta, S. Žumer, and Ivan I. Smalyukh. “Topology and Self-Assembly of Defect-Colloidal Superstructure in Confined Chiral Nematic Liquid Crystals.” ***Phys Rev E*** 91, 012501 (2015).
17. M. Tasinkevych, M. Campbell, and I.I. Smalyukh. “Splitting, linking, knotting, and solitonic escape of topological defects in homeotropic nematic drops with handles”, ***Procs. Natl. Acad. Sci. USA*** 111, 16268-16273 (2014).
18. B. Senyuk, M. Varney, J. Lopez, S. Wang, N. Wu, and I. I. Smalyukh. “Gourd-shaped colloidal particles in cholesteric liquid crystal.” ***Soft Matter*** 10, 6014-6023 (2014).
19. M.C.M. Varney, Q. Zhang, M. Tasinkevych, N. Silvestre, K. A. Bertness, and I. I. Smalyukh. “Periodic dynamics, localization, and interaction of particles with confining surfaces & helicoidal structure of cholesteric liquid crystals.” ***Phys. Rev. E*** 89, 052505 (2014).
20. S. Copar, T. Porenta, P. J. Ackerman, M. B. Pandey, M. C. M. Varney, I. I. Smalyukh, and S. Žumer. “Topological Switching and Orbiting Dynamics of Colloidal Spheres Dressed with Chiral Nematic Solitons.” ***Scientific Reports*** 4, 7337 (2014).

Magnetostructural Phase Transitions and Multicaloric Materials

Shane Stadler, Louisiana State University, Department of Physics and Astronomy

Naushad Ali, Southern Illinois University, Department of Physics

Program Scope

The objective of this project is to discover and explore new solid-state caloric materials, and to understand the origins of their physical behaviors including magnetocaloric effects, barocaloric effects, and transport properties. Materials that exhibit extreme changes in magnetostructural and transport properties linked to first-order magnetostructural phase transitions near room temperature are relatively rare. In this project we study multifunctional and multicaloric materials with the goal of improving our understanding of the magnetostructural phase transitions that are responsible for their novel physical behaviors.

Recent Progress

I. Multicaloric Systems: One focus of our current research is on MnTX–based (T = Co, Ni, and X = Ge, Si) intermetallic compounds due to the temperature-induced magnetostructural transitions (MSTs) that are responsible for their shape-memory phenomena, giant magnetocaloric effects (MCEs), and volume anomalies near room temperature.[1-3] We had found previously two isostructurally substituted MnTX compounds that exhibit large magnetocaloric effects at a magnetostructural transition near room temperature, namely, $(MnNiSi)_{1-x}(MnFeGe)_x$ and $(MnNiSi)_{1-x}(FeCoGe)_x$.[4,5] These materials both exhibit magnetostructural transitions in temperature ranges that could be tuned through room temperature through slight variation of composition or through the application of hydrostatic pressure. The maximum magnetic entropy changes in both materials ranged from 60 J/kgK to greater than 100 J/kgK (for ΔH = 5T), depending on the specific composition. Another important observation, however, was the pronounced temperature shifts of the magnetostructural transitions in these materials with hydrostatic pressure (up to -10 K/kbar).

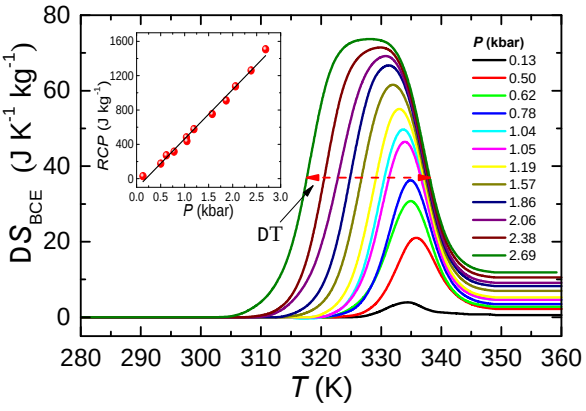

Fig. 1. The entropy change (ΔS) as a function of temperature and pressure of the compound with x = 0.38. ΔT ~ 25 K is the full width at half max (dashed arrow) of the ΔS curve with P = 2.69 kbar. The inset shows the RCP as a function of pressure (P).

These results were the motivation for barocaloric measurements, and calorimetery measurements were subsequently carried out in which heat flow

was measured as a function of temperature at different constant hydrostatic pressures, and others where the temperature change was measured upon on decompression. These measurements revealed a giant **inverse barocaloric effect** (BCE), the entropy changes (ΔS_{BCE}) of which are shown in Fig. 1 for different applied hydrostatic pressures. There are a couple of features to note in Fig. 1. First, the maximum value of ΔS_{BCE} at P = 2.69 kbar is 73.7 J kg^{-1} K^{-1}, and is comparable with the entropy change found in recently reported ferrielectric ammonium sulfate (AS) with (60 J kg^{-1} K^{-1} for 1.0 kbar).[5] Next, the full width half maximum of the curve for P=2.69 kbar is about ΔT_{FWHM}=25 K. From this we can calculate the relative cooling power (RCP = $\Delta T_{FWHM} \times \Delta S_{max}$) reaches nearly 1500 J/kg (see the inset of Fig. 1).[6]

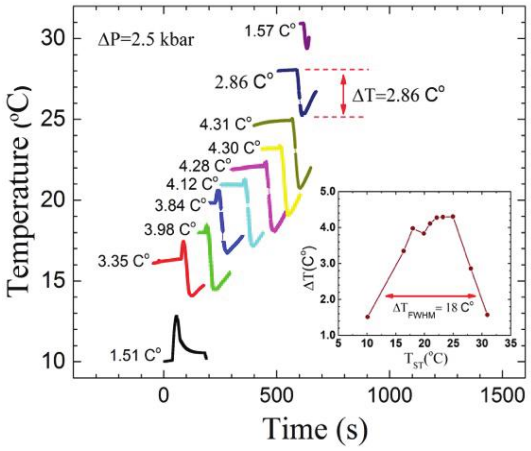

Fig. 2. The preliminary data on $(MnNiSi)_{1-x}(FeCoGe)_x$ (x=0.39). Each curve represents a different starting temperature. The inset shows the maximum temperature change (ΔT) versus the starting temperature T_{ST}.

The direct temperature change upon decompression was measured using the same calorimeter, and resulted in a temperature change of +3.2 K when decompressing from 2.5 kbar to atmosphere. The positive temperature change upon decompression is a verification of the inverse nature of the barocalroic effect in this system. However, in order to observe a negative temperature change upon compression, we had to construct a hydrostratic pressure device capable of measuring the temperature directly upon compression.

The temperature as a function of time is plotted in Figure 2 for $(MnNiSi)_{1-x}(FeCoGe)_x$ (x = 0.39) for different starting temperatures. For each curve, the temperature first increases as a consequence of the increasing pressure on the pressure conducting medium (an ethanol/methanol mixure) and on the compound before the magnetostructural transition is triggered. Upon further increase of pressure, the transition temperature is lowered through the operating temperature and the magnetostructural transition occurs. The inverse barocaloric effect connected with this transition then causes a sharp decrease in temperature, ΔT. The time duration of this decrease in each case is about 5 s, the time required to apply the 2.5 kbar hydrostatic pressure (same for all curves). The maximum ΔT = -4.31 ^{o}C (K) occurred for a starting temperature of about 25 ^{o}C (298 K), which was likely the starting temperature that allowed for the most complete magnetostructural transformation for a pressure change of 2.5 kbar. The inset shows ΔT_{max} as a function of starting temperature, showing a sigifiicant temperature change that spans 18 K.

With the previously published works on the magnetocaloric effect in these materials, the new results on the barocaloic effects demonstrate that this $(MnNiSi)_{1-x}(FeCoGe)_x$ is a giant multicaloric material. The impact of this material, and others like it, may appear in the development of systems that can utilize both effects in a thermal cycle. Another possibility is to use the pressure-induced

shift of the magnetostructural transition in a purely magnetocaloric device in order to circumvent the deleterious effects of thermal hysteresis in this type of material.

II. Direct ΔT_{ad} Measurements in Ni-Mn-In Compounds: The magnetic properties and the reversibility of the magnetocaloric effects in $Ni_{50}Mn_{35}In_{15}$ (and other related Ni-Mn-In alloys) have been studied at the magnetostructural phase transition (MST).[7,8] Direct adiabatic temperature change (ΔT_{ad}) measurements were carried out using an extraction-insertion method in magnetic fields up to 14 T. The MST between the martensitic phase (MP) with low magnetization (paramagnetic or antiferromagnetic) and a nearly ferromagnetic austenitic phase were detected from thermomagnetic measurements, M(T,H), at applied magnetic fields up to 5 T. The MST temperature was found to be nearly independent of magnetic field for H < 5 T, and shifted to lower temperature with the further increase of magnetic field to 14 T. A large and nearly reversible inverse magnetocaloric effect (MCE) with $\Delta T_{ad} \sim -11$ K for a magnetic field change of $\Delta H = 14$ T was observed at the MST. The irreversibility of ΔT_{ad} was found to be 1 K. A direct ΔT_{ad} of +7 K for ΔT_{ad} = 14 T was observed at the second order ferromagnetic-paramagnetic phase transition. The obtained results have been discussed in terms of the suppression of antiferromagnetic correlations with the application of a strong magnetic field, and a reversibility of the initial magnetic state of the MP with applied magnetic field when the MST coincides with T_C.

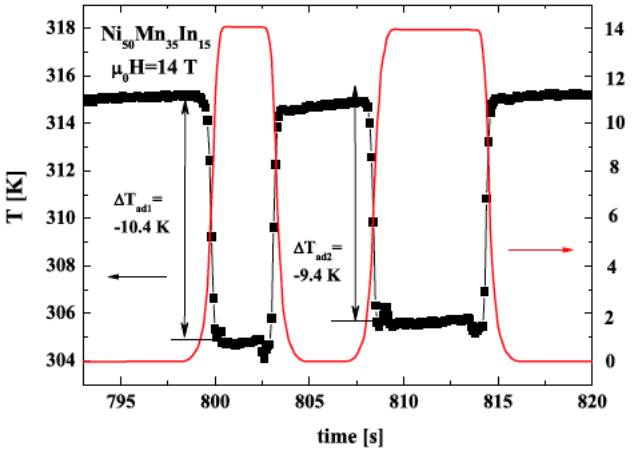

Fig. 3. The adiabatic temperature (left axis) as a function of time and applied field (right axis) for ΔH =14 T for multiple magnetization cycles.

III. Effects of Pressure on Metamagnetic Transitions in $DyRu_2Si_2$: Pressure-dependent magnetization measurements have been carried out on $DyRu_2Si_2$, from which we have estimated the volume magnetostriction and total entropy change (ΔS_T) as a function of hydrostatic pressure.[9] We observed multi-step metamagnetic transitions in the M(H) curves at atmospheric pressure (see Figure 4), the features of which diminished at intermediate pressures (P = 0.588

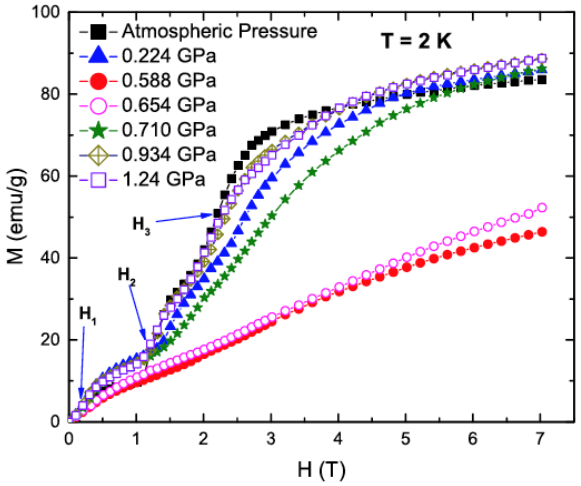

Fig. 4. The magnetization (M) vs. magnetic field (H) for $DyRu_2Si_2$ at T = 2 K at various hydrostatic pressures.

GPa and 0.654 GPa) and reappeared at higher pressures (P = 1 GPa). Moreover, the saturation magnetization decreased at intermediate pressures, following a near-linear dependence on increasing field, indicating a weaker magnetic ordering. At higher pressures, the saturation magnetization increased again, and the M(H) curves resembled those measured at atmospheric pressure. This trend of pressure dependence was also observed in the ΔS_T vs. T curves measured at various pressures. At intermediate pressures, the entropy changes ΔS_T decreased, whereas these values gradually increased with higher applied pressures. The origin of this pressure-dependent behavior may lie with the change of the a/c ratio with pressure. As pointed out by Szytula *et al*. in RT_2X_2 systems, the magnetic interaction is governed by the Ruderman–Kittel–Kasuya-Yosida (RKKY) model and the a/c ratio plays a crucial role in defining the nature and strength of the interaction.[10]

Future Plans

We have many projects in progress, one of which is a study of rare-earth doped Heusler alloys $Ni_{50-x}R_xMn_{35}Sn_{15}$ (x =0 and 1, R = La, Pr, Sm). We have observed a linear increase in the cell parameters as the RE atom changes from Sm to La, consistent with the increasing metallic radii of the RE elements (Sm = 1.802 Å, Pr = 1.828 Å, and La= 1.877 Å), resulting in a shift of the MST from 190 K to 260 K. The physical origin of the shift in martensitic transition temperature, the exact site occupancy of RE atoms, and the site-specific magnetic moments of Ni and Mn has yet to be explained. Among other things, we intend to explore the magneto-optic properties of these compounds.

Another project is a study of the effects of hydrostatic pressure on Ni-Mn-X systems. In particular, we will investigate Ni_2MnGa, which shows separated first and second order transitions, and $Ni_2Mn_{75}Cu_{25}Ga$, with those same transitions coupled into a single MST. Modified Arrott plot techniques will be applied to the separated transitions and then to the coupled one in order to evaluate the utility of Arrott plot techniques to coupled transitions.

References

[1]E. Liu *et al.,* Nature Commun. **3**, 873 (2012).
[2]T. Samanta *et al.,* Appl. Phys. Lett. **100**, 052404 (2012).
[3]C. L. Zhang *et al.,* Appl. Phys. Lett. **103**, 132411 (2013).
[4]T. Samanta *et al.,* Phys. Rev. B **91**, 020401(R) (2015).
[5]P. Lloveras *et al.,* Nature Commun. **6**, 8801 (2015).
[6]T. Samanta *et al.,* arXiv:1602.07584v1 [cond-mat.mtrl-sci]
[7]A. Quetz *et al.,* J. Alloys Compd. **683**, 139 (2016).
[8] Y. Koshkid'ko *et al.,* J. Alloys Compnd. **695**, 3348 (2017).
[9] A. Us Saleheen *et al.,* J. Appl. Phys. **121**, 045101 (2017).
[10] A. Szytula and J. Leciejewicz, *Handbook on the Physics and Chemistry of Rare Earths* (Elsevier Science Publishers B.V., 1989), Chap. 83, pp. 133–211.

Publications

[1] A. Us Saleheen, T. Samanta, M. Khan, Ph. W. Adams, D. P. Young, I. Dubenko, N. Ali, and Shane Stadler, "The influence of hydrostatic pressure on the magnetic and magnetocaloric properties of $DyRu_2Si_2$," J. Appl. Phys. **121**, 045101 (2017) [DOI: 10.1063/1.4874466]

[2] S. Pandey, A Quetz, A. Aryal, I. Dubenko, D. Mazumdar, S. Stadler, and N. Ali, "Thermosensitive Ni-based magnetic particles for self-controlled hyperthermia applications," J. Magn. Magn. Mater. **427**, 200 (2017). [DOI: 10.1016/j.jmmm.2016.11.049]

[3] A. Novikov, A. Solokov, E. A. Gan'shina, A. Quetz, I. S. Dubenko, S. Stadler, N. Ali, I. S. Titov, I. D. Rodionov, E. Lähderanta, A. Zhukov, A. B. Granovsky, and R. Sabirianov, "Probing the electronic structure of Ni-Mn-In-Si based Heusler alloy thin films using magneto-optical spectra in martensitic and austenitic phases," J. Magn. Magn. Mater. **432**, 455 (2017) [DOI: 10.1016/j.jmmm.2017.02.012]

[4] Y. Koshkid'ko, S. Pandey, A Quetz, A. Aryal, I. Dubenko, J. Cwik, E. Dilmieva, A. Granovsky, E. Lähderanta, A. Zhukov, S. Stadler, and N. Ali, "Inverse magnetocaloric effects in metamagnetic Ni-Mn-In-based alloys in high magnetic fields," J. Alloys Compnd. **695**, 3348 (2017) [DOI: 10.1016/j/jallcom.2016.12.032]

[5] S. Pandey, A. Quetz, P. J. Ibarra Gaytan, C. F. Sanchez-Valdes, A. Aryal, I. Dubenko, D. Mazumdar, J. L. Sanchez-Llamazares, S. Stadler, and N. Ali, "Magnetic, thermal, and magnetocaloric properties of $Ni_{50}In_{14.5}B_{0.5}$ ribbons," Adv. Mater. Lett. **8**, 1 (2017). [DOI: 10.5185/amlett.2017.1452]

[6] S. Pandey, A. Quetz, A. Aryal, A. Us Saleheen, I. Dubenko, D. Mazumdar, S. Stadler, and N. Ali, "Enhancement of ferromagnetism by substituting Cu for Mn in Ni-Mn-In-B Heusler alloys," Adv. Mater. Lett. **8**, 2 (2017). [DOI: 10.5185/amlett.2017.1403]

[7] M. Khan, O. Alshammari, B. Balasubramanian, B. Das, D. J. Sellmyer, A. Us Saleheen, and S. Stadler, "Controlling the microstructure and associated magnetic properties of $Ni_{0.2}Mn_{3.2}Ga_{0.6}$ melt-spun ribbons by annealing," AIP Adv. **7**, 056230 (2017). [DOI: 10.1063/1.4977892]

[8] S. Pandey, A. Quetz, A. Aryal, I. Dubenko, D. Mazumdar, S. Stadler, and N. Ali, "Large inverse magnetocaloric effects and giant magnetoresistance in Ni-Mn-Cr-Sn Heusler alloys," Magnetochemistry **3**, 3 (2017). [DOI: 10.3390/magnetochemistry3010003]

[9] S. Pandey, A. Quetz, A. Aryal, A. Us Saleheen, I. Rodionov, M. Blinov, M. Prudnikova, I. Dubenko, V. Prudnikov, D. Mazumdar, A. Granovsky, S. Stadler, and N. Ali, "Effects of the partial substitution of Ni by Cr on the transport, magnetic, and magnetocaloric properties of $Ni_{50}Mn_{37}In_{13}$," AIP Advances **7**, 056433 (2017) [DOI: 10.1063/1.4978909]

[10] S. Pandey, A. Quetz, A. Aryal, I. Dubenko, D. Mazumdar, S. Stadler, and N. Ali, "Magnetic, structural, and magnetocaloric properties of Ni-Si and Ni-Al thermoseeds for self-controlled hyperthermia," International Journal of Hyperthermia (accepted for publication, March 2017) [DOI: 10.1080/02656736.2017.1312562]

[11] A. Aryal, et al., "Magnetostructural phase transitions and magnetocaloric effects in as-cast $Mn_{1-x}Al_xCoGe$ compounds," J. Alloys Compnd. (2017) (Accepted for publication)

[12], S. Pandey et al., "Giant field-induced adiabatic temperature changes in In-based off-stoichiometric Heusler alloys," J. Appl. Phys. (accepted for publication, March 2017).

[13] A. Aryal, A. Quetz, S. Pandey, T. Samanta, I. Dubenko, D. Mazumdar, S. Stadler, and N. Ali, "Phase transitions and magnetocaloric and transport properties in off-stoichiometric $GdNi_2Mn_x$," J. Appl. Phys. **119**, 043905 (2016). [DOI: 10.1063/1.4940877]

[14] M. Khan, A. B. Karki, T. Samanta, D. Browne, S. Stadler, I. Vekhter, A. Pandey, P. W. Adams, and D. P. Young, "Complex superconductivity in the noncentrosymmetric compound Re_6Zr," Phys. Rev B **94**, 144515 (2016) [DOI: 10.1103/PhysRevB.94.144515]

[15] I. Dubenko, A. Granovsky, E. Lahderanta, M. Kashirin, V. Makagonov, A. Aryal, A. Quetz, S. Pandey, I. Rodionov, T. Samanta, S. Stadler, D. Mazumdar, and N. Ali, "Comparing magnetostructural transitions in $Ni_{50}Mn_{18.75}Cu_{6.25}Ga_{25}$ and $Ni_{49.80}Mn_{34.66}In_{15.54}$ Heusler alloys," J. Magn. Magn. Mater. **401**, 1145 (2016). [DOI:10.1016/j.jmmm.2015.11.025]

[16] Book Chapter: Novel Functional Magnetic Materials (Springer Series in Materials Science **231**), Chapter 2: *Magnetic, Magnetocaloric, Magnetotransport, and Magneto-optical, Properties of Ni–Mn–In-Based Heusler Alloys: Bulk, Ribbons, and Microwires,* I. Dubenko, N. Ali, S. Stadler, A. Zhukov, V. Zhukova, B. Hernando, V. Prida, V. Prudnikov, E. Gan'shina, and A. Granovsky, Springer International Publishing Switzerland (2016). ISBN 978-3-319-26104-1 [DOI 10.1007/978-3-319-26106-5]

[17] A. Quetz, Y. S. Koshkid'ko, I. Titov, I. Rodionov, S. Pandey, A. Aryal, P. J. Ibarra-Gaytan, V. Prudnikov, A. Granovsky, I. Dubenko, T. Samanta, J Cwik, J. L. Sanchez Llamazares, S. Stadler, E. Lahderanta, and N. Ali, "Giant reversible inverse magnetocaloric effects in $Ni_{50}Mn_{35}In_{15}$ Heusler alloys," J. Alloys Compd. **683**, 139 (2016). [DOI: 10.1016/j.jallcom.2016.05.106]

[18] A. Sokolov, E. Kirianov, A. Zlenko, A. Quetz, A. Aryal, S. Pandey, I. Dubenko, S. Stadler, N. Ali, N. Al-Aqrash, and R. Sabirianov, "Magnetic and magneto-transport studies of substrate effects on the martensitic transformation in a NiMnIn shape memory alloy," AIP Advances **6**, 056211 (2016). [DOI: 10.1063/1.4943537]

[19] The effects of substituting Ag for In on the magnetoresistance and magnetocaloric properties of Ni-Mn-In Heusler alloys, S. Pandey, A. Quetz, A. Aryal, I. Dubenko, T. Samanta, D. Mazumdar,

S. Stadler, and N. Ali, "Magnetic and magneto-transport studies of substrate effects on the martensitic transformation in a NiMnIn shape memory alloy," AIP Advances **6**, 056213 (2016). [DOI: 10.1063/1.4943537]

[20] G. Morrison, J. Prestigiacomo, N. Haldolaarachchige, B. K. Rai, D. P. Young, S. Stadler, E. Morosan, and J. Y. Chan, "Synthesis and anisotropic properties of single crystalline $Ln_2Ru_3Al_{15+x}$ (Ln = Gd, Tb)," J. Solid State Chem. **236**, 186 (2016) [DOI: 10.1016/j.jssc.2015.08.009]

[21] T. Samanta, D.L. Lepkowski, A. Saleheen, A. Shankar, J. Prestigiacomo, I. Dubenko, A. Quetz, I. W. H. Oswald, G. T. McCandless, J. Y. Chan, P. W. Adams, D. P. Young, N. Ali, and S. Stadler, "Hydrostatic pressure-induced modifications of structural transitions lead to large enhancements of magnetocaloric effects in MnNiSi-based systems," Phys. Rev. B **91**, 020401(R) (2015). [DOI: 10.1103/PhysRevB.91.020401]

[22] T. Samanta, D.L. Lepkowski, A. Saleheen, A. Shankar, J. Prestigiacomo, I. Dubenko, A. Quetz, I.W.H. Oswald, G.T. McCandless, J.Y. Chan, P.W. Adams, D. P. Young, N. Ali, and S. Stadler, "Effects of hydrostatic pressure on magnetostructural transitions and magnetocaloric properties in $(MnNiSi)_{1-x}(FeCoGe)_x$," J. Appl. Phys. **117** (12), (2015). [DOI: 10.1063/1.4916339]

[23] I. Dubenko, A. Quetz, S. Pandey, A. Aryal, M. Eubank, I. Rodionov, V. Prudnikov, A. Granovsky, A. Lahderanta, T. Samanta, A. Saleheen, S. Stadler, and N. Ali, "Multifunctional properties related to magnetostructural transitions in ternary and quaternary Heusler alloys," J. Mag. Mag. Mat. **383**, 186 (2015). [http://dx.doi.org/10.1016/j.jmmm.2014.10.083]

[24] S. Pandey, A. Quetz, I. D. Rodionov, A. Aryal, M. I. Blinov, I. S. Titov, V. N. Prudnikov, A. B. Granovsky, I. Dubenko, S. Stadler, and N. Ali, "Magnetic, transport, and magnetocaloric properties of boron-doped Ni-Mn-In alloys," J. Appl. Phys. **117**, 183905 (2015); [http://dx.doi.org/10.1063/1.4921052]

[25] S. Pandey, A. Aryal, A. Quetz, M. Eubank, T. Samanta, I. Dubenko, S. Stadler, and N. Ali, "Influence of copper substitution on the magnetic and magnetocaloric properties of NiMnInB alloys," J. Appl. Phys. **117**, 17A737 (2015). [dx.doi.org/10.1063/1.4916809]

[26] A. Aryal, A. Quetz, S. Pandey, M. Eubank, T. Samanta, I. Dubenko, S. Stadler, and N. Ali, "Phase Diagram and Magnetocaloric Effects in $Ni_{1-x}Cr_xMnGe_{1.05}$," J. Appl. Phys. **117**, 17A711 (2015). [DOI: dx.doi.org/10.1063/1.4907765]

[27] Yu.S. Koshkidko, A. Quetz, S.Pandey, A. Aryal, I. S. Dubenko, S. Stadler, N. Ali, J. Cwik, I. Titov, M. Blinov, M.V. Prudnikov, V.N. Prudnikova, E. Lähderanta, and A.B. Granovskii, "Magnetocaloric effect in $Ni_{50}Mn_{35}In_{15}$ Heusler Alloy in low and strong magnetic fields, I.D. Rodionov," JETP Lett. **101**, 385 (2015) [DOI: 10.1134/S0021364015060107]

DOE Award # DE-SC0007043

Georgia State University Research Foundation

Quantum Nanoplasmonics Theory

Mark I. Stockman, PI, Vadym Apalkov, co-PI

Date of Report: April 06, 2017

Research period covered by the Report is one year: April 1, 2016 – March 31, 2017.

Overall during this period of 2016-2017, the grant provided a major support acknowledged in publications of Refs. [1-5]. The following publications received a supplementary support from the grant for this period: Refs. [6-8].

1 Program Scope

This is a program of fundamental theoretical studies. The main focus is on ultrafast and strong field quantum phenomena in nanostructured and nanofilm solids induced by ultrashort and intense laser pulses.

2 Recent Progress

The following major subprojects comprise the main goal and scope of this program:

1. *Novel Quantum Nanooptics and Nanoplasmonics: Phenomena in Condensed Matter in Strong Ultrafast Fields.*

   Advanced laser sources presently allow generation of femtosecond optical pulses with close to one optical oscillation, highly-stabilized phase, and the field strength exceeding that of crystal fields, on the order of 2-3 V/Å. We study theoretically novel phenomena caused by such fields.

   1.1. We have introduced Attosecond Nanoscale Nearfield Sampling (ANNS) [2]. This phenomenon and a nanoplasmonics method based on it were proposed theoretically in our article [9]. The promise of ultrafast light-field-driven electronic nanocircuits has stimulated the development of the new research field of attosecond nanophysics. An essential prerequisite for advancing this new area is the ability to characterize optical near fields from light interaction with nanostructures, with sub-cycle resolution. Here we experimentally demonstrate and theoretically interpret attosecond near-field retrieval for a tapered gold nanowire. By comparison of the results to those obtained from noble gas experiments and trajectory simulations, the spectral response of the nanotaper near field arising from laser excitation can be extracted.

   1.2. Recent advances in attosecond science in combination with the well-established techniques of nanofabrication have led to the new research field of attosecond nanophysics. One central goal is the characterization and manipulation of electromagnetic fields on the attosecond and nanometer scale. This has so far remained challenging both theoretically and experimentally. One major obstacle is the inhomogeneity of the electric fields. We have presented a general model, which allows for the description of attosecond streaking in near fields [5]. It permits the classification into different regimes as well as the reconstruction of the electric fields at the surface. In addition, we discuss the case of parallel polarization of the streaking fields to the surface, which has so far not been

considered for attosecond streaking from metallic surfaces. Finally, we review recent measurements of the electric field and response function of a gold nanotaper. Our results are highly relevant for future attosecond streaking experiments in inhomogeneous fields.

1.3. At the heart of ever growing demands for faster signal processing is ultrafast charge transport and control by electromagnetic fields in semiconductors. Intense optical fields have opened fascinating avenues for new phenomena and applications in solids. Because the period of optical fields is on the order of a femtosecond, the current switching and its control by an optical field may pave a way to PHz optoelectronic devices. Schiffrin et. al. [10] have shown reversible semimetallization in fused silica on a femtosecond time scale by using a few-cycle strong field ~ 1 V/Å. The strong Wannier-Stark localization and Zener-type interband tunneling were expected to drive this ultrafast semimetallization. Wider spread of this technology demands better understanding of whether the strong field behavior is universally similar for different dielectrics. In this article, we have employed a carrier-envelope-phase stabilized, few-cycle strong optical field to drive the semimetallization in sapphire, calcium fluoride and quartz and to compare this phenomenon and show its remarkable similarity between them [7]. The similarity in response of these materials, despite the significant differences in their physical properties, suggests the universality of the physical picture explained by the localization of Wannier-Stark states. Our results pave the way toward PHz-rate optoelectronics.

2. *New Nanoplasmonic Phenomena in Novel 2D Nano-Materials.*

There is a wide class of novel two-dimensional materials whose properties span major classes of solids, from insulators (for instance, hexagonal boron nitride, h-BN), to semiconductors such as transitional metal dichalcogenides (such as $MoSe_2$, WS_2) and black phosphorus, to Dirac semimetals such as graphene. While the bulk of topological insulators is a narrow-band semiconductor, their surfaces are Dirac semimetals whose electrons possess spin-momentum locking. A remarkable property of these materials is that, in contrast to common plasmonic metals, their carrier density can be controlled by electric or chemical bias.

2.1. Black phosphorus (BP) is an emerging two-dimensional material with intriguing physical properties. It is highly anisotropic and highly tunable by means of both the number of monolayers and surface doping. Here, we investigated [1] experimentally and theoretically the near-field properties of a-few-atomic-monolayer nanoflakes of BP. We discover near-field patterns of bright outside fringes and a high surface polarizability of nanofilm BP consistent with its surface-metallic, plasmonic behavior at mid-infrared frequencies <1176 cm^{-1}. We conclude that these fringes are caused by the formation of a highly polarizable layer at the BP surface. This layer has a thickness of ~1 nm and exhibits plasmonic behavior. We estimate that it contains free carriers in a concentration of $n \approx 1.1 \times 1020$ cm^{-3}. Surface plasmonic behavior is observed for 10-40 nm BP thicknesses but absent for a 4-nm BP thickness. This discovery opens up a new field of research and potential applications in nanoelectronics, plasmonics and optoelectronics.

2.2. We have proposed an electronic interferometry in graphene's reciprocal space without a magnetic field, employing strong ultrafast circularly polarized optical pulses [4]. The reciprocal space interferograms contain information on the electronic spectra, topological properties (Berry flux) of graphene, and on the waveform and chirality of the excitation optical pulses. These can be measured using time-resolves angle-resolved photoemission spectroscopy (TR-ARPES) with attosecond ultraviolet pulses. The predicted effects

provide unique opportunities in fundamental studies of two-dimensional topological materials and in applications to future petahertz light-wave-driven electronics.

2.3. We have theoretically studied the interaction of crystalline topological insulator (CTIs), characterized by surface quadratic gapless bands, with an ultrashort (few-femtosecond) optical pulse [8]. The electron dynamics in such an optical pulse is determined by a strong lattice-momentum dependence of the interband dipole coupling, which is anisotropic and singular at the degeneracy point. The interband mixing induced by the ultrashort pulse results in a finite conduction band population, the distribution of which in the reciprocal space is correlated with the profile of the interband dipole matrix elements and has high contrast. The number of such high-contrast regions depends on the polarization direction of the optical pulse. The ultrashort pulse also causes an electrical current and a net charge transfer through the system in the direction of the maximum field.

2.4. Epsilon-near-zero (ENZ) materials constitute a novel class of materials whose optical properties have been predicted to be unusual and potentially promising for applications. Among them are synthetic metal-dielectric metamaterials and also natural materials such as metals near the bulk-plasmon frequency, highly-doped semiconductors, and also silicon carbide close to the optical phonon frequencies. In our research [3], from the fundamental principle of causality we have shown that with a very low (asymptotically zero) intrinsic dielectric loss do necessarily possess a very low (asymptotically zero) group velocity of electromagnetic wave propagation. This leads to the loss function being singular and causes high nonradiative damping of the optical resonators and emitters (plasmonic nanoparticles, quantum dots, chromophore molecules) embedded into them or placed at their surfaces. Rough ENZ surfaces do not exhibit hot spots of local fields suggesting that surface modes are overdamped. Reflectors and waveguides also show very large losses both for realistic and idealized ENZ materials.

2. Future Plans

We intend to further investigate behavior of solids in strong fields. The emphasis will be made on the fundamental problems related to the reduction of $\mathcal{P}$- and $\mathcal{T}$-symmetries of the solids by ultrafast strong fields. We will investigate such a novel problem as a strong field ultrafast imprinting of its symmetry on a two-dimensional solid causing a long-time chirality and currents, both electrical and spin-currents. A number of such expected effects are related to the valley selectivity of such solids with respect to chiral (circular-polarized) exciting radiation. Another class of effects to be investigated is behavior of solids in combined strong stationary and optical fields. An example may be a sharp metal tip under a large positive bias subjected to a strong field of plasmon polaritons. Similar systems are studied and are of high interest for atomic probe tomography and microscopy (APT-M). Finally, based on recent published results [11] and our own work on the spaser biomedical applications [12], we will aim at an explanation and theory of extraordinary sensitivity of a generating spaser to its environment, which allows one to use spasers for ultrasensitive environmental and biomedical probes.

3. Publications Resulting from the Grant and References

1. Y. Abate, S. Gamage, Z. Li, V. Babicheva, M. H. Javani, H. Wang, S. B. Cronin, and M. I. Stockman, *Nanoscopy Reveals Surface-Metallic Black Phosphorus*, Light Sci. Appl. **5**, e16162-1-7 (2016).
2. B. Förg, J. Schötz, F. Süßmann, M. Förster, M. Krüger, B. Ahn, W. Okell, K. Wintersperger, S. Zherebtsov, A. Guggenmos, V. Pervak, A. Kessel, S. Trushin, A. Azzeer, M. Stockman, D. E. Kim, F. Krausz, P. Hommelhoff, and M. Kling, *Attosecond Nanoscale near-Field Sampling*, Nat. Commun. **7**, 11717-1-7 (2016).
3. M. H. Javani and M. I. Stockman, *Real and Imaginary Properties of Epsilon-near-Zero Materials*, Phys. Rev. Lett. **117**, 107404-1-6 (2016).
4. H. K. Kelardeh, V. Apalkov, and M. I. Stockman, *Attosecond Strong-Field Interferometry in Graphene: Chirality, Singularity, and Berry Phase*, Phys. Rev. B **93**, 155434-1-7 (2016).
5. J. Schötz, B. Förg, M. Förster, W. A. Okell, M. I. Stockman, F. Krausz, P. Hommelhoff, and M. F. Kling, *Reconstruction of Nanoscale near Fields by Attosecond Streaking*, IEEE J. Sel. Top. Quant. Elec. **23**, 1-11 (2017).
6. Y. Abate, D. Seidlitz, A. Fali, S. Gamage, V. E. Babicheva, V. S. Yakovlev, M. I. Stockman, R. Collazo, D. E. Alden, and N. Dietz, *Nanoscopy of Phase Separation in $In_xga_{1-x}n$ Alloys*, ACS Appl Mater Inter **8**, 23160−23166 (2016).
7. O. Kwon, T. Paasch-Colberg, V. Apalkov, B.-K. Kim, J.-J. Kim, M. I. Stockman, and D. E. Kim, *Semimetallization of Dielectrics in Strong Optical Fields*, Sci. Rep. **6**, 21272-1-9 (2016).
8. S. A. Oliaei Motlagh, V. Apalkov, and M. I. Stockman, *Interaction of Crystalline Topological Insulator with an Ultrashort Laser Pulse*, Phys. Rev. B **95**, 085438-1-8 (2017).
9. M. I. Stockman, M. F. Kling, U. Kleineberg, and F. Krausz, *Attosecond Nanoplasmonic Field Microscope*, Nat. Phot. **1**, 539-544 (2007).
10. A. Schiffrin, T. Paasch-Colberg, N. Karpowicz, V. Apalkov, D. Gerster, S. Muhlbrandt, M. Korbman, J. Reichert, M. Schultze, S. Holzner, J. V. Barth, R. Kienberger, R. Ernstorfer, V. S. Yakovlev, M. I. Stockman, and F. Krausz, *Optical-Field-Induced Current in Dielectrics*, Nature **493**, 70-74 (2013).
11. R.-M. Ma, S. Ota, Y. Li, S. Yang, and X. Zhang, *Explosives Detection in a Lasing Plasmon Nanocavity*, Nat. Nano **9**, 600-604 (2014).
12. E. I. Galanzha, R. Weingold, D. A. Nedosekin, M. Sarimollaoglu, J. Nolan, W. Harrington, A. S. Kuchyanov, R. G. Parkhomenko, F. Watanabe, Z. Nima, A. Biris, A. I. Plekhanov, M. I. Stockman, and V. P. Zharov, *Spaser as a Biological Probe*, Nat. Commun., (In Print) (2017).

Tuning Spin Functionality at Interfaces through Complex Oxide Heteroepitaxy

PI: Yuri Suzuki
Department of Applied Physics, Stanford University

Program Scope

The *main research objective* of the program is to develop novel paradigms for *static and dynamic tuning* of quasi-two dimensional magnetic functionality in complex oxide thin films and heterostructures. In this program we have focused on the role of octahedral rotations due to lattice strain, electrical gating of the structures as well as coherent epitaxial strain to tune the magnetic functionality in complex oxide thin films and heterostructures. Atomically precise complex oxide thin films and heterostructures with spin functionality comprise a new class of oxide materials that may form the basis for the development of a more energy efficient spin-based electronics.

Our recent focus has been on three categories of materials based on *transition metal oxide compounds*:

(i) heterostructures in which octahedral rotations at the interfaces generate unexpected spin functionality not observed in the bulk;
(ii) heterostructures in which electrical gating of the interfaces gives rise to dynamical tuning of spin functionality;
(iii) thin films in which chemical pressure and epitaxial strain can turn on and off a ferromagnetic ground state

Recent Progress

Highlights of recent work include (i) demonstrating ferromagnetism switchable by octahedral rotations at the interfaces of $CaRuO_3/CaMnO_3$ superlattices, (ii) demonstrating ferromagnetism tunable by octahedral rotations at the interfaces of $LaNiO_3/CaMnO_3$ superlattices, (iii) demonstrating dynamical tuning of ferromagnetism at $CaRuO_3/CaMnO_3$ interfaces by electrical gating and (iii) demonstrating tunability of ferromagnetism in epitaxial $PrCoO_3$ thin films via chemical pressure and epitaxial strain.

Interfacial Ferromagnetism Tuned by Octahedral Rotations in $LaNiO_3/CaMnO_3$ superlattices.[1,2,3]

Despite recent progress in identifying new complex ground states at interfaces, isolating, and controlling the underlying mechanisms behind these emergent properties remains among the most challenging materials physics problems to date. In particular, generating ferromagnetism localized at the interface of two non-ferromagnetic materials is of fundamental and technological interest. Moreover, the ability to turn the ferromagnetism on and off would shed light on the origin of such emergent phenomena and is promising for spintronic applications.

We have previously demonstrated the emergence of interfacial ferromagnetism in one single unit cell of $CaMnO_3$ at each interface in $CaMnO_3/CaRuO_3$ superlattices.[4] The result was rather surprising as in the bulk $CaMnO_3$ is an antiferromagnetic insulator and $CaRuO_3$ is an itinerant metal. However through a combination of neutron reflectivity, exchange biased hysteresis loops,

scanning transmission electron microscopy/ electron energy loss spectroscopy and x-ray magnetic circular dichroism, we were able to conclusively demonstrate that Mn double exchange interactions in a single unit cell of $CaMnO_3$ at the interface mediated by itinerant electrons from the adjacent $CaRuO_3$ layer was the origin of the ferromagnetism.

More recently, we discovered that ferromagnetism confined within one unit cell at the interface of $CaRuO_3$ and $CaMnO_3$ can be switched on and off by changing the symmetry of the oxygen octahedra connectivity at the boundary.[1] More specifically, crystallographic symmetry-mismatch across the interfaces, associated with incommensurate tilt and rotation of the MnO_6 and RuO_6 octahedra, can modulate and even entirely suppress the interfacial ferromagnetism residing within a single unit cell of the $CaMnO_3$ layer. Our results indicate that the creation of discontinuities in the interfacial structural symmetry inhibits electron transfer from $CaRuO_3$ to $CaMnO_3$, destabilizing the ferromagnetism and illustrating the power of controlling charge transfer at interfaces.

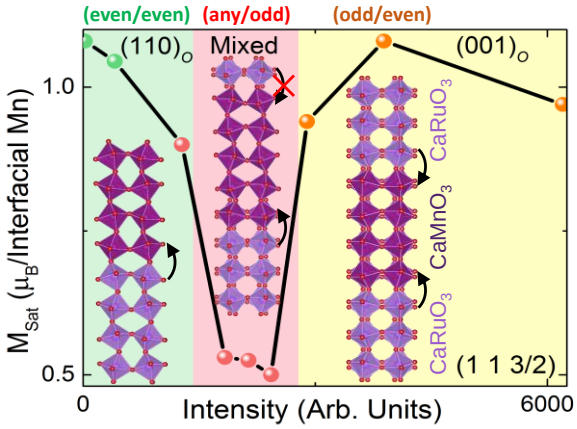

Figure 1. Magnetization versus intensity of the half order x-ray peak (1 1 3/2). Superlattices with odd layers of $CaMnO_3$ showed suppressed magnetization and always exhibited moderate (1 1 3/2) peak intensity indicative of the $(001)_{ortho}$ domain configuration as well as moderate (0 ½ 3/2) peak intensity indicative of the $(110)_{ortho}$ domain configuration. Superlattices with even layers of $CaMnO_3$ exhibited the highest magnetization and showed either high (1 1 3/2) peak intensity or high (01/2 3/2) peak intensity, indicating that they are mono-domain.

Figure 1 shows that superlattices with odd number of $CaMnO_3$ layers always have a mixed domain configuration and lower magnetization while those with even numbers of $CaMnO_3$ layers have a mono-domain configuration. The mixed domain gives rise to an incommensurate tilt and rotation in the two materials that suppresses charge transfer and therefore ferromagnetism at one of the interfaces. Further detailed studies showed that it is indeed the ferromagnetism is suppressed at the interface where $CaRuO_3$ is grown on a $CaMnO_3$ layer.

One of the guiding design principles for developing novel functionality in complex oxides systems is octahedral connectivity. In superlattices composed of perovskites with different crystal symmetries, variation of the relative ratio of the constituent layers as well as the individual layer thicknesses gives rise to non-equilibrium crystal symmetries that, in turn, lead to unprecedented control of interfacial ferromagnetism.[2] We have shown how octahedral connectivity can be used to stabilize non-equilibrium crystal symmetries in coherently strained

$LaNiO_3/CaMnO_3$ $(LaNiO_3)_N/(CaMnO_3)_M$ superlattices. In the $CaRuO_3$/ $CaMnO_3$ superlattices, the relaxed strain state of the superlattices meant that the superlattice layers could orient independently from one another. However, by studying coherently strained superlattices composed of constituent materials with different bulk crystal symmetries, we can use the $LaNiO_3$ and $CaMnO_3$ layer thicknesses to stabilize non-equilibrium crystal symmetries. In our superlattices, the magnitude of octahedral rotations in $CaMnO_3$ is determined by the $LaNiO_3$ layer thickness. However, the orientation of these octahedral rotations in $CaMnO_3$ is controlled by the $CaMnO_3$ layer thickness. Together, these structural modifications in $LaNiO_3/CaMnO_3$ superlattices enable control of the interfacial ferromagnetic properties over a large range of magnitudes, leading to enhanced ferromagnetism. This demonstrates that octahedral connectivity is a new path forward for engineering interfacial ferromagnetism.

In addition to octahedral connectivity, effects of polar compensation need to be taken into account for $LaNiO_3/CaMnO_3$ but not for $CaRuO_3$/ $CaMnO_3$ superlattices due to polarity mismatch of the constituent materials.[3] By focusing on LNO/CMO superlattices with only four unit cells of CMO, we are able to reduce the contribution of itinerant electron mediated ferromagnetic double exchange and highlight the polar compensation effect. In insulating superlattices, we have identified a small but significant ferromagnetic contribution from a Ni^{2+} - Mn^{4+} superexchange interaction at the interface driven by polarity mismatch. In metallic superlattices, this contribution is combined with a ferromagnetic double exchange interaction that increases with LNO thickness. Together these results indicate that interfacial ferromagnetism is attributed to charge transfer driven by polarity mismatch as well as double exchange.

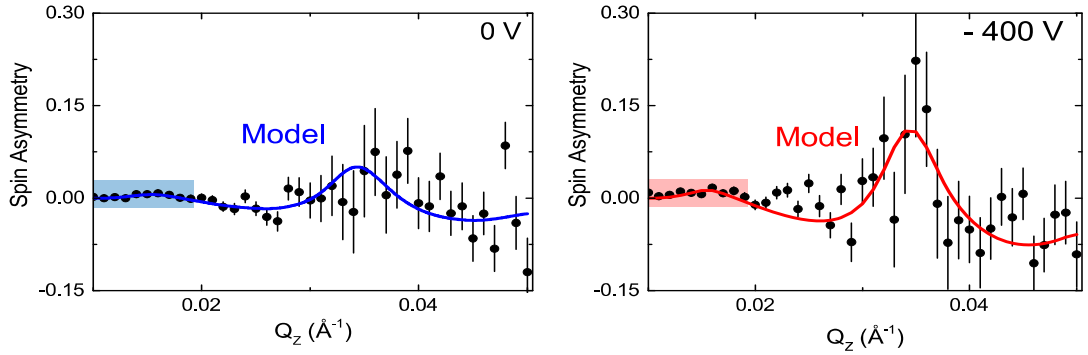

Figure 2. (a) Spin asymmetry of a $CaRuO_3/CaMnO_3$ interface after cooling in 700 mT without a bias; (b) Spin asymmetry of the same sample after cooling in 700 mT with a bias of -400 V. The solid lines indicate the model fitting that corresponds to 1μB in zero bias and 3μB at -400V.

Dynamically tuning $CaRuO_3/CaMnO_3$ interfaces.[5] We have demonstrated the dynamical tuning of interfacial ferromagnetism by electrically gating $CaRuO_3/CaMnO_3$ interfaces.[1] These results are of great significance as they demonstrate a promising route for the electrical field control of magnetism and tunable ferromagnetism in low power spintronic devices. Basically the electrical gate modifies the amount of charge transfer across $CaRuO_3/CaMnO_3$ interfaces. These carriers in the charge transfer mediate the Mn double exchange interaction, and hence the ferromagnetism, in a single unit cell of $CaMnO_3$.

Using polarized neutron reflectometry, we are able to detect the ferromagnetic signal arising from a single atomic monolayer of $CaMnO_3$, manifest as a spin asymmetry in the reflectivity.

We find that the application of an electric field of 600 kV/m across the bilayer induces a significant increase in this spin asymmetry. Figure 2 shows the neutron reflectivity data under the application of an electric field and corresponding fits to the data indicating an increase in magnetic moment from 1 μ_B to 3 μ_B per Mn ion from zero to a -400V bias. Modeling of the reflectivity suggests that this increase corresponds to a transition from canted antiferromagnetism to full ferromagnetic alignment of the Mn^{4+} ions at the interface. This increase from 1 μ_B to 3 μ_B per Mn is indicative of a strong magnetoelectric coupling effect, and such direct electric field control of the magnetization at an interface has significant potential for spintronic applications.

Epitaxial $PrCoO_3$ thin films.[6] We have demonstrated that both epitaxial strain and chemical pressure can be used to tune the ferromagnetic ground state in epitaxial cobaltite thin films.[4] Although none of the undoped cobaltites of the form $ACoO_3$ are ferromagnetic in bulk form, in our previous work we have shown that a ferromagnetic ground state, with Co in a non-zero spin state, can be stabilized in epitaxial $LaCoO_3$ and $PrCoO_3$ thin films under epitaxial tensile strain. We have now demonstrated that the ferromagnetic ground state can be tuned by chemical pressure or epitaxial strain. Epitaxial $PrCoO_3$ thin films are consistently ferromagnetic on $SrTiO_3$ single crystal substrates below 65 K. Under slightly smaller tensile strains on $(La,Sr)(Al,Ta)O_3$ substrates, $PrCoO_3$ thin films are not consistently ferromagnetic. Films under minimal or compressive strain do not exhibit any ferromagnetism. More recently, we have found that chemical pressure in the form of Y doping of the Pr site (i.e., $Pr_{0.7}Y_{0.3}CoO_3$) completely destabilizes a ferromagnetic ground state. These results indicate the importance of A-site cation choice for Co spin-state and Co-O-Co exchange interactions, offering another dimension to tune magnetic order in thin film cobalt perovskites.

References

1. A. J. Grutter, A. Vailionis. J.A. Borchers, B. J. Kirby, C. L. Flint, C. He, E. Arenholz, and Y. Suzuki, *Nano Letters* **16** 5647−5651 (2016).

2. C. Flint, A. Vailionis, H. Zhou, and Y. Suzuki, submitted to *Nano Letters* (2017).

3. C. L. Flint, A. N'Diaye, P. Shafer, E. Arenholz, and Y. Suzuki, submitted to *Physical Review Materials* (2017).

4. C. He, A.J. Grutter, M. Gu, N.D. Browning, Y. Takamura, B.J. Kirby, J.A. Borchers, J.W. Kim, M.R. Fitzsimmons, X. Zhai, V.V. Mehta, F.J. Wong, and Y. Suzuki, *Physical Review Letters* **109** 197202 (2012).

5. A. J. Grutter, C. He, B. J. Kirby, J. A. Borchers, C. L. Flint, E. Arenholz, and Y. Suzuki, *Physical Review Letters* **115** 047601 (2015).

6. Ted D. Sanders, Urusa S. Alaan, Matthew T. Gray, Shameek Bose, Matthew Taylor, Mariona Cabero, Virat Mehta, Maria Varela, Chris Leighton, Yuri Suzuki, submitted to *Journal of Magnetism and Magnetic Materials* (2017).

Publications

1. A. J. Grutter, C. He, B. J. Kirby, J. A. Borchers, C. L. Flint, E. Arenholz, and Y. Suzuki, "Electric Field Control of Interfacial Ferromagnetism in $CaMnO_3/CaRuO_3$ Heterostructures," *Physical Review Letters* **115** 047601 (2015).

2. A.J. Grutter, D.A. Gilbert, U.S. Alaan, E. Arenholz, B.B. Maranville, J. A. Borchers, Y. Suzuki, Kai Liu, and B. J. Kirby, "Reversible Control of Magnetism in $La_{0.67}Sr_{0.33}MnO_3$ Through Chemical Induced Oxygen Migration," *Applied Physics Letters* **108** 082405 (2016).

3. A. J. Grutter, A. Vailionis. J.A. Borchers, B. J. Kirby, C. L. Flint, C. He, E. Arenholz, and Y. Suzuki, "Interfacial Symmetry Control of Emergent Ferromagnetism," *Nano Letters* **16** 5647−5651 (2016).

4. Ted D. Sanders, Urusa S. Alaan, Matthew T. Gray, Shameek Bose, Matthew Taylor, Mariona Cabero, Virat Mehta, Maria Varela, Chris Leighton, Yuri Suzuki, "Magnetism in Epitaxial $PrCoO_3$ and $Pr_{0.7}Y_{0.3}CoO_3$ Films," submitted to *Journal of Magnetism and Magnetic Materials* (2017).

5. C. Flint, A. Vailionis, H. Zhou, and Y. Suzuki, "Tuning interfacial ferromagnetism in $LaNiO_3/CaMnO_3$ superlattices by Stabilizing Non-Equilibrium Crystal symmetry," submitted to *Nano Letters* (2017).

6. C. L. Flint, A. N'Diaye, P. Shafer, E. Arenholz, and Y. Suzuki, "The Role of Polar Compensation in Interfacial Ferromagnetism of $LaNiO_3/CaMnO_3$ Superlattices," submitted to *Physical Review Materials* (2017).

Harnessing Order Parameter in Ternary II-IV-V_2 Semiconductors

Adele C. Tamboli, National Renewable Energy Lab

Program Scope

Recent advances in semiconductor growth, characterization, and theory have enabled a new understanding that controlled disorder can be used to deterministically modify materials. In particular, the use of cation disorder as a new free parameter to enable tailored properties in optoelectronic semiconductors is now possible. In this program, we are developing a systematic understanding and control of cation order parameter and its impact on properties in II-IV-V_2 semiconductors, a class of compounds with structure and properties similar to III-Vs, but with a doubled conventional unit cell size due to the substitution of group II and IV elements for group III cations. Building off a foundation of work on III-V ordering, we are exploring a set of materials for optoelectronics with similar performance to III-Vs but wider tunability though chemical complexity. We are studying phosphide and nitride materials, representing the two different structure types available in II-IV-V_2 materials. These materials can be readily integrated with III-Vs as well as silicon, enabling applications ranging from optoelectronics spanning the visible spectrum, to extremely efficient yet inexpensive photovoltaics, to platforms for improved lasers and optical computing.

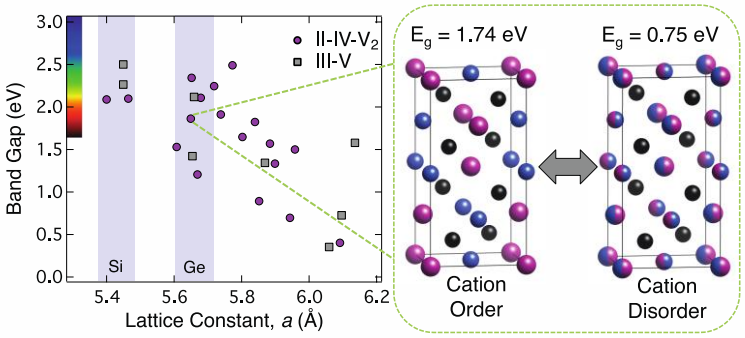

Fig. 1. Theoretical predictions and some experimental evidence have suggested that the band gap of II-IV-V_2 materials may be tunable by as much as 1 eV by tuning cation disorder. This would enable an alternative route to property tuning compared to traditional alloying approaches. *TOC graphic from publication [1].*

Recent Progress

In the first year of this project, we have begun developing techniques to enable understanding and control of cation disorder in ternary nitrides and phosphides. This work has included three key aspects: theory, growth, and characterization. To develop the appropriate frameworks, we have begun by considering two materials previously developed under EERE programs for photovoltaic applications, $ZnSnN_2$ and $ZnSiP_2$. Longer term, we will focus on $ZnGeN_2$ and $ZnGeP_2$, which we expect to enable more precise control of cation disorder.

A review of the field [1] revealed significant recent progress in understanding and control of cation disorder in $ZnSnP_2$ bulk crystals [2] and $ZnGeN_2$ nanowires [3], as well as an overall trend predicting increased tendency towards cation disorder (characterized by the ratio of melting point to disorder transition temperature) as a function lower tetragonal distortion (c/a closer to the ideal ratio of 2) (Fig. 2). Our decision to focus on $ZnGeX_2$ compounds is due to the observation that $ZnSnX_2$ disorders so readily that it can be difficult to control, and $ZnSiX_2$ (as well as most Cd-containing compounds) are unlikely to disorder. Recent work on $ZnSnP_2$ (Fig. 2) shows that bulk materials can be made with high order parameter using extremely slow cooling, which may not be practically achievable in thin films, and that these materials with controlled order parameter do show some of the predicted band gap tuning [2]. A recent study of $ZnGeN_2$ showed that this material can have controlled order parameter when grown in a more typical thin film configuration with varying growth temperature [3].

To enable a wide range of experimental conditions and high-throughput experimentation, we are using two very different growth techniques for each material type: combinatorial sputtering and epitaxial growth. These two different techniques enable access to very different chemical spaces, as combinatorial sputtering is a very far from equilibrium, low temperature technique that is expected to result in highly disordered films, and epitaxial growth enables slow growth rates and very controlled conditions for extremely crystalline films. Nitride epitaxy utilizes a molecular beam epitaxy system designed for GaN growth, with an expanded set of source materials. For combinatorial growth, we are using an ultra-high vacuum sputter chamber with an electron cyclotron resonance source to provide activated nitrogen. For phosphide materials, we have constructed a custom growth chamber for epitaxy,

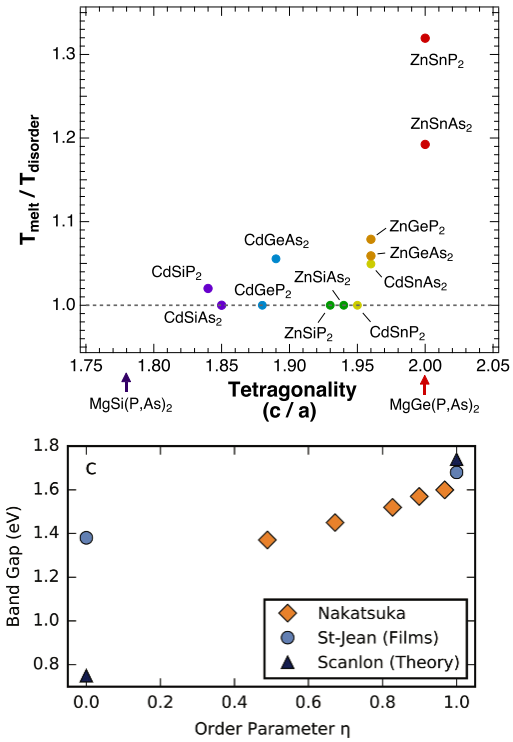

Fig. 2. (Top) The tendency of a material to disorder, as expressed by the ratio of its melting point to its order/disorder transition temperature, is directly related to its tetragonal distortion. (Bottom) $ZnSnP_2$ is one of the materials most likely to disorder, but can be formed in a more ordered structure by slow cooling of bulk materials. This results in measured band gap tuning of 0.4 eV. [1]

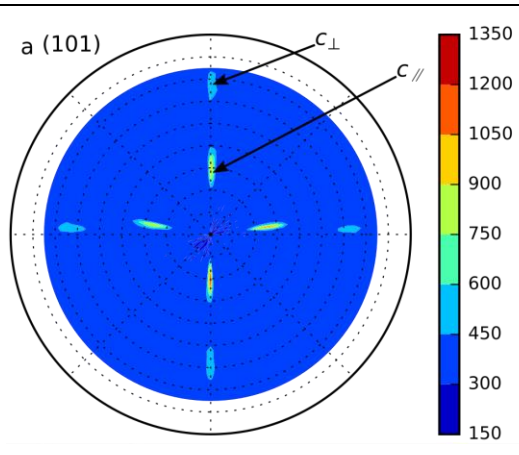

Fig. 3. XRD pole figure showing evidence of epitaxial $ZnSiP_2$ growth on Si.

which has recently been used to grow epitaxial $ZnSiP_2$ on Si using a combined chemical vapor deposition and molecular beam epitaxy approach (Fig. 3). We plan to begin $ZnGeP_2$/Si depositions soon using GeH_4 instead of SiH_4 for the group IV source. We hope to purchase a combinatorial phosphide sputtering chamber in the near future to complement epitaxial phosphide growth.

Using $ZnSnN_2$ thin films grown by combinatorial sputtering for a previous project, we are testing methods for determining the order parameter in II-IV-V_2 films. $ZnSnN_2$ has been predicted to form in two different "ordered" crystal structures with similar formation energies (space groups $Pna2_1$ and $Pmc2_1$), and in addition, there are two different disordered structures that may form [4]. All four structures are nearly indistinguishable from the ordered structures and each other by standard X-ray diffraction techniques due to the weak intensity of low angle ordering-related peaks (Fig. 4). To attempt to distinguish these structures, we have performed measurements of X-ray absorption and high-resolution diffraction at SLAC. The diffraction data does not show any evidence of low-angle peaks that would be characteristic of ordered materials, but our calculations have predicted that even small amounts of disorder (~10%) can cause these peaks to disappear. The key difference between the two disordered structures is whether or not they locally obey the octet rule, which is unlikely to be measurable using any type of X-ray diffraction (green and red curves). We expect the absorption data to provide information about local bonding and chemical environment that might reveal the presence or absence of octet rule violations, which are predicted to have a significant impact on material properties such as band gap and carrier localization. Analysis of this data is ongoing, and involves computational efforts to provide insight into differences in density of states for these different structures.

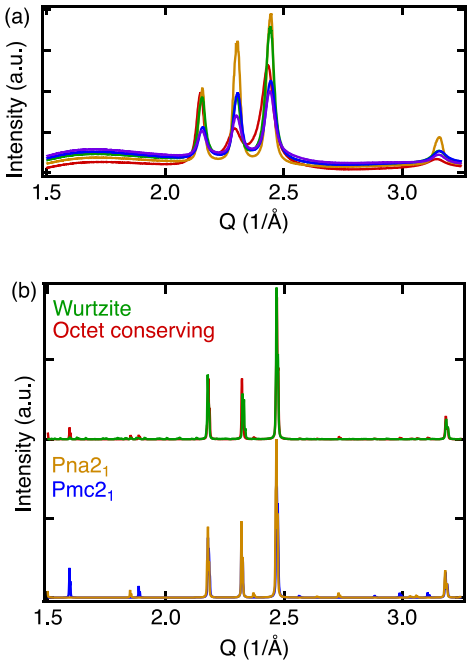

Fig. 4. (a) Experimental X-ray diffraction data for $ZnSnN_2$ (different colors correspond to varying Zn/Sn ratios) shows no evidence of low-angle peaks indicative of ordering. (b) Calculated XRD patterns for the two ordered structures and two different types of disorder.

Future Plans

We plan to extend our growth, characterization, and modeling framework enable control and understanding of cation disorder in $ZnGeP_2$ and $ZnGeN_2$. Computational frameworks are currently being developed using $ZnSnN_2$ as a model system to predict the evolution of the band structure and carrier localization as a function of crystal structure and concentration of octet-rule-violating motifs, as well as formation energy differences between the possible

structures. Preliminary investigations have agreed well with experimental results on $ZnSnN_2$, and we plan to apply these techniques to $ZnGeP_2$ and $ZnGeN_2$. In parallel, synthesis of $ZnGeN_2$ thin films will commence using both combinatorial and epitaxial growth, as our growth chambers come back online after upgrades for this project. Work to synthesize epitaxial $ZnGeP_2$ on Si will commenced soon, and films willbe optimized, focusing first on understanding the impact of growth temperature and post-growth annealing. When these films are of sufficient quality, we plan to apply the same synchrotron techniques we have used for $ZnSnN_2$ to characterize order parameter, linking this property to optical properties such as absorption onset and photoluminescence. Ultimately, the goal of this program is to create a complete understanding of how to control cation order, and its impact on optoelectronic properties, as understood through the lens of two model systems.

References

1. Aaron D. Martinez, Angela N. Fioretti, Eric S. Toberer and Adele C. Tamboli, *Synthesis, Structure, and Optoelectronic Properties of II-IV-V_2 Materials.* J. Mater. Chem. A, Advance Article (2017)
2. S. Nakatsuka and Y. Nose, J. Phys. Chem. C, 2016, 121(2), 1040–1046.
3. E. W. Blanton, K. He, J. Shan and K. Kash, J. Cryst. Growth, 2017, 461, 38–45.
4. P. C. Quayle, E. W. Blanton, A. Punya, G. T. Junno, K. He, L. Han, H. Zhao, J. Shan, W. R. L. Lambrecht and K. Kash, Phys. Rev. B: Condens. Matter Mater. Phys., 2015, 91, 205207.

Publications (2016-2017)

1. Aaron D. Martinez, Angela N. Fioretti, Eric S. Toberer and **Adele C. Tamboli**, *Synthesis, Structure, and Optoelectronic Properties of II-IV-V_2 Materials.* J. Mater. Chem. A, Advance Article, 2017 [Invited review, *Emerging Investigators* themed issue]. DOI: 10.1039/C7TA00406K

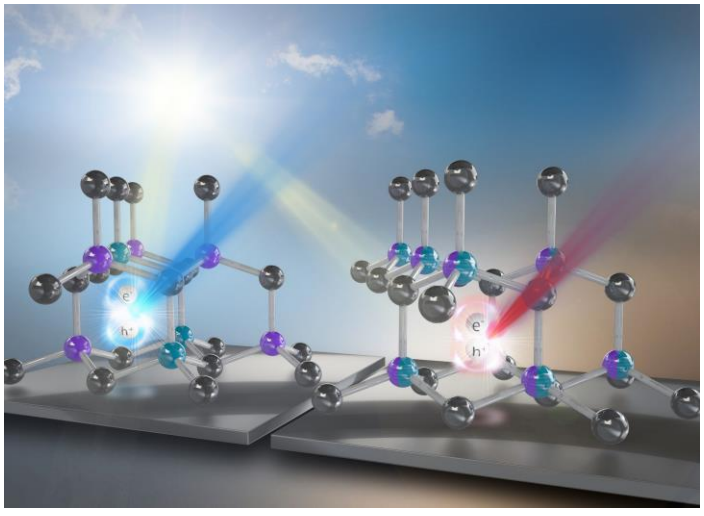

Back cover art for JMCA review illustrates the predicted band gap tunability in $ZnSnN_2$. *Illustration by Joshua Bauer (NREL).*

Non-equilibrium dynamics of interacting light-matter systems

Hakan E. Tureci, Department of Electrical Engineering, Princeton University

Program Scope

This projects aims to study the fundamental physics and technological applications of (i) superconducting circuits that contain one or multiple qubits coupled to a common electromagnetic environment and driven out of equilibrium by oscillatory sources, and (ii) the dynamics and control of exciton-polariton systems. The project will pursue the development of advanced quantum microwave engineering techniques that can efficiently deal with large, possibly complex 2D and 3D superconducting oscillators coupled to multiple Josephson-junction based artificial atoms. This includes in particular the accurate calculation of spectral densities seen by single qubits as well as interaction kernels in multi-qubit systems. We will also develop computational techniques to deal with the dynamics and control of exciton-polariton condensates in multi-cavity systems that are pumped spatially inhomogeneously.

Recent Progress

We have developed a theoretical and computational framework [1] to study the dynamics of a Josephson Junction (JJ) artificial atom capacitively coupled to an open multimode superconducting resonator. The effective equations of motion of the JJ qubit were derived by integrating out the EM degrees of freedom exactly, while encoding their effect in the (classical) Green's function (GF) of the EM background. The dissipation of the resonator modes are accounted for exactly by employing a spectral representation for the GF in terms of a complete set of non-Hermitian modes of the resonator. We derive Heisenberg-Langevin equations for the qubit without resorting to the rotating wave, two-level, Born or Markov approximations. We solved these equations for the quench dynamics of the qubit, capturing accurately the non-Markovian features of the dynamics in a way that is valid for any coupling strength.

We also undertook a preliminary study of exciton-polariton condensates [2]. The goal was to develop a modal description of polariton condensation in incoherently pumped inorganic systems. A temporal coupled mode theory was developed that captures the multi-mode condensate dynamics in the presence of non-linear interactions and arbitrary spatial pumping conditions. We have shown that our computational technique agrees very well with a full integration of the generalized Gross-Pitaevskii equations in diverse dynamical regimes, while providing physical insight specific to spectral methods that FTDT-variety brute force integrators lack.

Future Plans

In the next period we plan to

- Study the Lamb shift and Purcell decay rates of JJ qubits in open superconducting cavities. Any calculation of these quantities so far has been found in the literature to lead

to divergent results unless a cutoff is introduced. Some preliminary work has been completed in this direction indicating that a dynamical cutoff is introduced self-consistently by the hybridization of the qubit with the modes of a resonator.

- Investigate the driven qubit- cavity system. This will require the extension of our methodology to include external microwave drives.
- Investigate quantum transport of excitations in a lattice of superconducting oscillators. The goal will be to design a system for optimal transport of information and energy at the quantum level, between two sites of such a lattice. Some preliminary work is already completed in this direction.
- Continue our study of exciton- polariton systems to analyze non- equilibrium dynamics in coupled lattices with the computational technique developed in the first period.

Publications

1. Non-Markovian dynamics of a superconducting qubit in an open multimode resonator, M. Malekakhlagh, A. Petrescu, Hakan E. Tureci, Phys. Rev. A **94**, 063848 (2016).
2. Non-Hermitian coupled-mode theory for incoherently pumped exciton-polariton condensates, S. Khan, Hakan E. Tureci, Phys. Rev. A **94**, 053856 (2016).

Uncovering and surmounting loss mechanisms in light emitters

Principal Investigator: Chris G. Van de Walle, University of California, Santa Barbara

Program Scope

Nitride light-emitting diodes (LEDs) have enabled solid-state lighting. However, the widespread adoption and range of possible applications of nitride optoelectronics continues to be limited by efficiency droop under high-current-density operating conditions and losses due to radiative and nonradiative recombination of carriers at defects. These problems are exacerbated in the case of green and UV nitride light emitters. We are developing and applying new theoretical approaches to uncover the fundamental reasons for efficiency limitations in light emitters. Our methodology for calculating radiative and nonradiative recombination at point defects is based on advanced first-principles calculations, taking full account of accurate electronic structure and electron-phonon interactions. Radiative and nonradiative recombination rates are calculated without any fitting to experiment. Point-defect assisted Shockley-Read-Hall recombination is being quantified for impurities and point defects relevant to light-emitting diode structures. Our overall goal is to generate the fundamental knowledge that is essential for improving efficiencies, and to provide guidelines for overcoming the limitations.

Recent Progress

In the present phase of the project we focus on the effect of defect-assisted nonradiative mechanisms that may limit the performance of light-emitting devices. We address these issues using first-principles techniques based on density functional theory (DFT). Evaluation of defect-related properties requires accurate band gaps and treatment of localized states; we therefore employ a hybrid functional [1], which has been demonstrated to provide accurate electronic and atomic structure of these materials, and allows quantitative comparison with experiment.

A major goal of our project is to understand the microscopic origin of Shockley-Read-Hall (SRH) recombination in light emitters. SRH recombination is proportional to the first power of the carrier density, and limits the peak efficiency in LEDs. Recombination consists of two nonradiative capture events: electron capture and hole capture, as illustrated in Fig. 1. We build on the methodology that we developed to calculate carrier capture coefficients [2] to identify efficient SRH recombination centers that would be detrimental to the performance of nitride light emitters.

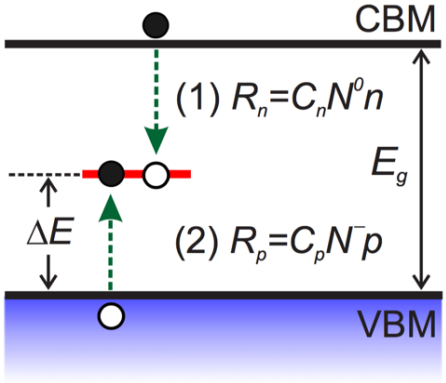

Fig. 1: Schematic energy band diagram depicting SRH recombination at a defect level in a material with a band gap E_g. Recombination proceeds via electron capture at a rate R_n and hole capture at the rate R_p. $N^{0,-}$ are defect concentrations, n,p are electron and hole carrier densities and $C_{n,p}$ are the nonradiative electron and hole capture coefficients.

In one part of the project we focused on the role of point defects. We elucidated the microscopic mechanisms by which gallium vacancy complexes with hydrogen (V_{Ga}-3H) and oxygen (V_{Ga}-O_N-2_H) [P1] can act as efficient SRH recombination centers in nitride light emitters operating in the green and yellow region of the spectrum. We find the total SRH coefficients increase significantly as the InGaN band gap decreases, as can be seen in Fig. 2 for the example of V_{Ga}-3H in InGaN. SRH *A* coefficients on the order of 10^7 s^{-1} are associated with large reductions in the efficiency of nitride light emitters [3].

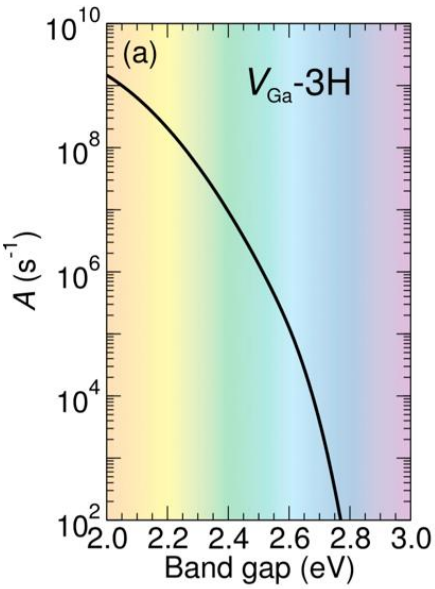

Fig 2: SRH *A* coefficient due to the V_{Ga}-3H complex versus the band gap of the InGaN alloy assuming a defect density of 10^{16} cm^{-3} and a temperature of 120°C. The color spectrum indicates the corresponding wavelengths of light.

In parallel to this effort we also undertook an investigation of impurities and their role as efficient SRHs center [P2]. Large concentrations of unintentional Ca incorporation have recently been observed in nitride devices grown by molecular beam epitaxy [4]. We identified calcium incorporated on the gallium site (Ca_{Ga}) as a center that can lead to SRH *A* coefficients exceeding 10^6 s^{-1} for InGaN band gaps below 2.5 eV, highlighting the importance of limiting the unintentional incorporation of Ca during growth.

To explain efficient SRH processes in wide-band-gap III-nitride semiconductors and their alloys we identified the crucial role played by the *electronic excited states* of defects. For the gallium vacancy complex with oxygen (V_{Ga}-O_N) [P3] and for iron impurities that substitute on the gallium site (Fe_{Ga}) in GaN [P4]—defects that based on the position of the defect levels in the band gap are expected to be inefficient SRH centers—we demonstrated the excited states enhance the SRH rates by orders of magnitude. In the case of Fe_{Ga} the recombination pathway due to the excited states of iron (illustrated in Fig. 3) leads to SRH coefficients on the order of 10^{-8} s^{-1} in GaN, in excellent agreement with experiment.

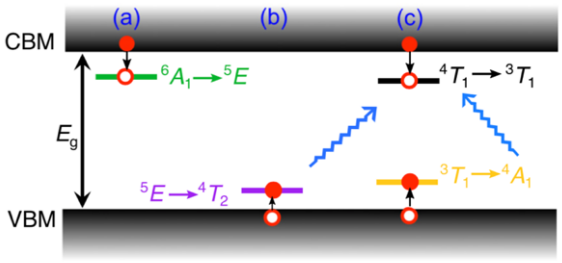

Fig. 3: Nonradiative recombination cycle due to Fe in GaN. (a) Electron and (b) hole capture that initializes the SRH process that proceeds via the excited states (c) of Fe. Spin-conserving intra-defect relaxations are illustrated with the blue arrows.

For LEDs operating at higher carrier densities, Auger processes present a fundamental obstacle that hinder operation of LEDs at high current densities [3]. In order to understand the various mechanisms that contribute to Auger recombination in nitride LEDs, we performed an in-depth first-principles study for InGaN alloys [P5]. Our investigations took into account the role of direct Auger processes and indirect Auger processes due to alloying, charged defects

and phonons. Illustrated in Fig. 4 is a summary of these various contributions to the hole-hole-electron (hhe) Auger process in InGaN. We conclude that indirect Auger processes mediated by short-wavelength phonons and by alloy scattering dominate the Auger coefficient in InGaN, while defect scattering had a weaker effect on the overall Auger process.

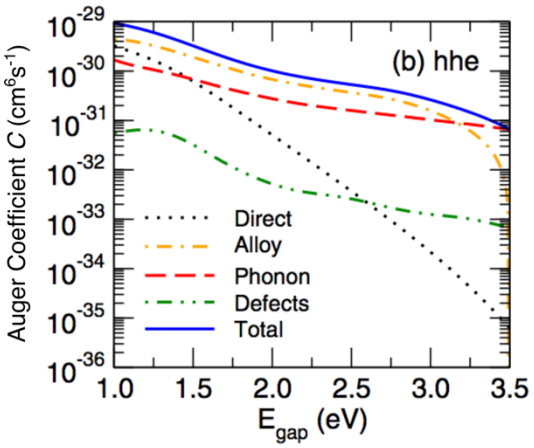

Fig. 4: Summary of the calculated indirect and direct hhe Auger recombination mechanisms in InGaN for a free electron and hole concentration of 10^{19} cm^{-3} and a temperature of 300K.

The efficiency of III-nitride devices is also limited by the presence of polarization fields in the quantum wells. Accurate values for spontaneous and piezoelectric polarization are necessary for analysis of experimental results and for device design. The spontaneous polarization constants are defined with respect to a reference structure, and for the wurtzite III-nitrides, the zinc-blende structure has been used as a reference. Our investigations have now made clear that use of the zinc-blende structure as a reference results in a spurious contribution to the spontaneous polarization differences between materials. In a reformulated approach, we define polarization discontinuities using a consistent reference based on a layered hexagonal structure [P6].

Future Plans

We will continue our investigations of the properties of point defects and impurities in III-nitride materials and their alloys and their impact on nonradiative recombination. Specifically, we will focus on transition metals and their complexes with point defects and impurities such as oxygen and carbon. There is growing evidence that transition metals are unintentionally incorporated during the growth of nitride devices.

Building on our expertise in investigating nonradiative recombination processes, we plan to study the role of nonradiative processes in methylammonium lead halides. These materials have come to the forefront for use in highly efficient solar cells. To achieve high conversion efficiencies a complete understanding of possible nonradiative loss mechanisms is required. Auger recombination has been flagged as a potential loss mechanism.

References

[1] J. Heyd, G. E. Scuseria, and M. Ernzerhof, "Hybrid functionals based on a screened Coulomb potential", J. Chem. Phys. **118**, 8207 (2003); **124**, 219906 (2006).

[2] A. Alkauskas, Q. Yan, and C. G. Van de Walle, "First-principles theory of nonradiative carrier capture via multiphonon emission", Phys. Rev. B **90**, 075202 (2014).

[3] A. David, and M. Grundmann, “Droop in InGaN light-emitting diodes: A differential carrier lifetime analysis”, Appl. Phys. Lett. **96,** 103504 (2010)

[4] E.C. Young, N. Grandjean, T.E. Mates, and J.S. Speck, “Calcium impurity as a source of non-radiative recombination in (In,Ga)N layers grown by molecular beam epitaxy”, Appl Phys. Lett. **109**, 212103 (2016).

Publications

[P1] C. E. Dreyer, A. Alkauskas, J. L. Lyons, J. S. Speck, and C. G. Van de Walle, “Gallium vacancy complexes as a cause of Shockley-Read-Hall recombination in III-nitride light emitters”, Appl. Phys. Lett. **108**, 141101 (2016).

[P2] J.-X Shen, D. Wickramaratne, C. E. Dreyer, A. Alkauskas, E. Young, J. S. Speck, C. G. Van de Walle, “Calcium as a nonradiative recombination center in InGaN”, Appl. Phys. Express **10**, 021001 (2017)

[P3] A. Alkauskas, C. E. Dreyer, J. L. Lyons, and C. G. Van de Walle, “Role of excited states in Shockley-Read-Hall recombination in wide-band-gap semiconductors”, Phys. Rev. B **93**, 201304 (2016).

[P4] D. Wickramaratne, J-X. Shen, C. E. Dreyer, M. Engel, M. Marsman, G. Kresse, S. Marcinkevičius, A. Alkauskas, C.G. Van de Walle, “Iron as a source of efficient Shockley-Read-Hall recombination in GaN”, Appl. Phys. Lett. **109**, 162107 (2016).

[P5] E. Kioupakis, D. Steiauf, P. Rinke, K. T. Delaney, and C. G. Van de Walle, “First-principles calculations of indirect Auger recombination in nitride semiconductors”, Phys. Rev. B, **92**, 035207 (2015).

[P6] C. E. Dreyer, A. Janotti, C. G. Van de Walle, and D. Vanderbilt, “Correct Implementation of Polarization Constants in Wurtzite Materials and Impact on III-Nitrides”, Phys. Rev. X **6**, 021038 (2016).

[P7] A. Alkauskas, M. D. McCluskey, and C. G. Van de Walle, “Tutorial: Defects in semiconductors—Combining experiment and theory”, J. Appl. Phys. **119**, 181101 (2016).

[P8] J. L. Lyons, A. Alkauskas, A. Janotti, and C. G. Van de Walle, “First-principles theory of acceptors in nitride semiconductors”, Phys. Stat. Sol. B **252**, 900 (2015).

Mesoscale Design of Magnetoelectric Heterostructures and Nanocomposites

Dwight Viehland, Materials Science and Engineering, Virginia Tech
Shashank Priya, Mechanical Engineering, Virginia Tech

Program Scope

Our focus is on investigating the mesoscale physics and interfacial interactions of two-phase (magnetostrictive and piezoelectric) magnetoelectric (*ME) composites at varying length and temporal scales through artificially designed anisotropic microstructures and domain configurations*. The specific objectives are to: (1) Develop simulated heterostructure and nanostructured ferroic thin/thick layers on semi-conducting, piezoelectric and ferromagnetic substrates in order to create varying interfacial behavior, (2) Through high resolution microscopy and atomic scale probing techniques, provide quantitative understanding of field-dependent ME behavior and tunable magnetic anisotropy of heterostructures and nanostructures in multi-dimensional composites, (3) Design and model self-biasing (ME response in the absence of DC bias) nanostructured films.

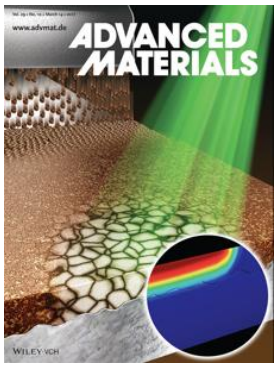

Fig.1 Adv. Mater. 29 (10), 1605688 (2017). Schematic representation of laser annealed RT deposited composite films on Metglas.

Recent Progress

(i) ME response in laser annealed PZT films on amorphous Metglas foil

Laser annealing coupled with the aerosol deposition (AD) method was developed to integrate PZT on amorphous metglas (25 μm-thick) (**Fig. 1**) at room temperature for achieving superior ME response.[1] Dimensions of PZT film were varied (2-11 μm) to achieve varying interfacial coupling coefficient (*k*).[1] The theoretical magnitude of magnetoelectric coefficient (α_{ME}) as a function of volume fraction of PZT (f_{PZT}) and interface coupling factor (*k*) can be expressed through Equation 1:[2]

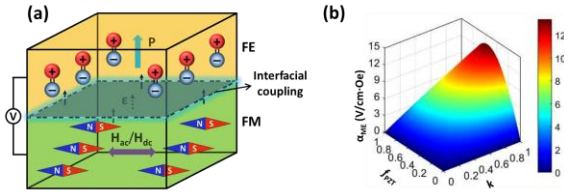

Fig.2 (a) Schematic representation of the direct magnetoelectric effect in a 2-2 configuration ferroelectric (FE)/ferromagnetic (FM) composite system (the numbers 2-2 refers to the connectivity of the phases in free space). (b) Theoretically predicted ME voltage coefficients (α_{ME}) of the PZT/Metglas composite as a function of volume fraction of the PZT (f_{PZT}) layer and the interface coupling factor (*k*) based on the Equation 1.[1]

$$\alpha_{ME} = \frac{-kf(1-f)(q_{11}^m + q_{12}^m)d_{31}^p}{kv(s_{11}^m + s_{12}^m)\varepsilon_{33}^p + (1-f)(s_{11}^p + s_{12}^p)\varepsilon_{33}^p - 2k(1-f)(d_{31}^p)^2} \qquad (1)$$

where the superscripts "*p*" and "*m*" represent the piezoelectric and magnetostrictive phases, respectively; *k* is the interface coupling factor; *f* denotes the volume fraction of the piezoelectric phase; ε_{33} and d_{31} are dielectric and piezoelectric constants; q_{ij} is piezomagnetic coefficient; and s_{ij}^p s_{ij}^p, and s_{ij}^m s_{ij}^p, and s_{ij}^m and s_{ij}^m are elastic compliances.[2] The results are plotted in **Fig. 2b**.[1] According to this analysis, ME coefficient of the composite with 6 μm-thick PZT film and 25 μm thick Metglas layer (for fPZT = 0.193 and k = 1) was found to be ~ 7 V/cm•Oe under off-resonance condition.[1] Experimentally we were able to replicate this magnitude of ME coefficient in

PZT/Metglas bilayer ME composite. This observation that variable *k* can have such dramatic influence on the ME response provides fundamental basis for further understanding the role of interfaces in governing the off-resonance direct ME output for film-based ME composites.

Below we provide some more process details and discussion of the experimental results for the films shown in Fig. 1. Room-temperature grown and laser annealed ferroelectrics as compared to conventional high-temperature grown materials is a new field of research with tremendous possibilities. All the laser annealed PZT samples exhibited a reasonably low dielectric loss in the range of 5-7%, over the frequency range of 1 kHz - 100 kHz.[1] At the driving frequency of 1 kHz, the value of dielectric constant, ε, for the PZT films with different thicknesses was found to be in the range of 720-900, which is comparable to the values of the films deposited on Si/Pt substrate followed by normal furnace annealing. This indicates that the laser annealing of PZT films did not cause any interfacial reaction between the PZT and amorphous Metglas layers and microstructural evolution was compatible with that obtained from traditional processes. The values of saturation polarization (P_s) and remnant polarization (P_r) under a maximum applied field of 700 kV/cm were in the ranges of 58-85 μC/cm^2 and 7-15 μC/cm^2, respectively. A significant improvement occurred in ε and P_s with increasing PZT thickness up to 6 μm, after which an opposite trend in these properties were observed. The difference in crystallinity (due to laser annealing) of the PZT films with varying thickness was considered a major contributor to the observed changes in the electrical response. Interestingly, the electrical properties were found to be degraded for thicker (> 6 μm) PZT film. Since all the PZT/Metglas samples with different thickness were fabricated under the same processing conditions, the volume fraction of annealed PZT phase and its degree of crystallinity were considered to contribute to the thickness dependent properties of the PZT/Metglas composites.

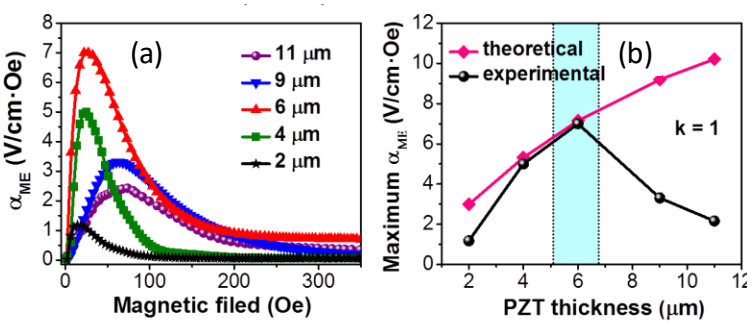

Fig.3 (a) ME voltage coefficients (α_{ME}) of laser annealed PZT/Metglas samples having different thickness. (b) Variations of maximum α_{ME} with the PZT film thickness.[1]

Fig. 3a shows the measured ME responses from the room-temperature grown laser annealed PZT/Metglas composites with varying thicknesses of PZT films. The sample with 6 μm thick PZT film on Metglas exhibited the largest α_{ME} (7 V/cm·Oe) as predicted by the theoretical calculation (see **Fig. 2b**). The changes in magnitude of ME coefficient with variation in the PZT film thickness are shown **Fig. 3b**. These results suggest the existence of an optimum thickness to achieve a maximum ME coupling between PZT and Metglas under given experimental conditions. The theoretical ME coefficients determined for the PZT films having different thicknesses on Metglas substrate, under ideal interface coupling (k=1), are compared with the corresponding experimental data in **Fig. 3b**. The trend in experimental values of α_{ME} followed the trend calculated from Equation 1. The thickness dependency of α_{ME} was attributed to the differences in the degree of crystallinity and the extent of annealing of the PZT film. The increase in domain switching with increase in crystallized volume of a ferroelectric phase gives rise to enhanced piezoelectricity and improved ME voltage output.

A close matching of the measured and calculated α_{ME} values for the 4 and 6 μm thick PZT films on Metglas substrate indicates the optimum fraction of crystallized volume of the PZT phase

after laser annealing, which in turn result in adequate combination of mechanical compliance (mechanical impedance matching with the MS layer) and electromechanical properties. The ME output results also suggested that there exists a strong and near-perfect interface bonding ($k \approx 1$), facilitating efficient strain transfer between PZT and Metglas. Theoretically, the ME voltage coefficient should increase continuously with increase in thickness of the PZT film (grown on 25 μm thick MS substrate) up to 33 μm (volume fraction $f_{PZT} = 0.56$), but the experimental data did not exhibit such trend. This phenomenon was considered to be related with the extent of laser interaction in thicker PZT films.

(ii) Electric field controlled magnetic states of $BiFeO_3$ (BFO) via strain

We have investigated the E-field controlled magnetic states of $BiFeO_3$ (BFO) via strain. BFO thin films were epitaxially deposited on $Pb(Mn_{1/3}Nb_{2/3})O_3$-30at%$PbTiO_3$ (PMN-30PT) single crystal substrates by pulsed laser deposition (PLD). The deposition conditions, such as laser energy density and film thickness, were optimized to ensure high quality films. The crystal structure was determined to be rhombohedral. Electric fields were applied on PMN-PT in both out-of-plane and in-plane directions, which in both cases induced a reversible change of in-plane strain.

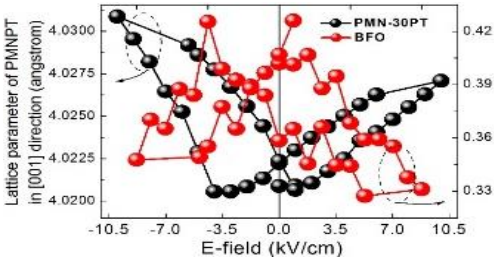

Fig.4 lattice parameter of PMNPT and in-plane strain of BFO vs E-field curve.

For example, in **Fig. 4**, an in-plane strain was measured by x-ray diffraction. We found that the lattice parameters of BFO could be tuned by about 0.4% under E-field applied on PMN-PT. Butterfly-like strain vs E-field curves were observed in the BFO layer, transferred from the substrate. In addition, reciprocal space mapping (RSM) measurements revealed that applied electric fields resulted in a change of the magnetic domain distribution in the BFO layer. These results clearly demonstrate important induced structural changes with application of electric field to the substrate.

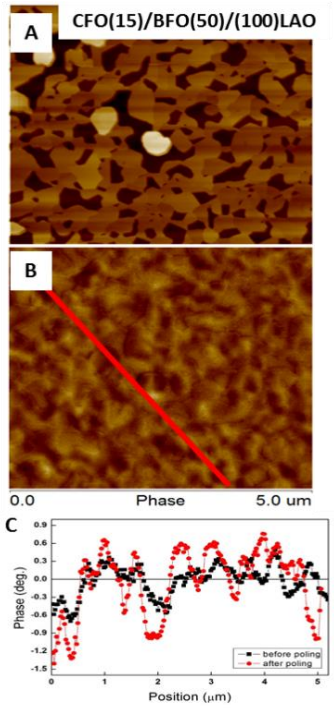

Fig.5 (A) AFM and (B) MFM images of CFO/T-phase BFO sample. (C) MFM phase signal before and after poling by tip bias.

Next, tetragonal structured BFO (T-phase BFO) and $CoFe_2O_4$ (CFO), CFO/T-phase BFO, nanocomposites were deposited on top of (001) $LaAlO_3$ (LAO) substrates. For comparisons, a control group CFO/R-phase BFO was deposited on (001) $SrTiO_3$ (STO). Although the CFO and BFO layers were deposited separately, after annealing at 725°C for 30min, the CFO top layer developed a self-assembled platform-like morphology with BFO on LAO (**Fig. 5a**), This phase distribution was different from the nanopillar CFO/R-phase BFO one previously reported on STO. Magnetic force microscopy (MFM) images revealed that each platform contained multiple magnetic domains, whose distribution could be adjusted by applying a tip bias (see **Figs. 5b and 5c**). However, studies of the control group showed that each nanopillar remained as a single domain that barely changed under tip bias. Hysteresis loops measured by a vibrating sample

magnetometer showed a strong thickness effect of the CFO layer's coercive field, in particular along the out-of-plane direction. For CFO/T-phase BFO, the coercive field was increased from 630Oe to 2100Oe as the thickness of the CFO layer was increased from 15nm to 30nm; but for the CFO/R-phase BFO heterostructure, the coercive field dropped from 3300Oe to 2100Oe. In addition, a weak exchange bias was found in both samples due to the ferrimagnetic CFO/antiferromagnetic BFO interface. Furthermore, field cooling measurement suggested that the R-phase and T-phase BFO may have different types of stable antiferromagnetic states, C-type and G-type, respectively.

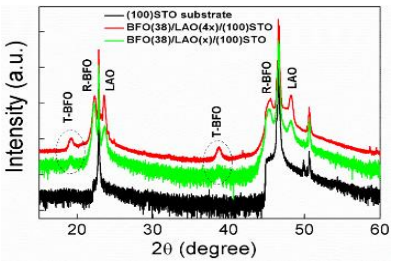

Fig.6 XRD patterns of BFO/LAO/(100)STO samples with different thickness.

Finally, to realize mixed-phase (both T and R) BFO on PMN-PT heterostructures, which may be beneficial to domain engineering of BFO, a heterostructure of BFO/LAO was fabricated on a (001) STO substrate. As shown in **Fig. 6**, the XRD patterns present both T-phase and R-phase BFO peaks, as well as epitaxial LAO peaks on the STO substrate.

Future Plans

In the room-temperature grown laser annealed PZT films, we have demonstrated significantly high ME response and just started to probe the influence of laser penetration and induced heat diffusion on microstructural evolution of the PZT films having a thickness up to 6 μm. We will continue this investigation to quantify the effect of crystallinity in thicker films through the modulation of laser wavelength, scanning speed, intensity, and sample temperature to achieve enhanced ME response. We will further investigate the effect of mechanical impedance matching (compliance matching between piezoelectric and magnetostrictive layer) on the magnetoelectric coupling. For this, substrates with difference compliance will be investigated. These samples and results will provide data points required to model the role of localized mechanisms such as interfacial anisotropy, charge transport, and coupling between magnetic-ferroelectric domains. In future, laser assisted synthesis will provide opportunity for the integration of ME devices at room temperature, which is especially important for conserving the cost and energy. Reducing the synthesis times from hours to minutes provide huge energy savings.

We further plan to investigate the ability to drive magnetic cycloid→AFM and cycloid→cycloid transformations by electric field. We are studying how to thermodynamically tune these transformations by compositional modifications that alter the required epitaxial strain needed to poise the material near the transformation point. We are also investigating various buffer layers that can stabilize mixed phase behavior which can lead to significantly enhanced magnetic and magnetoelectric property characteristics. Thermodynamically, these spin transformations are believed to be driven by flexo-magnetic effects. We are depositing BFO on particular substrates that favor strong flexural effects, and plan to study the structural and spin transformations driven by strain gradients.

References

[1] Haribabu Palneedi, Deepam Maurya, Gi-Yeop Kim, Venkateswarlu Annapureddy, Myoung-Sub Noh, Chong-Yun Kang, Jong-Woo Kim, Jong-Jin Choi, Si-Young Choi, Sung-Yoon Chung, Suk-Joong L. Kang, Shashank Priya, and Jungho Ryu, Advanced Materials **29** (10), 1605688 (2017).

[2] M. I. Bichurin, V. M. Petrov, and G. Srinivasan, Physical Review B **68** (5), 054402 (2003).

Publications

Peer reviewed Journals:

1) *Unleashing the full potential of magnetoelectric coupling in film heterostructure,* H. Palneedi, D. Maurya, G.-Y. Kim, V. Annapureddy, M. S. Noh, C.-Y. Kang, J. -W. Kim, J.-J. Choi, S. -Y. Choi, S.-Y. Chung, S.-J. L. Kang, S. Priya, and J. Ryu, ***Advanced Materials***, 2017, 29, 1605688.
2) *Modulated Magneto-Thermal Response of $La_{0.85}Sr_{0.15}MnO_3$ and $(Ni_{0.6}Cu_{0.2}Zn_{0.2})Fe_2O_4$ Composites for Thermal Energy Harvesters,* Hyun-Cheol Song, Deepam Maurya, Jinsung Chun, Yuan Zhou, Myung-Eun Song, David Gray, Nana Kwame Yamoah, Dhananjay Kumar, Austin McDannald, Menka Jain, Shashank Priya, ***Energy Harvesting and System****, 2017, DOI: https://doi.org/10.1515/ehs-2016-0016.*
3) *Enhanced torsional actuation and stress coupling in Mn-modified $0.93(Na_{0.5}Bi_{0.5}TiO_3)$-$0.07BaTiO_3$ lead-free piezoceramic system,* Pelin Berik, Deepam Maurya, Prashant Kumar, Min Gyu Kang & Shashank Priya, ***Science and Technology of Advanced Materials***, 2016, DOI: 10.1080/14686996.2016.1254569.
4) *Tailoring the Magnetoelectric Properties of $Pb(Zr,Ti)O_3$ Film Deposited on Amorphous Metglas Foil by Laser Annealing*, Haribabu Palneedi, Insung Choi, Gi-Yeop Kim, Venkateswarlu Annapureddy, Deepam Maurya, Shashank Priya, Jong-Woo Kim, Keon Jae Lee, Si-Young Choi, Sung-Yoon Chung, Suk-Joong L. Kang, and Jungho Ryu, ***J. Am. Ceram. Soc***., 2016, 1–8, DOI: 10.1111/jace.14270.
5) *Giant Magnetoelectric Effect in PZT Thin Film Deposited on Nickel*, Reema Gupta, Monika Tomar, Vinay Gupta, Yuan Zhou, Anuj Chopra, Shashank Priya, A. S. Bhalla and R. Guo, ***Energy Harvesting and Systems*** 2016, 3(2), 181–188.
6) *Status and Perspectives of Multiferroic Magnetoelectric Composite Materials and Applications*, Haribabu Palneedi, Venkateswarlu Annapureddy, Shashank Priya, and Jungho Ryu, ***Actuators***, 2016, 5(1), 9; doi:10.3390/act5010009.
7) *Self-Biased Magnetoelectric Composites: An Overview and Future Perspectives*, Yuan Zhou, Deepam Maurya, Yongke Yan, Gopalan Srinivasan, Eckhard Quandt, Shashank Priya, ***Energy Harvesting and Systems***, 2015, 2329-8774, DOI: 10.1515/ehs-2015-0003.
8) *Enhanced off-resonance magnetoelectric response in laser annealed PZT thick film grown on magnetostrictive amorphous metal substrate*, Haribabu Palneedi, Deepam Maurya, Gi-Yeop Kim, Shashank Priya, Suk-Joong L. Kang, Kwang-Ho Kim, Si-Young Choi and Jungho Ryu, ***Appl. Phys. Lett.*** 2015, 107, 012904.
9) *Integration of lead-free ferroelectric thin films on HfO_2/Si (100) for high performance non-volatile memory applications*, S. Kundu, D. Maurya, D., M. Clavel, Y. Zhou, N. N. Halder, M. K. Hudait, P. Banerji, S. Priya, ***Scientific Reports***, 2015, 5, 8494.
10) *Lead-free epitaxial ferroelectric material integration on semiconducting (100) Nb-doped $SrTiO_3$ for low-power non-volatile memory and efficient ultraviolet ray detection,S.* Kundu, M. Clavel, P. Biswas, B. Chen, H. -C. Song, P. Kumar, N. N. Halder, M. Hudait, P. Banerji, M. Sanghadasa, S. Priya, ***Scientific Reports***, 2015, 5, 12415, DOi: 10.1038/srep12415.
11) *Integration of $SrTiO_3$ on Crystallographically Oriented Epitaxial Germanium for Low-power Device Applications*, M. K. Hudait, M. Clavel, Y. Zhu, P. Goley, S. Kundu, D. Maurya, and S. Priya, ***ACS Appl. Mater. Interfaces***, 2015, 7 (9), pp 5471–5479.

12) C. Chen, S. Lv, J.J. Li, Z. Wang, X. Liang, Y.X. Li, D. Viehland, K. Nakajima, and Y. Ikuhara, "Two-dimensional electron gas at the Ti-diffused BiFeO3/SrTiO3 interface, Appl. Phys. Lett. 107 article number: 031601, DOI: 10.1063/1.4926732 (July 2015).
13) *Soft mode phonon dynamics and phase transition in Aurivillius type structures*, D. Maurya, F.-C. Sun, D. George, S. K. Nayak, A. Pramanick, M.-G. Kang, H. –C. Song, A. Charkhesht**,** S. Pamir Alpay, G. A. Khodaparast, N. Q. Vinh, and S. Priya, (under review in **PRL**).
14) M. Gao, J.F. Li, and D. Viehland "*Magnetoelectricity of CoFe2O4/Tetragonal Phase BiFeO3 nanocomposites*" (in preparation).

Book Chapters:

1) Applications of Multiferroic Magnetoelectric Composites in Multiferroic Materials: Properties, Techniques, and Applications (Edited by Junling Wang), Yuan Zhou, Jong-Woo Kim, Shuxiang Dong, Shashank Priya, Junling Wang, and Jungho Ryu, Taylor & Francis Group, Ch. 8, pages 215-254, 2016, DOI: 10.1201/9781315372532-9.
2) Recent advances in piezoelectric and magnetostrictive materials and phenomena in Composite Magnetoelectrics: Materials, Structures, and Applications (Editor: G Srinivasan, S Priya, N Sun), Shashank Priya, Su Chul Yang, Deepam Maurya, Yongke Yan, Woodhead publishing, Ch. 6, page 103-153, 2015.

Project title: Fundamental Piezotronic and Piezo-phototronic Effects in Nanowires

PI: Zhong Lin Wang

Affiliations: Georgia Institute of Technology

Program Scope

One dimensional (1D) semiconductors with wurtzite structure, such as GaN, ZnO and CdS nanowires, exhibit superior semiconductor, piezoelectric and mechanical properties, making them excellent candidates for novel electronic, opto-electronic devices and integrated systems. In 2006, our group firstly demonstrated the conversion of mechanical energy into electricity based on 1D semiconductor nanowires,[1] considering the coupling between piezoelectricity and semiconductor properties. This result has led to emerging fields of piezotronics and piezo-phototronics. Mechanical-deformation-induced piezoelectric polarization and corresponding piezoelectric polarization charges (*piezo-charges*), can effectively tune/control the distribution and transport properties of the charge carriers in the semiconductors; this is the piezotronic effect[2,3,4]. The piezo-phototronic effect[5,6] is a three-way coupling effect among piezoelectric polarization potential (*piezo-potential*), semiconducting properties and photoexcitation. Optoelectronic processes of charge carriers within semiconductors, such as generation, transport, separation and recombination can be controlled/tuned by introducing piezo-charges created and presented at the local interface.

By working on this program, we continue to focus on exploring and understanding the fundamental of the piezotronic and piezo-phototronic effects based on 1D semiconductor nanowires:

(1) Clarifying the fundamentals of the generation and distribution of the piezo-potential and piezo-charges inside the semiconductors under external straining; exploring the change rules of the induced piezo-potential and piezo-charges with the change of external strain; verifying the mechanical deformation-induced piezo-potential by applying external strains in opposite directions.

(2) Utilizing multi-field coupling finite-element-analysis method to calculate the generation and distribution of the induced piezo-potential and the piezo-charges inside the piezoelectric semiconductors under straining. The theoretical simulation results can also be used to confirm the experimental observations and better understanding the physical mechanisms.

(3) Optimizing the electric transport and/or optoelectric properties of semiconductor devices formed with 1D piezoelectric nanowires, by introducing the piezotronic and piezo-phototronic

effects; modulating the performances of 1D axial or coaxial heterostructured semiconductor devices by tuning the local energy band and dynamics of local free charge-carriers at the heterojunction interfaces, and thus control the corresponding electric transport and optoelectric processes for functional applications.

Recent Progress

- Piezo-Phototronic Effect in a Quantum Well Structure

Starting from the basic piezoelectricity equation, Schrödinger equation, Poisson equation, and Fermi's golden rule, a self-consistent theoretical model is proposed to study the piezo-phototronic effect in the framework of perturbation theory in quantum mechanics. The validity and universality of this model are well-proven with photoluminescence measurements in a single GaN/InGaN quantum well and multiple GaN/InGaN quantum wells. This study provides important insight into the working principle of nanoscale piezo-phototronic devices as well as guidance for the future device design.

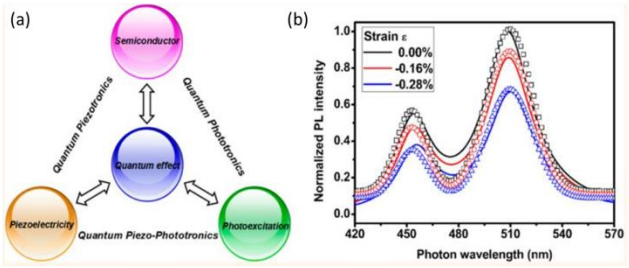

Figure 1. (a) Multifield coupling among the theory of semiconductors, piezoelectricity, photoexcitation, and quantum effects.(b) InGaN/GaNquantum structure PL spectrum of the under different compressive strains.

- Piezotronic Effect Modulated Heterojunction Electron Gas in AlGaN/AlN/GaN Heterostructure Microwire

we utilize strain-induced piezoelectric polarization charges to modify the energy band profile at local heterojunctions as an effective way for physical properties modulations of HEG. By introducing the piezotronic effect to AlGaN/AlN/GaN heterostructure microwires, at room temperature, the conductance is increased by 165% under −1.78% compressive strains, and reduced by 48% under 1.78% tensile strains. This study provides in-depth understanding about the piezotronic-effect modulation of low-dimensional electron gas in heterostructured nanomaterials, with potential applications in HEMTs and MEMS/NEMS.

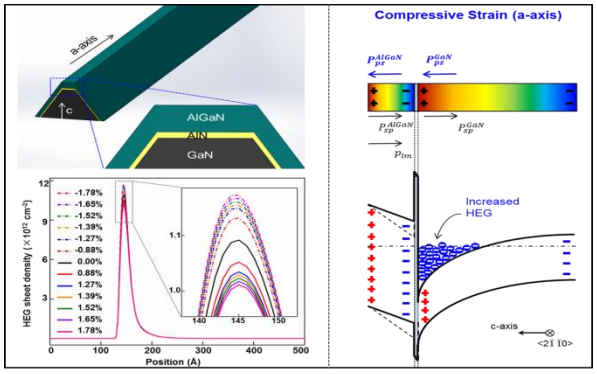

Figure 2. The schematic structure of the AlGaN/AlN/GaN heterostructure microwire, the calculated heterojunction electron gas density as a function of the external strain and the corresponding physical mechanism.

- Enhancing the Efficiency of Silicon-Based Solar Cells by the Piezo-Phototronic Effect

We fabricate a silicon-based nanoheterostructure (p+-Si/p-Si/n+-Si (and n-Si)/n-ZnO nanowire (NW) array) photovoltaic device and demonstrate the enhanced device performance through significantly enhanced light absorption by NW array and effective charge carrier separation by the piezophototronic effect. The strain-induced piezoelectric polarization charges created at n-doped Si-ZnO interfaces can effectively modulate the corresponding band structure and electron gas trapped in the n+-Si/n-ZnO NW nanoheterostructure and thus enhance the transport process of local charge carriers. The efficiency of the solar cell was improved from 8.97% to 9.51% by simply applying a static compress strain. This study indicates that the piezo-phototronic effect can enhance the performance of a large-scale silicon-based solar cell, with great potential for industrial applications.

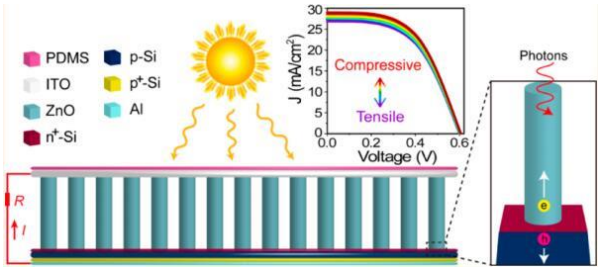

Figure 3. The schematic image of the fabricated Si-based Solar cell with piezoelectric semiconductor ZnO nanowires and experimental data about performances enhancement by the piezo-phototronic effect.

Future Plans

(1) Studying the piezotronic and piezo-phototronic effects at low temperature conditions; focusing on fundamentals of the piezotronic and piezo-phototronic effects in a wide range of semiconductor materials, such as III-Nitride nanowires, 2D materials, perovskites, *et.al;* introducing the piezotronic and piezo-phototronic effects into the emerging material systems for novel devices design.

(2) Exploring the practical applications of the piezotronic and piezo-phototronic effects in integrated nanowire array devices for intelligent mapping and imaging; developing high-performances, high-sensitive active sensor by introducing the piezotronic and piezo-phototronic effects.

References

1. Wang, Z. L.; Song, J. H. *Science* 2006, 312, 242-246.
2. Wang, Z. L. *Adv Mater* 2012, 24, 4632-4646.
3. Wang, Z. L. *Nano Today* 2010, 5, 540-552.
4. Wang, Z. L. *Mrs Bull* 2012, 37, 814-827.

Publications

1. Wang, X., Yu, R., Jiang, C., Hu, W., Wu, W., Ding, Y., Wang, Z. L. (2016). *Advanced Materials*, *28*(33), 7234-7242.

2. Wu, W., Wang, L., Yu, R., Liu, Y., Wei, S. H., Hone, J., & Wang, Z. L. (2016). *Advanced Materials*, *28*(38), 8463-8468.

3. Wang, Z., Yu, R., Wang, X., Wu, W., & Wang, Z. L. (2016). *Advanced Materials*, *28*(32), 6880-6886.

4. Pradel, K. C., Ding, Y., Wu, W., Bando, Y., Fukata, N., & Wang, Z. L. (2016). *ACS applied materials & interfaces*, *8*(7), 4287-4291.

5. Wang, L., Liu, S., Wang, Z., Zhou, Y., Qin, Y., & Wang, Z. L. (2016). *ACS nano*, *10*(2), 2636-2643.

Plasmon-mediated electrochemical reactions: using optical readouts to probe plasmonic nanoparticle activity

Andrew J. Wilson, Padmanabh B. Joshi, Natalia Y. Molina, Katherine A. Willets. Department of Chemistry, Temple University. Philadelphia, PA 19122

Program Scope

This program is focused on understanding how the role of nanoparticle structure impacts plasmon-mediated electrochemical reactions on the surface of nanoparticle electrodes. To do this, optically-active redox probes are used as reporters, which show changes in their emissive properties as their redox state is modulated. The benefit of using optically-active redox probes is that they enable the study of electrochemical reactions at the surface of single nanoparticles, which is extremely challenging using traditional electrochemical readouts. Moreover, by using super-resolution imaging techniques, it is possible to determine regions of local electrochemical activity on the surface of single nanoparticles, allowing the relationships among plasmon excitation, nanoparticle structure, and surface chemistry to be uncovered.

Recent Progress

Recent progress in three distinct areas will be discussed: (i) using surface-enhanced Raman scattering (SERS) from Nile Blue on gold nanoparticle arrays to decouple the role of nanoparticle shape from the impact of plasmon excitation on electrochemical activity, (ii) discriminating nanoparticle electrochemical activity from substrate activity for single molecule electrochemical studies, and (iii) introducing indirect optical reporters for studying non-optically active redox reactions, such as proton reduction. In the first activity, we have shown that the size of gold nanodisk electrodes leads to a shift in the half-wave potential of a Nile Blue probe, using both differential pulse voltammetry (DPV) and surface-enhanced Raman scattering (SERS) as independent readouts (Figure 1). In these experiments, gold nanodisk arrays are fabricated using a polystyrene-polymethylmethacrylate (PS-PMMA) block copolymer as a template. By varying the molecular weight of the polymer, disks of varying size are prepared on a transparent indium tin oxide (ITO) substrate and selectively functionalized with Nile Blue. The intensity of the SERS response of the tethered Nile Blue modulates with the redox state of the probe, with high or low intensity associated with the molecule in the

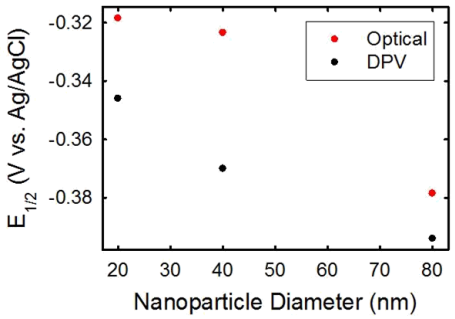

Figure 1. Half-wave potential of Nile Blue as a function of nanodisk size using DPV and SERS.

oxidized or reduced state, respectively.[1,2] From the potential-dependent SERS and DPV response, the half wave potential of Nile Blue is calculated as a function of the size of the gold nanodisk electrode (Figure 1). Two trends appear in the data: (1) the half-wave potential systematically grows more negative as the diameter of the nanoparticle increases and (2) the half-wave potential is more positive for the SERS measurements than the DPV measurements. This latter trend is not observed on smooth gold or ITO electrodes, suggesting that plasmon excitation may be responsible for the observed shift. However, both the SERS and DPV data for these nanoparticle experiments showed a deviation in the tethered Nile Blue electrochemistry relative to Nile Blue bulk solution, with the appearance of two redox peaks and a change in the pH sensitivity of the probe. Systematic investigation revealed that both the chemistry and the length of the linker used to tether the molecule to the surface impacted the (spectro)electrochemistry of the probe.[3,4] With this improved understanding of the redox chemistry of the Nile Blue probe, future directions include resuming studies similar to the work in Figure 1 to map out the relationships among particle size, plasmon excitation, and surface chemistry and their impact on electrochemical reactions.

The second activity involves studying single molecule electrochemical events on single nanoparticle electrodes to further add to our understanding of plasmon-mediated electrochemistry by including information about the role of local nanoparticle structure. For these studies, single nanoparticles are prepared synthetically and drop cast onto ITO-coated coverglass to create a working electrode. Cresyl Violet is used as the redox probe using fluorescence as a readout: similar to Nile Blue, the emission from this molecule is high in its oxidized form and low in its reduced form. By applying an oxidizing potential to the working electrode, single Cresyl Violet oxidation events are observed as bright fluorescent bursts on the surface of the nanoparticle (Figure 2, red arrows). Using super-resolution localization strategies, we can map out where electrochemical events occur on the nanoparticle surface.[1,2] However, one challenge with these studies is background from Cresyl Violet turnover events occurring on the ITO rather than the nanoparticle surface (as shown for gold nanowires on ITO, Figure 2B, top row). These background events can completely obscure Cresyl Violet events on the surface of the nanowire during early times after an oxidizing potential is applied. To address this, several surface passivation strategies have been attempted, including electrografted polymers and phosphonic acid layers, yielding mixed results to date.

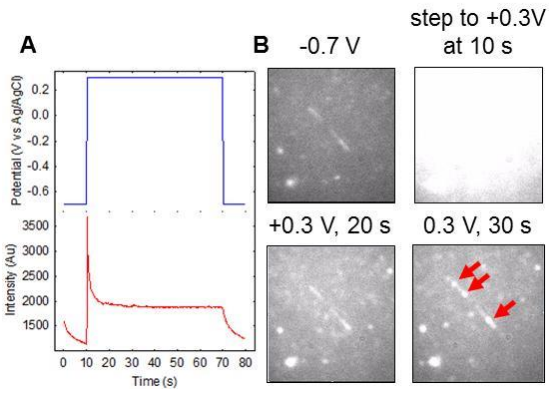

Figure 2. (A) Applied potential waveform and (B) resulting fluorescence images of Cresyl Violet interacting with a gold nanowire/ITO working electrode. Single Cresyl Violet turnover events at the nanowire are indicated by red arrows.

The third activity involves using a non-electroactive probe, fluorescein, to study a non-optically active electrochemical reaction, hydrogen reduction. The strategy enables us to extend our studies from model electrochemical systems to energy-relevant reactions. For this work, fluorescein was chosen as a probe because it is strongly fluorescent at high pH and weakly fluorescent at low pH. Thus, as protons in water are reduced to hydrogen gas at more negative potentials, a local pH increase occurs at the surface of the electrode, yielding a sudden rise in the emission from the fluorescein reporter. Figure 3 shows representative optical response data as well as the corresponding voltammograms for this system as a function of different scan rates and buffer concentrations using gold island films deposited on ITO as the working electrode. Under fast scan rates, the optical response is near linear at low buffer concentrations (Figure 3A), but reaches a saturation intensity under higher buffer concentrations (Figure 3C) that corresponds to the onset potential at which hydrogen production occurs (Figure 3D). For slower scan rates, the optical response shows hysteresis at low buffer concentrations (Figure 3E) and an unexpected loss of intensity at the high buffer concentration (Figure 3G) that corresponds to the onset potential of hydrogen production (Figure 3H). Thus, the conditions under which the experiments are run must be carefully optimized to yield insight into hydrogen reduction with this optical probe.

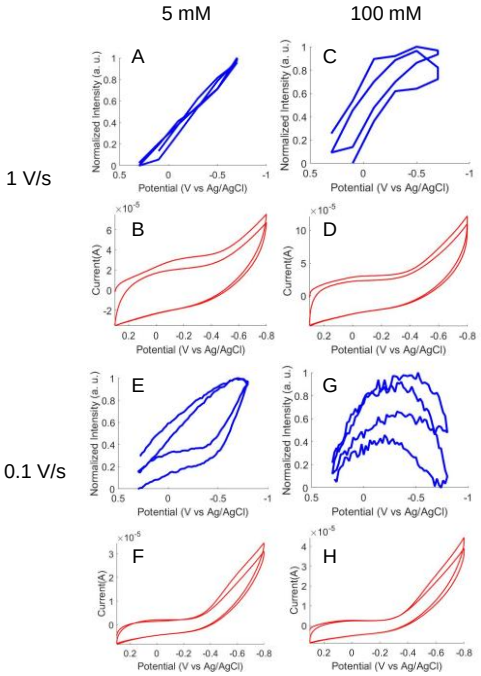

Figure 3. Optical and electrochemical readouts of proton reduction on gold island film substrates as a function of buffer concentration (5 mM vs. 100 mM) and scan rate (1 V/s vs. 0.1 V/s). (Blue traces) Fluorescence intensity response of fluorescein dye as a function of applied potential and thus pH and (red curves) corresponding hydrogen evolution voltammograms. Phosphate buffer, pH = 4. [Dye] = 1 µM.

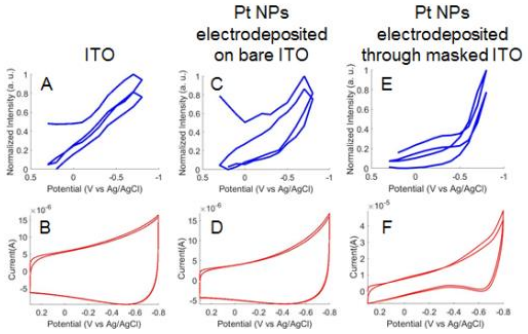

Figure 4. Optical (top row) and electro-chemical (bottom row) response to hydrogen evolution for a series of electrodes. Phosphate buffer, pH = 4, 10 mM. scan rate = 0.5 V/s. [Dye] = 1 µM (A-B), 0.1 µM (C-F).

Similar to the single molecule cresyl violet studies described above, decoupling the response associated with the supporting ITO substrate from the nanostructures is an ongoing challenge. In principle, ITO should have a significant overpotential relative to other materials, such as platinum. Experiments in which platinum nanoparticles are introduced onto ITO show near identical electrochemical and optical responses when compared to bare ITO (Figure 4, A-D),

indicating that the current response is dominated by the substrate. However, we have recently attempted a masking strategy using the PS-PMMA block copolymer templates described above to create voids on the ITO through which platinum is electrodeposited. For these masked substrates, the optical data shows a sharp rise in intensity at the onset potential for hydrogen production as expected (Figure 4E), suggesting that with sufficient passivation of the ITO substrate, this system shows promise for understanding hydrogen evolution using optical readouts.

Future Plans

A significant challenge with the current studies is isolating the electrochemical response due to the plasmonic nanostructures from the electrochemical activity associated with the supporting substrate and remains a focus of future work. For the SERS-active arrays in activity one, we solved this problem by tethering the Nile Blue molecule to the nanoparticle surface, although this affected the electrochemical behavior of the probe. However, we now understand how the tethering impacts the electrochemical response of the Nile Blue and can focus on mapping out the full plasmonic response of this system as a function of plasmon resonance, laser excitation, and even surface chemistry (to recreate synthesized nanostructures). For activity two involving single molecule super-resolution fluorescence imaging of electrochemical turnover events, preliminary data using phosphonic acid as a passivation layer on the ITO support has shown promise and will continue to be optimized using gold nanowires as a model plasmonic electrode, before moving to smaller structures such as nanorods or nanoprisms. For the third activity using indirect optical readouts of non-optically active electrochemical reactions, phosphonic acid surface passivation of the ITO has not yet shown success, so further exploration is required if this system will be useful for studying non-optically active electrochemical reactions.

References

(1) Weber, M. L.; Wilson, A. J.; Willets, K. A. Characterizing the Spatial Dependence of Redox Chemistry on Plasmonic Nanoparticle Electrodes Using Correlated Super-Resolution Surface-Enhanced Raman Scattering Imaging and Electron Microscopy. *J. Phys. Chem. C* **2015**, *119*, 18591-18601.

(2) Wilson, A. J.; Willets, K. A. Visualizing Site-Specific Redox Potentials on the Surface of Plasmonic Nanoparticle Aggregates with Superlocalization SERS Microscopy. *Nano Lett.* **2014**, *14*, 939-945.

(3) Wilson, A. J.; Molina, N. Y.; Willets, K. A. Modification of the Electrochemical Properties of Nile Blue through Covalent Attachment to Gold As Revealed by Electrochemistry and SERS. *J. Phys. Chem. C* **2016**, *120*, 21091-21098.

(4) Wilson, A. J.; Willets, K. A. Unforeseen distance-dependent SERS spectroelectrochemistry from surface-tethered Nile Blue: the role of molecular orientation. *Analyst (Cambridge, U. K.)* **2016**, *141*, 5144-5151.

Publications

K.A. Willets, A.J. Wilson, V.Sundaresan, P.B. Joshi. “Super-resolution imaging and plasmonics.” *Chem. Rev.* DOI: 10.1021/acs.chemrev.6b00547. (2017)

A.J. Wilson, N.Y. Molina, K.A. Willets. “Modification of the electrochemical properties of Nile Blue through covalent attachment to gold as revealed by electrochemistry and SERS.” *J. Phys. Chem. C*. 120, 21091 (2016).

B. Xu, H. Li, H. Li, A.J. Wilson, L. Zhang, K. Chen, K.A. Willets, F. Ren, J. Grossman, S. Ren. “Chemically driven interfacial coupling in charge-transfer mediated functional superstructures.” *Nano Letters*. 16, 2851 (2016)

B. Xu, Z. Luo, W. Gao, A.J. Wilson, C. He, X. Chen, G. Yuan, H.L. Dai, Y. Rao, K.A. Willets, Z. Dauter, S. Ren. “Solution-processed molecular opto-ferroic crystals.” *Chemistry of Materials*. 28, 2441 (2016).

B. Xu, Z. Luo, A.J. Wilson, K. Chen, W. Gao, G. Yuan, H.D. Chopra, X. Chen, K.A. Willets, Z. Dauter, S. Ren. “Multifunctional charge-transfer single crystals through supramolecular assembly." *Advanced Materials*. 28, 5322 (2016).

A.J. Wilson and K.A. Willets. “Molecular plasmonics.” Invited review. *Annual Reviews of Analytical Chemistry*. 9, 27 (2016).

A.J. Wilson, K. Marchuk, K.A. Willets. “Imaging electrogenerated chemiluminescence at single gold nanowire electrodes.” *Nano Lett*. 15, 6100 (2015).

M.L. Weber, A.J. Wilson, K.A. Willets. “Characterizing the spatial dependence of redox chemistry on plasmonic nanoparticle electrodes using correlated super-resolution surface-enhanced Raman scattering imaging and electron microscopy.” *J. Phys. Chem. C.* 119, 18591 (2015).

Interfacial Design for Aqueous Photoelectrochemical Cells and Solar Flow Batteries

Yiying Wu, The Ohio State University

Program Scope

Solid-electrolyte interfaces play crucial roles in controlling interfacial charge transfer and electrode stability, and represent one of the "transformative opportunities" as described in "Challenges at the Frontiers of Matter and Energy: Transformative Opportunities for Discovery Science", a DOE report from the Basic Energy Sciences Advisory Committee in 2015. The central theme of this project is to design amphiphilic interfacial molecules that form bilayer protection on semiconductor surfaces in aqueous solutions: an inner hydrophobic layer that prevents water from penetration and an outer layer that maintains the wetting of the electrode surface). The central theme of this renewal proposal is to design amphiphilic push-pull dyes that form bilayer protection on semiconductor surfaces in aqueous solutions: an inner hydrophobic layer that prevents water from penetration and an outer layer that maintains the wetting of the electrode surface. The push-pull design also promotes efficient vectorial electron transfer at the electrode/electrolyte interfaces. This project will focus on aqueous electrolytes, especially in strongly acidic conditions due to the relevance in solar water splitting and flow batteries.

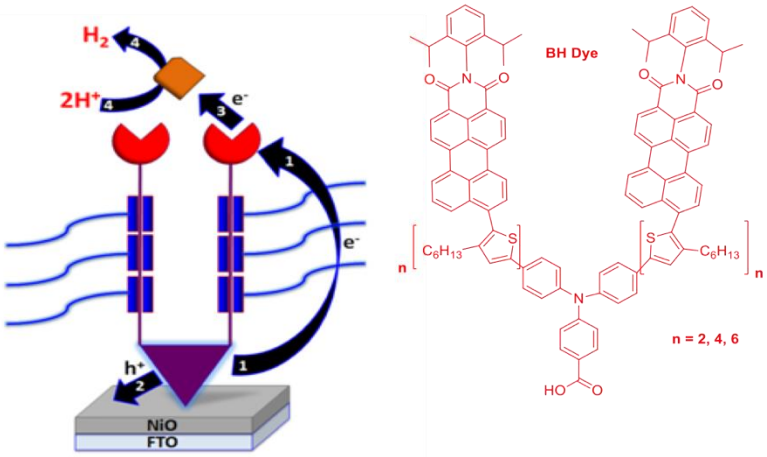

Schematic bilayer dye design that protects NiO from acid etching (left) and the molecular structure of the BH dyes (right)

Recent Progress

Oxide semiconductors display a Nernstian pH dependence on their flat band potentials due to surface protonation. We proposed that the BH4 dye's hydrophobic/hydrophilic properties induce a self-assembled structure similar to that of lipid bilayer membranes on the NiO surface therefore preventing both dye desorption and semiconductor degradation in aqueous electrolytes (see figure). In order to confirm the protection strategy and self-assembly of our bilayer dye design, the semiconductor-dye-electrolyte interface was probed by determining the flat-band potential dependence on pH of NiO films with and without our BH4 dye using Mott-Schottky

plots. The BH4 sensitized NiO film showed a constant flat band potential of 0.86 ± 0.03 V vs NHE between pH 1 – 5, while the bare showed a 62 mV/pH shift in the flat-band potential indicating that the P1 sensitized NiO films have open sites for proton adsorption. The results confirm the unique protection strategy of our membrane mimicking BH4 dye. The interfacial electron transfer kinetics between the BH dyes and NiO has also been probed by transient absorption (TA) spectroscopy. The photo-excited BH dye molecule is found to have ~10ps(~200ps) lifetimes in solution. The study of the dye-sensitized NiO samples exhibits that the subsequent fast hole injection undergoes within tens of picoseconds. The recombination between the reduced dye and electrode spans from hundreds of picoseconds to tens of microseconds. In addition, the synthesis of a new amphiphilic dye, incorporating hydrophilicity into a previously reported hydrophobic BH dye via the addition of multiple polyethylene glycol (PEG) chains is in good progress.

Future Plans

The first task is to complete the synthesis of amphiphilic dyes by adding hydrophilic PEG functional groups to the PMI unit and fully characterize dye/NiO interfaces and interfacial charge transfer. In addition, p-type wide-bandgap semiconductors with good transparency and high hole mobility such as CuI and CuSCN will be explored to replace NiO. The dye anchoring on CuI and CuSCN will be investigated, and the charge carrier dynamics at the semiconductor/dye/electrolyte interface will be measured.

Publications

1. Z. Huang, M. He, M. Yu, K. Click, D. Beauchamp, Y. Wu, "Dye-Controlled Interfacial Electron Transfer for High-Current Indium Tin Oxide Photocathodes", *Angew. Chem.*, 127, no. 23 (2015): 6961 – 6965.
2. Draskovic, Thomas; Yu, Mingzhe; Wu, Yiying. "2H-CuScO2 Prepared by Low Temperature Hydrothermal Methods and Post-Annealing Effects on Optical and Photoelectrochemical Properties", *Inorganic Chemistry,* 54, no. 11 (2015): 5519 - 5526.
3. M. Yu, W. D. McCulloch, D. R. Beauchamp, Z. Huang, X. Ren, Y. Wu, "Aqueous Lithium-Iodine Solar Flow Battery for the Simultaneous Conversion and Storage of Solar Energy", *J. Am. Chem. Soc.*, 137, no. 26 (2015): 8332 – 8335.
4. Huang, Z., Luo, W., Ma, L., Yu, M., Ren, X., He, M., Polen, S., Click, K., Garrett, B., Lu, J., Amine, K., Hadad, C., Chen, W., Asthagiri, A. and Wu, Y. , "Dimeric [Mo2S12]2− Cluster: A Molecular Analogue of MoS2 Edges for Superior Hydrogen-Evolution Electrocatalysis", *Angew. Chem.*, 127, no. 50 (2015): 15396 – 15400.
5. B.R. Garrett, A. Awad, M. He, K.A. Click, C.B. Durr, J.C. Gallucci, C.M. Hadad, Y. Wu "Dimeric FeFe-Hydrogenase Mimics Bearing Carboxylic Acids: Synthesis and Electrochemical Investigation", *Polyhedron*, 103 (2016): 21 – 27.

6. Mingzhe Yu, William David McCulloch, Zhongjie Huang, Brittany B Trang, Jun Lu, Khalil Amine and Yiying Wu, “Solar-Powered Electrochemical Energy Storage: an Alternative to Solar Fuels”, *J. Mater. Chem. A*, 2016, 4, 2766-2782.
7. Kevin A. Click, Damian R. Beauchamp, Zhongjie Huang, Weilin Chen, and Yiying Wu, “Membrane-Inspired Acidically Stable Dye-Sensitized Photocathode for Solar Fuel Production”, *J. Am. Chem. Soc.*, 2016, *138* (4), pp 1174–1179.
8. William D. McCulloch, Mingzhe Yu, and Yiying Wu, “pH-Tuning a Solar Redox Flow Battery for Integrated Energy Conversion and Storage“, *ACS Energy Letters.* 2016, *1* (3), pp 578–582.
9. Click, Kevin; Schockman, Bradley; Dilenschneider, Justin; McCulloch, William; Garrett, Benjamin; Yu, Yongze; He, Mingfu; Curtze, Allison; Wu, Yiying "Bilayer Dye Protected Aqueous Photocathodes for Tandem Dye Sensitized Solar Cells", *J. Phys. Chem. C*, 2017 accepted.

Enhancement of spin-lattice coupling in nanoengineered oxide films and heterostructures by laser MBE

Xiaoxing Xi, Department of Physics, Temple University, Philadelphia, PA 19122

Program Scope

The objective of the proposed research is to investigate nanoengineered oxide films and heterostructures that are predicted to show desirable physical properties. The main focus of the project is short-period superlattices grown by atomic layer-by-layer laser MBE from separate oxide targets (for example, growing $SrTiO_3$ from SrO and TiO_2 targets). The atomic layer-by-layer mode of the laser MBE growth is superior to the conventional laser MBE in broadening the thermodynamic space for the synthesis of short-period superlattices and new designer materials.

Recent Progress

1. Atomic Layer-by-Layer Laser MBE

The principle of ALL-Laser MBE is schematically illustrated in Fig. 1A. Separate oxide targets are used – instead of using a compound target of $SrTiO_3$, targets of SrO and TiO_2 are switched back and forth as they are alternately ablated by a UV laser beam. In conventional PLD or laser MBE using a compound target, all elements are ablated at once and the film grows unit cell by unit cell. In ALL-Laser MBE using separate targets, on the other hand, the film is constructed one atomic layer at a time.

Figure 1B shows the RHEED intensity oscillations as the targets of SrO and TiO_2 are alternately ablated. When Sr/Ti > 1 the peak intensity increases and a "double" peak appears. When Sr/Ti < 1 the peak intensity decreases. When Sr/Ti = 1 the intensity and shape of the oscillation peaks are constant. Furthermore, insufficient or excess pulses in each cycle cause RHEED intensity beating (Fig. 1C) while it remains constant for 100% layer coverage (Fig. 1D).

ALL-Laser MBE is versatile: it works for non-polar film on non-polar substrate (homoepitaxy of $SrTiO_3$), polar film on polar substrate ($La_5Ni_4O_{13}$ on $LaAlO_3$), and polar film on non-polar substrate ($LaAlO_3$ on $SrTiO_3$). It allows one to push the thermodynamic boundary further in stabilizing new phases than reactive MBE and PLD. For example, $La_5Ni_4O_{13}$, the Ruddlesden-Popper phase with n = 4, has never been reported in the literature because

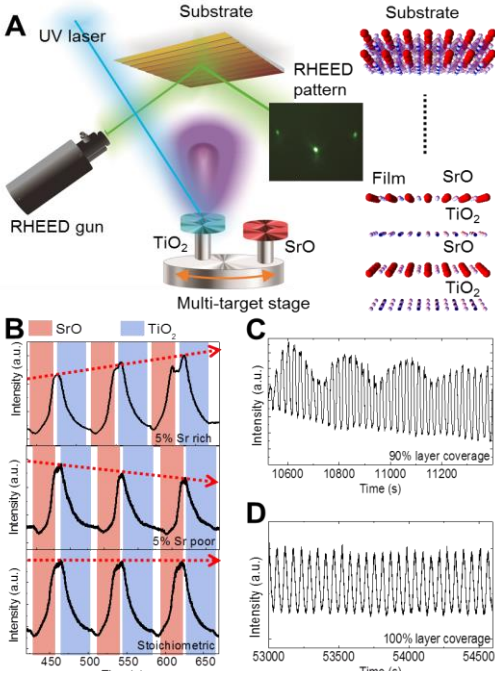

Figure 1 (**A**) Schematic of ALL-Laser MBE. (**B**) RHEED diffracted spot intensity during the atomic layer-by-layer growth of $SrTiO_3$ films for the cases of Sr-rich, Sr-poor, and stoichiometric deposition, respectively. (**C**) RHEED intensity beating when 0.9 monolayers of SrO and TiO_2 are deposited during each target switching cycle. (**D**) RHEED intensity oscillations for a stoichiometric sample with full layer coverage.

it needs atomic layer-by-layer growth at high oxygen pressures, not possible with other growth techniques. ALL-Laser MBE makes it possible.

2. Mechanism of the 2D Electron Gas at $LaAlO_3/SrTiO_3$ Interface

Since the discovery of the interfacial 2D electron gas in the $LaAlO_3/SrTiO_3$ system,[1] its mechanism has been a subject of controversy. According to the electronic reconstruction mechanism, because the atomic layers are charge neutral in $SrTiO_3$ but charged in $LaAlO_3$, a positive diverging electric potential is built up in a $LaAlO_3$ film grown on a TiO_2-terminated $SrTiO_3$ substrate. This leads to the transfer of half of an electron from the $LaAlO_3$ film surface to $SrTiO_3$ when the $LaAlO_3$ layer is thicker than 4 unit cells, creating a 2D electron gas at the interface with a sheet carrier density of $3.3\times10^{14}/cm^2$ for sufficiently thick $LaAlO_3$.[2] A serious inconsistency with this mechanism is that the carrier densities reported experimentally are invariably lower than the expected value[2] except under conditions where reduction of $SrTiO_3$ substrate is suspected.[3] Oxygen vacancies in $SrTiO_3$ are known to contribute to conductivity, but all reported conducting $LaAlO_3/SrTiO_3$ interfaces have been grown at low oxygen pressures (< 10 mTorr), and annealing in oxygen is often required; higher oxygen pressures during the PLD growth result in insulating samples or 3D island growth.[4]

Because we grow the $LaAlO_3$ film one atomic layer at a time, we were able to grow conducting $LaAlO_3/SrTiO_3$ interfaces at a high oxygen pressure with ALL-Laser MBE. Starting from a TiO_2-terminated $SrTiO_3$ substrate, we grew 10 unit-cell-thick $LaAlO_3$ films by alternately ablating La_2O_3 and Al_2O_3 targets under an oxygen pressure of 37 mTorr. Furthermore, we grew $LaAlO_3$ films of different cation stoichiometry, $LaAl_{1+y}O_{3(1+0.5y)}$, by varying the number of laser pulses on the Al_2O_3 target. The RHEED intensity oscillations during the growth of a stoichiometric film are shown in Fig. 2A. The RHEED intensity remain close to the substrate level throughout the growth. The 2D growth was also confirmed by the sharp RHEED spots in Fig. 2B for the 10 unit-cell film. The AFM image for the film in Fig. 2C shows an atomically flat surface.

The high oxygen pressure helps to prevent the possible oxygen reduction in $SrTiO_3$, ensure that the $LaAlO_3$ films are sufficiently oxygenated. Figure 2D shows x-ray absorption spectroscopy (XAS) spectra with different linear polarizations and the Ti $L_{2,3}$ x-ray linear dichroism (XLD) signals are shown in Fig. 2E for different $LaAl_{1+y}O_{3(1+0.5y)}$ stoichiometry. No Ti^{3+} related features around 462 eV, which have been linked to oxygen deficiency,[6] are observed. Rather, the spectra are similar to the fully oxygenated samples.[6] Figure 2F shows the Ti $L_{2,3}$ x-ray magnetic circular dichroism (XMCD) signals obtained from opposite circularly polarized XAS spectra. Very small XMCD signals were observed, consistent with the fully oxygen annealed samples and very weak ferromagnetism.[6]

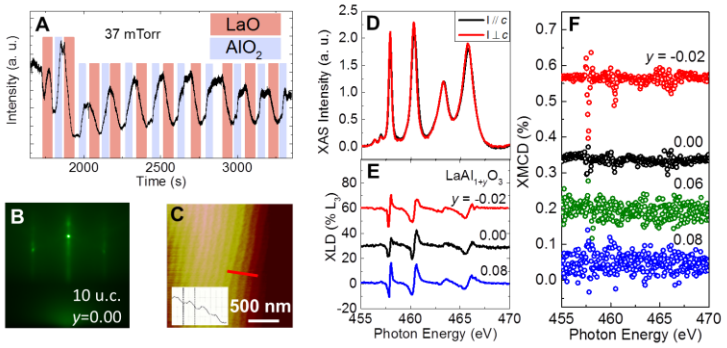

Figure 2 (**A**) RHEED intensity oscillation during the growth of a $LaAlO_3$ film on a $SrTiO_3$ substrate at an oxygen pressure of 37 mTorr. (**B**) RHEED pattern after the growth of a 10 unit-cell stoichiometric $LaAlO_3$ film. (**C**) AFM topographic images of the 10 unit-cell $LaAlO_3$ film on $SrTiO_3$. (**D**) Ti XAS spectra for a 10 unit-cell stoichiometric $LaAlO_3$ film. (**E**) Ti $L_{2,3}$-edges XLD spectra for 3 $LaAl_{1+y}O_{3(1+0.5y)}/SrTiO_3$ samples with y = -0.02, 0.00, and 0.08. (**F**) XMCD for 4 $LaAl_{1+y}O_{3(1+0.5y)}$ films with y = -0.02, 0.00, 0.06, and 0.08.

In $LaAl_{1+y}O_{3(1+0.5y)}$, either Al vacancies or La vacancies in the off-stoichiometric films lead to oxygen vacancies in order to keep the charge neutrality.[5] As a result, the charge on the $[LaO_{1+y}]$ layer is $+(1-2y)$ and on the $[Al_{1+y}O_{2+0.5y}]$ layer is $-(1-2y)$. In the electronic reconstruction picture, instead of the charge transfer of half of an electron in the case of stoichiometric $LaAlO_3$, $(0.5-y)$ electrons will be transferred to resolve the polar discontinuity at the interface. The sheet carrier density depends linearly on y, *i.e.* $n_s = (1-2y)\times 3.3\times 10^{14}/cm^2$ for sufficiently thick $LaAlO_3$.[5] For the 10 unit-cell $LaAlO_3$ films used in this work, the dependence becomes $n_s = (1-2y)\times 3.3\times 10^{14}/cm^2 - 1.6\times 10^{14}/cm^2 = (1.7-2y\times 3.3)\times 10^{14}/cm^2$.[2]

The temperature and stoichiometry dependences of the sheet resistance, sheet carrier density, and mobility are shown in Fig. 3A-F, respectively, for the 10 unit-cell $LaAl_{1+y}O_{3(1+0.5y)}$ films. All of the films are conducting with sheet resistance around 10^4 Ω/□ at 300 K. The low temperature upturn has $-\ln T$ dependence characteristic of the Kondo effect. This may be attributed to the inevitable defects at the $LaAlO_3/SrTiO_3$ interface, consistent with the weak magnetism shown by Fig. 2F. The sheet carrier density is around $10^{14}/cm^2$ for all the samples, close to the expected value of $1.7\times 10^{14}/cm^2$.

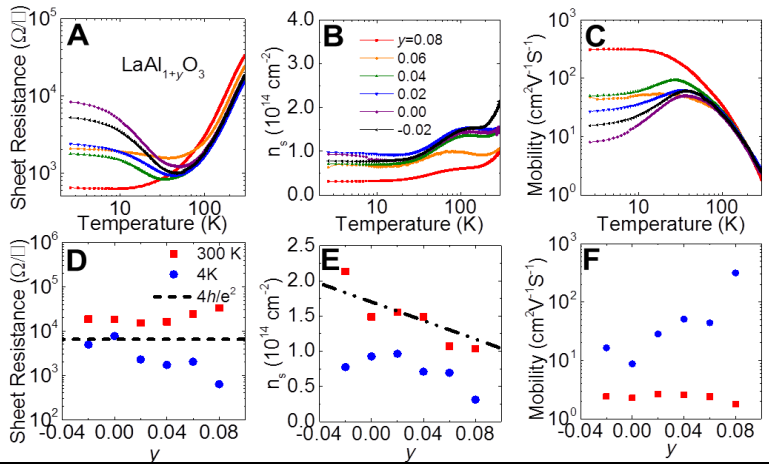

Figure 3 (**A**) Sheet resistance, (**B**) carrier density, and (**C**) Hall mobility as functions of temperature for a series of 10 unit-cell $LaAl_{1+y}O_{3(1+0.5y)}$ films. (**D**) Sheet resistance, (**E**) sheet carrier density, and (**F**) Hall mobility as functions of film stoichiometry at 300 K (red squares) and 4 K (blue dots). The dashed line in (**D**) is the quantum resistance limit $h/4e^2$. The dashed line in (**E**) indicates the theoretical value of sheet carrier density for 10 unit-cell films with different stoichiometry under the assumption of pure electronic reconstruction.[2]

The central result of our work is the dependence of sheet carrier density on the stoichiometry of $LaAl_{1+y}O_{3(1+0.5y)}$ shown in Fig. 3E. The black dashed line represents $n_s = (1.7-2y\times 3.3)\times 10^{14}/cm^2$, which is expected by the electronic reconstruction hypothesis for the 10 unit-cell films.[2] The red squares, which denote 300 K sheet carrier density, overlap with the dashed line. No additional mechanism is employed to explain our data. The quantitative agreement between our experimental result and the theoretical prediction provides a strong support to the electronic reconstruction mechanism. The key differences between our result and the previous reports are the high oxygen pressure during the film growth and the high film crystallinity. The high oxygen pressure suppresses the likelihood of oxygen vacancies in $SrTiO_3$. Well oxygenated samples produced during film growth can avoid possible defects when sufficient oxygen is provided only after the growth by annealing.

3. Strain-Engineered Oxygen Vacancies in $CaMnO_3$ Thin Films

Using ALL-Laser MBE, we synthesized high-quality singlec-rystalline $CaMnO_3$ films with systematically varying oxygen vacancy defect formation energies as controlled by coherent tensile strain. The systematic increase of the oxygen vacancy content in $CaMnO_3$ as a function of applied

in-plane strain is observed and confirmed experimentally using high-resolution soft x-ray XAS in conjunction with bulk-sensitive hard x-ray photoemission spectroscopy (HAXPES). The relevant defect states in the densities of states are identified and the vacancy content in the films quantified using the combination of first-principles theory and core−hole multiplet calculations with holistic fitting. The strain-induced oxygen-vacancy formation and ordering are a promising avenue for designing and controlling new functionalities in complex transition-metal oxides.

Future Plans

The project has ended. Future funding will be sought to continue the research in oxide heterostructures using ALL-Laser MBE.

References

1. Hwang, H. Y. *et al*. Emergent phenomena at oxide interfaces. *Nature Mater.* 11, 103-113 (2012).
2. Cancellieri, C. *et al*. Electrostriction at the $LaAlO_3/SrTiO_3$ interface. *Phys. Rev. Lett.* **107**, 056102 (2011).
3. Siemons, W. *et al*. Origin of charge density at $LaAlO_3$ on $SrTiO_3$ heterointerfaces: possibility of intrinsic doping. *Phys. Rev. Lett.* **98**, 196802 (2007).
4. Ariando *et al*. Electronic phase separation at the $LaAlO_3/SrTiO_3$ interface. *Nat. Commun.* **2**,188 (2011).
5. Sato, H. K., Bell, C., Hikita, Y. & Hwang, H. Y. Stoichiometry control of the electronic properties of the $LaAlO_3/SrTiO_3$ heterointerface. *Appl. Phys. Lett.* 102, 251602 (2013).
6. Salluzzo, M. *et al*. Origin of interface magnetism in $BiMnO_3/SrTiO_3$ and $LaAlO_3/SrTiO_3$ heterostructures. *Phys. Rev. Lett.* **111**, 087204 (2013).

Publications

1. Guozhen Liu, Qingyu Lei, Matthäus A. Wolak, Qun Li, Long-Qing Chen, Christopher Winkler, Jennifer Sloppy, Mitra L. Taheri, and Xiaoxing Xi, Epitaxial strain and its relaxation at the $LaAlO_3/SrTiO_3$ interface, J. Appl. Phys. 120, 085302 (2016).
2. Ravini U. Chandrasena, Weibing Yang, Qingyu Lei, Mario U. Delgado-Jaime, Kanishka D. Wijesekara, Maryam Golalikhani, Bruce A. Davidson, Elke Arenholz, Keisuke Kobayashi, Masaaki Kobata, Frank M. F. de Groot, Ulrich Aschauer, Nicola A. Spaldin, Xiaoxing Xi,and Alexander X. Gray, Strain-Engineered Oxygen Vacancies in $CaMnO_3$ Thin Films, Nano Lett. 17, 794 (2017).
3. Qingyu Lei, Maryam Golalikhani, Bruce A. Davidson, Guozhen Liu, Darrell G. Schlom, Qiao Qiao, Yimei Zhu, Ravini U. Chandrasena, Weibing Yang, Alexander X. Gray, Elke Arenholz, Andrew K. Farrar, Dmitri A. Tenne, Minhui Hu, Jiandong Guo, Rakesh K Singh, X. X. Xi, Constructing oxide interfaces and heterostructures by atomic layer-by-layer laser molecular beam epitaxy, npj Quant. Mater. 2, 10 (2017).

Electronics without Semiconductors by Functionalized Boron Nitride Nanotubes

Yoke Khin Yap

Department of Physics, Michigan Technological University, 1400 Townsend Drive, Houghton, MI 49931, USA.

Program Scope

The far reaching goal of this research project is to experimentally investigate single walled (SW) heterojunctions of boron nitride nanotubes and carbon nanotubes (BNNT/CNT junctions) with specific zigzag, armchair, or chiral structures. According to theory, [1-4]

- Zigzag BNNT/CNT junctions (Figure1a) are insulator/semiconductor junctions. They have flat band structures and tunable direct band gaps (~0.5 to 2.0 eV) at the interface. Thus these BNNTs/CNTs junctions can be used as nanoferromagnetic materials, spintronic and tunable photonic devices etc..
- Armchair BNNT/CNT junctions (Figure 1b) are insulator/semimetal junctions with tunable direct band gap, and applicable for Schottky devices, quantum dots, etc..

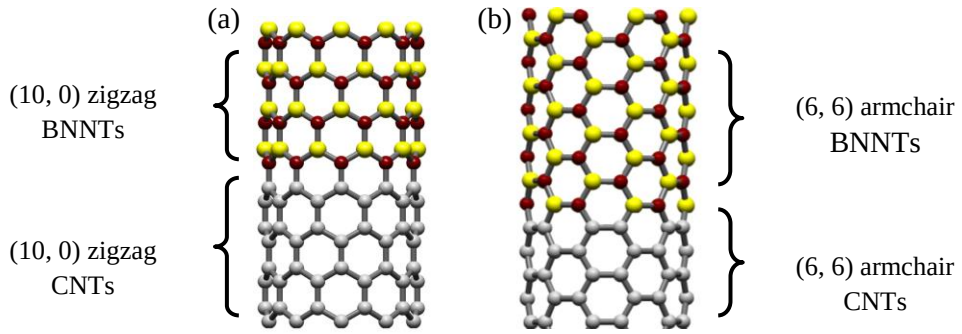

Figure 1. Ball-and-stick representations of (a) a zigzag (10, 0) and (b) an armchair (6,6) BNNT/CNT junctions.

This ultimate goal is currently not realistic because the science and engineering on chirality controls of both BNNTs and CNTs are not well established. In particular, technology to grow SW-BNNTs is still not fully achievable in the field.

Instead, the **major objectives of the current project are** to

1) Understand the science behind the synthesis of co-axial multiwalled (MW) BNNT/CNT junctions.
2) Investigate the novel physical properties of BNNT/CNT junctions, and their precursors that we have discovered during the pass funding period, including a) branching BNNT/CNT junctions, b) graphene-BNNT junctions, and c) quantum-dots functionalized BNNTs (QDs-BNNTs).

Recent Progress

BNNT/CNT Heterojunctions

We have continue the study of branching BNNT/CNT heterojunctions. Results suggested that branching BNNT/CNT junctions are insulator-semimetal junctions applicable as Schottky switches with non-linear current-voltage (I-V) behaviors. Unfortunately, we can did not detect gate effect on branching junctions. We believe that this is due to the presence of Fe catalyst particles at the junctions, which causes shielding effect of the applied gate potential. Therefore, we have devoted our efforts into the formation of coaxial BNNT/CNT junctions without using catalyst particles. As shown in Figure 2, co-axial BNNT/CNT junctions are formed. Further optimization is needed to improve the synthesis yield before we proceed for the characterization of their electronic properties.

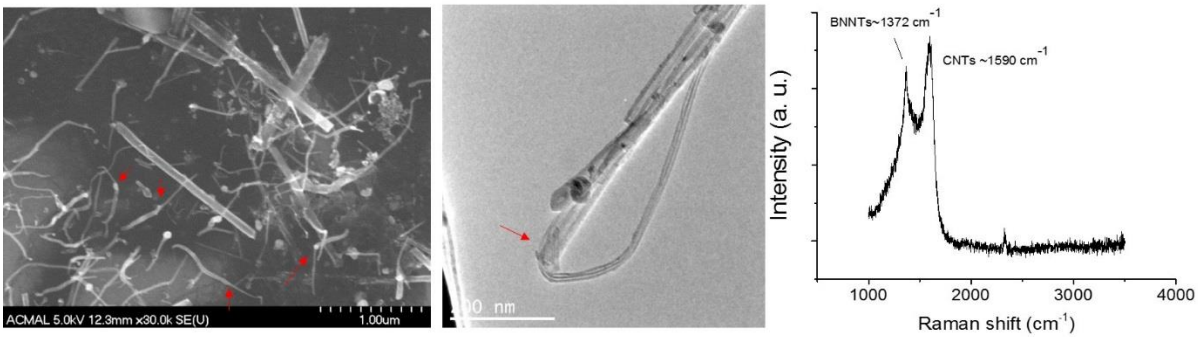

Figure 2. SEM and TEM images of co-axial BNNT/CNT junctions and the Raman spectra.

Electronics without Semiconductor by QDs-BNNTs

During the course of investigating the branching BNNT/CNT junctions, we have discovered a new class of functional materials: quantum-dots functionalized BNNTs (QDs-BNNTs).[5] These QDs-BNNTs consist of crystalized gold NPs on one side of the BNNTs. At low bias voltages, this QDs-BNNT is insulating. By applying increasing bias voltages, this QDs-BNNT allowed current to flow

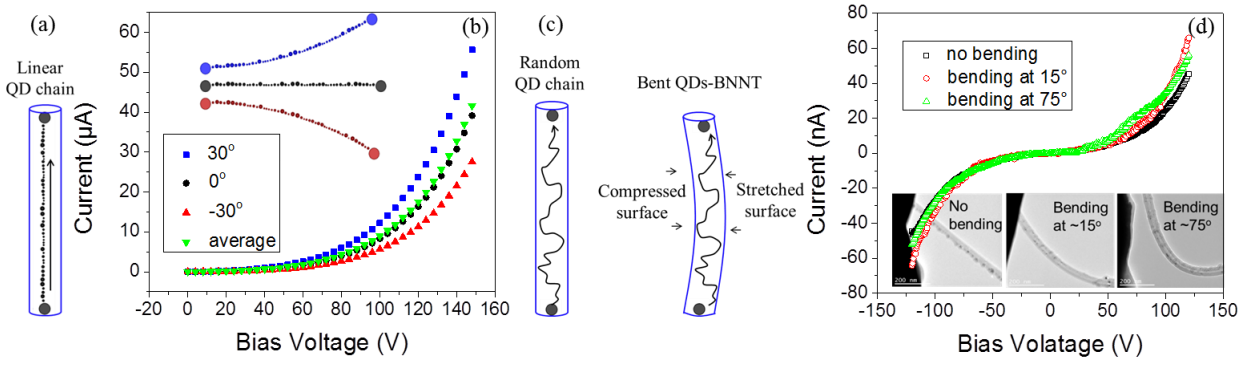

Figure 3. (a) Tunneling current on a QDs-BNNT with linear QD chain, and (b) the simulated I-V characteristic at various bending angle. (c) Tunneling current on a QDs-BNNT with randomized QD chain, and (d) the experimental I-V characteristic at various bending angle.

due to electron tunneling across the QDs. These tunneling field effect transistors (T-FETs) represent a new class of electronic switches with the use of any semiconducting property.

More recently, we reported on the switching behavior of QDs-BNNTs in flexible electronics. As shown in Figure 2a, tunneling current would confine along the path of the linear QD chain. The I-V behaviors of such QDs-BNNTs would be sensitive to the bending of the nanotubes as simulated and shown in Figure 2b. This is due to the change in the distance between QDs upon tensile or compressive stress. This is different for a QDs-BNNT with randomized QDs as shown in Figure 2c. Here the path of tunneling current is nonlinear, follow the path of QDs that has smallest QD gaps (minimum tunneling resistance and tunneling junction width). Statistically, this current path will be equally affected by bending at both the compressed and the stretched surfaces. While the current flow will be enhanced at the compressed surface but will be compensated by the degradation occurred at the stretched surface. This averaging effect led to I-V behaviors that is not sensitive to bending as experimentally proven (Figure 2d).

Better understanding on T-FETs based on QDs-BNNTs

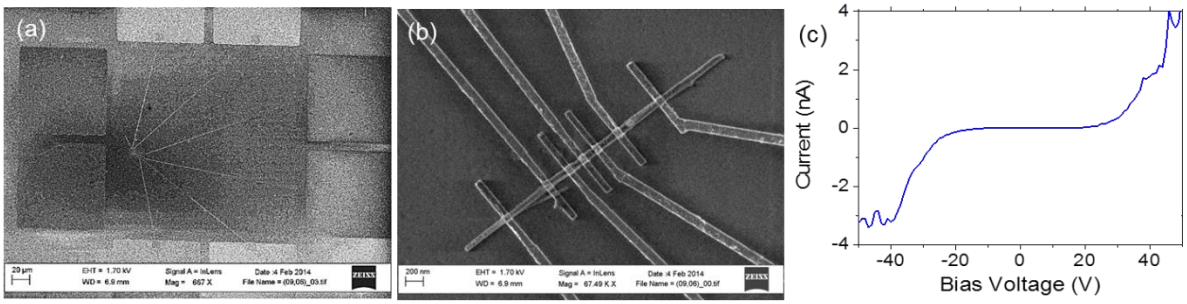

Figure 4. SEM images of the T-FET device and the typical I-V characteristic.

We have attempted to fabricate T-FETs with thinner gate oxide (150nm of HfO_2). As shown in Figure 4a, a QDs-BNNT is connected with a series of seven electrode leads to the surrounding microelectrode pads. The distance between two leads is ~100nm to 500nm (Figure 4b). Unfortunately, these switches shown low tunneling current (a few nA) and high threshold potential (~25V, Figure 4c). Further evaluation indicates that some of the distances between QDs are larger than 10nm and are not uniform. This is due to the fact that we used scanning electron microscopy (SEM) to judge the gaps of QDs when we optimize the synthesis of QDs-BNNTs. The resolution of SEM did not allow us to identify the better synthesis condition for QDs with smaller gap (negative fault signal).

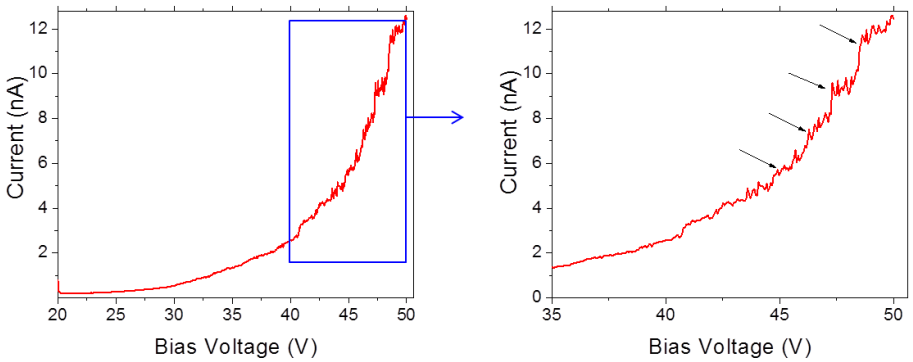

Figure 5. I-V characteristic of QDs-BNNTs detected at T=8.8K.

Therefore, we have switch our study to optimize the synthesis of QDs-BNNTs based on size evaluation of transmission electron microscopy (TEM)

Coulomb Staircase Detection

As suggested by our simulation, T-FETs fabricated by QDs-BNNTs are single electron transistors. To verify this, 4-probe scanning tunneling microscopy (STM) was used to perform *I-V* measurement on QDs-BNNTs at liquid He temperatures. As shown in Figure 5, the evidence of Coulomb staircase is detected near the threshold potential at T=8.8K. Again, the threshold potential is large for this series of tested samples.

Improve Uniformity of QDs-BNNTs

By using TEM imaging, we have further improved the uniformity of QDs on BNNTs as shown in Figure 6. As shown, QDs with diameter <10nm, spacing between QDs ~2-4nm can be deposited at one side of the BNNTs at a length scale of >1 μm. We are now preparing a series of these "optimized" QDs-BNNTs such that devices can be fabricated. Unfortunately, we are still struggling to make more devices due to the failure of electron beam deposition and lift-off issues during the lithography processes.

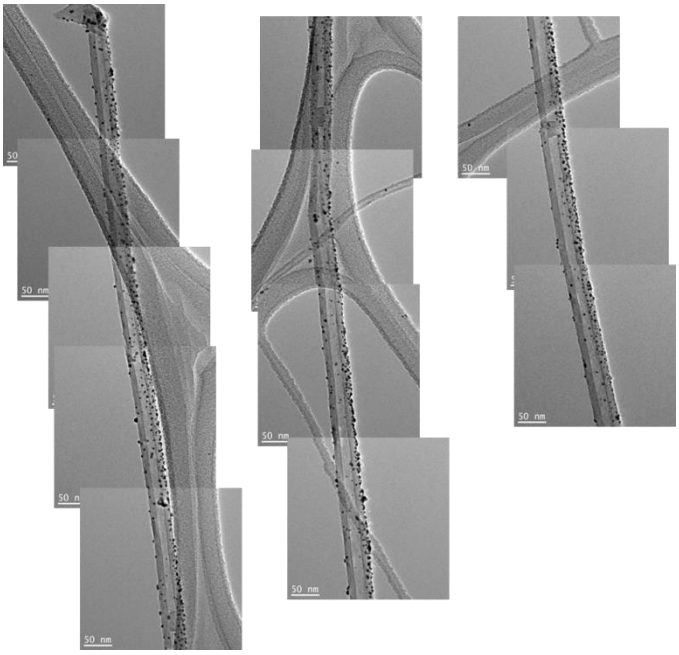

Figure 6. TEM images of uniform QDs deposited on BNNTs.

Future Plans

We have successfully synthesized co-axial BNNT/CNT junctions. However, there is still a mismatch between the diameters of BNNTs (~20-50nm) and CNTs (~8-15nm). Therefore, this will need to be addressed before we can achieve high-yield synthesis and characterization of their electronic properties. By using the refined approach, we are now able to synthesized QDs-BNNTs with more uniform QD sizes and gaps. We are now attempting to fabricate more devices base on QDs-BNNTs, in collaboration with the Center for Nanophase Materials Sciences (CNMS) in Oak Ridge National Laboratory. These devices will then be investigated for their plasmonic effects.

References

1 Blase, X., Charlier, J. C., DeVita, A. & Car, R. Theory of composite BxCyNz nanotube heterojunctions. *Appl Phys Lett* **70**, 197-199 (1997).

2 Okada, S., Igami, M., Nakada, K. & Oshiyama, A. Border states in heterosheets with hexagonal symmetry. *Phys Rev B* **62**, 9896-9899 (2000).

3 Okada, S. & Oshiyama, A. Magnetic ordering in hexagonally bonded sheets with first-row elements. *Phys Rev Lett* **87**, 146803 (2001).
4 Choi, J., Kim, Y. H., Chang, K. J. & Tomanek, D. Itinerant ferromagnetism in heterostructured C/BN nanotubes. *Phys Rev B* **67**, 125421 (2003).
5 Lee, C. H., Qin, S. Y., Savaikar, M. A., Wang, J. S., Hao, B. Y., Zhang, D. Y., Banyai, D., Jaszczak, J. A., Clark, K. W., Idrobo, J. C., Li, A. P. & Yap, Y. K. Room-Temperature Tunneling Behavior of Boron Nitride Nanotubes Functionalized with Gold Quantum Dots. *Adv Mater* **25**, 4544-4548 (2013).

Publications

1. Vyom Parashar, Corentin P. Durand, Boyi Hao, Rodrigo G. Amorim, Ravindra Pandey, Bishnu Tiwari, Dongyan Zhang, Yang Liu, An-Ping Li and Yoke Khin Yap, "Switching Behaviors of Graphene-Boron Nitride Nanotube Heterojunctions," *Scientific Reports* **5**, Article number: 12238 (2015) doi:10.1038/srep12238.
2. Boyi Hao, Anjana Asthana, Paniz Khanmohammadi Hazaveh, Paul L. Bergstrom, Douglas Banyai, Madhusudan A. Savaikar, John A. Jaszczak, and Yoke Khin Yap, "New Flexible Channels for Room Temperature Tunneling Field Effect Transistors," *Scientific Reports* **6**, 20293; doi: 10.1038/srep20293 (2016).
3. (Invited) Yoke Khin Yap, "Transistors without Semiconductors by Functionalized Boron Nitride Nanotubes," Symposium H01 Low Dimensional Nanoscale Electronic and Photonic Devices 8 in the 228th Electrochemical Society (ECS) Meeting (October 11-15, 2015) Phoenix, AZ.
4. (Invited) Yoke Khin Yap, "Transistors without Semiconductors by Functionalized Boron Nitride Nanotubes," Symposium G Multifunctional Inorganic One-dimensional Nanostructures: Status and Potential. 5th Int. Conf. of Smart and Multifunctional Materials, Structures, and Systems, June 5-9, 2016, Perugia, Italy.
5. (Invited) Yoke Khin Yap, "Transistors without Semiconductors by Functionalized Boron Nitride Nanotubes," Symposium NM3: Nanotubes and Related Nanostructures. 2016 Materials Research Society Fall Meeting, Nov 27-Dec 2, 2016, Boston, MA.

One-dimensional carrier confinement in semiconductor excitonic nanoshells.

Mikhail Zamkov,

The Center for Photochemical Sciences, Department of Physics Bowling Green State University, Bowling Green, Ohio 43403. zamkovm@bgsu.edu

Program Scope

The emerging generation of quantum dot optoelectronic devices offers an appealing advantage of a tunable semiconductor band gap enabled by a small particle size. Reducing a nanocrystal diameter, however, increases the density of inter-particle boundaries in a film, ultimately causing an inefficient charge flow in quantum dot assemblies.[1,2] To address this issue, we aim to develop an inverse energy-gradient nanoparticle architecture, which promotes the surface localization of excitons. In this "nanoshell" geometry, the quantum-confined properties are realized despite nanoparticle dimensions exceeding the exciton Bohr radius. The assembly of such nanostructures features fewer grain boundaries, leading to enhanced conductance of solution-processed films. The proposed employment of semiconductor nanoshells exhibiting a 1D carrier confinement offers a viable strategy for developing ordered, electrically-coupled nanoparticle assemblies. This methodology could be extended to a wide range of applications, including photocathodes, field-effect transistors, and photodetectors.

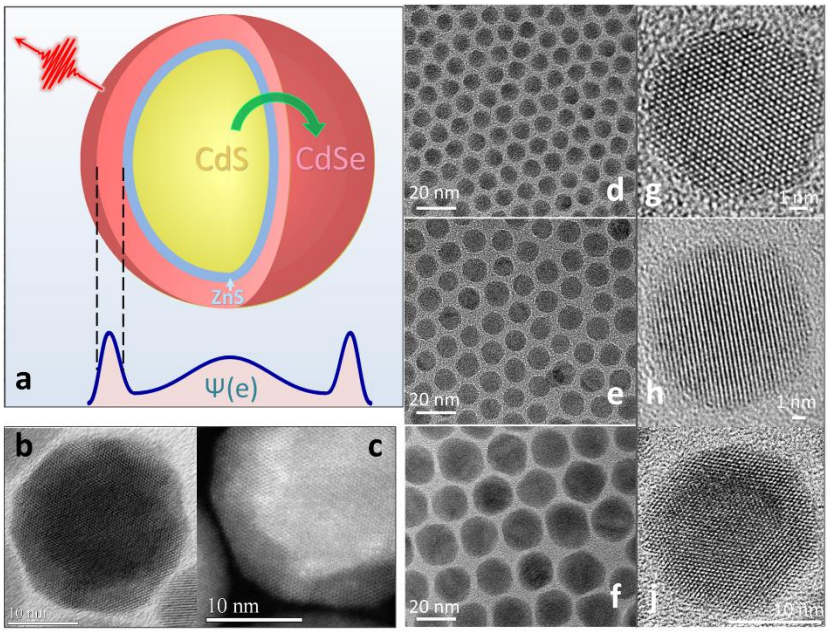

Figure 1. (a). Schematic of a CdS/CdSe nanoshell (NS). An intermediate ZnS layer decouples CdS and CdSe domains promoting the shell-localization of photoinduced charges. (b). TEM image of a typical CdS/CdSe NS. (c). The corresponding HAADF-STEM image of a CdS/CdSe NS. (d, g). 8.6-nm CdS core NCs (e, h). 11.6–nm nanostructures resulting from the addition of successive ZnS and CdS layers onto 8.6-nm CdS core NCs. (f, j). CdS/CdSe NS featuring ~ 4 nm of CdSe (total diameter ≈ 19.6 nm). The core/shell morphology can be seen in the high-resolution TEM image.

Recent Progress

We report on the synthesis of inverse energy-gradient CdS/CdSe nanostructures supporting the formation of two-dimensional excitons in the shell domain. The developed nanocrystal geometry places a wide-gap semiconductor (CdS) at the core of the composite nanoparticle in order to funnel the photoinduced energy into the low-gap CdSe shell layer (Fig. 1a). As a result, the quantum confinement is achieved in nanoparticles of up to 30

nanometer in size for which all spatial dimensions exceed the exciton Bohr radius (Figs. 1b and 1c). The formation of excitons in the CdSe shell was manifested through the size-tunable emission (Fig. 2b) and enhanced radiative lifetimes. Transient absorption measurements were employed to further elucidate the dynamics of the photoinduced energy relaxation in CdS/CdSe nanoshells. It was shown that the excitation of a bulk-like CdS core domain resulted in ~3-ps energy transfer to the CdSe shell with minimal carrier losses (Fig. 3b).

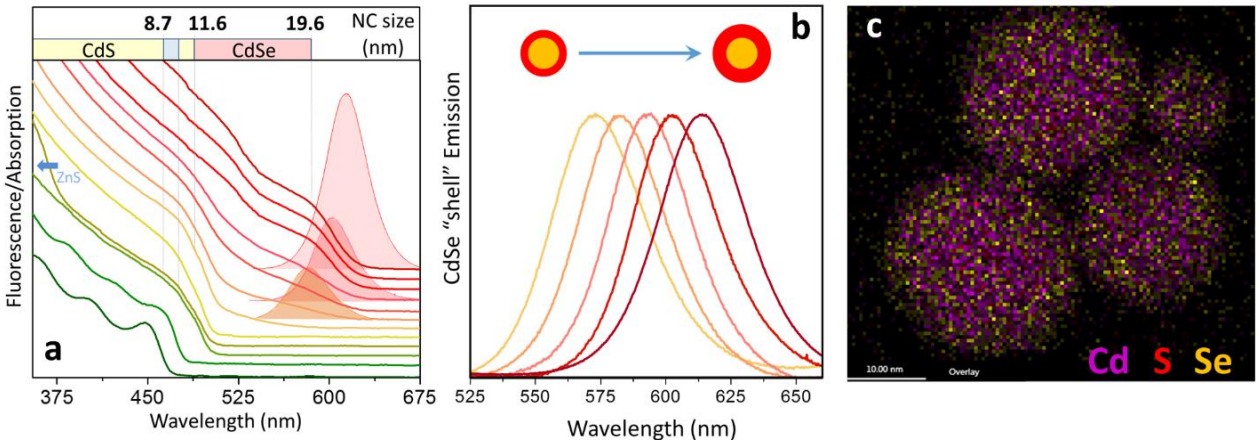

Figure 2. (a). Evolution of the absorption and emission spectra associated with the successive stages of the nanoshell growth. The corresponding nanoparticle diameter is indicated at the top of the figure. (b). Evolution of the steady state emission spectra corresponding to the growing size of the CdSe shell. The "bulk" core diameter is ≈ 11 nm. (c). Atomic element mapping using a STEM energy dispersive x-ray detector.

The spatial confinement of photoinduced charges in the shell of a composite nanoparticle can lead to several interesting properties that reflect the unique dimensionality of nanoshell architecture. For instance, the shell-localization of excitons gives rise to a ten-fold increase in room-temperature radiative lifetimes (τ_{Rad}), compared to spherical quantum dots. Provided that a proper surface passivation is devised, the developed nanoshell geometry could therefore enable long-lived excitons in CdSe NCs with lifetimes in excess of 600 ns. Together with a surface confinement of photoinduced charges, such long-lived excitations should promote enhanced surface reactivity, which is useful for applications in photocatalysis, light sensitization, and biological/chemical sensing.

Another appealing aspect of the demonstrated architecture is an intrinsically greater conductivity of disordered nanoshell solids compared to analogous films of spherical QDs (Fig. 3a), which was tentatively attributed to a relatively lower interfacial area associated with nanoshell assemblies. In order to obtain a relative estimate of the nanoshell solid conductivity, we have compared the photocurrents of spherical CdSe NC films with the similarly processed assembly of CdS/CdSe nanoshells (Fig. 3a). Both solids were developed on FTO substrates and capped with small-area 30-nm Au electrodes. The thickness of each film was chosen to yield a target optical extinction value that was determined by integrating the product of the excitation light spectral density and the photon absorption probability for each film, $n_{WL}(\lambda)\times(1\text{-}10^{-A(\lambda)})$. The original bulky ligands on nanoparticle surfaces were displaced using dimethylformamide (DMF) ligand stripping strategy[3] followed by mild annealing at 120 ºC. A thin layer of CdS was grown on both

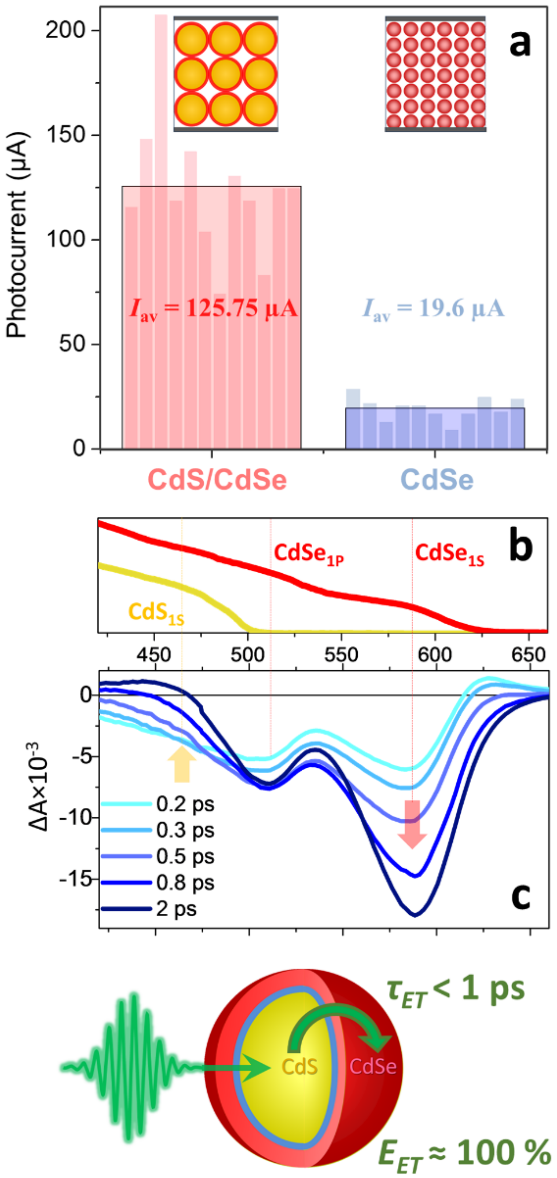

Figure 3. (a). Photocurrent measurements in similarly processed solids of CdS/CdSe nanoshell (red) and spherical CdSe NCs (blue). (b). Absorption profiles of CdS core NCs and CdS/CdSe nanoshells showing the three lowest-energy absorbing transitions. (c). TA spectra indicating a rapid transfer of the excitation energy from the core (CdS) to the shell (CdSe) domain of heterostructured nanocrystals, which depletes the CdS excited state population in 3 ps.

nanoparticle types prior to film deposition in an effort to suppress charge trapping on surfaces and promote inter-shell fusion during annealing. The size of spherical CdSe NCs in a reference sample was approximately 3.9 nm while the total diameter of nanoshells was 19.6 ± 1.0 nm (CdSe shell thickness ~ 4 nm). According to Fig. 3a, the photocurrent of nanoshell solids (averaged over 12 pixels) surpassed that of similarly processed CdSe NC films by a factor of 7. Such a considerable improvement in the photocurrent value provides additional evidence that solids featuring large-size nanoparticles exhibit better charge transport.

We expect that the developed nanoshell architecture could potentially be extended to a broader range of semiconductors (e.g. CdS/PbS, ZnS/CdS) facilitating the development of quantum confined solids offering improved charge transport characteristics.

Future Plans

The future expansion of the program will be continued along two main fronts: (*i*) – the synthesis of nanoshells utilizing CdS/PbS and PbS/CdS/CdSe (dual-emitting) semiconductor combinations and, (*ii*) – exploring the conductivity of CdS/CdSe and CdS/PbS nanoshells in thin film devices.

The proposed investigation of CdS/PbS nanoshells is aimed to improve the light-harvesting characteristics of quantum dot photovoltaics. Our preliminary data indicates that the employment of large grain, quantum-confined CdS/PbS nanoshells in thin film electronics will lead to enhanced diffusion-mobility products. The proof-of-concept experiments on the synthesis of CdS/PbS nanoshells and the investigation of their optoelectronic properties have already been performed. A seven-fold increase in photoconductivity of nanoshells compared to spherical nanoparticles was likewise observed in our recent experiments utilizing CdS/CdSe nanocrystal films (see Fig. 3a). We have also succeeded in the synthesis of dual-emitting PbS/CdS/CdSe dot-shell nanocrystals. These nanostructures

support the formation of excitons both in the core and the shell domains resulting in the two emission bands at 620 nm (CdSe) and ~ 900 nm (PbS), respectively. The dual emission from a single nanoparticle offers attractive opportunities for sensing applications and will be explored towards controlling the ratio of visible to IR emission intensities as well as understanding the environmental factors affecting the core/shell emission balance.

References

1. Carey, G. H.; Abdelhady, A. L.; Ning, Z.; Thon, S. M.; Bakr, O. M.; Sargent, E. H. Colloidal Quantum Dot Solar Cells. *Chem. Rev.* **2015**, *115*, 12732–12763.
2. Kagan, C.R.; Lifshitz, E.; Sargent, E. H.; Talapin, D. V. Building devices from colloidal quantum dots. *Science* **2016**, *353*, 6302.
3. Baumgardner, W. J.; Whitham, K.; Hanrath, T. Confined-but-Connected Quantum Solids via Controlled Ligand Displacement. *Nano Lett.* **2013**, *13*, 3225–3231.

Publications

Razgoniaeva, N.; Moroz, P.; Yang M.; Budkina D. S.; Eckard H.; Augspurger, M.; Khon, D.; Tarnovsky, A. N.; Zamkov, M. One-dimensional carrier confinement in “giant” CdS/CdSe excitonic nanoshells. **2017**. *Under Review* (Submitted on Feb. 27th)

Elucidation of Hydrogen Interaction Mechanisms with Metal Doped Carbon Nanostructures

Ragaiy Zidan (PI), Joseph A. Teprovich Jr., Patrick A. Ward, Aaron L. Washington
Savannah River National Laboratory, Aiken, SC 29808
E-mail: Ragaiy.Zidan@srnl.doe.gov
In Collaboration with:
Puru Jena
Department of Physics, Virginia Commonwealth University, Richmond, VA 23284

Program Scope

This program continues to support the Office of Basic Energy Sciences (BES) mission through the development of a basic understanding of the interaction mechanisms of hydrogen and hydrides with carbon nanostructures, resulting in the formation of unique nanomaterials with novel characteristics. The fundamental understanding and knowledge of these novel characteristics will allow us to predict and ultimately control material properties at the electronic, atomic, and molecular level, which can have profound impacts on new energy technologies and support other relevant aspects of the DOE missions. Through fundamental studies and characterization of metal hydrides over the past 60+ years it was discovered that these materials can be utilized in other energy storage and conversion systems. This led to the development of new and novel technologies such as nickel metal hydride batteries, hydrogen sorption coolers for satellites, switchable mirrors, and thermal energy storage systems. Our research on M_x-C_{nano}-H_y systems has mirrored the evolution of traditional metal hydrides in energy storage and conversion because we have demonstrated that our materials are also multi-modal. This has led to the discovery of new phenomenon in the M_x-C_{nano}-H_y systems such as fast ion conduction in the solid state and tunable photophysical properties. Through a synergistic experimental and theoretical methodology we are investigating these new and exciting avenues parallel with the ability to chemisorb and physisorb hydrogen in these materials.

Recent Progress

Previous theoretical work by the Jena group has explored the possibility of using halide free electrolytes for next generation electrolytes in lithium ion batteries with a focus on boron-based super-halogens as anion building blocks for electrolytes. Super-halogens mimic the chemistry of halogen atoms, but have electron affinities that far exceed those of a halogen. It has been determined that boron-based super-halogens (BH_4^-, $B_3H_8^-$, $CB_{11}H_{12}^{-2}$ and $B_{12}H_{12}^{-2}$) have Li^+ and H_2O binding energies lower than commonly used halogenated electrolytes, thus suggesting this class of materials is worthy of further study for this application. The lack of fluorine in these super-halogens is advantageous because hydrofluoric acid will not form in the presence of moisture or at elevated temperatures as is the case for the widely utilized $LiPF_6$ based liquid electrolytes. This important fact provides an extra safety factor during the lifetime of the battery. Additionally, the $M_2B_{12}H_{12}$ materials will not rapidly decompose releasing heat and hydrogen upon water exposure because they form stable crystalline hydrates with water. This is also another valuable added safety advantage for this material.

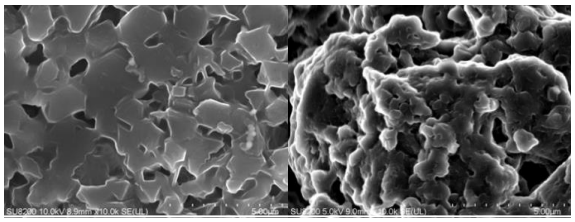

Fig. 1. SEM images of the "as synthesized" $Li_2B_{12}H_{12}$ (left) and the milled $Li_2B_{12}H_{12}$ (right).

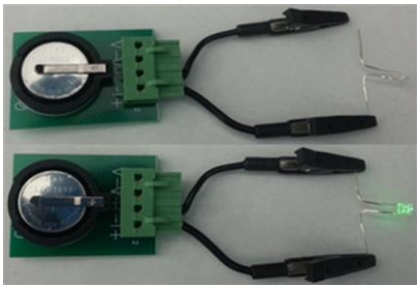

Fig. 2. (top) All solid state full cell ($Li/Li_2B_{12}H_{12}/LiCoO_2$) disconnected from the LED. (bottom) Same cell connected to the LED

Building on previous work in similar systems, we found that a defect rich structure can be imparted mechanochemically to $Li_2B_{12}H_{12}$ (Figure 1). This material in the solid state has an extremely high ionic conductivity of 0.31 mS/cm at room temperature with low activation energy for ionic conduction, 0.34 eV. Cyclic voltammetry and constant voltage cycling of the material demonstrated that the material is stable up to 6.0V (vs. Li/Li^+) and compatible with a metallic lithium electrode. Half and full cells showed good cycle stability even at room temperature utilizing $Li_2B_{12}H_{12}$ as a solid-state electrolyte. A coin cell capable of lighting an LED was also fabricated and tested at room temperature (Figure 2).

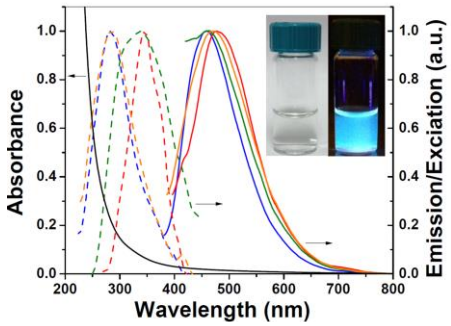

Fig. 3. UV-vis (solid black), excitation (dash), and emission (solid) spectra for $Li_2B_{12}H_{12}$ in: red- anhydrous solid state, blue- water, green- NMP, and orange- ethylene glycol. Inset shows a solution of $Li_2B_{12}H_{12}$ in visible and UV light.

To further characterize this material, the photophysical properties of $Li_2B_{12}H_{12}$ were also investigated. The UV-vis and photoluminescent excitation and emission spectra were measured in water, ethylene glycol, N-Methyl-2-pyrrolidone (NMP), and in the anhydrous solid state (Figure 3). Theses solvents were chosen due to the limited solubility of $Li_2B_{12}H_{12}$ in other common organic solvents. The UV-vis spectrum in all cases is relatively featureless with strong absorption in the UV below 300 nm. In all of the solvents examined, $Li_2B_{12}H_{12}$ has an emission maximum between 460 and 470 nm and shows bright blue emission upon UV excitation.

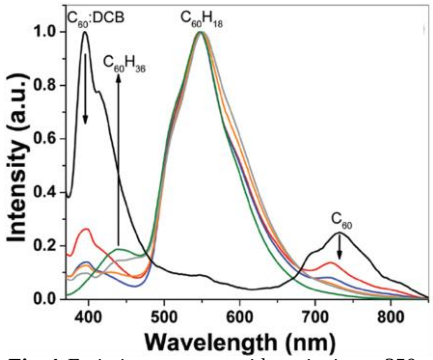

Fig. 4 Emission spectrum with excitation at 350 nm. Black: C_{60}, red: 6-$C_{60}H_x$, blue: 12-$C_{60}H_x$, orange: 24-$C_{60}H_x$, grey: 48-$C_{60}H_x$, and green: 72-$C_{60}H_x$ in o dichlorobenzene (DCB). C_{60}:DCB is the formation of an adduct between the solvent and C_{60}.

During our evaluation of $M_xC_{60}H_y$ systems for hydrogen storage, we observed that the material would change color as the amount of chemisorbed hydrogen was increased. This observation suggested that it might be possible to change and controllably manipulate the optical properties of C_{60} through the addition of hydrogen. Pure C_{60} in organic solvent has an emission maximum at ~740 nm with a very low quantum yield value of ~0.01 %. A series of hydrogenated C_{60} ($C_{60}H_x$) samples were prepared by varying the hydrogenation time from 6 to 72 hours to examine the effect its photophysical properties.

The geometries of $C_{60}H_x$ for a general x were calculated by starting with the Schlegel diagram which projects a three dimensional structure onto a two-dimensional plane. The candidate structures of $C_{60}H_x$ in the Schlegel diagram were suggested according to chemical considerations and semi empirical calculations. Using these structures as initial candidates, we

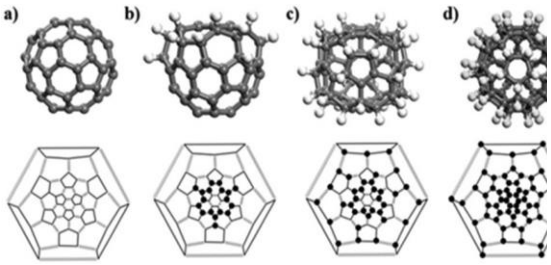

Fig. 5 Geometric calculated structures of (a) C_{60}, (b) $C_{60}H_{18}$, (c) $C_{60}H_{36}$, and (d) $C_{60}H_{60}$ in ball and stick model (upper panel) and Schlegel diagram (lower panel).

fully optimized $C_{60}H_x$ geometries without any symmetry constraints in order to yield the structures shown in Fig. 5. The results are plotted in Fig. 6. Notwithstanding small fluctuations, the HOMO–LUMO gaps of $C_{60}H_x$ generally increase as more hydrogen atoms are introduced. The continued increase of HOMO–LUMO gaps under hydrogenation is due to the change from sp^2 to sp^3 hybridization of C atoms as H atoms are successively attached. Thus, we show that introducing hydrogen defects (via C–H bond) can modulate the HOMO–LUMO gap of C_{60} over a large range and photophysical properties can be effectively tuned by hydrogenation process, in agreement with our experimental observation. Note that the HOMO–LUMO gap is calculated from the energy levels of isolated $C_{60}H_x$ molecules in their ground state. We didn't consider the geometric change and exciton binding effect in the excited state. Therefore it only provides a trend of the electronic transition responsible for the fluorescence observed in the system, and is consistent with the observed blue shift in the emission maximum as the hydrogen content increases.

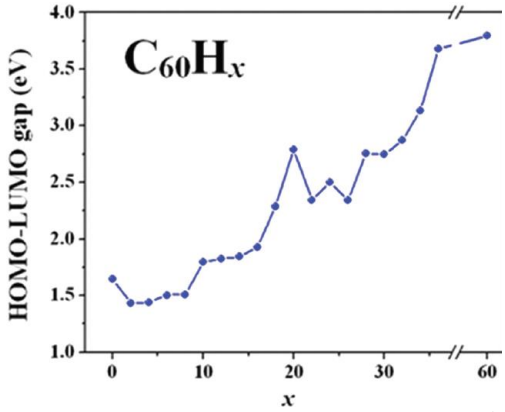

Fig. 6 Calculated HOMO–LUMO gaps responsible for the fluorescence of $C_{60}H_x$ species as a function of x calculated at the PBE level of theory.

One of the impediments in using light metal borohydrides as hydrogen storage materials is the presence of intermediate phases during decomposition which adversely affects their reversibility. Recent experiments indicate that the decomposition of $NaBH_4$ yields $Na_2B_{12}H_{12}$ as the intermediate phase, while decomposition of $Mg(BH_4)_2$ and $Y(BH_4)_3$ yields $Mg(B_3H_8)_2$ and $Y(B_3H_8)_3$, respectively. To understand why the intermediate phases are different for Na, Mg, and Y borohydrides, we carried out systematic calculations based on density functional theory to investigate the relative stability of $M[BH_4]_n$, $M[B_3H_8]_n$, and $M_2[B_{12}H_{12}]_n$ (M = Na, Mg, and Y; *n* is the valence of metal atom). The origin of these intermediate phases was shown to be due to the large electron affinity of BH_4, B_3H_8, and $B_{12}H_{12}$ and their relative binding energies to the metal cations.

Theoretical studies based on cluster motifs also revealed that the energy required to remove a hydrogen atom from a bimetallic borohydride such as $KAl(BH_4)_4$ is less than that from the corresponding monometallic borohydride, namely $Al(BH_4)_3$, thus making bimetallic borohydrides potential candidates for hydrogen-storage materials.

A synergistic study using both theory and experiment showed that the decomposition pathway of $Ca(BH_4)_2$ can be efficiently controlled by reaction temperature. That is, it decomposes into CaB_6 at a lower temperature range of 320 to 350 8C, but into amorphous boron at 400 to 450°C. We identified the formation of CaB_2H_6 as the crucial intermediate step on the way to CaB_6 that only forms at 320 to 350°C.

A topical review was also published that highlighted the multifunctional properties of metal borohydrides with applications in hydrogen storage, solid state electrolytes, as well as hybrid perovskite based solar cells.

Future Plans

- Evaluate hydrogen physisorption on fullerene derived nanocomposites with boron and nitrogen dopants
- Examine the mechanism of electrochemical intercalation/deintercalation of mono-, di-, and trivalent cations in a series of hydrogenated fullerenes
- Investigate ionic transport (Li^+, Na^+, and K^+) and dynamic anion reorientation (BH_4^-, $B_{12}H_{12}^{2-}$) in a series of boron based hydrides
- Continue to utilize a joint theoretical and experimental approach to the ration design and synthesis of new complex metal hydride systems

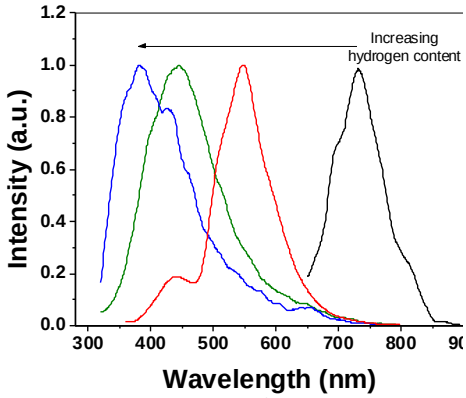

Fig. 7. Emission spectra of black: pure C_{60}, red: $C_{60}H_x$, green: $Li_6C_{60}H_x$, and blue: $Na_6C_{60}H_x$ in 1,2-dichlorobenzene.

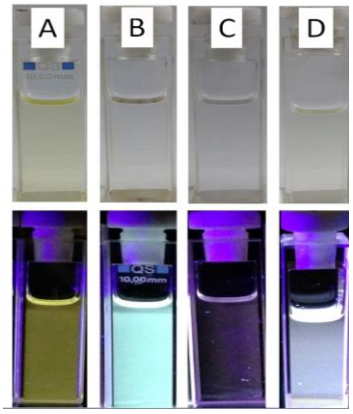

Fig. 8. Color photos of (A) $C_{60}H_x$, (B) $Li_6C_{60}H_x$, (C) $Na_6C_{60}H_x$, and (D) mixture of fulleranes that shows near white light emission. Top- room light, bottom- 365nm excitation.

Our interest in nano-carbon based dyes has been driven by their potential to be cheaper, sustainable, and non-toxic alternatives to traditional inorganic quantum dots (QD). In carbon based dyes such as carbon quantum dots (CQD), the use of surface chemistry and functional groups has been shown to be effective in changing the emissive state of a particular material. It has been proposed that the functional groups on the CQD surface could possibly serve dual roles in the overall emission from the system. The addition of hydrogen to CQD has been shown to shift the fluorescence maximum and increase the quantum yield. To understand the role of hydrogen in this and similar systems we utilized C_{60}, which can be controllably hydrogenated, as model system to understand the effect of hydrogen addition on fluorescence. In our previous work, we were only able to achieve up to $C_{60}H_{36}$ with un-doped C_{60}. To determine if the blue shift of the emission continues with successive hydrogen addition beyond $C_{60}H_{36}$, we examined the metal intercalated C_{60} materials. Previously, we were able to achieve ~40 hydrogen atoms per C_{60} with the Li intercalated sample and up to 60 hydrogen atoms per C_{60} with Na intercalation. The initial results for the Li and Na intercalated samples dissolved in 1,2-dichlorbenzene and the emission spectrum was measured (Figure 7). These samples were consistent with our previous theoretical work which showed that the emission maximum continues to shift to the blue with the successive addition of hydrogen to C_{60}. Owing to the fact that we can achieve emission over the entire visible spectrum by tuning the hydrogen content of C_{60}, we prepared a blended mixture of $C_{60}H_x$, $Li_6C_{60}H_x$, and $Na_6C_{60}H_x$ to prepare a white light emitting solution (Figure 8). We were also able to infuse polymethyl methacrylate (PMMA) with the same white light emitting mixture and were also able to demonstrate white light emission in the solid state. We are currently building on this work to understand how hydrogen defects can be utilized to manipulate and enhance the photophysical properties of this and similar carbon based systems.

Publications

1. Teprovich Jr., J, Colon-Mercado, H., Ward, P., Peters, B., Giri, S., Zhou, J., Greenway, S., Compton, R., Jena, P., and Zidan, R.: "Experimental and Theoretical Analysis of Fast Lithium Ionic Conduction in a $LiBH_4$-C_{60} Nanocomposite", *J. Phys. Chem. C*, **2014**, ***118***, 21755-21761.
2. Zu, G., Lu, K., Sun, Q., Kawazoe, Y., and Jena, P.: "Lithium-doped Triazine-based C_3N_4 Sheet for Hydrogen Storage at Ambient Temperature", *J. Comp. Mat. Science*, **2014**, *81*, 275-279.
3. Liu, Y., Giri, S., Zhou, J., and Jena, P.: "Intermediate phases during decomposition of metal borohydrides, $M(BH_4)_n$ (M=Na, Mg, Y)", J. Phys. Chem. C, **2014**, *118*, 28456-28461.
4. Liu, Y., Zhou, J., and Jena, P.: "Electronic Structure and Stability of Mono- and Bi-metallic Borohydrides and Their Underlying Hydrogen-Storage Properties – A Cluster Study", *J. Phys. Chem. C*, **2015**, *119*, 11056-11061.
5. Ward, P. A., Teprovich Jr., J. A., Compton, R. N., Schwartz, V., Veith, G. M., Zidan, R. "Evaluation of the physi- and chemisorption of hydrogen in alkali (Na, Li) doped fullerenes" *Int. J. Hydrogen Energy*, **2015**, *40*, 2710-2716.
6. Zhu, G., Sun, Q., Kawazoe, Y., and Jena, P.: "Porphyrin-based porous sheet: Optoelectronic properties and hydrogen storage", *Int. J. Hydrogen Energy*, **2015,** *40*, 3689-3696.
7. Yan, Y., Remhof, A., Rentsch, D., Giri, S., Jena, P., and Züttel, A.: "A Novel Strategy for Reversible Hydrogen Storage in $Ca(BH_4)_2$", *Chem. Commun.*, **2015**, *51*, 11008-11011.
8. Teprovich, Jr., J.A., Colon-Mercado, H., Washington, II, A.L., Ward, P.A., Greenway, S., Missimer, D.M., Hartman,H., Velten, J., Christian, J.H., Zidan, R. "Bi-functional $Li_2B_{12}H_{12}$ for energy storage and conversion applications: solid-state electrolyte and luminescent down-conversion dye" *J. Mater. Chem. A*, **2015**, *3*, 22853-33859.
9. Mohtadi, R., Remhof, A., and Jena, P.: "Complex Metal Borohydrides: Multifunctional Materials for Energy Storage and Conversion", *J. Phys. Cond. Mat.* **2016**, *28*, 353001 (invited topical review)
10. Teprovich Jr., J. A., Washington II, A. L., Dixon, J., Ward, P. A., Christian, J. H., Peters, B., Zhou, J., Giri, S., Sharp, D. N., Velten, J. A., Compton, R. N.; Jena, P., Zidan, R., "Investigation of hydrogen induced fluorescence in C_{60} and its potential use in luminescence down shifting applications" *Nanoscale* **2016**, *8*, 18760-18770.
11. Christian, J.H., Teprovich Jr., J.A., Wilson, J., Nicholson, J.C., Truong, T., Kesterson, M.R., Wiedenhöver, I., Baby, L.T., Anastasiou, M., Rijal, N., Washington II, A.L. "Developing Radiation Tolerant Polymer Nanocomposites Using C_{60} as an Additive" *RSC Adv.*, **2016**, *6*, 40785-40792.
12. Teprovich Jr., J.A., Weeks, J.A., Ward, P.A., Washington II., A.L., Zidan, R. "Fine tuning the fluorescent properties of C_{60} with hydrogen" *Int. J. Hydrogen Energy* (submitted, under review).

Patents Issued/Filed

Issued:

1. Ragaiy Zidan, Matthew S. Wellons "High capacity hydrogen storage nanocomposite materials, US 8945500, issued February 3, 2015
2. Ragaiy Zidan, Rana F. Mohtadi, Christopher Fewox, Premkumar Sivasubramanian "High capacity stabilized complex hydrides for hydrogen storage", US8883109, issued November 11, 2014
3. Aaron L. Washington, II, Joseph A. Teprovich, Ragaiy Zidan "Enhanced Superconductivity of Fullerenes" Notice of Allowance issued on 2/17/17; Publication number: 20160240765

Filed:

1. Ragaiy Zidan, Joseph A. Teprovich, Jr., Hector R Colon-Mercado, Scott D. Greenway, "Solid state electrolyte composites based on complex hydrides and metal doped fullerenes/fulleranes for batteries and electrochemical applications", Publication number: 20140356732, filed: June 4, 2014
2. Ragaiy Zidan, Joseph A. Teprovich, Aaron L. Washington, II "Novel carbon quantum dots and a method of making the same" Publication number: 2015141415, Filed: April 28, 2016

Author Index

Author Index

Participant List

Participant List

Name	Organization	E-mail Address
Ager, Joel	Lawrence Berkeley National Laboratory	jwager@lbl.gov
Alberi, Kirstin	National Renewable Energy Laboratory	Kirstin.Alberi@nrel.gov
Argyriou, Dimitri	AMES Laboratory	argyriou@ameslab.gov
Atwater, Harry	California Institute of Technology	haa@caltech.edu
Barnett, Scott	Northwestern University	s-barnett@northwestern.edu
Beratan, David	Duke University	david.beratan@duke.edu
Bergman, Leah	University of Idaho	Lbergman@uidaho.edu
Boehme, Christoph	University of Utah	boehme@physics.utah.edu
Boriskina, Svetlana	Massachusetts Institute of Technology	sborisk@mit.edu
Brener, Igal	Sandia National Laboratories	ibrener@sandia.gov
Cen, Cheng	West Virginia University	chcen@mail.wvu.edu
Chen, Gang	Massachusetts Institute of Technology	gchen2@mit.edu
Chen, Youping	University of Florida	ypchen2@ufl.edu
Chiang, Yet-Ming	Massachusetts Institute of Technology	ychiang@mit.edu
Chrzan, Daryl	Lawrence Berkeley National Laboratory	dcchrzan@berkeley.edu
Cohn, Joshua	University of Miami	cohn@physics.miami.edu
Crommie, Mike	Lawrence Berkeley National Laboratory	crommie@berkeley.edu
Cronin, Stephen	University of Southern California	scronin@usc.edu
Dahlberg, E Dan	University of Minnesota	dand@umn.edu
Dai, Hongjie	Stanford University	hdai1@stanford.edu
Dery, Hanan	University of Rochester	hanan.dery@rochester.edu
Eastman, Jeffrey	Argonne National Laboratory	jeastman@anl.gov
Egami, Takeshi	University of Tennessee	egami@utk.edu
Fan, Shanhui	Stanford University	shanhui@stanford.edu
Flagg, Edward	West Virginia University	edward.flagg@mail.wvu.edu
Fong, Dillon	Argonne National Laboratory	fong@anl.gov
Gartstein, Yuri	University of Texas, Dallas	yuri.gartstein@utdallas.edu
Giebink, Noel	Pennsylvania State University	ncg2@psu.edu
Gofryk, Krzysztof	Idaho National Laboratory	krzysztof.gofryk@inl.gov
Horwitz, James	U.S. Department of Energy	james.horwitz@science.doe.gov
Jarrahi, Mona	University of California, Los Angeles	mjarrahi@ucla.edu
Jena, Purusottam	Virginia Commonwealth University	pjena@vcu.edu

Kahn, Antoine	Princeton University	kahn@princeton.edu
Karimi, Farhad	University of Wisconsin, Madison	karimi2@wisc.edu
Karma, Alain	Northeastern University	a.karma@neu.edu
Knezevic, Irena	University of Wisconsin, Madison	irena.knezevic@wisc.edu
Koschny, Thomas	AMES Laboratory/Iowa State University	koschny@ameslab.gov
Kuno, Masaru	University of Notre Dame	mkuno@nd.edu
Li, Qiang	Brookhaven National Laboratory	qiangli@bnl.gov
Lin, Weiwei	Johns Hopkins University	wlin@jhu.edu
Lin, Shawn-Yu	Rensselaer Polytechnic Institute	sylin@rpi.edu
Liu, Feng	University of Utah	fliu@eng.utah.edu
Ma, Evan	Johns Hopkins University	ema@jhu.edu
Maroudas, Dimitrios	University of Massachusetts, Amherst	maroudas@ecs.umass.edu
Mascarenhas, Angelo	National Renewable Energy Laboratory	ajmascar@gmail.com
Maurya, Deepam	Virginia Tech	mauryad@vt.edu
McCluskey, Matthew	Washington State University	mattmcc@wsu.edu
Mishin, Yuri	George Mason University	ymishin@gmu.edu
Molina Lopez, Francisco	Stanford University	fmolina@stanford.edu
Neumeier, John	Montana State University	neumeier@montana.edu
Orbach, Raymond	University of Texas, Austin	orbach@austin.utexas.edu
Padilla, Willie	Duke University	willie.padilla@duke.edu
Pecharsky, Vitalij	AMES Laboratory	vitkp@ameslab.gov
Phan, Manh-Huong	University of South Florida	phanm@usf.edu
Rand, Barry	Princeton University	brand@princeton.edu
Ren, Shenqiang	Temple University	shenqiang.ren@temple.edu
Ren, Zhifeng	University of Houston	zren@uh.edu
Shi, Jing	University of California, Riverside	jing.shi@ucr.edu
Shi, Li	University of Texas, Austin	lishi@mail.utexas.edu
Shinar, Joseph	AMES Laboratory/Iowa State University	jshinar@iastate.edu
Sih, Vanessa	University of Michigan	vsih@umich.edu
Smalyukh, Ivan	University of Colorado, Boulder	ivan.smalyukh@colorado.edu
Soukoulis, Costas	AMES Laboratory	soukoulis@ameslab.gov
Stadler, Shane	Louisiana State University	stadler@phys.lsu.edu
Stern, Nathaniel	Northwestern University	n-stern@northwestern.edu
Stockman, Mark	Georgia State University	mstockman@gsu.edu
Suzuki, Yuri	Stanford University	ysuzuki1@stanford.edu
Tamboli, Adele	National Renewable Energy Laboratory	adele.tamboli@nrel.gov

Tang, Ming	Rice University	mt20@rice.edu
Tumas, William	National Renewable Energy Laboratory	bill.tumas@nrel.gov
Tureci, Hakan	Princeton University	tureci@princeton.edu
Vardeny, Zeev	University of Utah	val@physics.utah.edu
Virkar, Anil	University of Utah	anil.virkar@utah.edu
Wang, Zhong Lin	Georgia Institute of Technology	zhong.wang@mse.gatech.edu
Waldeck, David	University of Pittsburgh	dave@pitt.edu
Wickramaratne, Darshana	University of California, Santa Barbara	darshanaw@engineering.ucsb.edu
Willets, Katherine	Temple University	kwillets@temple.edu
Wu, Junqiao	Lawrence Berkeley National Laboratory	wuj@berkeley.edu
Wu, Yiying	Ohio State University	wu@chemistry.ohio-state.edu
Xi, Xiaoxing	Temple University	xiaoxing@temple.edu
Yang, Peidong	University of California, Berkeley	p_yang@berkeley.edu
Yap, Yoke Khin	Michigan Technological University	ykyap@mtu.edu
Zamkov, Mikhail	Bowling Green State University	zamkovm@bgsu.edu